

THIS WEEK

EDITORIALS

BIG DIG Skeleton in Leicester car park is identified as King Richard III **p.6**

WORLD VIEW Genetic privacy is impossible and self-defeating **p.7**



SHIFTY Tree-dwelling pigeons and doves evolved differently **p.9**

Unknown territory

Japan is making an overdue effort to regulate experimental stem-cell treatments. A clearly defined legal framework is needed to protect patients.

Millions of tourists flock to Japan each year to enjoy its rich cultural and historical heritage. But some visitors are shunning the usual tourist trail in favour of another attraction — experimental stem-cell treatments. In late December, the Japanese newspaper *The Mainichi* reported that a clinic in the Hakata district of Fukuoka in southwest Japan, which has links to the Seoul-based biotechnology firm RNL Bio, has been treating some 500 South Koreans a month with stem cells. Another report late last month in the *Asahi Shimbun* newspaper claimed to have found more than 20 clinics that advertise unproven stem-cell treatments in the country.

Some of the countries in which stem-cell tourism has taken off have immature regulatory systems, including China, Costa Rica and Ukraine. But why Japan?

For starters, Japan's regulations on stem-cell therapies are not just immature — they simply do not exist. Combine that with the nation's reputation for cleanliness and reliability, and Japan becomes the perfect place to give a veneer of legitimacy to an unproven therapy. The country is a "paradise for premature therapies" according to one article in the *Mainichi Shimbun* newspaper. Japan's health ministry has been slow to respond, but is now beginning to move on the issue.

Last week, a ministry subcommittee posted online some of its initial ideas for a new law to oversee the clinical use of stem cells. A final draft will be prepared this month for presentation to Japan's parliament in its upcoming session. Details remain fuzzy, but the document includes significant proposals, such as a requirement that stem-cell therapies be approved through clinical trials, that they take place only in registered and approved facilities and that providers set up ways to compensate their patients if things go wrong.

The introduction of such clearly defined rules and regulations, in contrast to Japan's usual preference for soft guidelines, is a positive and welcome step. Such guidance will be particularly helpful to local government officials, such as those in Fukuoka, who are reportedly stumped as to what to do about the stem-cell tourism there.

The problem is that the regulations with teeth will probably apply to only one of three classes of stem-cell treatment: that deemed the most risky, including procedures based on embryonic stem cells or induced pluripotent stem cells, the risks of which are unknown.

The other two categories are not yet well defined by the guidelines, but are likely to include therapies that are generally accepted and considered safe, as well as those that carry some degree of predictable risk. According to a government representative, a clinic that used these other classes would need only to get the approval of a local institutional review board and then notify the government that it is opening for stem-cell business. There would be no active monitoring by the government. The type of stem-cell treatment offered by RNL Bio — in which stem cells are extracted from a person's fat tissue and then expanded in the laboratory — would fall into one of these more loosely regulated categories, it seems. What, then, would prevent RNL Bio or other companies from

exploiting Japan's laxity, possibly to the detriment of patients?

Self-monitoring by clinics has already been exposed as problematic in the business of stem-cell therapy. The United States has a formidable regulatory system, but it is far from a shining example of how to oversee this emerging field. The state of Texas recently put into place

"Self-monitoring by clinics is problematic in the business of stem-cell therapy."

regulations that opened up the industry to any company that could pass inspection by local review boards, only to find that the review board that approved the state's highest profile stem-cell company had failed in its duties. The US Food and Drug Administration eventually got around to cracking down.

Regulators everywhere have a difficult job. Desperate patients, looking for any opportunity to try a therapy that could help them, feel deprived of their rights. And some companies complain — with some justification — that overly burdensome regulations are killing the development of promising therapies. Japan should learn from the situation in the United States and elsewhere. It must take care to look at potential loopholes in its laws that could allow unproven therapies on the market and put patients in danger. ■

In a hole

It is in Britain's best interests to keep looking for a site for a deep nuclear-waste repository.

The best way to dispose of nuclear waste is to bury it deep underground. With the right mixture of geology and engineering, researchers think, it should be possible to contain highly radioactive material safely for the many thousands of years that it will take to decay.

Scientists agree on this. The industry thinks the same way, and so do regulators, politicians and most environmental groups. Yet despite the expert endorsement, plans for a deep geological repository in Britain effectively ground to a halt last week, after a local council voted against plans to look for a suitable site. Some scientists view the rejection as a failure of local politics, but they are wrong.

The vote over whether to take early plans for a deep geological repository to the next stage came at a meeting of Cumbria County Council on 30 January. The work would have involved test drilling and surveys to try to find a suitable location for the 1,000 cubic metres of high-level waste and several thousand tonnes of spent fuel currently held in the United Kingdom.

Cumbria has always been the preferred site. At the opposite end of

the country from London, the county is already home to the Sellafield nuclear site that once produced plutonium for the nation's nuclear weapons. Sellafield still houses most of the country's nuclear waste, and so to build a repository nearby would be sensible, as long as the conditions are suitable.

The government has looked at Sellafield once before. In the 1980s, an independent group was set up to try to locate a geologically suitable waste dump in Britain. The body eventually settled on Sellafield, and set out to build a £200-million (US\$315-million) 'rock characterization facility' at the site. In 1997, the proposal was abandoned after local planners rejected it — in part, because of fears that the facility might become a de facto waste dump.

This time, the government vowed to do things differently. The old executive was abolished and in its place new plans were laid out that promised transparency, democratic inclusivity and scientific scrutiny. The plans mirror those of nations such as Finland and Sweden, which are successfully building waste repositories.

So why has the process come up empty again? The answer is a lack of political will at almost every level of government. Critics say that the Nuclear Decommissioning Authority, the body responsible for the repository, never did much to try to sell the facility to local residents or to address their concerns about what it might do to property prices or tourism. At a national level, politicians offered only the vaguest promise of 'economic development' in exchange for taking the waste. Meanwhile, local politicians advocated an alternative plan: to build more short-term storage at Sellafield, thereby creating jobs in the near-term without making long-term commitments.

The United Kingdom is not alone in its nuclear torpor. In the United States, efforts to build a repository are in the doldrums following a decision to withdraw from a proposed site at Yucca Mountain in Nevada. A panel has recommended a site-selection exercise similar to the one carried out in the United Kingdom, but there is little reason

to believe that it could do any better. The very act of looking at places other than Yucca Mountain will require a change to legislation — unlikely given the nation's current political paralysis.

In the meantime, the bills from neglecting the waste are piling up. The US Nuclear Regulatory Commission faces a costly lawsuit from states and utility companies seeking to have their nuclear waste taken away, as required by federal law. In the United Kingdom, the endless

"There are moral, financial and environmental reasons to make deep geological disposal work."

clean-up of Sellafield drags on; it has cost more than £67.5 billion so far, according to a report released this week by a parliamentary committee. At the Fukushima Daiichi nuclear plant in Japan, spent fuel stored above ground at reactors is likely to have been a major source of contamination following the earthquake and tsunami in 2011. At the last count, the clean-up there is expected to

cost trillions of yen, or hundreds of billions of dollars.

The bleak situation might encourage some on both sides of the Atlantic to search for a quick fix. Already, there is talk in the United Kingdom of officials trying to bypass Cumbria County Council by going directly to the local communities of Allerdale and Copeland, which supported the survey work. In the United States, some in industry would like to see the plans for a repository at Yucca Mountain revised, despite Nevada's promise to fight it tooth and nail. Advocates of these solutions may feel that they are in the right, but they are guilty of political myopia: although it might be possible to nudge the projects forward briefly, they would quickly become bogged down again in a mire of legal and civil challenges.

It seems likely that both nations must start again. Scientists can help by reminding politicians that there are moral, financial and environmental reasons to make deep geological disposal work. Given the enormous costs of inaction, it is in everyone's interest to keep trying. ■

Body of evidence

The identification of a long-dead king is not simply an academic event.

Headline writers and bloggers dusted off their copies of *The Complete Works of William Shakespeare* this week to gleefully report the identification of the skeleton of King Richard III, found beneath a car park in the English midlands. The fascination with Richard, the last king of the Plantagenet line and the last English monarch to fall in battle, goes beyond the known facts of the historical record; Richard is known as much as the misshapen villain of Shakespeare's play as the man who ruled until his violent death in 1485.

The king's mortal remains were identified by a mixture of science and history. The skeleton was male and about the right age, and radiocarbon dating suggests that he died around the end of the fifteenth century. Death was due to a forceful blow to the back of the head with a sharp blade, consistent with a sword or a fearsome medieval weapon called a halberd. He ate a high-protein diet containing plenty of seafood, so was clearly of high status. The spine was twisted, a sign of adolescent scoliosis, providing some basis for Shakespeare's deformed monster. The corpse was mutilated after death. It was found in the right place. And analysis of mitochondrial DNA from the bones matched samples taken from two descendants of Richard's family — the Canadian-born furniture maker Michael Ibsen and a second royal relative who chose to remain anonymous.

If that person chose to conceal their identity to avoid a media fuss, then they certainly made the right decision. The unveiling of the findings by researchers at the University of Leicester, UK, who found and

investigated the remains, at a press conference on Monday morning, led news bulletins and was immediately scrutinized and argued about online. Prominent historians scoffed at the media scrum and dismissed the academic significance of the find. Others accused them of jealousy and snobbery — would a similar discovery announced with equal fanfare by the University of Cambridge or Oxford face such hostility, they questioned?

Even some of those who praised the work could not resist bestowing a patronizing pat on the head, and pointed out that little old Leicester was enjoying its day in the Sun. (They may or may not have heard of DNA fingerprinting, which was developed by Alec Jeffreys in the same department of genetics that investigated the car-park skeleton.)

Certainly, the way the discovery was announced, the introduction of DNA evidence without the backing of a peer-reviewed paper, and the fact that there was a television documentary primed and ready to go will leave a sour taste in the mouth of some purists. The University of Leicester has managed to unite the two cultures of science and humanities in a way that few have before. "Science by press release" cried some scientists. "History by press conference" complained some historians.

They should get out more. The discovery of a 500-year-old slain King of England is an event that goes beyond the boundaries and the conventional audience of academia. The DNA evidence may be impossible for outsiders to verify until a paper is published, but molecular sleuthing alone will never be able to confirm the identity of the bones with total assurance anyway. And, given the strength of the other evidence, it does not need to. "There are lots of us out here

who've been intrigued by and researching this for years and years," one historian responded to an online critic. "This is really exciting for me — it's kind of the 15th century's Higgs Boson [sic] moment." Let them enjoy it. ■

➔ **NATURE.COM**
To comment online,
click on Editorials at:
go.nature.com/xhunjv



Genetic privacy needs a more nuanced approach

Because confidentiality of health data cannot be guaranteed, people should consider both the risks and advantages of sharing them, argues Misha Angrist.

The US National Institutes of Health has warned that research is at a “crucial juncture”. Bioethicists are fretting. Scientists are anxious. And all because an article in *Science* last month raised doubts about the privacy of volunteers who hand over their genetic data (M. Gymrek *et al. Science* 339, 321–324; 2013). “Oh my God, we really did this,” said Yaniv Erlich of the Massachusetts Institute of Technology in Cambridge to *The New York Times*, after his group managed to cross-reference information from public databases to put names to samples of DNA donated to research. One can imagine law enforcement salivating at the prospect of turning a bloodstain into a name and address.

Yet what the scientists did is not shocking or all that new. The DNA re-identification bogeyman has lurked at the door for years. The warning signs were there in 2005 when a precocious 15-year-old boy called Ryan Kramer found his sperm-donor father. Just as Erlich and his colleagues would do years later, Kramer used a combination of Y-chromosome data — his own in this case — and genealogical searching of public records to track down a donor dad who had almost certainly been promised anonymity by the sperm bank.

No responsible scientist can guarantee absolute privacy. Researchers know this and many volunteers accept it, yet official discussion of the issue remains firmly rooted in the twentieth century. Like whales and rainforests, research participants are viewed only as helpless things that must be protected. I suspect that much of the present hand-wringing has less to do with the welfare of these people and more to do with protecting researchers and their institutions from legal action.

Because information about individuals’ health can be used to discriminate against them, the privacy provisions of the US Health Insurance Portability and Accountability Act of 1996 (HIPAA) were revised in 2003 to create a category of protected health information that can be used or disclosed only under certain conditions.

Although genetic data are considered protected health information under the HIPAA, many of the protections disappear when the information is ‘de-identified’ — that is, the 18 identifiers specified in the act (including names, addresses, birthdates and the like) are removed. And because genetic information is not one of those 18 identifiers, it does not need to be removed from health records to follow the letter of HIPAA privacy. If researchers do not know who you are, and cannot easily find out, then their obligations to you diminish by orders of magnitude. Furthermore, their protocols are less likely to need full review by an institutional review board; their grant applications become less onerous; and their technology costs go down.

One can see, then, how the Kramers of the world pose a problem not just to sperm donors, but also to biomedical research. What if the absence of the 18 identifiers isn’t enough to

protect someone’s identity?

A few weeks ago, the US Department of Health and Human Services had the perfect opportunity to address this issue when it released its 563-page reboot of the HIPAA. But although it addressed genetic information explicitly, the de-identification criteria were summarily brushed off in a single sentence on page 416: “The Privacy Rule’s de-identification standard is outside the scope of this rulemaking.”

The risks of re-identification from genomic data sources were partly responsible for the launch of the Personal Genome Project (about which I have written a book and on whose unpaid board of directors I serve). The project’s approach has been to eschew any promises of privacy and confidentiality. To date, it has more than 2,000 participants, all of whom have agreed to make public, and potentially identifiable, any genomic, medical, environmental and trait data collected about

them during the study. I am one of them.

Such open consent is not for everyone. Many of the risks — from identity theft to being framed for crimes — are clear. So why would anyone enrol?

Fairness, for one: I can, if I want, access my sequence and other ‘omic’ data at any time, day or night. So, too, can a poorly funded geneticist in a tiny lab in Slovenia or Kenya. My data are not privy only to the select few running the study.

Second, research will work better if scientists have more information about the people they study. If an investigator wants to study the genome of someone with an anxiety disorder, ear pits and male pattern baldness, he or she is free to look me up. If someone is interested in induced pluripotent stem cells from a human male,

mine are available from the Coriell Institute for Medical Research in Camden, New Jersey. If we agree that part of the mission of biomedical science is to understand the relationship between genotype and phenotype, it is surely helpful to have access to a cohort’s unredacted phenotypes before its members die (at which point they are no longer considered ‘human subjects’ in the eyes of the government).

Third, some genomic information is going to be medically useful. A few months ago, Bloomberg News reporter and Personal Genome Project participant John Lauer learned that he was predisposed to a rare blood disorder, signs of which he can keep watch for. Finally, as Erlich and Kramer have shown, de-identification is increasingly difficult. Privacy and confidentiality are important principles. But being identifiable has some benefits, and being anonymous has some costs; science will be better off when it acknowledges this reality. ■

Misha Angrist is an assistant professor at the Duke University Institute for Genome Sciences and Policy in North Carolina and author of *Here is a Human Being: At the Dawn of Personal Genomics*.
e-mail: misha.angrist@duke.edu

IT IS SURELY
HELPFUL
TO HAVE ACCESS TO
A COHORT’S
UNREDACTED
PHENOTYPES BEFORE
ITS MEMBERS DIE.

➔ **NATURE.COM**
Discuss this article
online at:
go.nature.com/uvx1dx

RESEARCH HIGHLIGHTS

Selections from the
scientific literature

ECOLOGY

Mosquitoes battle for territory

Competition from an invasive species has resulted in declining numbers of a resident US mosquito during the past few decades, but the resident looks to be evolving resistance to the invader's tactics.

The Asian tiger mosquito (*Aedes albopictus*) arrived in and spread throughout the southeastern United States in the 1980s. It outcompetes the resident yellow-fever mosquito (*Aedes aegypti*) through satyrization — the invasive males mate with resident females but prevent the females from producing offspring. Irka Bargielowski and her colleagues at the University of Florida in Vero Beach exposed *A. aegypti* females to *A. albopictus* males in cages and looked for evidence of insemination. Females from regions where the two species have lived together for the past 20 years were less likely to be inseminated than were those from areas that have not been invaded.

The results show a potential for the recovery of yellow-fever mosquito populations, the authors say. *Proc. Natl Acad. Sci. USA* <http://dx.doi.org/10.1073/pnas.1219599110> (2013)

MICROBIOLOGY

The bacterial alchemist

A species of bacterium forms tiny nuggets of gold to combat the toxic effects of the dissolved form of the element.

The bacterium *Delftia acidovorans* lives in extensive communities — known as biofilms — that coat



MICROBIOLOGY

Microbes in malnutrition

More than a million children around the world die from malnutrition each year, but the condition does not result from diet alone — the make-up of microbes in the gut also has a role.

A team led by Jeffrey Gordon at Washington University in St. Louis, Missouri, studied 317 pairs of twins in Malawi. Of these, the authors identified pairs in which one twin had developed a form of severe acute malnutrition called kwashiorkor (pictured). The microbial profiles of these malnourished twins differed from those of their healthy siblings. When both children received therapeutic diets, the malnourished twins' microbiota began to resemble that of their healthy siblings, but it reverted when the children returned to traditional Malawian foods.

The findings could explain the apparent benefit of using antibiotics to treat kwashiorkor, a regime investigated by Mark Manary, also at Washington University in St. Louis, and his group. They conducted a trial with 2,767 Malawian children — including those in Gordon and co-workers' study — in which all children received therapeutic diets and some were treated with antibiotics. Of those given the antibiotic cefdinir, 4.1% died, compared with 7.4% of the children who received a placebo. *Science* 339, 548–554 (2013); *New Engl. J. Med.* 368, 425–435 (2013)

gold nuggets. A team led by Nathan Magarvey at McMaster University in Hamilton, Ontario, exposed the microbe to a gold solution and discovered that gold particles formed outside the bacterial membrane. Genomic and biochemical analysis revealed that the microbe secretes a peptide, called delftibactin, that binds to gold ions to form gold particles. Strains in which the genes involved in producing delftibactin were inactivated showed decreased growth in the presence of soluble gold, suggesting that the peptide detoxifies gold ions.

Nature Chem. Biol. <http://dx.doi.org/10.1038/nchembio.1179> (2013)

For a longer story on this research, see go.nature.com/dtahlh

ATMOSPHERIC SCIENCE

Jet-stream shifts linked to ozone

Antarctic ozone depletion, rather than rising greenhouse gas levels, is the prime culprit for the shifting jet stream in the Southern Hemisphere, a study using observational data has found — supporting previous modelling results.

The westerly jet stream has been shifting southward for the past few decades, affecting weather and climate. Sukyoung Lee and Steven Feldstein at Pennsylvania State University in University Park analysed data on four different wind patterns that fluctuate on short timescales. They found that ozone loss contributes about 50% more than greenhouse gases towards the jet-stream changes.

Alterations in the westerly jet stream during the summer have been linked to variations in rain patterns and storm locations.

Science 339, 563–567 (2013)

STEPHEN MORRISON/EPA/CORBIS



ECOLOGY

Cats are enemy number one

Free-ranging domestic cats in the United States kill many more birds and mammals than previously thought, making them possibly the top anthropogenic killer of US wildlife.

Scott Loss at the Smithsonian Conservation Biology Institute, Washington DC, and his colleagues conducted a systematic review of studies on cat population sizes and predation behaviour. They analysed the data to estimate mortality caused by US domestic cats — including those living on farms, pet cats that spend at least some of their time outdoors, stray cats fed by humans and feral felines. The researchers estimate that these cats kill 1.4 billion to 3.7 billion birds and 6.9 billion to 20.7 billion mammals annually, possibly exceeding other human-related causes of death such as habitat destruction or collisions with vehicles or buildings.

These numbers suggest that cats could be endangering some species in certain regions, the authors say. *Nature Commun.* 4, 1396 (2013)

PHYSICS

A tabletop neutron source

Researchers interested in using neutrons to probe materials currently need

access to particle accelerators or fission reactors, but a tabletop neutron-imaging device may be on the way. Markus Roth at the Technical University of Darmstadt, Germany, and his colleagues used a 200-terawatt laser at the Los Alamos National Laboratory in New Mexico to generate a high-energy neutron beam that can be directed at neutron-absorbing objects.

The team produced the beam by sending laser pulses into a deuterium-rich plastic target, knocking deuterons (which consist of a proton and a neutron) into a beryllium rod that then shot neutrons forwards. The researchers' technique used less than one-quarter of the laser energy and generated an order of magnitude more neutrons in a forward directed beam than previous methods.

The group hopes that its approach could be used to create a portable neutron source for use in university laboratories.

Phys. Rev. Lett. 110, 044802 (2013)

EVOLUTION

Bird behaviour spurs evolution

Shifts in environmental conditions are thought to drive evolutionary change, but biologists have debated whether the way that animals interact with their environment also plays a part. A study of pigeons and doves suggests that changes in behaviour can drive alterations in the birds' shapes.

Oriol Lapiedra of the Centre for Ecological Research and Forestry Applications in Barcelona, Spain, and his colleagues used evolutionary models to pinpoint links between changes

COMMUNITY CHOICE

The most viewed papers in science

MOLECULAR BIOLOGY

Protein production on the clock

HIGHLY READ
on www.plosbiology.org in January

The molecular clock not only controls the rhythmic expression of genes with physiological roles, but also regulates the creation of ribosomes — molecular machines that translate messenger RNA

into protein.

Frédéric Gachon at the University of Lausanne in Switzerland and his colleagues found that mRNAs that encode components of the translation machinery — including some involved in making ribosomes — are rhythmically expressed in the livers of mice. Production of these RNAs peaks in the nocturnal animals shortly before nightfall, when the energy needed for protein synthesis is most likely to be available.

PLoS Biol. 11, e1001455 (2013)

in behaviour and physical characteristics in 156 species of dove and pigeon (one, *Caloenas nicobarica*, pictured). The authors found that when some birds changed from terrestrial to tree-based foraging behaviour, this accelerated the evolution of shorter hindlimb bones and longer tails — traits that are useful in an arboreal lifestyle.

However, the demands of foraging in trees seems to limit further diversification, potentially representing an “evolutionary dead-end”, the authors say.

Proc. R. Soc. B <http://dx.doi.org/10.1098/rspb.2012.2893> (2013)

REPRODUCTIVE BIOLOGY

Puberty controlled by DNA changes

Sexual maturation in female mammals is controlled by specific changes to the chemical groups attached to DNA — a type of ‘epigenetic’ change — which results in

the coordinated action of multiple genes.

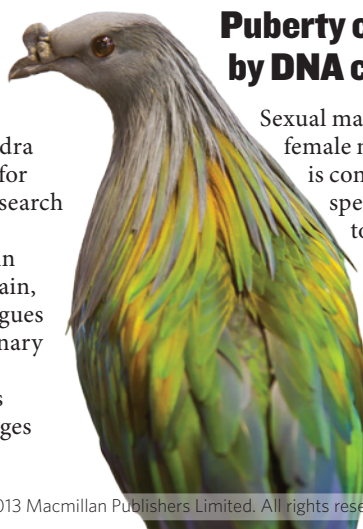
Puberty begins with a rise in the secretion of gonadotropin-releasing hormone (GnRH) by a region of the brain called the hypothalamus, but the mechanism that coordinates the genes involved has been unclear. Alejandro Lomniczi and Sergio Ojeda at Oregon Health & Science University in Portland and their colleagues report that decreasing levels of a gene-silencing molecule called EED may control the process in rats. EED regulates the expression of a gene called *Kiss1*, which encodes a protein that helps to stimulate GnRH production. The addition of methyl groups to the regulatory region of the EED gene lowers EED expression just before the onset of puberty, resulting in a rise in *Kiss1* activity and more frequent pulses of GnRH from the hypothalamus.

Nature Neurosci. <http://dx.doi.org/10.1038/nn.3319> (2013)

NATURE.COM

For the latest research published by Nature visit:

www.nature.com/latestresearch



SEVEN DAYS

The news in brief

POLICY

US immigration bill

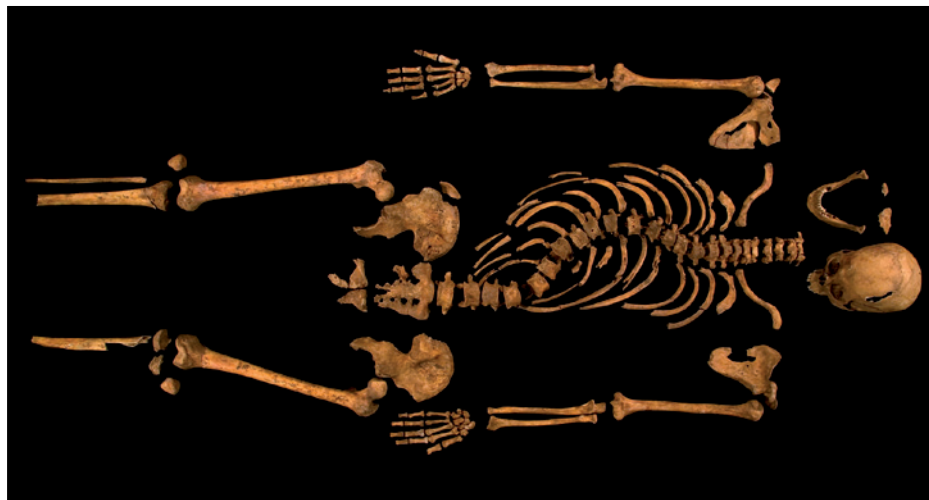
In a bid to attract and retain more skilled workers, US lawmakers introduced legislation on 29 January that is intended to ease current immigration limits. Under the proposed law, several groups would be exempted from the annual cap of 140,000 employment-based visas — including foreigners who earn advanced degrees in science, technology, engineering and mathematics in the United States, as well as outstanding professors and researchers. The Senate measure follows close on the heels of immigration-reform plans announced by lawmakers and President Barack Obama. See go.nature.com/zafspz for more.

Insecticide ban

The European Commission has proposed a two-year suspension of the use of insecticides that have been linked to declines in honeybees. If the proposal is accepted by European Union member states, three neonicotinoids — imidacloprid, thiamethoxam and clothianidin — would be banned from use on oilseed rape, sunflower, maize (corn) and cotton. Member states are likely to vote on the idea on 25 February. The move follows a report from the European Food Safety Authority in Parma, Italy, that highlighted concerns over neonicotinoid use. See go.nature.com/v3zdne for more.

UK nuclear waste

Plans for a deep repository to hold nuclear waste are on hold in Britain, following a vote on 30 January by Cumbria County Council to block further investigations at the only candidate site.



King Richard III unearthed

Archaeologists at the University of Leicester, UK, announced on 4 February that a skeleton uncovered last September is that of Richard III, a fifteenth-century king of England. The most telling sign was the skeleton's curved spine (pictured), a deformity immortalized in

Shakespeare's unflattering portrayal of the king. But the team cited other pieces of evidence, including the location of the burial; the fact that the body had apparently suffered numerous wounds; carbon dating; and mitochondrial DNA. See go.nature.com/cbysgv and page 6 for more.

The detailed geological investigations would have been precursors to building the £12-billion (US\$19-billion) underground facility. "I do not feel that we have the support of most of the people of Cumbria," Eddie Martin, the Conservative leader of the council, told BBC News. "We needed much more certainty and assurance about the science and the safety." See page 5 for more.

Polio killings

Two polio-vaccination workers were killed by a roadside bomb on 31 January in northwestern Pakistan, and a policeman guarding immunization teams was killed two days earlier in another part of the country. The violence follows a series of deadly attacks on health workers during a December

campaign to help eradicate polio (see *Nature* 493, 8; 2013), which had to be partly suspended. It is not clear whether the latest roadside bombing was intended to target health workers.

HPV vaccination

An international cooperation of public and private entities will fund the immunization of 180,000 girls in eight developing countries against human papillomavirus (HPV), the cause of most cervical cancers. The GAVI Alliance, based in Geneva, Switzerland, announced on 4 February that it would roll out the programme in Laos and seven African countries — Ghana, Kenya, Malawi, Niger, Sierra Leone, Tanzania and Madagascar. It plans to expand the initiative to more than 20 countries and

1 million girls by 2015. See go.nature.com/zplabr for more.

BUSINESS

Antisense success

The US Food and Drug Administration has approved an anti-cholesterol drug based on antisense technology, which uses synthetic DNA to inhibit messenger RNA and 'silence' target genes. The drug, Kynamro (mipomersen), which prevents production of a protein involved in carrying cholesterol, was approved on 29 January and will be used only to treat patients with a severe form of familial hypercholesterolaemia, a rare condition that causes very high levels of blood cholesterol. Kynamro was developed by Isis Pharmaceuticals of Carlsbad,

UNIV. LEICESTER

T. J. KIRKPATRICK/CORBIS

California. It will be the only antisense drug on the market at present. See go.nature.com/aicoww for more.

Pfizer split

On 1 February, pharmaceutical giant Pfizer spun out its animal-health business Zoetis in an initial public offering valued at US\$2.24 billion. Zoetis, headquartered in Madison, New Jersey, earned \$4.2 billion in fiscal year 2011. The spin-off is part of Pfizer's plan to pare down its business: in November, the New York-based company sold off its nutrition business to the Swiss food firm Nestlé for \$11.85 billion. Pfizer will continue to own about 80% of Zoetis stock.

FACILITIES

US collider fate

The only remaining particle collider in the United States has been flagged for possible closure. The Nuclear Science Advisory committee voted on 29 January to designate the Relativistic Heavy Ion Collider (RHIC) at Brookhaven National Laboratory in Upton, New York, as the most likely of three facilities to be closed if nuclear-science budgets remain flat. The RHIC produces multi-million-degree plasmas of quarks and gluons that are now also being studied at Europe's Large

Hadron Collider at CERN, near Geneva. See go.nature.com/oliczf for more.

PEOPLE

Bulgaria scandal

Bulgaria's science and education minister, Sergei Ignatov, was fired on 28 January after a government inquiry confirmed that he had been responsible for mismanagement of research money. Stefan Vodenicharov, the current president of the Bulgarian Academy of Sciences, has been nominated to replace him. Last November, scientists accused the Bulgarian Science Fund, which is overseen by the science ministry, of funnelling competitive grants towards poor-quality projects proposed by researchers with close ties to the fund (see *Nature* **491**, 649; 2012). The fund's two top officials, Rangel Gjurov and Hristo Petrov, both resigned from their leadership positions last week. See go.nature.com/ftdgvw for more.

Chu to step down

Steven Chu (**pictured**) announced on 1 February that he will soon step down as head of the US Department of Energy (DOE), a move that had been widely anticipated. In a letter to DOE employees, Chu highlighted a string of accomplishments, including



starting the Advanced Research Projects Agency-Energy, founding five Energy Innovation Hubs for applied research and overseeing a doubling in the country's production of solar and wind energy. See go.nature.com/dafanx for more.

RESEARCH

Satellite success

South Korea put a satellite into orbit on 30 January — the country's first successful attempt from its own soil. The launch, from the Naro Space Center, at the southern end of the peninsula, came seven weeks after rival North Korea launched its first satellite into orbit. South Korea's rocket was built in partnership with Russia, and had failed on attempts in 2009 and 2010. The country plans to develop its own rocket by 2018. See go.nature.com/frn39p for more.

COMING UP

10 FEBRUARY

The Large Hadron Collider shuts down for almost two years of upgrades. See page 16 for more.

11 FEBRUARY

NASA launches its eighth Landsat satellite to take images of Earth. See page 13 for more.

No NIH racial bias

A study has challenged the idea that grant-making at the US National Institutes of Health (NIH) is biased against black researchers, a major concern for the agency since a 2011 report made that claim (D. K. Ginther *et al.* *Science* **333**, 1015–1019; 2011). The latest analysis, published on 31 January (J. Yang *et al.* *J. Informetrics* **7**, 318–324; 2013), found that black faculty members actually performed similarly, if not better than, their white counterparts with similar productivity levels in both total NIH funding and in number of NIH-funded projects. See go.nature.com/klekyb for more.

TB vaccine blow

A leading candidate for a sorely needed new vaccine against tuberculosis (TB) has failed to protect children against the disease in a major clinical trial. The results of the MVA85A vaccine trial in South Africa, published in *The Lancet*, show that it seems to have “no significant efficacy” against tuberculosis. The results are a major blow to the TB research community; MVA85A could have served as a booster to the ‘BCG’ vaccine, which is used worldwide against the disease but has patchy efficacy. See go.nature.com/9ppuob for more.

➔ **NATURE.COM**

For daily news updates see:
www.nature.com/news

SOURCE: POINT CARBON

TREND WATCH

Prices for allowances to emit a tonne of carbon dioxide on Europe's carbon-trading market are still in free fall. The cause is a slump in industrial activity which means that the region's emissions are now far below the cap set by politicians, leaving the market awash in unneeded allowances. Thomson Reuters Point Carbon, a consultancy firm in Oslo, estimates an oversupply of about 2 billion tonnes of carbon allowances up to 2020 (equivalent to one year's emissions from all the polluters in the scheme).

EUROPE'S CARBON PRICE PLUNGES

Carbon prices in the European Union's emissions-trading scheme have fallen sharply since the start of 2013.



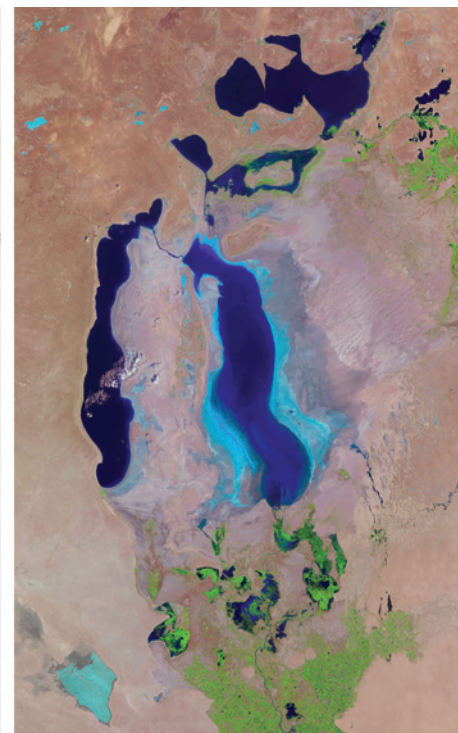
NEWS IN FOCUS

SOUTH KOREA Hydrogen fluoride spills cast doubt on industrial safety **p.15**

PHYSICS CERN collider will gather strength during two-year rest **p.16**

DRUG DISCOVERY European consortium aims to refill the pipeline **p.20**

ECOSYSTEMS Why global warming may doom tropical species **p.22**



Images from the Landsat satellite series show the Aral Sea in central Asia shrinking significantly from 1977 to 2010 because of water diversion.

EARTH SCIENCE

Landsat 8 to the rescue

NASA prepares to launch satellite that will continue historic record of global change.

BY JEFF TOLLEFSON

When Landsat 5 fell silent on 6 January, scientists across the globe mourned its passing but gave thanks for its fortitude. The satellite had lasted a record-breaking 28 years, snapping images of the changing planet from melting glaciers to burning rainforests, while its successors faltered. Landsat 6 failed during launch and Landsat 7, at 13 years old, is partially blind and has limited fuel. With the passing of Landsat 5, the future of the world's longest-running — and perhaps most influential — set of data on global change rests with Landsat 8, which is scheduled to launch next week from Vandenberg Air Force Base in California.

“Landsat 8 is the most important NASA

Earth-observing mission in over a decade,” says Greg Asner, an ecologist at the Carnegie Institution for Science in Stanford, California, who uses Landsat data to track tropical-forest trends. After making do for years with ageing and impaired orbiters, “we are getting our eyes back in the sky”, says Asner. “Those eyes are going to be extremely good.”

From the first launch in 1972, Landsat was designed to provide a global record of land-cover and land-use change. The earliest satellites captured images at several visible-light and near-infrared frequencies, all with a resolution of 80 metres. Landsats 4 and 5 reached 30-metre resolution and could see farther into the infrared, to aid studies of soil moisture and vegetation. Landsat 7 added a multi-spectral sensor that can achieve 15-metre resolution.

Through careful calibration, the programme has built up a continuous 40-year record of observations at the original frequencies, spanning a period of huge change for the planet.

The latest mission, commissioned in 2002, had a tortuous birth. NASA originally intended to buy data from a privately owned satellite, then formulated a plan to mount Landsat sensors on a separate set of polar-orbiting satellites. Only in 2005 did the administration of then-president George W. Bush call for an independent craft, formally known as the Landsat Data Continuity Mission.

The size of a large jeep, the US\$855-million spacecraft will circle Earth at an altitude of about 700 kilometres, carrying sensors of even higher precision than its predecessors. Instead of scanning the terrain below it with a ▶

► mirror and sending the signal to a few sensors, it will capture instantaneous views of a 185-kilometre swathe of Earth, using some 7,000 sensors for each bandwidth. The result is more data from each location and better image quality. “The data are much more sensitive to change across the landscape and over time,” says Jim Irons, project scientist for the mission at NASA’s Goddard Space Flight Center in Greenbelt, Maryland. “Maybe we will be able to better differentiate corn from sorghum, for example, or maple trees from oak trees.”

The spacecraft will also be the first in the Landsat series to collect data in an ‘ultra-blue’ band, particularly useful for studying oceans and atmospheric aerosols. Another new data stream will be a shortwave infrared band that is sensitive to cirrus clouds, which are powerful players in Earth’s climate.

Landsat has endured major changes in ideology and organization during its lifetime, notably in the 1980s and 1990s, when Congress gave control of the satellites and all data to a private company. Images sold for several thousand dollars each, limiting analysis to an elite corps of scientists. The government regained control in 2001, however, and from 2008 the US Geological Survey, which oversees the data, opened up the archive as a free global resource. Access exploded. Whereas the agency once sold around 15,000 images a year, annual downloads now average about 3 million.

“It provided for data democracy,” says Mike Wulder, a research scientist at the Canadian Forest Service in Victoria and a member of the Landsat science advisory team. “Landsat really is a global resource.”

The data helped to spark a digital revolution among remote-sensing specialists, who have developed tools to exploit massive computing resources and stitch together high-resolution records of global change over time and space. Other space-borne imagers, such as the Moderate Resolution Imaging Spectroradiometer (MODIS) on NASA’s Terra and Aqua satellites, can take snapshots of larger areas at a single pass, but with much lower resolutions.

With Landsat, “we can get the detail and the enormous geographic coverage,” says Asner. “This alone puts Landsat at the very forefront in land-cover and land-use change monitoring.”

Landsat 8 is scheduled to begin operations 90 days after entering orbit, although the first images could arrive within three or four weeks. The satellite might not live as long as its predecessor, which NASA engineers have put forward as a candidate to Guinness World Records, but Irons believes that Landsat 8 will make its own mark. “I do not think it hyperbole to suggest that all seven billion of us will benefit from the Landsat continuity mission.” ■

NUCLEAR ENERGY

Quake fears rise at Japan’s reactors

Commissioners say that geological faults make some reactors too dangerous to restart.

BY DAVID CYRANOSKI

Plans to restart some of Japan’s 50 nuclear reactors, which have been idle since the Fukushima Daiichi disaster in March 2011, have hit an obstacle — and his name is Kunihiro Shimazaki. Buoyed by a new cabinet keen on nuclear power, the nuclear industry wants to get the plants back online to meet the country’s energy demands. But before it can do so, Shimazaki and a group of 16 other geophysicists working for the country’s Nuclear Regulation Authority (NRA) must confirm the industry’s claims that the plants do not face a serious earthquake threat.

To judge by his initial reports, Shimazaki won’t accept the claims lightly. On 28 January, Shimazaki, an NRA commissioner who warned in 2004 that Fukushima’s coast was more vulnerable to tsunamis than regulators had claimed, angered proponents of nuclear energy by reporting his group’s conclusion that there is probably an active fault under the Tsuruga nuclear plant, which was due to restart. If, as expected, the NRA endorses that finding, the plant won’t be allowed to operate.

But the team’s evaluations have been questioned, and not just by the nuclear industry. Seismologists dispute whether the faults that Shimazaki’s researchers are finding meet the NRA’s definition of ‘active’, meaning that they have generated an earthquake in the past 120,000 years or so. In some cases, say the critics, the fractures are not dangerous and some may not even be faults at all.

“They are being overly cautious just to avoid criticism,” says Koji Okumura, a palaeoseismologist at Hiroshima University who was on an expert subcommittee of the cabinet’s Nuclear Safety Commission until it was replaced by the NRA in September 2012. “They think they’re like Superman coming in to save us from the bad guys.”

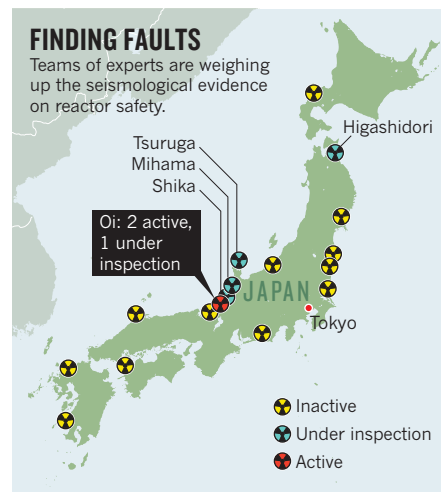
Shimazaki’s team is evaluating five plants, comprising 12 reactors in total, plus the shuttered Monju experimental fast breeder reactor (see ‘Finding faults’). Four of the five plants are due to restart; at the fifth, two of the four reactors

are already running. What the team is finding is often at odds with the industry’s assessment.

The Tsuruga plant’s reactors, for example, are 250 metres from a known fault. Excavations by the plant’s owner, the Japan Atomic Power Company, showed that the ground had shifted across the fault, suggesting that the fault had been active. But the company’s experts had concluded that the movement had happened before the 120,000-year threshold.

When Shimazaki’s experts examined the company’s trench, they found signs of more recent movement, and evidence that an extension of the fault runs directly beneath one of the reactors. “If you look at the displacement and slant, it looks like it’s a continuation” of a fracture running under the reactor, he says.

Problems also turned up in a survey by the Kansai Electric Power Company (KEPCO) of its Oi plant, which houses Japan’s only two running reactors. The plant is bisected by a fault, which KEPCO says is inactive. But Shimazaki says that crucial data from the original trench dug by KEPCO’s researchers are missing. And in December, Shimazaki announced that his group had found an active fault near the Higashidori plant, at which one reactor is idle, one is under construction and two more are planned. A full report is expected soon, but the Tohoku Electric Power Company, which operates the plant, says that it will produce data proving that the faults are not active.



➤ **NATURE.COM**
For more on Japan's
earthquake and
nuclear crisis see:
nature.com/japanquake

► mirror and sending the signal to a few sensors, it will capture instantaneous views of a 185-kilometre swathe of Earth, using some 7,000 sensors for each bandwidth. The result is more data from each location and better image quality. “The data are much more sensitive to change across the landscape and over time,” says Jim Irons, project scientist for the mission at NASA’s Goddard Space Flight Center in Greenbelt, Maryland. “Maybe we will be able to better differentiate corn from sorghum, for example, or maple trees from oak trees.”

The spacecraft will also be the first in the Landsat series to collect data in an ‘ultra-blue’ band, particularly useful for studying oceans and atmospheric aerosols. Another new data stream will be a shortwave infrared band that is sensitive to cirrus clouds, which are powerful players in Earth’s climate.

Landsat has endured major changes in ideology and organization during its lifetime, notably in the 1980s and 1990s, when Congress gave control of the satellites and all data to a private company. Images sold for several thousand dollars each, limiting analysis to an elite corps of scientists. The government regained control in 2001, however, and from 2008 the US Geological Survey, which oversees the data, opened up the archive as a free global resource. Access exploded. Whereas the agency once sold around 15,000 images a year, annual downloads now average about 3 million.

“It provided for data democracy,” says Mike Wulder, a research scientist at the Canadian Forest Service in Victoria and a member of the Landsat science advisory team. “Landsat really is a global resource.”

The data helped to spark a digital revolution among remote-sensing specialists, who have developed tools to exploit massive computing resources and stitch together high-resolution records of global change over time and space. Other space-borne imagers, such as the Moderate Resolution Imaging Spectroradiometer (MODIS) on NASA’s Terra and Aqua satellites, can take snapshots of larger areas at a single pass, but with much lower resolutions.

With Landsat, “we can get the detail and the enormous geographic coverage,” says Asner. “This alone puts Landsat at the very forefront in land-cover and land-use change monitoring.”

Landsat 8 is scheduled to begin operations 90 days after entering orbit, although the first images could arrive within three or four weeks. The satellite might not live as long as its predecessor, which NASA engineers have put forward as a candidate to Guinness World Records, but Irons believes that Landsat 8 will make its own mark. “I do not think it hyperbole to suggest that all seven billion of us will benefit from the Landsat continuity mission.” ■

NUCLEAR ENERGY

Quake fears rise at Japan’s reactors

Commissioners say that geological faults make some reactors too dangerous to restart.

BY DAVID CYRANOSKI

Plans to restart some of Japan’s 50 nuclear reactors, which have been idle since the Fukushima Daiichi disaster in March 2011, have hit an obstacle — and his name is Kunihiro Shimazaki. Buoyed by a new cabinet keen on nuclear power, the nuclear industry wants to get the plants back online to meet the country’s energy demands. But before it can do so, Shimazaki and a group of 16 other geophysicists working for the country’s Nuclear Regulation Authority (NRA) must confirm the industry’s claims that the plants do not face a serious earthquake threat.

To judge by his initial reports, Shimazaki won’t accept the claims lightly. On 28 January, Shimazaki, an NRA commissioner who warned in 2004 that Fukushima’s coast was more vulnerable to tsunamis than regulators had claimed, angered proponents of nuclear energy by reporting his group’s conclusion that there is probably an active fault under the Tsuruga nuclear plant, which was due to restart. If, as expected, the NRA endorses that finding, the plant won’t be allowed to operate.

But the team’s evaluations have been questioned, and not just by the nuclear industry. Seismologists dispute whether the faults that Shimazaki’s researchers are finding meet the NRA’s definition of ‘active’, meaning that they have generated an earthquake in the past 120,000 years or so. In some cases, say the critics, the fractures are not dangerous and some may not even be faults at all.

“They are being overly cautious just to avoid criticism,” says Koji Okumura, a palaeoseismologist at Hiroshima University who was on an expert subcommittee of the cabinet’s Nuclear Safety Commission until it was replaced by the NRA in September 2012. “They think they’re like Superman coming in to save us from the bad guys.”

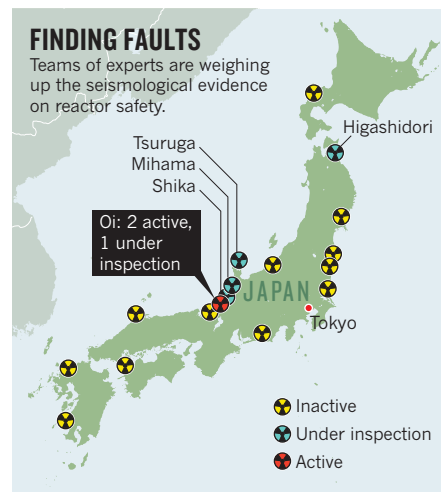
Shimazaki’s team is evaluating five plants, comprising 12 reactors in total, plus the shuttered Monju experimental fast breeder reactor (see ‘Finding faults’). Four of the five plants are due to restart; at the fifth, two of the four reactors

are already running. What the team is finding is often at odds with the industry’s assessment.

The Tsuruga plant’s reactors, for example, are 250 metres from a known fault. Excavations by the plant’s owner, the Japan Atomic Power Company, showed that the ground had shifted across the fault, suggesting that the fault had been active. But the company’s experts had concluded that the movement had happened before the 120,000-year threshold.

When Shimazaki’s experts examined the company’s trench, they found signs of more recent movement, and evidence that an extension of the fault runs directly beneath one of the reactors. “If you look at the displacement and slant, it looks like it’s a continuation” of a fracture running under the reactor, he says.

Problems also turned up in a survey by the Kansai Electric Power Company (KEPCO) of its Oi plant, which houses Japan’s only two running reactors. The plant is bisected by a fault, which KEPCO says is inactive. But Shimazaki says that crucial data from the original trench dug by KEPCO’s researchers are missing. And in December, Shimazaki announced that his group had found an active fault near the Higashidori plant, at which one reactor is idle, one is under construction and two more are planned. A full report is expected soon, but the Tohoku Electric Power Company, which operates the plant, says that it will produce data proving that the faults are not active.



➤ **NATURE.COM**
For more on Japan's
earthquake and
nuclear crisis see:
nature.com/japanquake

Meanwhile, surveys at the other two plants and the Monju reactor are set to begin this year. But critics are questioning the group's methods.

Okumura says that some of what Shimazaki's experts are citing as active faults could well be the result of landslides. He says the group lacks specialists on rocks and sediments — a limitation that the NRA says it has addressed by consulting the relevant experts.

Others are concerned that the group has been too quick to conclude that the fractures they have identified are dangerous. "There are fractures everywhere you look," says Haruo Yamazaki, a seismotectonics researcher at Tokyo Metropolitan University. He says the debate should focus on what, if any, damage the reactors would suffer if the faults moved.

Shimazaki says that the NRA will weigh up

the plants' vulnerability to earthquake damage as it evaluates the seismology reports. But the plants will face more hurdles if regulations being drafted by the NRA become law without changes. Due to take effect in July, new requirements for vents and radiation filters could mean that the Oi reactors would have to be shut down immediately and others could not restart without modifications. ■

CHEMICAL SAFETY

Alert over South Korea toxic leaks

Government moves to tighten oversight after string of hydrogen fluoride accidents.

BY SOO BIN PARK IN GUMI, SOUTH KOREA

By mid-December, the chill winter winds had stripped South Korea's trees bare. But around the city of Gumi, about 280 kilometres south of Seoul, blighted branches still bore a shroud of brown, withered leaves — reminders of the chemical accident that shook the region some three months earlier. At the edges of arable fields, red placards waved in the breeze: "Contaminated by the hydrofluoric acid leak," they warned. "Not edible."

On 27 September 2012, about eight tonnes of highly toxic hydrogen fluoride (HF) gas, which dissolves in the moisture in air to form droplets of corrosive hydrofluoric acid, burst from the Hube Global chemical plant in Gumi. The leak killed five workers and injured at least 18 others, including plant employees and emergency personnel.

Thousands of local citizens say that inhaling the acid has damaged their health. Exposure to HF can trigger an irregular heartbeat and cause fluid build-up in the lungs, and the long-term health effects include chronic lung disease. The government has said that it will pay about 36.4 billion won (US\$33.4 million) in compensation to citizens and local businesses.

This may sound like a freak accident — but it was not. On 15 January, about 2,500 litres of hydrofluoric acid escaped at a factory in Cheongju, injuring one person. And on 28 January, a worker died during a hydrofluoric acid leak at a Samsung Electronics computer-chip plant in Hwaseong. In the wake of the incidents, experts are raising questions about safety in the country's research-intensive chemical and microelectronics industries, and the government is investigating what went wrong.

"South Korea tends to focus on resolving accidents only when death occurs, but action to prevent such accidents is still severely lacking," says Lim Hyun-Sul, a researcher in

preventive medicine at Dongguk University in Gyeongju. Lim, who has been treating patients for HF exposure since the 1990s, says that preparation is key. "Protocols must be pre-



Government investigators survey the impact of a hydrogen fluoride leak.

pared thoroughly in advance, including education of factory workers, firefighters, medical doctors and public servants about the risks of toxic chemicals."

HANDLE WITH CARE

Hydrofluoric acid is commonly used by the electronics industry to etch patterns into silicon chips, and as South Korea has become one of the world's leading electronics exporters in recent years, annual consumption of HF has risen sharply. According to the Ministry of Environment, 26 businesses each handled around 10 tonnes of HF in 2001; by 2010,

the number of these large-scale handlers had almost tripled, and in 2011, 545 companies were registered as producers or distributors of the gas.

A mistake by Hube Global workers may have caused the Gumi disaster. Surveillance-camera footage seen by *Nature* shows two workers attempting to connect a hose to a valve on top of a HF tank. Neither is wearing protective gear. Suddenly, white vapour gushes from the tank, engulfing the workers and killing them instantly. Prosecutors have indicted three Hube Global executives on suspicion of negligence resulting in death, citing the absence of proper safety equipment and a lax attitude to safety regulations.

The disaster was compounded by the regional government's response. "Both the immediate and the long-term response to the hydrofluoric acid release from the South Korean government seemed to be really chaotic and uncontrolled," says Neal Langerman, who runs the consulting company Advanced Chemical Safety, based in San Diego, California.

Some firefighters failed to use chemical-protective clothing and self-contained breathing apparatus because they did not initially understand the threat posed by HF. Almost a day passed before they began using calcium hydroxide to neutralize the acid, which is standard procedure after such a leak.

Meanwhile, residents nearby were exposed to HF for about four hours before local authorities decided to evacuate them. The following day, they were told to return after investigators found no HF in the air. But thousands of residents soon complained of nausea, chest pains and rashes, suggesting that the all-clear had been sounded too early. Eleven days after the accident, the national government designated the area a 'special disaster zone', and residents began to leave again.

Evacuated residents finally returned ►

► to their homes in late December, after investigators reported that hydrofluoric acid concentrations had dropped to safe levels. Officials have allowed farming to resume, and work has restarted at Hube Global. But some experts worry that residents should stay away until there has been a more rigorous assessment of safety at the plant. "Three months is not sufficient time for thorough investigations of this incident," says Langerman.

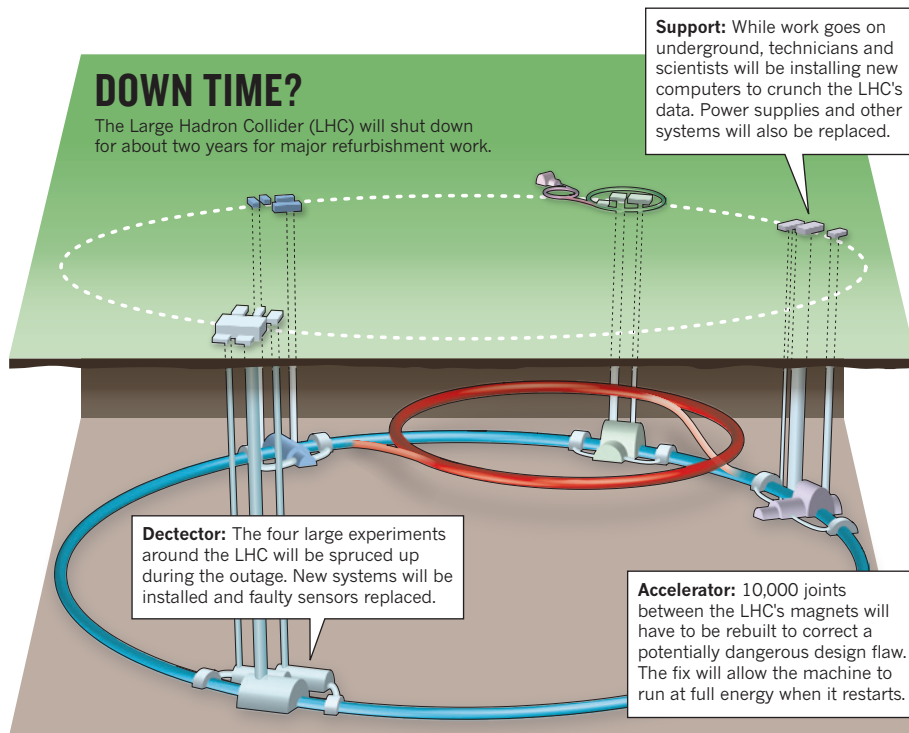
Lim adds that long-term monitoring of air and water is essential. "Once underground water gets tainted, there is a possibility that fresh water could become polluted," he says. A stream that lies just 1.5 kilometres from the Hube Global plant flows into the Nakdong River, which supplies water to more than 10 million people in the surrounding area.

So far, more than 12,000 people have claimed compensation for their injuries, and Woo Kuck Hyeun, an occupational and environmental physician at Soon Chun Hyang University Hospital in Gumi, is leading a follow-up study of those exposed to the gas. "It's almost an unprecedented case, so we are facing a lot of trial and error," he says.

Woo explains that the survey is modelled on a two-year health investigation that followed a 1987 leak at an oil refinery in Texas, when 18 tonnes of HF were released (H. H. Dayal *et al. Ann. Epidemiol.* 2, 213–230; 1992). In contrast to the accident at Gumi, however, the authorities there acted quickly to contain the leak. Within seven minutes of the release, water was used to contain and hydrate the escaping gas; within 20 minutes, a 0.8-kilometre evacuation zone was established.

The response to the Gumi accident has already been the subject of a parliamentary inquiry, and South Korea's government has promised to establish a centre that will work with local branches of the environment ministry to oversee the use of dangerous chemicals. Lim says that the regional approach is an important step. "Most chemical plants are located out of Seoul, so it's too late to wait for government agents coming from the capital to deal with an accident."

Meanwhile, the clean-up near Gumi continues. On 13 December, the government began burning about 9,100 tonnes of crops and trees killed by the gas, leaving the scene of the accident even more barren than before. "Surrounded by thousands of blighted trees, and watching them every day, recreated the trauma," says Kim Sangho, an elementary-school teacher, explaining why he has not yet returned to his home. "It's nothing different from the Fukushima accident," he adds. "What kind of people would buy the agricultural products from my village even if the government says they are absolutely safe?" ■



PARTICLE PHYSICS

LHC set to halt for upgrades

Maintenance, improvement work and data analysis will keep scientists busy as collider's planned closure begins.

BY GEOFF BRUMFIEL

With the discovery of the Higgs boson or something very like it under its belt, the world's most powerful particle collider is ready to take a well-earned rest. The Large Hadron Collider (LHC) will shut down on 11 February ahead of around two years of upgrade work.

The break, known as LS1 for 'long stop one', is needed to correct several flaws in the original design of the collider, which is located underground at CERN, Europe's particle-physics laboratory near Geneva in Switzerland. The fixes will allow the collider to almost double the energy at which it smashes protons together.

But there will be no long holiday for the thousands of physicists who depend on the LHC for their data. A bruising schedule of maintenance, upgrades and forward planning will keep the scientists who work on the collider's detectors busy (see 'Down time?'). Meanwhile, graduate students and postdocs will be poring over the past three years' worth of data, refining their

measurements of the Higgs-like particle discovered last summer and searching for any unusual signals. "It's absolutely not time off," says Dave Charlton, the deputy spokesman for ATLAS, the largest detector at the LHC.

The LHC's spectacular run got off to a shaky start in 2008. Shortly after operators fired it up, a single bad electrical connection caused coolant to vaporize, triggering an explosion that damaged an entire sector of the machine (see *Nature* 455, 436–437; 2008). Repairs took more than a year, and a subsequent review revealed potentially dangerous flaws in the original design, according to Steve Myers, CERN's director for accelerators. The worst lay in a system of copper bars designed to draw current away from delicate superconducting cables in the event of an emergency shutdown or failure. The way in which the bars had been installed made them vulnerable to failure, Myers says.

To protect the machine from further disaster, the accelerator team made the decision to run the collider at half power until all 10,000 copper connections could be repaired and

additional safety measures put in place. These repairs will begin almost immediately after the LHC switches off and will involve hundreds of people working double shifts, Myers says. The goal is to restart the collider at its full design energy of 14 teraelectronvolts by December 2014, but the complex schedule will be extraordinarily tight. “There’s no margin,” he says.

CATHEDRALS OF SCIENCE

Meanwhile, crews responsible for the underground detectors will take advantage of their first full access to the machines in more than three years. “The experiments at the LHC are a lot like satellites,” says Paolo Guibellino, the spokesman for ALICE, a detector that collects data on collisions of heavy ions such as lead and gold.

The innards of the instruments — the largest of which is 46 metres long and 25 metres wide, half the size of Notre Dame cathedral in Paris — have been largely inaccessible since the LHC began running in 2009. Now, hard-hat-wearing scientists responsible for the machinery will pull them open to conduct repairs and upgrades. ALICE, for example, will get a new set of instruments designed to track electrons and photons flying from collisions.

Meanwhile, above

ground, the team will replace banks of computers charged with capturing and analysing millions of events per second. The upgrades will help researchers to deal with the torrent of data expected when the machine roars to life. Similar work will be going on at ATLAS, says Charlton.

Other physicists will scrutinize the collisions that have already been detected. Last July, the teams working on ATLAS and another detector, the Compact Muon Solenoid (CMS), announced compelling evidence for the Higgs boson, a long-predicted particle and part of the proposed mechanism that endows other particles with mass (see *Nature* **487**, 147–148; 2012). But the detectors have accumulated double the amount of data since then. “We’re past the discovery and now in the measurement phase,” Charlton says.

Teams will work into the summer to try to determine the ‘spin’ of the new particle (theory predicts 0). Researchers will also try to further nail down its mass and behaviour to see whether it is really the long-sought particle, or something else masquerading as a Higgs boson. Such a particle or particles would look much like the Higgs predicted by theorists and could do the job of helping to endow other particles with mass, but might differ in important ways that would hint at new physics beyond the current set of predictions.

Theorists, too, will be taking a second look at

the data gathered so far, says John Ellis, a theoretical physicist at King’s College London. In their rush to discover the Higgs, experimentalists conducted only the easiest analyses. “The experiments went for the low-hanging fruit,” he says. There may be signals of something new hidden in the data.

Ellis plans to continue hunting through the data for signs of physics beyond the standard model. In particular, he hopes to turn up some hint of supersymmetry — a theory to which he has devoted years. Supersymmetry predicts a zoo of new particles, but none has so far appeared inside the detectors.

The teams will also spend the break looking towards the future. CMS spokesman Joe Incandela says the group is thinking about ways to make the most of the LHC’s new potency. “We have to start thinking already about replacement detectors for the early 2020s,” he says. Although the CMS will keep its magnets and metal superstructure, the plan is to eventually replace almost all of its electronic innards with new, state-of-the-art gear.

With the onset of the shutdown, the rhythm of the lab will change. Twenty-four-hour running shifts will come to an end, as will the frantic late-night analyses of the Higgs. But nobody is planning lengthy holidays, Incandela says. “Believe it or not, there’s not a lot of time to do everything we need to do.” ■

NATURE.COM
For more on the
LHC’s hunt for the
Higgs boson see:
nature.com/lhc

UNIVERSITIES

Campus girds for lean times

Plush San Francisco medical hub seeks to safeguard academic research.

BY ERIKA CHECK HAYDEN

A visitor to Mission Bay could be forgiven for thinking that the US economic downturn is a myth. The 23-hectare research campus of the University of California, San Francisco (UCSF), boasts freshly planted parks, new labs and the offices of biotechnology and pharmaceutical companies, alongside a construction site for a 289-bed medical centre slated to open in 2015.

When the first building opened at Mission Bay ten years ago, the project's US\$3-billion cost and its status as lynchpin of a city redevelopment plan made it one of the most ambitious clinical-research campuses ever built — and an expensive bet on the growth of the academic biomedical-research enterprise. Now, with tight budgets at the US National Institutes of Health (NIH) squeezing research grants and US health-care reform threatening hospital revenue, the world has changed. Mission Bay is a case study of the threats to medical-research hubs — and the strategies, from investment to philanthropy, that could keep them afloat. “The business model of these places won't look like it always has,” says Peter Bach, a health-care policy analyst at the Memorial Sloan-Kettering Cancer Center in New York.

UCSF is saddled with expenses that universities elsewhere do not face. Among them are the building costs for its medical centre, expanding retirement payments for California state employees and cuts in state funding — factors that could pull its budget into the red by 2015. On top of this, the medical centre is opening at a time when cost controls built into US President Barack Obama's health-care reform could erode the hospital revenues that have helped to support research at such places. Income from the existing UCSF medical centre, for example, funnelled \$295 million

to university operations over the past decade.

Perhaps worse is the increasing restriction of the NIH's budget, which will cause big problems at UCSF, one of the countries biggest recipients of the agency's research dollars. “The big squeeze for a place like UCSF, or any major

start-ups and taking royalties off of biotechnology companies has been very profitable” for universities, says Uwe Reinhardt, a health-care economist at Princeton University in New Jersey. “That's the wave of the future.”

UCSF administrators are also banking on private philanthropy to support Mission Bay, where around one-third of construction funds came from donations. The plush design of the new hospital and its proximity to labs in which treatments are pioneered could inspire donors, they say. “When you start to combine clinical care with innovative science, that's going to excite a lot of people, including donors,” says Peter Carroll, a prostate-cancer surgeon and director of strategic planning and clinical services for the university's existing cancer centre.

Cancer is one area of medicine that should still prove profitable for the new centre. Treatment involves equipment, operations and drugs that can cost tens or hundreds of thousands of dollars, and generates high revenues that are unlikely to be eroded as much as those from other areas of medicine. That is partly because the ageing of the US population means that cancer incidence will explode in the next ten years, and partly because the arcane health-insurance system pays generously for cancer services and drugs.

However they do it, observers say, UCSF and other crown jewels of US academic medicine will weather the current financial storm and keep their research robust. These centres offer specialized care, some of it available nowhere else, that is well reimbursed by insurers. They are also seen by local law-makers as crucial to the communities they serve; UCSF, for instance, is the second-largest employer in San Francisco. “I have never seen a case where academic health centres didn't work out their problems and become hugely profitable again,” says Reinhardt. ■



The ten-year-old Mission Bay campus is adapting to the era of austerity.

academic medical centre, is the complete drying up of academic funding of research,” says Bach.

Administrators hope that their evolving business plan will insure the site against the future. When workers broke ground at Mission Bay, critics warned that the campus would be a wasteland, isolated from the main UCSF site 4 kilometres away. But starting from scratch allowed space for academic labs and industry buildings to sit cheek by jowl, to accelerate the translation of basic research to the clinic and to attract industry investment.

The plan seems to be working. Old rail yards and warehouses have been replaced by seven major research buildings, outposts of nine companies — including major pharmaceutical manufacturers such as Bayer and Pfizer — and ten venture-capital firms poised to pick up and fund university projects. Start-ups that originated on the campus have raised \$230 million in follow-on capital and have hired 300 people, officials report. “This operation of incubating



Q&A



Taiwanese tycoon Samuel Yin on why he set up ‘Asian Nobels’ to reward neglected fields go.nature.com/kvtwtk

MORE NEWS

- Metastatic tumours change cell type to spread go.nature.com/ekto9t
- Diamond could make possible MRI of single molecules *in vivo* go.nature.com/st8f4e
- Panic reactions may bypass brain's ‘fear centre’ go.nature.com/xjnjjj

PODCAST



Ten things you don't know about ice; mystery genes in yeast; and the Indian Ocean's missing crust. go.nature.com/mzu7it



Robots in a facility in the Netherlands will screen molecules for biological activity.

DRUG DEVELOPMENT

Europe bets on drug discovery

Proponents hope consortium will revive flagging industry.

BY MONYA BAKER

Two sites shuttered by the pharmaceutical giant Merck, one in Scotland and one in the Netherlands, will soon be humming again with the work of drug discovery. But the hum will not be business as usual. It will be the sound of a public-private consortium placing a high-stakes wager: a nearly €200-million (US\$271-million) bet that it can boost a languishing pharmaceutical sector by fusing academic innovation with industrial-scale screening, using robots to test chemicals for biological activity.

"If it really works, it might provide a future model to operate early drug discovery," says Jörg Hüser, a champion of the idea who works at Bayer Healthcare in Wuppertal, Germany. The scheme, announced on 7 February, is sponsored by the Europe's Innovative Medicine Initiative. The European Commission's Seventh Framework Programme is contributing €80 million to the venture, with the remaining €116 million coming from in-kind contributions from industry partners and regional governments.

Called the European Lead Factory, the consortium consists of 30 academic and corporate partners, and aims to fill company pipelines with promising drug candidates. The current dearth of candidates, Hüser believes, is due to gaps in the range of biological targets that industry is pursuing and in the libraries

of compounds screened for activity against those targets.

To fill those gaps, the initiative will build and curate a collection of 500,000 molecules for screening, 300,000 of which will come from the seven large pharmaceutical partners. The rest — intended to cover classes of biologically active molecule that are poorly represented in current libraries — will be formulated and distributed in laboratory space in Newhouse, Scotland, that was closed by Merck in 2010.

CORPORATE FEEDBACK

Starting this July or August, the pharmaceutical partners will be able to use the library — including molecules from their competitors — in their own drug screens. Any academic group or company can also propose assays to test molecules in the library for biological activity. Lead-factory scientists will run these assays free of charge and confirm any promising results, working mainly in laboratory space closed by Merck in 2011 at Oss in the Netherlands. Follow-up work will be done at the University of Dundee in Scotland. Results will be provided confidentially to the groups that proposed the assays so that they can pursue further work and publications.

The hope is that members will build on the results to improve the molecules' biological properties and to gather evidence, such as tumour shrinkage, that the compounds may work as drugs. These molecules can then be

licensed back to companies for further development. The scheme hopes to become self-sustaining by requiring milestone payments as drugs move from laboratory to clinic and from additional partnerships and screening services.

"I think this is completely new," says Ton Rijnders, co-director of the initiative and scientific director of the non-profit research enabler Top Institute Pharma in Leiden, the Netherlands. An effort launched by the US National Institutes of Health in 2004 called the Molecular Libraries Program (MLP) built a 400,000-compound library of commercially available molecules, but its goal was not to find potential drugs but to identify biological pathways that might make good drug targets.

The European initiative, by contrast, aims to propel drug development. Both the chemicals in the screening library and results from the assays will be proprietary. Factory partners will get first right of refusal in licensing deals.

Such restrictions are essential if a compound is ever going to make the long journey from a screening hit to a viable drug candidate, say experts. "To justify the subsequent investments you have to make in hit-to-drug lead programmes, it is crucial that you can patent the results and protect them," says Hüser.

But others say that early hits are just entry points; the real value is created in subsequent work. "I've never worried about the notion that the MLP was a public collection," says Hugh Rosen, whose work at the Scripps Research Institute Molecular Screening Center in La Jolla, California, led to a compound now in clinical trials for multiple sclerosis.

The complexity of the European scheme makes some outsiders sceptical of whether it will succeed. Aled Edwards leads the Structural Genomics Consortium at the University of Toronto, Canada, in which some drug companies contribute both chemical analysis and screening support, but all data are publicly available. Keeping data open and focusing on specific drug mechanisms makes his consortium's approach much simpler. "Intellectual-property deals, assays coming from everywhere, multi-institutional agreements. Wow, that's hard," he says. "But they are very smart people who have done this before. So if anyone can do it, they can." ■

CORRECTIONS

The World View 'Scottish science is ready to go it alone' (*Nature* **493**, 579; 2013) attributed a recent debate on Scottish independence to the Royal Society of Edinburgh when it should have been the Royal Society of Chemistry.

The News story 'Coffee rust regains foothold' (*Nature* **493**, 587; 2013) gave the wrong year for the first major outbreak of the fungus in Costa Rica — it was 1989 not 1980.



SURVIVAL OF THE FLEXIBLE

Up in the foothills of the Rockies last summer, researchers from Colorado State University in Fort Collins fanned out along the banks of a stream. Some took the water's temperature and measured its speed and chemistry. Others waded in to catch insects using flat-bottomed nets. Aquatic ecologist LeRoy Poff combed through the haul, dropping the live stoneflies, caddis flies and mayflies into separate bins in a tackle box. Back at the lab, these would be further sorted under a microscope and then genetically barcoded — a way to catalogue the species.

Over the past year and a half, the team has run through the same procedure at 25 other streams in Colorado, and 26 in the Ecuadoran Andes, studying how variation in air temperature and water flow have affected insects in the two regions. The effort is part of a five-year project, called EVOTRAC (Evolutionary and Ecological Variability in Organismal Trait Response with Altitude and Climate), which seeks to understand how the evolutionary history of animals will influence their chances of survival in a world altered by global warming and other environmental changes.

The project was designed, in part, to test an influential hypothesis proposed in 1967 by ecologist Daniel Janzen. Janzen posited that tropical species have a hard time crossing mountains to expand into new territories because they are adapted to a fairly steady climate that never gets extremely hot or cold. At the time, global warming wasn't on the radar. But now Janzen's ideas have resurfaced as a guide to how climate change might affect biodiversity.

Although Janzen's hypothesis is widely accepted, much of it has never been tested directly. The EVOTRAC team, and other biologists, are now trying to remedy that — and to extend his idea about temperature to other environmental factors that are affected by climate,

Many tropical species never experience extreme heat or cold. That may doom them in a warming world.

BY HILLARY ROSNER



A mayfly from Ecuador could shed light on climate-change effects.

including stream conditions. If the hypothesis holds, it implies that tropical species may be particularly vulnerable to climate change, even though temperate and polar regions will warm much more than the tropics. The hypothesis could also help researchers to develop conservation plans for dealing with climate change.

JUST RIGHT

Janzen's pivotal idea came to him in the mid-1960s, when the young ecologist at the University of Kansas in Lawrence was travelling around Costa Rica with 20 US students and a Costa Rican assistant. The trip began in the assistant's home city of San José, which had a 'bland' climate that was, Janzen says, "not too hot, too cold, too wet or too dry". From there, they travelled to a dry tropical forest at sea level, where the weather was hotter. During a lecture, Janzen saw sweat pouring off his assistant. "And I looked at the students and none of them was sweating," says Janzen.

Later, when the group moved to a field station at 3,000 metres elevation in the cold, wet cloud forest, Janzen saw his assistant "sitting with piles of blankets on him. Everyone else was sitting there in khakis. I realized this guy has spent his life in San José, which is like sitting in a climate-controlled cabinet."

"The thought hit me," says Janzen, "that all these tropical animals and plants around me are living in whatever their temperature regime is. And it stays that way."

He reasoned that because tropical species are not exposed to seasonal extremes, they are locked into relatively narrow temperature ranges at specific elevations in the mountains. That prevents most of the creatures from spreading over mountains into adjacent valleys, which limits the flow of genes and increases the overall biodiversity in the tropics, he said.

When Janzen published his ideas¹, funders

RACHEL A. HARRINGTON

NATHALY QUIROZ

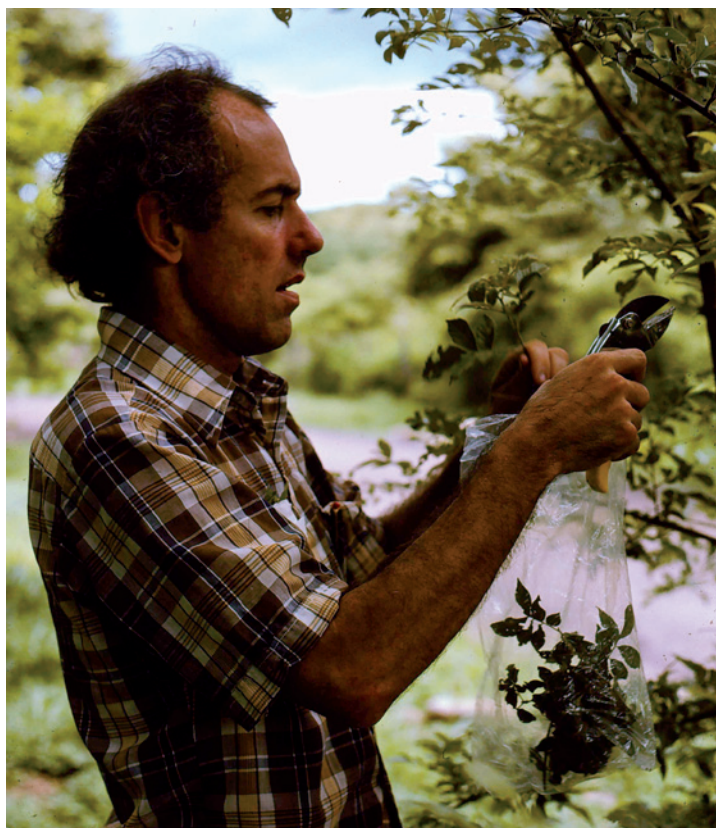
COURTESY OF DANIEL JANZEN

were not supporting the kind of big, interdisciplinary studies that would be required to test them. But when Cameron Ghalambor read Janzen's paper as a graduate student at the University of Montana in Missoula in the late 1990s, "it was one of the best papers I ever read", he says. He was struck by the idea that climate could shape so many aspects of a species' history and life cycle, and that this in turn could shape patterns of biodiversity. He told his adviser he wanted to pursue some of Janzen's ideas, but was shot down. "That's not something you can do in a PhD project," he recalls being told. "That's something you do over a lifetime."

But other biologists were already thinking along the same lines. "Janzen's theory is unique in that it couples climate variability, physiology and ecological and evolutionary principles," says Christy McCain, an evolutionary biologist at the University of Colorado Boulder. Inspired by Janzen's ideas, McCain spent nearly a decade compiling some 80 years of data on the ranges of 16,500 species that live on 170 mountains². "I looked at whether in fact range sizes were smaller on the low-latitude mountains," she says — the first part of what has come to be known as Janzen's climate variability hypothesis. Her results were published in 2009 (ref. 2). "Bats, birds, frogs, salamanders, lizards and snakes all show the trend. It's a linear decrease as you go from high to low latitude." Strangely, however, McCain found that the opposite was true with rodents, a fact she still struggles to explain.

Ghalambor, who is now at Colorado State, had reached a similar conclusion about Janzen's hypothesis in 2006 (ref. 3), when he and scientists from the University of Washington in Seattle analysed published studies of vertebrate ectotherms, such as reptiles, which are particularly sensitive to temperature. The team found, for instance, that the altitudinal ranges of tropical reptiles were more limited than those of temperate species. Ghalambor's group wondered whether Janzen's hypothesis could be used to test which species were likely to be most vulnerable to climate change.

In 2008, Ghalambor joined up with Raymond Huey, a co-author on the 2006 paper, and other researchers at the University of Washington to examine the physiological tolerance of lizards



Climate change has rekindled interest in Daniel Janzen's ideas from the 1960s.

and other ectotherms across different latitudes. The group found — just as Janzen's hypothesis suggests — that the optimum temperatures for tropical species are very close to what they currently experience, which means that the animals may not fare well as temperatures rise⁴.

"If you go to tropical lowland forests, the lizards that occur there are the least heat-tolerant lizards in the world," Huey says. The temperatures in a tropical forest never get much above 32°C and lizards there go into heat stress at 36°C or 37°C, he says.

The implication for a lizard, says Ghalambor, is that "a little bit of warming in the tropics quickly puts you outside your optimum".

REVISITING REPTILES

To put that idea to the test, Huey has now reunited with a group of scientists he has known since graduate school, who all studied lizards in Puerto Rico in the 1970s. Using their old data as a guide, the researchers are going back to make new measurements to determine whether the lizards on the island are adapting to warming temperatures or showing signs of stress.

Back in Colorado, Ghalambor began talking to Chris Funk, an evolutionary biologist who studies amphibians, about ways to test Janzen's hypothesis. They mentioned their interest to Poff, who is an expert on

aquatic insects. Poff was intrigued — and saw a parallel research opportunity to test other factors that influence species' ability to adapt or move. He had spent his career working on streams, which change from one season to the next because of variations in water flow. Extrapolating from Janzen's work, Poff wondered whether insects inhabiting streams that fluctuate strongly have evolved to tolerate much more variation than those living in more constant environments. So he teamed up with Ghalambor and Funk to test whether Janzen's hypothesis applies in the complex stream environment, where climate change is altering both temperature and water-flow patterns.

A year and a half into the EVOTRAC project, the scientists have yet to answer that question, but they have discovered that the streams in Colorado and Ecuador seem to contain many cryptic species — those that look the

same but are genetically distinct. If scientists have previously underestimated biodiversity in those spots, and the cryptic species are adapted to very specific ranges of temperature and water flow, then both locales could be more vulnerable to species loss than anyone has thought.

After a few hours collecting in the Colorado stream last summer, the EVOTRAC team packed up its collection of flies and headed back home. The two-hour drive wound through Poudre Canyon, 64 kilometres of forest that had been blackened by a massive wildfire just a few weeks earlier. There is a sense of urgency to the work. Record-breaking droughts and fires are taking a toll on the American West, and rapidly melting glaciers in Ecuador are altering rivers and streams at lower elevations. Climate change is already making its mark in the forests of both regions, even as researchers race to forecast how ecosystems will fare in the warming world. ■

Hillary Rosner is a freelance writer in Boulder, Colorado.

1. Janzen, D. H. *Am. Nat.* **101**, 233–249 (1967).
2. McCain, C. M. *Ecol. Lett.* **12**, 550–560 (2009).
3. Ghalambor, C. K., Huey, R. B., Martin, P. R., Tewksbury, J. J. & Wang, G. *Integr. Comp. Biol.* **46**, 5–17 (2006).
4. Deutsch, C. A. *et al. Proc. Natl Acad. Sci. USA* **105**, 6668–6672 (2008).



STEPHEN VOSS/REDUX/EVINE

Medicine man

As director of the NIH's bold new translational research centre, Christopher Austin has to show that he can jump-start a tortuous drug-discovery process.

BY MEREDITH WADMAN

In his last role two years ago with the Opera Vivente in Baltimore, Maryland, Christopher Austin played the Calvinist chaplain in Gaetano Donizetti's *Lucia di Lammermoor*. The story does not lack for drama: the heroine pulls out a knife in her wedding bed and stabs to death the husband who has been forced on her in place of her true love. On the heels of the murder, the chaplain "is the guy who is trying to bring order to chaos", says Austin, a bass-baritone who once considered a full-time career in opera.

Austin's most recent stage part has a certain resonance with his new day job. In September, he was appointed as director of the fledgling

NATURE.COM
For more on NCATS,
see:
go.nature.com/axfkbo

National Center for Advancing Translational Sciences (NCATS) at the US National Institutes of Health (NIH) in Bethesda, Maryland. In existence since December 2011, the centre has an ambitious — some say audacious — agenda that channels the central passion of both Austin and his boss, NIH director Francis Collins: to get more successful medicines into more patients, more quickly. That means forcing the agonizingly slow, failure-prone process of ‘translational research’ — the term of art for moving promising discoveries from the lab to the clinic — into a higher gear.

Passion runs high among the sceptics, too. Researchers both inside and outside the agency fear that NCATS — the first new centre at the NIH in more than a decade, funded at US\$575 million last year — will encroach on a finite pot of money that they say would be better spent probing the mechanisms of basic biology and disease. Others question the scale of its mission. “With the available resources, how are you going to achieve this?” asks Thomas Caskey, a molecular geneticist at Baylor College of Medicine in Houston, Texas. “To me, you cannot just take this money and be another biotechnology company and you certainly don’t have enough money to be a pharmaceutical company.”

NCATS will be neither, Austin responds. What will set it apart, he says, is a focus on overcoming obstacles on the road to drug development, from inadequate toxicology methods to inefficient clinical-trial recruitment, rather than actually producing the drugs. In an era in which more than 95% of drug candidates fail, and a novel drug takes 13 years and more than \$1 billion to develop, “NCATS has to be focused on logarithmic improvements in the process”, says Austin. “You can’t do this in a brute-force way. You have to do it differently. You have to drive the technology development.”

Austin’s fans say that if anyone has a shot at making this work, it is him. “This guy has got clinical training, industry training and scientific training. If you wanted me to pick a quarterback, this is the quarterback I’d pick,” says Lee Nadler, director of Harvard Catalyst, the NCATS-funded clinical and translational science centre based at Harvard University in Boston, Massachusetts. But whether quarterback or maestro, Austin has now to give the performance of his career. The biggest risk he faces lies in “not delivering something concrete within 12–24 months”, says Nadler. “Everybody is watching him.”

LOSING A LIFE

Austin learned early, and at first-hand, about the tragic shortcomings of medicine. One night in 1989, when he was a neurology resident on call at Massachusetts General Hospital in Boston, an ambulance brought in a middle-aged man with end-stage amyotrophic lateral sclerosis (ALS), a disease that slowly destroys muscle power but leaves brain function intact. Patients usually die when their breathing muscles give out.

The man had a ‘do not resuscitate’ order, but, because of a miscommunication, he had been revived by the paramedics. Furious that he had not been allowed to die at home, he demanded that his ventilator be turned off. Austin complied. Watched by his family and Austin, the man died slowly over three hours, in the end turning blue before his heart monitor flatlined. “It was like sitting through the crucifixion,” Austin recalls. “And I just said: ‘I can’t do this. There has got to be a better way.’”

Convinced that he had to do more, Austin began a postdoc in the lab of Connie Cepko, a geneticist at Harvard Medical School in Boston. There, he dived into developmental neurology, using new tracing techniques to reveal the migration of neural progenitor cells in the budding mouse cortex (C. P. Austin and C. L. Cepko *Development* **110**, 713–732; 1990).

“He was just really driven. He absolutely loves research,” says Cepko. She recalls the day that Austin’s wife went into labour with the couple’s first child at the Brigham and Women’s Hospital, around the corner. “I went to the lab and there was Chris sitting at his bench, pipetting away. I said, ‘Chris, aren’t you supposed to be in the delivery room?’ He said: ‘It’ll be a couple hours [yet].’”

Despite all the time he logged in the lab, Austin did not stop seeing

patients; at one point, he did a stint as the lone doctor in a hospital in rural Swaziland. But the distance from the elegant experiments of Cepko’s lab to the clinic increasingly bothered him. “That gulf was so wide,” says Austin. In 1995, when Edward Scolnick, research chief for the pharmaceutical company Merck, visited Harvard and announced that his firm was launching a genetics-based research operation that would redefine how it developed therapeutics, Austin immediately applied.

He spent the next seven years at Merck Research Laboratories in West Point, Pennsylvania, using the sequence that was beginning to come out of the Human Genome Project to seek targets for treating schizophrenia, bipolar disorder and Alzheimer’s disease. Austin’s know-how in identifying drug targets was “reversed” says Caskey, who was his boss at Merck, although he “never really did” the downstream drug development during which so many potential drugs founder. And Austin also

“He’s a guy with a sense of humour, which God knows to do that job you need.”

learned up close the disappointments of drug development: the Merck compounds that arose from his considerable work on the Alzheimer’s target γ -secretase were dropped by the company several years ago because of their side effects.

Eventually, Austin grew frustrated with the constraints of working for a huge drug company, where the need for profit made chasing cures for rare diseases such as ALS a non-starter.

He had already crossed paths with Collins, then the director of the NIH’s National Human Genome Research Institute. In August 2002, after Austin gave a talk on the NIH campus, Collins asked him to “come down here and help us figure out what to do with the genome”. Those were his exact words,” Austin recalls. By November, Austin was in place as Collins’s senior adviser for translational research.

THINKING BIG

Austin’s most prominent early project was the launch of the Molecular Libraries Program (MLP), a multi-centre effort to identify small molecules that academics could use to probe potential drug targets, and that sometimes formed the basis for drugs themselves. Many NIH officials envisioned a fairly modest effort for screening and tweaking molecules on the NIH campus. But Austin, with his commercial experience, thought on a different scale. He shopped high and low for the latest in high-throughput robotics systems and landed a deal with Kalypsys, a biotechnology firm based in San Diego, California. The company built him a one-of-a-kind, fully automated system that could, as an NIH YouTube video claimed, “boldly go where no robot had gone before”. In the space of five days, it could screen seven concentrations each of 400,000 compounds to test their activity against genes, proteins or cellular pathways implicated in a panoply of diseases. Before long, the robot was hosting a steady string of industry visitors who wanted to understand Austin’s technological leap.

In 2009, Austin launched a programme in which the NIH partners with companies, non-profit organizations and academics to try to move into clinical testing compounds that show promise against neglected diseases — including some from the MLP. The Therapeutics for Rare and Neglected Diseases programme, which is now part of NCATS, has already proved its worth, says Austin, with four compounds moving into clinical trials in the past 15 months. The trials include one launched

last month, which deploys cyclodextrin against a rare, fatal disorder of cholesterol metabolism, Niemann–Pick disease type C.

Austin's supporters say that he is no grey bureaucrat buried in the bowels of the NIH. He has proved, says Collins, “exceptionally effective” in building collaborations, whether with academics, industry veterans or earnest disease advocates. “He’s a guy with a sense of humour, which God knows to do that job you need,” adds Garret FitzGerald, director of the NCATS-supported Institute for Translational Medicine and Therapeutics at the University of Pennsylvania in Philadelphia. Last month, while speaking at the J.P. Morgan Healthcare Conference in San Francisco, California, Austin was asked whether it is true that he is an opera singer and whether, if so, he could sing a C for the audience.

“Yes, on both counts!” he sang loudly into the Colonial Room at the Westin St. Francis Hotel.

ROUGH START

In December 2010, Collins, early in his second year as NIH director, announced his intention to form a translational-medicine centre from existing components of the NIH, and to do so within a year — a veritable burst of speed in the government world. The reorganization would mean the dissolution of the NIH’s National Center for Research Resources, an entrenched institute with heavy investment in translational science and many constituents in basic research (see *Nature* 471, 15–16; 2011).

The next month, *The New York Times* ran a front-page story declaring that NIH officials “have decided to start a billion-dollar government drug development center to help create medicines” and that to do so Collins was willing to “cannibalize” other parts of the NIH. The reaction was fierce. Congressional Republicans, drug-industry executives and NIH-funded basic researchers blasted the agency for treading on private-sector prerogatives, for neglecting its basic-research mandate and for presuming that it could succeed where industry had been failing.

Perhaps the most damaging jab came from Roy Vagelos, former chief executive of Merck, at a congressional hearing last March. “Does anyone in the audience believe that there is something that NCATS is going to do that the industry thinks is critical and that they are not doing?” he asked. “That is incredible to think that. If you believe that, you believe in fairies.”

Collins rushed to defend the nascent centre’s mission. NCATS, he explained, would “complement and not compete with” industry, by taking on thorny problems in the technology of drug development to smooth the road to the clinic for all concerned. And, he assured his constituents, NCATS would not eat into the NIH’s basic-science dollars. Congress, at least, set aside its doubts, and funded NCATS in the dying days of 2011. The search for a director took nine months, and at least one other candidate was offered the job. But Austin, who had created many of the programmes that comprised NCATS, was a natural fit to head the centre. Besides, says Nadler, “Francis loves this guy”.

During a recent interview, Austin spontaneously countered the now-famous “fairies” criticism. On the NCATS to-do list, “are there things pharma hasn’t thought of doing? Maybe, but for the most part, no,” he says. However, he adds: “That’s not the right question. The right question is: what can they do within the confines of ... a profit-making organization? There’s a lot of things you just can’t do even if you want to.”

To underscore what sets NCATS apart from industry, Austin has been showcasing the centre’s first new programme, which makes available to

NIH-funded scientists 58 drugs tested in humans but abandoned by big drug firms for business reasons or because they didn’t work against the conditions that the companies had tested them on. The goal is to put those candidates to other uses. The programme has become a useful flagship for NCATS not least because it — unlike others in the opaque field of translational research — is easily explained to the public.

Austin also likes to talk about NCATS’s bid to overcome one of the biggest hurdles in the quest for new drugs: the discovery of harmful side effects when a compound is well into development. “This is a classic problem for NCATS to work on,” he says.

His solution, in part, is a programme in which NCATS is working with the Defense Advanced Research Projects Agency and the US Food and Drug Administration to put ten human tissues, from heart to brain and gut, on a chip that could then be used to screen potential drugs rapidly and efficiently for toxic effects. Another attack on toxicity can be found in the Tox21 programme, a collaboration between NCATS, the National Toxicology Program at the NIH’s National Institute of Environmental Health Sciences and the Environmental Protection Agency. It began in December 2011 to screen 10,000 environmental chemicals and approved drugs against every known human signalling pathway, to identify which molecules might have toxic effects.

In the longer term, one of Austin’s major goals is to find a better way to use NCATS’s biggest programme: the \$461-million Clinical and Translational Science Awards (CTSAs), which fund around 60 translational-medicine centres, each operating independently. The awards aim to train the next generation of translational researchers

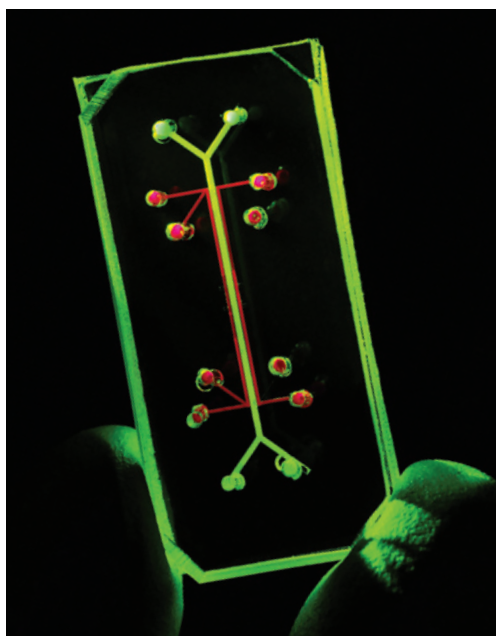
and to improve the full spectrum of that research, from discovering drug targets to answering health-delivery questions such as: do asymptomatic women really need routine manual pelvic exams? Since September, Austin has visited nine of the CTSAs — he has planned six more visits — to talk to principal investigators and other staff members. While praising the centres’ work, he says that they have so far mostly operated “without particular encouragement or direction from the NIH, and thus in a disjointed and uncoordinated fashion”. Austin wants to see a “CTSA 2.0” that will apply the consortium collectively to problems including clinical-trial recruitment, the development of better biomarkers and the rational use of electronic medical records in research. This can best be done “across a nationwide network focused on solving systematic problems”, says Austin.

Austin has not sung in an opera since the launch of NCATS. It is a fact of his current life that he regrets. “When I got this job,” he says, “I got more than one congratulatory note saying: ‘Now you really need to do the music. Because this is the only way that you’re gonna maintain your sanity.’”

Working out how to make that happen may be easier said than done; Opera Vivente folded during the economic meltdown, and Austin is logging 12–15-hour workdays. But he still sees the pursuit as intimately related to his chosen career.

“If you look at what NCATS is trying to do, and why I got into medicine in the first place — you are trying to understand the human condition. Fundamentally, that’s what opera does, that’s what it tries to explore. What makes people tick? And then, sometimes, how do you fix it?” ■

Meredith Wadman is a reporter for *Nature* in Washington DC.

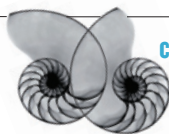


NCATS is helping to develop chips that mimic human tissues to screen for toxic effects of drugs.

WYSS INSTITUTE

COMMENT

RENEWABLES Energy from biomass has lots of potential **p.29**



CLASSICS Why *On Growth And Form* is in the scientific canon **p.32**

CONFLICT In conversation with Richard Rhodes, chronicler of science in war **p.34**

OBITUARY Brigitte Askonas, 'grand dame' of immunology, remembered **p.37**

VISUALS UNLIMITED/NATUREPL.COM



The impressive front of the Perito Moreno Glacier in southwest Argentina, part of the vast South American icefields.

Ten things we need to know about ice and snow

Understanding the molecular behaviour of frozen water is essential for predicting the future of our planet, says **Thorsten Bartels-Rausch**.

Ice is central to climate, geology and life. Understanding its behaviour is essential for predicting the future of our planet and unravelling the emergence of life in the Universe¹. Water ice frosts planets, moons and comets in our Solar System. On Earth, white polar ice caps reflect up to 90% of the Sun's incoming radiation. On average, 7% of the ocean's surface is frozen; sea ice alters ocean currents and limits the exchange of gases with seawater. Ice and snow coat 10% of the land permanently and up to half of the Northern Hemisphere in midwinter. These blankets of frozen water insulate the ground and the oceans.

Ice clouds concentrate airborne chemicals and are sites for atmospheric chemistry. Above the poles, clouds of ice grains host ozone-depleting reactions, forming holes in the stratospheric ozone layer at high latitudes that expose millions of people to increased ultraviolet radiation. Chemical reactions in snow on the ground can produce ozone and other environmental pollutants. Organic toxins and mercury accumulate in snow and can be released into rivers and oceans when the snow melts, where they enter the food web.

Yet the molecular mechanisms underlying these processes remain largely unknown². Without knowing more about how chemical

reactions proceed in ice and snow, and where they occur within the grain and crystal structure, it is impossible to build snow or ice-cloud modules for atmospheric and climate models or to extrapolate laboratory studies to environmental conditions with enough confidence.

In my view, the chemistry and physics of ice need to be studied more on a molecular scale if we are to address the massive environmental problems we face. Recent advances in computer simulations and in experimental techniques such as surface-sensitive spectroscopy, which can now be operated at temperatures and pressures ►

► relevant to ice in the environment, open the door to exciting future studies. Here, I summarize ten open questions about ice.

TEN QUESTIONS

How does ice form? Much about how and when water freezes is still unclear, even though this is essential for understanding Earth's climate and water cycle. We cannot predict with certainty when and where ice clouds will form in the atmosphere; areas of the sky remain humid when we would expect them to freeze. Do water droplets freeze from the surface first or crystallize from within? Which form of ice will they make?

Ice often forms easily on solid surfaces. To understand why that happens, the molecular bases of the interaction of water molecules with such surfaces need to be studied.

How does ice structure change? Ice crystals are composed of water molecules held in a regular tetrahedral arrangement by hydrogen bonding. Many crystalline structures of water are known, the most familiar being the hexagonal ice that forms snowflakes. As pressure and temperature vary, the water molecules adapt their arrangement to minimize energy, producing the different phases of ice.

These phase transitions are well understood macroscopically. Next, we need to be able to reproduce the molecular processes in those transitions in computer simulations or quantum-chemistry calculations over the whole temperature and pressure range. With these optimized models we might then tackle other questions such as the surface structure and how impurities react in ice.

How do different ice structures behave? In addition to ordered crystals, ice also comes in amorphous and 'metastable' forms — molecular arrangements that are long lived but not at minimum energy. This structural variety widens the possibilities for how readily ice crystals form, the chemical reactivity of ice clouds, how impurities are captured in comets, and the mechanical strength of icy bodies in space. Yet we know little about how these ices are structured, whether they mix with crystalline ice and where they occur.

Amorphous ice — loosely tetrahedral in molecular structure but not crystalline throughout — might form on comets when water condenses at extremely low temperatures. Metastable cubic ice, which seeds more readily than the hexagonal arrangement, can form in ice clouds. Examining these phases is tricky as they are difficult to access and are optically indistinguishable. In the laboratory, X-ray and neutron diffraction studies might be the answer.

What is the surface structure of ice? Molecular order breaks down at crystal surfaces. Hydrogen bonds exposed to the air also bind

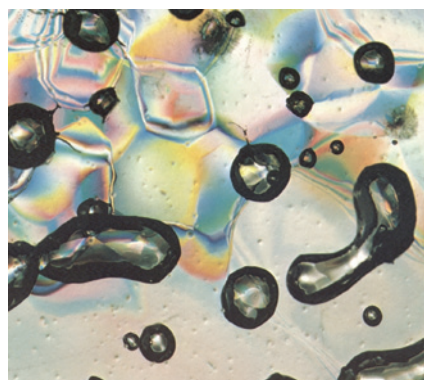
pollutants such as methanol, acetone, nitric acid and hydrochloric acid. The resulting networks of water molecules are irregular and difficult to describe, especially in ice that is warm and near its melting point, when the disorder spreads deep into the crystal.

We need to know the most essential things about this layer, such as its molecular structure and how that changes with temperature. And the layer's role in hosting impurities and chemical reactions is not clear. Surface-sensitive spectroscopy that can probe the bonding network of water molecules at near-ambient pressure, and thus of ice close to its melting point, could help answer these questions.

Where do impurities lie within ice? In the upper atmosphere and in space, water ice is often mixed with carbon monoxide, carbon dioxide, methane, sulphuric acid and nitric acid. Ice on the Earth's surface holds chemicals from sources such as sea salt, dust and pollution. Different impurities have been observed to boil off together from comets approaching the Sun, which suggests that they are trapped within the frozen material until the ice matrix vaporizes. But we don't know how these impurities are mixed in with the ice, or whether different types of ice, such as soft snow and compacted glaciers, hold contaminants in similar ways.

Some common crystalline structures associated with impurities have been identified in the laboratory. For example, nitric acid forms solid hydrates with frozen water that are crucial for ozone depletion in Earth's stratosphere. We must identify the phase, location and chemical environment of impurities within ice matrices in space, in clouds and on the ground. Surface-sensitive spectroscopy and diffraction are promising techniques in this regard.

How do reactions proceed in ice? At the South Pole, reactions of nitrous oxides released from snow produce enough ozone to raise the local concentration to levels seen in industrial areas. In the Arctic, mercury ions deposited from the atmosphere into the snow cover are chemically converted before



Ice core air bubbles capture ancient atmosphere.

being released back to the air. In space, molecules such as hydrogen, water, methanol, carbon oxides, ammonia and amino acids form on the surfaces of icy grains.

To get a better understanding of the chemical reactions that occur on surface films and in complex ice matrixes, we need to identify the dominant pathways and the locations of the impurities involved, given that reactivity on ice surfaces differs greatly from that within micro-pockets or bulk ice. Classical kinetic experiments could identify the chemical states of reactants.

Are there pockets of liquid in ice? Brine fills the pores and channels in sea ice, and sea salt in snow and impurities along grain boundaries in glacial ice can cause local melting to form internal pools. The presence of liquid changes the fate of impurities and the phase stability of ice, but in environmental ice we do not know how much liquid is trapped or where it is held.

In the lab, liquids in tiny ice pockets nanometres across freeze at temperatures tens of kelvin lower than normal. But whether such pockets exist in nature, and how much of the impurities they might capture, is not known. Observations are difficult at such small scales and it is hard to differentiate liquid and solid water optically. Microscopy using chemicals that enhance the contrast between liquid and solid phase could tackle these questions.

How do physical processes affect ice impurities? Chemicals from the atmosphere are absorbed rapidly by snow and creep deeper into glacial ice over centuries, altering the chemistry of air, snow and ice over time. Fluctuations in the levels of slowly diffusing pollutants, such as fluorides and methane-sulphonates, complicate the dating of the environmental record from ice cores.

The processes that dominate the spread of impurities in ice and snow, and their exchange with the atmosphere in clouds and on the ground, must be determined by measuring exchange rates and where exchange occurs within the ice structure. Surface adsorption, diffusion into the ice crystal or along grain boundaries, and trapping by liquid all affect the migration and fate of impurities. We can use spectroscopic techniques to follow these interactions at the molecular level.

How does ice growth affect impurities? Water molecules in the surface layers of ice and snow are continually evaporating and re-freezing. During the course of a day, as temperatures cycle between warm and cold, up to 60% of the molecules can be redistributed.

How do impurities respond when the shape, surface area and volume of the ice

changes so drastically? Laboratory and field studies reveal that mercury, hydrogen peroxide, hydrochloric acid and nitric acid are taken up more readily by growing than by stable ice. Experiments are needed to measure this uptake accurately and over a range of growth rates. Tracking uptake in individual growing ice crystals would be a good start.

How long will ice last? Satellite data indicate that the Arctic perennial sea-ice cover is declining by around 10% per decade. Glacier shrinkage at the Greenland and Antarctic ice sheets is accelerating. Our understanding of the observations is insufficient for us to predict the rate at which snow and ice could disappear from our planet in this century. Studying the impact of ice chemistry on molecular-scale melting processes will help us to predict the fate of Earth's snow and ice.

BACK TO THE LAB

How shall we answer these questions? Good starting points are existing research networks, such as the Air–Ice Chemical Interactions programme of the International Global Atmospheric Chemistry project, with which I am involved, the European Science Foundation's network on the microdynamics of ice, Micro-DICE, and the Arctic health-risks project ArcRisk, which is supported by the European Community.

These collaborations of scientists from different disciplines and countries should be broadened. We need to bring in materials scientists working on crystal and surface structures in metals, cell biologists who study the biota of frozen environments and food scientists who study how compounds change during freezing.

More funds for fundamental, laboratory-based experiments must be raised. I believe that all ten questions could be answered with an investment of €5 million (US\$7 million). Sadly, this will be difficult to find, but now that we have identified basic key questions, the time has come for complex, well-defined experiments in laboratories using sophisticated analytical techniques, including synchrotron facilities. Lack of recognition of the importance of ice chemistry may be one reason why many ice and snow research groups have moved into field studies. We need to reverse this flight and use the expertise gained over the past decades to understand the role of ice in the global Earth system — before it vanishes. ■

Thorsten Bartels-Rausch studies the surface chemistry of ice and snow at the Paul Scherrer Institute, Villigen, Switzerland.
e-mail: thorsten.bartels-rausch@psi.ch

1. Bartels-Rausch, T. *et al. Rev. Mod. Phys.* **84**, 885–944 (2012).
2. Bartels-Rausch, T. *et al. Atmos. Chem. Phys. Discuss.* **12**, 30409–30541 (2012).



Brazil distils vast quantities of fermenting sugarcane into alcohol for fuel.

Build a biomass energy market

Governments must offer incentives to drive a switch to biofuels and other renewables, argues **Heinz Kopetz**.

Biofuels — which include wood, straw, charcoal, ethanol derived from corn (maize) and methane-rich biogas — currently generate about 10% of the world's energy, or 53 exajoules¹. The majority goes towards heat, with the rest used for electricity and transportation (see 'Biomass boost'). But biofuels hold the potential to deliver at least one-quarter of the world's projected energy needs of 623 exajoules by 2035 (ref. 2). This would

help to limit global warming, create jobs in rural areas and improve energy security. To achieve it, countries will need to dramatically accelerate their development of biofuel technologies.

Some countries have made huge strides in this respect, notably Sweden, Austria, Brazil and China. Many others are not making the most of their resources: in Australia, for example, millions of tonnes of straw are still burned in fields after ▶

► the harvest each year; this 'waste' could be used to generate energy.

Critics often argue that the development of biofuels for transportation has caused more hunger in the world by eating up land that could be used to produce food, but there is little scientific evidence of that. In fact, the development of bioenergy goes hand in hand with increased investment and higher productivity in agriculture and forestry. And because many of the by-products are protein-rich, it could actually improve the food supply.

I believe that by making agriculture and forestry more efficient, we could boost the production of biofuels worldwide without displacing food production. Policy-makers need to be made more familiar with the options available and introduce incentives, taxes and subsidies that encourage households and industries to switch to bioenergy and provide investment for the long-term development of advanced fuels.

PLANT POWER

Biomass comprises 76% of all renewable sources of energy¹. The carbon it contains is captured by plants from the atmosphere through photosynthesis and released back into the atmosphere by decay or other processes of use. Biomass is therefore a carbon-neutral source of energy. By contrast, the carbon in fossil fuels stems from Earth's crust, so burning these fuels injects additional carbon into the atmosphere.

Every year, plants convert 4,500 exajoules of solar energy and 125 gigatonnes of carbon from the atmosphere into biomass — an

equivalent of almost 300 million tonnes of oil per day. Most plant material is broken down by microorganisms within the natural carbon cycle, but hundreds of exajoules per year remain exploitable³.

More than 80% of the biomass used for energy comes from forests, in the form of logs, wood chips, wood pellets, sawdust, bark and other by-products. Just one-third of the world's 4 billion hectares of forest is used for wood production or other commercial purposes⁴. And those that are managed have room to grow more feedstock than they currently do. In Sweden and Austria, for example, sustainable forests generate 4–8 cubic metres of wood per hectare per year. Simply improving forestry practices, as has been achieved in parts of Europe, and increasing the forest area by 200 million hectares could deliver an extra 25 exajoules of energy per year.

Similarly, better use of low-yielding grasslands, sparse woodlands and degraded land could deliver more biofuels without encroaching on food production. Of the 13 billion hectares of land worldwide, 12% is used for crops and 30% for livestock⁵. But a further 893 million hectares could accommodate rain-fed agriculture and new forests⁵. Planting 170 million hectares of this with energy crops could deliver 15 exajoules, and still leave space for feeding rising populations, urban development and biodiversity protection, and new forests⁵.

"Biofuels hold the potential to deliver at least one-quarter of the world's energy needs."

Admittedly, livestock production on the remaining land would have to be intensified and meat consumption limited.

In regions without bioenergy programmes, waste and most agricultural and forestry residues such as straw and bark are dumped in landfills, burned or left to rot, amounting to a loss of at least 60 exajoules.

THREE SECTORS

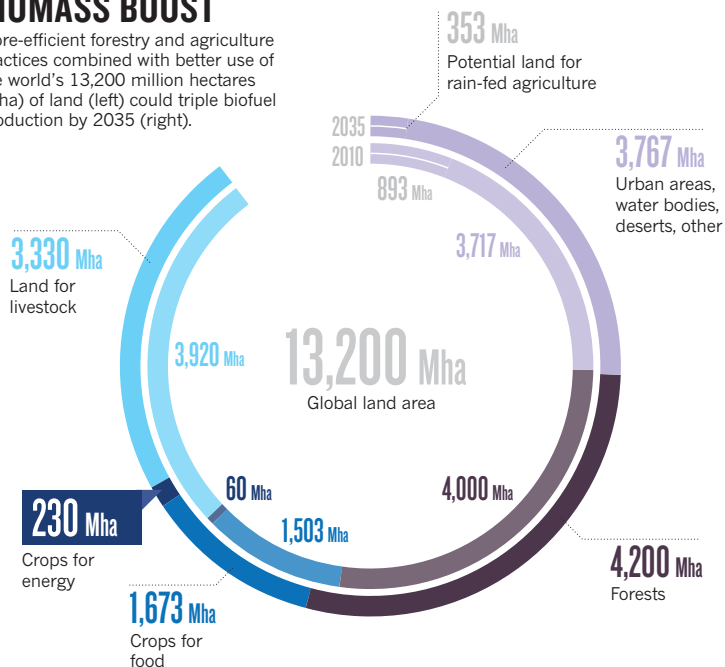
Because fossil fuels are used in the production of biomass — in planting, fertilizing, harvesting, transport and processing, the net emissions savings vary hugely depending on the method of production and on what the fuel is used to produce.

Heat — for cooking, hot water, space heating and industry — is the largest destination for biofuels, and it generates the highest net savings — of more than 95% in many cases, according to several bioenergy associations. Almost half of the world's population is thought to fuel stoves and boilers using firewood or charcoal, often from unsustainable forests³. Traditional charcoal production and stoves are inefficient, and their emissions are terrible for air quality and health. I believe that more-efficient stoves, such as those that use ethanol or wood pellets, would save up to 10 exajoules per year.

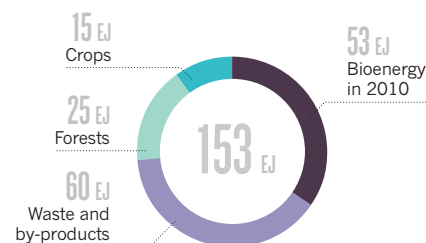
Wood-pellet stoves and boilers are well suited to suburban households because pellets are energy-dense and compact to store. Farms or companies with more storage space prefer wood chips, which are bulkier but cheaper. Wood powder injected into adapted oil burners has helped several Scandinavian companies to escape rising oil prices.

BIOMASS BOOST

More-efficient forestry and agriculture practices combined with better use of the world's 13,200 million hectares (Mha) of land (left) could triple biofuel production by 2035 (right).



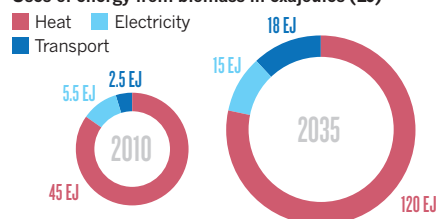
Extra sources of biomass for energy, targets for 2035



Sources of renewable energy, 2010



Uses of energy from biomass in exajoules (EJ)



In the Northern Hemisphere, fossil fuels still dominate the heat market, even though biomass is half the price of oil. But several countries are setting a good example. Thirty years ago, Sweden levied environmental taxes on fossil fuels, which made production of heat from biomass cheaper. Now, less than 5% of the nation's residential heat comes from coal or oil. Furthermore, the nation uses district heating to serve its densely populated downtown areas. In this system, a grid distributes hot water from a central heating source, such as a combined heat and power (CHP) plant, which burns biomass to produce electricity and feeds waste heat into the grid. CHP systems can be twice as efficient as those that produce electricity alone. Denmark and Finland also use district heating.

Italy has a booming wood-pellet market, which serves more than 15% of the nation's apartments. In Austria, government grants that cover 30% of the investment cost have encouraged companies and home owners to install biomass heating systems that burn wood chips or pellets, so that biomass fuels one-third of the heating market.

For electricity production, biofuels supply around 2% of the world's needs⁶. Germany uses biogas from energy crops, manure and waste to deliver about 2% of its electricity. CHP plants are the most efficient option.

Green transport is dominated by first-generation fuels such as ethanol and biodiesel, which are derived from corn, canola, soya beans, oil palm or sugarcane. Production has grown rapidly in the past decade, reaching 86 billion litres of ethanol and 20 billion litres of biodiesel in 2010. The grain and canola planted for biofuels delivered 64 million tonnes of protein feed worldwide — equivalent to 22 million hectares of soya beans. Globally, 1% of the agricultural land was used to produce the feedstock for these fuels and to yield 20% of the world's protein supply. I believe that government support for agriculture and cultivation of these fuels only on disused land could lead to greater yields without harming the food supply.

Another option for the transport sector is advanced biofuels, which are derived from cellulose or hemi-cellulose materials such as straw, wood residues or municipal refuse, or using algae. These are currently expensive, complex to produce and only just entering the commercial phase in small quantities in pilot or demonstration plants. The costs of feedstock and the logistics involved — such as collection, transport and storage — are often underestimated and the production costs are higher than those of fossil fuels. Advanced biofuel production will grow rapidly only with government support.

In sum, by 2035, biomass could deliver 120 exajoules (50% of the world's needs) for heat, 15 exajoules for transport and 18 exajoules (7%) for electricity. Altogether that



Elephant grass and straw can be used to fire power stations.

is one-quarter of the global energy needs — assuming that the growth in energy consumption slows down with the improved efficiency.

NEXT STEPS

The top priority should be heating: improving efficiency in developing countries and using biomass and district heating, rather than fossil fuels and electricity, in developed countries. Governments must tax fossil fuels, provide investment grants and support the construction of district heating grids.

Generating electricity from biomass — particularly biogas — would compensate for the intermittence of wind and solar electricity in renewable energy schemes. Because the cost of electricity from biomass is above market price, the best solution is a system of guaranteed sale prices for producers, financed by all consumers, as implemented in Germany more than 15 years ago.

For transportation, we should aim for a modest growth of first-generation biofuels, to 5–7 exajoules by 2035. Successful incentives to promote these fuels include tax exemptions or mandating a minimum share of biofuels, as is done in the European Union. For advanced biofuels, targeted subsidies would compensate for the higher production costs and encourage commercial-scale production.

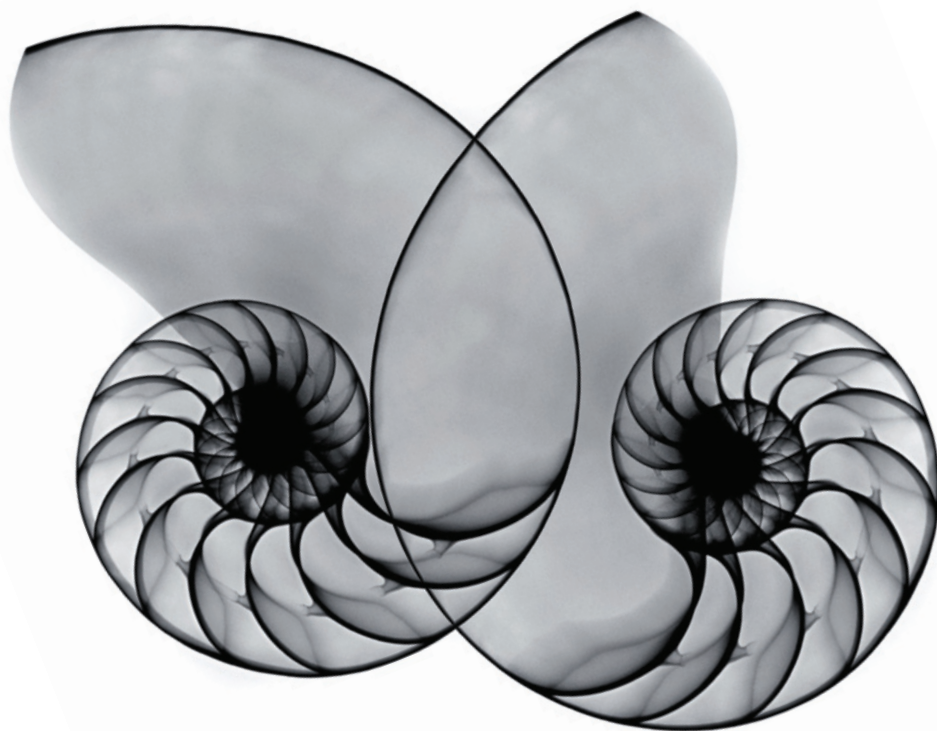
Fossil fuels receive more than US\$500 billion in subsidies worldwide every year and are well established on all markets. Without

targeted, long-term government policies, bioenergy will develop too slowly to help in the mitigation of climate change. Rural development based on sustainable agriculture and forestry will have to become an economic policy priority for governments and international organizations.

So that decision-makers can choose the best bioenergy strategies for their countries, I call on international organizations such as the Food and Agriculture Organization of the United Nations and the International Renewable Energy Agency to work with the World Bioenergy Association, of which I am president, to catalogue case studies of successful bioenergy policies. By building on the experience of others, countries can accelerate the transition to more-sustainable systems. ■

Heinz Kopetz is president of the World Bioenergy Association in Stockholm, Sweden.
e-mail: hg.kopetz@netway.at

1. International Energy Agency. *Key World Energy Statistics 2012* (2012).
2. International Energy Agency. *World Energy Outlook 2011* (2011).
3. World Bioenergy Association. *WBO Position Paper on Global Potential of Sustainable Biomass for Energy* (WBA, 2009).
4. Food and Agriculture Organization of the United Nations. *Global Forest Resources Assessment 2010* (FAO, 2010).
5. WWF, ECOFYS, Office for Metropolitan Architecture. *The Energy Report: 100% Renewable Energy by 2050* (2011).
6. REN 21. *Renewables 2012: Global Status Report* (2012).



IN RETROSPECT

On Growth and Form

Philip Ball celebrates a classic work on the mathematics that shape living structures, from antlers to cells.

Like Newton's *Principia*, D'Arcy Wentworth Thompson's *On Growth and Form* is a book more often name-checked than read. Both are hefty — Thompson's revised edition in 1942 weighed in at more than 1,000 pages, to the alarm of Cambridge University Press.

And both books stand apart from their age. Each contains ideas ahead of its time, yet seems rooted in earlier traditions. First published in 1917, with the modern synthesis of neo-Darwinian biology two or three decades away and genes still a nascent concept, *On Growth and Form* looked in some ways archaic by the time the second edition appeared — yet it continues to inspire.

Thompson's agenda is captured in the book's epigraph from statistician Karl Pearson (first published in this journal in 1901): "I believe the day must come when the biologist will — without being a mathematician — not hesitate to use mathematical analysis when he requires it." Thompson presents mathematical principles as a shaping agency that may supersede natural selection, showing how the structures of the living world often echo those in inorganic nature.

Thompson's route to this view was, like the man himself, idiosyncratic. The son of a Cambridge classicist, he went to Edinburgh to study medicine but switched to zoology at Cambridge — the same trajectory as Darwin. There he supplemented his income by teaching Greek. He returned to Scotland as (in effect) a marine biologist at the University of Dundee before moving a few miles down the North Sea coast to the University of St Andrews, where he occupied the Chair of Natural History.

His frustration at the 'Just So' explanations of morphology offered by Darwinians burst out in a 1894 paper presented at the British Association meeting; he argued that physical forces, not heredity, may govern biological form.

On Growth and Form elaborates at length on this theme. "In general no organic forms exist save such as are in conformity with physical and mathematical laws," he wrote. Thompson's demonstration of this claim takes him through a formidable range of

On Growth and Form

D'ARCY WENTWORTH THOMPSON
Cambridge University Press: 1917.

topics. To name a few: the mathematical laws that relate growth, flight and locomotion to mass and size (a topic currently experiencing a renaissance); the shapes of cells, bubbles and soap films; geometrical compartmentalization and honeycombs; corals; banded minerals; the intricate shells of molluscs and of the minuscule protozoan radiolarians; antlers and horns; plant shapes; bone microstructure; skeletal mechanics; and the morphological comparison of species.

The book's central motif is the logarithmic spiral, which appears on the plaque commemorating Thompson's former residence in St Andrews. He saw it first in foraminifera, and again in seashells, horns and claws, insect flight paths and the arrangement of leaves in some plants. This, to Thompson, was evidence of the universality of form and the reduction of diverse phenomena to a few mathematical governing principles.

How much influence did *On Growth and Form* have? Evolutionary and developmental biologists often genuflect to Thompson's breadth and imagination while remaining sceptical that he told us much of lasting value.

Thompson was reacting against the Darwinism of his age, whereby, in its first flush of enthusiasm, it seemed adequate to account for every feature with a plea to adaptation. Thompson's insistence that biological form had to make sense in engineering terms was a necessary reminder. But it did not challenge the idea that natural selection was evolution's scalpel — it merely imposed constraints on the forms that might emerge. When he sent the manuscript of *On Growth and Form* to his publisher, Thompson wrote: "where it undoubtedly runs counter to conventional Darwinism, I do not rub this in, but leave the reader to draw the obvious moral for himself."

Thompson believed that evolution could sometimes advance in a leap rather than a shuffle — still a hotly discussed issue. And the debate that Thompson tried to initiate about contingency versus necessity in biological form has not yet really been engaged. There are still biologists who believe that almost every feature of an organism must be adaptive. There are still open questions about how deterministic the course of evolution is.

This is one reason to keep *On Growth and Form* in the canon. Another is the modern appreciation of self-organization as a means of developing complex form and pattern from simple physical rules — evident, for example, in fractal patterns, animal swarming and perhaps even the subtle regularities of human society. Here Thompson is not as easy to enlist as a prophet as one might expect.

Many of the systems he looked at, such as the striped markings of animals, and the formation of polygonal crack networks, are now recognized as paradigmatic examples of spontaneous self-organization in complex systems. But Thompson often gives

such things only a glancing mention while either confessing that he has no real explanation or assuming that it must be a simple one. He says of the chemical precipitation patterns called Liesegang rings, "For a discussion of the *raison d'être* of this phenomenon, the student will consult the textbooks of physical and colloid chemistry." The student would have found little there in 1917, and some aspects of this chemistry are still being clarified.

The logarithmic spiral was, to Thompson, evidence of the universality of form.

The tradition from which Thompson's great work emerged was rather different from the early interest in complex systems by the likes of Henri Poincaré: it was indebted to the biophysics and biomechanics of anatomists such as Wilhelm His and Wilhelm Roux. It is probably this strand that ties Thompson most securely to the present, for much of cell biology now centres on how the mechanics of cell structures determine the fates, forms and functions of tissues. This undervalued aspect of biophysics is becoming more integrated into the rest of molecular biology, as we come to realize how much mesoscale mechanics modulates gene and protein behaviour.

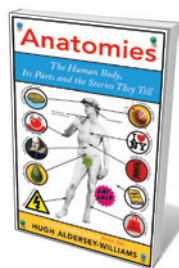
But much of the admiration for *On Growth and Form* expressed by fans such as Peter Medawar and Stephen Jay Gould stems from a more general consideration: Thompson's breadth of scholarship, coupled to the elegance of his writing. He was a classicist as well as a scientist (the many Greek and Latin quotes in *On Growth and Form* pass untranslated), and there is something of the antiquarian in his persona. At a time when science was succumbing to the specialization that has now become something of a liability, Thompson showed the value of synoptic thinkers who are prepared to risk being quite wrong here and there for the sake of an inspirational vision. Like the modern mavericks James Lovelock, Benoit Mandelbrot, Gould and Stephen Wolfram, he presented his ideas in an extended, almost incontinent, gush, rather than with a conventional succession of closely argued papers.

Such figures excite strong responses. They are sometimes exasperating. But we must make sure that they do not — in an age of Big Science, citation-counting, tenure battles and funding crises — become extinct. ■

Philip Ball is a writer based in London.
e-mail: p.ball@btinternet.com

The D'Arcy Thompson Zoology Museum at the University of Dundee, UK, is currently displaying the first works acquired through a grant from the Art Fund to build a collection of art inspired by Thompson's work. A special issue of *Interdisciplinary Science Reviews* on D'Arcy Thompson and his legacy will be published in March 2013.

Books in brief



Anatomies: The Human Body, Its Parts and the Stories They Tell

Hugh Aldersey-Williams VIKING 320 pp. £18.99 (2013)

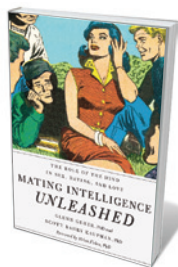
How comfortable are we with our corporeal selves? Hugh Aldersey-Williams, whose best-seller on the periodic table eulogized the elements, here turns a cultivated eye to the body eclectic, limbs, liver, lungs and all. He roves from Rembrandt's *The Anatomy Lesson of Dr Nicolaes Tulp* (1632) — with its intent crowd of medics round a pallid corpse — to his own observations of cadavers and their nested organs, so distinct in hue, density and texture. A seething melange of science and culture follows: the iconic status of the nose, the shapeliness of kidneys, extreme longevity and much more.



Constant Touch: A Global History of the Mobile Phone

Jon Agar ICON BOOKS 288 pp. £12.99 (2013)

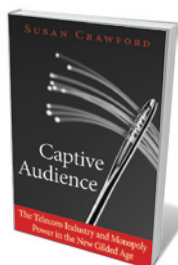
In this update to his 2003 history of the mobile phone, science and technology historian Jon Agar reassesses the ever-evolving nature of this multitasking machine clamped to the ears of billions. Agar reports on the developments with characteristically clear precision. His four-part chronicle deconstructs a typical mobile phone; traces its genesis and evolution, touching on regional differences; dives into the cultures embracing it, from phone-hacking journalists to African farmers; and, weaving in Apple's part in the story, ends with a bang at the smartphone.



Mating Intelligence Unleashed: The Role of the Mind in Sex, Dating, and Love

Glenn Geher and Scott Barry Kaufman OXFORD UNIVERSITY PRESS 320 pp. \$27.95 (2013)

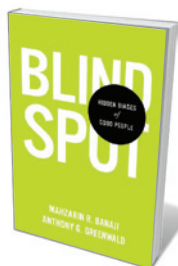
Human courtship is as convoluted as the human mind. In generating and maintaining relationships we can be master tacticians, deploying everything from humour and compassion to bling and 'bad boy' displays. It is this nexus of intelligence and mating that psychologists Glenn Geher and Scott Barry Kaufman explore in this lively, copiously researched treatise on the roles of factors from creativity to biases and emotional intelligence.



Captive Audience: The Telecom Industry and Monopoly Power in the New Gilded Age

Susan Crawford YALE UNIVERSITY PRESS 256 pp. £20 (2013)

The United States may be a pioneer of digitization but, says Susan Crawford, it has lost its early lead in broadband pricing and speed — and, in turn, Internet access. In her history-cum-analysis, telecommunications policy specialist Crawford avers that many US citizens pay significantly more than their counterparts elsewhere; and whereas more than half of South Korean households have fast fibre lines, the US figure is just 7%. With monopolies running US cable companies, it is time, she argues, for government regulation.



Blindspot: Hidden Biases of Good People

Mahzarin R. Banaji and Anthony G. Greenwald DELACORTE 272 pp. \$27 (2013)

Unconscious biases that guide behaviour act like retinal blindspots — even blindsight, in which people with brain damage can grab an object without consciously seeing it. So say psychologists Mahzarin Banaji and Anthony Greenwald, arguing that such quirks can trump ethical intent owing to adaptations that may have been evolutionarily advantageous. Starting with perceptual mistakes based on habits of thought (mindbugs), they cover psychological self-trickery in depth.

Correspondence

Royal Institution is ever more relevant

You mischaracterize the impact and continued relevance of the Royal Institution of Great Britain (RI) by presenting an incomplete picture (*Nature* **493**, 452; 2013).

In 2012 the RI delivered 87 evening events. Of the 46 held in the Faraday Theatre, the mean attendance was 288, much higher than might be expected from a small marketing budget. The thriving schools programme featured 136 lectures and workshops, reaching nearly 13,000 students last year alone. The RI runs mathematics and engineering masterclasses for schoolchildren at more than 140 UK locations. Our activities score very highly using the industry-standard Generic Learning Outcomes, which gauge enjoyment, inspiration, knowledge and understanding.

Thanks to its unique position and unrivalled heritage, the RI attracts the best scientists and science communicators across its programmes, including psychologist Stephen Pinker and physicist Brian Cox.

Even if one thinks that public talks are irrelevant in this age of “the Internet and mass media”, then the RI is still a powerful player. Our televised Christmas Lectures had an audience of 4.2 million in 2011.

The RI Channel website launched just over a year ago and showcases some 300 videos, which have so far attracted almost 1 million views. Some highlight recent RI events, others feature re-digitized footage from our archive, and there are high-quality videos from scientific institutions across the world.

I accept that mistakes made by the RI have led to the current situation. The growing popularity of its programmes — live, broadcast and online — isn't one of them.

Gail Cardew *Royal Institution of Great Britain, London.*
gail@ri.ac.uk

See go.nature.com/12ymkg for more debate on this topic.

Sometimes Bayesian statistics are better

David Vaux argues that experimental biologists should be better versed in classical statistics (*Nature* **492**, 180–181; 2012). We suggest that they might also join the shift to Bayesian statistics that is already under way in many other areas of science.

He defines the 95% confidence interval (CI) as “with 95% confidence, the population mean will lie in this interval”, adding that it is commonly used “to infer where the population mean lies, and to compare two populations”.

However, a 95% CI merely tells us that if we were to sample from the population many times and calculate a 95% CI for each sample, 95% of the calculated CIs would, on average, contain the true population mean. Because classical statistics concern conditional probabilities of data based on assumed true parameter values (namely, the plausibility of the observed or more extreme data, given our assumptions), the 95% CI does not allow a probabilistic inference about “where the population mean lies”.

Bayesian statistics, by contrast, provide conditional probabilities of parameter values — the plausibility of different parameter values — given the data. Bayesian statistics therefore allow for probabilistic inferences about the true population mean and other parameters (J. K. Kruschke *J. Exp. Psychol. Gen.* <http://doi.org/kdb>; 2012).

Researchers often confuse probabilities derived from classical statistics (*P* values, for example) with Bayesian posterior probabilities (G. Gigerenzer *J. Socio-Econ.* **33**, 587–606; 2004). This is because the latter represent what scientists are ultimately interested in: the conditional probability of parameter values or hypotheses, given the data.

Stefan Herzog, Dirk Ostwald

Max Planck Institute for Human Development, Berlin, Germany.
herzog@mpib-berlin.mpg.de

David Vaux replies: I agree that it is often preferable to use Bayesian rather than classical statistics, and that I did not give the full and precise definition of 95% confidence intervals in my Comment. However, the distinction is unimportant for experiments in which *N* is 3 or less (where *N* is the number of independent samples).

Cell and molecular biologists could learn from physicist Ernest Rutherford, who said: “If your experiment needs statistics, you ought to have done a better experiment.” Where *N* is small, they would do well to plot all data points, rather than showing any statistics, classical or Bayesian.

Species splitting puts conservation at risk

A worrying trend over the past decade has been the taxonomic splitting of mammal species, mostly by raising subspecies to species. Because of its potential bearing on conservation, we advise caution in this practice, which we maintain should be based solely on peer-reviewed evidence of biological validity.

This trend is mainly the result of a shift from the biological to the phylogenetic species concept. The biological species concept holds that species are groups of (actually or potentially) interbreeding populations. The phylogenetic species concept and its variants, by contrast, define species either as the smallest cluster sharing genetically transmitted characters, such that all individuals are unequivocally diagnosable on the basis of those characters, or as monophyletic assemblages. In these, all individuals sharing a common ancestor belong to one species, with common ancestry inferred on the basis of shared derived characters (see, for example, C. Groves and P. Grubb *Ungulate*

Taxonomy Johns Hopkins University Press, 2011).

As well as confusing the functional meaning of a species, taxon splitting could be detrimental to conservation. If threatened species are incorrectly split into several units and managed as such, for example in captive breeding or meta-population management, there could be unnecessary loss of genetic variation and an increased risk of extinction.

Such newly designated species call into question the suitability of Red List assessments and the legality of species identified under national laws and international agreements. It is vital to identify true species as conservation units, based on adequate sample sizes and on information pertaining to genetics, morphology and behaviour.

Frank E. Zachos* *Natural History Museum Vienna, Austria.*
frank.zachos@nhm-wien.ac.at
*On behalf of 6 co-signatories (see go.nature.com/4urduh for full list).

Another collider is not the way forward

You encourage the international particle-physics community to support Japan's offer to host the next big particle collider, the International Linear Collider (ILC; *Nature* **492**, 312; 2012). But the case for the ILC is not strong at this point, considering that the Large Hadron Collider (LHC) in Switzerland has revealed only one standard-model Higgs-boson-like particle so far.

The European strategy for particle physics will shortly be updated, but many European countries are hesitant to invest taxpayers' money in another large-scale collider (*Nature Physics* **9**, 1; 2013). Instead, the community should be focusing on the LHC, its future upgrades and other, smaller-scale physics projects.

Tommy Ohlsson *KTH Royal Institute of Technology, Stockholm, Sweden.*
tohsson@kth.se

Brigitte Askonas

(1923–2013)

The ‘grand dame’ of immunology.

Brigitte Askonas, widely known among immunologists as Ita, helped to establish many of the basic mechanisms and components behind the immune response to infection.

Askonas, who died on 9 January, was born in Vienna in 1923 to Czech parents. Her family left Austria in 1938 and settled in Canada in 1940. Educated at McGill University in Montreal, she moved to the United Kingdom in the late 1940s to do a PhD in biochemistry at the University of Cambridge. Then, in 1952, she obtained a staff position in the biochemistry division at the National Institute for Medical Research (NIMR) in Mill Hill, London, to study how milk proteins are made.

To quote Askonas, “the sticky nature of casein, the main milk protein, made it very difficult to purify any of the other milk proteins”. Soon after Askonas joined the NIMR, immunologist John Humphrey demonstrated in a seminar how adding purified antigen to blood serum caused antibodies in the serum to precipitate (antigens are foreign substances that prompt the production of neutralizing proteins or antibodies in the body). Askonas was intrigued and soon turned her attention to the immune system.

In the mid-1950s, Askonas started studying the assembly and secretion of antibody molecules in animals that had received injections of antigens. By 1957, immunology had progressed so much at the NIMR that Humphrey was asked to set up the first immunology division. He invited Askonas to become a founding member. The research effort expanded further after immunologist Peter Medawar became director of the NIMR in 1962. In the early 1960s, the institute became a worldwide centre of immunology research, with Askonas playing a central part — both as a pioneering researcher and as a shaper of the futures of the many young scientists who worked with her.

After studying the assembly and secretion of antibodies — also known as immunoglobulins, which are found throughout the body, including in serum and saliva — Askonas focused on the behaviour of B cells, a type of white blood cell that produces antibodies.

In particular, she looked at which antibodies were produced after different antigens were administered to animals. She established that B cell clones producing particular antibodies rapidly dominated specific neutralizing responses.



In the 1960s, very little was known about how the immune system handles antigens. Askonas discovered that antigens were taken up and partially degraded by macrophages (another type of white blood cell) with a small amount of antigen being retained by the cells. In the late 1960s, Humphrey invited immunologist Emil Unanue to join the NIMR. Working with Askonas, Unanue showed that those macrophages that had retained remnants of antigen could very efficiently induce the production of neutralizing antibodies by B cells, providing the first findings in the nascent field of antigen processing and presentation.

In 1973, Askonas was elected a Fellow of the Royal Society. Three years later, she became head of the Division of Immunology at the NIMR. At this point she began her seminal work on the immune response to infectious agents, moving away from the ‘model antigens’ — extracted for example from chicken eggs — that were heavily studied at the time.

In the mid-1970s, Askonas and several colleagues, including her close friend Bridget Ogilvie, studied how trypanosomes, the protozoa that cause African sleeping sickness,

inhibit and evade the immune response. However, Askonas’s greatest interest became immune responses to viruses mediated by white blood cells called T cells. She focused mostly on influenza, and later also studied respiratory syncytial virus, which particularly afflicts infants.

Cytotoxic T lymphocytes are T cells that kill virally infected cells. Among the first to isolate and clone this type of T cell, Askonas and her colleagues showed that, unexpectedly, the T cells did not distinguish between influenza-virus variants within a serotype. These studies paved the way to understanding viral antigen presentation to T cells. (Her PhD student Alain Townsend went on to make several key findings.)

Askonas’s immense contributions to immunology were recognized by numerous awards and honours. In 2007, for example, she was elected a foreign associate of the US National Academy of Sciences. Last year, at the age of 89, she received an honorary doctorate from the University of Cambridge for achieving the greatest international prominence in her field.

It is impossible to list all the collaborators and trainees worldwide who benefited from Ita’s sharp mind and generosity. She was passionate about introducing young scientists to immunology and worked hard to support students from many countries, especially in the developing world. Many of the PhD students and postdocs she trained are now eminent scientists. She also trained many physicians in experimental immunology.

Ita remained inquisitive throughout. Culture and arts were deeply embedded in her family, and although a scientist through and through, she loved music and art, attending operas and art galleries with her numerous scientific friends. Over the years, she always made time to critically read drafts of papers and grant applications from many scientists, both young and old. She continued to contribute to many studies after her retirement as head of the NIMR immunology division, although she rarely accepted co-authorship.

It is difficult for immunologists to think of a world without Ita. We will miss her — as a force in immunology and as a dear friend. ■

Anne O’Garra is head of the Division of Immunoregulation at the Medical Research Council’s National Institute for Medical Research in Mill Hill, London.
e-mail: aogarra@nimr.mrc.ac.uk

FORUM: Microbiology

The life beneath our feet

Our planet's soils teem with microorganisms that regulate processes from crop productivity to carbon sequestration. Molecular analysis contributes hugely to the characterization of microbial communities, but how can we better understand their ecological functions? Two microbiologists discuss the advantages of data-mining approaches versus targeted experiments.

THE TOPIC IN BRIEF

- The diverse activities of mixed populations of soil microorganisms are fundamental to ecological processes (Fig. 1).
- These communities are also important indicators of responses to changed conditions.
- Rapid DNA sequencing and other molecular-analysis technologies can

provide large-scale data on the combined genomes of a microbial community, potentially revealing unanticipated community members or activities.

- But experiments that test hypotheses on microbe–environment associations may allow more direct identification and analysis of these processes.

Exploring Earth's dark matter

JANET K. JANSSON

Investigation of the crucial environmental parts played by microbes has accelerated with the advent of 'omics' technologies, which has been made possible by low-cost and high-throughput nucleic-acid sequencing, and advances in technologies for studying other biological macromolecules (proteins and metabolites). By studying the total composition of DNA (genomics), RNA (transcriptomics), proteins (proteomics) or metabolites (metabolomics) for multiple organisms, it is possible to produce 'meta-omic' data that encompass all microorganisms in a given habitat. So, can omics provide insight into microbial ecology that cannot be achieved using traditional methods? It is important to keep in mind that omics approaches are not themselves the science, but rather tools, and that the key difference between them and other methods is the amount of data they generate — and the potential that these 'big data' have to expand our knowledge.

Sequencing circumvented the need to generate pure cultures of microorganisms for many studies of microbial processes, but also revealed that most of the 'species' detected were unknown. This led to the concept of microbial life as Earth's 'dark matter', analogous to the unknown realms of the cosmos. In many ways, the challenges faced by astrophysicists and microbial ecologists are indeed

similar, and both fields rely on large quantities of data and supercomputing facilities. But, in microbial ecology, a lack of resources with which to analyse these data has led to a bottleneck in scientific discovery. So, should major investments be made in big-data infrastructure to support the analysis of Earth's microbial communities, similar to those afforded to astrophysics?

One critique against the use of omics in microbial ecology is that the resulting data are merely descriptive. The problem with this criticism is that we don't know what we don't know, similar to studies of the cosmos. There are an estimated 10^{24} stars in the Universe and 10^{30} bacteria on our planet, and I would argue that the discovery of a microbial species with potentially novel functions would be just as interesting as the discovery of a star. Until we dive in and use the best tools at our disposal to explore a given habitat, we often do not even know what questions to ask, or we may be asking the wrong questions.

There are numerous examples that illustrate how omics investigation of microbial samples from diverse environments can lead to discovery. Before metagenome sequencing of the Sargasso Sea¹, it was not known that Earth's oceans contain a predominance of bacteria with a previously unknown light-harvesting system called proteorhodopsin. Metagenomics

also led to the identification of ammonia-oxidizing archaea², which have subsequently been shown to be active in a variety of habitats. Furthermore, combining metagenomic studies with metatranscriptomic and/or metaproteomic studies can reveal which microbial functions are expressed under certain conditions. An example of this approach was the finding of active, yet uncultivated, alkane-degrading *Oceanospirillales* bacteria in the deep sea following the 2010 Deepwater Horizon oil spill in the Gulf of Mexico³.

Another promise of omics is that the data will themselves be hypothesis-generating. The Earth Microbiome Project⁴, which aims to systematically categorize the identities and functions of microbial communities across the planet, is illustrative of this point. One of the project's underlying hypotheses is that certain environmental features are correlated with specific combinations of microbial species, and that knowledge of these patterns can be used in a predictive capacity. For example, studies of the temporal variability of microorganisms in the English Channel, combined with environmental data, led to the proposal that such information could be used to predict the seasonal variability of specific microbes and their metabolic products, and this was shown to be the case⁵.

Although characterizing metagenomes from habitats with high microbial diversity, such as soil, remains challenging, the approach promises to provide a more comprehensive view of the composition and function of their microbial communities than has been possible to date. A recent example was the use of metagenomics to determine that permafrost-soil microbial communities are strongly affected by a short-term thaw⁶. A draft genome of a novel methane-producing bacterium was assembled from the permafrost soil, leading to the hypothesis that these bacteria have a major role in generating methane as the permafrost thaws and suggesting an avenue for further experimentation to test this hypothesis. As these tools are further refined and validated, they should lead to the discovery and understanding of more of our planet's microbial species and capabilities.

Janet K. Jansson is in the Earth Sciences Division, Lawrence Berkeley National Laboratory, Berkeley, California 94720, USA. e-mail: jrjansson@lbl.gov

Think before you sequence

JAMES I. PROSSER

Descriptions of soil microbial communities have been transformed by sequencing and, increasingly, by omics approaches. We must marvel at the technological advances that have made this possible, but they have not been matched by increases in our understanding of the ecology of such communities or links between community composition, diversity and ecosystem function. A potential reason, in my opinion, is an overemphasis on descriptive approaches to soil-microbial ecology compared with hypothesis-driven experiments.

Debates on the relative value of descriptive and data-mining approaches versus hypothesis-driven science are not new. The typical conclusion is that these methods are complementary, rather than mutually exclusive^{7,8}. Hypotheses are constructed to explain observed phenomena, and they may be influenced by existing knowledge, a situation even accepted by philosopher Karl Popper, who wrote⁹: “Some scientists find, or so it seems, that they get their best ideas when smoking; others by drinking coffee or whisky. Thus there is no reason why I should not admit that some may get their ideas by observing, or by repeating observations.”

Hypotheses lack value, however, if they are based solely on observations, or if they are relevant only to the data used to construct them. They are worthwhile if they incorporate novel ideas and flashes of inspiration; they can propose (ideally universal) explanations and mechanisms; and they generate predictions that can be tested by experimentation. It is this process, and not the initial observations, that truly increases understanding. Hypothesis-driven research can thus provide counter-observational, non-intuitive predictions and conceptual frameworks, and can indicate which techniques are, and are not, needed to test them.

Omics descriptions of microbial communities are therefore not analogous to attempts to determine the nature of dark matter in the Universe, which was discovered by, and is being investigated using, hypothesis-driven research. In practice, purely descriptive studies of microbial communities are rare. Most genomic studies compare the sequences present in different, or differently treated, soils, often alongside descriptions of the soils' properties and correlations between these sequences



Figure 1 | Data mining. The abundant microorganisms in Earth's soils perform myriad ecosystem services, many of which are still poorly understood or remain unrecognized. The best ways of identifying and studying these processes is a topic of debate in the ecology community.

and soil properties. Such studies are pointless unless they are used to generate hypotheses, but they are generally driven by a question, although this is often unstated or framed only vaguely. So these studies are, even if unconsciously, based on hypotheses — for example, that gene sequences provide useful information on microbial identity and function, and

“A hypothesis generated by a descriptive study lacks value, and does not increase understanding, unless it is tested by experiment.”

that soil properties influence the assembly and activity of the resident microbe communities. The ability of descriptive studies to increase understanding is obviously limited by the techniques used, which may or may not be relevant to underlying mechanisms. In addition, the non-explicit nature of the ideas that underlie such studies can compromise attempts to explain their findings, for example when assumptions are generated retrospectively or the experimental design is inadequate. It is also noteworthy that data used to generate a hypothesis cannot also be used to test the hypothesis or assess its value. Thus, a hypothesis generated by a descriptive study lacks value, and does not increase understanding, unless it is subsequently tested by experiment.

Unfortunately, the appetite for experimental testing seems to be smaller than that for further descriptive sequencing, even though the *raison d'être* for omic approaches is their greater potential explanatory power. This

may result, in part, from the reduced costs of sequencing. Generating large quantities of sequence data is inexpensive and relatively simple, and it is easier to describe and compare data than to construct and test hypotheses.

Of course, there are examples of hypothesis-driven omics research in microbial ecology. There is also no shortage of questions, ideas, concepts and ecological theory that omics can address, test and extend. Indeed, the enormous complexity and heterogeneity of the soil environment demands courage and intellectual effort in the construction and explicit stating of hypotheses, and critical and focused experimental testing of predictions. It seems to me that this approach offers a more efficient way to use limited resources than the relentless cataloguing and correlation of sequences from ever more soils. In my opinion, it is more challenging and requires greater thought — and is also more enjoyable and rewarding. ■

James I. Prosser is at the Institute of Biological and Environmental Sciences, University of Aberdeen, Aberdeen AB24 3UU, UK. e-mail: j.prosser@abdn.ac.uk

1. Venter, J. C. *et al.* *Science* **304**, 66–74 (2004).
2. Treusch, A. H. *et al.* *Environ. Microbiol.* **7**, 1985–1995 (2005).
3. Mason, O. U. *et al.* *ISME J.* **6**, 1715–1727 (2012).
4. www.earthmicrobiome.org
5. Gilbert, J. A. *et al.* *ISME J.* **6**, 298–308 (2012).
6. Mackelprang, R. *et al.* *Nature* **480**, 368–371 (2011).
7. Kell, D. B. & Oliver, S. G. *BioEssays* **26**, 99–105 (2004).
8. Casadevall, A. & Fang, F. C. *Infect. Immun.* **76**, 3835–3836 (2008).
9. Popper, K. R. *Realism and the Aim of Science* (ed. Bartley, W. W. III) 36 (Routledge, 1983).

SOLID-STATE PHYSICS

A new spin on spintronics

By harnessing the way charge carriers move in a magnetic field, computing blocks based on semiconductor junctions have been made that are reconfigurable and can be interconnected to perform complex logic functions. [SEE LETTER P.72](#)

SAYEEF SALAHUDDIN

Conventional computers rely on the controlled motion of charge in transistors, the basic building blocks of integrated circuits. It has been pointed out, however, that if one could devise electronic devices based on the spin of particles — a quantum-mechanical property responsible for magnetism — completely new computing technologies might emerge that could outperform their conventional analogues. Such 'spintronic' devices have attracted much attention among researchers worldwide¹. On page 72 of this issue, Joo *et al.*² describe a computing scheme that combines the physics of charge motion in a magnetic field with conventional electronic devices in a way that promises to provide a significant step towards a spintronic computing technology*.

Joo and colleagues' scheme hinges on the physics of the Lorentz force on charged particles. When a charged particle moves in a magnetic field, it experiences a force that deflects it in a specific direction. The direction of this force depends on the sign of the charge, the direction of the magnetic field and the direction of motion. It can be reversed by changing the sign of any of these three quantities. So, for example, if carriers move from left to right in a magnetic field, the force experienced by the negatively charged carriers will act in the opposite direction to that experienced by the positively charged carriers.

This property can be exploited in a semiconductor, in which mobile charges that are predominantly negative or positive can be created using a technique called 'doping'. Doping consists of adding a relatively small number of atoms of a different material from that of the host semiconductor to increase its negative (electrons) or positive ('holes') charges. A semiconductor that has mostly mobile electrons is said to be of the n-type category, whereas one that has mainly holes

is dubbed a p-type semiconductor. By combining n-type and p-type, many different p–n junctions can be made. These junctions are the basic building blocks of all semiconductor devices.

One such device is an avalanche diode, in which highly energetic carriers are injected beyond a specific electrical voltage from one side of the junction to the other. Owing to their high kinetic energy, these carriers can generate additional carriers by breaking chemical bonds as they collide with atoms near the junction. In turn, the additional carriers produce more carriers in a chain reaction that leads to an 'avalanche' of carriers (Fig. 1). Avalanche diodes are commercially available and are routinely used to provide voltage reference and electrical-surge protection in integrated circuits. Now, if an avalanche diode is placed in a magnetic field, it is conceivable that, owing to the Lorentz force, the energetic carriers will be deflected and will therefore need a larger voltage to reach the energy threshold above which they can multiply and produce a carrier avalanche. As a result, the current in the diode will decrease^{3–5}.

Joo and colleagues' computing scheme

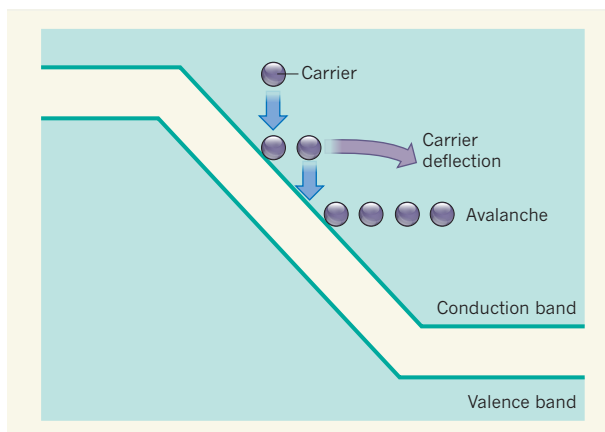


Figure 1 | Bending avalanche carriers. Charge carriers going through an avalanche multiplication process in a p–n semiconductor junction can be deflected by an applied magnetic field. Here, the junction is depicted through its energy-band diagram, which consists of the valence and conduction bands separated by an energy gap. The deflection leads to a reduction in the electrical current running through the junction. Joo *et al.*² have exploited this effect to develop basic computing blocks that can be interconnected to perform complex logic operations.

builds on these concepts. The key idea comes from the fact that, by introducing an asymmetry in the physical geometry of the diode, asymmetry can be created in the device's current–voltage behaviour such that the same voltage will yield a different amount of current for two opposite directions of the magnetic field. Take, for example, the case of a planar device that has two vertically separated p- and n-type semiconductor layers lying in a magnetic field whose direction is completely in the same plane as the device. Because of this in-plane field, charge carriers will be deflected more in one direction in the planar device than in the other. But if an out-of-plane field is applied in the same planar device, carriers will be deflected in all directions equally. For the in-plane field, the asymmetry in carrier deflection dictates that if the avalanche diode is in the 'on' state for a particular direction of the field, it will be 'off' when the field is reversed. Therefore, two avalanche diodes under two opposite directions of the applied field can provide a complementary pair that can be used, almost like conventional transistors, to build up computing blocks.

One interesting aspect of Joo and colleagues' work is the exploitation of mirror symmetry. Because oppositely charged carriers are deflected in opposite directions in the magnetic field, the behaviour of a device that has a top n/bottom p-layer configuration will be exactly opposite to a top p/bottom n one. Thus, the requirement to reverse the direction of the magnetic field to create the complementary pair can be replaced by simply interchanging the ordering of n and p layers. This strategy provides a significant advantage in terms of flexibility in designing complicated and interconnected computing blocks by leveraging existing expertise on semiconductor processing. Also, the fact that the direction of the magnetic field does not have to be reversed is highly advantageous for the operation of the device at low power and for overall scaling up of the technology.

However, improvement is needed before this computing scheme can be viable for practical applications. Even the need to generate a unidirectional magnetic field in an integrated microchip could consume significant energy. One possibility, which the authors suggest, would be to develop technologies in which the required field is produced by thin-film permanent magnets rather than by passing a current through a wire. However, integrating the materials needed for this purpose with conventional semiconductors poses a considerable challenge.

An attractive aspect of this technology is the reconfigurability of the computing blocks such that the

*This article and the paper under discussion² were published online on 30 January 2013.

same block can perform different logic functions depending on an external signal. But this can be achieved only if the magnetic field is reversed. The authors suggest using an effect called spin-transfer torque^{6,7} to attain this reversal. However, such an effect can work only on small magnets, and so this approach may not be scalable. Additionally, the use of energetic carriers in the avalanche diode requires a large amount of energy to be supplied to the diode from external circuits, which is then translated into the kinetic energy of the carriers. This may prove to be a bottleneck for low-power device operation. Nevertheless, none of these difficulties seems to be of a fundamental nature, and greater insight into the capabilities of this technology

may lead to completely new ways of doing computation. ■

Sayeef Salahuddin is in the Department of Electrical Engineering and Computer Sciences, University of California, Berkeley, Berkeley, California 94720, USA.
e-mail: sayeef@berkeley.edu

1. Insight: Spintronics *Nature Mater.* **11**, 367–416 (2012); available at go.nature.com/sarl9
2. Joo, S. *et al.* *Nature* **494**, 72–76 (2013).
3. Delmo, M. P., Yamamoto, S., Kasai, S., Ono, T. & Kobayashi, K. *Nature* **457**, 1112–1115 (2009).
4. Wan, C., Zhang, X., Gao, X., Wang, J. & Tan, X. *Nature* **477**, 304–307 (2011).
5. Lee, J. *et al.* *Appl. Phys. Lett.* **97**, 253505 (2010).
6. Slonczewski, J. C. *J. Magn. Magn. Mater.* **159**, L1–L7 (1996).
7. Berger, L. *Phys. Rev. B* **54**, 9353–9358 (1996).

NEUROSCIENCE

Salty sensations

Salt is important in health and disease, yet how mammals sense it is not completely clear. Evidence in worms suggests that TMC proteins, which are implicated in human hearing, are salt receptors involved in taste. SEE LETTER P.95

BERTRAND COSTE & ARDEM PATAPOUTIAN

Salt is one of the oldest and most common food seasonings. And, together with sweet, bitter, sour and the savoury taste umami, it forms the five modalities of taste¹. Salt is essential for survival, but its intake has to be tightly controlled because overconsumption impairs ion balance and regulation of blood pressure. Indeed, depending on its concentration, salt can be attractive or repulsive in many vertebrates and invertebrates. Little is known about how organisms sense the main component of salt, sodium chloride. In mice, epithelial sodium channels are required for the creatures to exhibit attractive responses to the taste associated with low salt concentrations, but not for them to show aversion to high salt concentrations². It is exciting, therefore, that on page 95 of this issue, Chatzigeorgiou *et al.*³ report a promising candidate for a salt sensor*.

The authors explored the function of transmembrane channel-like protein-1 (TMC-1) in the nematode worm *Caenorhabditis elegans*. The TMC family of multipass transmembrane proteins has eight known members in humans and two (TMC-1 and TMC-2) in *C. elegans*. TMC-1 mutations cause deafness in humans and mice, and in the absence of both TMC-1 and TMC-2 the hair cells of the mouse auditory system cannot show mechanosensory responses⁴. However, it is not clear whether TMCs are bona fide ion channels and/or a component of the elusive channel

complex of the hair-cell mechanotransducer.

Chatzigeorgiou *et al.* report that TMC-1 in *C. elegans* is expressed in a few sensory neurons, including the ASH neurons, which are important for avoidance of noxious stimuli such as nose touch (the worms reverse their direction when they bump into an object with their nose), hyperosmolarity, heavy metals, acids and high salt concentrations⁵. Notably, TMC-1 is detected in the sensory cilia of ASH neurons, the site of sensory transduction in these cells — consistent with a role for TMC-1 in sensory detection.

“These results establish that the TMC-1 protein contributes specifically to sodium sensing.”

behavioural studies following deletion of the *tmc-1* gene demonstrated the relevance of TMC-1 in sensing salt, but not other repulsive chemical or mechanical stimuli such as glycerol, copper and nose touch. They also showed that TMC-1-mediated aversion to salt is specific to sodium ions. In addition, the inability of *tmc-1*-mutant worms to avoid sodium chloride (NaCl) was overcome by inducing the expression of exogenous TMC-1 in ASH neurons.

These results establish that TMC-1 contributes specifically to sodium sensing in ASH neurons. But is TMC-1 sufficient to account for salt sensitivity? To address this question, Chatzigeorgiou *et al.* induced TMC-1 expression specifically in salt-insensitive ASK neurons and found that this protein confers salt

sensitivity *in vivo*. Remarkably, expression of *C. elegans* TMC-1 in four distinct mammalian cell lines induced sodium-activated conductance. The threshold of activation was about 140 millimolar NaCl, which is consistent with the NaCl concentrations that induce aversive responses in worms, mice⁶ and flies⁷.

TMC-1-induced cationic currents occur mainly in response to sodium and are insensitive to amiloride — a blocker of the epithelial sodium channels¹. Intriguingly, low NaCl concentrations (10–150 mM) are attractive to mice, and this attraction is blocked by amiloride. However, mice exposed to higher concentrations of NaCl show aversive responses that are insensitive to amiloride². In light of Chatzigeorgiou and colleagues' data, it seems that TMC-1 constitutes an amiloride-insensitive ion-channel component that, in worms, is activated by high sodium concentrations. The role of TMC proteins in the mammalian taste system remains to be explored.

Can the present data, obtained by genetic studies in worms, be reconciled with the proposal that TMC-1 and TMC-2 are part of the mechanotransduction apparatus in mammalian auditory hair cells⁴? Chatzigeorgiou and co-workers' findings suggest that TMC-1 is not involved in worm mechanotransduction. As for TMC-2, the authors show that *tmc-2* mutations do not exacerbate the effects of *tmc-1* mutations on the response to sodium, which suggests that TMC-2 is not required for salt detection. Nonetheless, as *tmc-2* transcripts are enriched in mechanoreceptors⁸, the role of TMC-2 in worm mechanotransduction — as well as other sensory systems — should be investigated.

By demonstrating that TMC-1 encodes a putative ion channel that is activated by extracellular sodium ions, Chatzigeorgiou *et al.* highlight another role for TMC proteins in sensory transduction. Given that the introduction of worm TMC-1 into human cells can induce sodium-activated currents, similarly cloning and characterizing mammalian TMC proteins could provide further insight into their function. Follow-up studies should confirm whether TMC proteins are pore-forming subunits of ion channels or whether they are modulators of as yet unidentified ion channels, as well as address their physiological role in various species. ■

Bertrand Coste is in the Ion Channels and Sensory Transduction Group, CRN2M, CNRS-Aix-Marseille University, Marseille 13015, France. **Ardem Patapoutian** is in the Molecular and Cellular Neuroscience Department, Dorris Neuroscience Center, The Scripps Research Institute, La Jolla, California, and at the Genomics Institute of the Novartis Research Foundation, San Diego, California 92121, USA.
e-mails: bertrand.coste@univ-amu.fr; apatapoutian@gnf.org

*This article and the paper under discussion³ were published online on 30 January 2013.

1. Yarmolinsky, D. A., Zuker, C. S. & Ryba, N. J. *Cell* **139**, 234–244 (2009).
2. Chandrashekar, J. *et al. Nature* **464**, 297–301 (2010).
3. Chatzigeorgiou, M., Bang, S., Wook Hwang, S. & Schafer, W. R. *Nature* **494**, 95–99 (2013).
4. Kawashima, Y. *et al. J. Clin. Invest.* **121**, 4796–4809 (2011).
5. Bargmann, C. I. & Kaplan, J. M. *Annu. Rev. Neurosci.* **21**, 279–308 (1998).
6. Bachmanov, A. A., Beauchamp, G. K. & Tordoff, M. G. *Behav. Genet.* **32**, 445–457 (2002).
7. Wang, Z., Singhvi, A., Kong, P. & Scott, K. *Cell* **117**, 981–991 (2004).
8. Smith, C. J. *et al. Dev. Biol.* **345**, 18–33 (2010).

FUNGAL BIOLOGY

Multiple mating strategies

Unusual strains of the pathogen *Candida albicans* have been found that contain a single set of chromosomes. Formation of such haploid strains weeds out damaged copies of genes to promote evolution in the human body. [SEE ARTICLE P.55](#)

NEIL A. R. GOW

Fungi exhibit the most complex and diverse strategies for mating and sexual reproduction in nature. The medical importance of the fungal pathogen *Candida albicans*, which causes infections in hundreds of millions of people each year¹, means that it has been highly studied, but the secrets of its life cycle are only now coming to light. Clinical isolates of the fungus are invariably diploid — they contain two of each of its eight chromosomes. But on page 55 of this issue, Hickman *et al.*² report the isolation of *C. albicans* strains that have shed one copy of each chromosome, leading to a haploid state. These haploid strains can mate to regenerate diploid strains, and can undergo all of the developmental life-cycle

stages normally seen in the organism. The implications of these findings are profound, in that they will help us to understand and study the evolution and pathogenesis of this fungus*.

Sexual reproduction is the engine of evolution among eukaryotes (organisms with membrane-bound organelles, including plants, animals and fungi). This reproduction is driven by a process of cell division called meiosis, in which haploid cells are formed from diploid parent cells. The advantage of sexual reproduction is that it enables gene pools to be constantly mixed, both by intra-chromosomal recombination (the exchange of DNA between paired chromosomes) and by the random assortment of chromosome

*This article and the paper under discussion² were published online on 30 January 2013.

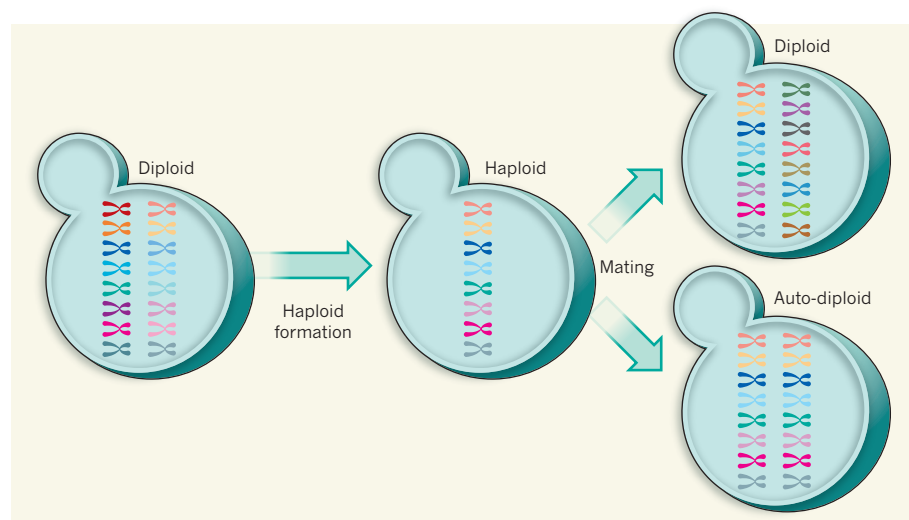


Figure 1 | Asexual evolution. The fungus *Candida albicans* typically exists in a diploid form, that is, it has two copies of each of its eight chromosomes. Hickman *et al.*² show that some rare strains of *C. albicans* undergo spontaneous haploid formation, by shedding one copy of each chromosome. These haploid strains can go on to re-form diploids by mating with another haploid strain, or by mating between themselves or duplicating their single chromosomes, to generate an auto-diploid. The strategy may be one of many that this fungus, which does not undergo normal sexual reproduction, has evolved to discard dangerous genetic variants and create fitter strains.

homologues (one-half of a chromosome pair) into the daughter cells. This process creates unique and genetically diverse individuals, some of which will have genotypes that are well suited for survival under changing environmental pressures. Inbreeding can unmask deleterious mutations when these are passed on in the germ line of both parents. Indeed, each human contains hundreds of seriously damaged genes, but these 'balanced lethal mutations' are compensated for by the presence of a fully functional copy of the gene from one parent. Outbreeding and meiosis therefore ensure evolutionary fitness and minimize the accumulation of harmful mutations.

But some organisms seem to be non-meiotic, so how do they cope? They have evolved other strategies to create genetic diversity, and *C. albicans* is a good example. Its genome contains most or all of the genes that would be required for sexual reproduction by meiosis, but meiosis has never been observed in this species. It has even been suggested that meiosis may be impossible in *C. albicans*, because of balanced lethal mutations scattered throughout the genome of diploid strains that would result in non-viable haploid progeny.

Some genetic variation will be introduced by recombination during mitosis (the replication of diploid cells) and by homozygosis (a process in which one of the two strands of DNA in the chromosomes becomes replicated at the expense of the other). But, in the absence of full meiosis, *C. albicans* uses other reproductive strategies that generate variability. The fungus can mate efficiently as long as it is in a mating-competent cell form called the opaque phase³ — in this phase, diploid cells fuse together to form tetraploid progeny^{4,5}. During this 'parasexual cycle', the tetraploid progeny gradually shed chromosomes to regenerate the diploid state⁶. This 'concerted chromosome loss' seems to be non-meiotic in that it does not result in the chromosome-segregation pattern that would be predicted from meiosis. *C. albicans* can also specifically duplicate some chromosomes to generate aneuploid strains (which have an abnormal number of chromosomes), a process that occurs under the selective pressure exerted by antibiotics⁷. Finally, same-sex mating of diploids (homothallism) has also been reported⁸.

Hickman and colleagues' results add to the repertoire of genetic-reassortment mechanisms for this apparently asexual organism. During a screen of *C. albicans* strains to find those that harbour genetically identical chromosome pairs (homozygous strains), the authors discovered rare strains that had lost a single copy of each of the eight chromosomes and become haploid, apparently by a concerted-chromosome-loss mechanism (Fig. 1). Although previous work had demonstrated that individual chromosomes could be lost⁶, this study establishes that true haploids

of *C. albicans* can be generated by this process, and that these are viable.

The authors found that these haploid strains arose both in laboratory cultures and during infections of mice. The haploids were fully competent to grow as yeasts or to form hyphal filaments (which can invade human tissues) as well as opaque-phase cells that could mate with cells of the opposite mating type. The haploids could also mate with themselves or duplicate single chromosomes to form spontaneous 'auto-diploids' (Fig. 1). The haploid and auto-diploid strains were, however, slower growing and less virulent than their parental heterozygous diploids, and were outcompeted by heterozygous diploid strains in mouse infection models. This accounts for the rareness of these haploid strains and why they have not previously been detected.

Interestingly, Hickman and colleagues also found that the two homologues of each chromosome were not equally likely to be lost during haploid formation. For five of the chromosome pairs, only one homologue was lost, suggesting that this process weeds out chromosomes that harbour lethal gene variants. The possibility therefore emerges that forming mating-competent haploid cells helps to eliminate lethal mutations from the population. The reduced fitness of haploid strains and homozygous auto-diploids relative to the parental diploids is presumably a result of uncovering harmful, but not lethal, mutations. This view is supported by the authors' observation that crossing non-identical haploid strains generated partially heterozygous strains with

notably increased fitness. Thus, this mechanism achieves many of the attributes of sexual reproduction, but without meiosis.

The revelation of this rare ability of *C. albicans* to generate haploid strains adds to the array of alternative mechanisms for genetic recombination used by this fungus in the apparent absence of meiosis. The identification of these strains also opens the way for the development of experimental technologies and resources that are difficult to construct in diploids. Libraries of fungal mutants can now be produced on a haploid background, and genetic crosses can be performed to combine genotypes of interest. *C. albicans* causes around 400,000 potentially lethal infections each year¹, and a better understanding of the pathogen's biology may help us to tackle these. ■

Neil A. R. Gow is at the Institute of Medical Sciences, University of Aberdeen, Aberdeen AB252ZD, UK.

e-mail: n.gow@abdn.ac.uk

1. Brown, G. D. *et al. Sci. Transl. Med.* **4**, 165rv13 (2012).
2. Hickman, M. A. *et al. Nature* **494**, 55–59 (2013).
3. Miller, M. G. & Johnson, A. D. *Cell* **110**, 293–302 (2002).
4. Magee, B. B. & Magee, P. T. *Science* **289**, 310–313 (2000).
5. Hull, C. M., Raisner, R. M. & Johnson, A. D. *Science* **289**, 307–310 (2000).
6. Bennett, R. J. & Johnson, A. D. *EMBO J.* **22**, 2505–2525 (2003).
7. Selmecki, A., Forche, A. & Berman, J. *Science* **313**, 367–370 (2006).
8. Alby, K., Schaefer, D. & Bennett, R. J. *Nature* **460**, 890–894 (2009).

ASTROPHYSICS

Going supernova

When massive stars die as supernovae, these explosions can be seen out to the 'edge of the Universe'. But the stars' nature is often unclear. New observations provide insight into the life of one such star before it exploded. SEE LETTER P.65

ALEXANDER HEGER

Massive stars die violently. Born with masses greater than about ten times that of the Sun, they end their lives as supernovae or powerful γ -ray bursts. But how do they look just before they die? On page 65 of this issue, Ofek *et al.*¹ report observations of an outburst from a massive star just 40 days before it exploded as a supernova. Rare observations such as these offer a means to probe the brief terminal phases of massive stars that are not otherwise easily accessible.

Before 1987, astronomers thought that massive stars evolve to become red supergiant stars and then explode. But then supernova SN 1987A, the closest supernova to be observed since the early seventeenth century,

was detected in the Small Magellanic Cloud², a nearby dwarf galaxy. Because of its proximity to Earth, researchers were able to look at archival data and identify what had been at the location of the supernova. It came as a surprise that the supernova's progenitor star³ was actually a blue, rather than a red, supergiant. But SN 1987A was an unusual case because of its proximity. Nowadays, large observational programmes are in place to study supernovae and their progenitors in nearby galaxies on a regular basis. Some of these programmes have found⁴, for example, that the progenitors are typically less massive than expected. But much remains unknown about their exact nature, particularly just before they explode.

Stars are powered by nuclear-fusion processes in their interior, where light elements

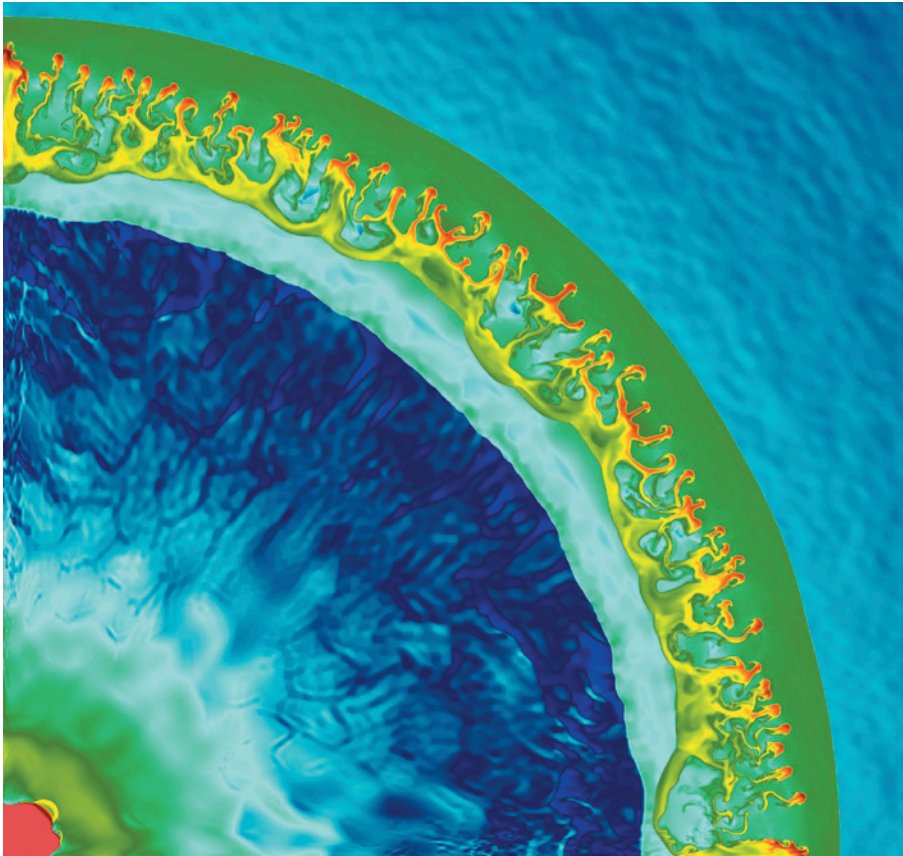


Figure 1 | Shell collision. The image shows a simulation of a collision between two shells of matter ejected by a massive star in two subsequent pulsational pair-instability supernova eruptions¹¹, only years apart, just before the star dies. Displayed is a slice through the upper-right corner of the event. The radius of the shell that contains collision fragments (red knots) is about 500 times the Earth–Sun distance. The colour coding represents gas density ranging from 10^{-11} to 10^{-16} grams per cubic centimetre, with red indicating the highest density and dark blue the lowest. (Image courtesy of Ke-Jung Chen, School of Physics and Astronomy, Univ. Minnesota.)

are forged into increasingly heavier ones⁵. They spend most of their time fusing hydrogen into helium. Then, all but the least-massive stars fuse helium into carbon and oxygen, a stage that takes most of their remaining lifetime. For stars born with more than about six to seven times the Sun's mass, fusion continues and carbon is converted into oxygen, neon and magnesium. For stars born with less than about eight to ten times the Sun's mass, fusion at the star's centre stops, and eventually the star becomes a white dwarf. More-massive stars continue the fusion process in their core at increasingly higher temperature and density, producing silicon and sulphur and finally elements near iron in the periodic table. These elements have the most tightly bound nuclei, and no energy can be gained from fusing them. This 'ash' accumulates in the star's centre and the star ultimately collapses owing to the pull of gravity. In most cases, the star explodes as a supernova, leaving behind a neutron star or a black hole⁶. But some of the most massive stars may contract rapidly soon after using up their carbon, burning much of their remaining fuel in just seconds. This could lead to complete disruption of the star in a powerful

explosion that leaves no remnant⁷, or in a series of supernova-like eruptions of shells of matter, known as pulsational pair-instability supernovae, shortly before the star dies. The collision of subsequent shells of ejecta can trigger some of the brightest observational displays in nature⁸ (Fig. 1).

The advanced burning stages of massive stars are peculiar. The star loses most of its energy, not in the form of observable light from its surface, but rather through neutrinos that escape from the hot centre and cool the star. As a result, these late stages proceed quickly relative to the star's total lifetime of a few million years: the fusion of carbon lasts hundreds of years, and silicon fusion may occur in just a week. Until recently, no sign of these advanced burning stages was expected to become visible at the star's surface, and so it was impossible to tell at which point a star was in its late evolutionary phase, or how soon it would go supernova. Measuring the neutrinos released would offer a window into this phase, but this is a difficult, if not currently impossible, task, even for the closest massive stars, such as Betelgeuse⁹.

In their study, Ofek and colleagues observed

an outburst of about 0.01 solar masses of material from a massive star just roughly one month before it exploded. They suggest that the progenitor star was a fairly massive object, about 50 solar masses. On the basis of statistical considerations, they argue that this eruption is causally related to the ensuing supernova explosion. If confirmed, this system would represent one of the few cases in which additional information has been obtained about the late life of a fairly massive progenitor star — other than that gained from analysing the composition of ejected material or from the supernova itself. Stars with initial masses larger than 20–25 solar masses are found to undergo eruptions. One extreme example of such an eruption is that experienced by the nearby, very massive star Eta Carinae, which may have shed 20 of its initial 150 solar masses in just a few years¹⁰. For most eruptions in massive stars, however, we know little about when they occur and what drives them.

Ofek *et al.* assessed their data within the framework of various theoretical models for such eruptions. They concluded that the timing and nature of the ejecta are best described by a model¹¹ based on hydrodynamic instabilities in the last stages of fusion. But more theoretical work is needed to model these eruptions and to understand the underlying mechanisms. It will also be interesting to investigate how these outbursts relate to other eruptive events observed in similarly massive stars but which are not connected to the final fusion stages. How can the different types of event be teased apart before the supernova is observed? Nevertheless, Ofek and colleagues' observations may change our understanding of the final evolutionary stages of the most massive stars, just as supernova SN 1987A did for their less-massive cousins. ■

Alexander Heger is in the Monash Centre for Astrophysics, School of Mathematical Sciences, Monash University, Victoria 3800, Australia.

e-mail: alexander.heger@monash.edu

1. Ofek, E. O. *et al.* *Nature* **494**, 65–67 (2013).
2. www.cbat.eps.harvard.edu/iauc/04300/04316.html
3. West, R. M., Lauberts, A., Schuster, H.-E. & Jorgensen, H. E. *Astron. Astrophys.* **177**, L1–L3 (1987).
4. Smartt, S. J. *Annu. Rev. Astron. Astrophys.* **47**, 63–106 (2009).
5. Woosley, S. E., Heger, A. & Weaver, T. A. *Rev. Mod. Phys.* **74**, 1015–1071 (2002).
6. Heger, A., Fryer, C. L., Woosley, S. E., Langer, N. & Hartmann, D. H. *Astrophys. J.* **591**, 288–300 (2003).
7. Heger, A. & Woosley, S. E. *Astrophys. J.* **567**, 532–543 (2002).
8. Woosley, S. E., Blinnikov, S. & Heger, A. *Nature* **450**, 390–392 (2007).
9. Odrzywolek, A., Misiaszek, M. & Kutschera, M. *Nucl. Phys. B Proc. Suppl.* **221**, 380 (2011).
10. Davidson, K. & Humphreys, R. M. (eds) *Eta Carinae and the Supernova Impostors* (Springer, 2012).
11. Quataert, E. & Shiode, J. *Mon. Not. R. Astron. Soc.* **423**, L92–L96 (2012).

Spin–orbit coupling in quantum gases

Victor Galitski^{1,2} & Ian B. Spielman¹

Spin–orbit coupling links a particle’s velocity to its quantum–mechanical spin, and is essential in numerous condensed matter phenomena, including topological insulators and Majorana fermions. In solid–state materials, spin–orbit coupling originates from the movement of electrons in a crystal’s intrinsic electric field, which is uniquely prescribed in any given material. In contrast, for ultracold atomic systems, the engineered ‘material parameters’ are tunable: a variety of synthetic spin–orbit couplings can be engineered on demand using laser fields. Here we outline the current experimental and theoretical status of spin–orbit coupling in ultracold atomic systems, discussing unique features that enable physics impossible in any other known setting.

A particle’s spin is quantized. In contrast to the angular momentum of an ordinary (that is, classical) spinning top, which can take on any value, measurements of an electron’s spin angular momentum (or just ‘spin’) along some direction can result in only two discrete values: $\pm\hbar/2$, commonly referred to as spin-up or spin-down. This internal degree of freedom has no classical counterpart; in contrast, a quantum particle’s velocity is directly analogous to a classical particle’s velocity. It is therefore no surprise that spin is a cornerstone for a variety of deeply quantum materials such as quantum magnets¹ and topological insulators². Spin–orbit coupling (SOC) intimately unites a particle’s spin with its momentum, bringing quantum mechanics to the forefront; in materials, this often increases the energy scale at which quantum effects are paramount.

The practical utility of any material is determined, not only by its intrinsic functional behaviour, but also by the energy or temperature scale at which that behaviour is present. For example, the quantum Hall effects—rare examples of truly quantum physics where the spin is largely irrelevant—are confined to highly specialized laboratories because these phenomena manifest themselves only under extreme conditions: at liquid-helium temperatures and high magnetic fields^{3,4}. The integer quantum Hall effect (QHE) was the first observed topological insulator, but it has a broken time-reversal symmetry. This is in contrast with a new class of topological insulators (see Box 1), which rely on SOC instead of magnetic fields for their quantum properties, and are expected to retain their quantum nature up to room temperature².

As fascinating and unusual as the existing topological world of spin–orbit-coupled systems is, all this physics is largely based on a non-interacting picture of independent electrons filling up a prescribed topological landscape. But there is clearly physics beyond this, as suggested by the fractional QHE materials, where interactions between electrons yield phenomena qualitatively different from those encountered in integer QHE. In fractional QHE systems, the charged excitations are essentially just fractions of an electron, with fractional charge: a new type of emergent excitation with no analogue elsewhere in physics. Furthermore, even non-Abelian excitations are possible: a system can be in one of many states of equal energy in which ‘non-Abelions’ exist at the same location, and differ only by the sequence of events that created them. At zero magnetic field, strong interactions and strong SOC can also give rise to fractionalization in topological insulators: the emergence of excitations that are fundamentally different from the constituent particles. We currently know little about these fractional topological insulators, but we do know that they should exist and we also expect them to be stable at a much larger range of

parameters and experimental temperatures than the fractional QHE: perhaps even up to room temperature in solids.

It is ironic then that we focus on the most fundamental behaviour of spin–orbit-coupled systems using ultracold atoms at nano-Kelvin temperatures. These nominally low temperatures are often deceiving, because what matters is not an absolute temperature scale, but rather the temperature relative to other energy scales in the system (for example, the Fermi energy), and from this perspective, ultracold atom systems are often not that cold⁵. However, ultracold atomic systems are among the simplest and most controllable of quantum many-body systems. Although only one type of SOC has been experimentally realized to date, realistic theoretical proposals to create a range of SOC’s abound, many of which have no counterpart in material systems^{6–10}. The laser-coupling technique first experimentally implemented by our team^{11,12}, and now implemented in laboratories around the world, is well suited to realize topological states with one-dimensional atomic systems¹³. In contrast to solid-state systems, in which we do not control or even know with certainty all details of the complicated material structure, ultracold atoms are remarkable in that most aspects of their environment can be engineered in the laboratory. Also, their tunable interactions and their single-particle potentials are both well characterized: the full atomic Hamiltonian is indeed known. This provides a level of control unprecedented in condensed matter and allows one to address basic physics questions at the intersection of material science and many-body theory. To study material systems, theorists create ‘spherical-cow’ models of real materials, whereas in cold atom physics experimentalists can actually make spherical cows.

Interactions—even the simple contact interactions present in cold atom systems—enrich the physics of quantum systems by engendering new phases and phenomena. For example, when combined with SOC, the celebrated superfluid–Mott-insulator transition^{14,15} gives rise to numerous magnetic phenomena in both the insulating and superfluid phases^{16,17}. Such interacting systems are often impossible to treat exactly with current theoretical techniques, but cold atom experiments can directly realize these systems and shed light on the complicated and often exotic physics mediated by the strong interactions. Likewise, by asking basic questions such as how strong interactions can destroy topological insulators—or create them—we can understand the mechanisms underlying fractional topological insulators. These exotic quantum states have not yet been observed, but are present in realistic theoretical descriptions of ultracold atoms with SOC^{18,19}.

Ultracold atoms with synthetic SOC’s⁸ can not only shed light on the outstanding problems of condensed matter physics, but also yield completely

¹Joint Quantum Institute, National Institute of Standards and Technology, and University of Maryland, Gaithersburg, Maryland 20899, USA. ²Condensed Matter Theory Center, University of Maryland, College Park, Maryland 20742, USA.

BOX 1

Topological matter

Topological insulators² are strongly spin–orbit-coupled materials that have seemingly mutually exclusive properties: they are both insulating and metallic at the same time. In their interior (bulk), electrons cannot propagate, whereas their surfaces are highly conducting. To get an insight into the complicated theory of these exotic materials, let us recall that electrons in an insulator fully occupy a certain number of allowed energies (bands) in such a way that the highest occupied state is separated from the lowest empty one by a gap of forbidden energies. Hence, a non-zero energy is required to excite an electron across the gap (that is, to make it move) and small perturbations have almost no effect on the insulator. From this perspective, it is as good as vacuum: nothing moves inside. It may seem that any two such insulators ('vacua') should be indistinguishable, but it is not so! If we ask whether one insulator can be smoothly deformed into another without breaking certain symmetries or turning it into a metal along the way, we find that it is not always possible. Insulators are divided into qualitatively different categories, including trivial insulators (which are much like vacuum) and topological insulators, characterized by a non-zero integer topological index, related to the momentum-dependent spin in spin–orbit-coupled materials such as occurs in HgTe/CdTe quantum wells² (preserving time-reversal symmetry) or from the magnetic field in quantum Hall systems (breaking time-reversal symmetry). Integers cannot change smoothly one into another, but whenever we have a surface of a topological insulator—that is, a boundary with a true vacuum—we do effectively enforce a transition between the media characterized by different integers, say 1 and 0, and the only way to cross between them is either to break symmetries or to close the gap abruptly, that is to create a boundary metal. This is why the topological boundary states are so robust: they are squeezed in between the two vacua (the usual vacuum and the twisted one—the topological insulator) and have nowhere to go.

Although superconductors are very different from insulators in their electromagnetic properties, the characterizations of their excitation spectra are closely related. A superconductor is a condensate of electron pairs (Cooper pairs) behaving like a superfluid. Because it is energetically favourable to form electron pairs in a superconductor, it takes energy to break a pair to create single electrons, just as it takes energy to move an electron across an energy gap in an insulator. So, a superconductor is an insulator for its fermionic excitations and as such can be characterized by topological integers with similar consequences, including boundary states. But the boundary states are unusual at the edges of a topological superconductor, which get filled by weird chargeless and spinless entities: linear combinations of an electron and a hole (an absentee electron). Under certain circumstances these can also become Majorana fermions (zero-energy particles that are their own antiparticle) which were predicted in spin–orbit-coupled systems and might have been observed there³³.

new phenomena with no analogue elsewhere in physics. A notable example of such a unique system is that of spin–orbit-coupled bosons with just two spin states: a synthetic spin-half system. The existence of such particles with real spin-half is prohibited in fundamental physics owing to Pauli's spin-statistics theorem, but synthetic symmetries—imposed by restricting the states available to the atoms—relax these constraints, allowing bosons with pseudo-spin-half to exist²⁰. SOC also results in a wide array of new many-body quantum states, including a zoo of exotic quantum spin states in spin–orbit-coupled Mott insulators^{16,17,21}, unusual spin–orbit-coupled Bose–Einstein condensates (BECs) with a symmetry protected degenerate ground state²², and perhaps even strongly correlated composite fermion phases analogous to the fractional QHE states in electron systems¹⁸. These are just a few examples of phenomena from a trove of exciting physics that is waiting to be uncovered in this emerging and fast-developing field.

Basics of SOC

In any context, SOC requires symmetry breaking because the coupling strength is related to velocity as measured in a preferred reference frame (such as an electron's velocity with respect to its host crystalline lattice, or an atom's velocity with respect to a reference frame defined by its illuminating laser beams). Conventional SOC thus results from relativistic quantum mechanics, where the spin is a fundamental and inseparable component of electrons as described by the Dirac equation. In the non-relativistic limit, the Dirac equation reduces to the familiar Schrödinger equation, with relativistic corrections including an important term coupling the electron's spin to its momentum and to gradients of external potentials. This is the fundamental origin of SOC, which underlies both the $L \cdot S$ coupling—linking the electronic orbital angular momentum L to its spin angular momentum S —familiar in atomic and molecular systems and all spin–orbit phenomena in solids. SOC can most simply be understood in terms of the familiar $-\mu \cdot B$ Zeeman interaction between a particle's magnetic moment μ parallel to the spin, and a magnetic field B present in the frame moving with the particle.

SOC is most familiar in traditional atomic physics where it gives rise to atomic fine-structure splitting, and it is from this context that it acquires its name: a coupling between an electron's spin and its orbital angular momentum about the nucleus. The electric field produced by the charged nucleus gives rise to a magnetic field in the reference frame moving with an orbiting electron (along with an anomalous factor of two resulting from the electron's non-inertial trajectory encircling the atomic centre of mass), leading to a momentum-dependent effective Zeeman energy.

In materials, the connection to a momentum-dependent Zeeman energy is particularly clear. For example, the Lorentz-invariant Maxwell's equations dictate that a static electric field $E = E_0 e_z$ in the laboratory frame (at rest, where $e_{x,y,z}$ are the three Cartesian unit vectors defining the x , y and z directions in space) gives a spin–orbit magnetic field $B_{SO} = (E_0 \hbar / mc^2) \times (k_x e_y - k_y e_x)$ in the frame of an object moving with momentum $\hbar k$, where c is the speed of light in vacuum and m is the particle's mass. The resulting momentum-dependent Zeeman interaction $-\mu B \approx \sigma_x k_y - \sigma_y k_x$ is known as Rashba SOC²³. This often arises from the built-in electric field in two-dimensional semiconductor heterostructures resulting from asymmetries of the confining potential²⁴, and is depicted in Fig. 1. Figure 1d plots a typical spin–orbit dispersion relation, where the minima for each spin state (red or blue) is displaced from zero; in the case of Rashba SOC, this dispersion is axially symmetric, meaning that this double-well structure is replicated for motion in any direction in the e_x – e_y plane. Because of the momentum-dependent Zeeman interaction, the equilibrium alignment of a particle's magnetic moment depends on its velocity. Quantum-mechanically, this implies that the quantum-mechanical eigenstates are generally momentum-dependent superpositions of the initial $|\uparrow\rangle$ and $|\downarrow\rangle$ spin states.

In most condensed matter systems, electrons move in a crystal potential and when there is a potential gradient on the average, effective spin–orbit interactions arise. These usually originate either from a lack of mirror symmetry in two-dimensional systems leading to the Rashba SOC described above²³, or from a lack of inversion symmetry in bulk crystals, leading to other forms of SOC such as the linear Dresselhaus SOC²⁵, described by a Zeeman interaction $-\mu \cdot B \approx \sigma_x k_x - \sigma_y k_y$, reminiscent of that of Rashba SOC.

SOC phenomena are ubiquitous in solids and have been known to exist since the early days of quantum mechanics and band theory. However, rapid developments in the field of spintronics²⁶ have recently moved these phenomena back to the forefront of condensed matter research. This renewal of interest was stimulated by a number of exciting proposals for spintronic devices, whose functionality hinges on an electric-field-dependent coupling between the electron spin and its momentum. Apart from these potential useful applications, spin–orbit-coupled systems turned out to display an amazing variety of fundamentally new and fascinating phenomena: spin-Hall effects^{27,28}, topological insulators², Majorana¹³ and Weyl fermions²⁹, exotic spin textures in disordered systems³⁰, to name just a few.

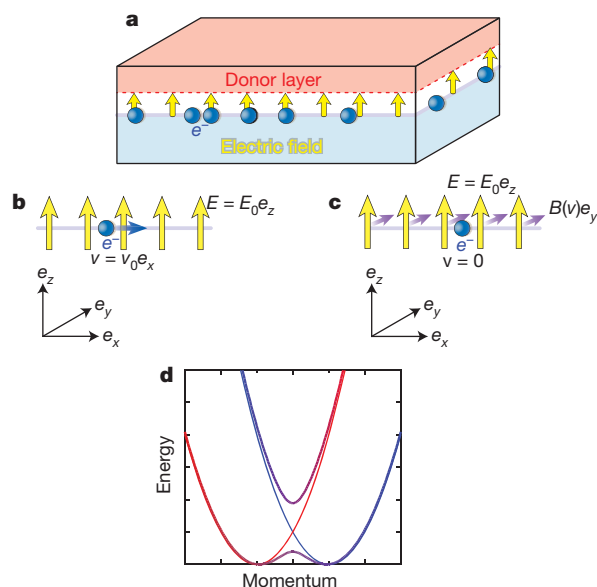


Figure 1 | Physical origin of SOC in conventional systems. **a**, Structural inversion-symmetry breaking. In materials, SOC requires a broken spatial symmetry. For example, the growth profile of two-dimensional GaAs electron (or hole) systems can create an intrinsic electric field, thereby breaking inversion symmetry. **b**, Model system in laboratory frame. The effective model system consists of an electron confined in the e_x – e_y plane (in this example moving along e_x) in the presence of an electric field along e_z . **c**, Model system in electron's frame. In the rest frame of the electron, the Lorentz-transformed electric field generates a magnetic field along e_y (yielding a Zeeman shift) that depends linearly on the electron's velocity. **d**, Dispersion of resulting Rashba SOC. For such systems the SOC is linear, and the usual free-particle $mv^2/2 = p^2/2m$ dispersion relation is altered in a spin-dependent way. In this case, pure Rashba SOC shifts the free-particle dispersion relations for each spin state away from zero (red and blue curves). The crossing point of these curves can be split by an applied magnetic field (smoothly shaded curve).

The problem of synthesizing Majorana fermions stands out as perhaps the most active and exciting area of research combining both profound fundamental physics and a potential for applications. Indeed, Kitaev noticed that a Majorana fermion, being a linear combination of a particle and a hole, should not couple much to external sources of noise and as such should be protected from its debilitating effects and decoherence³¹. Furthermore, when many such Majorana entities are put together, they can form a non-Abelian network capable of encoding and processing topological quantum information and may be ideal for quantum computing applications³². Spin-orbit-coupled superconductors in a magnetic field can host Majorana fermions³³, and creating such topological fermionic superfluids in spin-orbit-coupled quantum gases appears to be within experimental reach, and perhaps cold atoms may become the first experimental platform to create and manipulate non-Abelian quantum matter.

Synthetic SOC in cold atomic gases

As we have seen, SOC links a particle's spin to its momentum, and in conventional systems it is a relativistic effect originating from electrons moving through a material's intrinsic electric field. This physical mechanism for creating SOC—requiring electric fields at the level of trillions of volts per metre for significant SOC—is extremely inaccessible in the laboratory. Such fields exist inside atoms and materials, but not in laboratories. Instead, we engineer SOC in systems of ultracold atoms, using two-photon Raman transitions—each driven by a pair of laser beams with wavelength λ —that change the internal atomic 'spin'.

Physically, this Raman process corresponds to the absorption of a single photon from one laser beam and its stimulated re-emission into the second. Each of these photons carries a tiny momentum with magnitude $p_R = h/\lambda$, called the photon recoil momentum (h is Planck's

constant). Conservation of momentum implies that the atom must acquire the difference of these two momenta (equal to $2p_R$ for counter-propagating laser beams). In most materials, the photon recoil is negligibly small; indeed, in conventional condensed matter systems, the 'optical transitions' are described as having no momentum change. Ultracold atoms, however, are at such low temperatures that the momentum of even a single optical photon is quite large. Thus, as first put forward by Higbie and Stamper-Kurn³⁴, Raman transitions can provide the required velocity-dependent link between the spin and momentum: because the Raman lasers resonantly couple the spin states together when an atom is moving, its Doppler shift effectively tunes the lasers away from resonance, altering the coupling in a velocity-dependent way. Remarkably, nearly all SOC phenomena present in solids can potentially be engineered with cold atoms (and some already have), but in contrast to solids where SOC is an intrinsic material property, synthetic SOC in cold atoms can be controlled at will. Furthermore, unlike the common electron, laser-dressed atoms with their pseudo-spins are not constrained by fundamental symmetries; this leads to a remarkably broad array of 'synthetically engineered' physical phenomena not encountered anywhere else in physics.

Figure 2 depicts the currently implemented technique for creating SOC in ultracold atoms^{12,35–38}. The first step, shown in Fig. 2a, is to select from the many available internal atomic states a pair of states, which we will associate with the pseudo-spin states $|\uparrow\rangle$ and $|\downarrow\rangle$ that together comprise the atomic 'spin'. Two counterpropagating laser beams, which here define the x axis, couple this selected pair of atomic states to the atoms' motion along e_x . Reminiscent of the case for Rashba SOC shown in Fig. 1d, this coupling alters the atom's energy–momentum dispersion, although here only motion along the x direction is affected (Fig. 2c). In the standard language, both Rashba and Dresselhaus SOC are present, and have equal magnitude, giving the effective Zeeman shift $-\mu \cdot B \approx -\sigma_y k_x$. In solids, this symmetric combination of the Rashba and Dresselhaus coupling is called the "persistent spin-helix symmetry point", where it on the one hand allows spin control via SOC, but on the other minimizes the undesirable effect of spin memory loss³⁰.

Given that the effect of SOC on a single particle is equivalent to that of a momentum-dependent Zeeman magnetic field, the particle's dispersion relation (for example, the familiar kinetic energy $mv^2/2 = p^2/2m$ for a free particle) is split into two sub-bands corresponding to two spin-split components, now behaving differently (measured in Fig. 2c). For the linear SOC on which we focus, the band splitting simply shifts the minimum of the dispersion relation by an amount depending on the particle's internal state and the laser coupling strength. This effect, depicted in Fig. 2b, was first measured indirectly in ref. 12, where a BEC was prepared in a mixture of $|\uparrow\rangle$ and $|\downarrow\rangle$ in each of the two minima of the dispersion, and the momentum of the two spins was measured as a function of laser intensity. More recently, the full dispersion curve was measured spectroscopically³⁸, clearly revealing the spin-orbit-coupled structure as a function of momentum (Fig. 2c).

A panoply of SOC can be created, with additional lasers linking together additional internal states. Figure 3 shows a realistic example in which three internal atomic states can be coupled, producing a tunable combination of Rashba and Dresselhaus SOC³⁹. In these cases, one of the three initial atomic states is shifted by a large energy, leaving behind two pseudo-spins comprising a two-level system⁶. A further extension can generate an exotic three-dimensional analogue either to the Rashba SOC, which we call Weyl SOC, that cannot exist in materials¹⁰, or to types of SOC with more than the usual two spin states⁹.

Many-body physics

An example of a unique quantum phenomenon made possible in ultracold atomic systems is that of spin-orbit-coupled BECs. The main ingredient of these exotic many-body states are laser-dressed bosons with states $|\uparrow\rangle$ and $|\downarrow\rangle$ that create a synthetic spin-half system. Because the Pauli spin-statistics theorem prohibits the existence of bosons with real spin-half, this is already a weird and interesting

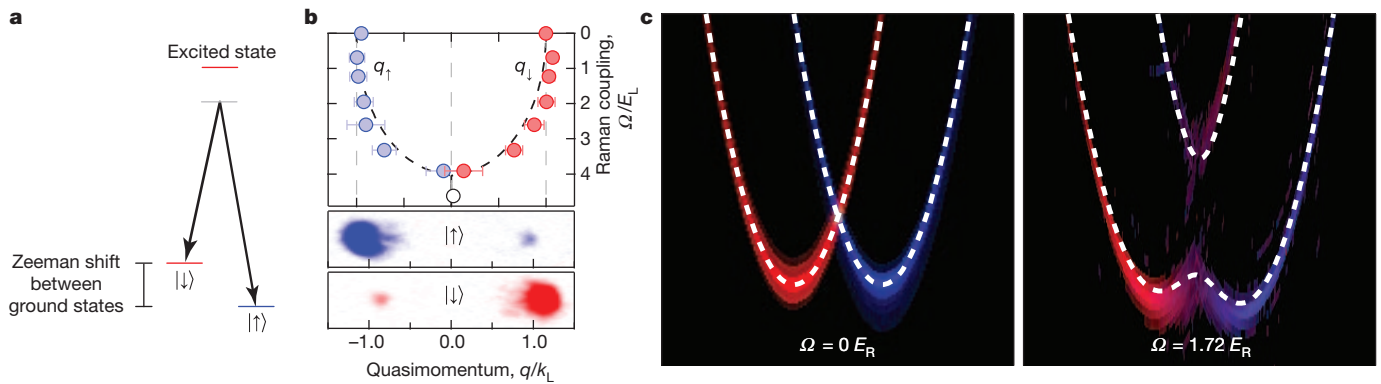


Figure 2 | Laser coupling schemes. **a**, Typical level diagram. In our experiments, a pair of lasers—often counter-propagating—couple together a selected pair of atomic states labelled by $|\uparrow\rangle$ and $|\downarrow\rangle$ that together comprise the atomic ‘spin’. These lasers are arranged in a two-photon Raman configuration that uses an off-resonant intermediate state (grey). These lasers link atomic motion along the x direction to the atom’s spin creating a characteristic spin-orbit coupled energy-momentum dispersion relation. **b**, Minima location. Measured location of energy minimum or minima, where as a function of laser

intensity the characteristic double minima of SOC dispersion move together and finally merge¹². The uncertainties reflect the standard deviation of about 10 measurements. Taken from figure 1 in ref. 12. **c**, Dispersion measured in ^6Li . Complete dispersion before and after laser coupling measured in a ^6Li Fermi gas (data reproduced with permission of M. Zwierlein, from figure 2 of ref. 38), compared with the predicted dispersion (white dashed curves), showing the typical spin-orbit dispersion relations depicted in Fig. 1d.

entity, but when many such entities are brought together in a spin-orbit-coupled system, the weirdness increases further. As the temperature is lowered, the bosons tend to condense, but in contrast to the conventional BEC, where the zero-momentum state is the unique state with lowest energy (the ground state is non-degenerate), spin-orbit bosons can have energy-momentum dispersion with several lowest-energy states (the ground state is degenerate). For example, for Rashba and Dresselhaus SOC (Fig. 2c) there are two such minima; for pure Rashba SOC there is a continuous ring of minima (Fig. 1d); for the Weyl-type SOC there is a sphere of minima¹⁰. This is in contrast with the more conventional case of spinor BECs, which include two or more spin states, but do not alter the energy-momentum dispersion relation.

The bosons’ ‘indecisiveness’ about what state to condense into is partially resolved by their interactions, which limits the states with lowest energy. But unless the interactions break a ‘synthetic time-reversal’ (Kramers) symmetry, some degeneracy must remain, leading to the possibility of exotic states. For example, repulsive bosons with a non-equal combination of Rashba and Dresselhaus SOC are predicted to condense into a strongly entangled many-body ‘cat’ state, where the whole condensate is simultaneously in a superposition of states with equal and opposite momentum. Such many-body cat states have long been sought in various experiments, but have never been convincingly observed. The spin-orbit BECs, existing in a double-well ‘potential’ in momentum space (for example, Fig. 1d) are promising in this regard

because robust arguments support the existence of many-body cat states²²: (1) the symmetry protection of the exact spin degeneracy from splitting and (2) an argument based on the Heisenberg uncertainty relation, which suggests that for the repulsive bosons to stay as far as possible from each other in real space, they should be as close as possible in dual momentum space. An experimental realization of such a many-body cat state would be a major scientific development.

On the experimental front, there are already exciting developments, which include the first realization of an Abelian SOC (corresponding to the persistent spin helix symmetry point, where Rashba and Dresselhaus SOC are identical; see Box 2 for a discussion of the connection to Abelian and non-Abelian gauge fields) and observation of a spin-orbit-coupled BEC with rubidium atoms^{12,35,36}. Exactly as expected, the time-of-flight images of cold spin-orbit coupled bosons feature two peaks that correspond to left- and right-moving condensates flying apart in opposite directions. They however do not represent a cat state (where all the atoms are either in the left-moving or all in the right-moving condensate), but rather are either in a ‘striped’ state (where all of the atoms are in the same state, which involves both positive and negative momenta), or in a phase-separated state of the right- and left-moving condensates in the Abelian spin-orbit system^{12,40–42}; see Fig. 2b.

Spin-orbit-coupled ultracold fermions are intriguing⁸: even the behaviour of two interacting fermions is fundamentally altered with the addition of SOC. Without SOC and in one spatial dimension, any attraction between two fermions, no matter how weak, always gives

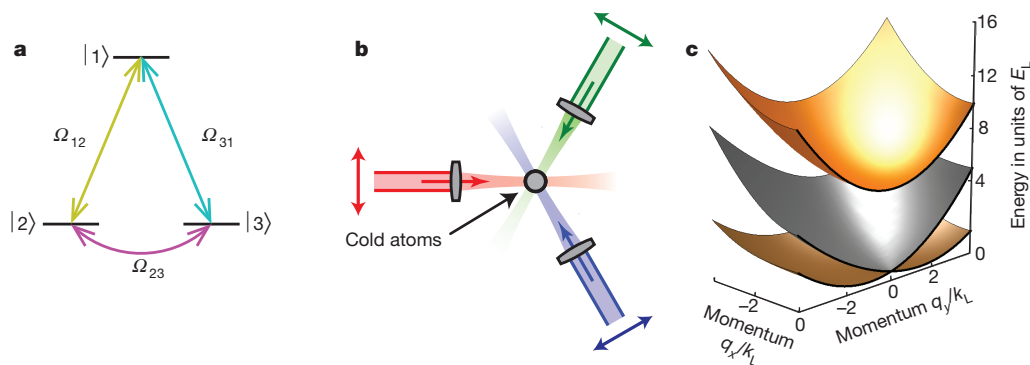


Figure 3 | Generalized SOC. Going beyond current experiments, more complicated forms of SOC may be created. These require both more laser beams and more internal states. **a**, Coupling scheme. Each state is coupled by a two-photon Raman transition, each produced by a pair of the beams shown in

b. The configuration depicted in **a** and **b** could realize a tunable combination of Rashba and Dresselhaus SOC in the alkali atoms³⁹; the outcome is equivalent to that of the well-known tripod configuration⁶ with detuning, but practical in the alkali atoms. **c**, Resulting coupled dispersion relation.

BOX 2

Connection to gauge fields

The forms of SOC discussed in this review are all examples of static gauge fields, which can be mathematically included in the atomic Hamiltonian as $H = (p - A)^2/2m$. The most elementary example of a gauge field is the electromagnetic vector potential defined by $A = A/q$, where q is the electric charge of the particle. This vector potential defines magnetic and electric fields through its spatial and temporal properties: a uniform time-independent vector potential is of no physical consequence. A gauge field A is non-Abelian when the components of the vector $A = (A_x, A_y, A_z)$ are non-commuting operators, for example $A_x A_y \neq A_y A_x$. Such non-Abelian gauge potentials are generic in problems ranging from nuclear magnetic resonance to molecular collisions⁶¹. Using techniques related to those discussed here⁶², it is possible to engineer artificial magnetic¹¹ and electric fields in ultracold atoms. In addition, two recent experiments have demonstrated two alternative techniques for creating artificial gauge fields: in the first, a spatially staggered magnetic field was generated using Raman-assisted tunnelling in a two-dimensional optical lattice^{63,64}; and in the second, an artificial vector potential was created by carefully shaking a one-dimensional optical lattice⁶⁵. An intriguing direction for continued research is to create non-Abelian analogues of the electric and magnetic fields that result from variations in non-Abelian gauge fields^{6,7}, which would lead to quantum-gas analogues to the spin-Hall effect⁶⁶. An exciting direction of research here is engineering dynamic gauge fields in which the field is a dynamical quantum degree of freedom with analogues in quantum electro- and chromo-dynamics^{67–69}.

rise to the formation of a molecule. In two dimensions, the resulting molecular pairing is suppressed but not absent, with an exponentially small binding energy, and in three dimensions there is a threshold below which there is no molecular state. However, in systems with many fermions, many-body effects guarantee the formation of Cooper pairs in any dimension, as long as attraction is present. The crossover between a BEC of molecules to a Bardeen–Cooper–Schrieffer (BCS) condensate of pairs is a smooth transition between physics described in terms of simple ‘native’ molecules to the truly many-body physics of Cooper pairs^{43,44}. SOC provides a completely different avenue for enhancing the pairing between two fermions. The ground-state of the Rashba SOC Hamiltonian consists of a one-dimensional ring in momentum and that of the Weyl SOC is a two-dimensional sphere. This reduces the effective dimensionality and thereby strongly enhances molecular pairing. This ensures that there is no threshold for molecular formation in such spin–orbit systems and that the BEC–BCS crossover is strongly modified^{10,45–47}. The many-body physics of the BCS side is greatly affected as well. The main difficulty in realizing topological fermionic superfluids is the creation of the unconventional pairing mechanism between the atoms^{48,49}. Such topological pairing has proved difficult to achieve using p -wave Feshbach resonances owing to debilitating effects of three-body losses⁵⁰. SOC can create effective interactions too: for example, in analogy to the d -wave interactions recently demonstrated between colliding BECs⁵¹, stable p -wave interactions generated by synthetic spin–orbit are expected and pave the way to atomic topological superfluids^{52–54}. Experimentally, SOC in atomic Fermi systems has been realized in two laboratories^{37,38}, where the basic physical phenomena at the single-particle level were confirmed.

Outlook

Spin–orbit-coupled cold atoms represent a fascinating and fast-developing area of research significantly overlapping with traditional condensed matter physics, but importantly containing completely new phenomena not realizable anywhere else in nature. There is great potential for new experimental and theoretical understanding.

Spin–orbit-coupled BECs and degenerate Fermi gases have now been realized in a handful of laboratories: the experimental study of these systems is just beginning. The immediate outlook centres on implementing the full range of SOC that currently exist only in theoretical proposals: so far only one form of SOC has been engineered in the laboratory. To realize the true promise of these systems, a central experimental task is to engineer SOC that link spin to momentum in two and three dimensions (non-Abelian, and without an analogue in material systems). An unfortunate reality of light-induced gauge fields, as currently envisioned, is the presence of off-resonant light scattering—spontaneous emission—that leads to atom loss, heating of the quantum gas, or both. In the alkali atoms, this heating cannot be fully mitigated by selecting different laser parameters (such as wavelength): as a result, an important direction of future research is finding schemes, or selecting different atomic species, in which this problem is mitigated or absent.

Another goal of research using synthetic spin–orbit-coupled fermions is to realize topological insulating states in optical lattices. A recent breakthrough in condensed matter physics is the understanding that the quantum Hall states represent only a small fraction of a zoo of topological states. A complete classification of those has by now been achieved for fermion systems in thermodynamic limit^{55,56}. This leads to fundamentally different classes of Hamiltonians. For example, no non-trivial insulators exist in three dimensions if time-reversal invariance is allowed to be broken, but the now-famous Z_2 classification exists otherwise⁵⁷. There are nine symmetry classes in each spatial dimension, although not all of them have been realized in solids.

In materials, the symmetries are usually ‘non-negotiable’ while in ‘synthetic’ spin–orbit systems, the symmetries and lack thereof can be controlled at will, opening the possibility of creating and controlling topological states, including topological phases that are not realizable in solids. The ability to tune synthetic couplings suggests that a larger class of non-Abelian gauge structures is within immediate experimental reach. These structures do not have analogues, or even names in solid state physics, but are most appropriately characterized as SU(3)-SOCs. They can be created by focusing on a three-level manifold of dressed states, as opposed to two-level manifold corresponding to spin-up and spin-down states for the usual SOC. The general coupling of the three internal dressed degrees of freedom to particle motion cannot be spanned by three spin matrices, but requires 3×3 Gell–Mann matrices⁵⁸, which form generators of the SU(3) group that has been well studied in the context of elementary particle physics. The algebraic structure, geometry and topology of this complicated group are very different from the familiar spin case, and these differences will have profound observable manifestations.

A completely different way to create such topological matter is related to the non-equilibrium physics of spin–orbit-coupled systems. It is easy to experimentally engineer dynamic synthetic SOC and gauge fields with a prescribed time dependence, providing the opportunity to realize interesting dynamic structures, such as Floquet topological insulators⁵⁹ and Floquet Majorana fermions⁶⁰.

We expect that the most exciting physics in atomic SOC systems will rely on interactions, and lie at the intersection of experiment and theory. What is the physics of spin–orbit-coupled Mott insulators and the corresponding superfluid-to-insulator phase transition? What is the ground state of the Rashba bosons, which were recently argued to undergo a statistical transmutation into fermions? How is the BEC–BCS transition altered by SOC? Each of these questions can only be answered in a partnership between experiment and theory: the underlying physics is so intricate that the correct answer is difficult to anticipate without direct measurement, and the meaning of these measurements can be inexplicable without theoretical guidance.

Received 28 September; accepted 11 December 2012.

1. Balents, L. Spin liquids in frustrated magnets. *Nature* **464**, 199–208 (2010).
2. Hasan, M. Z. & Kane, C. L. Topological insulators. *Rev. Mod. Phys.* **82**, 3045–3067 (2010).

3. von Klitzing, K., Dorda, G. & Pepper, M. New method for high-accuracy determination of the fine-structure constant based on quantized Hall resistance. *Phys. Rev. Lett.* **45**, 494–497 (1980).
4. Tsui, D. C., Stormer, H. L. & Gossard, A. C. Two-dimensional magnetotransport in the extreme quantum limit. *Phys. Rev. Lett.* **48**, 1559–1562 (1982).
5. Bloch, I., Dalibard, J. & Zwerger, W. Many-body physics with ultracold gases. *Rev. Mod. Phys.* **80**, 885–964 (2008).
6. Osterloh, K., Baig, M., Santos, L., Zoller, P. & Lewenstein, M. Cold atoms in non-abelian gauge potentials: from the Hofstadter “Moth” to lattice gauge theory. *Phys. Rev. Lett.* **95**, 010403 (2005).
This paper was an initial proposal suggesting a method of creating SOC in cold atoms (equivalent to a non-Abelian gauge field), in a lattice potential.
7. Ruseckas, J., Juzeliūnas, G., Ohberg, P. & Fleischhauer, M. Non-abelian gauge potentials for ultracold atoms with degenerate dark states. *Phys. Rev. Lett.* **95**, 010404 (2005).
This paper was an initial proposal suggesting a method of creating SOC in cold atoms (equivalent to a non-Abelian gauge field) in the continuum.
8. Liu, X.-J., Borunda, M. F., Liu, X. & Sinova, J. Effect of induced spin–orbit coupling for atoms via laser fields. *Phys. Rev. Lett.* **102**, 046402 (2009).
9. Juzeliūnas, G., Ruseckas, J. & Dalibard, J. Generalized Rashba–Dresselhaus spin–orbit coupling for cold atoms. *Phys. Rev. A* **81**, 053403 (2010).
10. Anderson, B. M., Juzeliūnas, G., Galitski, V. M. & Spielman, I. B. Synthetic 3D spin–orbit coupling. *Phys. Rev. Lett.* **108**, 235301 (2012).
11. Lin, Y.-J., Compton, R. L., Jiménez-García, K., Porto, J. V. & Spielman, I. B. Synthetic magnetic fields for ultracold neutral atoms. *Nature* **462**, 628–632 (2009).
12. Lin, Y.-J., Jiménez-García, K. & Spielman, I. B. Spin-orbit-coupled Bose–Einstein condensates. *Nature* **471**, 83–86 (2011).
This work demonstrated the first observation of SOC in an atomic quantum gas, and observed a quantum phase transition in the resulting two-component spin-orbit-coupled BECs.
13. Sau, J. D., Lutchyn, R. M., Tewari, S. & Das Sarma, S. Generic new platform for topological quantum computation using semiconductor heterostructures. *Phys. Rev. Lett.* **104** (2010).
14. Fisher, M. P. A., Weichman, P. B., Grinstein, G. & Fisher, D. S. Boson localization and the superfluid–insulator transition. *Phys. Rev. B* **40**, 546–570 (1989).
15. Greiner, M., Mandel, O., Esslinger, T., Hansch, T. W. & Bloch, I. Quantum phase transition from a superfluid to a Mott insulator in a gas of ultracold atoms. *Nature* **415**, 39–44 (2002).
16. Radić, J., Di Ciolo, A., Sun, K. & Galitski, V. Exotic quantum spin models in spin–orbit-coupled Mott insulators. *Phys. Rev. Lett.* **109**, 085303 (2012).
17. Cole, W., Zhang, S., Paramakanti, A. & Trivedi, N. Bose–Hubbard models with synthetic spin–orbit coupling: Mott insulators, spin textures, and superfluidity. *Phys. Rev. Lett.* **109**, 085302 (2012).
18. Levin, M. & Stern, A. Fractional topological insulators. *Phys. Rev. Lett.* **103**, 196803 (2009).
19. Sedrakyan, T. A., Kamenev, A. & Glazman, L. I. Composite fermion state of spin–orbit-coupled bosons. *Phys. Rev. A* **86**, 063639 (2012).
20. Ashhab, S. & Leggett, A. J. Bose–Einstein condensation of spin-1/2 atoms with conserved total spin. *Phys. Rev. A* **68**, 063612 (2003).
21. Cai, Z., Zhou, X. & Wu, C. Magnetic phases of bosons with synthetic spin–orbit coupling in optical lattices. *Phys. Rev. A* **85**, 061605 (2012).
22. Stanešcu, T., Anderson, B. & Galitski, V. Spin-orbit coupled Bose–Einstein condensates. *Phys. Rev. A* **78**, 023616 (2008).
23. Bychkov, Y. A. & Rashba, E. I. Oscillatory effects and the magnetic susceptibility of carriers in inversion layers. *J. Phys. Chem.* **17**, 6039–6045 (1984).
24. Meier, L. *et al.* Measurement of Rashba and Dresselhaus spin–orbit magnetic fields. *Nature Phys.* **3**, 650–654 (2007).
25. Dresselhaus, G. Spin-orbit coupling effects in zinc blende structures. *Phys. Rev.* **100**, 580–586 (1955).
26. von Zutic, I., Fabian, J. & Das Sarma, S. Spintronics: fundamentals and applications. *Rev. Mod. Phys.* **76**, 323–410 (2004).
27. Sinova, J. *et al.* Universal intrinsic spin Hall effect. *Phys. Rev. Lett.* **92**, 126603 (2004).
28. Kato, Y. K., Myers, R. C., Gossard, A. C. & Awschalom, D. D. Observation of the spin Hall effect in semiconductors. *Science* **306**, 1910–1913 (2004).
29. Burkov, A. A. & Balents, L. Weyl semimetal in a topological insulator multilayer. *Phys. Rev. Lett.* **107**, 127205 (2011).
30. Koralek, J. D. *et al.* Emergence of the persistent spin helix in semiconductor quantum wells. *Nature* **458**, 610–613 (2009).
31. Kitaev, A. Y. Unpaired Majorana fermions in quantum wires. *Phys.-Usp.* **44**, 131–136 (2001).
This paper proposed that Majorana fermions can exist at the end of one-dimensional superconducting wires, an idea that is directly relevant to one-dimensional atomic Fermi gases with SOC.
32. Alicea, J., Oreg, Y., Refael, G., von Oppen, F. & Fisher, M. P. A. Non-Abelian statistics and topological quantum information processing in 1D wire networks. *Nature Phys.* **7**, 412–417 (2011).
33. Mourik, V. *et al.* Signatures of Majorana fermions in hybrid superconductor–semiconductor nanowire devices. *Science* **336**, 1003–1007 (2012).
34. Higbie, J. & Stamper-Kurn, D. M. Periodically dressed Bose–Einstein condensate: a superfluid with an anisotropic and variable critical velocity. *Phys. Rev. Lett.* **88**, 090401 (2002).
This paper proposed loading quantum degenerate gases into the laser-dressed states used in current SOC experiments.
35. Fu, Z., Wang, P., Chai, S., Huang, L. & Zhang, J. Bose–Einstein condensate in a light-induced vector gauge potential using 1064-nm optical-dipole-trap lasers. *Phys. Rev. A* **84**, 043609 (2011).
36. Zhang, J.-Y. *et al.* Collective dipole oscillations of a spin–orbit coupled Bose–Einstein condensate. *Phys. Rev. Lett.* **109**, 115301 (2012).
37. Wang, P. *et al.* Spin-orbit coupled degenerate Fermi gases. *Phys. Rev. Lett.* **109**, 095301 (2012).
This was the first observation of SOC in an atomic Fermi gas.
38. Cheuk, L. *et al.* Spin-injection spectroscopy of a spin–orbit coupled Fermi gas. *Phys. Rev. Lett.* **109**, 095302 (2012).
This paper describes the observation of SOC in an atomic Fermi gas, and a direct spectroscopic measurement of the SOC dispersion relation.
39. Campbell, D. L., Juzeliūnas, G. & Spielman, I. B. Realistic Rashba and Dresselhaus spin–orbit coupling for neutral atoms. *Phys. Rev. A* **84**, 025602 (2011).
40. Wang, C., Gao, C., Jian, C.-M. & Zhai, H. Spin-orbit coupled spinor Bose–Einstein condensates. *Phys. Rev. Lett.* **105**, 160403 (2010).
41. Ho, T.-L. & Zhang, S. Bose–Einstein condensates with spin–orbit interaction. *Phys. Rev. Lett.* **107**, 150403 (2011).
42. Wu, C.-J., Mondragon-Shem, I. & Zhou, X.-F. Unconventional Bose–Einstein condensations from spin–orbit coupling. *Chin. Phys. Lett.* **28**, 097102 (2011).
43. Giorgini, S., Pitaevskii, L. P. & Stringari, S. Theory of ultracold atomic Fermi gases. *Rev. Mod. Phys.* **80**, 1215–1274 (2008).
44. Ketterle, W. & Zwerlein, M. W. Making, probing and understanding ultracold Fermi gases. In *Proc. International School of Physics “Enrico Fermi”, Course CLXIV (Varenna, 20–30 June 2006)* (eds Inguscio, M., Ketterle, W. & Salomon, C.) 95–287 (IOS Press, 2008).
45. Chaplik, A. V. & Magarill, L. I. Bound states in a two-dimensional short range potential induced by the spin–orbit interaction. *Phys. Rev. Lett.* **96**, 126402 (2006).
46. Gong, M., Tewari, S. & Zhang, C. BCS–BEC crossover and topological phase transition in 3D spin–orbit coupled degenerate Fermi gases. *Phys. Rev. Lett.* **107**, 195303 (2011).
47. Yu, Z.-Q. & Zhai, H. Spin-orbit coupled Fermi gases across a Feshbach resonance. *Phys. Rev. Lett.* **107**, 195305 (2011).
48. Veilleux, M., Sheehy, D., Radzihovsky, L. & Gurarie, V. Superfluid transition in a rotating Fermi gas with resonant interactions. *Phys. Rev. Lett.* **97**, 250401 (2006).
49. Levinsen, J., Cooper, N. R. & Gurarie, V. Strongly resonant *p*-wave superfluids. *Phys. Rev. Lett.* **99**, 210402 (2007).
50. Regal, C. A., Ticknor, C., Bohn, J. L. & Jin, D. S. Tuning *p*-wave interactions in an ultracold Fermi gas of atoms. *Phys. Rev. Lett.* **90**, 053201 (2003).
51. Williams, R. A. *et al.* Synthetic partial waves in ultracold atomic collisions. *Science* **335**, 314–317 (2012).
52. Zhang, C., Tewari, S., Lutchyn, R. M. & Das Sarma, S. *p_x+ip_y* superfluid from *s*-wave interactions of fermionic cold atoms. *Phys. Rev. Lett.* **101**, 160401 (2008).
53. Massignán, P., Sanpera, A. & Lewenstein, M. Creating *p*-wave superfluids and topological excitations in optical lattices. *Phys. Rev. Lett.* **105**, 053607 (2010).
54. Seo, K., Han, L. & Sá de Melo, C. Emergence of Majorana and Dirac particles in ultracold fermions via tunable interactions, spin–orbit effects, and Zeeman fields. *Phys. Rev. Lett.* **109**, 105303 (2012).
55. Schnyder, A. P., Ryu, S., Furusaki, A. & Ludwig, A. W. W. Classification of topological insulators and superconductors in three spatial dimensions. *Phys. Rev. B* **78**, 195125 (2008).
56. Kitaev, A. Periodic table for topological insulators and superconductors. *AIP Conf. Proc.* **1134**, 22–30 (2009).
57. Moore, J. E. & Balents, L. Topological invariants of time-reversal-invariant band structures. *Phys. Rev. B* **75**, 121306(R) (2007).
58. Gell-Mann, M. Symmetries of baryons and mesons. *Phys. Rev.* **125**, 1067–1084 (1962).
59. Lindner, N. H., Refael, G. & Galitski, V. Floquet topological insulator in semiconductor quantum wells. *Nature Phys.* **7**, 490–495 (2011).
60. Jiang, L. *et al.* Majorana fermions in equilibrium and driven cold atom quantum wires. *Phys. Rev. Lett.* **106**, 220402 (2011).
61. Shapere, A. & Wilczek, F. *Geometric Phases in Physics* (World Pacific, 1989).
62. Dalibard, J., Gerbier, F., Juzeliūnas, G. & Ohberg, P. Artificial gauge potentials for neutral atoms. *Rev. Mod. Phys.* **83**, 1523–1543 (2011).
63. Jaksch, D. & Zoller, P. Creation of effective magnetic fields in optical lattices: the Hofstadter butterfly for cold neutral atoms. *N. J. Phys.* **5**, 56 (2003).
64. Aidelburger, M. *et al.* Experimental realization of strong effective magnetic fields in an optical lattice. *Phys. Rev. Lett.* **107**, 255301 (2011).
65. Struck, J. *et al.* Tunable gauge potential for neutral and spinless particles in driven optical lattices. *Phys. Rev. Lett.* **108**, 225304 (2012).
66. Zhu, S.-L., Fu, H., Wu, C. J., Zhang, S. C. & Duan, L. M. Spin Hall effects for cold atoms in a light-induced gauge potential. *Phys. Rev. Lett.* **97**, 240401 (2006).
67. Bermudez, A. *et al.* Wilson fermions and axion electrodynamics in optical lattices. *Phys. Rev. Lett.* **105**, 190404 (2010).
68. Zohar, E., Cirac, J. & Reznik, B. Simulating compact quantum electrodynamics with ultracold atoms: probing confinement and nonperturbative effects. *Phys. Rev. Lett.* **109**, 125302 (2012).
69. Banerjee, D. *et al.* Atomic quantum simulation of dynamical gauge fields coupled to fermionic matter: from string breaking to evolution after a quench. *Phys. Rev. Lett.* **109**, 175302 (2012).

Acknowledgements We acknowledge the financial support of the NSF through the Physics Frontier Center at JQI; the ARO with funds from the Atomtronics MURI, DARPA’s OLE Program (I.B.S.), and directly (V.G.).

Author Contributions Each author contributed equally to writing this review.

Author Information Reprints and permissions information is available at www.nature.com/reprints. The authors declare no competing financial interests. Readers are welcome to comment on the online version of the paper. Correspondence should be addressed to I.B.S. (ian.spielman@nist.gov).

The ‘obligate diploid’ *Candida albicans* forms mating-competent haploids

Meleah A. Hickman¹, Guisheng Zeng², Anja Forche³, Matthew P. Hirakawa⁴, Darren Abbey¹, Benjamin D. Harrison¹, Yan-Ming Wang², Ching-hua Su⁵, Richard J. Bennett⁴, Yue Wang² & Judith Berman^{1,6}

Candida albicans, the most prevalent human fungal pathogen, is considered to be an obligate diploid that carries recessive lethal mutations throughout the genome. Here we demonstrate that *C. albicans* has a viable haploid state that can be derived from diploid cells under *in vitro* and *in vivo* conditions, and that seems to arise through a concerted chromosome loss mechanism. Haploids undergo morphogenetic changes like those of diploids, including the yeast–hyphal transition, chlamydospore formation and a white–opaque switch that facilitates mating. Haploid opaque cells of opposite mating type mate efficiently to regenerate the diploid form, restoring heterozygosity and fitness. Homozygous diploids arise spontaneously by auto-diploidization, and both haploids and auto-diploids show a similar reduction in fitness, *in vitro* and *in vivo*, relative to heterozygous diploids, indicating that homozygous cell types are transient in mixed populations. Finally, we constructed stable haploid strains with multiple auxotrophies that will facilitate molecular and genetic analyses of this important pathogen.

The opportunistic fungal pathogen *C. albicans* has been studied extensively since the 1800s and has been considered a strictly diploid organism with no haploid state. The diploid nature of the organism has complicated genetic and genomic analyses of *C. albicans* biology and virulence. Studies in the 1960s through the early 1980s debated the ploidy of *C. albicans*, and proposed that a haploid state existed based on cell size heterogeneity¹, parasexual genetics² and estimates of DNA content by fluorimetry^{1,3}. Haploid clinical isolates were reported^{2,3}, but were later found to be diploid in genome content or were shown to be non-*albicans* *Candida* species (T. Suzuki, personal communication and Supplementary Fig. 1). Research supporting the diploid nature of the organism included DNA content measurements that suggested a genome size similar to that of diploid *Saccharomyces cerevisiae*^{4,5}, molecular studies that demonstrated the need to delete two gene copies to produce a null mutant^{6,7}, genetic studies that demonstrated heterozygosity of specific alleles^{8,9}, and ultimately the complete genome sequence, which revealed heterozygosity throughout much of the genome¹⁰. This, together with the predominantly clonal nature of *C. albicans* within an individual host^{11,12}, was interpreted as evidence that the organism spent most, if not all, of its life cycle in a diploid state.

The ‘obligate diploid’ nature of *C. albicans* was proposed to be due to recessive lethal mutations dispersed throughout the genome^{13,14}. However, studies of *C. albicans* chromosome monosomy^{15,16}, recombination¹⁷ and haplotype mapping¹⁸ demonstrated that homozygosity of certain chromosomes can occur, arguing against this balanced lethal mutation hypothesis. A diploid–tetraploid parasexual cycle was also discovered in *C. albicans* and shown to involve a switch to the ‘opaque’ physiological state that renders cells mating-competent^{19,20}, conjugation between opaque diploids to form tetraploids^{21,22}, and subsequent ploidy reduction resulting in diploid progeny that often carry multiple aneuploid chromosomes^{18,23}. Importantly, specific aneuploid chromosomes can provide a selective advantage under stressful conditions such as exposure to antifungal drugs²⁴. Parasexual ploidy reduction

in tetraploids occurs via a non-meiotic process termed ‘concerted chromosome loss’. This process can facilitate the rapid generation of diversity through the production of homozygous and aneuploid progeny, under conditions where outcrossing in the host is unlikely²⁵. If a haploid state for *C. albicans* were to exist, it could facilitate the elimination of lethal alleles from the population. Furthermore, mating between different haploids could promote adaptation to changing conditions within the mammalian host. With the advent of whole-genome approaches that can distinguish ploidy states, it is now possible to ask if *C. albicans* exists, even transiently, in the tetraploid or the haploid state.

Detection of haploid *C. albicans* cells

Haploid *C. albicans* was serendipitously discovered during experiments to follow loss of heterozygosity (LOH) at multiple independent loci. Using a multiply marked derivative of SC5314, the laboratory reference strain¹⁰, we selected for an initial LOH event at the *GAL1* locus (encoding galactokinase) by growth on 2-deoxygalactose (2-DOG) and subsequently screened for additional LOH events at four other heterozygous loci. Importantly, growth in 2-DOG does not affect LOH rates (Supplementary Fig. 2) and as such, the selection for cells with an LOH event does not artificially induce LOH. Amongst the approximately 2,500 galactokinase-negative (Gal[−]) isolates, 42 showed additional LOH events and intriguingly one strain, Haploid I, was homozygous for all of the markers tested, as well as for multiple single nucleotide polymorphisms (SNPs) on every chromosome. Analysis of DNA content in Haploid I by flow cytometry indicated that the genome had half the amount of DNA of that in a diploid control (Fig. 1a).

Once we became aware that haploid *C. albicans* cells could be detected, we used flow cytometry to screen isolates from many sources, including *in vitro* stresses²⁶, from which one haploid isolate (Haploid IV) was identified amongst small colonies growing in the presence of fluconazole (in the halo of an E-test strip), a commonly

¹Department of Genetics, Cell Biology & Development, University of Minnesota, Minneapolis, Minnesota 55455, USA. ²Institute of Molecular and Cell Biology, Agency for Science, Technology & Research, Singapore 138673, Singapore. ³Bowdoin College, Brunswick, Maine 04011, USA. ⁴Department of Molecular Microbiology and Immunology, Brown University, Providence, Rhode Island 02912, USA.

⁵Department of Microbiology and Immunology, Taipei Medical University, Taipei, Taiwan. ⁶Department of Molecular Microbiology and Biotechnology, George Wise Faculty of Life Sciences Tel Aviv University, Ramat Aviv, 69978 Israel.

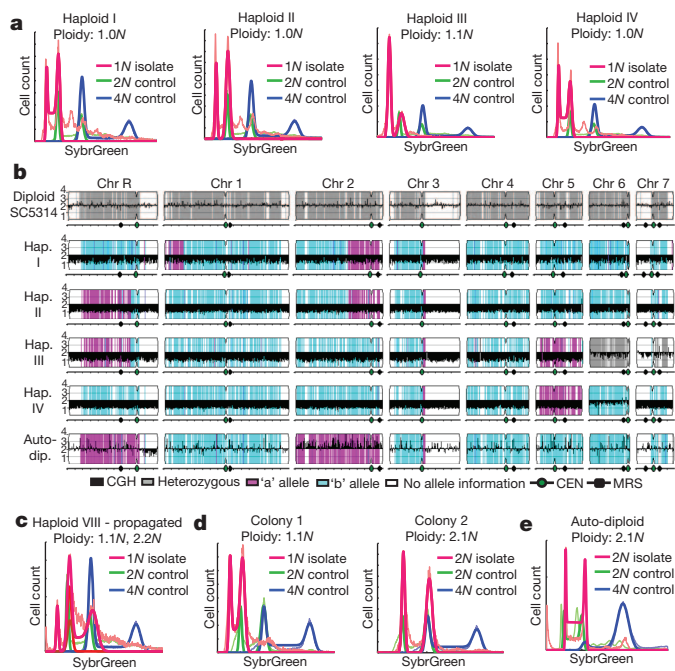


Figure 1 | *C. albicans* haploid and auto-diploid genotypes. **a**, Flow cytometry analysis of DNA content of haploid strains (red) compared to diploid (SC5314, green) and tetraploid (RBY18, blue) control strains. Thin lines, raw data; bold lines, 'best fit' data as described in the Methods Summary. **b**, SNP/CGH array analysis of indicated strains (left) showing copy number (\log_2 ratio, black) and SNP allele information (grey, heterozygous; magenta, allele 'a'; cyan, allele 'b'; white, no SNP data). CEN, centromere; Chr, chromosome; MRS, major repeat sequence. **c**, Flow cytometry after prolonged propagation of a haploid revealed a mixture of ploidies within a single population (c), whereas single colonies from this haploid (d) show distinct haploid (left) and diploid (right) ploidy. **e**, Flow cytometry of a homozygous auto-diploid.

used antifungal drug. We also screened *C. albicans* cells isolated from *in vivo* mouse models of candidaemia²⁷ and candidiasis²⁸ and discovered several additional isolates with 1N DNA content. The overall population of post-*in vivo* isolates screened for ploidy included approximately 300 isolates from YPD plates (Gal⁺), and approximately 740 isolates from the 2-DOG selection plates (Gal⁻), and only the 2-DOG-resistant (2-DOG^R) colonies contained isolates that were haploid. We found that 3.2% of 2-DOG^R colonies from the OPC model were haploid (10 out of 312), whereas 1.2% of 2-DOG^R colonies from the systemic model were haploid (5 out of 431). Because LOH frequencies *in vivo* are $\sim 10^{-3}$ (ref. 29), this indicates that detectable haploids arose at a frequency of 1–3 per 100,000 cells. Loss of *GAL1* is often, but not always, associated with the haploid state (for example, Haploid IV), especially in diploid progenitors that are heterozygous for this locus. In total, we characterized eleven strains with haploid (or close to haploid) flow cytometry profiles (Fig. 1a, Supplementary Fig. 3 and Supplementary Table 1) that were derived from multiple independent and varied sources.

Because previous reports of haploid *C. albicans*³ included misidentified species (Supplementary Fig. 1), we determined if these newly identified isolates were bona fide *C. albicans* by PCR amplifying and sequencing the mating type-like (*MTL*) locus. All isolates contained sequences identical to either the *MTLa* or *MTL α* alleles of SC5314 (Supplementary Fig. 4 and data not shown). Next, we analysed the haploid genomes by hybridization to SNP/CGH (comparative genome hybridization) arrays³⁰ to determine allelic ratios and relative chromosome copy numbers. Six isolates were completely euploid (Fig. 1b and Supplementary Fig. 5); in the remaining five haploids, one or two chromosomes (chromosomes 6 and 7) were disomic.

These disomic chromosomes were heterozygous except in one isolate (Haploid IV) where the disomic chromosome (chromosome 6) was homozygous.

Based on the *C. albicans* haplotype map³⁰, each haploid chromosome primarily contained alleles from only one parental homologue with few, if any, obvious crossovers detectable (Fig. 1b and Supplementary Fig. 5). This implies that haploids did not arise through conventional meiosis, which usually requires at least one crossover per chromosome³¹. The few crossovers detected probably arose by mitotic recombination before selection for LOH events. For example, Haploid I was isolated following selection for loss of *GAL1*, which is within the crossover region on chromosome 1. Furthermore, in *C. albicans* haploids (Fig. 1b and Supplementary Fig. 5), the majority of disomic chromosomes were heterozygous, which would arise after mis-segregation of homologues in meiosis I. Such meiosis I mis-segregation is not seen in *Drosophila* male meioses, which lack recombination³²; it is seen in *Candida lusitanae* meiotic progeny, which undergo high levels of recombination³³. The low level of genetic recombination together with the presence of heterozygous disomic chromosomes remains most consistent with random homologue segregation in *C. albicans*. Accordingly, we propose that haploids arise through a concerted chromosome loss mechanism similar to that described for the diploid–tetraploid *C. albicans* parasexual cycle²³, although a non-conventional meiotic program cannot be completely discounted.

The existence of haploids refutes the argument that recessive lethal alleles are present on each *C. albicans* homologue^{13,14}. Nonetheless, the absence of some chromosomal homologues from the haploid progeny indicates that recessive lethal alleles may exist. Indeed, only the 'b' homologues for chromosomes 3, 4, 6, 7 and most of chromosome 1 were detected in the haploids analysed (Fig. 1b and Supplementary Fig. 5). Interestingly, a similar homologue bias was seen in diploid parasexual progeny derived from SC5314 (ref. 18). In contrast, homologues of chromosome 5, which carries the *MTL*, appeared in equal numbers (six *MTLa* and five *MTL α*) and were entirely of one or the other parental haplotype. Similarly, both homologues of chromosomes R and 2 were observed. As such, homologues from more than half the chromosomes (chromosomes 3, 4, 6, 7 and most of chromosome 1) potentially carry at least one recessive lethal mutation and may limit the frequency with which viable haploids arise. Accordingly, we propose that haploidization may provide an effective mechanism for eliminating recessive lethal mutations from the predominantly diploid populations of *C. albicans*.

Auto-diploidization of haploids

In the course of these studies, prolonged propagation of haploid isolates yielded cultures with a mixed population of haploid and diploid cells (Fig. 1c). Subsequent colony purification yielded distinct haploid and/or diploid populations (Fig. 1d). Surprisingly, some haploid isolates also diploidized during the process of strain shipping, which involved storage, transit and revival from partial dehydration on a solid surface. For example, a potential haploid isolate identified in Taiwan was sent to Minnesota on sterile filter paper. Once revived and grown in liquid culture, the genome was diploid (Fig. 1e) and homozygous for all SNPs (Fig. 1b, 'auto-dip.'). indicating auto-diploidization from a haploid phase. Whereas homozygous diploids could arise through mitotic defects or by self-mating³⁴, mating between cells of the same mating type was not detectable, as discussed below. Thus, we suggest that auto-diploids arise through mitotic defects that may be analogous to the auto-diploidization events in vertebrate haploid stem-cell cultures^{35–37}.

Haploid morphogenesis and mating

Consistent with reduced ploidy content in other yeast species³⁸, haploid *C. albicans* cells were smaller, on average, for both cell and nuclear size compared to diploid cells (Fig. 2a and Supplementary Fig. 6). The

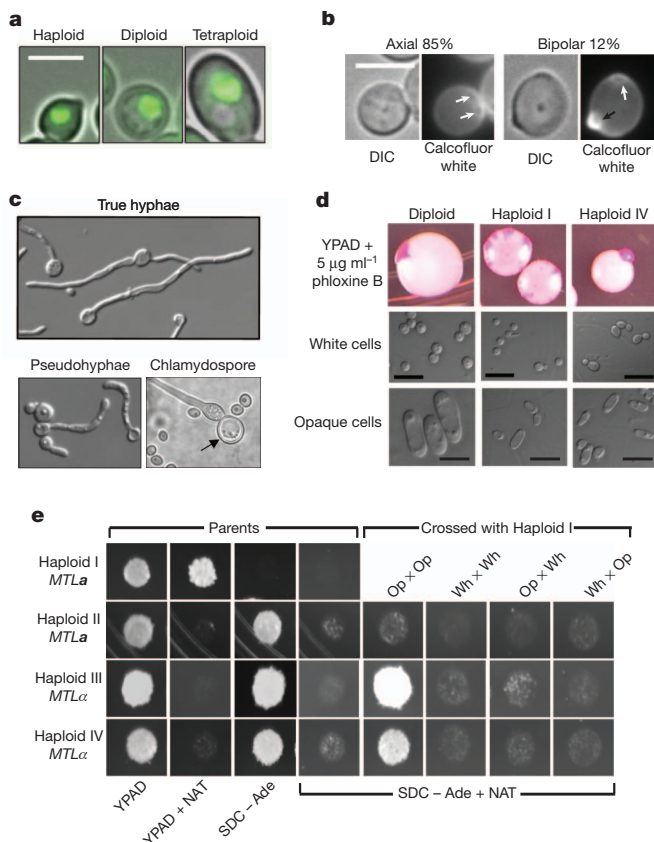


Figure 2 | Morphology and mating competency of haploid *C. albicans*.

a, Representative differential interference contrast microscopy (DIC) images of haploid, diploid and tetraploid cells overlaid with fluorescence images of their nuclei. **b**, Calcofluor white staining revealed primarily cells with the axial budding pattern, 15% with a bipolar budding pattern ($n = 72$) and 3% that were difficult to resolve. White arrows, previous bud scars; black arrow, newest bud. Scale bars, 5 μm . **c**, Haploids form true hyphae, pseudohyphae and chlamydospores in serum, RPMI and corn meal agar media, respectively. **d**, White-opaque switching detected as pink colony sectoring (top) and by microscopy of cells from white and pink/opaque sectors. Diploid, *MTLa/MTL α 1 Δ α 2 Δ* (YJB12234); Haploid I, *MTLa*; Haploid IV, *MTL α* . **e**, Mating between haploid cells. 'Parents': Haploid I (*MTLa NAT1 ade2 Δ*), Haploid II (*MTLa ADE2*), Haploids III and IV (*MTL α ADE2*) showing growth on media indicated. 'Crossed with Haploid I': opaque (Op) or white (Wh) cells from Haploid I were mixed with opaque and/or white cells from Haploids II, III or IV and plated to medium selective for mating products. Ade, adenine; NAT, nourseothricin; YPAD, yeast peptone dextrose media with adenine.

bud site selection patterns of haploids, like diploid *C. albicans*, were predominantly axial, with a small fraction of cells displaying a bipolar budding pattern (Fig. 2b)³⁹. Significantly, under conditions that induce morphogenesis of diploid *C. albicans* to form true hyphae, pseudohyphae and chlamydospores^{40,41}, similar morphogenetic events occurred in haploids (Fig. 2c).

C. albicans diploid cells that are homozygous at the *MTL* locus can undergo a transcriptionally induced switch to the opaque state that renders them competent for mating^{19,42}. Similarly, haploids readily switched from the white (Wh) to the opaque (Op) state, as detected by colony sectoring (Fig. 2d). Haploid opaque cells had elongated opaque-like cell morphology⁴³, yet were considerably smaller than diploid opaque cells (Fig. 2d). Importantly, haploid opaque cells of opposite mating type were mating competent. Mating between cells with complementary genetic markers resulted in the formation of heterozygous diploids (Fig. 2e, Op \times Op). In contrast, neither opaque cells of the same mating type, nor white cells of opposite mating type, mated efficiently (Fig. 2e). This is consistent with opposite mating types and the opaque state being prerequisites for conventional

mating^{19,42}. Thus, we propose that haploids participate in a non-meiotic haploid-diploid parasexual cycle.

Reduced growth and virulence of haploids

The products from haploid **a** and α mating were heterozygous for *MTL* (Supplementary Fig. 7), near-diploid in genome content (Supplementary Fig. 7), and probably inherited the extra aneuploid copies of chromosome 6 and/or chromosome 7 from their *MTL α* parent. All the haploid isolates grew significantly slower than SC5314 (Fig. 3a and Supplementary Fig. 8, $P < 0.001$ for all haploids). However, the mating products grew significantly faster than either of their haploid parents (Fig. 3a), as expected if heterozygosity restores fitness through the complementation of recessive alleles⁴⁴. Consistent with this, auto-diploids had growth rates indistinguishable from their haploid progenitors (Fig. 3a and Supplementary Fig. 8), with the single exception of Haploid VIII ($P = 0.02$). We propose that the low fitness of haploids, as well as their corresponding auto-diploids, is a consequence of unmasking recessive alleles that reduce growth potential. Furthermore, the variability in fitness between haploids is probably due to the specific combination of alleles inherited by each haploid isolate.

Notably, the diploid mating products from haploid crosses grew more slowly than the highly heterozygous diploid SC5314. The generation of robust and diverse diploid progeny from haploid mating would require outcrossing, which is predicted to occur infrequently^{11,12}, as many humans are colonized with a single strain of *C. albicans*. As it seems that some lethal mutations have accumulated on one of the two homologues for more than half the chromosomes (Fig. 1 and Supplementary Fig. 5), mating between related haploids

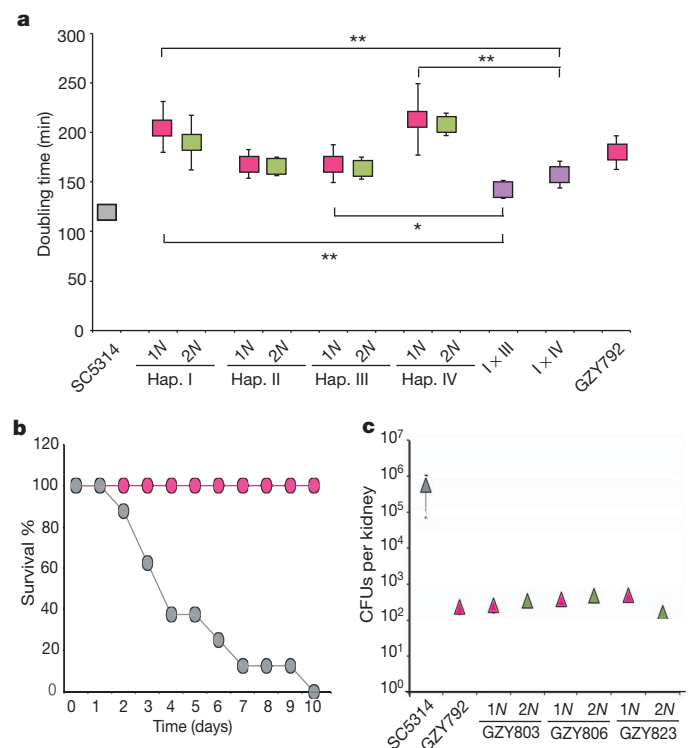


Figure 3 | Haploid growth *in vitro* and *in vivo*. **a**, Growth (doubling times in YPAD) of control diploid, haploids (pink), their auto-diploid derivatives (green), and heterozygous, mating products I \times III and I \times IV (purple). Error bars reflect one standard deviation from the mean. $*P < 0.01$, $**P < 0.001$, Student's *t*-test. **b**, Survival of mice (tail vein systemic candidiasis model) following inoculation with Haploid II (pink) or its diploid progenitor, YJB12419 (grey). **c**, Recovery of colony-forming units (CFUs) from mouse kidneys (three mice per yeast strain) 48 h post-infection.

would not re-establish complete genome heterozygosity. Thus, even though the formation of haploids potentially eliminates lethal mutations, continued inbreeding between related haploids would perpetuate homozygosity of most chromosomes and consequently would reduce overall fitness.

Consistent with reduced growth rates *in vitro*, Haploid II was avirulent in a mouse model of systemic candidiasis (Fig. 3b) and was cleared from the mouse after 10 days. However, after 48 h of infection with a haploid strain, cells could be recovered (Supplementary Fig. 9a) and the majority of these isolates remained haploid. Subsequent *in vivo* experiments compared the colony-forming units (CFUs) of haploids, auto-diploids and SC5314 isolated from mouse kidneys 48 h post-inoculation in individual and direct competition experiments (Fig. 3c and Supplementary Fig. 9b). The number of CFUs recovered from mice inoculated with haploids and auto-diploids was several orders of magnitude lower than the number of CFUs recovered from mice inoculated with SC5314 (Fig. 3c). Furthermore, competition experiments indicated that haploids and auto-diploids showed similar fitness *in vivo*, as both of these forms were outcompeted by heterozygous diploids (Supplementary Fig. 9b). Similar to growth rates *in vitro*, the low fitness of haploids and their corresponding auto-diploids *in vivo* indicates that it is not the diploid state *per se* that is beneficial to growth, but rather extensive allelic heterozygosity, as shown with SC5314. From these data, we propose that haploid formation may not be rare, but that haploids probably represent a very small fraction of the overall population owing to their low competitive fitness relative to heterozygous diploids.

Haploid strains as genetic tools

The haploid state greatly facilitates experimental approaches such as classical genetic screens for recessive alleles and a single round of gene-knockout phenotyping. To illustrate this potential, a set of auxotrophic *C. albicans* strains was derived from a relatively stable haploid, GZY792 (Fig. 4a and Supplementary Fig. 10), and genes important for morphogenesis in diploids (*HGC1*, *RVS167*, *SLA1*, *SEC3* and *ACE2*) were deleted in a single step (Fig. 4c). The resulting mutants showed morphogenesis defects closely resembling those of the corresponding diploid null mutants (Fig. 4d)^{45–48}. Furthermore, because the deleted genes map to all eight chromosomes (Fig. 4c), the ability to delete each gene in a single step confirms that all chromosomes were monosomic in the parental haploid.

Concluding remarks

In summary, *C. albicans* can no longer be considered to be an obligate diploid. Rather, it has the ability to form haploids that subsequently mate to form diploids or undergo auto-diploidization. The lower fitness of haploids and auto-diploids suggests they will not persist in the population and thus should be detected only rarely. Nonetheless, efficient mating between viable haploids can produce heterozygous diploids that have increased fitness, presumably owing to the complementation of detrimental recessive alleles. Furthermore, the reduction to a haploid state can serve as a vehicle to eliminate recessive lethal alleles from a heterozygous diploid population. We propose that *C. albicans* rapidly generates genetic diversity by producing a broad range of different ploidy states, including haploid, diploid, tetraploid and aneuploid²⁵. Each of these ploidy states are mating competent and genetic outcrossing can introduce, albeit infrequently, further genetic diversity into the population. Whereas the ploidy reduction mechanism(s) used by *C. albicans* remain elusive, the discovery of a haploid form and the potential for a haploid–diploid parasexual cycle significantly expands our ability to manipulate, and thereby better understand, this opportunistic pathogen. Furthermore, this study reveals how whole-genome analyses can lead to a re-evaluation of common assumptions about genomic structure in microbial organisms.

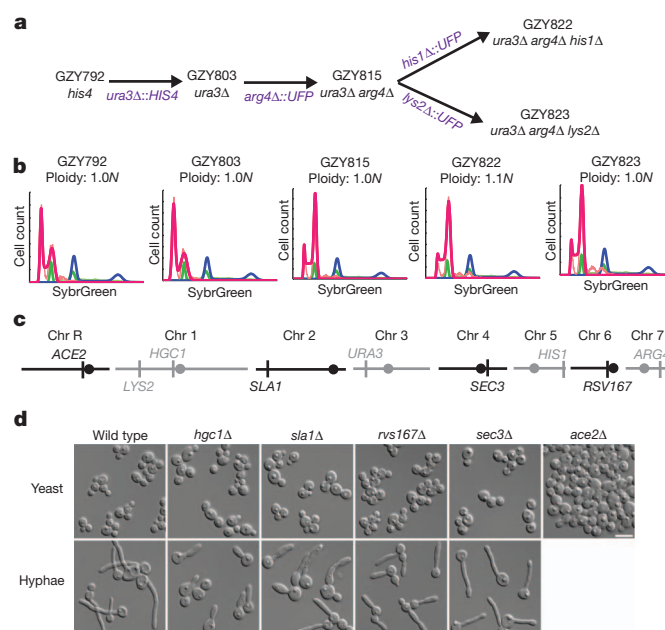


Figure 4 | Auxotrophic haploid strains enable one-step gene deletions.

a, Series of strains constructed from a stable haploid isolate, GZY792 (*MTLα*, *his4*), which was isolated after propagation for 30 passages, screening for ploidy by flow cytometry and selection of isolates that were consistently haploid. GZY803 (*ura3Δ*) was constructed by disruption of *URA3* with *HIS4*. Other auxotrophies were generated by the *URA*-flipper approach⁵⁰. **b**, Flow cytometry of these auxotrophic strains. **c**, Genes disrupted in one-step map to all eight chromosomes. Circles, centromere position. **d**, Cell morphology phenotypes of haploid mutants grown in minimal media (yeast) or media supplemented with 20% FBS at 37 °C (hyphae) are similar to phenotypes seen for the corresponding diploid null mutants.

METHODS SUMMARY

For full details please refer to the Supplementary Methods. This study was carried out in strict accordance with the recommendations in the Guide for the Care and Use of Laboratory Animals as defined by the National Institutes of Health (PHS Assurance #A3284-01) and National Advisory Committee For Laboratory Animal Research of Singapore (NACLAR). Animal protocols were reviewed and approved by the Institutional Animal Care and Use Committee (IACUC) of Brown University and ASTAR (#110686). All animals were housed in a centralized and AAALAC-accredited research animal facility that is fully staffed with trained husbandry, technical and veterinary personnel. Haploid isolates recovered from mouse models of bloodstream²⁷ and oropharyngeal²⁸ infections were identified by plating dilutions of kidney or tongue tissue homogenates onto YPD and onto 2-DOG medium to identify Gal[−] cells. Colonies from YPD and 2-DOG plates were analysed by flow cytometry to determine cell ploidy. For preparation of samples for flow cytometry, cells were collected during mid-log phase, fixed with ethanol, stained with SybrGreenI and analysed using a FACScaliber. Mating³⁴, *in vitro* growth³⁰ and *in vivo*⁴⁹ assays were performed as previously described.

Full Methods and any associated references are available in the online version of the paper.

Received 27 July; accepted 21 November 2012.

Published online 30 January 2013.

- van der Walt, J. P. Sexually active strains of *Candida albicans* and *Cryptococcus albidus*. *Antonie van Leeuwenhoek* **33**, 246–256 (1967).
- Sarachek, A., Rhoads, D. D. & Schwarzhoff, R. H. Hybridization of *Candida albicans* through fusion of protoplasts. *Arch. Microbiol.* **129**, 1–8 (1981).
- Suzuki, T., Nishibayashi, S., Kuroiwa, T., Kanbe, T. & Tanaka, K. Variance of ploidy in *Candida albicans*. *J. Bacteriol.* **152**, 893–896 (1982).
- Olaiya, A. F. & Sogin, S. J. Ploidy determination of *Candida albicans*. *J. Bacteriol.* **140**, 1043–1049 (1979).
- Riggsby, W. S., Torres-Bauza, L. J., Wills, J. W. & Townes, T. M. DNA content, kinetic complexity, and the ploidy question in *Candida albicans*. *Mol. Cell. Biol.* **2**, 853–862 (1982).

6. Kelly, R., Miller, S. M., Kurtz, M. B. & Kirsch, D. R. Directed mutagenesis in *Candida albicans*: one-step gene disruption to isolate *ura3* mutants. *Mol. Cell. Biol.* **7**, 199–208 (1987).
7. Kurtz, M. B. & Marrinan, J. Isolation of *hem3* mutants from *Candida albicans* by sequential gene disruption. *Mol. Gen. Genet.* **217**, 47–52 (1989).
8. Magee, P. T., Kakar, S. & Kwon-Chung, K. in *Genetic Analysis of Candida albicans by Complementation* (ed. Schessinger, D. M.) 230–233 (American Society of Microbiology, 1983).
9. Whelan, W. L., Partridge, R. M. & Magee, P. T. Heterozygosity and segregation in *Candida albicans*. *Mol. Gen. Genet.* **180**, 107–113 (1980).
10. Jones, T. *et al.* The diploid genome sequence of *Candida albicans*. *Proc. Natl Acad. Sci. USA* **101**, 7329–7334 (2004).
11. Gräser, Y. *et al.* Molecular markers reveal that population structure of the human pathogen *Candida albicans* exhibits both clonality and recombination. *Proc. Natl Acad. Sci. USA* **93**, 12473–12477 (1996).
12. Bounoux, M.-E. *et al.* Mating is rare within as well as between clades of the human pathogen *Candida albicans*. *Fungal Genet. Biol.* **45**, 221–231 (2008).
13. Whelan, W. L. & Soll, D. R. Mitotic recombination in *Candida albicans*: recessive lethal alleles linked to a gene required for methionine biosynthesis. *Mol. Gen. Genet.* **187**, 477–485 (1982).
14. Sarachek, A. & Weber, D. A. Segregant-defective heterokaryons of *Candida albicans*. *Curr. Genet.* **10**, 685–693 (1986).
15. Barton, R. C. & Gull, K. Isolation, characterization, and genetic analysis of monosomic, aneuploid mutants of *Candida albicans*. *Mol. Microbiol.* **6**, 171–177 (1992).
16. Janbon, G., Sherman, F. & Rustchenko, E. Monosomy of a specific chromosome determines L-sorbose utilization: a novel regulatory mechanism in *Candida albicans*. *Proc. Natl Acad. Sci. USA* **95**, 5150–5155 (1998).
17. Andaluz, E. *et al.* Rad52 function prevents chromosome loss and truncation in *Candida albicans*. *Mol. Microbiol.* **79**, 1462–1482 (2011).
18. Forche, A. *et al.* The parasexual cycle in *Candida albicans* provides an alternative pathway to meiosis for the formation of recombinant strains. *PLoS Biol.* **6**, e110 (2008).
19. Miller, M. G. & Johnson, A. D. White-opaque switching in *Candida albicans* is controlled by mating-type locus homeodomain proteins and allows efficient mating. *Cell* **110**, 293–302 (2002).
20. Soll, D. R., Lockhart, S. R. & Zhao, R. Relationship between switching and mating in *Candida albicans*. *Eukaryot. Cell* **2**, 390–397 (2003).
21. Magee, B. B. & Magee, P. T. Induction of mating in *Candida albicans* by construction of *MTLa* and *MTL α* strains. *Science* **289**, 310–313 (2000).
22. Hull, C. M., Raisner, R. M. & Johnson, A. D. Evidence for mating of the 'asexual' yeast *Candida albicans* in a mammalian host. *Science* **289**, 307–310 (2000).
23. Bennett, R. J. & Johnson, A. D. Completion of a parasexual cycle in *Candida albicans* by induced chromosome loss in tetraploid strains. *EMBO J.* **22**, 2505–2515 (2003).
24. Selmecki, A., Forche, A. & Berman, J. Aneuploidy and isochromosome formation in drug-resistant *Candida albicans*. *Science* **313**, 367–370 (2006).
25. Berman, J. & Hadany, L. Does stress induce (para)sex? Implications for *Candida albicans* evolution. *Trends Genet.* **28**, 197–203 (2012).
26. Forche, A. *et al.* Stress alters rates and types of loss of heterozygosity in *Candida albicans*. *mBio* **2**, e00129–11 (2011).
27. Forche, A. *et al.* A system for studying genetic changes in *Candida albicans* during infection. *Fungal Genet. Biol.* **39**, 38–50 (2003).
28. Solis, N. V. & Filler, S. G. Mouse model of oropharyngeal candidiasis. *Nature Protocols* **7**, 637–642 (2012).
29. Forche, A., Magee, P. T., Selmecki, A., Berman, J. & May, G. Evolution in *Candida albicans* populations during a single passage through a mouse host. *Genetics* **182**, 799–811 (2009).
30. Abbey, D., Hickman, M., Gresham, D. & Berman, J. High-resolution SNP/CGH microarrays reveal the accumulation of loss of heterozygosity in commonly used *Candida albicans* strains. *G3 (Bethesda)* **1**, 523–530 (2011).
31. Mancera, E., Bourgon, R., Brozzi, A., Huber, W. & Steinmetz, L. M. High-resolution mapping of meiotic crossovers and non-crossovers in yeast. *Nature* **454**, 479–485 (2008).
32. Tsai, J.-H. & McKee, B. D. Homologous pairing and the role of pairing centers in meiosis. *J. Cell Sci.* **124**, 1955–1963 (2011).
33. Reedy, J. L., Floyd, A. M. & Heitman, J. Mechanistic plasticity of sexual reproduction and meiosis in the *Candida* pathogenic species complex. *Curr. Biol.* **19**, 891–899 (2009).
34. Alby, K., Schaefer, D. & Bennett, R. J. Homothallic and heterothallic mating in the opportunistic pathogen *Candida albicans*. *Nature* **460**, 890–893 (2009).
35. Yi, M., Hong, N. & Hong, Y. Generation of medaka fish haploid embryonic stem cells. *Science* **326**, 430–433 (2009).
36. Freed, J. J. & Mezger-Freed, L. Stable haploid cultured cell lines from frog embryos. *Proc. Natl Acad. Sci. USA* **65**, 337–344 (1970).
37. Elling, U. *et al.* Forward and reverse genetics through derivation of haploid mouse embryonic stem cells. *Cell Stem Cell* **9**, 563–574 (2011).
38. Mortimer, R. K. Radiobiological and genetic studies on a polyploid series (haploid to hexaploid) of *Saccharomyces cerevisiae*. *Radiat. Res.* **9**, 312–326 (1958).
39. Chaffin, W. L. Site selection for bud and germ tube emergence in *Candida albicans*. *Microbiology* **130**, 431–440 (1984).
40. Berman, J. & Sudbery, P. E. *Candida albicans*: a molecular revolution built on lessons from budding yeast. *Nature Rev. Genet.* **3**, 918–932 (2002).
41. Citiulo, F., Moran, G. P., Coleman, D. C. & Sullivan, D. J. Purification and germination of *Candida albicans* and *Candida dubliniensis* chlamydospores cultured in liquid media. *FEMS Yeast Res.* **9**, 1051–1060 (2009).
42. Lockhart, S. R. *et al.* In *Candida albicans*, white-opaque switchers are homozygous for mating type. *Genetics* **162**, 737–745 (2002).
43. Slutsky, B. *et al.* White-opaque transition: a second high-frequency switching system in *Candida albicans*. *J. Bacteriol.* **169**, 189–197 (1987).
44. Crow, J. & Kimura, M. Evolution in sexual and asexual populations. *Am. Nat.* **99**, 439–450 (1965).
45. Wang, Y. CDKs and the yeast-hyphal decision. *Curr. Opin. Microbiol.* **12**, 644–649 (2009).
46. Kelly, M. T. *et al.* The *Candida albicans* *CaACE2* gene affects morphogenesis, adherence and virulence. *Mol. Microbiol.* **53**, 969–983 (2004).
47. Zeng, G., Wang, Y.-M. & Wang, Y. Cdc28–Cln3 phosphorylation of Sla1 regulates actin patch dynamics in different modes of fungal growth. *Mol. Biol. Cell* **23**, 3485–3497 (2012).
48. Douglas, L. M., Martin, S. W. & Konopka, J. B. BAR domain proteins Rvs161 and Rvs167 contribute to *Candida albicans* endocytosis, morphogenesis, and virulence. *Infect. Immun.* **77**, 4150–4160 (2009).
49. Noble, S. M., French, S., Kohn, L. A., Chen, V. & Johnson, A. D. Systematic screens of a *Candida albicans* homozygous deletion library decouple morphogenetic switching and pathogenicity. *Nature Genet.* **42**, 590–598 (2010).
50. Morschhäuser, J., Michel, S. & Staib, P. Sequential gene disruption in *Candida albicans* by FLP-mediated site-specific recombination. *Mol. Microbiol.* **32**, 547–556 (1999).

Supplementary Information is available in the online version of the paper.

Acknowledgements We would like to thank M. McClellan, K. Matter, E. Voigt and F. Y. Chan for technical assistance, S. Filler and J. Becker for work involving mouse models of infection, F. M. Chang and T. Y. Ou for contributing to the isolation of the progenitor of GZY792, and L. Burrack, J. Heitman, M. Kupiec, K. Nielsen and N. Pavelka for comments on the manuscript. M.A.H. is supported by an NRSA post-doctoral fellowship (F32GM096536-02). A.F. is supported by the National Institute of Allergy and Infectious Diseases (NIAID) (R15-AI090633-01A1 and R01 AI0624273). M.P.H. is supported by a training grant for Graduate Assistance in Areas of National Need (P200A100100). B.D.H. is supported by the National Institute of Dental & Craniofacial Research (T32DE007288). R.J.B. is supported by the NIAID (AI081560 and AI081704) and a PATH Award from the Burroughs Wellcome Fund. Y.W. is supported by Agency for Science, Technology, & Research, Singapore. J.B. is supported by the NIAID (AI0624273).

Author Contributions M.A.H. performed flow cytometry analysis, SNP/CGH hybridizations, species identification, white-opaque switching and mating assays, and *in vitro* growth assays. Y.W. and G.Z. designed and analysed auxotrophs, morphogenesis mutants and *in vivo* growth experiments; G.Z. constructed the mutants; Y.-M.W. collected isolates post-*in vivo*. A.F. and C.-h.S. initially isolated haploid/homozygous isolates. D.A. developed the flow cytometry analysis and SNP/CGH pipelines. M.P.H. performed virulence and *in vivo* competition assays. B.D.H. collected and analysed cell and nuclear size data and budding patterns. M.A.H. and J.B. assembled the data and wrote the manuscript with editorial input from A.F., R.J.B. and Y.W.

Author Information Reprints and permissions information is available at www.nature.com/reprints. The authors declare no competing financial interests. Readers are welcome to comment on the online version of the paper. Correspondence and requests for materials should be addressed to J.B. (jberman@umn.edu or jberman@post.tau.ac.il).

METHODS

Haploid screening from the mouse models of infection. Bloodstream infections were performed by injecting 10^6 cells of parent strain AF7 (*gal1Δ::URA3/GAL1*), into the tail vein of 13 outbred ICR male mice (22–25 g, Harlan)²⁷. When moribund (at 5–7 days), mice were anaesthetized using isoflurane, euthanized, and both kidneys were removed. Kidneys were combined, homogenized with 1 ml of water. 1:1,000 dilutions of kidney homogenates were plated for total cell count onto YPD, and 1:10 dilutions of the same homogenate were plated onto 2-DOG medium to obtain Gal[−] colony counts at 3 days.

For the oropharyngeal model of infection²⁸, Balb/C mice were immunosuppressed with cortisone on days −1, 1 and 3 of infection. Calcium alginate swabs were saturated with a suspension of 10^6 cells per ml of YJB9318 (*gal1Δ::URA3/GAL1*) under their tongues for 75 min. Mice were euthanized at 1, 2, 3 and 5 days post-infection. 1:1,000 dilutions of tongue tissue homogenates were plated for total cell count onto YPD, and 1:10 dilutions of the same homogenate were plated onto 2-DOG medium to obtain Gal[−] colony counts at 3 days. Importantly, to confirm that 2-DOG resistant cells only arose during *in vivo* passage and were not selected for by plating on 2-DOG medium, a *gal1/gal1* strain and a *gal1/GAL1* heterozygote strain were plated onto 2-DOG medium and observed for growth. 2-DOG resistant colonies grew up from the *gal1/gal1* mutant but not from the *GAL1/gal1* heterozygote by day 3 after plating²⁷. Therefore, we used a cut-off of day 3 for picking 2-DOG resistant colonies after plating.

Approximately 300 colonies were transferred from YPD plates and ~740 colonies from 2-DOG plates (312 from OPC and 431 BSI isolates) into 96-well plates containing 50% glycerol and stored at −80 °C. All *C. albicans* cells isolated following *in vivo* passaging were analysed by flow cytometry to determine cell ploidy.

Flow cytometry preparation and analysis. Mid-log phase cells were collected, washed and resuspended in 50:50 TE (50 mM Tris, pH 8; 50 mM EDTA) and fixed with 95% ethanol. Cells were washed with 50:50 TE and treated with 1 mg ml^{-1} RNase A and then 5 mg ml^{-1} proteinase K. Cells were washed with 50:50 TE and resuspended in SybrGreenI (1:85 dilution in 50:50 TE) incubated overnight at 4 °C. Stained cells were collected and resuspended in 50:50 TE and analysed using a FACScaliber. Whole-genome ploidy was estimated by fitting DNA content data with a multi-Gaussian cell cycle model that assumes the G2 peak has twice the fluorescence of the G1 peak and that minimizes S-phase cell contribution to the error function. Ploidy values were calculated by comparing the ratio of peak locations in experimental samples to those of diploid and tetraploid controls.

Mating assays. Opaque or white cells were mixed together in equal cell numbers and incubated on Spider media³⁴ for 18 h before replica-plating onto SDC − Ade + NAT (to select for mating products), as well as YPAD, YPAD + Nat, SDC − Ade and SDC − Ade + NAT to detect parental auxotrophies and then photographed 24 h later.

***In vitro* growth assays.** Strains were grown in YPD media supplemented with adenine, uridine and histidine in a 96-well microtitre plate and absorbance at 600 nm was measured every 15 min with a plate reader (Tecan Sunrise) for 24 h. Doubling times were calculated as previously described³⁰.

***In vivo* assays.** For virulence assays, eight mice per *C. albicans* strain were inoculated with $\sim 6.0 \times 10^5$ CFUs by tail vein injection⁴⁹. For survival assays, three mice per strain were inoculated by tail vein injection, both kidneys were collected at 48 h and CFUs were determined by plating on YPAD. Ploidy of randomly selected isolates was determined by flow cytometry.

Structural basis for viral 5'-PPP-RNA recognition by human IFIT proteins

Yazan M. Abbas¹, Andreas Pichlmair^{2,3*}, Maria W. Górna^{2*}, Giulio Superti-Furga² & Bhushan Nagar¹

Interferon-induced proteins with tetratricopeptide repeats (IFITs) are innate immune effector molecules that are thought to confer antiviral defence through disruption of protein-protein interactions in the host translation-initiation machinery. However, it was recently discovered that IFITs can directly recognize viral RNA bearing a 5'-triphosphate group (PPP-RNA), which is a molecular signature that distinguishes it from host RNA. Here we report crystal structures of human IFIT5, its complex with PPP-RNAs, and an amino-terminal fragment of IFIT1. The structures reveal a new helical domain that houses a positively charged cavity designed to specifically engage only single-stranded PPP-RNA, thus distinguishing it from the canonical cytosolic sensor of double-stranded viral PPP-RNA, retinoic acid-inducible gene I (RIG-I, also known as DDX58). Mutational analysis, proteolysis and gel-shift assays reveal that PPP-RNA is bound in a non-sequence-specific manner and requires a 5'-overhang of approximately three nucleotides. Abrogation of PPP-RNA binding in IFIT1 and IFIT5 was found to cause a defect in the antiviral response by human embryonic kidney cells. These results demonstrate the mechanism by which IFIT proteins selectively recognize viral RNA, and lend insight into their downstream effector function.

The innate immune system relies on several germ-line-encoded receptors to distinguish self from non-self molecules in order to mount an appropriate early defence response. During viral infection, non-self molecules are derived from viral genomes generally in the form of double-stranded RNA (dsRNA) or PPP-RNA that is not protected by a 5'-cap. The canonical host proteins responsible for sensing or interacting with these foreign nucleic acids include the Toll-like receptors, RIG-I-like receptors and nucleotide oligomerization domain (NOD)-like receptors¹. Recently, an unbiased proteomics approach discovered that the IFITs could also directly engage PPP-RNA².

IFITs are among the most potently expressed proteins of a group of interferon-stimulated genes (ISGs)³, which are the culmination of virally triggered signalling pathways that lead to the production of interferon (IFN)- α , IFN- β and other cytokines. They are evolutionarily conserved from mammals to fish, with four well-characterized paralogues in humans: IFIT1 (also known as p56 and ISG56), IFIT2 (also known as p54 and ISG54), IFIT3 (also known as p60 and ISG60) and IFIT5 (also known as p58 and ISG58), ranging in mass from 54 to 56 kDa. IFITs are composed of tetratricopeptide repeats (TPRs), degenerate helix-turn-helix motifs of 34 amino acids in length, which are usually present in multiple copies as tandem arrays that generate solenoid-type scaffolds well-suited for mediating protein-protein interactions⁴ (Supplementary Figs 1 and 2).

IFITs have been implicated in modulating several biological processes, including inhibition of translation initiation, cell proliferation, and migration, in addition to mediating antiviral effects³. Most of these functions are thought to occur through disruptive protein-protein interactions between IFITs and host cellular factors. Through their TPRs, human IFIT1 and IFIT2 were shown to inhibit key steps during translation initiation by interacting with the 'e' or 'c' subunits of eIF3 (refs 5, 6). However, the unexpected finding that IFITs can bind RNA suggested a more direct role: after infection or interferon

stimulation, it was found that IFITs form large multiprotein complexes with other family members and several different RNA-binding proteins, leading to viral clearance². Like RIG-I, productive binding of both IFIT1 and IFIT5 were shown to depend on the presence of cytosolic PPP-RNAs^{2,7,8}. However, crystallographic and biochemical analyses of RIG-I bound to RNA revealed that it is a dsRNA-specific translocase⁹, which optimally interacts with blunt-ended PPP-RNA¹⁰⁻¹⁵. The mechanism by which IFITs recognize PPP-RNA is unknown.

We describe here the crystal structure of full-length human IFIT5 with and without PPP-RNAs, as well as an N-terminal, protease-resistant fragment of human IFIT1 (nIFIT1). The structures reveal a novel arrangement of TPR domains that directly bind PPP-RNA in a non-sequence-specific manner and, to our knowledge, represent the first example of a TPR protein bound to a nucleic acid ligand. Structure-guided biochemical analysis of IFIT5 indicated that only single-stranded RNA (ssRNA) can be accommodated within the protein, which undergoes a compaction upon binding. Finally, functional analysis in human embryonic kidney (HEK) cells reveals a reduction of viral replication only in the presence of proper PPP-RNA binding by IFIT1 or IFIT5.

Crystal structures of IFIT5 and nIFIT1

We crystallized and determined the structures of full-length human IFIT5 (residues 1–482) at 2.1 Å resolution and an N-terminal fragment of IFIT1 (residues 7–279) at 1.9 Å resolution using single-wavelength anomalous diffraction. The structure of IFIT5 reveals a helical domain with approximate dimensions of 80 Å × 55 Å × 40 Å (Fig. 1a, b). In most multi-TPR-containing proteins, such as O-linked N-acetylglucosamine transferase, the relationship between successive TPRs is regular and repeating, such that they form open-ended super-helical structures with distinct convex and concave surfaces^{4,16}. In IFIT5, of its total 24 α -helices, 18 form canonical TPRs (TPRs 1–9; Fig. 1a), whereas the remaining 6 helices intervene between the TPRs

¹Department of Biochemistry, and Groupe de Recherche Axé sur la Structure des Protéines, McGill University, Montreal, Quebec H3G 0B1, Canada. ²CeMM Research Center for Molecular Medicine of the Austrian Academy of Sciences, 1090 Vienna, Austria. ³Max Planck Institute of Biochemistry, 82152 Martinsried/Munich, Germany.

*These authors contributed equally to this work.

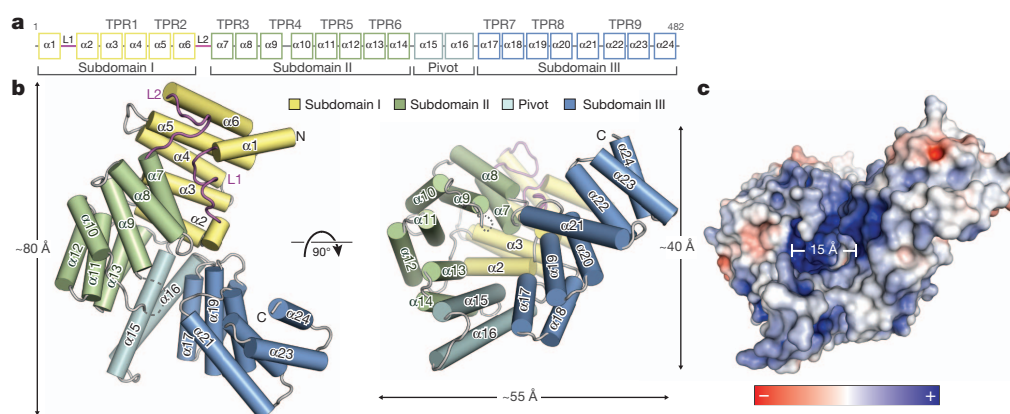


Figure 1 | Structural overview of human IFIT5. **a**, Secondary structure, TPR motif and subdomain organization of IFIT5. **b**, Orthogonal views of IFIT5 with helices represented as cylinders. **c**, Surface representation of IFIT5 coloured by electrostatic potential (using APBS) from negative ($-5kTe^{-1}$; red) to positive ($+5kTe^{-1}$; blue).

such that the regular repeating relationship between them is disrupted. This results in the formation of three distinct bundles of TPRs (subdomains I, II and III) oriented with respect to one another to give the overall protein a relatively closed clamp-shaped structure (Fig. 1a and Supplementary Fig. 5a).

The topology of subdomain I is unusual in that its two canonical TPRs ($\alpha 3$ to $\alpha 6$) are capped off on both ends by helices $\alpha 1$ and $\alpha 2$, preventing its further propagation into a superhelix. This is facilitated by a connecting 17-residue loop (L1) containing a highly conserved Cys-His-Phe-Thr-Trp pentapeptide motif that is invariant among nearly all of the IFIT proteins (Supplementary Fig. 2), and forms a single turn of a helix that packs against the concave inner face of subdomain I (Supplementary Fig. 4). This same arrangement of subdomain I is also found in the structure of nIFIT1 (root mean squared deviation, 1.4 Å; Supplementary Fig. 3) and is probably a defining characteristic of all IFIT proteins given the high TPR and sequence conservation in subdomains I and II (Supplementary Figs 1 and 2).

The remainder of the IFIT5 structure forms a superhelix encompassing subdomains II and III, as well as a pair of extended non-TPR helices ($\alpha 15$ and $\alpha 16$) that form a pivot point between the latter two subdomains (Fig. 1b). Subdomain II forms a canonical four-TPR-repeat domain in which, notably, its first helix ($\alpha 7$) interacts with

subdomain I in a manner reminiscent of TPR protein–ligand interactions observed previously¹⁷ (Supplementary Fig. 4). This leads to the concave surface of subdomain II forming one wall of a large cavity in the centre of the protein closed off at its base by helix $\alpha 2$ (Fig. 1b). The same TPR–ligand relationship between subdomains I and II is also maintained in the nIFIT1 structure (Supplementary Fig. 3).

The rest of the cylindrical cavity is created by the intervening pivot helices and the N-terminal TPRs from subdomain III. Subdomain III begins with two typical TPRs followed by an interrupting helix ($\alpha 21$), which inverts the direction of the final TPR9 such that it forms an S-shaped appendage at the carboxy terminus with two potential ligand-interacting concave surfaces (Fig. 1b and Supplementary Fig. 5b). The deep pocket formed by this atypical arrangement of TPRs is approximately 28 Å deep by 15 Å wide, and is lined with an expansive collection of positively charged residues well-suited for the accommodation of nucleic acid (Fig. 1c).

IFIT5 specifically binds PPP-RNAs

To understand the structural basis for RNA binding by IFIT5, we *in vitro* transcribed 5'-triphosphate-bearing, short oligonucleotides of cytidine, uridine and adenosine, purified each PPP-RNA in complex with IFIT5 (Supplementary Fig. 6) and determined their structures

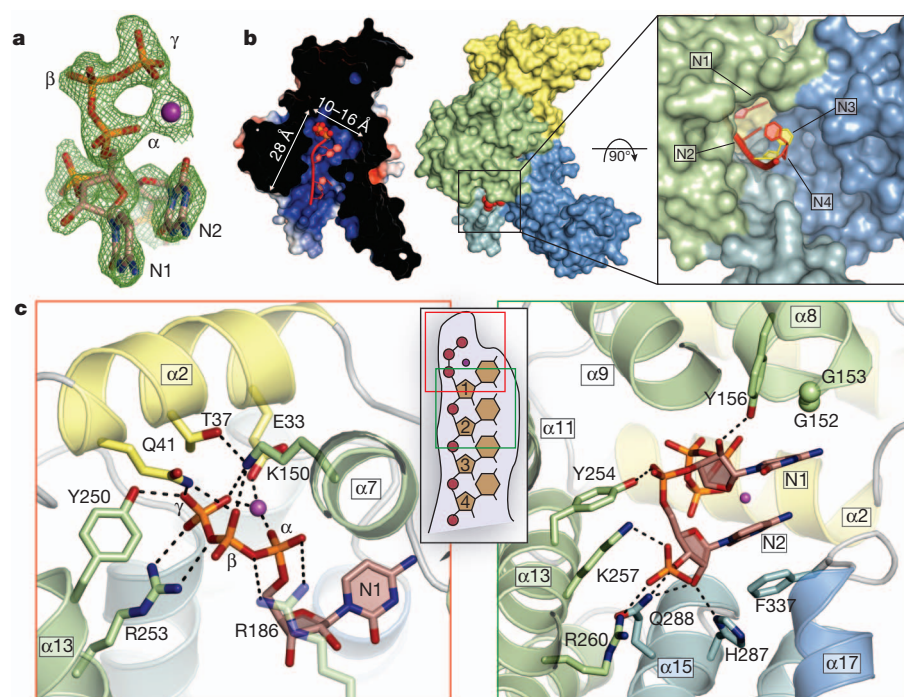


Figure 2 | Structure of IFIT5 bound to PPP-RNA. **a**, $F_o - F_c$ electron-density map of the triphosphate and first two nucleotides contoured at 3.5 σ before inclusion of RNA into the model. The metal ion is indicated with a purple sphere. **b**, Left, cross-section of the complex coloured by surface electrostatic potential. The triphosphate is shown as spheres and RNA nucleotides are shown in red. Middle, surface representation of IFIT5 bound to PPP-RNA coloured by subdomain. Protruding RNA is shown as red spheres. Right, close-up view looking down the axis of the RNA-binding pocket. **c**, Close-up view of the residues making specific contacts with the triphosphate group (left) and the first two nucleotides, N1 and N2 (right). Helices are coloured according to the subdomain to which they belong. Hydrogen bond and salt-bridge interactions are indicated with black dashed lines.

at resolutions of 1.86 Å (oligo-C), 2.0 Å (oligo-U) and 2.5 Å (oligo-A) using molecular replacement with the unliganded structure. All of the structures were similar, and therefore we initially describe the general features of the IFIT5-oligo-C complex as it was the highest resolution structure. Difference Fourier maps revealed strong positive electron density within the central positively charged pocket from which the 5'-triphosphate and the first four nucleotides of the RNA could be reliably modelled (Fig. 2a and Supplementary Fig. 10a). The 5'-triphosphate group is nestled deep within the pocket and makes a multitude of electrostatic interactions with protein side chains from helix $\alpha 2$ (Glu 33, Thr 37 and Gln 41) located at the very base of the pocket, and residues from the concave inner surface of subdomain II (Lys 150, Tyr 250 and Arg 253) (Fig. 2c). Arg 187 in IFIT1 was previously identified to be required for RNA interaction; the homologous residue in IFIT5 (Arg 186) makes a weak salt-bridge with the α - and β -phosphates, and van der Waals contacts with the first ribose moiety. These RNA-interacting residues are for the most part conserved in sequence and structure between IFIT5 and IFIT1 (Supplementary Figs 2 and 7), the only IFITs that have been shown to bind PPP-RNA with strong affinity². One notable exception is Thr 37, which is replaced in IFIT1 by Arg 38, suggesting slight differences in RNA recognition between IFIT1 and IFIT5. Conversely, in IFIT3, which is known to not bind PPP-RNA², Tyr 250 is substituted with a negatively charged residue, Asp 242, and Arg 186 with His 182 (Supplementary Fig. 2), both of which would interfere directly with RNA binding.

Interestingly, a metal ion that bridges the α - and γ -phosphates also seems to be an integral part of PPP-RNA recognition as it neutralizes the negative charge in this region from Glu 33 (Fig. 2c and Supplementary Fig. 8). On the basis of ligand distances and geometry, the ion is probably Mg^{2+} from the *in vitro* transcription reactions, but could potentially also be Na^+ (a component of the crystallization buffer). It is unlikely that capped messenger RNA (mRNA) can be accommodated within this pocket owing to size constraints. In addition, given the critical interactions made with the γ -phosphate and the metal ion, the pocket is unlikely to accept 5'-monophosphorylated or 5'-hydroxylated RNA with considerable affinity. Thus, the structure of the IFIT5 TPR domains have evolved to specifically engage PPP-RNA, and in doing so, distinguish between self and non-self nucleic acids.

Following the 5'-triphosphate end of the RNA, the first two nucleotides (N1, N2) are stably bound along the pocket before the third and fourth nucleotides (N3, N4) begin to protrude from the mouth of the pocket (Fig. 2b). Well-defined density is observed for the phosphodiester backbone and ribose sugars (Supplementary Fig. 10a), which also form several specific interactions with the protein (Fig. 2c). In particular, the 5'-phosphate of N2 hydrogen bonds with Tyr 254, and the 5'-phosphate of N3 makes a salt-bridge with Arg 260 and Lys 257, and hydrogen bonds with Gln 288 (Fig. 2c). The 5'-phosphate of N4 interacts with Arg 294, and weak electron density was observed for the 5'-phosphate of a fifth nucleotide (Supplementary Figs 10a and 11a). The 2'-hydroxyl of the ribose sugars also make specific interactions with the protein, but in this case, interactions that are dependent on the sugar pucker. N1 adopts a C2'-endo conformation (commonly found in B-form double-stranded DNA; Supplementary Fig. 9) and hydrogen bonds with Tyr 156 (Fig. 2c), whereas N2 and N3 are C3'-endo (as found in A-form dsRNA) and interact through their 2'-hydroxyls with His 287 and Gln 288, and Arg 294 and Asp 343, respectively (Fig. 2c and Supplementary Fig. 11a).

PPP-RNA recognition is non-sequence specific

To investigate the potential for sequence-specific interactions at the 5'-end, we compared the crystal structures of IFIT5 in complex with the different RNAs. In both the oligo-C and oligo-U complexes, the pyrimidine base at position 1 is abutted from the top by van der Waals interactions with Tyr 156 and two glycine residues from the loop of TPR3 (between $\alpha 7$ and $\alpha 8$), and from the bottom by non-specific

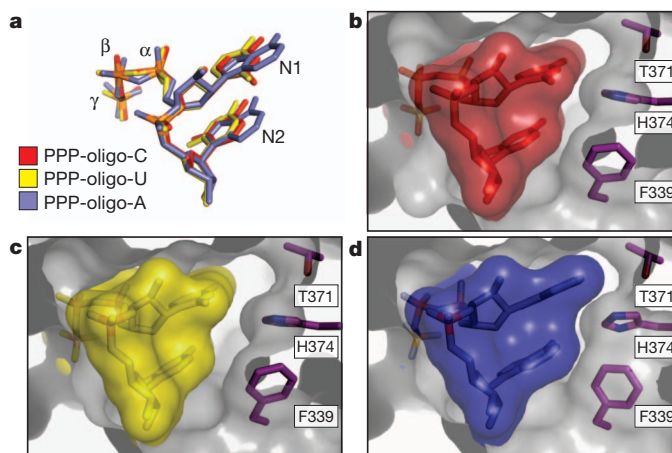


Figure 3 | The interaction between IFIT5 and PPP-RNA is non-sequence specific. Close-up of the RNA-binding pocket in an orientation similar to that shown in Fig. 2b, right panel. **a**, Alignment of the first two nucleotides from the three IFIT5-RNA complexes. **b**, **c**, Surface and stick representation of the first two nucleotides within the IFIT5-oligo-C and IFIT5-oligo-U complexes. The protein surface is depicted as a transparent grey cutaway. **d**, IFIT5-oligo-A complex. Detailed binding between the protein and all nucleotides is depicted in Supplementary Fig. 12.

stacking interactions against the second base, which in turn stacks with Phe 337 (Fig. 2c). Notably, the first two bases do not make any specific hydrogen bonds with protein residues and there is ample space adjacent to the pyrimidine ring edges, suggesting that the larger purine bases can also be easily accommodated (Fig. 3). The structure of the oligo-A complex confirms this notion and reveals that the adenine rings reach further out into the periphery making additional non-specific van der Waals contacts with Thr 371, His 374 and Phe 339, which were absent with the pyrimidine bases (Fig. 3b–d).

The remaining bases stack against Phe 339 in a manner analogous to that observed for the first two bases (Fig. 2b and Supplementary Fig. 11) and interact with a mobile loop from TPR4. Thus, IFIT5 seems to have evolved the capacity to accommodate any 5'-PPP-RNA sequence that may potentially be present in a viral genome.

PPP-RNA binding involves a conformational change

Because the RNA-binding site in IFIT5 is a deep and narrow pocket, the means by which RNA enters is unclear. Superposition of the RNA-bound and -free forms of IFIT5 reveal that the RNA-bound state is more compact, with the largest motions occurring at the pivot helices between subdomain III and the rest of the protein (Fig. 4a and Supplementary Fig. 13). These motions position several key residues from the different subdomains for optimal interaction with the RNA. Moreover, limited proteolysis of IFIT5 in the presence and absence of RNA supports the notion of compaction and stabilization of the protein in the RNA-bound form (Fig. 4b and Supplementary Fig. 15).

To better understand the nature of the conformational change upon RNA binding, we used small-angle X-ray scattering (SAXS) measurements, which provide information on macromolecular size, state and flexibility directly in solution^{18,19}. SAXS analysis revealed reductions in the radius of gyration (R_g , ~ 2.5 Å), the maximum dimension (D_{max} , ~ 25 Å) and the volume ($\sim 14,000$ Å³) of the protein upon addition of RNA (Fig. 4c and Supplementary Fig. 14). The scattering curves show good agreement between solution (R_g , 28.2 Å) and crystal structure (R_g , 27.5 Å) for the RNA-bound form (Supplementary Fig. 14h), in contrast to the unliganded form, which displays considerable differences (solution R_g , 30.6 Å; crystal structure R_g , 28.3 Å). This suggests that in solution, the unliganded protein is either more open or possibly flexible. To discern between these possibilities, we subjected the SAXS data to a Porod–Debye analysis, which provides information on the degree of flexibility present in the

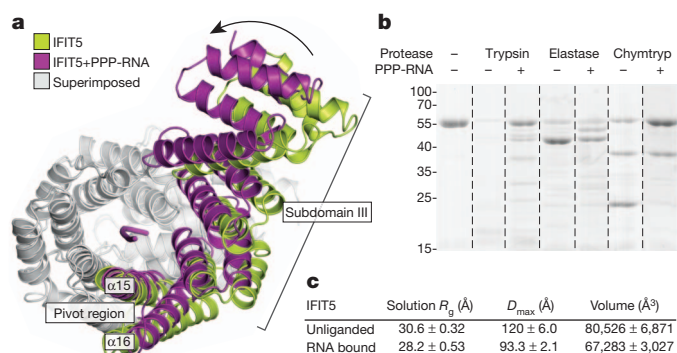


Figure 4 | IFIT5 undergoes a conformational change upon binding PPP-RNA. **a**, Comparison of IFIT5 bound to PPP-RNA (magenta) and the unbound form (green). Superimposed regions are coloured light grey. **b**, SDS-polyacrylamide gel electrophoresis of limited protease digestion of IFIT5 in the presence and absence of RNA taken from each experiment at the 15-min time point (see also Supplementary Fig. 15). Chymotrypsin, chymotrypsin. **c**, Summary of SAXS results. Measurements are the average from three concentrations, with the corresponding standard deviation.

scattering sample¹⁹. For both unliganded and RNA-bound IFIT5, the Porod–Debye plot showed characteristic plateaus that indicate the presence of distinct conformations for both species (Supplementary Fig. 14k, l). Thus, unliganded IFIT5 probably exists in a more open conformation in solution than that observed in the crystal structure, facilitating RNA entry.

IFIT5 and IFIT1 bind only PPP–ssRNAs

The internal diameter of the RNA-binding pocket in IFIT5 is roughly 15 Å, leaving no room to accommodate dsRNA, which would require a diameter of greater than 21 Å. Moreover, at least three bases are necessary to span the length of the pocket, suggesting that IFIT5 is potentially a sensor for PPP–ssRNA, or base-paired PPP–RNA with a minimum three-nucleotide overhang. By contrast, foreign PPP–RNA species in the cytosol that optimally activate RIG-I seem to require blunt-ended RNAs, which are thought to be the most potent immune-stimulant of RIG-I (ref. 15).

To assess the recognition of distinct PPP–RNA species by IFITs, we used gel-shift assays. A 44-nucleotide ssRNA with no predicted secondary structure within the 5′ 22 nucleotides was *in vitro* transcribed, to which complementary RNA strands of 15–20 nucleotides were annealed to generate dsRNA with blunt ends and various 5′-overhangs. Consistent with the crystal structure, we found that IFIT5 could shift both PPP–ssRNA and PPP–dsRNA with at least three-nucleotide overhangs, but could not efficiently shift blunt-ended PPP–RNA or PPP–dsRNA with 1–2-nucleotide overhangs (Fig. 5a and Supplementary Fig. 16). Similarly, IFIT1 could only shift PPP–ssRNA or PPP–dsRNA with at least five-nucleotide overhangs (Supplementary Fig. 16). As a negative control we used IFIT3, which could not shift any species of RNA (Fig. 5a and Supplementary Fig. 16d). Thus, owing to the limitations imposed by their RNA-binding pockets, IFIT5 and IFIT1 can engage only PPP–RNAs that have single-stranded 5′-ends.

Functional validation of PPP–RNA binding to IFITs

To examine the functional relevance of residues involved in binding PPP–RNA, we used PPP–RNA-coated beads to pull down c-Myc-tagged wild-type and mutant IFIT5 and IFIT1 expressed in HEK293 cells. We began by first corroborating that IFIT5, like IFIT1, could be pulled down by RNA only when it is triphosphorylated at the 5′-end (Supplementary Fig. 17a), and that replacing the triphosphate with 5′-cap, 5′-monophosphate or 5′-hydroxyl diminishes the binding (Fig. 5b). The affinity of PPP–RNA for IFIT5 is between 250–500 nM (Fig. 5b), similar to that found previously for IFIT1 (ref. 2).

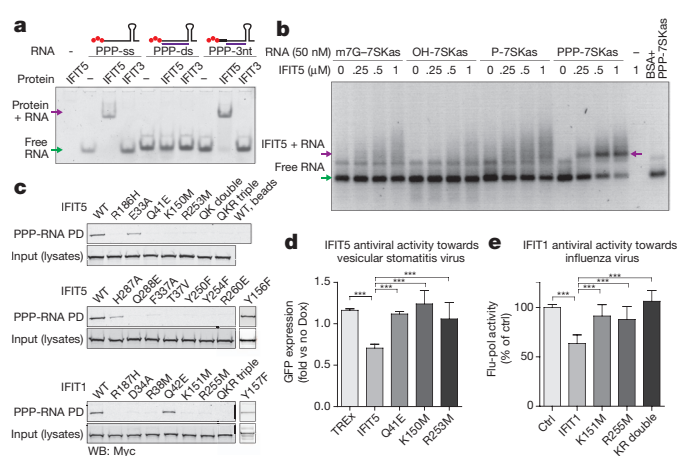


Figure 5 | Functional analyses of IFIT binding to PPP–RNA. **a**, Mobility shift assay between IFIT5 or IFIT3 and ssRNA, dsRNA with blunt ends, or dsRNA with a three-nucleotide (3nt) overhang as indicated by the schematics above each set of lanes. PPP is indicated by red spheres, *in vitro* transcribed top strand is indicated by the black line, and synthetic complementary RNA is shown in purple. **b**, Agarose gel-shift assay between IFIT5 and the various RNAs indicated. 7SKas, 7SKantisense; BSA, bovine serum albumin; m7G; 7-methyl-guanosine cap. **c**, Biotinylated RNA pull-downs (PD) of wild-type (WT) and mutant IFIT1 and IFIT5 from HEK293 cell lysates. QK double indicates Q41E/K150M and QKR triple indicates Q41E/K150M/R253M. Y156F and Y157F were carried out separately, and the appropriate positive and negative controls are described in Supplementary Fig. 17. **d**, **e**, PPP–RNA binding is required for antiviral activities of IFIT5 and IFIT1. **d**, Replication of vesicular stomatitis virus expressing green fluorescent protein (GFP) in doxycycline (Dox)-inducible HEK Flp-In TREx cells expressing IFIT5 (and mutants). Average fold change (± s.d.) in doxycycline-treated versus untreated cells of ten measurements. **e**, Influenza virus in 293T cells transfected with IFIT1 (and mutants). Average percentage (± s.d.) of influenza polymerase (flupol) activity as compared to control (ctrl) of four independent experiments done in duplicate measurements. *** $P < 0.001$ (one-way analysis of variance, Tukey’s multiple comparison test).

Next, we mutated key RNA contacts within the pocket and found that in most cases, a single-residue substitution was sufficient to abolish RNA binding *in vitro* (Fig. 5c). All residues recognizing the PPP–RNA were critical for binding, with the exception of Glu 33, Tyr 156 and His 287 (see Supplementary Fig. 17). Homologous mutations in IFIT1 also lead to abrogation of RNA binding. Thus, the PPP–RNA-binding pocket identified here is probably involved in a similar mode of recognition in other IFIT family members.

Finally, to investigate whether the RNA-interacting residues are important for the antiviral activity of IFIT5 against virus infection, we used HEK293 Flp-In TREx cells that inducibly express IFIT5, and IFIT5 mutants that have lost their ability to bind PPP–RNA. Consistent with the mutational analysis, IFIT5 mutants were impaired in their ability to restrict growth of vesicular stomatitis virus compared to wild-type IFIT5 (Fig. 5d). Similarly, IFIT1 lacking the ability to bind PPP–RNA was not able to inhibit the activity of an influenza virus polymerase (Fig. 5e), consistent with the notion that binding to PPP–RNA is critical for the antiviral activity of IFIT1.

Discussion

The structural basis for IFIT recognition of foreign RNA described here validates the new paradigms put forth for how this family of interferon-stimulated genes carry out their effector functions, and brings to the forefront the versatility of the TPR motif in recognizing diverse ligands, paralleling established receptors of the innate immune system such as those containing leucine-rich repeats¹.

In addition to using protein–protein interactions to confer downstream antiviral activity^{2,3,5,6}, the principal molecular role of IFITs seems to be initiated by direct recognition of foreign PPP–ssRNAs.

PPP-RNAs are found within the genome of negative-sense ssRNA viruses such as influenza and vesicular stomatitis virus. Other RNA viruses, such as positive-sense viruses which have 5'-capped genomes, can also generate cytosolic PPP-RNAs as replicative intermediates during their life cycle. Hence, the evolution of a binding site to specifically recognize PPP-RNA allows IFITs to distinguish self from non-self RNAs, as cytosolic host ssRNAs bear a 5'-monophosphate (on ribosomal RNA and transfer RNA)^{20,21} or are 5'-capped (in the case of mRNA). In doing so, one possible mechanism for IFIT function may be to latch onto the ends of viral RNA, preventing it from being properly replicated or packaged into progeny virions.

Recent studies have suggested a role for IFIT proteins in sensing the 5'-cap methylation status of some viral RNA (for example, West Nile virus, poxvirus and coronavirus)^{22–24}. A 5'-cap is present on positive-sense virus genomes, but most viruses also have the ability to either hijack a cap from host mRNA or encode machinery to add a 5'-cap structure to their mRNA, thereby potentially circumventing IFIT recognition²⁵. Although a 5'-cap cannot be accommodated within the RNA-binding pocket of IFIT5 identified here, we do not preclude the possibility that higher order complexes of IFITs may be able to recognize capped viral RNAs.

Finally, given that bacterial mRNAs also bear a free 5'-PPP and can access the cytosol during infection to potentiate induction of IFN- β ²⁶, it is plausible that IFITs could also have a role in anti-bacterial innate immunity. Taken together, it is clear that unravelling the structural details that underlie IFIT biology will improve our understanding of the complex interplay between pathogens and host innate immunity, and hopefully pave the way for the development of new immunotherapeutics.

Note added in proof: While this paper was under review, the crystal structure of unliganded IFIT2 was published²⁷.

METHODS SUMMARY

For crystallization, all constructs were cloned into a modified pET28a vector containing an N-terminal, Ulp1-cleavable His₆-SUMO tag²⁸ and expressed in *Escherichia coli*. Proteins were purified using standard Nickel-affinity, ion-exchange, and size-exclusion chromatography. PPP-RNAs were generated by *in vitro* transcription. Crystals of nIFIT1, IFIT5 and IFIT5 in complex with PPP-RNA were grown from a sparse matrix screen (see Supplementary Information). The structures of nIFIT1 and IFIT5 were solved by single-wavelength anomalous diffraction phasing of selenomethionine-derivatized protein, and the complexes with PPP-RNA were solved by molecular replacement using unliganded IFIT5 as a search model. Pull-downs with PPP-RNA and functional assays with HEK Flp-in TREx cells are described elsewhere². Full methods can be found in Supplementary Information.

Received 2 March; accepted 13 November 2012.

Published online 13 January 2013.

- Barbalat, R., Ewald, S. E., Mouchess, M. L. & Barton, G. M. Nucleic acid recognition by the innate immune system. *Annu. Rev. Immunol.* **29**, 185–214 (2011).
- Pichlmair, A. *et al.* IFIT1 is an antiviral protein that recognizes 5'-triphosphate RNA. *Nature Immunol.* **12**, 624–630 (2011).
- Fensterl, V. & Sen, G. C. The ISG56/IFIT1 gene family. *J. Interferon Cytokine Res.* **31**, 71–78 (2011).
- Main, E. R. G., Xiong, Y., Cocco, M. J., D'Andrea, L. & Regan, L. Design of stable α -helical arrays from an idealized TPR motif. *Structure* **11**, 497–508 (2003).
- Guo, J., Hui, D. J., Merrick, W. C. & Sen, G. C. A new pathway of translational regulation mediated by eukaryotic initiation factor 3. *EMBO J.* **19**, 6891–6899 (2000).
- Terenzi, F., Hui, D. J., Merrick, W. C. & Sen, G. C. Distinct induction patterns and functions of two closely related interferon-inducible human genes, ISG54 and ISG56. *J. Biol. Chem.* **281**, 34064–34071 (2006).
- Pichlmair, A. *et al.* RIG-I-mediated antiviral responses to single-stranded RNA bearing 5'-phosphates. *Science* **314**, 997–1001 (2006).

- Hornung, V. *et al.* 5'-Triphosphate RNA is the ligand for RIG-I. *Science* **314**, 994–997 (2006).
- Myong, S. *et al.* Cytosolic viral sensor RIG-I is a 5'-triphosphate-dependent translocase on double-stranded RNA. *Science* **323**, 1070–1074 (2009).
- Wang, Y. *et al.* Structural and functional insights into 5'-ppp RNA pattern recognition by the innate immune receptor RIG-I. *Nature Struct. Mol. Biol.* **17**, 781–787 (2010).
- Lu, C. *et al.* The structural basis of 5' triphosphate double-stranded RNA recognition by RIG-I C-terminal domain. *Structure* **18**, 1032–1043 (2010).
- Kowalinski, E. *et al.* Structural basis for the activation of innate immune pattern-recognition receptor RIG-I by viral RNA. *Cell* **147**, 423–435 (2011).
- Luo, D. *et al.* Structural insights into RNA recognition by RIG-I. *Cell* **147**, 409–422 (2011).
- Jiang, F. *et al.* Structural basis of RNA recognition and activation by innate immune receptor RIG-I. *Nature* **479**, 423–427 (2011).
- Schlee, M. *et al.* Recognition of 5' triphosphate by RIG-I helicase requires short blunt double-stranded RNA as contained in panhandle of negative-strand virus. *Immunity* **31**, 25–34 (2009).
- Jinek, M. *et al.* The superhelical TPR-repeat domain of O-linked GlcNAc transferase exhibits structural similarities to importin α . *Nature Struct. Mol. Biol.* **11**, 1001–1007 (2004).
- Zhang, Y. & Chan, D. C. Structural basis for recruitment of mitochondrial fission complexes by Fis1. *Proc. Natl Acad. Sci. USA* **104**, 18526–18530 (2007).
- Putnam, C. D., Hammel, M., Hura, G. L. & Tainer, J. A. X-ray solution scattering (SAXS) combined with crystallography and computation: defining accurate macromolecular structures, conformations and assemblies in solution. *Q. Rev. Biophys.* **40**, 191–285 (2007).
- Rambo, R. P. & Tainer, J. A. Characterizing flexible and intrinsically unstructured biological macromolecules by SAS using the Porod-Debye law. *Biopolymers* **95**, 559–571 (2011).
- Xiao, S., Scott, F., Fierke, C. A. & Engelke, D. R. Eukaryotic ribonuclease P: a plurality of ribonucleoprotein enzymes. *Annu. Rev. Biochem.* **71**, 165–189 (2002).
- Fromont-Racine, M., Senger, B., Saveanu, C. & Fasiolo, F. Ribosome assembly in eukaryotes. *Gene* **313**, 17–42 (2003).
- Daffis, S. *et al.* 2'-O methylation of the viral mRNA cap evades host restriction by IFIT family members. *Nature* **468**, 452–456 (2010).
- Züst, R. *et al.* Ribose 2'-O-methylation provides a molecular signature for the distinction of self and non-self mRNA dependent on the RNA sensor Mda5. *Nature Immunol.* **12**, 137–143 (2011).
- Szretter, K. J. *et al.* 2'-O methylation of the viral mRNA cap by West Nile virus evades ifit1-dependent and -independent mechanisms of host restriction *in vivo*. *PLoS Pathog.* **8**, e1002698 (2012).
- Decroly, E., Ferron, F., Lescar, J. & Canard, B. Conventional and unconventional mechanisms for capping viral mRNA. *Nature Rev. Microbiol.* **10**, 51–65 (2012).
- Sander, L. E. *et al.* Detection of prokaryotic mRNA signifies microbial viability and promotes immunity. *Nature* **474**, 385–389 (2011).
- Yang, Z. *et al.* Crystal structure of ISG54 reveals a novel RNA binding structure and potential functional mechanisms. *Cell Res.* **22**, 1328–1338 (2012).
- Mossessova, E. & Lima, C. D. Ulp1-SUMO crystal structure and genetic analysis reveal conserved interactions and a regulatory element essential for cell growth in yeast. *Mol. Cell* **5**, 865–876 (2000).

Supplementary Information is available in the online version of the paper.

Acknowledgements We thank S. Labiuk and P. Grochulski for X-ray data collection performed on beamline 08ID-1 at the Canadian Light Source, which is supported by the Natural Sciences and Engineering Research Council of Canada, the National Research Council Canada, the Canadian Institutes of Health Research (CIHR), the Province of Saskatchewan, Western Economic Diversification Canada, and the University of Saskatchewan. Thanks also to all laboratory members for discussions and technical assistance. B.N. is supported by a Canada Research Chair, a Career Development Award from the Human Frontiers Science Program (CDA 0018/2006-C/1) and an operating grant from the CIHR (CIHR grant MOP-82929). Work in the G.S.-F. laboratory is funded by the Austrian Academy of Sciences and the i-FIVE ERC grant. A.P. is an EMBO Long-Term Fellowship recipient (ATLF 463-2008). Y.M.A. was supported by the CIHR Strategic Training Initiative in Chemical Biology.

Author Contributions B.N., G.S.-F., Y.M.A., M.W.G. and A.P. designed the project. B.N., Y.M.A., A.P., M.W.G. and G.S.-F. wrote the manuscript. Y.M.A. performed all of the structural and biochemical analyses, and carried out proteolysis and gel-shift experiments. M.W.G. performed the mutagenesis, pull-down and gel-shift experiments and A.P. performed functional experiments and pull-down experiments.

Author Information Coordinates and structure factors have been deposited in the Protein Data Bank under accession numbers 4HOQ, 4HOR, 4HOS, 4HOT and 4HOU. Reprints and permissions information is available at www.nature.com/reprints. The authors declare no competing financial interests. Readers are welcome to comment on the online version of the paper. Correspondence and requests for materials should be addressed to B.N. (bhushan.nagar@mcgill.ca) or G.S.-F. (gsperti@cemm.oeaw.ac.at).

An outburst from a massive star 40 days before a supernova explosion

E. O. Ofek¹, M. Sullivan^{2,3}, S. B. Cenko⁴, M. M. Kasliwal⁵, A. Gal-Yam¹, S. R. Kulkarni⁶, I. Arcavi¹, L. Bildsten^{7,8}, J. S. Bloom^{4,9}, A. Hoshino⁶, D. A. Howell^{8,10}, A. V. Filippenko⁴, R. Laher¹¹, D. Murray¹², E. Nakar¹³, P. E. Nugent^{4,9}, J. M. Silverman^{4,14}, N. J. Shaviv¹⁵, J. Surace¹¹ & O. Yaron¹

Some observations suggest that very massive stars experience extreme mass-loss episodes shortly before they explode as supernovae^{1–4}, as do several models^{5–7}. Establishing a causal connection between these mass-loss episodes and the final explosion would provide a novel way to study pre-supernova massive-star evolution. Here we report observations of a mass-loss event detected 40 days before the explosion of the type II_n supernova SN 2010mc (also known as PTF 10tel). Our photometric and spectroscopic data suggest that this event is a result of an energetic outburst, radiating at least 6×10^{47} erg of energy and releasing about 10^{-2} solar masses of material at typical velocities of $2,000 \text{ km s}^{-1}$. The temporal proximity of the mass-loss outburst and the supernova explosion implies a causal connection between them. Moreover, we find that the outburst luminosity and velocity are consistent with the predictions of the wave-driven pulsation model⁶, and disfavour alternative suggestions⁷.

Type II_n supernovae are a diverse class of transient events, spectroscopically defined by narrow and/or intermediate-width hydrogen emission lines (up to a few thousand km s^{-1} wide)^{8–10}. These emission lines probably originate from optically thin circumstellar matter ionized by the supernova shock and/or radiation field. The spectra and light curves of these supernovae are interpreted as signatures of interaction between the supernova ejecta and mass that has been expelled before the explosion^{11–13}. The most likely detection of a progenitor before its explosion as a type II_n supernova³ involved a luminous blue variable (LBV)—a class of objects which are known for their vigorous eruptive mass-loss events¹⁴. Very recently, a massive star in the nearby galaxy NGC 7259, namely SN 2009ip, had a series of outbursts^{15–17} with a typical expelled-matter velocity of about 500 km s^{-1} , possibly followed by a supernova event^{18,19} exhibiting P Cygni lines with velocities of $\sim 10^4 \text{ km s}^{-1}$. Another event that showed an outburst before its supernova explosion is SN 2006jc, which is further discussed in Supplementary Information section 7.

The Palomar Transient Factory^{20,21} (PTF), a ground-based, wide-field survey, discovered the type II_n SN 2010mc²² in images obtained on 2010 August 20.22 (UTC dates are used throughout this paper). It is located at right ascension 17 h 21 min 30.68 s, declination $+48^\circ 07' 47.4''$ (J2000.0), at redshift $z = 0.035$, which corresponds to a luminosity distance of 153 Mpc. Our continuing search for precursor events in pre-explosion images of nearby type II_n supernovae observed by PTF revealed a positive precursor detection for this supernova. Here we measure time relative to 2010 August 20.22, which corresponds to the onset of the supernova explosion (the main event visible in Fig. 1). The initial bump in the pre-supernova light curve emerged at day -37 relative to the supernova discovery date, and peaked at an absolute

magnitude of about -15 ($\sim 2.25 \times 10^{41} \text{ erg s}^{-1}$) in the R_{PTF} band. The main supernova explosion then brightened for two weeks and peaked at an R_{PTF} absolute magnitude of -18.4 ($\sim 5.2 \times 10^{42} \text{ erg s}^{-1}$), radiating a total bolometric luminosity of $\sim 3 \times 10^{49} \text{ erg}$, while the precursor bump radiated $\sim 6 \times 10^{47} \text{ erg}$ (or more, due to the unknown bolometric correction).

Spectra of the supernova, showing a blue continuum with Balmer emission lines, are presented in Fig. 2. The continuum becomes redder

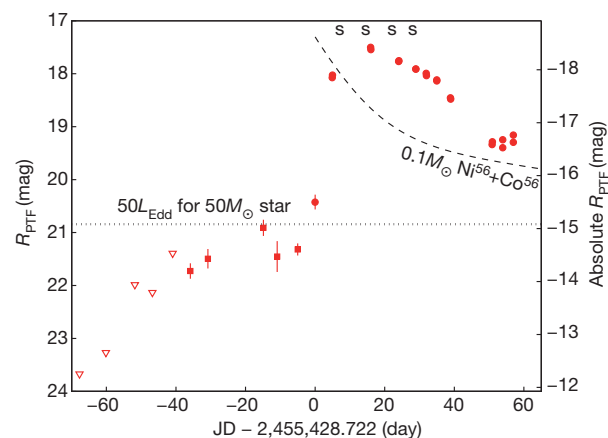


Figure 1 | The light curve of SN 2010mc as obtained with the Palomar 48-inch telescope. Red circles, data based on individual images; squares, based on coadded images; open triangles, 3σ upper limits derived from coadded images. Error bars, 1σ . The object magnitudes are given in the PTF magnitude system^{27,28}. The left-hand y axis shows the R -band apparent magnitude; the right-hand y axis indicates the R -band absolute magnitude. Other data sets discussed in the Supplementary Information, including those from the Palomar 60-inch and Swift-UVOT, are listed in Supplementary Table 3. All the photometric and spectroscopic data are available via the WISEREP website²⁹. Dashed line at top right, the expected luminosity from the radioactive decay of an ejected mass of $0.1 M_{\odot}$ of Ni^{56} (which decays to Co^{56} , which decays to Fe^{56}). Assuming that at late times the optical depth is sufficiently large to convert the radioactive energy to optical luminosity, but not too large so it will go into PdV work, this line represents an upper limit on the total amount of Ni^{56} in the ejecta; it was set to coincide with the latest observation of the supernova at Julian date $\text{JD} \approx 2,455,758$ (see Supplementary Table 3). The dotted line represents a bolometric luminosity equal to 50 times the Eddington luminosity L_{Edd} for a $50 M_{\odot}$ star (order of magnitude estimate of the mass of the progenitor assuming it is a massive star). The right edges of the “S” symbols above the light curve indicate the epochs at which we obtained spectra (see Fig. 2). A full version of this light curve, including the late-time observations, is shown in Supplementary Information.

¹Benoziyo Center for Astrophysics, Weizmann Institute of Science, 76100 Rehovot, Israel. ²School of Physics and Astronomy, University of Southampton, Southampton SO17 1BJ, UK. ³Department of Physics (Astrophysics), University of Oxford, Keble Road, Oxford OX1 3RH, UK. ⁴Department of Astronomy, University of California, Berkeley, California 94720-3411, USA. ⁵Observatories of the Carnegie Institution for Science, 813 Santa Barbara Street, Pasadena, California 91101, USA. ⁶Division of Physics, Mathematics, and Astronomy, California Institute of Technology, Pasadena, California 91125, USA. ⁷Kavli Institute for Theoretical Physics, Kohn Hall, University of California, Santa Barbara, California 93106, USA. ⁸Department of Physics, Broida Hall, University of California, Santa Barbara, California 93106, USA. ⁹Lawrence Berkeley National Laboratory, 1 Cyclotron Road, Berkeley, California 94720, USA. ¹⁰Las Cumbres Observatory Global Telescope Network, 6740 Cortona Drive, Suite 102, Goleta, California 93117, USA. ¹¹Spitzer Science Center, California Institute of Technology, M/S 314-6, Pasadena, California 91125, USA. ¹²Physics Department, University of Wisconsin–Milwaukee, Milwaukee, Wisconsin 53211, USA. ¹³School of Physics and Astronomy, Tel-Aviv University, 69978 Tel-Aviv, Israel. ¹⁴Department of Astronomy, University of Texas, Austin, Texas 78712-0259, USA. ¹⁵Racah Institute of Physics, The Hebrew University, 91904 Jerusalem, Israel.

with time, and its slope corresponds to an effective temperature of more than 16,000 K at day five, dropping to about 8,000 K at day 27. The H α line has an initial width of $\sim 3 \times 10^3 \text{ km s}^{-1}$ at day 6, decreasing to $\sim 10^3 \text{ km s}^{-1}$ at day 14. A broad (10^4 km s^{-1}) P Cygni profile emerges by day 27. The spectra also show He I lines with decreasing strength, presumably due to the drop in temperature.

The nature of the precursor bump is very intriguing and can potentially tell us a great deal about the supernova explosion and the progenitor. The only interpretation that is fully consistent with the photometric and spectroscopic evidence is that the first bump represents an outburst from the SN progenitor about one month before explosion, while the brighter bump is initiated by a full explosion of the star a few weeks later. Below we analyse this model in the context of the photometric and spectroscopic data. In Supplementary Information section 6, we discuss some alternative models and conclude that they are unlikely.

The mass ejected by the precursor burst can be estimated in various independent ways. By requiring that the precursor integrated bolometric luminosity, $E_{\text{bol,prec}}$, be lower than the kinetic energy of the precursor outburst (moving at velocity v_{prec} in km s^{-1}) which powers it, we can set a lower limit on the mass ejected in the precursor outburst, $M_{\text{prec}} \gtrsim 2E_{\text{bol,prec}} v_{\text{prec}}^{-2} \approx 1.5 \times 10^{-2} (v_{\text{prec}}/2,000)^{-2} M_{\odot}$. The outburst velocity is estimated from the line widths of 1,000–3,000 km s^{-1} , seen in the early-time spectra of the supernova. As this mass was presumably ejected over a period of about one month (that is, the outburst duration), the effective annual mass-loss rate is about 10 times higher. A similar order-of-magnitude argument can be used to put an upper limit on the mass in the precursor outburst. If some of the supernova bolometric energy, $E_{\text{bol,SN}}$, is due to interaction between the supernova ejecta, moving at v_{SN} (in km s^{-1}), and the precursor shell, and assuming high efficiency of conversion of the kinetic energy to luminosity, then $M_{\text{prec}} \lesssim 2E_{\text{bol,SN}} v_{\text{SN}}^{-2} \approx 3 \times 10^{-2} (v_{\text{SN}}/10^4)^{-2} M_{\odot}$.

Another method to estimate the mass in the ejecta is based on the H α emission-line luminosity and the radius of the photosphere, which is determined from a black-body fit to the spectra (Supplementary Fig. 2). This method, derived in Supplementary Information section 2, sug-

gests a mass-loss rate of $\gtrsim 10^{-1} M_{\odot} \text{ yr}^{-1}$, or a total ejected mass of $\gtrsim 10^{-2} M_{\odot}$, if we assume a month-long outburst in which material is ejected at a velocity of 2,000 km s^{-1} .

Another independent method for estimating the mass in the circumstellar matter is based on the rise time of the supernova. Because photons diffuse through material between the supernova and the observer, the supernova rise time gives us an upper limit on the diffusion timescale and therefore the total intervening mass. As the supernova rise time was about one week, this argument suggests that if the shell is spherically symmetric its total mass cannot exceed about $0.4 M_{\odot}$ (see Supplementary Information section 5). Therefore, the kinetic-energy arguments, the H α luminosity and the diffusion timescale are consistent with each other (and with the X-ray limits derived in Supplementary Information section 3), and indicate that the total mass lost during the outburst is of the order of $\sim 10^{-2} M_{\odot}$.

Our model for the sequence of events is presented in Fig. 3. In a nutshell, this model suggests that the precursor outburst ejected $\sim 10^{-2} M_{\odot}$ at a velocity of 2,000 km s^{-1} about one month before the supernova explosion. Shortly after the supernova explosion, this ejected material was engulfed by the supernova ejecta. At later times, after the optical depth decreases, we start seeing indications of the high velocity of the supernova ejecta. We discuss some less likely alternative models in Supplementary Information section 6.

A surprising result is the short time between the outburst and the explosion, which is a tiny fraction ($\sim 10^{-8}$) of the lifetime of a massive star. Even if massive stars have multiple mass-loss episodes (with mass loss $\gtrsim 10^{-2} M_{\odot}$) during their lifetime, the number of such episodes cannot exceed $\sim 5,000$; otherwise, the mass lost will exceed a typical stellar mass. A conservative estimate shows that so far it might be possible to detect such an outburst in a sample of up to about 20 nearby type II supernovae, which have deep pre-explosion observations (see Supplementary Information section 7). Therefore, the probability of observing a random burst one month before the explosion is 0.1%. We conclude that such outbursts are either causally related to, or at least two orders of magnitude more common before, the final stellar explosion.

When considering where such an eruption could originate, one is led to the stellar core, as the binding energy it can liberate by contraction and nuclear reactions is sufficiently large. Because the actual luminosity is most probably neutrino-dominated, the Kelvin–Helmholtz timescale for this contraction could be short enough to explain the precursor's rapid rise in luminosity. However, the energy liberated at the core must reach the envelope. This requires an efficient energy-transport mechanism⁶. There are several proposed mechanisms that predict high mass-loss rates before the final stellar explosion. Recently, it was suggested⁶ that in some massive stars the super-Eddington fusion luminosities, shortly before core collapse, could drive convective motions that in turn excite gravity waves that propagate towards the stellar surface. The dissipation of these waves could unbind up to several solar masses of the stellar envelope. Alternatively, it was suggested⁷ that the mass loss is driven by a common-envelope phase²³ due to the spiralling-in of a neutron star into a giant companion core (a so-called Thorne–Żytkow object), unbinding the companion envelope and setting up accretion onto the neutron star that collapses into a black hole and triggers a supernova explosion shortly thereafter. This model, however, predicts an outflow velocity that is considerably lower than the one observed in the precursor of SN 2010mc, and is therefore disfavoured. Another possible mechanism is the pulsational pair instability supernova²⁴. However, current models predict that the mass ejected in these events will probably be much larger than the $10^{-2} M_{\odot}$ seen in SN 2010mc^{5,25}.

The velocity and energetics of the precursor of SN 2010mc are consistent with the predictions of the wave-driven outburst mechanism⁶. However, a more detailed theoretical investigation is required in order to test whether this model is consistent with all the observational evidence. In Supplementary Information section 8, given the observed precursor luminosity, we theoretically derive the mass loss (using the wave-driven outburst mechanism) to be $\sim 0.05 M_{\odot}$, in excellent agreement with

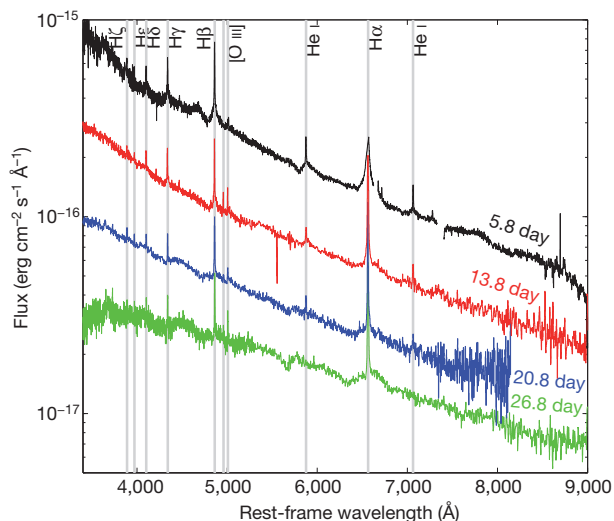


Figure 2 | Spectra of SN 2010mc, showing prominent Balmer emission lines. The early-time spectra are well fitted by a narrow component ($\sim 10^2 \text{ km s}^{-1}$; the fit includes the instrumental line broadening) and a broad component extending to $\sim 3 \times 10^3 \text{ km s}^{-1}$ at the first epoch, and decreasing to 10^3 km s^{-1} at the second epoch. At later epochs the Balmer H α line develops a P Cygni profile (similar to that of normal type II supernovae) with a velocity difference between the absorption bottom and the emission peak of $\sim 10^4 \text{ km s}^{-1}$. At the first epochs we also detect He I lines, some of which are marked on the plot. They become weaker (see Supplementary Fig. 2) at later epochs, presumably owing to the decrease in the effective temperature (Supplementary Fig. 2). This, as well as the absence of He II lines, indicates that our temperature estimate (Supplementary Fig. 2) is reasonable.

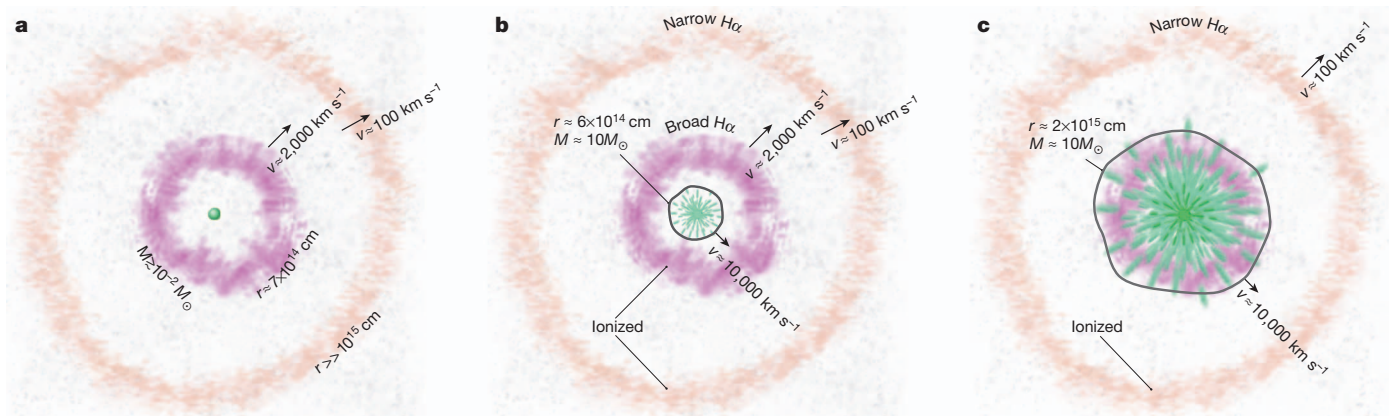


Figure 3 | Qualitative sketch of the proposed model for SN 2010mc. **a**, At day ~ 0 (relative to the supernova explosion time), an inner shell (purple) with a mass of $\sim 10^{-2} M_{\odot}$, ejected about one month earlier during the precursor outburst and moving at velocity v of about $2,000$ km s $^{-1}$, is located at a radius r of $\sim 7 \times 10^{14}$ cm. An outer shell (orange), found at a large radius and moving at about 100 km s $^{-1}$ (up to 10^3 km s $^{-1}$), was ejected at earlier times. This indicates that the progenitor probably had multiple mass-loss episodes in the past tens to hundreds of years before the explosion. **b**, At day ~ 5 , the supernova shock front (dark grey line) moving at $\sim 10,000$ km s $^{-1}$ is ionizing the inner and outer shells which produce the broad and narrow H α emission seen in the early-time spectra. **c**, At day ~ 20 , the supernova shock engulfs the inner shell, and the intermediate-width

($\sim 2,000$ km s $^{-1}$) component of the H α line disappears. Instead we detect a $1,000$ km s $^{-1}$ line, presumably due to material ejected during previous, but probably recent, mass-loss episodes and that is found at larger distances from the supernova. We note that inspection of the supernova light curve shows that around day 50 there is an indication of a possible rebrightening, perhaps resulting from the supernova ejecta colliding with such additional material ejected at earlier times. At day ~ 20 , the photospheric temperature decreases and it becomes optically thinner, and therefore we begin seeing an H α P Cygni profile with a velocity of $\sim 10,000$ km s $^{-1}$. This line becomes even stronger on day 27. This reflects the unshocked ejecta below the interaction zone.

our mass-loss estimates. Furthermore, we note that the velocity of the precursor ejecta is higher than predicted by other models⁷. Finally, we note that the mass-loss velocity in SN 2010mc is considerably higher than the one observed in SN 2009ip¹⁸, although the mass-loss rate was similar²⁶.

Received 14 October; accepted 18 December 2012.

1. Dopita, M. A., Cohen, M., Schwartz, R. D. & Evans, R. The 1984 supernova in NGC 3169 — evidence for a superwind. *Astrophys. J.* **287**, L69–L71 (1984).
2. Chugai, N. N. & Danziger, I. J. Supernova 1988Z — low-mass ejecta colliding with the clumpy wind. *Mon. Not. R. Astron. Soc.* **268**, 173–180 (1994).
3. Gal-Yam, A. & Leonard, D. C. A massive hypergiant star as the progenitor of the supernova SN 2005gl. *Nature* **458**, 865–867 (2009).
4. Ofek, E. O. et al. Supernova PTF 09uj: a possible shock breakout from a dense circumstellar wind. *Astrophys. J.* **724**, 1396–1401 (2010).
5. Woosley, S. E., Blinnikov, S. & Heger, A. Pulsational pair instability as an explanation for the most luminous supernovae. *Nature* **450**, 390–392 (2007).
6. Quataert, E. & Shiode, J. Wave-driven mass loss in the last year of stellar evolution: setting the stage for the most luminous core-collapse supernovae. *Mon. Not. R. Astron. Soc.* **423**, L92–L96 (2012).
7. Chevalier, R. A. Common envelope evolution leading to supernovae with dense interaction. *Astrophys. J.* **752**, L2 (2012).
8. Schlegel, E. M. A new subclass of Type II supernovae? *Mon. Not. R. Astron. Soc.* **244**, 269–271 (1990).
9. Filippenko, A. V. Optical spectra of supernovae. *Annu. Rev. Astron. Astrophys.* **35**, 309–355 (1997).
10. Kiewe, M. et al. Caltech Core-Collapse Project (CCCP) observations of type II supernovae: typical properties and implications for their progenitor stars. *Astrophys. J.* **744**, 10 (2012).
11. Chugai, N. N. & Danziger, I. J. A massive circumstellar envelope around the type-II supernova 1995G. *Astron. Lett.* **29**, 649–657 (2003).
12. Ofek, E. O. et al. SN 2006gy: an extremely luminous supernova in the galaxy NGC 1260. *Astrophys. J.* **659**, L13 (2007).
13. Smith, N. et al. SN 2006gy: Discovery of the most luminous supernova ever recorded, powered by the death of an extremely massive star like η Carinae. *Astrophys. J.* **666**, 1116–1128 (2007).
14. Owocki, S. Hot-star mass-loss mechanisms: winds and outbursts. *Astron. Soc. Pacif. Conf. Ser.* **425**, 199–208 (2010).
15. Smith, N. et al. Discovery of precursor LBV outbursts in two recent optical transients: the fitfully variable missing links UGC 2773-OT and SN 2009ip. *Astron. J.* **139**, 1451–1467 (2010).
16. Pastorello, A. et al. Multiple major outbursts from a restless luminous blue variable in NGC 3432. *Mon. Not. R. Astron. Soc.* **408**, 181–198 (2010).
17. Foley, R. J. et al. The diversity of massive star outbursts. I. Observations of SN 2009ip, UGC 2773 OT2009-1, and their progenitors. *Astrophys. J.* **732**, 32 (2011).
18. Mauerhan, J. C. et al. The unprecedented third outburst of SN 2009ip: a luminous blue variable becomes a supernova. Preprint at <http://arXiv.org/abs/1209.6320> (2012).

19. Prieto, J. L., Brimacombe, J., Drake, A. J. & Howerton, S. The rise of the remarkable type II supernova SN 2009ip. Preprint at <http://arXiv.org/abs/1210.3347> (2012).
20. Law, N. M. et al. The Palomar Transient Factory: system overview, performance, and first results. *Publ. Astron. Soc. Pacif.* **121**, 1395–1408 (2009).
21. Rau, A. et al. Exploring the optical transient sky with the Palomar Transient Factory. *Publ. Astron. Soc. Pacif.* **121**, 1334–1351 (2009).
22. Ofek, E. O. et al. X-ray emission from supernovae in dense circumstellar matter environments: a search for collisionless shocks. Preprint at <http://arXiv.org/abs/1206.0748> (2012).
23. Taam, R. E. & Ricker, P. M. Common envelope evolution. *New Astron. Rev.* **54**, 65–71 (2010).
24. Rakavy, G., Shaviv, G. & Zinamon, Z. Carbon and oxygen burning stars and pre-supernova models. *Astrophys. J.* **150**, 131–162 (1967).
25. Quimby, R. M. et al. Hydrogen-poor superluminous stellar explosions. *Nature* **474**, 487–489 (2011).
26. Ofek, E. O. et al. SN 2009ip: Constraints on the progenitor mass-loss rate. *Astrophys. J.* (submitted).
27. Ofek, E. O. et al. The Palomar Transient Factory photometric calibration. *Publ. Astron. Soc. Pacif.* **124**, 62–73 (2012).
28. Ofek, E. O. et al. The Palomar Transient Factory photometric catalog 1.0. *Publ. Astron. Soc. Pacif.* **124**, 854–860 (2012).
29. Yaron, O. & Gal-Yam, A. WISEREP — An interactive supernova data repository. *Publ. Astron. Soc. Pacif.* **124**, 668–681 (2012).

Supplementary Information is available in the online version of the paper.

Acknowledgements We thank E. Quataert and M. Cantiello for discussions. The VLA is operated by the National Radio Astronomy Observatory, a facility of the US National Science Foundation (NSF) operated under cooperative agreement by Associated Universities, Inc. This paper is based on observations obtained with the Samuel Oschin Telescope as part of the Palomar Transient Factory project. We are grateful for the assistance of the staff at the various observatories where data were obtained. We acknowledge support from the Arye Dissentnik career development chair, the Helen Kimmel Center for Planetary Science, the Israeli Ministry of Science, the Royal Society, the NSF, the Israeli Science Foundation, the German-Israeli Foundation, ERC, the US Department of Energy, Gary and Cynthia Bengier, the Richard and Rhoda Goldman Fund, the Christopher R. Redlich Fund, and the TABASGO Foundation.

Author Contributions E.O.O. initiated the search for precursor outbursts and wrote the paper, M.S. wrote the image-subtraction pipeline, S.B.C. reduced the Swift-UVOT observations, M.M.K. reduced the P60 observations, A.G.-Y. helped with the spectroscopic analysis, L.B., E.N. and N.J.S. contributed to the theoretical interpretation, A.V.F. assisted with the spectroscopy and edited the paper, D.A.H., D.M. and J.M.S. conducted the spectroscopic observations or reductions, O.Y. helped write the paper, and S.R.K., I.A., J.S.B., R.L., P.E.N. and J.S. built the PTF hardware and software infrastructure.

Author Information Reprints and permissions information is available at www.nature.com/reprints. The authors declare no competing financial interests. Readers are welcome to comment on the online version of the paper. Correspondence and requests for materials should be addressed to E.O.O. (eran@astro.caltech.edu).

Reconstructing state mixtures from diffraction measurements

Pierre Thibault¹ & Andreas Menzel²

Progress in imaging and metrology depends on exquisite control over and comprehensive characterization of wave fields. As reflected in its name, coherent diffractive imaging relies on high coherence when reconstructing highly resolved images from diffraction intensities alone without the need for image-forming lenses^{1–3}. Fully coherent light can be described adequately by a single pure state. Yet partial coherence and imperfect detection often need to be accounted for, requiring statistical optics or the superposition of states^{4,5}. Furthermore, the dynamics of samples are increasingly the very objectives of experiments⁶. Here we provide a general analytic approach to the characterization of diffractive imaging systems that can be described as low-rank mixed states. We use experimental data and simulations to show how the reconstruction technique compensates for and characterizes various sources of decoherence quantitatively. Based on ptychography^{7,8}, the procedure is closely related to quantum state tomography and is equally applicable to high-resolution microscopy, wave sensing and fluctuation measurements. As a result, some of the most stringent experimental conditions in ptychography can be relaxed, and susceptibility to imaging artefacts is reduced. Furthermore, the method yields high-resolution images of mixed states within the sample, which may include quantum mixtures or fast stationary stochastic processes such as vibrations, switching or steady flows.

Recent experimental advances have provided cleaner probes to investigate ever more complex systems. However, state mixtures often have to be used to accurately describe the statistical nature of the system under investigation. In the context of imaging, we categorize the occurrence of mixed states into three distinct groups, illustrated in Fig. 1: fluctuations in the probing radiation, commonly grouped under the concept of partial coherence (Fig. 1a), mixed states within the object of interest (Fig. 1b) and detector point spread (Fig. 1c). Although any such source of decoherence affects the measured intensity distribution in a specific way, they all share the common signature of reducing the so-called fringe or speckle visibility in the diffracted intensities (Fig. 1d).

Decoherence is often an unwanted complication, and much experimental effort is spent in reducing its impact. The need for coherence effectively imposes severe constraints on the setup, such as a high-brilliance source, negligible vibrations of all components, a static sample or ultra-short pulses and often a drastic reduction of usable flux. At hard X-ray synchrotron sources, for instance, the necessary coherence filtering reduces flux by several orders of magnitude. In the past few years, progress has been made to accommodate more permissive conditions. In some instances, imaging with a partially coherent wavefront can be cast as a blind deconvolution problem⁹. However, preconditions for this approach are frequently unsatisfied. Until now the general problem of how to mitigate decoherence in data analysis has largely remained unexplored.

Here we show that stationary mixed states of any origin can be reconstructed by using ptychography. Used with X-rays¹⁰, electrons¹¹ and visible light¹², ptychography is a coherent diffractive imaging technique that allows the simultaneous reconstructions of the incident

wavefront and the sample transmission. Producing a ptychogram requires a sequence of diffraction measurements in which the object is scanned through a spatially confined illumination, or ‘probe’. The probe is assumed constant, and the specimen’s interaction with it is assumed to be adequately described by a multiplicative transmission function. Consequently, a fully coherent ptychography measurement can be written as a set of simple products of probe and object. Sampling takes place in reciprocal space, in which the phase information in the scattered field is discarded and only intensities I are recorded as a function of the momentum transfer \mathbf{q} .

We show in the Supplementary Information how such a measurement can be recast in probabilistic terms by following von Neumann’s analysis of quantum mechanics¹³. Thus, the expectation value of any observable can conveniently be expressed in terms of an operator, here \hat{I}_{jq} , where j indexes the position in the ptychographic scan, and a density operator, usually represented by a density matrix ρ :

$$I_{jq} = \text{Tr} \hat{I}_{jq} \rho \quad (1)$$

where Tr denotes the trace operator. Reconstructing the density matrix from such measurements of a set of observables is precisely the task of quantum state tomography. The key requirement for a reconstruction to succeed is that the measurements are tomographically complete; for example, that they span the entire parameter space of the system. Formally, this requires the density matrix to be of sufficiently low rank and that it can be sampled by sufficiently many independent measurements. Stating that ρ is of rank r means that there exists a spectral decomposition of ρ with r orthogonal states. Beyond the fully coherent

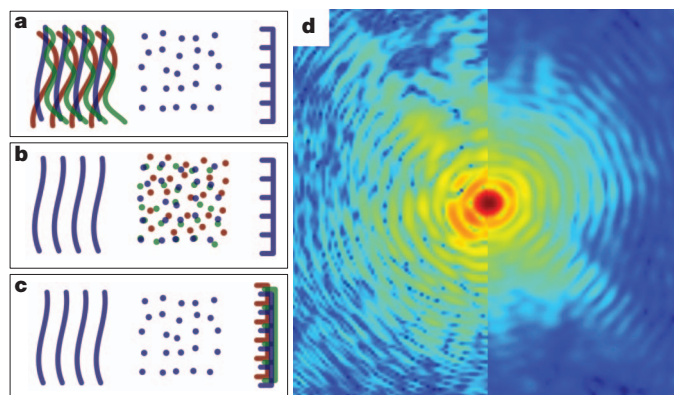


Figure 1 | Decoherence in scattering experiments. **a**, Mixed states within the probing radiation may include all sources of mixing that manifest themselves as transverse partial coherence or finite bandwidth. **b**, Mixed states in the sample may occur from quantum mixtures and fast stationary stochastic processes such as vibrations, switching or steady flows. **c**, The spatial extent over which two detections cannot be discerned corresponds effectively to a mixed state in the detector plane. **d**, The signature of decoherence in far-field diffraction is a decrease in ‘visibility’ of the scattered intensity distribution. Here the right half of the simulated diffraction pattern shows the effect of sample vibration.

¹Physics Department, Technische Universität München, 85748 Garching bei München, Germany. ²Paul Scherrer Institut, 5232 Villigen PSI, Switzerland.

case ($r = 1$), ptychography can be generalized to mixed states ($r > 1$) of various origins, and the reconstruction problem amounts to finding tomographically complete sets for probe and object states. When the object is in a pure state, this spectral decomposition is equivalent to the mode expansion of the mutual coherence function¹⁴, as recently used for coherent diffractive imaging to allow reconstructions with partial transverse¹⁵ and longitudinal coherence¹⁶ from a single diffraction pattern.

Determining the conditions under which a solution is trustworthy is a central concern for any inverse problem. Increasing the dimension of the density matrix adds a large number of degrees of freedom, which intuitively calls for an equal increase in measured data. This claim is supported by recent work in compressed sensing^{17,18}, which confirms that, if the ensemble of measurement operators satisfies certain conditions, the increase in measured data should scale with the rank r of the density matrix to be reconstructed. The formal result does not apply completely to ptychography because of the need to concurrently reconstruct the object transmission function. However, simulations indicate that the rank scaling rule seems to apply in a wide range of situations. In practice this condition amounts to ensuring that the scanned area is covered by a larger number of measurement points. The fact that the use of finer sampling, or a larger overlap of adjacent probe positions, helps in solving the problem is consistent with the Wigner distribution point of view, taken in early formulations of both ptychography^{19,20} and quantum state tomography²¹. In these implementations, dense sampling effectively maps the complete phase space. Conversely, this general result also explains why ptychographic reconstructions can succeed with a relatively small number of diffraction patterns in comparison with the extents of the reconstructed images.

Adapting existing algorithms to the new problem formulation is rather straightforward (see also Supplementary Information). Most reconstruction algorithms use projections^{22,23}, one of which is to ensure that the model for the wave leaving the object complies with measured data. This Fourier magnitude projection can be seen as projecting any point in the complex plane onto a circle whose square radius is equal to the measured intensity. Reconstruction of the low-rank density matrix uses an equivalent projection in which the circle is replaced by a higher-dimensional quadric form. Maximum-likelihood refinement^{24,25} is also readily adapted through a modification of the intensity model. Any of these modified algorithms yields, if it converges, a set of r modes that span the rank space of ρ . All the reconstructions below use the difference map implementation⁷ followed by maximum-likelihood refinement²⁵.

We demonstrate our findings with X-ray data from a simple ptychography experiment. The setup, shown in Fig. 2a, is described elsewhere⁷. The monochromatic beam was apertured by slits and focused by a Fresnel zone plate onto a test sample made from nano-fabricated gold pillars. First, the slit opening was smaller than the area that can be considered coherent. Then the horizontal slits were opened fourfold, significantly exceeding the coherence length of the incident X-ray beam. Typical far-field diffraction patterns obtained in either case are shown in Fig. 2.

As expected, reconstruction from the high-coherence data set poses no problem. However, even in this case, only about 80% of the illumination is carried by the dominant coherent mode, and imaging artefacts can be reduced by allowing for multiple modes (see Supplementary Fig. 3). Reconstructions from the low-coherence data set are shown in Fig. 3. An attempt that assumed full coherence failed to produce a faithful image of the sample. When reconstructing—without a priori wavefront characterization—12 modes in the illumination, image retrieval converged to the result shown in Fig. 3b. The five most significant modes obtained from this reconstruction are shown in Fig. 3c. The relative power of the dominant mode, as measure of coherence, is seen to be slightly less than 40%.

The immediate consequence of our result is a reduced susceptibility to systematic errors while simultaneously relaxing experimental conditions. Acquisition times can be reduced by admitting higher—albeit less coherent—flux, thereby alleviating long-term stability requirements for the instrumentation. Reconstruction of the illumination modes also has intrinsic interest, for instance for metrological applications to complement interferometric techniques^{26,27}. Derived quantities such as the complex degree of coherence are readily computed from the reconstructed modes and are in good agreement with other experimental measurements (see Supplementary Fig. 2). Through detailed simulations we have verified that multiple additional sources of decoherence are similarly accounted for, including sample vibrations²⁸ and partial coherence in an unfocused probe. Similarly, the loss of visibility caused by the detector point spread can be included in the density matrix (see Supplementary Fig. 3). Decoherence effects caused by the detector point spread are thus transferable to illumination properties, a fact that can be interpreted as a consequence of Cowley's reciprocity principle²⁹.

The formalism we present also opens new imaging applications, because the reconstruction of sample mixtures (Fig. 1b) can be implemented in a manner completely analogous to the cases discussed so far. The wide-sense stationary processes to be thus characterized include continuous sample movement, stochastic equilibrium fluctuations,

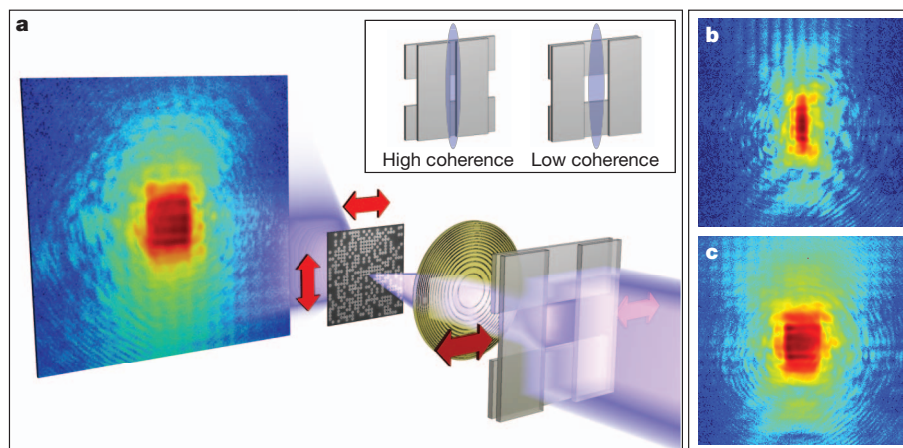


Figure 2 | Ptychography with partly coherent X-rays. **a**, A portion of the incident beam, selected by slits, is focused with a Fresnel zone plate onto the specimen, which is scanned in both transverse directions. The order-sorting aperture is not shown, for clarity. The scattered intensities are collected on a

detector in the far field. The inset shows two different openings of the horizontal slits as well as elongated ellipses representing the approximate area over which the beam is coherent. **b**, **c**, One of the measured diffraction patterns in high-coherence mode (**b**) and in low-coherence mode (**c**).

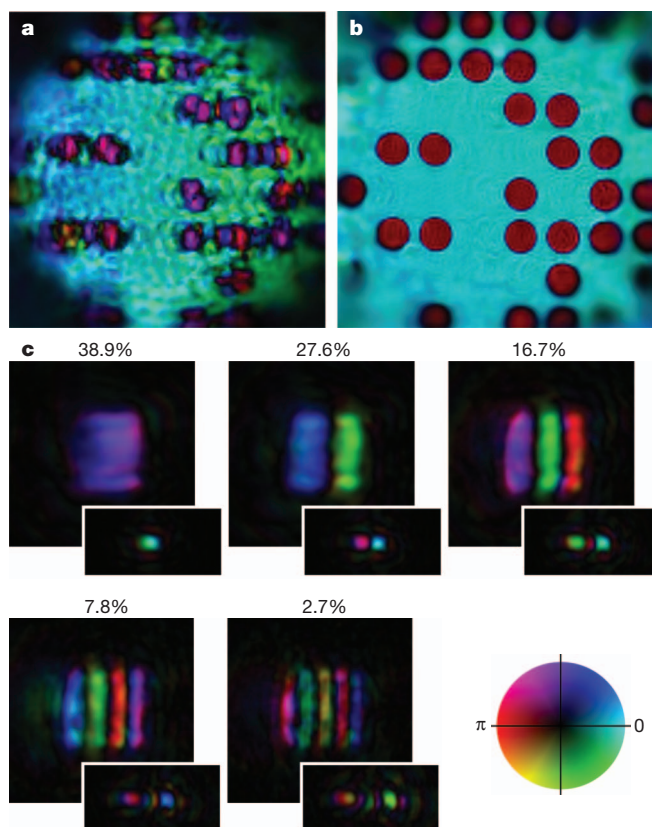


Figure 3 | Reconstruction from the low-coherence X-ray experiment.

a, Reconstructed transmission function when the incoming wavefield is assumed to be fully coherent, that is, ρ is of rank one. **b**, Reconstructed transmission function with an incoming wavefield composed of $r = 12$ independent modes. **c**, The five dominant modes reconstructed simultaneously with the sample, represented in Fourier space. Complex amplitudes in the sample plane are shown in the insets. In accordance with the shorter horizontal coherence length, variation in all modes is essentially only along the horizontal direction.

steady flows and periodic variations. Typically, to characterize such dynamics, intensity fluctuation spectroscopy⁶ or related techniques are employed and, when spatially inhomogeneous, statistics can be characterized by scanning-probe techniques. Applying ptychography to such fluctuation microscopy³⁰ enhances its resolving power and sensitivity.

To demonstrate the potential of mixed-sample-state reconstruction, we simulated an Ising toy model comprising 4×4 quantum dots, illustrated in Fig. 4a. Each quantum dot can be in two possible spin states, which we assume to produce contrast in a scattering experiment. The equilibrium configuration follows the usual rules of Ising models given by identical ferromagnetic couplings between all first neighbours and a temperature well above the Curie point. The four central couplings, shown in red, were chosen to be antiferromagnetic. This model is simple enough to have a configuration space of manageable size and is sufficiently well understood for validation of a simulated imaging experiment. In our simulation we assumed that the dynamics are fast; that is, that all possible configurations are explored during each single exposure. The extent of the simulated probe function is such that two neighbouring quantum dots can be illuminated simultaneously.

Reconstruction from the simulated data set follows the same principles as described above. Here, the illumination was assumed to be a pure state, and the density matrix representing the mixed state of the sample was sufficient to describe the statistics of the entire experiment. Sixteen modes were reconstructed in total, of which the four dominant ones are shown in Fig. 4b. As a result of symmetry, the expectation

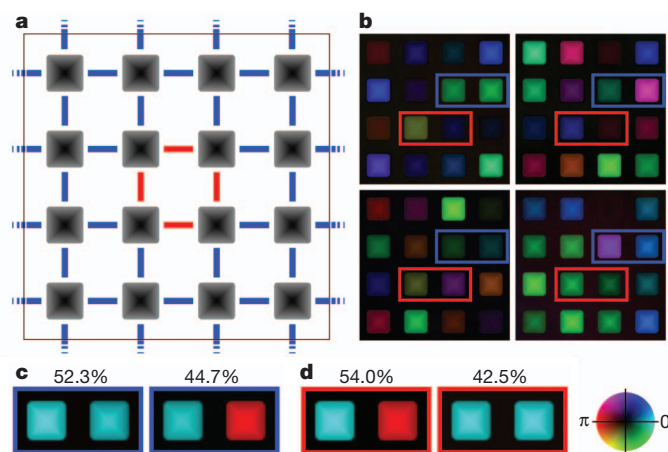


Figure 4 | Imaging a simulated Ising model. **a**, In the sample layout, grey squares mark individual spins, which incur a $\pm\pi/2$ phase shift on the illumination. Blue lines represent ferromagnetic couplings, $J = -1$, red lines antiferromagnetic ones, $J = +1$. Periodic boundary conditions apply. The configurations are Boltzmann distributed with a temperature five times the Curie temperature for the infinite two-dimensional Ising model. **b**, The four dominant modes after subtraction of the mean. Consistent with the probe size, long-range symmetries are not reconstructed. **c**, **d**, The results of orthogonalization of neighbouring spins, outlined by blue and red frames in **b**, for a ferromagnetic bond (**c**) and an antiferromagnetic bond (**d**). The relative mode amplitudes are in good agreement with expected values.

value of any spin is zero. Still, the reconstruction reliably images each quantum dot because of the decoherence that its fluctuation causes. What is more, correlations between dots on length scales shorter than the illumination are encoded in the diffraction data. These short-range correlations are well reconstructed when orthogonalization is applied to two neighbouring spins (Fig. 4c, d). The obtained relative powers are quantitatively consistent with the ferromagnetic and antiferromagnetic couplings. Beyond magnetic systems, we see potential applications of our method in the direct imaging of spin-density wave domains, of quantum oscillator modes and of steady flows in nanofluidics. Our simulations indicate that reconstruction can succeed even in cases where decoherence occurs concurrently in the illumination and the object. However, in such cases, coupling of object and probe modes may be unavoidable because, for instance, decoherence caused by global translations of the sample has the same effect as translations of the illumination.

The mixed-state formulation of ptychography presented in this letter helps to address some of the most limiting experimental challenges. Acceptance of some degree of partial coherence and robustness to detector point spread improves reconstruction quality and reliability and makes further instruments useable or a higher flux accessible, thus widening the applicability of ptychographic imaging. Bridging intensity fluctuation techniques with coherent diffractive imaging, the principles introduced in this paper allow dynamical systems to be imaged with only the most basic of assumptions; that is, wide-sense stationary statistics that can be described by low-rank density matrices. Steady-state fluctuations in both quantum and classical systems can be reconstructed unambiguously with high resolving power, offering new insight into fluctuations at phase boundaries, defects and points of excitation.

METHODS SUMMARY

Experiments were conducted at the cSAXS beamline (X12SA) at the Swiss Light Source, Paul Scherrer Institut, Villigen, at an X-ray wavelength of 2 Å. Longitudinal coherence was determined by the bandwidth of $\Delta E/E \approx 0.02\%$ of the double-crystal Si(111) monochromator. As described in the text, transverse-coherence filtering was achieved with movable slits about 33 m from the source. The coherence length at the slits was estimated to be about $200\ \mu\text{m} \times 20\ \mu\text{m}$ (horizontal \times vertical). The same slits determined the part of the Fresnel zone

plate that was illuminated to create the probe. The zone plate had been manufactured as described in ref. 31 with 1,000-nm-thick gold structures, a diameter of 200 μm and a finest zone width of 100 nm. The same manufacturing process was used for the sample, which consisted of a pseudorandom array of gold structures with diameter 500 nm on a rectangular grid with pitch 750 nm. A PILATUS-II single-photon counting hybrid pixel detector³² was positioned 7.18 m from the sample. Over roughly 7 m the volume between sample and detector was flushed with helium to reduce absorption and scattering. Scans, shown in Fig. 3, comprised sample movements along concentric circles. Six such circles, with an increase in diameter of $\Delta r = 0.25 \mu\text{m}$ and $5n$ points on the n th shell¹⁰, resulted in data acquisition at 90 positions for a field of view of about 5 μm diameter. The acquisition time was typically 2 s per position.

Received 26 June; accepted 16 November 2012.

- Miao, J., Charalambous, P., Kirz, J. & Sayre, D. Extending the methodology of X-ray crystallography to allow imaging of micrometre-sized non-crystalline specimens. *Nature* **400**, 342–344 (1999).
- Eisebitt, S. *et al.* Lensless imaging of magnetic nanostructures by X-ray spectroholography. *Nature* **432**, 885–888 (2004).
- Abbey, B. *et al.* Keyhole coherent diffractive imaging. *Nature Phys.* **4**, 394–398 (2008).
- Mandel, L. & Wolf, E. Coherence properties of optical fields. *Rev. Mod. Phys.* **37**, 231–287 (1965).
- Goodman, J. W. *Statistical Optics* (Wiley, 2000).
- Sutton, M. A review of X-ray intensity fluctuation spectroscopy. *C. R. Phys.* **9**, 657–667 (2008).
- Thibault, P. *et al.* High-resolution scanning X-ray diffraction microscopy. *Science* **321**, 379–382 (2008).
- Maiden, A. M. & Rodenburg, J. M. An improved ptychographical phase retrieval algorithm for diffractive imaging. *Ultramicroscopy* **109**, 1256–1262 (2009).
- Clark, J. N. & Peele, A. G. Simultaneous sample and spatial coherence characterisation using diffractive imaging. *Appl. Phys. Lett.* **99**, 154103 (2011).
- Dierolf, M. *et al.* Ptychographic X-ray computed tomography at the nanoscale. *Nature* **467**, 436–439 (2010).
- Putkunz, C. *et al.* Atom-scale ptychographic electron diffractive imaging of boron nitride cones. *Phys. Rev. Lett.* **108**, 1–4 (2012).
- Maiden, A. M., Rodenburg, J. M. & Humphry, M. J. Optical ptychography: a practical implementation with useful resolution. *Opt. Lett.* **35**, 2585–2587 (2010).
- von Neumann, J. Wahrscheinlichkeitstheoretischer Aufbau der Quantenmechanik. *Nachr. Ges. Wiss. Göttingen Math.-Phys. Kl.* 245–272 (1927).
- Wolf, E. New theory of partial coherence in the space-frequency domain Part I: spectra and cross spectra of steady-state sources. *J. Opt. Soc. Am.* **72**, 343–351 (1982).
- Whitehead, L. W. *et al.* Diffractive imaging using partially coherent X rays. *Phys. Rev. Lett.* **103**, 243902 (2009).
- Abbey, B. *et al.* Lensless imaging using broadband X-ray sources. *Nature Photon.* **5**, 420–424 (2011).
- Candès, E. J. & Recht, B. Exact matrix completion via convex optimization. *Found. Comput. Math.* **9**, 717–772 (2009).
- Gross, D. Recovering low-rank matrices from few coefficients in any basis. *IEEE Trans. Inf. Theory* **57**, 1548–1566 (2011).
- Rodenburg, J. M. & Bates, R. H. T. The theory of super-resolution electron microscopy via Wigner-distribution deconvolution. *Phil. Trans. R. Soc. Lond. A* **339**, 521–553 (1992).
- Chapman, H. N. Phase-retrieval X-ray microscopy by Wigner-distribution deconvolution: signal processing. *Scanning Microsc.* **11**, 67–80 (1997).
- Raymer, M. G. Measuring the quantum mechanical wave function. *Contemp. Phys.* **38**, 343–355 (1997).
- Fienup, J. R. Phase retrieval algorithms: a comparison. *Appl. Opt.* **21**, 2758–2769 (1982).
- Elser, V. Phase retrieval by iterated projections. *J. Opt. Soc. Am. A Opt. Image Sci. Vis.* **20**, 40–55 (2003).
- Guizar-Sicairos, M. & Fienup, J. R. Phase retrieval with transverse translation diversity: a nonlinear optimization approach. *Opt. Express* **16**, 7264–7278 (2008).
- Thibault, P. & Guizar-Sicairos, M. Maximum-likelihood refinement for coherent diffractive imaging. *N. J. Phys.* **14**, 063004 (2012).
- Pfeiffer, F. *et al.* Shearing interferometer for quantifying the coherence of hard X-ray beams. *Phys. Rev. Lett.* **94**, 164801 (2005).
- Cerbino, R. *et al.* X-ray-scattering information obtained from near-field speckle. *Nature Phys.* **4**, 238–243 (2008).
- Clark, J. N. *et al.* Dynamic sample imaging in coherent diffractive imaging. *Opt. Lett.* **36**, 1954–1956 (2011).
- Cowley, J. M. Image contrast in a transmission scanning electron microscope. *Appl. Phys. Lett.* **58**, 58–59 (1969).
- Treacy, M. M. J., Gibson, J. M., Fan, L., Paterson, D. J. & McNulty, I. Fluctuation microscopy: a probe of medium range order. *Rep. Prog. Phys.* **68**, 2899–2944 (2005).
- Gorelick, S., Guzenko, V. A., Vila-Comamala, J. & David, C. Direct e-beam writing of dense and high aspect ratio nanostructures in thick layers of PMMA for electroplating. *Nanotechnology* **21**, 295303 (2010).
- Henrich, B. *et al.* PILATUS: a single photon counting pixel detector for x-ray applications. *Nucl. Instrum. Methods Phys. Res. A* **607**, 247–249 (2009).

Supplementary Information is available in the online version of the paper.

Acknowledgements We thank M. Dierolf for discussions and help in the algorithm implementation; A. Diaz for help during the measurements; C. Kewish for providing the sample, which had been produced by J. Vila Comamala; V. Elser for pointing us to relevant literature; and F. Pfeiffer, M. Bech and I. Zanette for helping to improve the manuscript. This work is supported in part by a European Research Council Starting Grant, under project OptimaX (no. 279753).

Author Contributions A.M. and P.T. designed and conducted the experiment. P.T. analysed the data and prepared the simulations. Both authors worked together to refine the methods, interpret results, write the manuscript and create the figures.

Author Information Reprints and permissions information is available at www.nature.com/reprints. The authors declare no competing financial interests. Readers are welcome to comment on the online version of the paper. Correspondence and requests for materials should be addressed to P.T. (pierre.thibault@tum.de).

Magnetic-field-controlled reconfigurable semiconductor logic

Sungjung Joo^{1,2}, Taeyueb Kim^{1,2}, Sang Hoon Shin³, Ju Young Lim³, Jinki Hong², Jin Dong Song³, Joonyeon Chang¹, Hyun-Woo Lee⁴, Kungwon Rhie², Suk Hee Han¹, Kyung-Ho Shin¹ & Mark Johnson⁵

Logic devices based on magnetism show promise for increasing computational efficiency while decreasing consumed power. They offer zero quiescent power and yet combine novel functions such as programmable logic operation and non-volatile built-in memory^{1–5}. However, practical efforts to adapt a magnetic device to logic suffer from a low signal-to-noise ratio and other performance attributes that are not adequate for logic gates. Rather than exploiting magnetoresistive effects that result from spin-dependent transport of carriers, we have approached the development of a magnetic logic device in a different way: we use the phenomenon of large magnetoresistance found in non-magnetic semiconductors in high electric fields^{6,7}. Here we report a device showing a strong diode characteristic that is highly sensitive to both the sign and the magnitude of an external magnetic field, offering a reversible change between two different characteristic states by the application of a magnetic field. This feature results from magnetic control of carrier generation⁸ and recombination in an InSb p–n bilayer channel⁹. Simple circuits combining such elementary devices are fabricated and tested, and Boolean logic functions including AND, OR, NAND and NOR are performed. They are programmed dynamically by external electric or magnetic signals, demonstrating magnetic-field-controlled semiconductor reconfigurable logic at room temperature. This magnetic technology permits a new kind of spintronic device, characterized as a current switch rather than a

voltage switch, and provides a simple and compact platform for non-volatile reconfigurable logic devices.

High-electric-field magnetoresistance typically studied in Si (refs 6, 7, 10–12) has also been observed as a large magnetoconductance in an HgCdTe diode⁸. This large magnetoresistance effect derives from Lorentz forces acting on energetic carriers. Here we introduce a modified avalanche diode structure that adopts a structural asymmetry in the form of a p–n bilayer channel, thereby leading to an asymmetry in the dependence of recombination on the polarity of a magnetic field, B . The result is a current–voltage characteristic strongly dependent on magnetic field. As a second modification, we enhance the avalanche characteristics by use of a semiconductor with a small bandgap, resulting in very high magnetoconductance. Specifically, we chose InSb, which has a bandgap of 0.17 eV and an electronic effective mass that is 0.013 times the free electron mass.

We fabricated devices as follows. Sample NP had a p–n junction composed of a 0.2- μm -thick n-type InSb layer at the top, and a 6- μm -thick p-type InSb layer at the bottom of the channel (Fig. 1a). The channel width was 10 μm , and the length was 120 μm . The p-type layer in sample NP was characterized after removing the n-type by wet etching; we obtained values of carrier density and mobility (at 300 K) of $2.4 \times 10^{18} \text{ cm}^{-3}$ and $2.3 \times 10^2 \text{ cm}^2 \text{ V}^{-1} \text{ s}^{-1}$, respectively. To investigate the n-type layer, an auxiliary device, sample N, was fabricated with growth conditions identical to the n-type in sample NP, and its

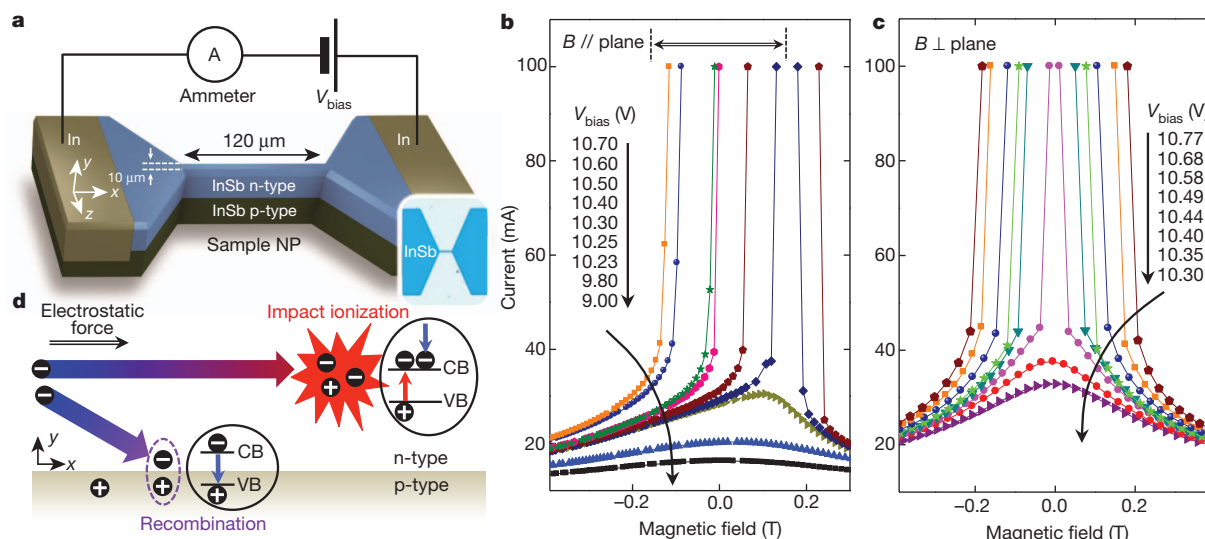


Figure 1 | Magnetoconductance tunable by external voltage. **a**, Schematic diagram and micrograph (bottom right inset) of an InSb device, sample NP. **b**, A family of plots of current versus magnetic field for sample NP (orientation $B // \text{plane}$, see main text). For a given bias voltage, there is a transition to a high-current state at a characteristic onset value of magnetic field. In the field region

designated by a horizontal arrow (\leftrightarrow), the I – B characteristic resembles that of an electrical diode. **c**, A family of I – B plots for orientation $B \perp \text{plane}$ (see main text). **d**, Schematic illustration of carrier transport processes in the channel. CB and VB represent the conduction band edge and valence band edge, respectively.

¹Spin Convergence Research Center, KIST, Seoul 130-650, South Korea. ²Department of Display and Semiconductor Physics, Korea University, Sejong 339-700, South Korea. ³Nano Photonics Research Center, KIST, Seoul 130-650, South Korea. ⁴Department of Physics, Pohang University of Science and Technology, Pohang 790-784, South Korea. ⁵Naval Research Laboratory, Washington DC 20375, USA.

carrier density and mobility (at 300 K) were $2 \times 10^{16} \text{ cm}^{-3}$ and $7.8 \times 10^4 \text{ cm}^2 \text{ V}^{-1} \text{ s}^{-1}$, respectively. The thickness of the n-type layer in sample NP was less than the electron mean free path ($\sim 0.4 \mu\text{m}$) of sample N. All measurements in this study were performed at room temperature using d.c. voltage sources. The current was intentionally limited to 100 mA to protect the device from damage. Two magnetic field configurations were used: B perpendicular to the x - z plane (that is, along the y axis in Fig. 1a) and B parallel to the x - z plane (along the z axis in Fig. 1a).

The unique $I(V, B)$ characteristic of our NP device is shown in Fig. 1b. We plot a family of traces showing channel current I as a function of magnetic field B ($B \parallel \text{plane}$) for a variety of bias voltages, V_{bias} . Considering data in the field region $-0.15 \text{ T} < B < +0.15 \text{ T}$ (designated by a horizontal arrow, \leftrightarrow), each current trace monotonically increases with increasing field and there is an abrupt change in magnitude at a field value that represents the onset of the high-current state. This behaviour is similar to the characteristic of a p-n junction diode if the bias voltage is replaced by the magnetic field. Our device therefore can be considered to be a magnetic-field version of an electrical diode. Although conventional p-n junction diodes have a fixed onset voltage called the knee voltage, the onset field of our devices varies according to V_{bias} .

We define the magnetoconductance ratio (MC) of our devices as the ratio of the maximum to the minimum value of $I(B)/V_{\text{bias}}$ (that is, $\text{MC} = I_{\text{max}}/I_{\text{min}}$) for a given bias voltage. The maximum current is limited at 100 mA, which artificially limits the magnetoconductance ratio. For magnetic fields ranging between -0.2 and 0.2 T , MC is a numeric factor greater than five. Because the device shows such an abrupt change in current, a high-current state (ON, digital '1') can be defined as an output current of 100 mA. A low-current state (OFF, digital '0') is similarly defined as an output current of 40 mA or less.

The structural asymmetry caused by the p-n bilayer channel distinguishes magnetoresistance in our structure from that in other devices. Conductivity is sensitive to a carrier generation process

induced by impact ionization¹³ and transport is influenced by field-dependent recombination rates (Fig. 1d)^{14,15}. A large field along the negative z axis deflects energetic carriers in the n-type layer towards the p-n interface by a Lorentz force. Enhanced recombination depletes the carrier population and diminishes the current. By contrast with Fig. 1b, the data for $B \perp \text{plane}$ in Fig. 1c are symmetric with respect to the sign of magnetic field because the Lorentz force deflection is in the plane and does not affect recombination. Carrier generation at high bias was verified by Hall measurements, and magnetic-field-dependent recombination was confirmed using a photoconductivity measurement (Supplementary Information section 2).

New functionalities for information processing are enabled by the unique properties of our device; we fabricated several circuits and demonstrated magnetic-field-controlled reconfigurable Boolean logic gates at room temperature. We begin with a simple reconfigurable AND/OR gate, and then extend this gate to perform most of the Boolean logic functions. We further show that our device can be programmed by external binary parameters. These demonstrations rely on the magnetic conductance characteristics displayed in Fig. 1b, where the onset of the high-current state is a function of bias voltage.

An AND/OR gate was prepared to elucidate the principle of logic operation with our devices. We manufactured two devices (NP1 and NP2) with nearly identical structure and electrical properties, which are, for the purpose of this explanation, the same as those of sample NP. Each device was mounted on a separate sample holder, and an external magnetic field was applied to both sample holders. By rotating each sample holder, the orientation of the magnetic field applied to the devices could be controlled individually (Supplementary Fig. 1). Figure 2a depicts the circuit and field configurations. The field ($B \parallel \text{plane}$) has an orientation either positive or negative along the z axis. The corresponding current-voltage curves for NP1 are displayed in Fig. 2b, and show an abrupt increase of current at the threshold voltage, V_{th} . The key feature of this circuit is that current I is the same for NP1 and NP2 in series, and the current has the high-state value $I = 100 \text{ mA}$

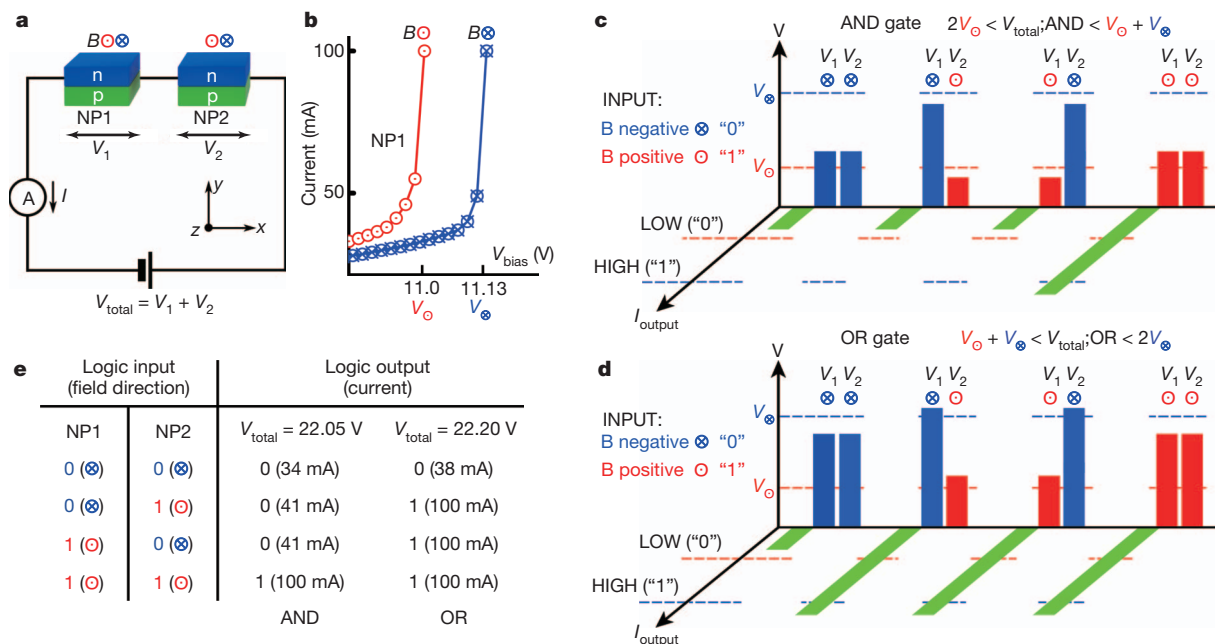


Figure 2 | Programmable logic operation demonstrated by an AND/OR gate. Positive (⊙) or negative (⊗) magnetic fields of -0.1 T and 0.1 T are applied to devices with orientation $B \parallel \text{plane}$. **a**, The circuit used for demonstration of reprogrammable Boolean logic. V_1 and V_2 are the voltage drops across samples NP1 and NP2, respectively. Binary logic inputs are positive (negative) magnetic field, corresponding to binary 1 (0). Logic output is high (low) current, corresponding to binary 1 (0). The Boolean operation to be performed is programmed by setting the bias voltage V_{total} to 22.05 V for the

AND operation or 22.20 V for the OR operation. **b**, Current-voltage characteristics of NP1. The threshold voltage of NP1 and NP2 at the negative field, V_{th} , is 11.13 V, and that at the positive field, V_{th} , is 11.0 V. **c**, Schematic explanation of AND gate operation, described in the main text. **d**, Schematic explanation of OR gate operation, described in the main text. **e**, Truth table summary of the operations described in **c** and **d**. Experimentally measured output values are included (all values were reproducible).

only if the voltage drops across devices NP1 and NP2 (referred to as V_1 and V_2) exceed the threshold voltages, that is, $V_1 > V_{th,1}$ and $V_2 > V_{th,2}$. If not, either $V_1 < V_{th,1}$ or $V_2 < V_{th,2}$, and the current has the low-state value. To describe binary logic operations, we define the inputs as the polarity of field B at NP1 and NP2, B positive (negative) corresponding to binary 1 (0) and represented in Fig. 2 by symbol \odot (\otimes). The logical output is a high (low) current with value $I = 100$ mA ($I < 40$ mA) corresponding to binary 1 (0). The simple circuit of Fig. 2a is a reconfigurable gate, with either the AND or the OR logic function determined by the applied voltage, V_{total} .

The operation of programmable Boolean logic is illustrated in Fig. 2c and d. The V axis represents the voltage across each device, the I_{output} axis represents the output current, and bar plots for four different input configurations are staggered along the horizontal axis. Symbols V_{\odot} and V_{\otimes} represent the values of V_{th} for positive and negative field, respectively. In Fig. 2c, V_{total} is given a value of 22.05 V, in the range $2V_{\odot} < V_{total} < V_{\odot} + V_{\otimes}$. The vertical bars represent the voltage drops across each of the two devices, red (blue) corresponding to a device in the presence of positive (negative) field. The sum of the heights of the bars is constant for each of the four configurations. In the first configuration, NP1 and NP2 are in negative field, the inputs are binary 0 and 0, voltages V_1 and V_2 are both less than the threshold voltages $V_{th,1}$ and $V_{th,2}$ (V_{\otimes} on the V axis), and the output current is necessarily low, OUTPUT = 0. In the second and third cases, one device is in a positive field and the other a negative field; the inputs are 0 and 1, $V_1 < V_{th,1}$ and $V_2 < V_{th,2}$, and OUTPUT = 0. In the final case, both NP1 and NP2 are in positive field, the inputs are binary 1 and 1, $V_1 > V_{th,1}$ and $V_2 > V_{th,2}$, and OUTPUT = 1. The truth table is summarized in Fig. 2e and represents the operation of an AND gate. In Fig. 2d, V_{total} is given a higher value of 22.20 V, in the range $V_{\odot} + V_{\otimes} < V_{total} < 2V_{\odot}$. For inputs 0 and 0, we have $V_1 < V_{th,1}$ and $V_2 < V_{th,2}$ and OUTPUT = 0. For other configurations, we have $V_1 > V_{th,1}$ and $V_2 > V_{th,2}$ and OUTPUT = 1. The truth table (Fig. 2e) represents the operation of an OR gate. The summary provided by Fig. 2e includes values of output current that were experimentally measured in our circuit at room temperature. These results demonstrate that an external parameter, the total voltage bias,

can be used to program dynamically the functional operation of the circuit as either an AND gate or an OR gate.

Such reprogrammability can be extended to other Boolean logic functions. Magnetic field is a pseudovector and its sign changes when taking a mirror image of a physical system¹⁶. Hence, a system is invariant under the substitution of its mirror image and reversal of the field direction. We introduce PN devices as mirror images of NP devices. NP devices have an n-type layer above a p-type layer, whereas PN devices have a reverse stack, an n-type beneath a p-type layer. Mirror reflection with respect to the p–n interface ensures the mirror image relation between these two types, and a PN device can be replaced by an NP with reversed magnetic field direction. Equivalently stated, PNs in Fig. 3 can be considered as NPs with logical negation at the inputs, because the Boolean negation for 1 (positive field) corresponds to 0 (negative field).

We now describe a wide variety of reconfigurable Boolean operations that are demonstrated in Fig. 3. PN and NP devices were distinguished from each other while mounting them on the sample holder (see Methods). Two NP devices, NP3 and NP4, and two PN devices, PN1 and PN2, have V_{\odot} of 10.35, 10.11, 12.4 and 12.8 V, respectively, and V_{\otimes} of 10.47, 10.23, 12.0 and 12.65 V, respectively. NP3 and PN1 were mounted on one sample holder, and NP4 and PN2 were mounted on the other.

When V_{NOT} is zero, no current flows in the PN devices and the output is determined entirely by the NP devices and V_{COPY} (see Fig. 3a for V_{NOT} and V_{COPY}). The output of the circuit in Fig. 3a is low (high) current for the input \otimes (\odot), when $V_{\odot, NP3} < V_{COPY}$ ($= 10.42$ V) $< V_{\otimes, NP3}$. This represents the logical COPY function. The circuit shown in Fig. 3b can be simplified as a series connection of NP3 and NP4 with a bias of V_{COPY} , representing the same circuit as that in Fig. 2a and performing the same reprogrammable AND/OR functions. Similarly, when V_{COPY} is zero, the NP devices carry no current, and the PN devices and bias V_{NOT} determine the output. Recalling the mirror symmetry relation that a PN can be treated as an NP if the logical inputs \odot and \otimes are interchanged, the circuit of Fig. 3a performs the NOT function and the circuit of Fig. 3b performs NOR/NAND functions.

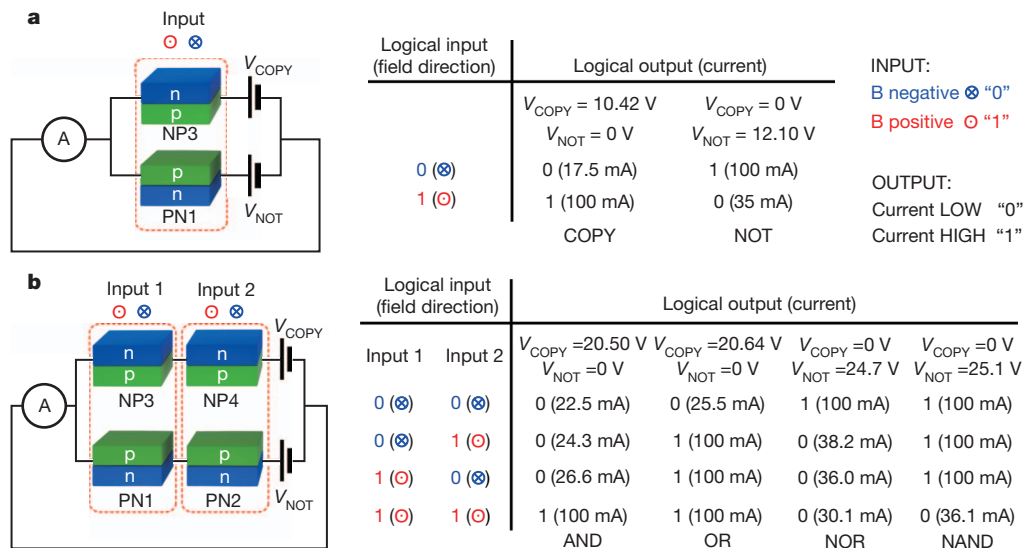


Figure 3 | Demonstration of various Boolean operations. Left, a pair of NP and PN devices, shown boxed by red dotted lines, receives a common input signal (magnetic field): one pair is NP3 and PN1 and the second pair is NP4 and PN2. NP and PN devices are driven by bias voltage V_{COPY} and V_{NOT} , respectively. Right, the total current is a summation of the currents driven by these two voltage sources, and the logic output is determined by this total current. Experimentally measured output currents are listed in parentheses for

various bias voltages and input values. The outputs of the circuit shown in **a** represent the Boolean logic function COPY or NOT, and those of circuit shown in **b** represent AND, OR, NOR or NAND functions. Thus, several elementary functions are possible with a single circuit system: two functions for the circuit shown in **a** and four functions for the circuit shown in **b**. Each function can be programmed by pre-setting the bias voltage values.

Experimental results for the two circuits are listed in the truth tables in Fig. 3, demonstrating that our reconfigurable logic gates provide the basic Boolean operations, with each logic function programmed by pre-setting the bias voltages. Complex operations can be accomplished by building on these elementary functions. We further experimentally demonstrate logic gates for which the function is programmed using a binary parameter, positive or negative field directions \odot and \otimes , rather than bias voltage (Supplementary Fig. 2). Binary programming avoids errors that might arise from narrow margins of control voltage.

We have demonstrated unique performance characteristics of p-n bilayer avalanche diodes by fabricating devices with dimensions of the order of 10 μm and using external magnetic fields. However, digital electronics applications require integrated devices fabricated with sub-micrometre feature size. Issues for the miniaturization of our device can be divided into two parts, the diode current channel and the source of local magnetic field. The minimum size of the channel is determined by the 'dead space', the distance that a carrier travels before acquiring enough energy from the electric field to participate in impact ionization. For an electric field of the order of 10^5 V cm^{-1} , which is less than values used in commercial avalanche diodes, the dead space of about 20 nm for InSb represents a scaling limit for our device. Avalanche diodes with Si (ref. 17) and AlAsSb (ref. 18) channels having 100-nm dimensions have already been demonstrated. Because the Lorentz force is determined by carrier mobility in diffusive systems and high mobility can be maintained at small sizes, the magnetic field sensitivity of our devices should be scalable.

The second issue is the source of magnetic field. An appropriate integrated source of field can be provided by fabricating a patterned ferromagnetic element next to a passivated device channel. The fringe field associated with the ferromagnetic element has a magnitude that depends on the mean distance to the channel, but is roughly 0.2 T for a distance of 200 nm (ref. 19). Of greater importance, the magnetic field polarity can be controlled by switching the magnetization orientation of the ferromagnet between one of two bistable directions along a uniaxial anisotropy axis. The magnetization state of the ferromagnet is efficiently 'written' by spin transfer torque (STT) switching²⁰. This technique scales with current density, and therefore STT writing scales with device area. A typical write current density is approximately $1 \times 10^6 \text{ A cm}^{-2}$ (refs 2, 20). For ferromagnetic elements with dimensions of the order of 100 nm, appropriate write current pulses have amplitude 0.2 mA and duration 2 ns.

Following these considerations, our InSb avalanche diode, if reduced to dimensions of channel length, width and thickness of roughly 100 nm, is expected to have a threshold voltage V_{th} of about 9 mV and an output of 40 μA in the low-current state. Provided that output is limited to five times the low-current value, the high-current output is 0.2 mA. Unlike voltage-controlled semiconductor devices, magnetization switching is driven by current. Our device is a current switch, and the 0.2-mA output is sufficiently large to provide STT write current input to a subsequent device. Our device is therefore unique in the field of spintronics because it is intrinsically adapted to device fan-out, a requirement for digital logic applications.

Our device, if scaled to submicrometre feature size with a patterned ferromagnetic element, promises further advantages. It is important to note that magnetization orientation is maintained as a non-volatile state because of the bistability of magnetic hysteresis. Our approach could be called non-volatile reconfigurable logic. By adding a magnetic memory device to an elementary logic unit such as an AND or OR gate, any circuit or sub-circuit would remember its most recent configuration and the latest logical result. Circuits, blocks of circuits, or entire chips could be powered off when not in use, followed by 'instant-on' performance when powered up for an operation. Compared to complementary metal oxide semiconductor (CMOS) devices which need power in quiescent mode, both the duty cycle and the average power could be reduced substantially. The energy per operation would be a characteristic parameter, rather than operating power. For a 2-ns pulse

duration, we estimate the largest dissipation in the channel (high-current state) would be 3.6 fJ and an STT write process would dissipate 40 aJ, if the size of the channel and ferromagnetic element were of the order of 100 nm. As a final note, four of our magnetic diodes are adequate to perform the four Boolean functions in our reconfigurable gate (see Fig. 3). This promises that a future version of our device would be more compact than a comparable logic unit in a CMOS gate array, and could lead to higher packing density and faster operating speed. Of greater importance, our architecture for logic operation offers dynamic reconfigurability, as demonstrated in this study. This reconfiguration could be performed in a single clock cycle in the future device.

METHODS SUMMARY

An indium antimonide (InSb) wafer was grown on a GaAs substrate using molecular beam epitaxy²¹. A wafer grown without intentional doping showed n-type conduction with a carrier density of nearly intrinsic level. p-Type layers were obtained by beryllium doping during the growth process. The device shape was defined by conventional photolithographic techniques and formed by low-energy ion milling and subsequent wet-chemical etching. Ohmic electrodes were made by electron-beam evaporation of indium. A d.c. voltage source and an ammeter were connected through the electrodes.

To avoid Joule heating, a copper block was installed on the sample holder (Supplementary Fig. 1). Devices were mounted on this copper block with Apiezon H grease, which is a thermal conductor (but an electrical insulator) and provides thermal contact to the copper block. Electric currents were measured in steps of bias voltage sweep or magnetic field sweep. For each measurement step, a current value was collected after applying d.c. voltage for a sufficient time (~ 3 s) to guarantee an electrical steady state. During the time interval (>10 s) between successive measurement steps, the bias voltage was reduced to 0 V to minimize Joule heating in the devices.

Both NP and PN devices consist of an n-type layer grown on a p-type layer, and their fabrication processes were the same. NP devices were mounted on sample holders with the n-type layer on the top and the p-type layer on the bottom. However, PN devices were mounted by turning the n-type layer down to the sample holders, resulting in the p-type layer on the top and the n-type layer on the bottom. An electrical insulator (Apiezon H grease) was used to prevent leakage current between the devices and the surface of sample holders.

Received 31 July; accepted 20 November 2012.

Published online 30 January 2013.

1. Moodera, J. S. & Leclair, P. Spin electronics: a quantum leap. *Nature Mater.* **2**, 707–708 (2003).
2. Ney, A., Pampuch, C., Koch, R. & Ploog, K. H. Programmable computing with a single magnetoresistive element. *Nature* **425**, 485–487 (2003).
3. Dery, H., Dalal, P., Cywinski, L. & Sham, L. J. Spin-based logic in semiconductors for reconfigurable large-scale circuits. *Nature* **447**, 573–576 (2007).
4. Xu, P. *et al.* An all-metallic logic gate based on current-driven domain wall motion. *Nature Nanotechnol.* **3**, 97–100 (2008).
5. Behin-Aein, B., Datta, B. D., Salahuddin, S. & Datta, S. Proposal for an all-spin logic device with built-in memory. *Nature Nanotechnol.* **5**, 266–270 (2010).
6. Delmo, M. *et al.* Large positive magnetoresistive effect in silicon induced by the space-charge effect. *Nature* **457**, 1112–1115 (2009).
7. Wan, C. *et al.* Geometrical enhancement of low-field magnetoresistance in silicon. *Nature* **477**, 304–307 (2011).
8. Lee, J. *et al.* An electrical switching device controlled by a magnetic field-dependent impact ionization process. *Appl. Phys. Lett.* **97**, 253505 (2010).
9. Hong, J. *et al.* Magnetic field dependent impact ionization in InSb. Preprint at <http://arxiv.org/abs/1206.1094v1> (2012).
10. Schoonus, J. J. H. M., Bloom, F. L., Wagemans, W., Swagten, H. J. M. & Koopmans, B. Extremely large magnetoresistance in boron-doped silicon. *Phys. Rev. Lett.* **100**, 127202 (2008).
11. Delmo, M. P., Kasai, S., Kobayashi, K. & Ono, T. Current-controlled magnetoresistance in silicon in non-Ohmic transport regimes. *Appl. Phys. Lett.* **95**, 132106 (2009).
12. Ciccarelli, C., Park, B. G., Ogawa, S., Ferguson, A. J. & Wunderlich, J. Gate controlled magnetoresistance in a silicon metal-oxide-semiconductor field-effect-transistor. *Appl. Phys. Lett.* **97**, 082106 (2010).
13. Sze, S. M. *Semiconductor Devices, Physics and Technology* 2nd edn, 78, 118 (Wiley and Sons, 2002).
14. Chovet, A. Study of recombination processes from the magnetoconcentration effect. *Phys. Status Solidi A* **28**, 633–645 (1975).
15. Cristoloveanu, S. & Lee, J. H. Magnetoconcentration and related galvanomagnetic effects in non-intrinsic semiconductors. *J. Phys. C* **13**, 5983–5997 (1980).
16. Fulling, S. A., Sinyakov, M. N. & Tischchenko, S. V. *Linearity and the Mathematics of Several Variables* 343 (World Scientific, 2000).

17. Massey, D. J. *et al.* Impact ionization in submicron silicon devices. *J. Appl. Phys.* **95**, 5931–5933 (2004).
18. Xie, J. J. *et al.* Excess noise characteristics of thin AlAsSb APDs. *IEEE Trans. Electron. Dev.* **59**, 1475–1479 (2012).
19. Hong, J. *et al.* Local Hall effect in hybrid ferromagnetic/semiconductor devices. *Appl. Phys. Lett.* **90**, 023510 (2007).
20. Hosomi, M. *et al.* A novel nonvolatile memory with spin torque transfer magnetization switching: spin-RAM. In *Proc. Electron Devices Meeting, 2005* 459–462 (IEDM Technical Digest, IEEE International, 2005).
21. Lim, J. Y., Song, J. D., Ahn, J.-P., Rho, H. & Yang, H. S. Effect of thin intermediate-layer of InAs quantum dots on the physical properties of InSb films grown on (001) GaAs. *Thin Solid Films* **520**, 6589–6594 (2012).

Supplementary Information is available in the online version of the paper.

Acknowledgements This work was supported by the KIST vision 21 programme, NRF grants funded by MEST (2010-0000506, 2011-0012386 and 2012-0005631), the industrial strategic technology development programme funded by MKE (KI002182), the Dream project, MEST (2012K001280), GRL and the Office of Naval Research.

Author Contributions J.H. and J.D.S. planned the project and supervised the research. S.J. and T.K. fabricated the devices and collected the data. J.D.S., S.H.S. and J.Y.L. grew the materials. J.C., H.-W.L., K.R., S.H.H. and K.-H.S. analysed and discussed the data. J.C., J.H. and M.J. wrote the manuscript, which was edited and approved by all co-authors.

Author Information Reprints and permissions information is available at www.nature.com/reprints. The authors declare no competing financial interests. Readers are welcome to comment on the online version of the paper. Correspondence and requests for materials should be addressed to J.H. (jkhongikhong@korea.ac.kr) or J.D.S. (jdsong@kist.re.kr).

Towards practical, high-capacity, low-maintenance information storage in synthesized DNA

Nick Goldman¹, Paul Bertone¹, Siyuan Chen², Christophe Dessimoz¹, Emily M. LeProust², Botond Sipos¹ & Ewan Birney¹

Digital production, transmission and storage have revolutionized how we access and use information but have also made archiving an increasingly complex task that requires active, continuing maintenance of digital media. This challenge has focused some interest on DNA as an attractive target for information storage¹ because of its capacity for high-density information encoding, longevity under easily achieved conditions^{2–4} and proven track record as an information bearer. Previous DNA-based information storage approaches have encoded only trivial amounts of information^{5–7} or were not amenable to scaling-up⁸, and used no robust error-correction and lacked examination of their cost-efficiency for large-scale information archival⁹. Here we describe a scalable method that can reliably store more information than has been handled before. We encoded computer files totalling 739 kilobytes of hard-disk storage and with an estimated Shannon information¹⁰ of 5.2×10^6 bits into a DNA code, synthesized this DNA, sequenced it and reconstructed the original files with 100% accuracy. Theoretical analysis indicates that our DNA-based storage scheme could be scaled far beyond current global information volumes and offers a realistic technology for large-scale, long-term and infrequently accessed digital archiving. In fact, current trends in technological advances are reducing DNA synthesis costs at a pace that should make our scheme cost-effective for sub-50-year archiving within a decade.

Although techniques for manipulating, storing and copying large amounts of existing DNA have been established for many years^{11–13}, one of the main challenges for practical DNA-based information storage is the difficulty of synthesizing long sequences of DNA *de novo* to an exactly specified design. As in the approach of ref. 9, we represent the information being stored as a hypothetical long DNA molecule and encode this *in vitro* using shorter DNA fragments. This offers the benefits that isolated DNA fragments are easily manipulated *in vitro*^{11,13}, and that the routine recovery of intact fragments from samples that are tens of thousands of years old^{14,15} indicates that well-prepared synthetic DNA should have an exceptionally long lifespan in low-maintenance environments^{3,4}. In contrast, approaches using living vectors^{6–8} are not as reliable, scalable or cost-efficient owing to disadvantages such as constraints on the genomic elements and locations that can be manipulated without affecting viability, the fact that mutation will cause the fidelity of stored and decoded information to reduce over time, and possibly the requirement for storage conditions to be carefully regulated. Existing schemes used for DNA computing in principle permit large-scale memory^{1–16}, but data encoding in DNA computing is inextricably linked to the specific application or algorithm¹⁷ and no practical storage schemes have been realized.

As a proof of concept for practical DNA-based storage, we selected and encoded a range of common computer file formats to emphasize the ability to store arbitrary digital information. The five files comprised all 154 of Shakespeare's sonnets (ASCII text), a classic scientific paper¹⁸ (PDF format), a medium-resolution colour photograph of the European Bioinformatics Institute (JPEG 2000 format), a 26-s excerpt from Martin Luther King's 1963 'I have a dream' speech (MP3 format) and a Huffman code¹⁰ used in this study to convert bytes to base-3

digits (ASCII text), giving a total of 757,051 bytes or a Shannon information¹⁰ of 5.2×10^6 bits (see Supplementary Information and Supplementary Table 1 for full details).

The bytes comprising each file were represented as single DNA sequences with no homopolymers (runs of ≥ 2 identical bases, which are associated with higher error rates in existing high-throughput sequencing technologies¹⁹ and led to errors in a recent DNA-storage experiment⁹). Each DNA sequence was split into overlapping segments, generating fourfold redundancy, and alternate segments were converted to their reverse complement (see Fig. 1 and Supplementary Information). These measures reduce the probability of systematic failure for any particular string, which could lead to uncorrectable errors and data loss. Each segment was then augmented with indexing information that permitted determination of the file from which it originated and its location within that file, and simple parity-check error-detection¹⁰. In all, the five files were represented by a total of 153,335 strings of DNA, each comprising 117 nucleotides (nt). The perfectly uniform fragment lengths and absence of homopolymers make it obvious that the synthesized DNA does not have a natural (biological) origin, and so imply the presence of deliberate design and encoded information².

We synthesized oligonucleotides (oligos) corresponding to our designed DNA strings using an updated version of Agilent Technologies' OLS (oligo library synthesis) process²⁰, creating $\sim 1.2 \times 10^7$ copies of each DNA string. Errors occur only rarely (~ 1 error per 500 bases) and independently in the different copies of each string, again enhancing our method's error tolerance. We shipped the synthesized DNA in lyophilized form that is expected to have excellent long-term preservation characteristics^{3,4}, at ambient temperature and without specialized packaging, from the USA to Germany via the UK. After resuspension, amplification and purification, we sequenced a sample of the resulting library products at the EMBL Genomics Core Facility in paired-end mode on the Illumina HiSeq 2000. We transferred the remainder of the library to multiple aliquots and re-lyophilized these for long-term storage.

Our base calling using AYO²¹ yielded 79.6×10^6 read-pairs of 104 bases in length, from which we reconstructed full-length (117-nt) DNA strings *in silico*. Strings with uncertainties due to synthesis or sequencing errors were discarded and the remainder decoded using the reverse of the encoding procedure, with the error-detection bases and properties of the coding scheme allowing us to discard further strings containing errors. Although many discarded strings will have contained information that could have been recovered with more sophisticated decoding, the high level of redundancy and sequencing coverage rendered this unnecessary in our experiment. Full-length DNA sequences representing the original encoded files were then reconstructed *in silico*. The decoding process used no additional information derived from knowledge of the experimental design. Full details of the encoding, sequencing and decoding processes are given in Supplementary Information.

Four of the five resulting DNA sequences could be fully decoded without intervention. The fifth however contained two gaps, each a run

¹European Bioinformatics Institute, Wellcome Trust Genome Campus, Hinxton CB10 1SD, UK. ²Agilent Technologies, Genomics-LSSU, 5301 Stevens Creek Boulevard, Santa Clara, California 95051, USA.

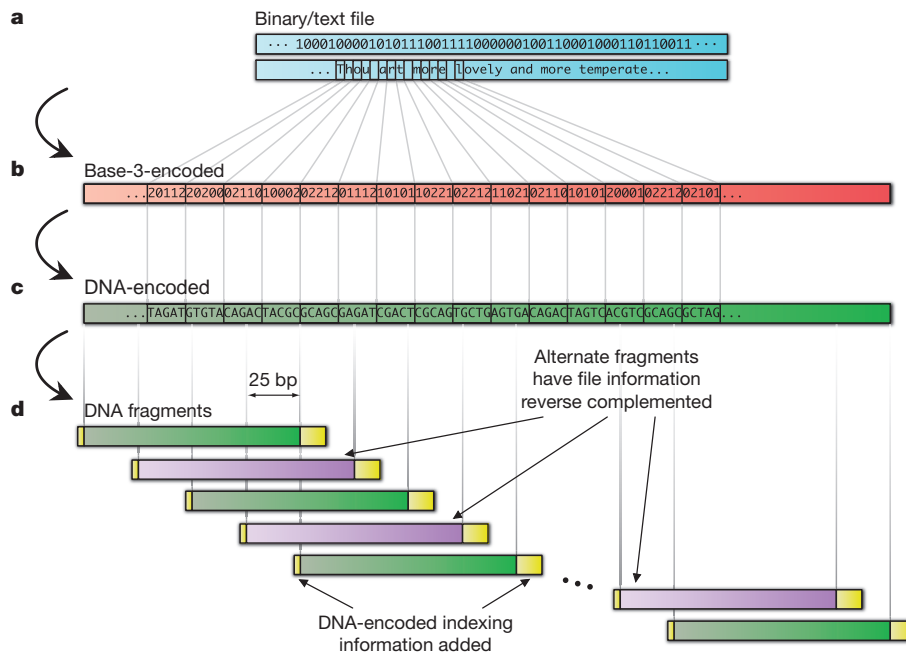


Figure 1 | Digital information encoding in DNA. Digital information (a, in blue), here binary digits holding the ASCII codes for part of Shakespeare's sonnet 18, was converted to base-3 (b, red) using a Huffman code that replaces each byte with five or six base-3 digits (trit). This in turn was converted *in silico* to our DNA code (c, green) by replacement of each trit with one of the three nucleotides different from the previous one used, ensuring no homopolymers

were generated. This formed the basis for a large number of overlapping segments of length 100 bases with overlap of 75 bases, creating fourfold redundancy (d, green and, with alternate segments reverse complemented for added data security, violet). Indexing DNA codes were added (yellow), also encoded as non-repeating DNA nucleotides. See Supplementary Information for further details.

of 25 bases, for which no segment was detected corresponding to the original DNA. Each of these gaps was caused by the failure to sequence any oligo representing any of four consecutive overlapping segments. Inspection of the neighbouring regions of the reconstructed sequence permitted us to hypothesize what the missing nucleotides should have been (see Supplementary Information) and we manually inserted those 50 bases accordingly. This sequence could also then be decoded. Inspection confirmed that our original computer files had been reconstructed with 100% accuracy.

An important issue for long-term digital archiving is how DNA-based storage scales to larger applications. The number of bases of synthesized DNA needed to encode information grows linearly with the amount of information to be stored, but we must also consider the indexing information required to reconstruct full-length files from short fragments. As indexing information grows only as the logarithm of the number of fragments to be indexed, the total amount of synthesized DNA required grows sub-linearly. Increasingly large parts of each fragment are needed for indexing however and, although it is reasonable to expect synthesis of longer strings to be possible in future, we modelled the behaviour of our scheme under the conservative constraint of a constant 114 nt available for both data and indexing information (see Supplementary Information). As the total amount of information increases, the encoding efficiency decreases only slowly (Fig. 2a). In our experiment (megabyte scale) the encoding scheme is 88% efficient; Fig. 2a indicates that efficiency remains >70% for data storage on petabyte (PB, 10^{15} bytes) scales and >65% on exabyte (EB, 10^{18} bytes) scales, and that DNA-based storage remains feasible on scales many orders of magnitude greater than current global data volumes²². Figure 2a also shows that costs (per unit information stored) rise only slowly as data volumes increase over many orders of magnitude. Efficiency and costs scale even more favourably if we consider the synthesized fragment lengths available using the latest technology (Supplementary Fig. 5).

As the amount of information stored increases, decoding requires more strings to be sequenced. A fixed decoding expenditure per byte of

encoded information would mean that each base is read fewer times and so is more likely to suffer decoding error. But extension of our scaling analysis to model the influence of reduced sequencing coverage on the per-decoded-base error rate (see Supplementary Information) revealed that error rates increase only very slowly as the amount of information encoded increases to a global data scale and beyond (Supplementary Table 4). This also suggests that our mean sequencing coverage of 1,308 times was considerably in excess of that needed for reliable decoding. We confirmed this by subsampling from the 79.6×10^6 read-pairs to simulate experiments with lower coverage. Figure 2b indicates that reducing the coverage by a factor of 10 (or even more) would have led to unaltered decoding characteristics, which further illustrates the robustness of our DNA-storage method.

DNA-based storage might already be economically viable for long-horizon archives with a low expectation of extensive access, such as government and historical records^{23,24}. An example in a scientific context is CERN's CASTOR system²⁵, which stores a total of 80 PB of Large Hadron Collider data and grows at 15 PB yr^{-1} . Only 10% is maintained on disk, and CASTOR migrates regularly between magnetic tape formats. Archives of older data are needed for potential future verification of events, but access rates decrease considerably 2–3 years after collection. Further examples are found in astronomy, medicine and interplanetary exploration²⁶. With negligible computational costs and optimized use of the technologies we employed, we estimate current costs to be $\$12,400 \text{ MB}^{-1}$ for information storage in DNA and $\$220 \text{ MB}^{-1}$ for information decoding. Modelling relative long-term costs of archiving using DNA-based storage or magnetic tape shows that the key parameters are the ratio of the one-time cost of synthesizing the DNA to the recurrent fixed cost of transferring data between tape technologies or media, which we estimate to be 125–500 currently, and the frequency of tape transition events (Supplementary Information and Supplementary Fig. 7). We find that with current technology and our encoding scheme, DNA-based storage may be cost-effective for archives of several megabytes with a ~ 600 – $5,000$ -yr horizon (Fig. 2c). One order of magnitude reduction in synthesis costs reduces this to ~ 50 – 500 yr; with two orders

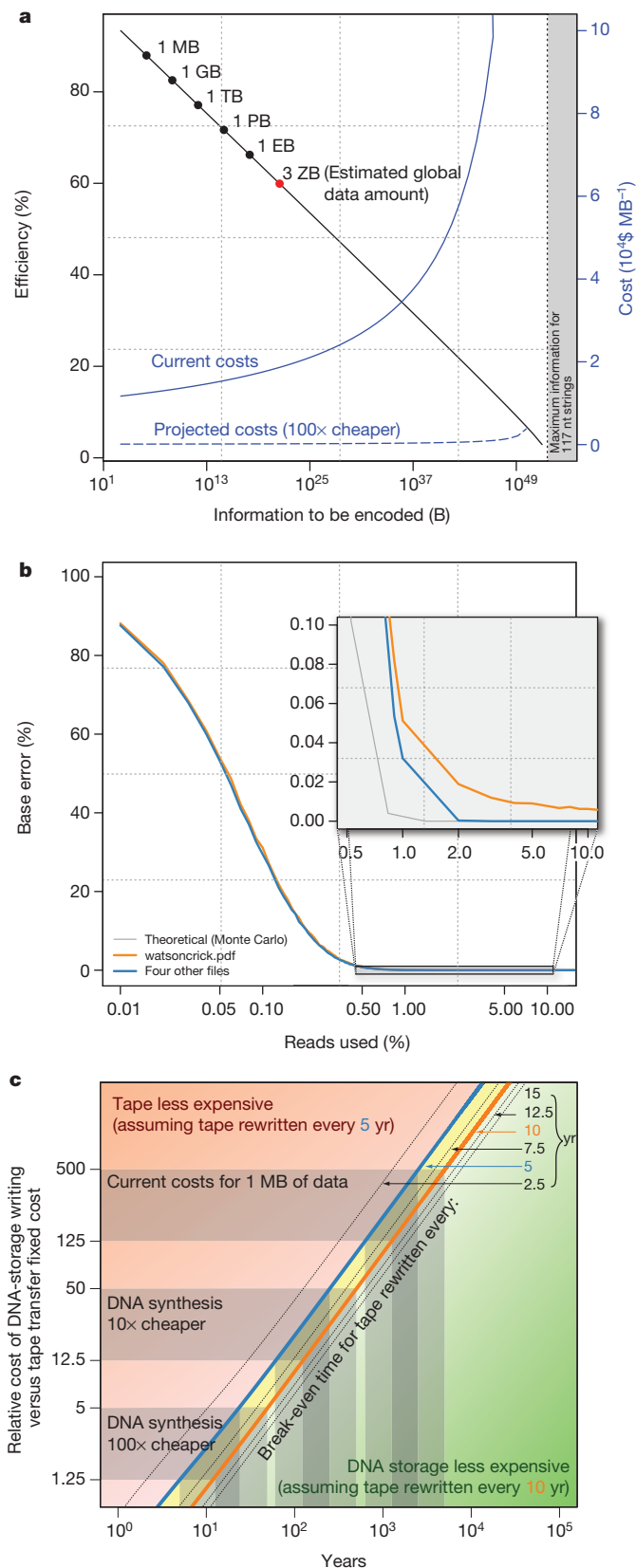


Figure 2 | Scaling properties and robustness of DNA-based storage.

a, Encoding efficiency and costs change as the amount of stored information increases. The x axis (logarithmic scale) represents the total amount of information to be encoded. Common data scales are indicated, including the three zettabyte (3 ZB , 3×10^{21} bytes) global data estimate, shown red. The black line (y -axis scale to left) indicates encoding efficiency, measured as the proportion of synthesized bases available for data encoding. The blue curves (y -axis scale to right) indicate the corresponding effect on encoding costs, both at current synthesis cost levels (solid line) and in the case of a two-order-of-magnitude reduction (dashed line). **b**, Per-recovered-base error rate (y axis) as a function of sequencing coverage, represented by the percentage of the original 79.6×10^6 read-pairs sampled (x axis; logarithmic scale). The blue curve represents the four files recovered without human intervention: the error is zero when $\geq 2\%$ of the original reads are used. The grey curve is obtained by Monte Carlo simulation from our theoretical error rate model. The orange curve represents the file (watsoncrick.pdf) that required manual correction: the minimum possible error rate is 0.0036%. The boxed area is shown magnified in the inset. **c**, Timescales for which DNA-based storage is cost-effective. The blue curve indicates the relationship between break-even time beyond which DNA storage is less expensive than magnetic tape (x axis) and relative cost of DNA-storage synthesis and tape transfer fixed costs (y axis), assuming the tape archive has to be read and rewritten every 5 yr. The orange curve corresponds to tape transfers every 10 yr; broken curves correspond to other transfer periods as indicated. In the green-shaded region, DNA storage is cost-effective when transfers occur more frequently than every 10 yr; in the yellow-shaded region, DNA storage is cost-effective when transfers occur every 5–10 yr; in the red-shaded region tape is less expensive when transfers occur less frequently than every 5 yr. Grey-shaded ranges of relative costs of DNA synthesis to tape transfer are 125–500 (current costs for 1 MB of data), 12.5–50 (achieved if DNA synthesis costs are reduced by one order of magnitude) and 1.25–5 (costs reduced by two orders of magnitude). Note the logarithmic scales on both axes. See Supplementary Information for further details.

both processes can be accelerated through parallelization (Supplementary Information).

The DNA-based storage medium has different properties from traditional tape- or disk-based storage. As DNA is the basis of life on Earth, methods for manipulating, storing and reading it will remain the subject of continual technological innovation. As with any storage system, a large-scale DNA archive would need stable DNA management²⁷ and physical indexing of depositions. But whereas current digital schemes for archiving require active and continuing maintenance and regular transferring between storage media, the DNA-based storage medium requires no active maintenance other than a cold, dry and dark environment^{3,4} (such as the Global Crop Diversity Trust's Svalbard Global Seed Vault, which has no permanent on-site staff²⁸) yet remains viable for thousands of years even by conservative estimates. We achieved an information storage density of $\sim 2.2 \text{ PB g}^{-1}$ (Supplementary Information). Our sequencing protocol consumed just 10% of the library produced from the synthesized DNA (Supplementary Table 2), already leaving enough for multiple equivalent copies. Existing technologies for copying DNA are highly efficient^{11,13}, meaning that DNA is an excellent medium for the creation of copies of any archive for transportation, sharing or security. Overall, DNA-based storage has potential as a practical solution to the digital archiving problem and may become a cost-effective solution for rarely accessed archives.

Received 15 May; accepted 12 December 2012.

Published online 23 January 2013.

- Baum, E. B. Building an associative memory vastly larger than the brain. *Science* **268**, 583–585 (1995).
- Cox, J. P. L. Long-term data storage in DNA. *Trends Biotechnol.* **19**, 247–250 (2001).
- Anchordouy, T. J. & Molina, M. C. Preservation of DNA. *Cell Preserv. Technol.* **5**, 180–188 (2007).
- Bonnet, J. et al. Chain and conformation stability of solid-state DNA: implications for room temperature storage. *Nucleic Acids Res.* **38**, 1531–1546 (2010).
- Clelland, C. T., Risca, V. & Bancroft, C. Hiding messages in DNA microdots. *Nature* **399**, 533–534 (1999).
- Kac, E. *Genesis* (1999); available at <http://www.ekac.org/geninfo.html> (accessed 10 May 2012).

of magnitude reduction, as can be expected in less than a decade if current trends continue (ref. 13, and <http://www.synthesis.cc/2011/06/new-cost-curves.html>), DNA-based storage becomes practical for archives with a horizon of less than 50 yr. The speed of DNA-storage writing and reading are not competitive with current technology, but

7. Ailenberg, M. & Rotstein, O. D. An improved Huffman coding method for archiving text, images, and music characters in DNA. *Biotechniques* **47**, 747–754 (2009).
8. Gibson, D. G. *et al.* Creation of a bacterial cell controlled by a chemically synthesized genome. *Science* **329**, 52–56 (2010).
9. Church, G. M., Gao, Y. & Kosuri, S. Next-generation digital information storage in DNA. *Science* **337**, 1628 (2012).
10. MacKay, D. J. C. *Information Theory, Inference, and Learning Algorithms* (Cambridge Univ. Press, 2003).
11. Erlich, H. A., Gelfand, D. & Sninsky, J. J. Recent advances in the polymerase chain reaction. *Science* **252**, 1643–1651 (1991).
12. Monaco, A. P. & Larin, Z. YACs, BACs, PACs and MACs: artificial chromosomes as research tools. *Trends Biotechnol.* **12**, 280–286 (1994).
13. Carr, P. A. & Church, G. M. Genome engineering. *Nature Biotechnol.* **27**, 1151–1162 (2009).
14. Willerslev, E. *et al.* Ancient biomolecules from deep ice cores reveal a forested southern Greenland. *Science* **317**, 111–114 (2007).
15. Green, R. E. *et al.* A draft sequence of the Neandertal genome. *Science* **328**, 710–722 (2010).
16. Kari, L. & Mahalingam, K. in *Algorithms and Theory of Computation Handbook* Vol. 2, 2nd edn (eds Atallah, M. J. & Blanton, M.) 31–1–31–24 (Chapman & Hall, 2009).
17. Păun, G., Rozenberg, G. & Salomaa, A. *DNA Computing: New Computing Paradigms* (Springer, 1998).
18. Watson, J. D. & Crick, F. H. C. Molecular structure of nucleic acids. *Nature* **171**, 737–738 (1953).
19. Niedringhaus, T. P., Milanova, D., Kerby, M. B., Snyder, M. P. & Barron, A. E. Landscape of next-generation sequencing technologies. *Anal. Chem.* **83**, 4327–4341 (2011).
20. LeProust, E. M. *et al.* Synthesis of high-quality libraries of long (150mer) oligonucleotides by a novel depurination controlled process. *Nucleic Acids Res.* **38**, 2522–2540 (2010).
21. Massingham, T. & Goldman, N. All Your Base: a fast and accurate probabilistic approach to base calling. *Genome Biol.* **13**, R13 (2012).
22. Gantz, J. & Reinsel, D. *Extracting Value from Chaos* (IDC, 2011).
23. Brand, S. *The Clock of the Long Now* (Basic Books, 1999).
24. Digital archiving. History flushed. *Economist* **403**, 56–57 (28 April 2012); available at <http://www.economist.com/node/21553410> (2012).
25. Bessone, N., Cancio, G., Murray, S. & Taurelli, G. Increasing the efficiency of tape-based storage backends. *J. Phys. Conf. Ser.* **219**, 062038 (2010).
26. Baker, M. *et al.* in *Proc. 1st ACM SIGOPS/EuroSys European Conf. on Computer Systems* (eds Berbers, Y. & Zwaenepoel, W.) 221–234 (ACM, 2006).
27. Yuille, M. *et al.* The UK DNA banking network: a “fair access” biobank. *Cell Tissue Bank.* **11**, 241–251 (2010).
28. Global Crop Diversity Trust. Svalbard Global Seed Vault. (2012); available at <http://www.croptrust.org/main/content/svalbard-global-seed-vault> (accessed 10 May 2012).

Supplementary Information is available in the online version of the paper.

Acknowledgements At the University of Cambridge: D. MacKay and G. Mitchison for advice on codes for run-length-limited channels. At CERN: B. Jones for discussions on data archival. At EBI: A. Löytynoja for custom multiple sequence alignment software, H. Marsden for computing base calls and for detecting an error in the original parity-check encoding, T. Massingham for computing base calls and advice on code theory and K. Gori, D. Henk, R. Loos, S. Parks and R. Schwarz for assistance with revisions to the manuscript. In the Genomics Core Facility at EMBL Heidelberg: V. Benes for advice on Next-Generation Sequencing protocols, D. Pavlinić for sequencing and J. Blake for data handling. C.D. is supported by a fellowship from the Swiss National Science Foundation (grant 136461). B.S. is supported by an EMBL Interdisciplinary Postdoctoral Fellowship under Marie Curie Actions (COFUND).

Author Contributions N.G. and E.B. conceived and planned the project and devised the information-encoding methods. P.B. advised on oligo design and Next-Generation Sequencing protocols, prepared the DNA library and managed the sequencing process. S.C. and E.M.L. provided custom oligonucleotides. N.G. wrote the software for encoding and decoding information into/from DNA and analysed the data. N.G., E.B., C.D. and B.S. modelled the scaling properties of DNA storage. N.G. wrote the paper with discussions and contributions from all other authors. N.G. and C.D. produced the figures.

Author Information Data are available at <http://www.ebi.ac.uk/goldman-srv/> DNA-storage and in the Sequence Read Archive (SRA) with accession number ERP002040. Reprints and permissions information is available at www.nature.com/reprints. The authors declare competing financial interests: details are available in the online version of the paper. Readers are welcome to comment on the online version of the paper. Correspondence and requests for materials should be addressed to N.G. (goldman@ebi.ac.uk).

Northern Hemisphere forcing of Southern Hemisphere climate during the last deglaciation

Feng He¹, Jeremy D. Shakun², Peter U. Clark³, Anders E. Carlson^{1,3,4}, Zhengyu Liu^{1,5}, Bette L. Otto-Bliesner⁶ & John E. Kutzbach¹

According to the Milankovitch theory, changes in summer insolation in the high-latitude Northern Hemisphere caused glacial cycles through their impact on ice-sheet mass balance¹. Statistical analyses of long climate records supported this theory, but they also posed a substantial challenge by showing that changes in Southern Hemisphere climate were in phase with or led those in the north². Although an orbitally forced Northern Hemisphere signal may have been transmitted to the Southern Hemisphere³, insolation forcing can also directly influence local Southern Hemisphere climate, potentially intensified by sea-ice feedback^{4–6}, suggesting that the hemispheres may have responded independently to different aspects of orbital forcing. Signal processing of climate records cannot distinguish between these conditions, however, because the proposed insolation forcings share essentially identical variability⁷. Here we use transient simulations with a coupled atmosphere–ocean general circulation model to identify the impacts of forcing from changes in orbits, atmospheric CO₂ concentration, ice sheets and the Atlantic meridional overturning circulation (AMOC) on hemispheric temperatures during the first half of the last deglaciation (22–14.3 kyr BP). Although based on a single model, our transient simulation with only orbital changes supports the Milankovitch theory in showing that the last deglaciation was initiated by rising insolation during spring and summer in the mid-latitude to high-latitude Northern Hemisphere and by terrestrial snow–albedo feedback. The simulation with all forcings best reproduces the timing and magnitude of surface temperature evolution in the Southern Hemisphere in deglacial proxy records^{8,9}. AMOC changes associated with an orbitally induced retreat of Northern Hemisphere ice sheets¹⁰ is the most plausible explanation for the early Southern Hemisphere deglacial warming and its lead over Northern Hemisphere temperature; the ensuing rise in atmospheric CO₂ concentration provided the critical feedback on global deglaciation^{9,11}.

To identify the physical mechanisms associated with the onset of the last deglaciation, we conducted four single-forcing transient simulations in addition to a transient simulation with all forcings¹² (hereafter ALL), using the Community Climate System Model version 3 (CCSM3) of the US National Center for Atmospheric Research: ORB (22–14.3 kyr BP), forced only by transient variations of orbital configuration¹³ (Figs 1a and 2a, b); GHG (22–14.3 kyr BP), forced only by transient variations of atmospheric greenhouse gas concentrations¹⁴ (Fig. 1a); MOC (19–14.3 kyr BP), forced only by transient variations of meltwater fluxes from the Northern Hemisphere (NH) and Antarctic ice sheets¹² (Fig. 1b, c); and ICE (19–14.3 kyr BP), forced only by quasi-transient variations of ice-sheet orography and extent based on the ICE-5G (VM2) reconstruction¹⁵. All other forcing factors for each single-forcing simulation were held constant at their Last Glacial Maximum value. See Methods for further details.

For comparison with model results, we constructed Southern Hemisphere (SH) regional proxy temperature stacks from records

south of the equatorial region (15–90° S), with four surface air temperature (SAT) records used to construct an Antarctic stack, five sea surface temperature (SST) records for the South Atlantic stack, six SST

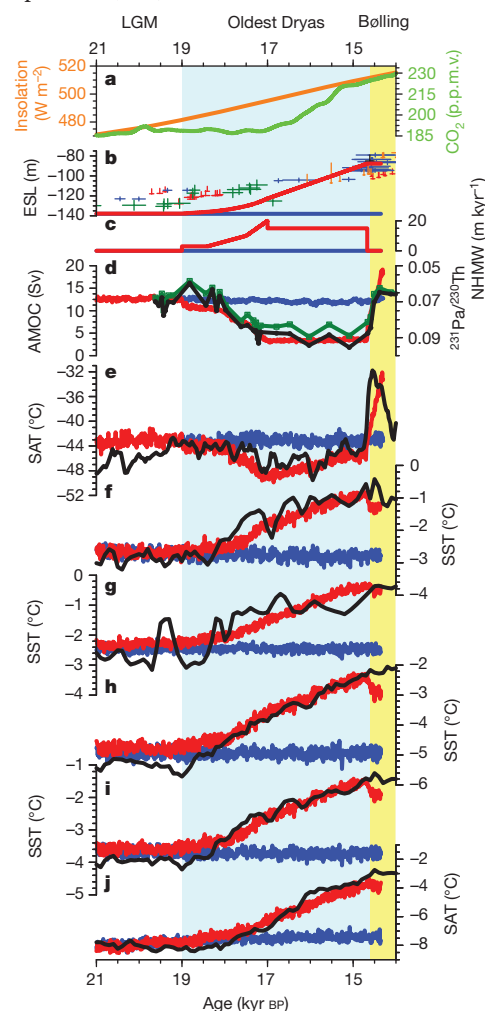


Figure 1 | Comparison of data and models for SH regional temperature stacks. **a**, Insolation on 21 June at 60° N (ref. 13) and atmospheric CO₂ concentration¹⁴. **b**, Eustatic sea level²⁸. Age error bars, ± 2 s.d. **c**, NH meltwater (NHMW) fluxes¹², in metres of global sea level rise per 1,000 years. **d**, Pa/Th ratio at Bermuda (GGC5 core) as a proxy for AMOC export²⁹, and model maximum AMOC transport (below 500 m). Sv, Sverdrup (1 Sverdrup = 10^6 m³ s⁻¹). **e**, Greenland SAT based on GISP2 ice core³⁰ and from simulations (model offset by -4.5 °C). **f–i**, Regional SST stack in the South Atlantic (**f**), the Indian Ocean (**g**), the South Pacific (**h**) and the SH Ocean (**i**). **j**, Regional SAT stack over Antarctica. In **d–j**: black, reconstruction; red, simulation ALL; blue, simulation ORB (10-year annual averages). LGM, Last Glacial Maximum.

¹Center for Climatic Research, Nelson Institute for Environmental Studies, University of Wisconsin-Madison, Madison, Wisconsin 53706, USA. ²Department of Earth and Planetary Sciences, Harvard University, Cambridge, Massachusetts 02138, USA. ³College of Earth, Ocean, and Atmospheric Sciences, Oregon State University, Corvallis, Oregon 97331, USA. ⁴Department of Geoscience, University of Wisconsin-Madison, Madison, Wisconsin 53706, USA. ⁵Department of Atmospheric and Oceanic Sciences, University of Wisconsin-Madison, Madison, Wisconsin 53706, USA. ⁶Climate and Global Dynamics Division, National Center for Atmospheric Research, Boulder, Colorado 80307, USA.

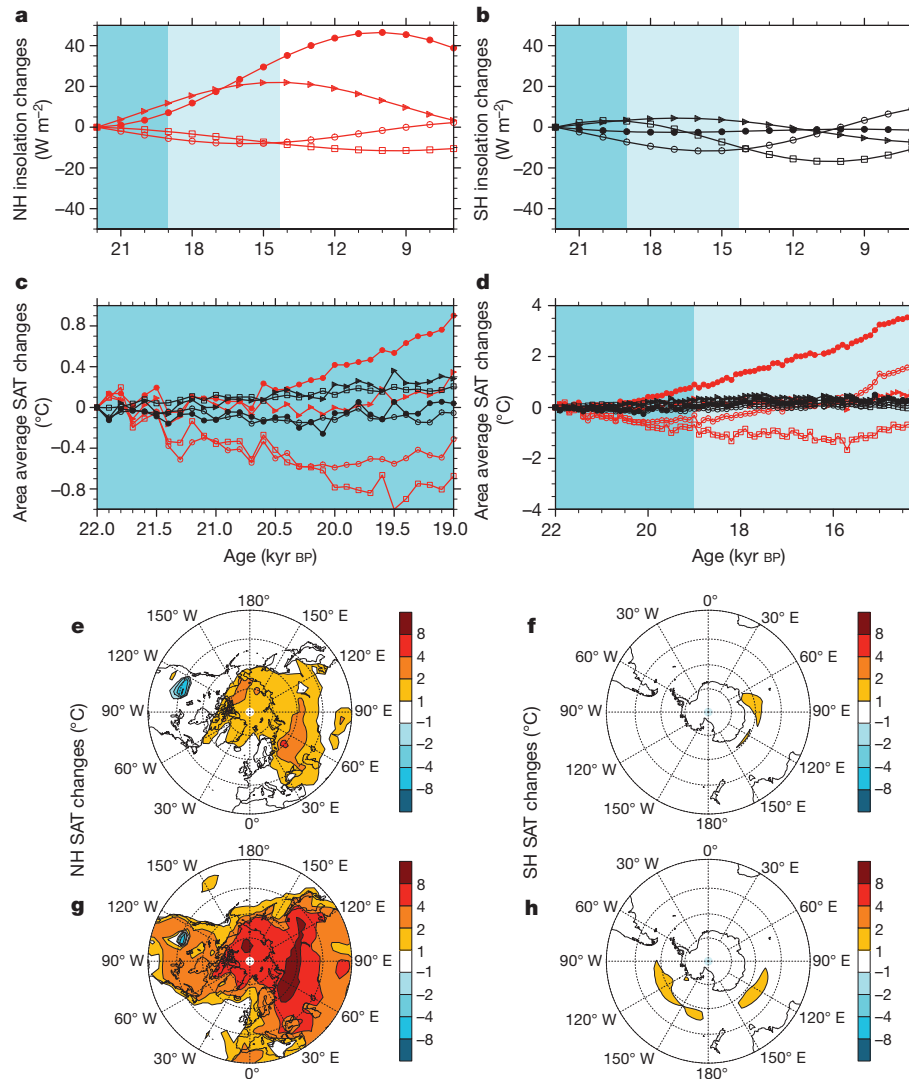


Figure 2 | Comparison of the deglacial warming between the NH and the SH in simulation ORB. **a, b**, Insolation changes at the top of the atmosphere in seasonal averages¹³: NH mid–high latitude (40–90° N) (**a**) and SH mid–high latitude (40–90° S) (**b**). **c, d**, NH (red) and SH (black) mid–high latitude area average SAT in seasonal averages between 22 and 19 kyr BP (**c**) and between 22 and 14.3 kyr BP (**d**). **e, f**, Pattern of SAT changes between 19 and 22 kyr BP in NH

summer (June–August) (**e**) and SH autumn (March–May) (**f**). **g, h**, Pattern of SAT changes between 22 and 14.3 kyr BP in NH summer (June–August) (**g**) and SH winter (June–August) (**h**). In **a–d**: triangles, March–May; filled circles, June–August; open circles, September–November; squares, December–February. The seasons are fixed angular seasons^{16,17}.

records for the South Pacific stack, two SST records for the Indian Ocean, and the combined 13 SH SST records for the SH SST stack (Supplementary Table 1). The simulated deglacial temperature evolution at the locations of each proxy record is used to derive the corresponding regional deglacial temperature stacks for each transient CCSM3 simulation, providing a direct data–model comparison (Supplementary Figs 1–5).

Simulation ALL captures the timing and much of the amplitude of deglacial warming recorded in SH proxy temperature records between the Last Glacial Maximum and the onset of Bølling warming (22–15 kyr BP) (Fig. 1 and Supplementary Figs 6 and 7). Moreover, the deglacial temperature evolution in the proxy and model ALL stacks identifies the SH lead over the NH, with the onset of deglacial warming starting 19–18 kyr BP in the SH, more than 1 kyr earlier than over Greenland (Fig. 1 and Supplementary Fig. 8). The linear summation of the four single-forcing transient simulations (hereafter simulation SUM) also reproduces the temperature changes in simulation ALL (Fig. 3 and Supplementary Fig. 9), suggesting that the transient climatic responses in these regions are linearly proportional to the changes in the four simultaneous forcings in the coupled climate model.

We use the results from the ORB simulation to evaluate the different hypotheses of orbital forcing of climate during the early deglacial period^{3–6}. After correcting for the calendar effect^{16,17}, which is most pronounced in the SH spring season, we find that the apparent deglacial increase of mid-latitude to high-latitude SH spring insolation^{4,6} disappears (Supplementary Figs 10 and 11). The initial increase of the mid-latitude to high-latitude NH spring–summer insolation between 22 and 19 kyr BP was about threefold that in the SH (Fig. 2a, b). Furthermore, the decrease in surface albedo from the melting of terrestrial snow cover in the NH results in additional net solar flux absorption in the NH (Supplementary Figs 12–15). Consequently, NH summers in simulation ORB warm by up to 2 °C in the Arctic and by up to 4 °C over Eurasia, with an area average of 0.9 °C warming in mid to high latitudes in the NH (Fig. 2c, e). In contrast, the simulated area-average SH maximum seasonal temperature change (March–May or December–February) from 22–19 kyr BP increases by only 0.3 °C, with limited regional Southern Ocean warming of less than 2 °C (Fig. 2c, f).

The increase in NH spring–summer insolation continued to exceed the increase in SH insolation throughout the Oldest Dryas (19–14.3 kyr BP), and was about tenfold the anomaly in SH autumn

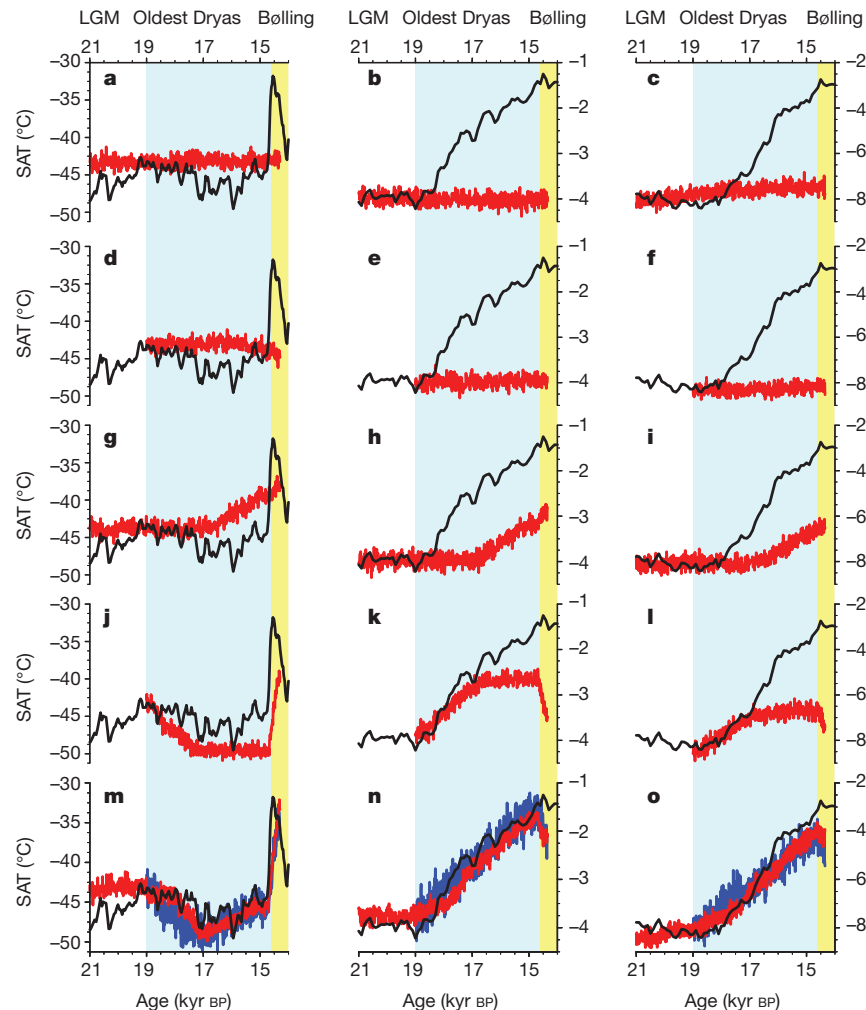


Figure 3 | Early deglacial warming in single-forcing transient simulations. **a–c**, Summit Greenland SAT (GISP2) (**a**), SH SST stack (**b**) and Antarctic SAT stack (**c**) in simulation ORB. **d–o**, As for **a–c**, but for simulations ICE (**d–f**), GHG (**g–i**), MOC (**j–l**) and ALL/SUM (**m–o**). All model variables are

shown in 10-year annual averages. Proxy reconstructions are shown in black. In **a–l**, single-forcing simulations are shown in red. In **m–o**, simulation ALL is shown in red, and simulation SUM is shown in blue. LGM, Last Glacial Maximum.

insolation at the end of the Oldest Dryas (Fig. 2a, b). Concurrently, simulated NH summers warm by up to 4 °C in the Arctic and up to 8 °C over Eurasia, mostly due to the snow–albedo feedback (Supplementary Figs 16–19), with an area average of 3.5 °C warming in mid-latitude to high-latitude regions of the NH (Fig. 2d, g). The simulated area-average winter temperature warming in the SH from 22 to 14.3 kyr BP is, however, less than 0.5 °C, with limited regional Southern Ocean warming of less than 2 °C (Fig. 2d, h).

Our ORB simulation thus supports the Milankovitch theory in showing that substantial summer warming occurs in the NH at the end of the Last Glacial Maximum as a result of the larger increase in high-latitude spring–summer insolation in the NH and greater sensitivity of the land-dominated northern high latitudes to insolation forcing from the snow–albedo feedback. This orbitally induced warming probably initiated the retreat of NH ice sheets¹⁰ and helped sustain their retreat during the Oldest Dryas. In contrast, insolation forcing causes significantly less warming in the SH, particularly during the early deglacial period. Most notably, the ORB simulation fails to produce any of the warming seen in the SH regional SST stacks during the Oldest Dryas (Fig. 1). Over Antarctica, the simulated ORB stack shows only ~0.5 °C of deglacial warming, a 90% underestimation of the reconstructed warming in the Antarctic proxy stack (Fig. 1 and Supplementary Figs 9, 20 and 21). Our transient simulations thus suggest that SH orbital forcing alone is too weak to account for the SH warming during the last deglaciation, which can be attributed to

the weak response of SH sea ice to the local insolation forcing that was previously suggested to be a strong feedback for amplifying SH orbital changes^{4–6} (Supplementary Figs 22–24). An additional shortcoming of hypotheses invoking SH insolation forcing to trigger deglaciation, such as austral spring insolation or summer duration, is that these particular quantities are strong functions of precession and thus cannot readily account for the association between terminations and high obliquity¹⁸.

At the onset of the SH deglacial warming 19–17 kyr BP, simulation ALL reproduces the antiphase annual changes in SAT over Greenland and Antarctica, with 4–6 °C of cooling over Greenland and ~1.5 °C of warming over Antarctica, capturing the timing and much of the reconstructed SH warming (Fig. 3 and Supplementary Figs 25 and 26). In a similar manner to the ORB simulation, the ICE and GHG simulations fail to reproduce significant temperature change in the SH during this interval, as a result of the lack of major changes in ice sheets and concentrations of atmospheric greenhouse gases. In contrast, simulation MOC accounts for almost all of the temperature changes in simulations SUM and ALL (Supplementary Fig. 26), suggesting that the onset of SH warming represents a bipolar seesaw response to the decrease in AMOC associated with the orbitally forced NH ice-sheet retreat that began 20–19 kyr BP¹⁰.

Further support for the role of the bipolar seesaw 19–17 kyr BP comes from the spatial correlation between data and model temperatures from 80 proxy records that span both hemispheres^{8,9} (Fig. 4). Among all the single forcing transient simulations, only simulation

MOC shows variability and significant spatial correlation ($P < 0.01$) with the 80 proxy records in terms of the deglacial temperature change during this time, with most of the warming occurring at SH proxy locations and most of the cooling at NH locations (Fig. 4). Simulation MOC also accounts for the significant correlation between the proxy and simulations ALL and SUM during this period (Fig. 4).

The bipolar seesaw 19–17 kyr BP was followed by global warming 17–15 kyr BP from the deglacial increase in CO_2 concentration beginning at ~ 17.5 kyr BP⁹. Simulation ALL reproduces the in-phase changes among SATs over Greenland and Antarctica and SSTs in the SH (Fig. 3 and Supplementary Figs 27 and 28), whereas simulations ORB and ICE fail to produce significant temperature changes during this interval, because of the cancellation of the seasonal temperature changes from the orbital forcing and the lack of major changes in ice-sheet size. With a weak AMOC 17–15 kyr BP, simulation MOC produces continued but weak warming of SST in the SH and SAT in Antarctica because of thermal inertia in SH oceans during the bipolar seesaw 19–17 kyr BP. Simulation GHG accounts for most of the temperature change in simulations ALL and SUM, suggesting that forcing by greenhouse gases is the dominant mechanism for synchronizing deglacial warming over Greenland and Antarctica and in SSTs in the SH 17–15 kyr BP.

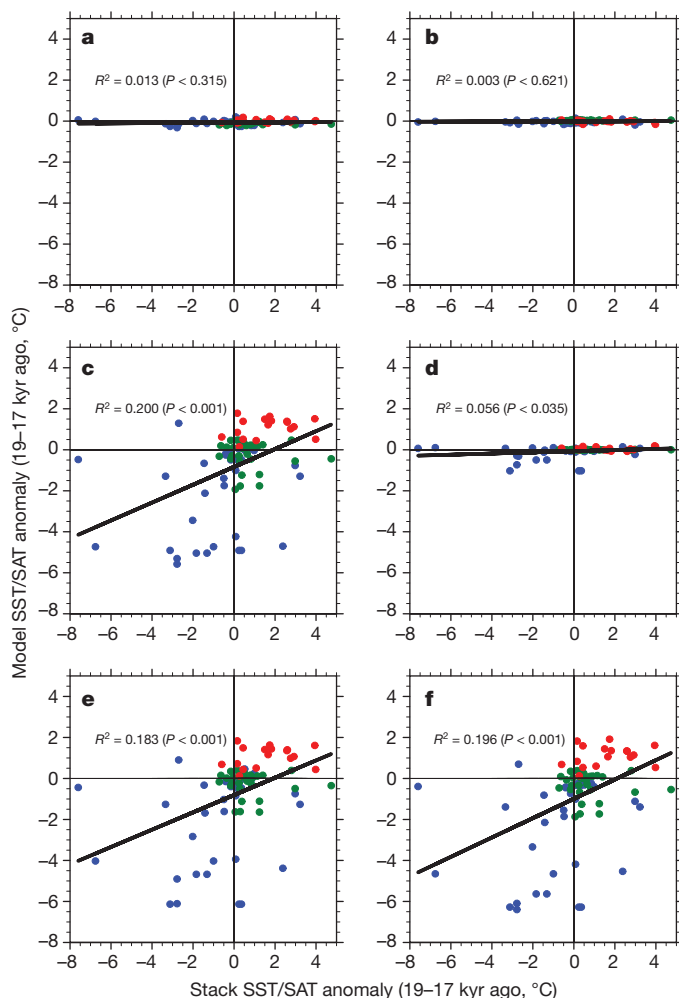


Figure 4 | Spatial correlation of temperature changes of deglacial proxy temperature records⁹ and transient simulations between 19 and 17 kyr BP. a, ORB; b, GHG; c, MOC; d, ICE; e, ALL; f, SUM. In the 80 deglacial temperature records, 33 records are from NH mid-high latitude (15° – 90° N blue), 30 are from the tropics (green) and 17 are from the SH mid-high latitude (15° – 90° S, red). Temperature changes in the model are based on 300-year annual averages between 17.15–16.85 kyr BP and 19.0–18.7 kyr BP. The solid black line denotes the least-square regression line.

The increase in CO_2 concentration during deglaciations is fundamentally tied to Southern Ocean processes¹⁹ and closely tracks Antarctic temperature changes²⁰. The dominance of NH meltwater forcing in triggering SH warming in our model implies that the initial increase in deglacial CO_2 concentration was in turn related to this NH forcing. Moreover, the timing and duration of the steps in the deglacial CO_2 record have been associated with AMOC reductions^{21,22}, further supporting the importance of NH meltwater in triggering and maintaining the deglacial increase in CO_2 concentration. At the same time, the dominant role of CO_2 in driving deglacial warming in simulation ALL suggests a positive feedback between melting ice sheets and increasing CO_2 concentration¹¹, with attendant NH meltwater playing the key role in transferring NH deglaciation to the SH and sustaining the deglacial increase in CO_2 concentration. In contrast, the weak response of the Southern Ocean in simulation ORB throughout the first half of the deglaciation suggests that local insolation contributed little to the increase in CO_2 concentration^{4,5}.

Our results therefore support the Milankovitch theory in identifying a strong NH response to NH insolation forcing. Our results also provide a physical mechanism that can explain the apparent inconsistency between the Milankovitch theory and the early deglacial warming of the SH: the SH lead is caused by the bipolar seesaw (initially induced by NH orbital forcing) that warms the SH and cools the NH^{3,23}. The impact of SH orbital variations and simulated sea-ice feedback^{4–6} are substantially weaker than the bipolar seesaw and cannot account for the $\sim 1.5^{\circ}\text{C}$ warming in the SH regional proxy temperature stacks 19–17 kyr BP. Much of the SH warming during the last deglaciation was therefore driven initially by NH forcing and subsequently by increasing concentrations of atmospheric greenhouse gases. We suggest that our results may apply to each of the major deglaciations of the past 450 kyr. Given the muted Antarctic temperature response to insolation forcing and NH ice-sheet changes simulated in our model, and that Antarctic temperature may consistently lead CO_2 concentration^{24,25}, NH meltwater forcing associated with large ice sheets provides a viable mechanism for triggering SH deglacial warming and the attendant increase in CO_2 concentration¹⁹, which is consistent with records showing that a decrease in AMOC is a common feature of terminations^{21,26,27}.

METHODS SUMMARY

We conducted four single-forcing transient simulations of the last deglaciation (ORB, ICE, GHG and MOC) with CCSM3 of the US National Center for Atmospheric Research, to test the impact of these different forcings in the transient simulation ALL¹², and to investigate the contribution of each individual forcing to early deglacial warming in the SH. As in simulation ALL, all single-forcing transient simulations include dynamic vegetation feedback and a fixed annual cycle of aerosol forcing. Similar to simulation ALL, simulations ORB and GHG were branched off from an equilibrium Last Glacial Maximum simulation¹². Simulation ORB was forced only by transient variations in orbital configuration¹³ of the past 22 kyr, and simulation GHG was forced only by transient variations in greenhouse gas concentrations of the past 22 kyr (ref. 14). All other forcing factors for simulations ORB and GHG are held constant with the values of 22 kyr BP. Both simulations MOC and ICE were branched off at 19 kyr BP from simulation ALL. Simulation MOC was forced only by transient variations of NH meltwater fluxes that were identical to those applied in simulation ALL¹². In simulation ICE, continental ice-sheet orographies and extents were modified on the basis of the time resolution of the ICE-5G (VM2) reconstruction¹⁵; that is, once per 1,000 years for 19–17 kyr BP, and once per 500 years from 17 kyr BP onwards. All other forcing factors for simulations MOC and ICE are held constant with the values of 19 kyr BP.

The SH regional temperature stacks were derived from the deglacial proxy records⁹ that contain most published high-resolution (median resolution 200 years), well-dated (636 radiocarbon dates) temperature records from the last deglaciation; these therefore represent the current state of knowledge on SH deglacial temperature variability. The data were linearly interpolated to 100-year resolution and combined as averages to yield mean temperature time series for the regional temperature stacks.

Received 21 August; accepted 27 November 2012.

1. Milanković, M. *Canon of Insolation and the Ice-age Problem* [Kanon der Erdbestrahlung und seine Anwendung auf das Eiszeitenproblem] Belgrade. 1941. (Israel Program for Scientific Translations, 1969).

2. Hays, J. D., Imbrie, J. & Shackleton, N. J. Variations in Earth's orbit—pacemaker of ice ages. *Science* **194**, 1121–1132 (1976).
3. Imbrie, J. *et al.* On the structure and origin of major glaciation cycles. 1. Linear responses to Milankovitch forcing. *Paleoceanography* **7**, 701–738 (1992).
4. Stott, L., Timmermann, A. & Thunell, R. Southern hemisphere and deep-sea warming led deglacial atmospheric CO₂ rise and tropical warming. *Science* **318**, 435–438 (2007).
5. Huybers, P. & Denton, G. Antarctic temperature at orbital timescales controlled by local summer duration. *Nature Geosci.* **1**, 787–792 (2008).
6. Timmermann, A., Timm, O., Stott, L. & Menviel, L. The roles of CO₂ and orbital forcing in driving Southern Hemispheric temperature variations during the last 21 000 yr. *J. Clim.* **22**, 1626–1640 (2009).
7. Huybers, P. Antarctica's orbital beat. *Science* **325**, 1085–1086 (2009).
8. Shakun, J. D. & Carlson, A. E. A global perspective on Last Glacial Maximum to Holocene climate change. *Quat. Sci. Rev.* **29**, 1801–1816 (2010).
9. Shakun, J. D. *et al.* Global warming preceded by increasing carbon dioxide concentrations during the last deglaciation. *Nature* **484**, 49–54 (2012).
10. Clark, P. U. *et al.* The Last Glacial Maximum. *Science* **325**, 710–714 (2009).
11. Ruddiman, W. F. Ice-driven CO₂ feedback on ice volume. *Clim. Past Discuss.* **2**, 43–55 (2006).
12. Liu, Z. *et al.* Transient simulation of last deglaciation with a new mechanism for Bolling–Allerod warming. *Science* **325**, 310–314 (2009).
13. Berger, A. L. Long-term variations of daily insolation and Quaternary climatic changes. *J. Atmos. Sci.* **35**, 2362–2367 (1978).
14. Joos, F. & Spahni, R. Rates of change in natural and anthropogenic radiative forcing over the past 20,000 years. *Proc. Natl Acad. Sci. USA* **105**, 1425–1430 (2008).
15. Peltier, W. R. Global glacial isostasy and the surface of the ice-age earth: the ICE-5G (VM2) model and GRACE. *Annu. Rev. Earth Planet. Sci.* **32**, 111–149 (2004).
16. Timm, O., Timmermann, A., Abe-Ouchi, A., Saito, F. & Segawa, T. On the definition of seasons in paleoclimate simulations with orbital forcing. *Paleoceanography* **23**, PA2221 (2008).
17. Chen, G. S., Kutzbach, J. E., Gallimore, R. & Liu, Z. Y. Calendar effect on phase study in paleoclimate transient simulation with orbital forcing. *Clim. Dyn.* **37**, 1949–1960 (2011).
18. Huybers, P. & Wunsch, C. Obliquity pacing of the late Pleistocene glacial terminations. *Nature* **434**, 491–494 (2005).
19. Fischer, H. *et al.* The role of Southern Ocean processes in orbital and millennial CO₂ variations—a synthesis. *Quat. Sci. Rev.* **29**, 193–205 (2010).
20. Pedro, J. B., Rasmussen, S. O. & van Ommen, T. D. Tightened constraints on the time-lag between Antarctic temperature and CO₂ during the last deglaciation. *Clim. Past* **8**, 1213–1221 (2012).
21. Cheng, H. *et al.* Ice age terminations. *Science* **326**, 248–252 (2009).
22. Denton, G. H. *et al.* The last glacial termination. *Science* **328**, 1652–1656 (2010).
23. Crowley, T. J. North Atlantic deep water cools the Southern Hemisphere. *Paleoceanography* **7**, 489–497 (1992).
24. Caillon, N. *et al.* Timing of atmospheric CO₂ and Antarctic temperature changes across termination. III. *Science* **299**, 1728–1731 (2003).
25. Hansen, J. *et al.* Climate change and trace gases. *Phil. Trans. R. Soc. A* **365**, 1925–1954 (2007).
26. McManus, J. F., Oppo, D. W. & Cullen, J. L. A 0.5-million-year record of millennial-scale climate variability in the North Atlantic. *Science* **283**, 971–975 (1999).
27. Martrat, B. *et al.* Four climate cycles of recurring deep and surface water destabilizations on the Iberian margin. *Science* **317**, 502–507 (2007).
28. Carlson, A. E. & Clark, P. U. Ice-sheet sources of sea level rise and freshwater discharge during the last deglaciation. *Rev. Geophys.* **50**, RG4007 <http://dx.doi.org/10.1029/2011RG000371> (2012).
29. McManus, J. F., Francois, R., Gherardi, J. M., Keigwin, L. D. & Brown-Leger, S. Collapse and rapid resumption of Atlantic meridional circulation linked to deglacial climate changes. *Nature* **428**, 834–837 (2004).
30. Cuffey, K. M. & Clow, G. D. Temperature, accumulation, and ice sheet elevation in central Greenland through the last deglacial transition. *J. Geophys. Res.* **102** (C12) 26383–26396 (1997).

Supplementary Information is available in the online version of the paper.

Acknowledgements We thank O. Timm and A. Timmermann for fruitful discussions, and G. Chen for providing the conversion code for fix-angular calendar. We thank the University Corporation for Atmospheric Research for continuous development of the community Earth system model. This research used resources of the Oak Ridge Leadership Computing Facility, located in the National Center for Computational Sciences at Oak Ridge National Laboratory, which is supported by the Office of Science of the Department of Energy under contract DE-AC05-00OR22725. F.H. is supported by the US National Science Foundation (AGS-0902802, AGS-1203430) and the Climate, People, and the Environment Program. P.U.C. and J.D.S. were supported by the Paleoclimate Program of the National Science Foundation through project PALEOVAR (06023950-ATM). This is CCR contribution no. 1130.

Author Contributions F.H. and Z.L. conceived this study. F.H. initiated and performed all the single-forcing transient simulations and wrote the manuscript with P.U.C. J.D.S. provided and synthesized the proxy data. A.E.C. and P.U.C. constructed the meltwater forcing schemes with F.H., Z.L. and B.O.-B. Z.L. and B.O.-B. initiated the transient simulation project and provided the computational resources. J.E.K. helped interpret the calendar effect of insolation. All authors discussed the results and provided input on the manuscript.

Author Information Reprints and permissions information is available at www.nature.com/reprints. The authors declare no competing financial interests. Readers are welcome to comment on the online version of the paper. Correspondence and requests for materials should be addressed to F.H. (fenghe@wisc.edu).

Diversity loss with persistent human disturbance increases vulnerability to ecosystem collapse

A. S. MacDougall¹, K. S. McCann¹, G. Gellner¹ & R. Turkington²

Long-term and persistent human disturbances have simultaneously altered the stability and diversity of ecological systems, with disturbances directly reducing functional attributes such as invasion resistance, while eliminating the buffering effects of high species diversity^{1–4}. Theory predicts that this combination of environmental change and diversity loss increases the risk of abrupt and potentially irreversible ecosystem collapse^{1–3,5–7}, but long-term empirical evidence from natural systems is lacking. Here we demonstrate this relationship in a degraded but species-rich pyrogenic grassland in which the combined effects of fire suppression, invasion and trophic collapse have created a species-poor grassland that is highly productive, resilient to yearly climatic fluctuations, and resistant to invasion, but vulnerable to rapid collapse after the re-introduction of fire. We initially show how human disturbance has created a negative relationship between diversity and function, contrary to theoretical predictions^{3,4}. Fire prevention since the mid-nineteenth century is associated with the loss of plant species but it has stabilized high-yield annual production and invasion resistance, comparable to a managed high-yield low-diversity agricultural system. In managing for fire suppression, however, a hidden vulnerability to sudden environmental change emerges that is explained by the elimination of the buffering effects of high species diversity. With the re-introduction of fire, grasslands only persist in areas with remnant concentrations of native species, in which a range of rare and mostly functionally redundant plants proliferate after burning and prevent extensive invasion including a rapid conversion towards woodland. This research shows how biodiversity can be crucial for ecosystem stability despite appearing functionally insignificant beforehand, a relationship probably applicable to many ecosystems given the globally prevalent combination of intensive long-term land management and species loss.

Biodiversity can stabilize ecological systems by functional complementarity, with different species thriving under different conditions thereby buffering the effects of environmental change^{1–5}. Despite an often demonstrated positive correlation between diversity and stability, however, the generality of this relationship remains unclear in natural systems, especially in those under persistent anthropogenic influences^{1,8,9}. Human land management is often persistent, by intentional (for example, fire suppression and overfishing) or inadvertent (for example, nitrogen pollution) disturbances that homogenize both resident diversity and environmental conditions. Persistent disturbances obscure diversity–stability relationships because they can affect ecosystem function independently of diversity^{1–3}, as when overgrazing directly decreases production and provides opportunities for invasion^{1,2}. Because persistent disturbances can also drive species loss, false positives may arise between diversity and ecosystem function, in which reductions in diversity and function are correlated but have weak mechanistic connections.

The homogenizing effect of human activity on environmental conditions and diversity may also increase the risk of abrupt and potentially irreversible changes after disturbance pulses, even when systems appear stable beforehand^{5–7}. The question of whether simpler systems

are more or less resistant to disturbance has characterized diversity–stability research for decades^{4,10–13}. Recent research typically supports the latter model, but data are often derived from shorter-term studies in constructed experimental communities⁴. It is unclear, however, whether these stability-regulating mechanisms operate in a similar manner in environmentally heterogeneous natural systems^{2,3}, and whether all measures of stability respond similarly in different environmental contexts (for example, the presence or absence of disturbance)¹. The stabilization of functional attributes after abrupt disturbances is assumed to derive from the asynchronous population-level responses of disturbance-resistant species, which maintain function at the aggregate community level as disturbance-sensitive species falter³. Yet in persistently managed systems characterized by the loss of environmental variability and diversity, species that are well-adapted to previous environmental conditions have often become rare or extinct¹³. These declines may have little functional significance as long as the existing conditions of persistent management are maintained¹⁴. However, this may create a hidden vulnerability to abrupt environmental change, analogous to reduced genetic diversity limiting the capacity for adaptive responses in populations.

Here we demonstrate this vulnerability to collapse in a degraded grassland system in western North America, where responses to abrupt disturbance were mediated by the levels of remnant diversity. As with most grasslands globally, long-term anthropogenic management has homogenized diversity and function (Supplementary Fig. 1). After approximately 150 years of fire suppression, most areas are dominated by high-biomass, low-diversity mixtures of exotic pasture grasses. Over a ten-year period along a naturally occurring diversity gradient, we experimentally re-introduced burning at two intervals: a ten-year press, and a five-year pulse with five years of recovery. The diversity gradient is associated with interactions among grass dominance, dispersal limitation and soil depth, with higher grass production on deeper soils, in the absence of fire, eventually displacing dispersal-limited native populations to areas with shallower soils that are also grass-dominated but with 24% less cover and 22% less production per plot (see Methods). We monitored four measures of stability in response to the immediate and longer term effects of re-introducing fire: resistance to species invasion, resilience of microhabitat conditions, resistance to plot-level extinction, and constancy of biomass production including grass litter (the major fuel source for fire). We quantified the direct effects of fire on stability (for example, the potential extinction of precariously rare native species after burning), versus those mediated by diversity (that is, whether species-rich areas were more resilient to the disturbance). We also contrasted relative abundance and biomass in the press and pulse treatments, to determine the stability of the responses to five years of burning when fire was once again suppressed.

In the absence of fire, based on decade-long data from control plots, we detected a negative association between stability and diversity by the persistent maintenance of low-diversity communities of introduced grasses (Fig. 1a, b). High-density near-monoculture populations can be unstable in nature owing to the intensification of density-dependent

¹Department of Integrative Biology, University of Guelph, Guelph, Ontario N1G 2W1, Canada. ²Department of Botany, and Biodiversity Research Center, University of British Columbia, Vancouver, British Columbia V6T 1Z4, Canada.

factors such as intraspecific competition and enemy attack³. Here, these limitations were weakened by anthropogenic management beginning in the mid-nineteenth century (Supplementary Fig. 1). Similar to an agricultural system in which a few species account for most production, the introduced grasses are more productive (Supplementary Table 1), maintain more environmentally homogeneous understory conditions (such as ground level light; Supplementary Fig. 2), and are less affected by climate variability than plots with high remnant diversity (Fig. 1a). Previous studies have shown how compensatory dynamics in species-rich systems buffer the effects of climatic variability¹⁵. We observed the opposite response, indicating that diversity–stability relationships can sometimes be more system-specific than universal¹. Stability was mechanistically explained by the dense canopy that was more than twice the height of native species (exotic canopy height: 157.3 ± 13.6 cm (mean \pm s.e.m.); native canopy height: 67.63 ± 9.1 cm) and a deep litter layer. Together, they significantly reduced variability in yearly biomass production (Fig. 1b) and ground level light availability (Supplementary Fig. 2), suppressed native plant diversity (Supplementary Table 1), and resisted invasion by woody plants (Supplementary Table 1). When combined with vegetative sprouting that maintains grass recruitment

despite low ground-level light, the net outcome is a species-poor but productive and temporally resilient grassland community that persists despite both the absence of burning and high regional rainfall levels typically associated with woodland ($\sim 1,000$ mm per annum).

The re-introduction of fire, however, caused this system to collapse within one growing season, with immediate dominance by invasive species, especially woody plants. Elton predicted simpler systems to be more prone to invasion¹¹; here, this was only true when the species-poor grassland suffered a sudden disturbance. Experimental burning transformed each stability measure, with significant shifts in species composition, biomass and light levels (Supplementary Table 1 and Supplementary Fig. 2), plus increased plot-level extinctions (Supplementary Table 1) and invasion by both woody plants and pernicious non-native herbaceous species including thistle and annual brome-grasses (Fig. 2 and Supplementary Table 1). These changes were explained by the acute sensitivity of the dominant grasses to burning, resulting in cover reductions to $<5\%$ m⁻² per species or their plot-level eradication (Supplementary Table 1). The most significant change was the rapid invasion by woody plants including late-successional tree species (for example, Douglas-fir (*Pseudotsuga menziesii*)). Typically, tree invasion of grassland is restricted by fire mortality and biotic interactions, which can maintain tree–grassland boundaries for decades^{16,17}. Here, grass elimination led to a significant influx of woody plants within one growing season, with this conversion representing a potentially irreversible state-change given that obligate grassland flora are rapidly extirpated under woodland canopies^{16,17}.

By contrast, woody plant invasion was inhibited in areas with high remnant diversity of native flora (Fig. 2). The underlying mechanisms

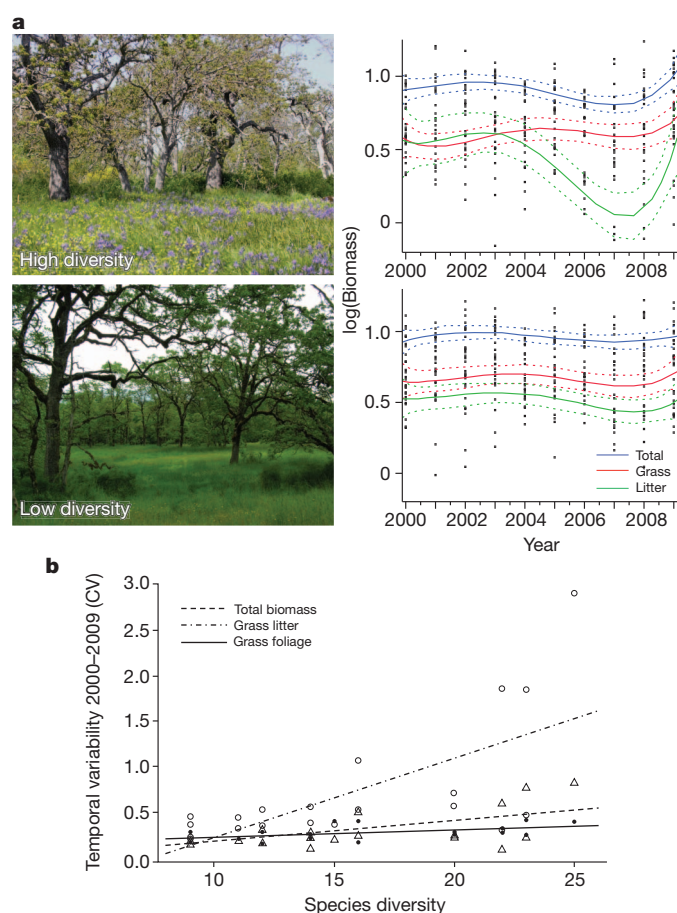


Figure 1 | Production responses to annual climatic variability. **a**, Annual biomass fluctuations in high (top) and low (bottom)-diversity plots. Trendlines are best-fit polynomials with 95% confidence intervals. All high-diversity measures fluctuate significantly with time (repeated-measures analysis of variance (ANOVA): grass $F_{1,9} = 2.2$, $P = 0.02$, litter $F_{1,9} = 4.0$, $P = 0.0002$, total $F_{1,9} = 5.8$, $P < 0.0001$). No biomass measure varies at low diversity (repeated-measures ANOVA: grass $F_{1,9} = 1.4$, $P = 0.2$, litter $F_{1,9} = 1.0$, $P = 0.4$, total $F_{1,9} = 1.49$, $P = 0.16$). **b**, Decadal variability in grass (filled circles), litter (open circles), and total production (triangles), by plot-level diversity. Variability is the coefficient of variation (CV) for the time series of each plot for 2000–2009. Variation increases as diversity increases (repeated-measures ANOVA: grass $F = 8.4$, $P = 0.009$, litter $F = 13.16$, $P = 0.002$, total biomass $F = 9.38$, $P = 0.007$).

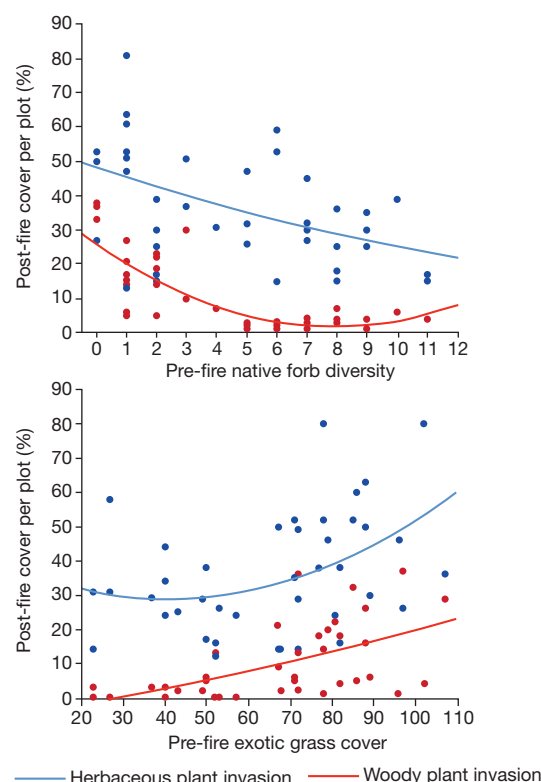


Figure 2 | Invasion by herbaceous exotics and woody plants after fire, in relation to pre-burn native forb diversity and exotic grass cover. All relationships were significant (best-fit trendlines for the relationship between pre-burn native forb cover versus woody plant invasion ($F_{2,39} = 28.2$; $P < 0.0001$) and non-woody plant invasion ($F_{2,39} = 4.9$; $P = 0.013$); for pre-burn exotic perennial grass cover versus woody plant invasion ($F_{2,39} = 8.6$; $P = 0.0008$) and non-woody plant invasion ($F_{2,39} = 4.1$; $P < 0.025$)). Control-plot data are pooled from the pulse- and press-burned treatments (see Methods).

explaining sudden ecosystem collapse have been difficult to determine^{5,7,18}. Here, collapse was associated with local processes connected to plot-level species diversity. Resistance to woody plant invasion occurred by rapid increase in cover of 30 rare native plants representing a range of life-history strategies, with per-species cover increasing by 1.5–4 times compared with unburned plots (Supplementary Table 1). Sampling-effect models predict that one or several species will determine recovery, with more diverse communities more likely to have these species present¹⁹. Here, the diversity response was explained by the aggregate responses of the entire native ground flora community, suggesting functional redundancy despite their life-history differences. Redundancy is often crucial for stability in complex systems, with one species capable of substituting for another²⁰. This was the case here, because no species was distributed widely enough beforehand to compensate solely for the effects of fire. As diversity increased, ground level light returned in the range of pre-burn levels in the same growing season (Supplementary Fig. 2), and woody plant recruitment did not change significantly (Fig. 2 and Supplementary Table 1). Not all stability responses were positively correlated, as above-ground biomass production—a common stability metric—decreased by approximately 34% in the forb-dominated community compared with exotic grassland (Supplementary Table 1). This last observation supports the notion that diversity responses can vary by environmental context and the type of stability being measured¹. Here, low-diversity communities were more stable in the absence of fire, with greater resistance to invasion and greater resiliency in biomass production to yearly climatic variability. High-diversity communities were more stable with sudden perturbation, with greater resilience to microclimatic change and invasion resistance, but were also significantly less productive than the undisturbed low-diversity community.

Diversity influenced not only invasion after burning but also the dynamics of the fire regime itself, on the basis of trait differences between the two dominant functional groups: grasses and forbs. Classic fire models often predict burning to promote fire-tolerant species that maintain fire by producing high-fuel loads, thereby creating a stabilizing positive feedback²¹. We found that forbs in high-diversity areas proliferated with fire but produced little persistent litter, thereby making the reoccurrence of high-intensity fires less likely owing to fuel scarcity. The reduction of burning, in turn, leads to the rapid re-emergence of grasses, as observed in our pulse experiment in which the cessation of burning in 2005 was followed by the rapid recovery of grass biomass to pre-burn levels within two growing seasons (Supplementary Fig. 3). This would once again increase the likelihood of fire. These wide fluctuations in fuel availability over short periods suggest the potential for fine-scale non-equilibrium dynamics in the presence of fire, with local communities oscillating between grass and forb dominance depending on feedbacks between litter availability and fire frequency (see modelling simulations in Supplementary Fig. 4 and Supplementary Information). Historical accounts from southeastern Vancouver Island in the mid-nineteenth century support this exact interpretation, with local species composition and production fluctuating widely even within a single growing season depending on the timing and intensity of fire²². Today, this spatially heterogeneous dynamism has been eliminated, with fire suppression homogenizing species diversity at site and regional levels and changing how the system responds to fire.

Our work demonstrates how persistent human activity can homogenize the structure and function of ecological systems, while simultaneously weakening diversity-related compensatory mechanisms needed to respond to sudden disturbance. These findings are consistent with previously demonstrated connections between diversity and ecosystem function, in which a larger portfolio of functional strategies within a community provides insurance against sudden environmental change^{1–4,23}. Given that many terrestrial systems possess this signature of compositional homogenization owing to persistent human activity, there may be a similar vulnerability to sudden environmental change that will be only evident after the collapse occurs.

METHODS SUMMARY

In May 2000 at peak growing season, 80 1 m⁻² treatment plots were established along a natural diversity gradient in a 10.8-ha oak savanna on Vancouver Island, British Columbia, Canada (Nature Conservancy of Canada). This grassland is part of the California Floristic Province, associated with the Mediterranean climate of coastal western North America that includes pronounced yearly variability in temperature and precipitation including the influence of the Pacific decadal oscillation^{22,24,25}. The pre-European fire season was July–October before the winter rainy season²². The savanna has 115 plant species (75% native) including grasses, forbs and woody plants. Exotic grasses dominate all plots along the gradient, with their combined covers in 2000 ranging from 54 to 129%. Native species can persist at all points along the diversity gradient, with their present-day restriction to areas of lower grass cover associated with competition, acute dispersal limitation and soil depth²⁴ (see Methods). Total plot diversity ranged from 4 to 25 species m⁻². The percentage cover of plants and bare soil, ground level light, and soil moisture were measured in all plots in May–June 2000–2009. Biomass was measured in half of the 80 plots annually; soil nitrogen levels were measured in these same plots in 2000 and two years after burning. Biomass was separated into live grass, litter and forbs, dried for two days at 68 °C, and weighed.

Burning was initiated in July 2000. Twenty plots were burned once each year from 2000–2009 during the summer fire period (July), in a press treatment to test the homogenizing effects of continuous burning on diversity, biomass and invasion. Twenty other plots were treated in the same way from 2000–2004, after which they were unburned for the next five years, in a pulse treatment to test the trajectory of vegetation recovery (see Methods for further details).

Full Methods and any associated references are available in the online version of the paper.

Received 30 August; accepted 20 December 2012.

- Ives, A. R. & Carpenter, S. R. Stability and diversity of ecosystems. *Science* **317**, 58–62 (2007).
- Hooper, D. U. *et al.* A global synthesis reveals biodiversity loss as a major driver of ecosystem change. *Nature* **486**, 105–108 (2012).
- Loreau, M. *From Populations to Ecosystems: Theoretical Foundations for a New Ecological Synthesis* (Princeton, 2010).
- McCann, K. S. The diversity–stability debate. *Nature* **405**, 228–233 (2000).
- Barnosky, A. D. *et al.* Approaching a state shift in Earth's biosphere. *Nature* **486**, 52–58 (2012).
- Kéfi, S. *et al.* Spatial vegetation patterns and imminent desertification in Mediterranean arid ecosystems. *Nature* **449**, 213–217 (2007).
- Rietkerk, M., Dekker, S. C., de Ruiter, P. C. & van de Koppel, J. Self-organized patchiness and catastrophic shifts in ecosystems. *Science* **305**, 1926–1929 (2004).
- Hector, A. Diversity favors productivity. *Nature* **472**, 45–46 (2011).
- Jackson, J. B. C. *et al.* Historical overfishing and the recent collapse of coastal ecosystems. *Science* **293**, 629–637 (2001).
- May, R. M. *Stability and Complexity in Model Ecosystems* (Princeton Univ. Press, 1973).
- Elton, C. S. *Ecology of Invasions by Animals and Plants* (Chapman & Hall, 1958).
- Yodanis, P. The stability of real ecosystems. *Nature* **289**, 674–676 (1981).
- Vonlanthan, P. *et al.* Eutrophication causes speciation reversal in whitefish adaptive radiations. *Nature* **482**, 357–362 (2012).
- Wittebolle, L. *et al.* Initial community evenness favours functionality under selective stress. *Nature* **458**, 623–626 (2009).
- Tilman, D., Reich, P. B. & Knops, J. M. H. Biodiversity and ecosystem stability in a decade long grassland experiment. *Nature* **441**, 629–632 (2006).
- Staver, A. C., Archibald, S. & Levin, S. A. The global extent and determinants of savanna and forest as alternative biome states. *Science* **334**, 230–232 (2011).
- Hirota, M., Holmgren, M., Van Nes, E. H. & Scheffer, M. Global resilience of tropical forest and savanna to critical transitions. *Science* **334**, 232–235 (2011).
- Scheffer, M. *et al.* Early-warning signals for critical transitions. *Nature* **461**, 53–59 (2009).
- Naeem, S. & Li, S. Biodiversity enhances ecosystem reliability. *Nature* **390**, 507–509 (1997).
- Wohl, D. L., Arora, S. & Gladstone, J. R. Functional redundancy supports biodiversity and ecosystem function in a closed and constant environment. *Ecology* **85**, 1534–1540 (2004).
- Bowman, D. M. J. S. *et al.* Fire in the earth system. *Science* **324**, 481–484 (2009).
- MacDougall, A. S., Beckwith, B. & Maslovat, C. Defining conservation strategies with historical perspectives: a case study from a degraded oak grassland ecosystem. *Conserv. Biol.* **18**, 455–465 (2004).
- Yachi, S. & Loreau, M. Biodiversity and ecosystem productivity in a fluctuating environment: the insurance hypothesis. *Proc. Natl Acad. Sci. USA* **96**, 1463–1468 (1999).
- MacDougall, A. S. Response of diversity and invasibility to burning in a northern oak savanna. *Ecology* **86**, 3354–3363 (2005).

25. Harley, C. D. G. & Paine, R. T. Contingencies and compounded rare perturbations dictate sudden distributional shifts during periods of gradual climate change. *Proc. Natl Acad. Sci. USA* **106**, 11172–11176 (2009).

Supplementary Information is available in the online version of the paper.

Acknowledgements We thank I. Banman, T. Ennis and C. Elder; the Garry Oak Ecosystem Recovery Team; the British Columbia Ministry of Forests, Lands, and Natural Resource Operations; the Municipality of North Cowichan, British Columbia; the Maple Bay Fire Department; and the many field technicians over ten years who assisted with this project. All burning was conducted with the assistance and approval of the Municipality of North Cowichan and the BC Ministry of Forests, Lands, and Natural Resource Operations. Thanks also to B. Gilbert, Y. Hautier, E. Harvey, L. Keshet, P. Arcese, M. Fuchs, D. Fraser, R. Hebda, H. Roemer, B. Costanzo, B. Beckwith,

G. Douglas, A. Ceska and M. Fairbairns. Funding was provided by NSERC, World Wildlife Fund Endangered Species Recovery Fund, Mountain Equipment Co-Op Environmental Research Fund, and the University of Guelph, with significant in-kind contributions from the Nature Conservancy of Canada.

Author Contributions Experimental design was by A.S.M. and R.T., fieldwork was by A.S.M., statistical analyses were by A.S.M. and G.G., supplementary methods and analysis were by G.G. and K.S.M., and writing was by A.S.M. with input from R.T., K.S.M. and G.G.

Author Information Reprints and permissions information is available at www.nature.com/reprints. The authors declare no competing financial interests. Readers are welcome to comment on the online version of the paper. Correspondence and requests for materials should be addressed to A.S.M. (amacdo02@uoguelph.ca).

METHODS

The study area was a species-rich remnant oak savanna, and supports communities of herbaceous ground flora in open areas surrounded by low-density patches of oak (*Quercus garryana*), Douglas-fir (*Pseudotsuga menziesii*) and shrubs (pictured in Fig. 1a). All experimental work occurred in open areas free from canopy cover. This system is part of the California Floristic Province, associated with the Mediterranean climate of coastal western North America that includes pronounced yearly variability in temperature and precipitation including the influence of the Pacific decadal oscillation^{22,24,25}.

The factorial field experiment was conducted along a natural diversity gradient, with all plots on the gradient dominated at the beginning of the experiment by two perennial agronomic grasses (*Poa pratensis* and *Dactylis glomerata*), with other exotic agronomic grasses occurring sporadically (*Alopecurus pratensis*, *Agrostis gigantea*, *Elymus repens* and *Phleum pratense*). Half of the 80 plots along the diversity gradient were randomly placed in areas with either deeper (range: 20 to >85 cm) or shallower (8 to 20 cm) soils, with depth of the glaciomarine clay-loam soils on the reserve varying owing to undulations in the underlying bedrock. The two areas do not differ in land-use history, although they are physically separated by an old cart-path (which we use for site access) that was avoided during plot placement in 2000. Soil depth in each plot was measured with an 85-cm rod driven to bedrock. Two burn and two control plots were paired in blocks (4 plots \times 10 blocks \times 2 soil depth zones = 80 plots), with blocking used to minimize the effects of fine-scale variability in soil depth and pre-burn cover of the dominant grasses on the analysis of burn responses. Plots were not selected based on diversity, which thus varied randomly. Plot diversity was surveyed each year starting in 2000, using a 20-cell 1-m² sampling frame laid over each plot. The percentage of cover was visually estimated to be 1% for each species, resulting in annual plot-level cover measures for the 115 species on the reserve from 2000–2009.

The natural diversity gradient on the site is correlated with exotic grass cover, grass litter cover and soil depth, with deeper soil plots having higher grass cover, more litter, and fewer native forb and native graminoid species²⁴. In the absence of long-term burning, the gradient is mechanistically influenced by the interaction between competition and dispersal limitation. All native species can establish, persist and reproduce along all parts of the diversity gradient, based on current distribution patterns plus experimental seed and seedling additions conducted on the reserve²⁴. Plant performance of most native species, however, is significantly constrained in areas of high exotic grass cover, with grass and litter cover reducing mean plant size, reproductive output, and seedling survival of most subordinate species^{24,26}. Although many native perennial forbs are long-lived bulb species that can persist for decades even among the dominant exotic grasses in areas of high production, their reduced fecundity combined with low establishment success increases the probability of their eventual displacement from areas with dense grass cover. They also demonstrate acute dispersal limitation^{24,26}, such that once species become displaced from deeper soil areas, the likelihood of re-colonization from remnant populations on areas with shallower soil is low.

There is no strong direct abiotic effect of soil depth on recruitment (that is, resistance to tree invasion on high diversity shallow-soil plots is not explained by moisture stress associated with shallower soils). Recruitment for all species, including woody plants and exotic herbaceous species, occurs during the winter–spring rainy season (November–March). When moisture becomes limiting in the summer drought period, seedlings in all areas have either matured sufficiently to avoid (senescence) or tolerate (rapidly-produced deep roots) the drought, or perish regardless of soil depth, because all areas along the diversity gradient become similarly moisture limited by early summer^{24,26}.

Burning was conducted in late July each year at the height of summer drought, the time of year when fires most often occurred before the late-nineteenth century²². Most native forbs have set seed and senesced by this time. Most agronomic grasses, by contrast, are at their reproductive peak such that burning eliminates both foliage and seed. The two most abundant native perennial grasses on the reserve (*Bromus carinatus* and *Elymus glaucus*) are similarly sensitive to burning, suggesting that fire suppression would have favoured their abundance before the arrival of the agronomic invaders.

Fires were ignited using a roofing torch, and typically lasted less than 1 min in each plot. Previous fire work on the reserve using thermocouple sensors measured peak temperatures from 133–408 °C at 50 cm above ground level, with no change in temperature 5 cm below the soil surface²⁴. There is no effect of litter biomass on fire intensity (for example, fire does not burn hotter in deeper soil areas with higher litter biomass)²⁴. Burning in the press experiment was conducted annually up to (and including) 2009, even when litter biomass after 2004 had dropped beyond levels that might naturally support fire. Burning was continued to test the homogenizing effects of repeated burning on vegetation compared to the pulse experiment (see modelling details below). Burning in the pulse experiment was conducted annually for five years (July 2000–2004) in the same manner as the press experiment. All analyses on the effects of fire on stability emphasized the 2000 pre-burn data against the responses that unfolded up to and including 2004.

Burning responses were measured as described above, with the percentage cover of vegetation, bare soil, light level at ground level, and soil moisture measured annually at peak growing season (May–June) from 2000 to 2009. Light was measured at five locations within each plot, with measurements at ground level and above canopy (quantum sensor: LiCor). Soil moisture measurements were taken with a 12-cm TDR hydrosense probe (Campbell Scientific). Soil NO₃, NH₄ and total nitrogen were measured in 10-cm deep \times 5-cm diameter soil cores before burning (2000) and after two years of burning (soil lab, University of British Columbia). Biomass data were not collected in 2005.

These data were used to calculate four measures of stability. ‘Resistance to species invasion’ was based on the establishment of woody plant species, and non-native herbaceous species that are known invaders elsewhere in North America. Establishing woody plants were both native (Douglas-fir, big-leaf maple (*Acer macrophyllum*), snowberry (*Symphoricarpos albus*)) and exotic species (scotch broom (*Cytisus scoparius*) and English hawthorn (*Crataegus laevigata*)). Herbaceous invaders were thistles (*Cirsium* spp.), annual brome grasses (*Bromus sterilis* and *Bromus hordeaceus*) and annual forbs (for example, *Trifolium dubium*, *Myosotis discolor* and *Valerianella locusta*). Because of the acute dispersal limitation by the native forbs, all diversity-mediated resistance to species invasion was determined by individuals present in plots at the beginning of the experiment (for example, burned plots with initial low native diversity in 2000 did not transition to plots with higher native diversity later during the experiment). ‘Resilience of microhabitat conditions’ was based on post-fire measures of ground level light, soil moisture, and soil nitrogen at the peak of the growing season. Neither soil nitrogen nor soil moisture was significantly affected by burning and is not discussed further²⁴. ‘Resistance to extinction’ was determined by comparing species composition in plots before and after burning, as well as comparing background levels of extinction in the control plots. ‘Constancy of biomass production’ was the yearly variation in biomass production of grasses, litter and forbs, and was tested in both control plots (Fig. 1) and burned plots.

To analyse our response data, we used repeated-measures ANOVA for multi-factorial analyses (for example, the interacting effects of forb diversity, grass cover, bare soil and light levels on post-fire tree invasion), generalized linear model Poisson regressions when testing the individual effects of plot-level diversity on various response measures (given that diversity was a count measure), and best-fit linear or polynomial regressions when testing the explanatory effects of continuous measures (for example, biomass). All data were log- or (log + 1)-transformed to improve normality. All analyses were done using JMP 8.0. For Fig. 1b, the population variability of each sample plot was calculated from biomass (log + 1) data using the coefficient of variation spanning the years 2000–2009. The community diversity of each plot was measured as the species richness from the first year (2000). Total biomass was calculated by summing the three community types (grass, forb and litter) for each year within each plot. Similarly, species richness for the total biomass measure was the sum of the species richness of all communities in the first year. Linear regression was used to find the relationship between species richness and population variability (coefficient of variation) across all plots. All these analyses were carried out using Wolfram Mathematica version 8.

26. MacDougall, A. S. & Turkington, R. Are invasive species the drivers or passengers of change in degraded ecosystems? *Ecology* **86**, 42–55 (2005).

Suppression of neuroinflammation by astrocytic dopamine D2 receptors via α B-crystallin

Wei Shao^{1*}, Shu-zhen Zhang^{1*}, Mi Tang^{1,2}, Xin-hua Zhang¹, Zheng Zhou¹, Yan-qing Yin¹, Qin-bo Zhou¹, Yuan-yuan Huang¹, Ying-jun Liu¹, Eric Wawrousek³, Teng Chen⁴, Sheng-bin Li⁴, Ming Xu⁵, Jiang-ning Zhou⁶, Gang Hu² & Jia-wei Zhou¹

Chronic neuroinflammation is a common feature of the ageing brain and some neurodegenerative disorders. However, the molecular and cellular mechanisms underlying the regulation of innate immunity in the central nervous system remain elusive. Here we show that the astrocytic dopamine D2 receptor (DRD2) modulates innate immunity through α B-crystallin (CRYAB), which is known to suppress neuroinflammation^{1,2}. We demonstrate that knock-out mice lacking *Drd2* showed remarkable inflammatory response in multiple central nervous system regions and increased the vulnerability of nigral dopaminergic neurons to neurotoxin 1-methyl-4-phenyl-1,2,3,6-tetrahydropyridine (MPTP)-induced neurotoxicity³. Astrocytes null for *Drd2* became hyper-responsive to immune stimuli with a marked reduction in the level of CRYAB. Preferential ablation of *Drd2* in astrocytes robustly activated astrocytes in the substantia nigra. Gain- or loss-of-function studies showed that CRYAB is critical for DRD2-mediated modulation of innate immune response in astrocytes. Furthermore, treatment of wild-type mice with the selective DRD2 agonist quinpirole increased resistance of the nigral dopaminergic neurons to MPTP through partial suppression of inflammation. Our study indicates that astrocytic DRD2 activation normally suppresses neuroinflammation in the central nervous system through a CRYAB-dependent mechanism, and provides a new strategy for targeting the astrocyte-mediated innate immune response in the central nervous system during ageing and disease.

Neuroglial cells are essential for the maintenance of brain homeostasis. Activated neuroglial cells contribute to immune deregulation and neuroinflammation, which are associated with ageing and a variety of neurodegenerative disorders⁴. The ageing of the human brain and progression of cognitive and motor function impairment in the elderly are accompanied with downregulation of DRD2 density in both the striatum and several extrastriatal regions in the normal brain^{5–7}. Recent data indicate that full sets of neurotransmitter receptors, including dopamine receptors, are expressed in microglia and astrocytes^{8–10}. Therefore, we asked whether the deficits in glial DRD2 signalling affect the innate immune response contributing to unbalanced brain homeostasis and disease progression.

To unravel the potential role of DRD2 in neuroinflammation, we examined the expression of an astroglial marker, glial fibrillary acid protein (GFAP) and a microglial marker, ionized calcium binding adaptor molecule 1 (IBA1) in global *Drd2*-knockout (*Drd2*^{−/−}) mice and their wild-type counterparts using immunohistochemistry. In young (2-month-old) *Drd2*-deficient mice, there was pronounced activation of astrocytes (~160%) in the substantia nigra (Fig. 1a, b). In old *Drd2*-null mice (16-month-old), the astrogliosis in the substantia nigra and striatum were also more severe than in age- and

gender-matched wild-type mice (Supplementary Fig. 2). Comparatively more microglial reactivity was seen in these animals (Fig. 1a, c and Supplementary Fig. 2a). To determine whether the *Drd2*-depletion-induced activation of glial cells contribute to neurodegeneration of nigral dopaminergic neurons, *Drd2*^{−/−} mice were treated with neurotoxin 1-methyl-4-phenyl-1,2,3,6-tetrahydropyridine (MPTP). This resulted in more severe loss of nigral dopaminergic neurons compared with their wild-type counterparts (Fig. 1d, e). This difference was associated with more severe inflammation in these brain regions of *Drd2*^{−/−} mice (Fig. 1a–c).

Further biochemical analysis showed that the enhanced vulnerability of nigral dopaminergic neurons was associated with aberrant expression of inflammatory mediators. In 2-month-old *Drd2*^{−/−} mice, there were pronounced increases in levels of CD68, an inflammatory protein expressed in macrophage/microglia, and interleukin (IL)-1 β in various regions of the central nervous system, but not in the immune organ thymus (Fig. 1f and Supplementary Fig. 3a). Quantitative PCR (qPCR) analysis revealed that the expression of pro-inflammatory mediator genes, including *IL-1 β* , *IL-2*, *IL-6*, *IL-12 β* , cyclooxygenase-2 (*COX-2*; genes also known as *Il1b*, *Il2*, *Il6*, *Il12b* and *Ptgs2*, respectively), and anti-inflammatory cytokine *IL-10* (also known as *Il10*), but not tumour necrosis factor- α (*TNF- α* , also known as *Tnfa*), were significantly increased in the striatum of *Drd2*-null mice compared to wild-type mice (Fig. 1g). Moreover, advanced age exacerbates inflammation (Supplementary Fig. 3b). In contrast, ablation of other dopamine receptor subtypes *Drd1* or *Drd3* only resulted in mild or no significant alteration in the levels of pro-inflammatory mediators in the central nervous system (Supplementary Figs 4 and 5). These data indicate that the absence of *Drd2* tipped the balance of cell signalling network towards activation of inflammatory genes in organ-specific and age-dependent manners.

To define the cell types responsible for *Drd2*-ablation-mediated inflammation, we assessed the levels of inflammatory mediators under basal conditions *in vitro*. Expression of major inflammatory mediators were not significantly altered in microglia and neurons isolated from *Drd2*-null pups compared to wild-type control (Fig. 2a and data not shown). In contrast, *Drd2*-null astrocytes produced more pro-inflammatory agents than their wild-type counterparts (Fig. 2b and Supplementary Fig. 6a–d). Interestingly, *Drd2*-null astrocytes and microglia showed a distinctive response to immune stimuli. Astrocytes null for *Drd2* showed a marked increase in the levels of pro-inflammatory mediators, but not NURR1¹¹, compared with wild-type astrocytes following exposure to the conditioned medium of toll-like receptor ligands lipopolysaccharide (LPS)-treated microglia (Fig. 2b and Supplementary Figs 6c, d and 7), indicating that *Drd2*-null astrocytes were hyper-responsive. Conversely, microglia from null

¹Institute of Neuroscience, State Key Laboratory of Neuroscience, Shanghai Institutes for Biological Sciences, Chinese Academy of Sciences, Shanghai 200031, China. ²Jiangsu Key Laboratory of Neurodegeneration, Department of Pharmacology, Nanjing Medical University, Nanjing, Jiangsu 210029, China. ³National Eye Institute, NIH, Bethesda, Maryland 20892, USA. ⁴Department of Forensic Science, Xi'an Jiaotong University School of Medicine, Xi'an, Shanxi 710061, China. ⁵Department of Anesthesia and Critical Care, University of Chicago, Chicago, Illinois 60637, USA. ⁶CAS Key Laboratory of Brain Function and Diseases, School of Life Science, University of Science and Technology of China, Hefei, Anhui 230027, China.

*These authors contributed equally to this work.

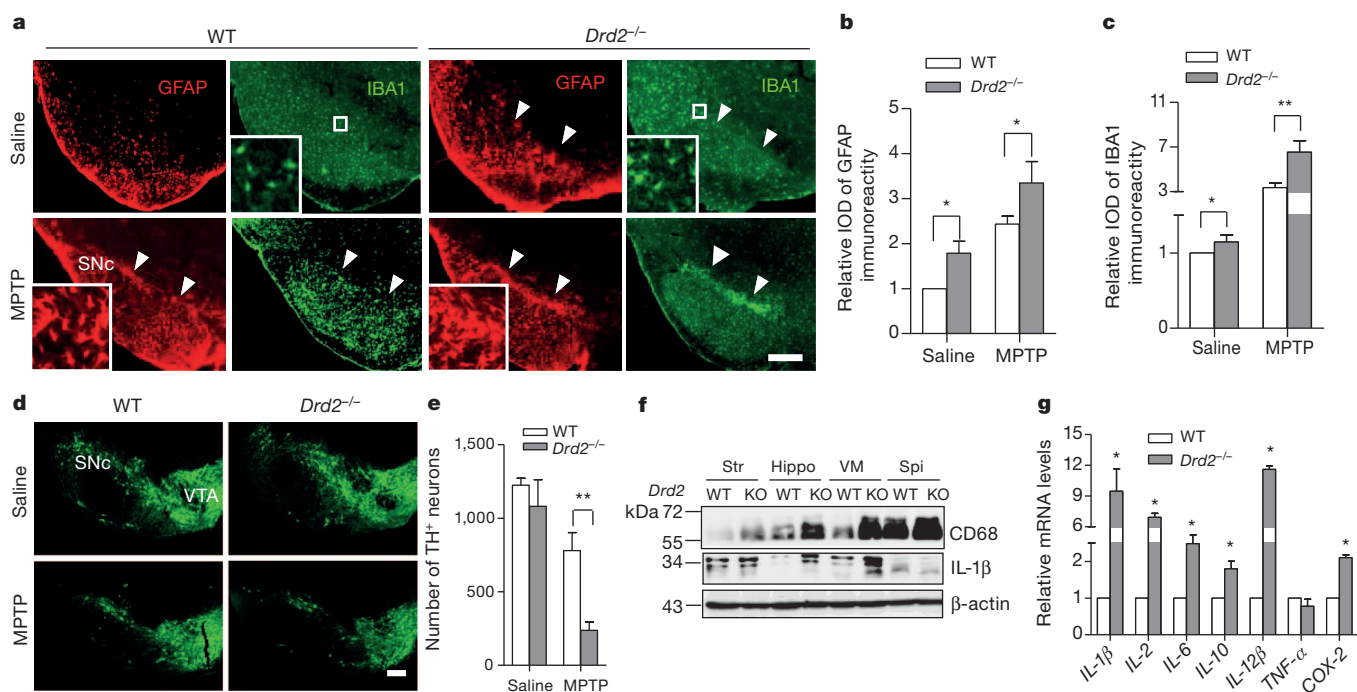


Figure 1 | More severe activation of astrocytes and microglia and pronounced inflammatory responses in global *Drd2*-deficient mice. **a–e**, Immunofluorescent histochemical staining for GFAP, IBA1 and tyrosine hydroxylase (TH) on the ventral mesencephalon of 2-month-old wild-type (WT) and *Drd2*^{-/-} mice administered with either saline or MPTP (**a**, **d**) and quantitative data (**b**, **c**, **e**) are shown. Inserts are enlarged views of the substantia nigra pars compacta (SNc) of the corresponding photo. Arrow heads indicate the SNc. Scale bar, 500 μm. Data are expressed as mean ± s.e.m. (**b**, *n* = 10 per group; **c**, **e**, *n* = 6 per group); **P* < 0.05; ***P* < 0.01

compared to control. IOD, integrated optical density. **f**, Representative western blots from two separate experiments showing CD68 and IL-1β expression in the various brain regions from 2-month-old WT and global *Drd2*^{-/-} mice. Hippo, hippocampus; Spi, spinal cord; Str, striatum; VM, ventral mesencephalon. **g**, Representative graph showing relative mRNA levels of inflammatory mediators in the striatum from WT and global *Drd2*^{-/-} mice. Data are expressed as mean ± s.e.m. (*n* = 4), **P* < 0.05 compared to control.

animals did not show a similar hyper-responsiveness when stimulated in culture with LPS (Fig. 2a). Furthermore, co-culture of mesencephalic dopaminergic neurons with *Drd2*-null astrocytes resulted in a significantly reduced survival of tyrosine-hydroxylase-positive neurons (Supplementary Fig. 6e).

To determine whether *Drd2*-deficiency-induced neuroinflammation occurs at the level of the substantia nigra in a non-cell autonomous fashion, we crossed *Drd2*^{fllox/fllox} mice with human GFAP (hGFAP)-Cre recombinase transgene¹² to generate *Drd2* conditional knockout mice, *Drd2*^{fllox/fllox}; hGFAP-Cre (hereafter referred to as *Drd2*^{hGFAP} cKO) in which *Drd2* is preferentially inactivated in astrocytes. Remarkable loss of *Drd2* messenger RNA was observed in cultured astrocytes, whereas no marked excision in striatal tissue was detected by qPCR analysis (Supplementary Fig. 8a, b), indicating that astrocytic DRD2 is of very low abundance in overall levels of DRD2 in the striatal tissue. In young knockout progeny at postnatal day (P) 10–16, mesencephalic dopaminergic neuron development was normal (Supplementary Fig. 8c, d). With advancing age, mesencephalic dopaminergic neurons were maintained, whereas the levels of inflammatory mediators in the substantia nigra of *Drd2*^{hGFAP} cKO mice were remarkably elevated (Fig. 2c, d), which is in accordance with Fig. 1a. *Drd2*^{hGFAP} cKO mice treated with MPTP showed no marked alteration in cell proliferation in the substantia nigra (Supplementary Fig. 9). The ventral tegmental area (VTA) was essentially devoid of activated glial cells (Supplementary Fig. 10). Selective deletion of *Drd2* in neuronal cells *in vivo* resulted in very mild increases in the levels of pro-inflammatory mediators (Supplementary Fig. 11). Taken together, these data indicate that astrocytic DRD2 is a key negative regulator for neuroinflammation.

To identify downstream effectors of *Drd2* that might be responsible for regulating inflammatory mediator production, DNA microarray

analysis was carried out to compare striatal gene transcript profiles between *Drd2*-null mice and their wild-type littermates. Reduction of αB-crystallin (CRYAB) was prominently detected in *Drd2*-null mice compared to wild-type counterparts (Supplementary Table 1 and Supplementary Fig. 12a). CRYAB is known as a small heat-shock protein with anti-inflammatory and neuroprotective activities^{1,2}. In the brain it is expressed primarily in astrocytes and oligodendrocytes^{2,13,14}. Ablation of *Drd2*, but not *Drd1*, resulted in remarkable reduction of CRYAB exclusively in the central nervous system (Supplementary Fig. 12b–f). Furthermore, we found that in either primary cultured astrocytes null for *Drd2* or the central nervous system tissue of *Drd2*^{hGFAP} cKO mice and tamoxifen (TAM)-inducible *Drd2*^{hGFAP} cKO mice, there was pronounced reduction of CRYAB compared to control animals (Fig. 3a and Supplementary Figs 8a, b and 12a, g, h). These analyses indicate that astrocytic DRD2 tightly controls CRYAB expression in astrocytes. Interestingly, some components of classical DRD2 signalling probably contributed to the inflammatory response because the TAM-inducible *Drd2*^{hGFAP} cKO mice displayed enhanced phosphorylated levels of GSK3β(Ser 9), GSK3β(Tyr 216) and p44/42 MAPK (Thr 202/Tyr 204) in the striatum (Supplementary Fig. 13).

To unravel the role of CRYAB on inflammatory mediator expression in astrocytes, we evaluated the impact of altering CRYAB expression. Small interfering RNA knockdown of *Cryab* in cultured astrocytes markedly upregulated pro-inflammatory mediators compared to control (Supplementary Fig. 14a–c). In the substantia nigra of adult *Cryab*-null mice, astrocytes were robustly activated, showing intense GFAP immunoreactivity, but no marked dopaminergic neuron loss in this brain region (Supplementary Fig. 15). Moreover, overexpression of Flag-tagged CRYAB in cultured *Drd2*-null astrocytes resulted in a marked reduction in the levels of

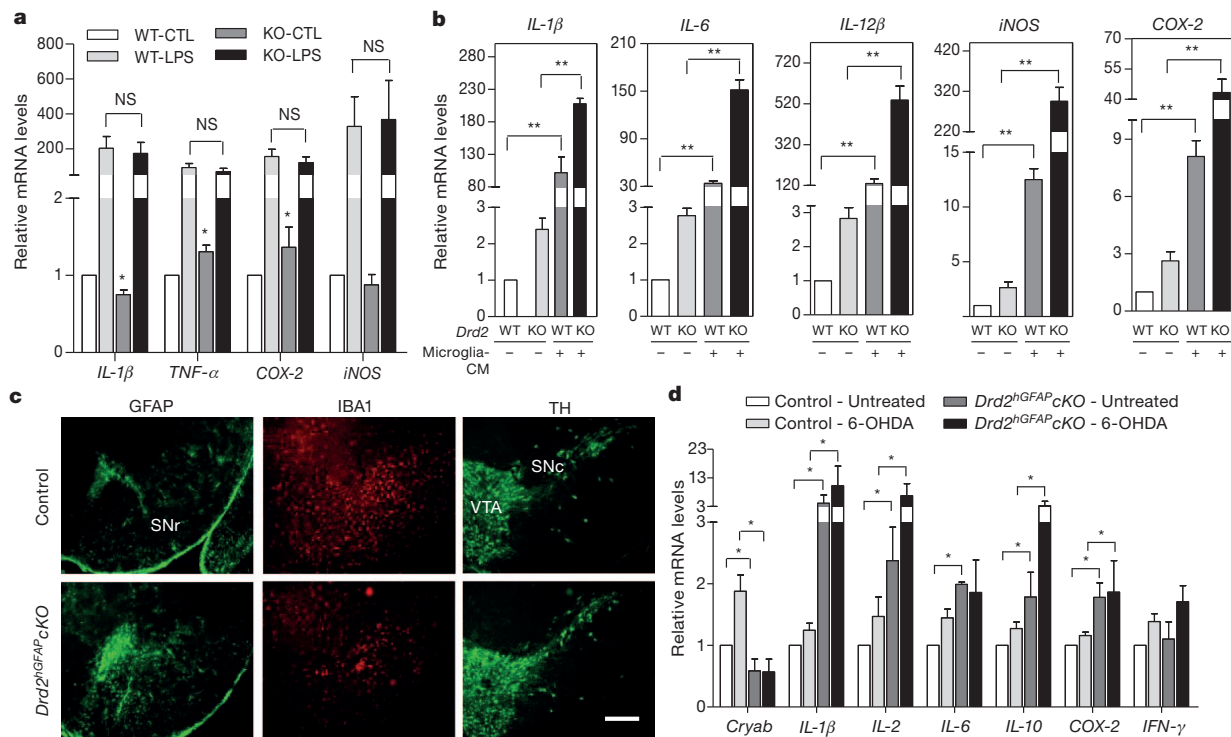
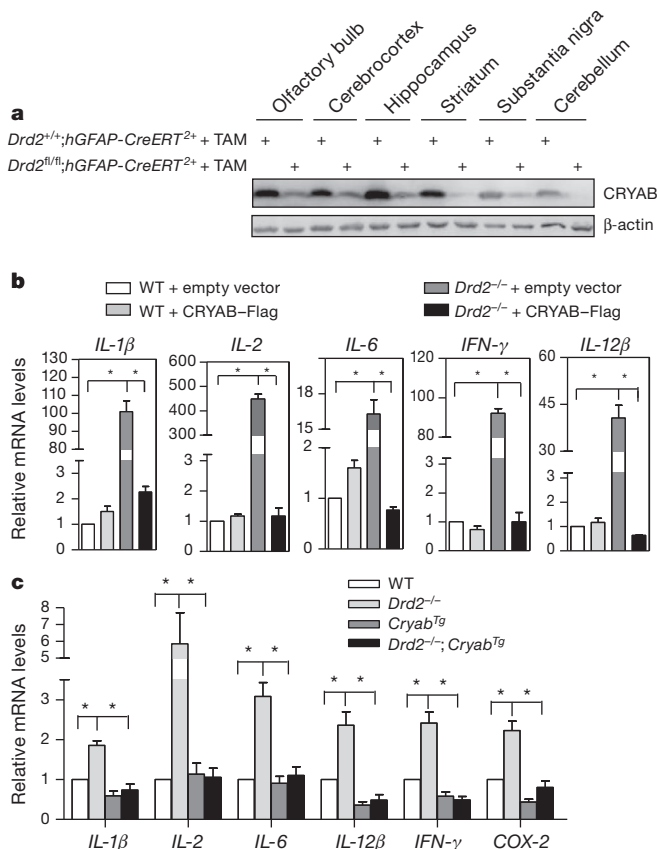


Figure 2 | Astrocytes from global *Drd2*^{-/-} mice are hyper-responsive. **a**, Representative graph showing relative mRNA levels of the indicated pro-inflammatory mediators from primary cultured microglia isolated from WT and global *Drd2*^{-/-} mice and stimulated with lipopolysaccharide (LPS). Data are expressed as mean \pm s.e.m. ($n = 10$); * $P < 0.05$; ** $P < 0.01$ compared to WT control. CTL, control; NS, not significant. **b**, Representative graph showing relative mRNA levels of *IL-1β*, *IL-6*, *IL-12β*, *iNOS* (also known as *Nos2*) and *COX-2* from primary cultured astrocytes isolated from WT and global *Drd2*^{-/-} mice and stimulated with the conditioned medium of

microglia treated with LPS for 24 h. **c**, Immunofluorescent histochemical staining for GFAP, IBA1 and TH on the ventral mesencephalon of 3-week-old *Drd2*^{hGFAP}*cKO* mice compared with control. SNr, substantia nigra pars reticulata. Scale bar, 200 μ m. **d**, Representative graph showing relative mRNA levels of *Cryab* and pro/anti-inflammatory mediators in 2-month-old *Drd2*^{hGFAP}*cKO* and control (*Drd2*^{+/+}*hGFAP-Cre*⁺) animals treated with or without 6-hydroxydopamine (6-OHDA). Data are expressed as mean \pm s.e.m. ($n = 3$); * $P < 0.05$.



pro-inflammatory mediators compared to control (Fig. 3b and Supplementary Fig. 14d–f). Furthermore, we crossed transgenic mice expressing the hamster *Cryab* gene under the control of hGFAP promoter to target expression to astrocytes (hereafter referred to as CRYAB^{Tg})¹⁴ with global *Drd2*^{-/-} mice. Overexpression of CRYAB remarkably inhibited the aberrant increase of pro-inflammatory mediators in the *Drd2*^{-/-} mice (Fig. 3c and Supplementary Fig. 14g). Together, these results indicate that CRYAB is required for *Drd2*-mediated suppression of inflammatory response in astrocytes. To investigate the physiological relevance of these findings, we examined expression of CRYAB in a MPTP-induced mouse model of Parkinson's disease¹⁵. We found intense CRYAB immunosignals in the substantia nigra and striatum of MPTP-treated wild-type mice, some of which were confined to reactive astrocytes (Supplementary Fig. 16).

To determine whether DRD2 signalling is required for suppression of inflammatory response *in vivo*, wild-type mice were treated with

Figure 3 | CRYAB overexpression suppresses *Drd2* deficiency-induced inflammation. **a**, Preferential depletion of *Drd2* in astrocytes results in marked reduction of CRYAB in the central nervous system. Western blot analysis of tissue lysates from the indicated central nervous system regions of 5-month-old inducible conditional *Drd2* knockout mice treated with tamoxifen (TAM). **b**, Transcript levels of the indicated genes evaluated in CRYAB-overexpressing *Drd2*-null astrocytes exposed to the conditioned medium from LPS-treated microglia by qPCR. Data are expressed as mean \pm s.e.m. ($n = 3$); * $P < 0.05$. **c**, CRYAB overexpression specifically targeting astrocytes suppresses the *Drd2*-deficiency-induced aberrant expression of the indicated inflammatory mediators in the striatum *in vivo* as shown by qPCR.

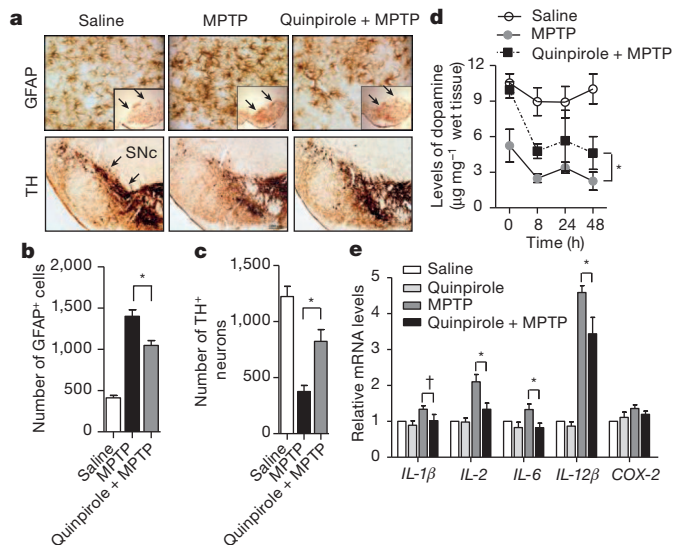


Figure 4 | *In vivo* activation of DRD2 inhibits astrogliosis and inflammation elicited by MPTP treatment. **a–c**, Immunohistochemical analysis of the ventral mesencephalon sections taken after 7 days from wild-type mice that received repeated quinpirole and MPTP administration. **b**, **c**, Quantitative data shown in **a**. Data are expressed as mean ± s.e.m. ($n = 6$); * $P < 0.05$. Scale bar, 200 μm. **d**, Measurement of striatal dopamine levels were performed in wild-type mice pretreated with quinpirole before MPTP treatment at various times (0, 8, 24, 48 h). Data are expressed as mean ± s.e.m. ($n = 6$); * $P < 0.05$. **e**, Transcript levels of the indicated genes evaluated in the striatum of wild-type mice treated with quinpirole or MPTP alone at 56 h after initial MPTP injection. Data are expressed as mean ± s.e.m. ($n = 6$); † $P = 0.058$, * $P < 0.05$.

quinpirole before MPTP administration (Supplementary Fig. 17a). Repeated quinpirole administration resulted in a marked reduction in the level of activation of astrocytes and microglia in the nigrostriatal pathway compared to control (Fig. 4a, b and Supplementary Fig. 17b, c, e, f). As expected, activation of DRD2 significantly prevented the MPTP-induced loss of nigral dopaminergic neurons and their terminals in the striatum (Fig. 4a, c and Supplementary Fig. 17b, d). Consistent with these results, quinpirole significantly attenuated the acute decrease of striatal dopaminergic levels, as shown by high-performance liquid chromatography (HPLC) measurement, and reduced the levels of pro-inflammatory mediators in the substantia nigra of MPTP-treated mice compared with the mice treated with MPTP alone (Fig. 4d, e). In contrast, *Drd2*-null mice as well as *Cryab*-null mice failed to show attenuation of astrocyte activation in the nigrostriatal pathway induced either by MPTP or 6-hydroxydopamine following quinpirole treatment, respectively (Supplementary Figs 18 and 19). Our data indicate that the use of a DRD2 agonist reduced the severity of the neuroinflammatory response when administered before MPTP.

Our results identify astrocytic DRD2 as an important component of neural network controlling innate immunity in the central nervous system. Astrocytic *Drd2* tightly controls the expression of CRYAB which accounts for the observed modulation of immune balance. By influencing CRYAB expression, DRD2 may modulate inflammatory response and maintain balance of immune state, representing a completely novel function in the central nervous system (Supplementary Fig. 1). Microglia has long been considered a key player in neuroinflammation^{11,16–18}. However, our data indicate that astrocytes are likely to play a previously unexpected but critical function in the modulation of neuroinflammation in the context of *Drd2* deficiency. These findings open up new avenues in the investigation of brain ageing and neuroinflammation-associated central nervous system disorders.

METHODS SUMMARY

Adult or neonatal C57BL/6 mice were from Shanghai Laboratory Animal Center, Chinese Academy of Sciences. *Drd2* (B6.129S2-*Drd2*^{tm1Low}/J), *Drd1* (B6.129S4-*Drd1a*^{tm1Jed}/J) heterozygous mice and *Cryab* transgenic mice (FVB-Tg(GFAP-CRYAB)141.6Mes/J) were purchased from the Jackson Laboratory. *Drd2*^{-/-} mice in a C57BL/6 (inbred) genetic background generated by 10 backcrosses were used in the entire study. *Drd2*-floxed mice were created by Shanghai Research Center for Model Organisms. *Cryab* and *Drd3* mutant mice in 129/Sv genetic background used in this study were characterized previously^{2,19,20}. hGFAP-Cre transgenic mice in a C57BL/6 genetic background, which was originally derived from FVB-Tg(GFAP-Cre)25Mes/J (Jackson Laboratory), were gifts from S. M. Duan. hGFAP-CreER^{T2} transgenic mice in a C57BL/6 genetic background were kindly provided by K. D. McCarthy²¹. Neuron-specific enolase (NSE)-Cre transgenic mice in a C57BL/6 genetic background were gifts from J. Fei. Genotyping was performed as previously described²². Western blotting, primary cell culture, immunohistochemistry, fluorescence intensity measurements, Affymetrix microarray analysis, qPCR and statistics were performed as described in Methods.

Full Methods and any associated references are available in the online version of the paper.

Received 1 August 2011; accepted 7 November 2012.

Published online 16 December 2012.

- Bhat, R. & Steinman, L. Innate and adaptive autoimmunity directed to the central nervous system. *Neuron* **64**, 123–132 (2009).
- Ousman, S. S. *et al.* Protective and therapeutic role for α B-crystallin in autoimmune demyelination. *Nature* **448**, 474–479 (2007).
- Langston, J. W., Ballard, P., Tetrud, J. W. & Irwin, I. Chronic Parkinsonism in humans due to a product of meperidine-analog synthesis. *Science* **219**, 979–980 (1983).
- Lucin, K. M. & Wyss-Coray, T. Immune activation in brain aging and neurodegeneration: too much or too little? *Neuron* **64**, 110–122 (2009).
- Seeman, P. *et al.* Human brain dopamine receptors in children and aging adults. *Synapse* **1**, 399–404 (1987).
- Kaasinen, V. *et al.* Age-related dopamine D2/D3 receptor loss in extrastriatal regions of the human brain. *Neurobiol. Aging* **21**, 683–688 (2000).
- Antonini, A. & Leenders, K. L. Dopamine D2 receptors in normal human brain: effect of age measured by positron emission tomography (PET) and [¹¹C]-raclopride. *Ann. NY Acad. Sci.* **695**, 81–85 (1993).
- Zhang, Y. & Barres, B. A. Astrocyte heterogeneity: an underappreciated topic in neurobiology. *Curr. Opin. Neurobiol.* **20**, 588–594 (2010).
- Bal, A. *et al.* Evidence for D₂ receptor mRNA expression by striatal astrocytes in culture: in situ hybridization and polymerase chain reaction studies. *Brain Res. Mol. Brain Res.* **23**, 204–212 (1994).
- Luo, X., Zhang, X., Shao, W., Yin, Y. & Zhou, J. Crucial roles of MZF-1 in the transcriptional regulation of apomorphine-induced modulation of FGF-2 expression in astrocytic cultures. *J. Neurochem.* **108**, 952–961 (2009).
- Saijo, K. *et al.* A Nurr1/CoREST pathway in microglia and astrocytes protects dopaminergic neurons from inflammation-induced death. *Cell* **137**, 47–59 (2009).
- Zhuo, L. *et al.* hGFAP-cre transgenic mice for manipulation of glial and neuronal function in vivo. *Genesis* **31**, 85–94 (2001).
- Iwaki, T., Kume-Iwaki, A., Liem, R. K. & Goldman, J. E. α B-crystallin is expressed in non-lenticular tissues and accumulates in Alexander's disease brain. *Cell* **57**, 71–78 (1989).
- Hagemann, T. L., Boelens, W. C., Wawrousek, E. F. & Messing, A. Suppression of GFAP toxicity by α B-crystallin in mouse models of Alexander disease. *Hum. Mol. Genet.* **18**, 1190–1199 (2009).
- Jackson-Lewis, V. & Przedborski, S. Protocol for the MPTP mouse model of Parkinson's disease. *Nature Protocols* **2**, 141–151 (2007).
- Rivest, S. Regulation of innate immune responses in the brain. *Nature Rev. Immunol.* **9**, 429–439 (2009).
- Saijo, K., Collier, J. G., Li, A. C., Katzenellenbogen, J. A. & Glass, C. K. An ADIOL-ER β -CtBP transrepression pathway negatively regulates microglia-mediated inflammation. *Cell* **145**, 584–595 (2011).
- Saijo, K., Crotti, A. & Glass, C. K. Nuclear receptors, inflammation, and neurodegenerative diseases. *Adv. Immunol.* **106**, 21–59 (2010).
- Brady, J. P. *et al.* α B-crystallin in lens development and muscle integrity: a gene knockout approach. *Invest. Ophthalmol. Vis. Sci.* **42**, 2924–2934 (2001).
- Xu, M. *et al.* Dopamine D3 receptor mutant mice exhibit increased behavioral sensitivity to concurrent stimulation of D1 and D2 receptors. *Neuron* **19**, 837–848 (1997).
- Casper, K. B., Jones, K. & McCarthy, K. D. Characterization of astrocyte-specific conditional knockouts. *Genesis* **45**, 292–299 (2007).
- Cai, L. *et al.* Ethanol-induced neurodegeneration in NRSF/REST neuronal conditional knockout mice. *Neuroscience* **181**, 196–205 (2011).

Supplementary Information is available in the online version of the paper.

Acknowledgements We thank B. Zhang and Y. J. Yan for technical assistance; L. Zhu for technical support in DNA microarray analysis; the Optical Imaging Center of ION and the Cell Biology Analysis Center of IBCB for technical support in confocal microscopy; T. L. Hagemann for providing the CRYAB construct; R. Quinlan for anti-CRYAB

antibodies, Y. Q. Ding for providing the *Drd1* and *Drd2* gene null mice; we also thank Shanghai Research Center for Model Organisms for creating *Drd2*-floxed mice. This work was supported by grants from the Chinese Academy of Sciences, National Basic Research Program of China (nos 2011CBA00408 and 2011CB504102), Natural Science Foundation of China (nos 31021063 and 31123002), and Shanghai Metropolitan Fund for Research and Development.

Author Contributions W.S., S.-z.Z. conducted most of the *in vivo* and *in vitro* experiments and the data analysis, M.T., Z.Z. prepared cell cultures, Y.-q.Y. and Y.-j.L. contributed to cell cultures; X.-h.Z. and Q.-b.Z. contributed to pilot experiments. Y.-q.Y.

and Y.-y.H. contributed to genotyping; E.W. provided CRYAB mutant mice; T.C, S.-b.L. and M.X. provided *Drd3* mutant mice; J.-n.Z., G.H. provided pathological samples and/or advice and J.-w.Z. supervised the project and wrote the manuscript.

Author Information All original microarray data have been deposited in the NCBI Gene Expression Omnibus under accession number GSE41638. Reprints and permissions information is available at www.nature.com/reprints. The authors declare no competing financial interests. Readers are welcome to comment on the online version of the paper. Correspondence and requests for materials should be addressed to J.-w.Z. (jwzhou@ion.ac.cn).

METHODS

Animals. Adult or neonatal C57BL/6 mice were from Shanghai Laboratory Animal Center, Chinese Academy of Sciences. *Drd2* (B6.129S2-*Drd2*^{tm1Low/J})²³, *Drd1* (B6.129S4-*Drd1*^{tm1Jcd/J})²⁴ heterozygous mice and *Cryab* transgenic mice (FVB-Tg(GFAP-CRYAB)141.6Mes/J) were purchased from the Jackson Laboratory (USA). *Drd2*^{-/-} mice in a C57BL/6 (inbred) genetic background generated by 10 backcrosses were used in the entire study. *Drd2*-floxed mice were created by the Shanghai Research Center for Model Organisms. Briefly, the floxed *Drd2* allele was generated by introduction of *loxP* sites flanking the coding region of exon 2 of the *Drd2* locus into the mouse genome. Recombinant embryonic stem cells were injected into C57BL/6 blastocysts to produce chimaeras which were then crossed to C57BL/6 mice to produce mice heterozygous for the floxed *Drd2* allele (*Drd2*^{fllox/+}). *Cryab* and *Drd3* mutant mice in the 129/Sv genetic background used in this study were characterized previously^{19,20,25}. Human glial fibrillary acidic protein promoter (hGFAP)-Cre transgenic mice in a C57BL/6 genetic background, which was originally derived from FVB-Tg(GFAP-Cre)25Mes/J (Jackson Laboratory), were gifts from S. M. Duan. Mice harbouring a TAM-inducible Cre recombinase transgene driven by the hGFAP promoter (hGFAP-CreER^{T2}) in a C57BL/6 genetic background were provided by K. D. McCarthy²¹. Neuron-specific enolase (NSE-Cre) transgenic mice in a C57BL/6 genetic background were gifts from J. Fei. Characterization and genotyping of these mice were described previously²². They were maintained on a 12 h light/dark cycle at 23 °C with food and water available *ad libitum*. All procedures performed were approved by the Institutional Animal Care and Use Committee and were in accordance with the US National Institutes of Health Guide for the Care and Use of Laboratory Animals.

Tamoxifen treatments. Tamoxifen (TAM, Sigma-Aldrich) was made freshly by dissolving in 95% sunflower seed oil/5% ethanol solution by bath sonication for 20–30 min at room temperature with intermittent vortexing. Final concentration of TAM was 10 mg ml⁻¹. Two-month-old mice were injected intraperitoneally with 40–50 mg kg⁻¹ with three cycles of TAM treatment at 1-month intervals. Each cycle consisted of daily injection for 5 consecutive days. The animals were killed at age of 5 months.

Western blot analysis and quantification. Western blotting was performed as described previously²⁶. The following primary antibodies were used: rabbit anti-CRYAB polyclonal antibody (pAb) (1:2,000; Stressgen); rabbit anti-IBA1 pAb (1:500; WAKO); mouse anti-GFAP monoclonal antibody (mAb) (1:1,000; Sigma-Aldrich); mouse anti-β-actin mAb (1:5,000; Sigma-Aldrich); rabbit anti-IL-1β pAb (1:1,000; Abcam); mouse anti-CD68 mAb (1:1,000; Abcam); rabbit anti-Nurr1 pAb (1:2,000; Santa Cruz Biotechnology); rabbit anti-phospho-JNK pAb (1:1,000; Cell Signaling); rabbit anti-p65 pAb (1:1,000; Santa Cruz Biotechnology); rabbit anti-phospho-p38 pAb (1:1,000; Cell Signaling); rabbit anti-phospho-ERK1/2 or ERK1/2 pAb (1:1,000; Cell Signaling); rabbit anti-phospho-AKT(Ser 473) or AKT pAb (1:1,000; Cell Signaling); rabbit anti-phospho-GSK3β(Ser 9) or phospho-GSK3β(Ser 216) or GSK3β pAb (1:1,000; Cell Signaling); rabbit anti-β-arrestin 2 pAb (1:1,000; Santa Cruz Biotechnology). The membrane was washed and incubated for 1 h at room temperature with the corresponding secondary antibodies: horseradish peroxidase (HRP)-conjugated goat anti-rabbit IgG (1:10,000; Jackson ImmunoResearch Laboratories); HRP-conjugated goat anti-mouse IgG (1:10,000; Jackson ImmunoResearch Laboratories). Peroxidase activity was detected with SuperSignal WestPico chemiluminescent substrate (Pierce Biotechnology) and visualized and digitized with ImageQuant (LAS-4000). Optical densities of bands were analysed by using ImageReader software (Fujifilm). Protein levels, quantified by computer analysis as the ratio between each immunoreactive band and the levels of β-actin, were expressed as a percentage of vehicle-treated control.

Immunofluorescence, confocal microscopy and image analysis. Sections or fixed cell cultures were incubated with one primary antibody followed by incubation with secondary antibody conjugated with either Alexa488 or Alexa555. The same sections were then incubated with another primary antibody, followed by incubation with the appropriate secondary antibody. Sections were imaged using either a cooled CCD (DP72, Olympus) on a microscope (BX51; Olympus) or a laser confocal microscope (Leica). Data were obtained and processed using Adobe Photoshop 7.0 software (Adobe Systems). In some cases, immunosignals were visualized by using 3,3'-diaminobenzidine (Sigma-Aldrich).

The following primary antibodies were used: rabbit anti-tyrosine hydroxylase pAb (1:500; Chemicon); mouse anti-CRYAB mAb (2D2B6, 1:200; Santa Cruz Biotechnology or 1:50, a gift from R. Quinlan); rabbit anti-IBA1 pAb (1:500; WAKO); rabbit anti-GFAP pAb (1:800; DAKO); mouse anti-GFAP mAb (1:1,000; Sigma-Aldrich); mouse anti-Cre (1:500; Millipore); mouse anti-tyrosine hydroxylase mAb (1:500; Chemicon).

Cell counting. The number of tyrosine-hydroxylase-positive cells was quantified in adult *Drd2*^{-/-} mutants and their littermates in brain cryosections with typical morphology of the substantia nigra, as described previously²⁷. Four series of

cryosections were collected and every fourth section (12 μm) was used for quantification of tyrosine-hydroxylase-positive neurons. The number of GFAP⁺ or IBA1⁺ cells was quantified using a similar approach. Numbers of tyrosine-hydroxylase-positive neurons in the ventral mesencephalic (VM) cultures were counted in each well.

Intensity analysis. Average intensities of tyrosine hydroxylase, GFAP or IBA1 were calculated using ImageJ by sampling a 28 × 28 pixel area, in the substantia nigra and striatum, in 40 images taken from 4–8 consecutive sections. Values are reported as average intensity above background ± s.e.m.

Primary astrocytic culture and transfection. Astrocytes were prepared from the striatum of Sprague–Dawley rats or *Drd2*-deficient and wild-type C57BL/6 mice at P0, as described previously²⁸. The neonatal striatum were trypsinized and dissociated and cells were plated at density of 5 × 10⁷ cells per 75 cm² flask (Corning) in DMEM/Ham's F12 medium containing 10% FBS (in some cases, 0.5% FBS was used). Culture media were changed 24 h later to complete medium and subsequently twice a week. Cultures were shaken to remove the top layer of cells sitting over the astroglial monolayer to yield mainly type-I astrocytes with a flat morphology between day 5 and 7. Before experimental treatments, astrocytic cultures were passaged once. Cells were allowed to reach 90% confluence. Cultures were transfected using a Nucleofector device (Amaxa) with the indicated plasmids or treated with compounds at various concentrations for the indicated incubation times. Untreated cells were included as controls in all experiments.

Primary microglia culture. Neonatal mice, age 1–3 days, were used for the microglia isolation. Microglial cultures were prepared as described previously²⁹ with a few modifications. Briefly, the neonatal brain were trypsinized and dissociated and cells were plated in a six-well-plate at a density of 5 × 10⁴ cells cm⁻² (Corning) in DMEM/Ham's F12 medium containing 10% FBS, penicillin and streptomycin at 37 °C in humidified 5% CO₂/95% air. Culture media were changed twice a week. Cells were allowed to reach 90% confluence. At day 9 *in vitro*, cultures were replated after trypsinization. At day 20 *in vitro*, cultures were mildly trypsinized with trypsin solution (0.07% trypsin in DMEM/Ham's F12) at 37 °C for 15–20 min. Floating cells (astrocytes and dead cells) were removed by rinsing cultures with D-Hanks' solution. The resulting enriched microglial cultures were maintained in DMEM/Ham's F12 complete medium containing 10% heat-inactivated FBS, penicillin and streptomycin until use. The purity (>99%) of these cultures was confirmed by IBA1 immunocytochemistry.

Preparation of conditioned medium. Postnatal striatal *Drd2*-null and wild-type microglia were allowed to grow to 90% confluence and treated with LPS (10 ng ml⁻¹) for 2 h¹¹. The conditioned medium was collected 24 h following washing of the culture. The conditioned medium was centrifuged before use.

Mesencephalic neuronal culture. Primary VM neuronal cultures were prepared as described previously³⁰. Briefly, fetuses obtained from pregnant rats on the 14th gestational day (E14, where E0 is the day of the vaginal plug) were used for preparation of VM neuronal cultures. The animals were killed with an overdose of pentobarbital sodium and the VM tissues were collected and digested with trypsin. Cell suspension was plated onto poly-L-lysine-coated 96-well plates at a density of 10⁵ cells per cm² in DMEM/Ham's F12 medium (Invitrogen) containing 10% fetal bovine serum (Invitrogen). Cells were maintained at 37 °C in a 95% air/5% CO₂ humidified atmosphere for 3 h, and the cells were then switched to Neurobasal medium with 2% B27 supplement (Invitrogen).

Isolation of total RNA and Affymetrix microarray analysis. Isolation of total RNA and Affymetrix microarray analysis were performed as described previously³¹. Briefly, the striatum of 2-month-old male mice were homogenized in TRIzol reagent (Invitrogen). Total RNA was purified and complementary DNA was synthesized. The complementary RNA was prepared and biotin-labelled. Twenty micrograms of fragmented cRNA were hybridized for 16 h at 45 °C to a Mouse 430 2.0 array (Affymetrix). All RNA samples were subjected to RNA quality control by inspection on an agarose gel and measurement of 260/280 nm absorbance ratios. Array hybridization was performed following the manufacturer's protocol and the arrays were scanned using a laser confocal microscope (Affymetrix). The array was repeated twice with different batches of sample. All original microarray data have been deposited in the NCBI Gene Expression Omnibus under accession number GSE41638.

Microarray data analysis. Primary analysis was performed using Affymetrix Genechip Operating System 1.2 (GCOS1.2) software, as described previously³¹, to select all of the probe sets that scored as 'present' in the control sample. The signal strengths of those probe sets were compared between *Drd2* KO and wild-type counterparts to identify any probe sets that showed increased or reduced expression in the KO sample for more than twofold compared with wild-type mice. Supplementary Table 1 showed the list of differentially expressed annotated genes and predicted genes identified using statistical analysis with Student's *t*-test, in combination with Benjamini–Hochberg (BH) multiple test correction.

Cryab knockdown. Knocking down *Cryab* (GenBank accession number NC_000011) was performed as described previously³². Mouse primary astrocytes were seeded 2×10^5 in six-well tissue culture dishes 36 h before transfection with small interfering RNA (siRNA) targeting *Cryab* or control siRNA (Jima) using Lipofectamine 2000 (Invitrogen) according to the manufacturer's protocol. siRNA duplexes used were: sense: r(GGCCCCAAUUAUCAAGCUA)dTdT; antisense: r(UAGCUUGAUAAUUUGGGCC)dTdT; non-silencing control siRNA: sense: r(UUCUCCGAACGUGUCACGU)dTdT; and antisense: r(ACGUGACACG UUCGGAGAA) dTdT. At 72 h after transfection, cells were collected for western blot or qPCR analysis.

In vivo experimental treatments. Adult mice were administered three intraperitoneal injections of 2 or 5 mg kg⁻¹ quinpirole (Sigma-Aldrich, lot number 096K4603), or 0.5 or 1 mg kg⁻¹ spiperone (Sigma-Aldrich), or vehicle (saline) at 8-h intervals before and after MPTP injection (Supplementary Fig. 17a). Mice were given intraperitoneal injections of 1-methyl-4-phenyl-1,2,3,6-tetrahydropyridine (MPTP; 20 mg kg⁻¹) administered four times at 2 h intervals as described previously¹⁵, and the total dose per mouse was 80 mg kg⁻¹. In some cases, mice received subacute MPTP administration. MPTP was given at 30 mg kg⁻¹ for four consecutive days and left for 3 days. At day 7 post-injection, the animals were killed by rapid decapitation, and the striatum and VM were dissected and processed for western blot or qPCR analysis. In some cases, animals were perfused with 4% paraformaldehyde in 0.1 M phosphate buffer (pH 7.4) and coronal cryo-sections at a thickness of 25 µm were prepared for immunohistochemistry.

In order to test whether a DRD2 agonist exerts suppressive effect on inflammatory response in mice with 129/Sv genetic background that are known to be relatively insensitive to MPTP, animals were perfused in the striatum unilaterally with neurotoxin 6-hydroxydopamine as described previously³³. Lesion of the nigrostriatal pathway was determined using tyrosine hydroxylase immunostaining.

RNA isolation and quantitative PCR. Brain tissue was homogenized in TRIzol reagent (Invitrogen). cDNA was synthesized from 1 µg of extracted total RNA using M-MLV Reverse Transcriptase kit (Invitrogen) according to the manufacturer's protocol. Quantitative PCR was performed with SYBR-Green premix Ex Taq (Takara) and detected by a Real Time PCR System (Roche LightCycler 480 or Rotorgene 6000). β -actin was used as an internal control gene. qPCR primers were designed using Primer Picking Program and their sequences were as follows:

Catalase, forward, 5'-GCATCGAGCCCAGCCCTGAC-3', reverse, 5'-TTGGGGGCACACCCTGGTT-3'; COX-2, forward, 5'-CCCTGCTGCCCGACACCTTC-3', reverse, 5'-CCAGCAACCCGGCCAGCAAT-3'; *Cryab*, forward, 5'-GCACGAAGAACGCCAGGACGA-3', reverse, 5'-GAATGGTGCCTCA GGGCCA-3'; *IL-1 β* , forward, 5'-TGCAGCTGGAGAGTGTGGATCCC-3', reverse, 5'-TGTGCTCTGCTTGTGAGGTGCTG-3'; *IL-2*, forward, 5'-CGCAC CACTTCAAGCTCCACTTC-3', reverse, 5'-ATTCTGTGGCCTGCTTGG GCAAG-3'; *IL-6*, forward, 5'-GGTGGCCCTGCCAGTATTCTC-3', reverse, 5'-GGTCCCAACACAGGATGA-3'; *IL-12 β* , forward, 5'-TGGTTTGCCA TCGTTTGTCTG-3', reverse, 5'-ACAGGTGAGGTTCAGTGTCTTCT-3'; IFN- γ , forward, 5'-GGCTGTACTGCCACGGCACA-3', reverse, 5'-CACCATCCTT

TTGCCAGTTCTCTCCA-3'; inducible NO synthase (iNOS), forward, 5'-GCTGCCTTCCTGCTGTGCA-3', reverse, 5'-CCTGACCATCTCGGGTGCG G-3'; *TNF- α* , forward, 5'-ACTTCGGGGTGATCGGTCCCC-3', reverse, 5'-TGGTTTGTCTACGACGTGGGCTAC-3'; *Hsp25* (also known as *Hspb1*), forward, 5'-CGGTGCTTACCCGGAAATA-3', reverse, 5'-AGGGGATAGGGAAAGA GGACA-3'; *Gpx1*, forward, 5'-TCGGACACCAGGAGAATGGCA-3', reverse, 5'-GAGCGCAGTGGGGTCGTAC-3'; *Gpx3*, forward, 5'-CCTTTTAAGCAGT ATGCAGGCA-3', reverse, 5'-CAAGCCAAATGGCCCAAGTT-3'; β -actin, forward, 5'-GAGATTACTGCCCTGGCTCCTA-3', reverse, 5'-TCATCGTA CTCCTGCTTGCTGAT-3'. Following PCR amplification, a first derivative melting-curve analysis was performed to confirm the specificity of the PCR. The relative fold difference in mRNA between samples was calculated by comparing the threshold cycle (C_t) at which product initially appeared above background according to: $2^{-(\Delta C_t)}$, where ΔC_t is the difference between control group and a treatment group.

Statistical analysis. Statistical analysis was performed using GraphPad software (GraphPad Prism v5.0; GraphPad Software). Data presented as mean \pm s.e.m. were submitted to one/two-way ANOVA followed by either Dunnett test or Student–Newman–Keul's test (as a post hoc test). $P < 0.05$ was considered as significant in statistics.

23. Kelly, M. A. *et al.* Pituitary lactotroph hyperplasia and chronic hyperprolactinemia in dopamine D2 receptor-deficient mice. *Neuron* **19**, 103–113 (1997).
24. Drago, J. *et al.* Altered striatal function in a mutant mouse lacking D1A dopamine receptors. *Proc. Natl Acad. Sci. USA* **91**, 12564–12568 (1994).
25. Ousman, S. S. *et al.* Protective and therapeutic role for α B-crystallin in autoimmune demyelination. *Nature* **448**, 474–479 (2007).
26. Li, A. *et al.* Apomorphine-induced activation of dopamine receptors modulates FGF-2 expression in astrocytic cultures and promotes survival of dopaminergic neurons. *FASEB J.* **20**, 1263–1265 (2006).
27. Sauer, H., Rosenblad, C. & Bjorklund, A. Glial cell line-derived neurotrophic factor but not transforming growth factor beta 3 prevents delayed degeneration of nigral dopaminergic neurons following striatal 6-hydroxydopamine lesion. *Proc. Natl Acad. Sci. USA* **92**, 8935–8939 (1995).
28. Menet, V. *et al.* Inactivation of the glial fibrillary acidic protein gene, but not that of vimentin, improves neuronal survival and neurite growth by modifying adhesion molecule expression. *J. Neurosci.* **21**, 6147–6158 (2001).
29. Saura, J., Tusell, J. M. & Serratos, J. High-yield isolation of murine microglia by mild trypsinization. *Glia* **44**, 183–189 (2003).
30. Guo, H. *et al.* Apomorphine induces trophic factors that support fetal rat mesencephalic dopaminergic neurons in cultures. *Eur. J. Neurosci.* **16**, 1861–1870 (2002).
31. Zhou, Q., Li, J., Wang, H., Yin, Y. & Zhou, J. Identification of nigral dopaminergic neuron-enriched genes in adult rats. *Neurobiol. Aging* **32**, 313–326 (2011).
32. Dimberg, A. *et al.* α B-crystallin promotes tumor angiogenesis by increasing vascular survival during tube morphogenesis. *Blood* **111**, 2015–2023 (2008).
33. Sauer, H. & Oertel, W. H. Progressive degeneration of nigrostriatal dopamine neurons following intrastriatal terminal lesions with 6-hydroxydopamine: A combined retrograde tracing and immunocytochemical study in the rat. *Neuroscience* **59**, 401–415 (1994).

tmc-1 encodes a sodium-sensitive channel required for salt chemosensation in *C. elegans*

Marios Chatzigeorgiou^{1*}, Sangsu Bang^{2*}, Sun Wook Hwang² & William R. Schafer¹

Transmembrane channel-like (TMC) genes encode a broadly conserved family of multipass integral membrane proteins in animals^{1,2}. Human *TMC1* and *TMC2* genes are linked to human deafness and required for hair-cell mechanotransduction; however, the molecular functions of these and other TMC proteins have not been determined^{3–6}. Here we show that the *Caenorhabditis elegans* *tmc-1* gene encodes a sodium sensor that functions specifically in salt taste chemosensation. *tmc-1* is expressed in the ASH polymodal avoidance neurons, where it is required for salt-evoked neuronal activity and behavioural avoidance of high concentrations of NaCl. However, *tmc-1* has no effect on responses to other stimuli sensed by the ASH neurons including high osmolarity and chemical repellents, indicating a specific role in salt sensation. When expressed in mammalian cell culture, *C. elegans* TMC-1 generates a predominantly cationic conductance activated by high extracellular sodium but not by other cations or uncharged small molecules. Thus, TMC-1 is both necessary for salt sensation *in vivo* and sufficient to generate a sodium-sensitive channel *in vitro*, identifying it as a probable ionotropic sensory receptor.

TMC1 is a gene strongly linked to deafness in humans^{1,3}, and mutant mice carrying semidominant (*Tmc1*^{Mhdabth}) or recessive (*Tmc1*^{dn}) *Tmc1* alleles are hearing-deficient^{3,4}. *Tmc1* is expressed in cochlear hair cells, and is required for hair-cell function⁵. Recently, knockout mice containing deletions of both *Tmc1* and a closely related gene, *Tmc2*, were shown to lack hair-cell mechanosensory potentials⁶. *Tmc1* and *Tmc2* are members of a larger family of putative multipass transmembrane proteins that includes eight proteins in humans, one in *Drosophila*, and two in *C. elegans*^{2,3}, one of which (*tmc-2*) is expressed in mechanoreceptors⁷. However, it is not known whether *Tmc* genes encode channel proteins, or whether *Tmc1* and *Tmc2* are components of the hair-cell mechanotransducer or are required indirectly for its activity.

To learn more about the function of the *C. elegans* *tmc-1* gene, we first investigated its expression pattern. In transgenic lines expressing a fluorescent reporter under the *tmc-1* promoter, expression was observed in a small number of neurons, including the ASH neurons, which are important for sensing chemical repellents⁸, high osmolarity and nose touch⁹ (Fig. 1a, b). Expression was also seen in other sensory neurons, including the ADF, ASE, ADL, AQR, PQR, URX and PHA cells (Supplementary Figs 1 and 2). To investigate the subcellular distribution of TMC-1, we expressed a translational fusion between the *tmc-1* coding region and mCherry in ASH under the *gpa-11* promoter (Fig. 1c). This TMC-1::mCherry fusion was localized to the cell body as well as the sensory cilia, the site of sensory transduction. These results indicated a possible role for TMC-1 in ASH sensory function.

To investigate the possible role of TMC-1 in sensory transduction, we assayed the effect of a *tmc-1* deletion allele on ASH-mediated behaviours. The ASH neurons are important for avoidance of diverse noxious stimuli, including nose touch, hyperosmolarity, heavy metals, acids and high concentrations of salt^{10–13}. *tmc-1* mutant animals showed no apparent defect in nose touch avoidance (Fig. 2c), suggesting that mechanosensation in ASH was unaffected by TMC-1. To assess ASH chemosensory function, we presented animals with various repulsive chemical stimuli, including CuCl₂, glycerol and high concentrations of salt, and assayed escape behaviour⁸. We observed that *tmc-1* mutants were strongly defective in the avoidance of NaCl concentrations above 100 mM (Fig. 2a, b). In contrast, responses to other soluble repellents as well as to hyperosmolarity were indistinguishable from wild type (Fig. 2c, d), indicating that *tmc-1* is not required generally for ASH function. In contrast, a loss-of-function mutation in the transient receptor potential vanilloid (TRPV) channel *osm-9* affected avoidance to all these stimuli (Fig. 2). Expression of a

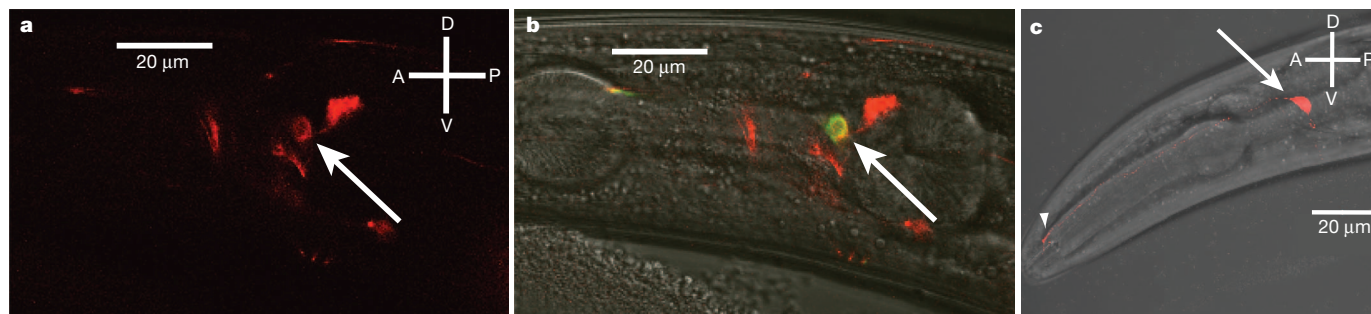


Figure 1 | Expression of TMC-1 in chemosensory neurons. **a, b,** Expression of the *tmc-1::mCherry* promoter fusion in the ASH neurons. Animals express the extrachromosomal array [jEx470[*tmc-1::mCherry*]] as well as [jEx239[*sra-6::YC3.60*]] which specifically labels the ASH neurons with the fluorescent protein yellow cameleon 3.60. Panel **a** shows an image of the expression pattern of the red fluorescent *tmc-1::mCherry* reporter; the ASH neuron is indicated by the arrow. Panel **b** is a differential interference contrast (DIC) and fluorescence image of the same animal showing co-localization of *tmc-1::mCherry* with

sra-6::YC3.60 in ASH. Expression was also seen in the following neurons: ADF, ASE, PHA, ADL, CEP, NSM, AQR, PQR and URX, and at lower frequency, AWC, AFD and BAG (see also Supplementary Figs 1 and 2). **c,** Localization of a TMC-1::mCherry protein fusion in the ASH neurons. Shown is a DIC/fluorescence image of a strain carrying a transgenic array [jEx483[*gpa-11::tmc-1::mCherry*]] in which the *tmc-1* cDNA is fused in frame to mCherry and expressed in ASH under the *gpa-11* promoter. The ASH sensory cilia (arrowhead) and cell body (arrow) are indicated. D, dorsal; V, ventral; A, anterior; P, posterior.

¹Cell Biology Division, MRC Laboratory of Molecular Biology, Hills Road, Cambridge CB2 0QH, UK. ²Department of Biomedical Sciences, Korea University College of Medicine, Seoul 136-705, Korea.

*These authors contributed equally to this work.

tmc-1 cDNA under the control of either the *sra-6* or *gpa-11* promoters, the expression of which overlaps only in ASH, rescued the *tmc-1* salt-avoidance defect (Fig. 2a, b), indicating that *tmc-1* functions in ASH. A double mutant of *tmc-1* and a loss-of-function mutation in the paralogous *tmc-2* gene was no more defective than the *tmc-1* single mutant (Fig. 2b). These results are consistent with TMC-1 acting as a salt sensor in ASH neurons.

The whole-cell neuronal responses of ASH neurons can be measured directly in intact animals by calcium imaging¹⁴. We used a transgenic line expressing a genetically encoded calcium indicator in ASH to assay the effects of *tmc-1* on calcium transients in the ASH cell body evoked by increases in external salt concentration¹⁵. In wild-type animals, we observed large calcium transients in ASH in response to high concentrations of NaCl (Fig. 3a), consistent with behavioural studies¹³. In contrast, the ASH neurons of the *tmc-1* deletion mutant showed little response to high salt concentrations (Fig. 3a, b). This salt-response defect could be rescued by expression of wild-type *tmc-1* under the control of either the *sra-6* or *gpa-11* promoters (Fig. 3a, b). *tmc-1* mutant animals showed normal calcium responses to other stimuli that activate ASH, including glycerol, copper, and nose touch, consistent with the behavioural data indicating that only salt sensation is defective in these animals (Fig. 3e and Supplementary Fig. 4). Thus, *tmc-1* is specifically required for salt sensation in the ASH neurons.

To examine the specificity of the TMC-1-dependent salt response, we used calcium imaging and behavioural assays to test the responses of ASH to salts other than NaCl. We observed that several chloride salts, including KCl, CaCl₂ and MgCl₂, evoked escape responses and ASH calcium transients when presented in high concentrations. These responses were unaffected (for MgCl₂ and CaCl₂) or only slightly

affected (for KCl) by the *tmc-1* mutation, indicating that TMC-1 is not required to sense these salts (Fig. 3d and Supplementary Figs 3b, 4c and 5a, b). We also observed that escape responses and ASH calcium transients were evoked by sodium acetate and sodium gluconate. We found that these responses were strongly reduced in the *tmc-1* deletion mutant and rescued when *tmc-1* was expressed cell-specifically in ASH (Fig. 3c and Supplementary Figs 3a and 6). The sodium gluconate avoidance phenotype of *tmc-1* mutants was only slightly enhanced by ASH ablation and was similar to that of ASH-ablated wild-type animals (Fig. 2e and Supplementary Fig. 3a), indicating that TMC-1 mediates most of the sodium response in ASH, and most of the TMC-1 independent response is due to sensing by other neurons. Mutation of *tmc-2* did not enhance the *tmc-1* mutant phenotype (Fig. 2e). Together, these data suggest that the ASH neurons contain a TMC-1-dependent salt sensor that responds specifically to sodium ions.

The finding that TMC-1 is specifically required for sodium responses in ASH raised the possibility that TMC-1 might itself be a salt-sensing receptor. To address this possibility, we tested whether ectopic expression of TMC-1 in worm neurons could confer the ability to sense sodium. We used the *srbc-64* promoter to express TMC-1 specifically in the ASK cells, amphid neurons that do not respond to salt (Fig. 3f, g) and use a cGMP-dependent mechanism to generate a calcium off-response to lysine and pheromones^{16,17}. In these *srbc-64::tmc-1* animals, we observed strong calcium responses to sodium gluconate in the ASK neurons (Fig. 3f, g), indicating that expression of *tmc-1* was sufficient to confer salt sensitivity. Moreover, *srbc-64::tmc-1* animals exhibited behavioural responses to sodium in a *tmc-1* mutant background (although surprisingly, attraction rather than repulsion), indicating the functionality of the ectopic TMC-1-mediated

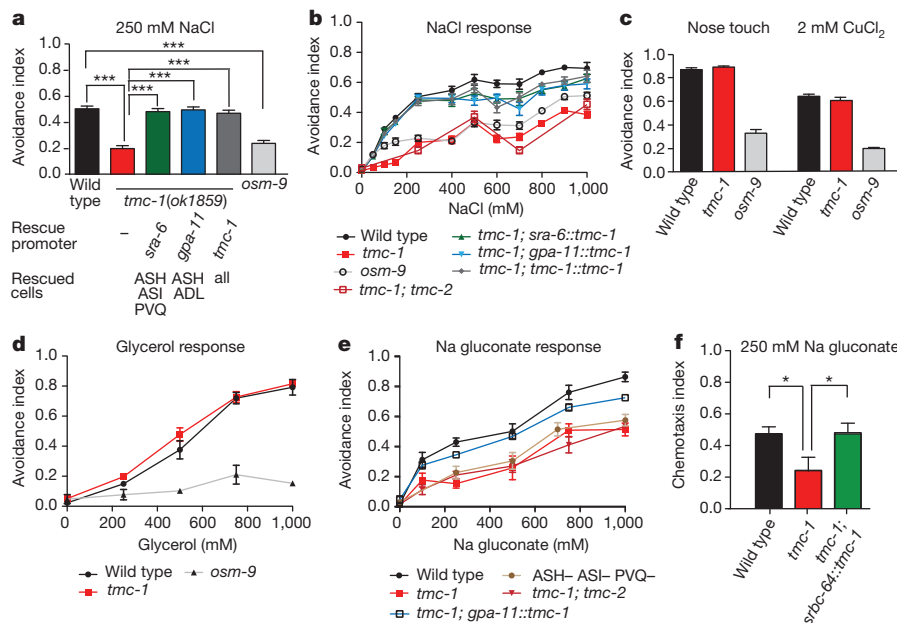


Figure 2 | *tmc-1* is specifically required for high salt avoidance behaviour. **a**, Effect of *tmc-1* on 250 mM NaCl avoidance. Escape behaviour was assessed using the drop test assay⁸. The avoidance index indicates the fraction of animals reversing following stimulus application; error bars for these and other panels indicate s.e.m. For each genotype at least 370 animals were tested in population drop assays. One-way ANOVA with Bonferroni correction was used to test significance. *tmc-1(ok1859)* animals were significantly different from wild type ($P < 0.0005$), whereas all *tmc-1* rescue lines were significantly different from *tmc-1(ok1859)* ($P < 0.0005$), but not from wild type. **b**, Dose response for NaCl avoidance. For each data point, at least 170 animals were tested. *tmc-1(ok1859)* were significantly different from wild-type ($P < 0.005$) for all concentrations, and all *tmc-1* rescue lines were significantly different from *tmc-1(ok1859)* at all concentrations ($P < 0.05$). **c**, Effect of *tmc-1* on other ASH-dependent escape behaviours. For each genotype at least 260 animals were tested for nose touch

avoidance and at least 320 animals for 2 mM CuCl₂ avoidance. No significant difference was observed between wild type and *tmc-1(ok1859)*. **d**, Dose response for glycerol avoidance. For each data point at least 70 animals were tested. No significant difference was detected between wild type and *tmc-1(ok1859)* across all concentrations. **e**, Dose response for sodium gluconate avoidance. For each data point, at least 70 animals were tested. *tmc-1(ok1859)* was significantly different from wild type across all concentrations ($P < 0.05$). The *tmc-1; gpa-11::tmc-1* rescue line (with error bars too small to be visible on the graph) was significantly different from *tmc-1(ok1859)* ($P < 0.05$). **f**, Chemotaxis behaviour to sodium gluconate of wild type, *tmc-1* mutant and animals with heterologous *tmc-1* expression in ASK. At least 790 animals were assayed for each genotype. Wild type was significantly different from *tmc-1(ok1859)* ($P < 0.05$) and *tmc-1; srbc-64::tmc-1* was significantly different ($P < 0.05$) from *tmc-1(ok1859)*.

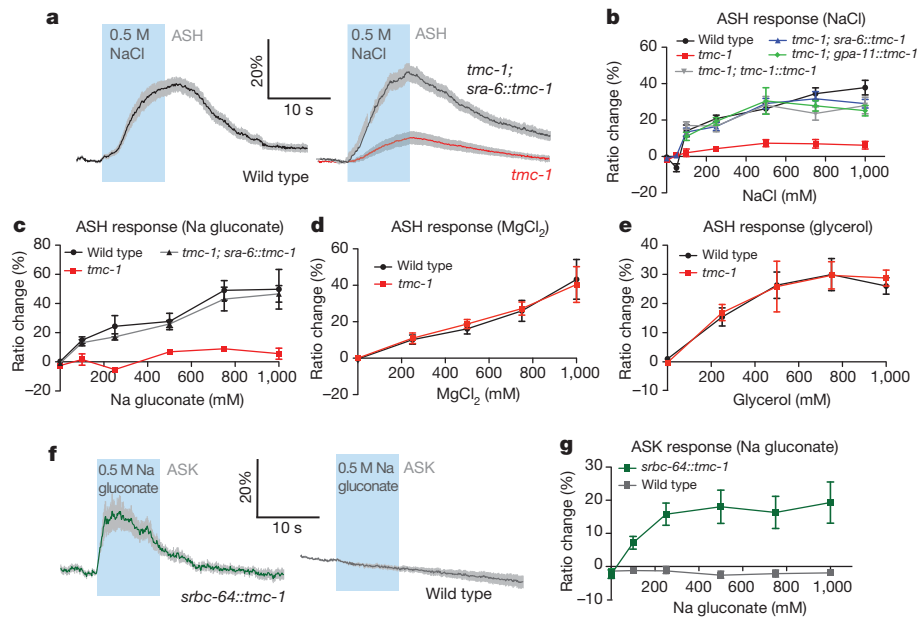


Figure 3 | *tmc-1* is specifically required for ASH chemosensory neuron responses to high salt concentration. **a**, ASH calcium responses to external salt stimulation. Shown are averaged traces of ASH calcium transients in wild type, *tmc-1* mutant and *tmc-1* ASH-rescued animals in response to a 10 s NaCl concentration up-step from 0 to 500 mM. Traces indicate average percentage change in R/R_0 where R is the fluorescence emission ratio and R_0 the baseline ratio; the grey band represents s.e.m. Statistical significance for all experiments was evaluated by one-way ANOVA with Bonferroni correction. The time of the NaCl up-step is shown in blue; $n \geq 13$. For the inset scale graphs in **a** and **f**, 20% indicates per cent change in the YFP/CFP emission ratio. **b**, Quantification of ASH calcium responses in mutant and rescued animals. For each data point $17 < n < 51$ animals were tested; error bars for this and other panels indicate s.e.m. For all concentrations ≥ 100 mM, the response of *tmc-1* was statistically different from wild type and all rescue lines ($P < 0.05$). **c**, Quantification of ASH calcium responses to sodium gluconate. For each data point $5 < n < 19$ animals

were tested. For all concentrations ≥ 100 mM, the response of *tmc-1* was statistically different from wild type and the rescue line ($P < 0.05$). **d**, Quantification of ASH calcium responses to $MgCl_2$. For each data point, $4 < n < 12$ animals were tested. For all concentrations the response of *tmc-1* was not statistically different from wild type. **e**, Quantification of ASH calcium responses to glycerol. For each data point $5 < n < 38$ animals were tested. For all concentrations the response of *tmc-1* was not statistically different from wild type. **f**, ASK calcium responses to sodium gluconate. Shown are averaged R/R_0 traces in wild type ($n = 12$), and *srbc-64::tmc-1* ($n = 15$) animals, which express TMC-1 ectopically in ASK, in response to a 10 s stimulation with 0.5 M sodium gluconate. **g**, Quantification of ASK calcium responses to sodium gluconate. For each data point $7 < n < 24$ animals were tested. For all concentrations ≥ 100 mM, the response of *srbc-64::tmc-1* was statistically different from wild type ($P < 0.05$).

salt responses in ASK (Fig. 2f). These results suggest that TMC-1 can be sufficient to generate a salt receptor *in vivo*.

To investigate this possibility further, we expressed a *C. elegans tmc-1* cDNA in Chinese hamster ovary (CHO-K1) cells and recorded electrophysiological responses of the transfected cells to external salt stimulation. The expressed TMC-1 protein was localized to the plasma membrane, as verified by confocal fluorescence imaging (Supplementary Fig. 8a–c). A 150 mM up-step in NaCl (from a baseline of 140 mM to 290 mM) evoked inward currents in TMC-1-expressing cells (Fig. 4a); in contrast, hypertonic stimulation using glucose, mannitol or *N*-methyl-D-glucamine (NMDG) chloride did not activate currents in these cells (Fig. 4a and Supplementary Figs 8e and 10d). Assaying over a range of NaCl concentrations, we estimated a half-maximum effective concentration (EC_{50}) for the TMC-1-dependent currents of 220 mM, with a threshold of approximately 140 mM and a plateau at approximately >400 mM (Fig. 4b). The Hill plot of the NaCl dose–response curve rose steeply (Hill coefficient of 4.5), suggesting cooperative gating by external salt. Together, these results indicate that heterologously expressed TMC-1 induces the formation of ion channels that are specifically sensitive to extracellular NaCl.

We performed additional experiments to learn more about the properties of the TMC-1-dependent channels. Chloride salts other than NaCl did not evoke robust current increases in TMC-1-expressing CHO-K1 cells (Fig. 4c and Supplementary Fig. 10a–c). In contrast, sodium salts with other anions (including Na gluconate) all elicited currents (Supplementary Fig. 11 and data not shown), suggesting that Na^+ is critical for TMC-1 activation. In the presence of external

calcium, extracellular NaCl evoked Ca^{2+} transients, suggesting that the expressed channels are permeable to Ca^{2+} ions (Fig. 4d), although indirect effects might contribute to this calcium signal. By measuring the reversal potentials of basal currents¹⁸, we quantified ion permeabilities of TMC-1 conductances; Na^+ ions were the most permeable (2.3-fold greater than Cs^+), whereas Ca^{2+} , K^+ and the large cation NMDG⁺ had lower indices (70%, 42% and 2% of Cs^+ permeability, respectively; Fig. 4e). Cl^- and other anions were about 7 to 12 times less permeable than Na^+ or K^+ (Supplementary Fig. 11f, h). Comparable permeability ratios of Cl^- to Na^+ and K^+ (8.7% and 6%), despite the different permeabilities of the two cations, may indicate that Cl^- must be chaperoned by counterions to permeate TMC-1 (Supplementary Fig. 11f). Although TMC-1-dependent currents were insensitive to piezo-driven membrane displacement (Supplementary Fig. 8f), responses to external salt were inhibited by $GdCl_3$, a non-specific blocker of stretch-activated channels (Fig. 4f and Supplementary Fig. 8g), which also blocks the *tmc-1*-dependent response of ASH to sodium gluconate (Supplementary Fig. 7). Overall, TMC-1 expression generates sodium-sensitive, gadolinium-blockable currents with a high Na^+ permeability, properties consistent with a salt sensor.

The production of salt-sensitive channels in TMC-1-expressing cells raises the possibility that TMC-1 itself might form a bona fide ion channel. Although the evidence is not definitive, several lines of evidence support this possibility. When we expressed TMC-1 heterologously in other mammalian cell lines (including HEK293T and HeLa cells), we observed sodium-sensitive inward currents similar to those in TMC-1 CHO-K1 cells (Supplementary Fig. 12a, b). This, together with the expression of an ectopic salt sensor in ASK

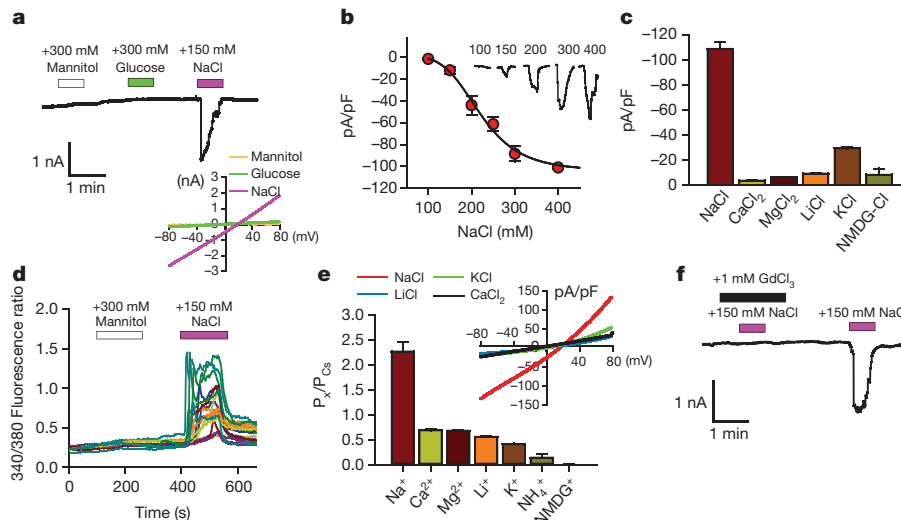


Figure 4 | Sodium-sensitive cation currents in TMC-1-expressing cells.

a, Inward currents were elicited in TMC-1-expressing CHO-K1 cells by external addition of 150 mM NaCl, but not by 300 mM mannitol or glucose, in whole-cell voltage-clamp recordings at -60 mV ($n = 7$) using native chloride conditions (see Methods). Unless otherwise indicated (see panels **b** and **e**), the external buffer contained 140 mM NaCl. When GFP was co-transfected, 76% of GFP-positive cells showed the inward current responses; mock-transfected or untransfected cells lacked such responses (Supplementary Fig. 8d). Inset, representative current-voltage relationship of NaCl-induced inward currents in TMC-1-expressing CHO-K1 cells. **b**, NaCl dose-response for inward current responses of TMC-1-expressing cells. Filled circles represent mean responses to extracellular NaCl ($n = 9$ –17 for each point); error bars for this and other panels indicate s.e.m. Fitting to the Hill equation gives a Hill coefficient of 4.5 and EC_{50} of 220 mM. **c**, Activation of currents in TMC-1-expressing CHO-K1 cells by other salts. Shown are mean current responses at -60 mV upon

addition of 300 mM of the indicated salt to the recording buffer ($n = 6$ –11). **d**, Intracellular Ca²⁺ levels were elevated in TMC-1 expressing CHO-K1 cells in response to addition of external 150 mM NaCl but not to 300 mM mannitol ($n = 34$). Mock-transfected or untransfected cells lacked such responses, as did transfected cells in Ca²⁺-free external buffer (Supplementary Fig. 9). **e**, Relative cation permeabilities of TMC-1 calculated from the reversal potentials of basal currents with CsCl in the internal solution and the indicated chloride salt in the external solution. Permeability ratios were 2.27 ± 0.19 for Na⁺ ($n = 13$), 0.42 ± 0.09 for K⁺ ($n = 14$), 0.57 ± 0.01 for Li⁺ ($n = 11$), 0.70 ± 0.02 for Ca²⁺ ($n = 11$), 0.69 ± 0.06 for Mg²⁺ ($n = 17$), 0.15 ± 0.06 for NH₄⁺ ($n = 5$) and 0.02 ± 0.01 for NMDG⁺ ($n = 17$) (mean \pm s.e.m.). Inset, representative current-voltage relationships of currents under different external salts in TMC-1-expressing CHO-K1 cells. **f**, 1 mM GdCl₃ blocked NaCl-induced inward currents in TMC-1-expressing CHO-K1 cells ($n = 11$).

(Fig. 3f, g), suggests that additional cell-type-specific ionotropic effectors are not required to express TMC-1-dependent ion channels. Moreover, TMC-1-dependent currents were neither voltage-sensitive nor significantly blocked by micromolar amiloride, suggesting that a DEG/ENaC or voltage-gated sodium channel is not involved (Supplementary Fig. 12c–e). These results are all consistent with TMC-1 encoding an ionotropic sensory receptor.

Thus, TMC-1 is a putative ion channel required for salt sensation in *C. elegans*, and meets several critical criteria expected of an authentic salt sensor. First, heterologously expressed TMC-1 forms salt-activated channels that respond specifically to extracellular sodium. Thus, external salt alters the properties of TMC-1 *in vitro* in a manner consistent with the requirements for *in vivo* chemosensation. Second, the ASH neurons of *tmc-1* mutants are strongly defective in responses to sodium, but respond normally to other stimuli including hyperosmolarity and chemical repellents. Thus, TMC-1 is specifically required *in vivo* for neuronal responses to salt. Finally, *tmc-1* mutants show strong, modality-specific defects in chemosensory behaviour with a focus in the ASH neurons. Therefore, the neuronal responses that require *tmc-1* are clearly linked to sensory behaviour. Taken together, these results argue strongly that TMC-1 is a salt sensor in *C. elegans* chemosensory neurons and may comprise a salt-activated channel.

Although much is known about the molecular mechanisms of sweet, sour, umami and bitter taste, the molecular basis of salt taste is poorly understood. In *C. elegans*, detection of salt concentration changes by neurons mediating chemosensory attraction requires a cGMP-gated channel^{15,19,20}; however, the receptors that might link this channel's activity to extracellular salt concentration are unknown. ASH responses to salt, as well as chemical, osmotic and mechanical stimuli, also require the TRPV channel OSM-9 (ref. 21), which may function as a nonspecific amplifier rather than a receptor²². In mammals and

insects, low-concentration salt taste requires the sodium-selective ENaC channel^{23,24}, whereas mammalian high-concentration salt taste may involve TRPV1 (ref. 25). However, on their own these channels, although sodium-permeable, are inhibited by external sodium^{26,27}. In contrast, the Hill coefficient of TMC-1-dependent channels indicates that they are not only sodium permeable but also sodium-activated²⁸, properties optimally suited for a salt chemosensor.

TMC proteins have been previously implicated in processes of sensory transduction, in particular hearing, but their mechanistic role in these processes has been unclear^{5,6}. Our results indicate that *C. elegans* TMC-1 may comprise an ion channel gated by a sensory stimulus, raising the possibility that other TMC proteins may constitute channels as well. We speculate that TMC proteins, including but not limited to mammalian TMC1, may function generally as ionotropic sensory receptors, although potentially gated by stimuli other than sodium. Because mammals contain several TMC proteins of unknown function, it is possible that one or more of these may play a role in sensory transduction processes such as touch or salt taste. With the recent finding that mammalian TMC1 and TMC2 are required for cochlear hair-cell mechanotransduction⁶, these molecules must be considered strong candidates for the mammalian hair-cell mechanotransducer.

METHODS SUMMARY

Strains and culture. All strains were grown using standard protocols at 20 °C on nematode growth medium (NGM) plates with OP50 bacteria as a food source. The *tmc-1* mutant strain was from the Caenorhabditis Genetics Center, and was backcrossed six times before use in experiments or crossing into other backgrounds. A complete list of strains is given in the Supplementary Information.

Confocal microscopy and dye-filling of neurons. Confocal imaging was done using a Zeiss LSM510 Meta confocal microscope with a $\times 60$ objective. Strains expressing both *tmc-1* and ASH-specific reporters were generated by standard genetic crosses.

Behavioural assays. For all the behavioural assays, we picked fourth larval stage animals and assayed them after 20 h growth at 20 °C. The repellent drop test was performed on unseeded NGM plates essentially as described previously⁸. We assayed attraction to sodium gluconate in gradient assays essentially as described previously²⁹. Details are in the Methods and Supplementary Information.

Calcium imaging of ASH and ASK neurons. Optical recordings were performed on a Zeiss Axioskop 2 upright compound microscope equipped with a Dual View beam splitter and a Uniblitz Shutter essentially as described previously³⁰.

tmc-1 mammalian transfection. Mammalian cells were seeded onto 12-mm glass coverslips and were transfected transiently with 800 ng of plasmids containing *tmc-1* plasmid DNA plus GFP using TransIT-LT1 (Mirus Bio). Cells were recorded 12–36 h later. Because Chinese hamster ovary (CHO-K1) showed the best efficiency (76% population of GFP-positive CHO-K1 cells were responsive versus 42% for HEK293T and 50% for HeLa cells), most of the experiments were conducted with CHO-K1 cells, unless otherwise described.

Electrophysiology. Whole-cell patch-clamp experiments were performed using a Multiclamp 700B amplifier (Molecular Devices). Details are provided in the Methods.

Full Methods and any associated references are available in the online version of the paper.

Received 16 March; accepted 18 December 2012.

Published online 30 January 2013.

- Kurima, K., Yang, Y., Sorber, K. & Griffith, A. J. Characterization of the transmembrane channel-like (TMC) gene family: functional clues from hearing loss and epidermodysplasia verruciformis. *Genomics* **82**, 300–308 (2003).
- Keresztes, G., Mutai, H. & Heller, S. TMC and EVER genes belong to a larger novel family, the TMC gene family encoding transmembrane proteins. *BMC Genomics* **4**, 24 (2003).
- Kurima, K. *et al.* Dominant and recessive deafness caused by mutations of a novel gene, *TMC1*, required for cochlear hair-cell function. *Nature Genet.* **30**, 277–284 (2002).
- Vreugde, S. *et al.* Beethoven, a mouse model for dominant, progressive hearing loss DFNA36. *Nature Genet.* **30**, 257–258 (2002).
- Marcotti, W., Erven, A., Johnson, S. L., Steel, K. P. & Kros, C. J. *Tmc1* is necessary for normal functional maturation and survival of inner and outer hair cells in the mouse cochlea. *J. Physiol. (Lond.)* **574**, 677–698 (2006).
- Kawashima, Y. *et al.* Mechanotransduction in mouse inner ear hair cells requires transmembrane channel-like genes. *J. Clin. Invest.* **121**, 4796–4809 (2011).
- Smith, C. J. *et al.* Time-lapse imaging and cell-specific expression profiling reveal dynamic branching and molecular determinants of a multi-dendritic nociceptor in *C. elegans*. *Dev. Biol.* **345**, 18–33 (2010).
- Hilliard, M. A., Bargmann, C. I. & Bazzicalupo, P. *C. elegans* responds to chemical repellents by integrating sensory inputs from the head and the tail. *Curr. Biol.* **12**, 730–734 (2002).
- Kaplan, J. M. & Horvitz, H. R. A dual mechanosensory and chemosensory neuron in *Caenorhabditis elegans*. *Proc. Natl Acad. Sci. USA* **90**, 2227–2231 (1993).
- Bargmann, C. I., Thomas, J. H. & Horvitz, H. R. Chemosensory cell function in the behavior and development of *Caenorhabditis elegans*. *Cold Spring Harb. Symp. Quant. Biol.* **55**, 529–538 (1990).
- Sambongi, Y. *et al.* Sensing of cadmium and copper ions by externally exposed ADL, ASE, and ASH neurons elicits avoidance response in *Caenorhabditis elegans*. *Neuroreport* **10**, 753–757 (1999).
- Hilliard, M. A., Bergamasco, C., Arbucci, S., Plasterk, R. H. & Bazzicalupo, P. Worms taste bitter: ASH neurons, QUL-1, GPA-3 and ODR-3 mediate quinine avoidance in *Caenorhabditis elegans*. *EMBO J.* **23**, 1101–1111 (2004).
- Hukema, R. K., Rademakers, S., Dekkers, M. P., Burghoorn, J. & Jansen, G. Antagonistic sensory cues generate gustatory plasticity in *Caenorhabditis elegans*. *EMBO J.* **25**, 312–322 (2006).
- Hilliard, M. A. *et al.* *In vivo* imaging of *C. elegans* ASH neurons: cellular response and adaptation to chemical repellents. *EMBO J.* **24**, 63–72 (2005).
- Suzuki, H. *et al.* Functional asymmetry in *Caenorhabditis elegans* taste neurons and its computational role in chemotaxis. *Nature* **454**, 114–117 (2008).
- Wakabayashi, T. *et al.* *In vivo* calcium imaging of OFF-responding ASK chemosensory neurons in *C. elegans*. *Biochim. Biophys. Acta* **1790**, 765–769 (2009).
- Jang, H. *et al.* Neuromodulatory state and sex specify alternative behaviors through antagonistic synaptic pathways in *C. elegans*. *Neuron* **75**, 585–592 (2012).
- Grimm, C., Kraft, R., Sauerbruch, S., Schultz, G. & Harteneck, C. Molecular and functional characterization of the melastatin-related cation channel TRPM3. *J. Biol. Chem.* **278**, 21493–21501 (2003).
- Coburn, C. M. & Bargmann, C. I. A putative cyclic nucleotide-gated channel is required for sensory development and function in *C. elegans*. *Neuron* **17**, 695–706 (1996).
- Komatsu, H., Mori, I., Rhee, J. S., Akaike, N. & Ohshima, Y. Mutations in a cyclic nucleotide-gated channel lead to abnormal thermosensation and chemosensation in *C. elegans*. *Neuron* **17**, 707–718 (1996).
- Colbert, H. A., Smith, T. L. & Bargmann, C. I. OSM-9, a novel protein with structural similarity to channels, is required for olfaction, mechanosensation, and olfactory adaptation in *C. elegans*. *J. Neurosci.* **17**, 8259–8269 (1997).
- Geffeney, S. L. *et al.* DEG/ENAC but not TRP channels are the major mechanoelectrical transduction channels in a *C. elegans* nociceptor. *Neuron* **71**, 845–857 (2011).
- Liu, L. *et al.* Contribution of *Drosophila* DEG/ENAC genes to salt taste. *Neuron* **39**, 133–146 (2003).
- Chandrasekar, J. *et al.* The cells and peripheral representation of sodium taste in mice. *Nature* **464**, 297–301 (2010).
- Lyall, V. *et al.* The mammalian amiloride-insensitive non-specific salt taste receptor is a vanilloid receptor-1 variant. *J. Physiol. (Lond.)* **558**, 147–159 (2004).
- Ohta, T., Imagawa, T. & Ito, S. Novel gating and sensitizing mechanism of capsaicin receptor (TRPV1): tonic inhibitory regulation of extracellular sodium through the external protonation sites on TRPV1. *J. Biol. Chem.* **283**, 9377–9387 (2008).
- Chraïbi, A. & Horisberger, J. D. Na self inhibition of human epithelial Na channel: temperature dependence and effect of extracellular proteases. *J. Gen. Physiol.* **120**, 133–145 (2002).
- Zhou, Y. & MacKinnon, R. Ion binding affinity in the cavity of the KcsA potassium channel. *Biochemistry* **43**, 4978–4982 (2004).
- Pocock, R. & Hobert, O. Hypoxia activates a latent circuit for processing gustatory information in *C. elegans*. *Nature Neurosci.* **13**, 610–614 (2010).
- Ezcurra, M., Tanizawa, Y., Swoboda, P. & Schafer, W. R. Food sensitizes *C. elegans* avoidance behaviours through acute dopamine signalling. *EMBO J.* **30**, 1110–1122 (2011).

Supplementary Information is available in the online version of the paper.

Acknowledgements We thank the *Caenorhabditis* Genetics Center and M. de Bono for strains, and A. Patapoutian, J. R. Holt, J. Hao, B. Zhao, D. Miller and R. Branicky for suggestions and comments on the manuscript. This research was supported by the Medical Research Council (W.R.S.) and grants to S.W.H. from the National Research Foundation of Korea (2012000540) and Korea Health technology R&D Project of Ministry of Health & Welfare (A111373).

Author Contributions M.C. and S.B. carried out the experiments and analysed the data. All the authors planned experiments and interpreted results. S.W.H. and W.R.S. supervised the research. W.R.S. wrote the paper with contributions from M.C. and S.W.H.

Author Information Reprints and permissions information is available at www.nature.com/reprints. The authors declare no competing financial interests. Readers are welcome to comment on the online version of the paper. Correspondence and requests for materials should be addressed to S.W.H. (sunhwang@korea.ac.kr) or W.R.S. (wschafer@mrc-lmb.cam.ac.uk).

METHODS

Drop test assays. The repellent drop test was performed on unseeded NGM plates essentially as described previously⁸. Animals (10 to 30) were picked from a culture plate and placed on a plate without food for a few seconds to avoid transferring food to the assay plates. The animals were then placed on the assay plate, allowed to settle for 10 min, then assayed using a capillary to deliver the stimulus. A drop of the stimulus solution was delivered near the tail of a moving animal; the response of a single animal to each drop delivered was recorded as either positive (when the animal stops moving forwards and reverses) or negative (when the animal continues moving forward) for escape behaviour. To consider the response positive, the avoidance reaction must be observed within a 4 s interval following the stimulation. Each animal was tested only once. All salts were dissolved in 1 mM MgSO₄, 1 mM CaCl₂ and 5 mM KPO₄. CuCl₂ was dissolved in M13 buffer. The animals lacking the ASH, ASI and PVQ neurons expressed the *egl-1* cell death gene under the control of the *sra-6* promoter (see strain list in Supplementary Methods). Statistical comparison between two strains was done using the *t*-test. Where more than one comparison was made, ANOVA with Bonferroni correction for multiple comparisons was used instead. Chemosensory attraction assays²⁹ are described in Supplementary Information.

Calcium imaging of ASH and ASK neurons. Filter-dichroic pairs used were excitation, 400–440 nm; excitation dichroic, 455 nm; CFP emission, 465–495 nm; emission dichroic, 505 nm; YFP emission, 520–550 nm. Individual adult worms (~24 h past L4 stage) were glued with Dermabond 2-octyl cyanoacrylate glue to pads composed of 2% agarose in extracellular saline (5 mM KCl, 1 mM CaCl₂, 5 mM MgCl₂, 20 mM D-glucose and 10 mM HEPES buffer, pH 7.2). Worms used for calcium imaging had similar levels of cameleon expression in sensory neurons as inferred from initial fluorescence intensity. The animals were placed under the microscope in a perfusion chamber (RC-26GLP, Warner Instruments) under constant flow rate (0.4 ml min⁻¹) of neuronal buffer using a perfusion pencil (AutoMate). Outflow was regulated using a peristaltic pump (Econo Pump, Biorad). Repellents were delivered using the perfusion pencil and manually controlled valves³⁰. Solutions contained the indicated amount of salt and in addition 1 mM MgSO₄, 1 mM CaCl₂ and 5 mM KPO₄. For salt experiments, the osmolarity of the pre and post stimulus solution was adjusted to match that of

the stimulus using sucrose as described¹⁵; similar results were obtained when sucrose was not included in the buffer solution (data not shown). The pH was adjusted to pH 7. Glycerol was dissolved in M13 buffer to a final concentration of 1 M or 0.5 M. Additional details of these experiments are given in the Supplementary Information.

Electrophysiology. Unless otherwise specified, the internal solution consisted of 140 mM CsCl, 5 mM EGTA, 10 mM HEPES, 2.0 mM MgATP, 0.2 mM NaGTP titrated to pH 7.2 with CsOH. For the native Cl⁻ condition, 20 KCl mM plus 120 mM potassium gluconate was used instead of 140 mM CsCl. The external bath solution except for Fig. 4e cation permeability experiments consisted of 140 mM NaCl, 5 mM KCl, 2 mM CaCl₂, 2 mM MgCl₂, 10 mM HEPES, titrated to pH 7.4 with NaOH. Responses were sampled at 20 kHz and calculated using Clampfit 10.3 software (Molecular Devices). To minimize junction potentials, we used a 3 M KCl agar salt bridge as the reference electrode. To generate the curve in Fig. 4b, the sodium concentration in the external buffer was changed to the indicated concentration; concentrations of other solutes were unchanged. The curve was fitted by the Hill equation ($I = I_{\max}/(1 + (EC_{50}/[NaCl])^n)$); *I*, current response; *I*_{max}, maximum current response from a given cell).

Cation permeabilities of TMC-1 were determined by current–voltage relationship experiments by using the following cationic solutions. The internal solution consisted of 150 mM CsCl and 10 mM HEPES (pH 7.3 with CsOH). The monovalent external solutions consisted of 300 mM NaCl (or 150 mM KCl or 150 mM LiCl for a measurement of K⁺ or Li⁺ permeability respectively) and 10 mM HEPES. The divalent external solutions consisted of 100 mM CaCl₂ (or 100 mM MgCl₂ for a measurement of Mg²⁺ permeability) and 10 mM HEPES. Reversal potentials were obtained from the current–voltage curves under an 800 ms voltage ramp protocol ranging from −80 mV to +80 mV at a holding potential of −60 mV. When the basal currents of a given cell were small, averaged current–voltage curves from multiple ramp trials on a same cell were used to obtain the reversal potential. To completely wash external NaCl before other cation applications, 150 mM CsCl plus 10 mM HEPES were used. The ratio of cation permeability (P_X/P_{Cs}) was determined for each test cation X from the reversal potential of the basal current (see Supplementary Information for more details).

Negligible immunogenicity of terminally differentiated cells derived from induced pluripotent or embryonic stem cells

Ryoko Araki^{1,2}, Masahiro Uda¹, Yuko Hoki¹, Misato Sunayama¹, Miki Nakamura¹, Shunsuke Ando¹, Mayumi Sugiura¹, Hisashi Ideno^{1,3}, Akemi Shimada³, Akira Nifuji^{1,3} & Masumi Abe¹

The advantages of using induced pluripotent stem cells (iPSCs) instead of embryonic stem (ES) cells in regenerative medicine centre around circumventing concerns about the ethics of using ES cells and the likelihood of immune rejection of ES-cell-derived tissues^{1,2}. However, partial reprogramming and genetic instabilities in iPSCs^{3–6} could elicit immune responses in transplant recipients even when iPSC-derived differentiated cells are transplanted. iPSCs are first differentiated into specific types of cells *in vitro* for subsequent transplantation. Although model transplantation experiments have been conducted using various iPSC-derived differentiated tissues^{7–10} and immune rejections have not been observed, careful investigation of the immunogenicity of iPSC-derived tissue is becoming increasingly critical, especially as this has not been the focus of most studies done so far. A recent study reported immunogenicity of iPSC- but not ES-cell-derived teratomas¹¹ and implicated several causative genes. Nevertheless, some controversy has arisen regarding these findings¹². Here we examine the immunogenicity of differentiated skin and bone marrow tissues derived from mouse iPSCs. To ensure optimal comparison of iPSCs and ES cells, we established ten integration-free iPSC and seven ES-cell lines using an inbred mouse strain, C57BL/6. We observed no differences in the rate of success of transplantation when skin and bone marrow cells derived from iPSCs were compared with ES-cell-derived tissues. Moreover, we observed limited or no immune responses, including T-cell infiltration, for tissues derived from either iPSCs or ES cells, and no increase in the expression of the immunogenicity-causing *Zg16* and *Hormad1* genes in regressing skin and teratoma tissues. Our findings suggest limited immunogenicity of transplanted cells differentiated from iPSCs and ES cells.

There are three major concerns about the adequacy of the design and conclusions of a previous study that reported immunogenicity of iPSC- but not ES-cell-derived teratomas¹¹. The first is that the immunogenicity of iPSCs was assessed by teratoma formation. Consistent with the focus on tumour immunity rather than transplant immunity, the causative gene identified in the regressing teratomas was tumour related¹³. Second, only a single ES-cell clone was included in the comparison of iPSC- and ES-cell-related immunogenicity. Third, the developmental ability of the iPSC and ES-cell lines used may have been compromised. Given that partial genome reprogramming can elicit immune responses and cause considerable variation among iPSC clones, the developmental abilities of iPSC and ES-cell clones should always be tested before such analyses. To evaluate better the immunogenicity of iPSCs, we conducted transplantation experiments involving terminally differentiated cells derived from iPSCs. Our experiments involved multiple ES-cell and iPSC lines (Supplementary Fig. 1a) that were established from an inbred mouse strain, C57BL/6, and were confirmed to have strong developmental capacities. We generated iPSCs by expressing plasmid-borne *Oct4* (also known as *Pou5f1*),

Sox2, *Klf4* and *Myc* genes¹⁴, and then selected clones that were free from genome-integration events (Supplementary Fig. 1b)¹⁵, as iPSCs with integrated transgenes elicit marked immune responses¹¹. Similar doubling times were measured for all the cell lines (Supplementary Fig. 1c). Germline transmission capability was confirmed for eight of ten iPSC clones and for six of seven ES-cell clones (Supplementary Table 1).

We used seven iPSC and five ES-cell lines in teratoma formation tests to obtain more conclusive results (Supplementary Fig. 2a). The tests in C57BL/6 wild-type mice were replicated a total of ten times for each of the twelve clones. We observed teratomas containing three germ layers¹⁵ at a high incidence rate for both types of pluripotent stem cells, with no statistical difference between iPSCs and ES cells (Fig. 1a). Next, we used immunohistochemical staining to investigate the infiltration of the teratomas by T cells (Supplementary Fig. 2b). We did not observe any T cells in most sections, although fewer than two T cells were detected in some sections. Although slight differences were observed among the cell lines, the profiles between iPSCs and ES cells were quite similar overall (Fig. 1b), and no statistically significant difference between iPSC- and ES-cell-derived teratomas was detectable (Fig. 1c).

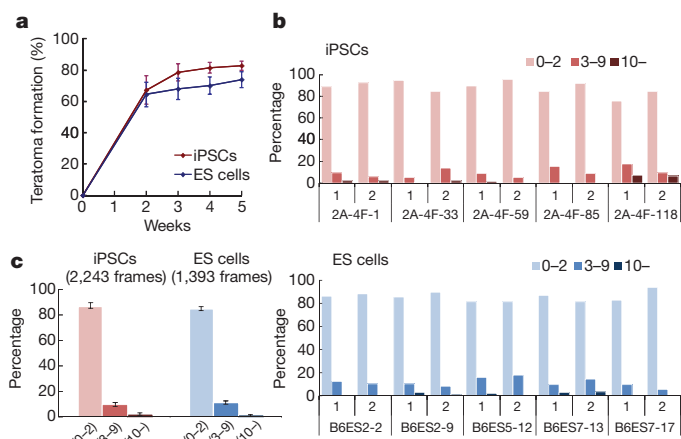


Figure 1 | Teratoma formation by iPSCs and ES cells. **a**, Time course of the appearance of teratomas after injection. Error bars show standard error of the mean (s.e.m.). iPSCs, $n = 7$; ES cells, $n = 5$. **b**, Frequency of T cells in each teratoma. Ten teratomas from iPSCs (red) and ten from ES cells (blue), two for each of five clones of both cell types, were stained with anti-CD3 antibody. More than 50 frames (each $0.382 \text{ mm} \times 0.507 \text{ mm}$) were randomly chosen for each teratoma. The numbers of T cells detected were categorized into three groups: 0–2, 3–9 or ≥ 10 T cells per frame. **c**, Summary of the data shown in **b** and the total number of frames investigated. Error bars show s.e.m. ($n = 10$).

¹Transcriptome Research Group, National Institute of Radiological Sciences, Chiba 263-8555, Japan. ²PRESTO, Japan Science and Technology Agency (JST), Kawaguchi 332-0012, Japan. ³Department of Pharmacology, School of Dental Medicine, Tsurumi University, Yokohama 230-8501, Japan.

Focusing on teratoma formation is not suitable for assessing the immunogenic responses of relevance to regenerative medicine. Given that teratomas are a type of tumour, it is not surprising that they elicit immunological reactions in transplant recipients. Indeed, in a further teratoma formation test using severe combined immunodeficiency (SCID) mice¹⁶ although, again, no difference was observed between iPSCs and ES cells, a similar frequency but a slight increase in size compared with wild-type mice was shown, indicating that certain immune systems respond to the teratomas derived from these two types of pluripotent stem cells (Supplementary Fig. 3). Hence, although we did not detect any significant T-cell infiltrations in various teratomas derived from either iPSCs or ES cells in our assay, we cannot rule out the possibility that substantial immune responses can be elicited under certain situations during teratoma formation in both types of pluripotent stem cells^{11,17}. On the other hand, considering that iPSCs themselves would not be implanted, and that the stem cells would first be converted into specific types of differentiated cells before transplantation, the immunogenicity of terminally differentiated cells derived from iPSCs is critically relevant to the long-term prospects of their use in regenerative medicine. We therefore prepared dermal and bone marrow tissues from the highly chimaeric mice developed from iPSCs or ES cells for subsequent transplantation experiments. These tissues were selected on the basis of the central roles they have in the immune system.

For each type of terminally differentiated cell, we initially set up our assay system by using a green fluorescent protein (GFP)-labelled iPSC clone, because it allowed us to monitor the donor cells after transplantation, even in a single-cell manner. We used a genome-integration-free iPSC clone, 2A-3F-EGFPtg-4, which was established from a C57BL/6-Tg(CAG-EGFP) mouse¹⁸ with *Oct4*, *Sox2* and *Klf4* genes; using Trichostatin A, we demonstrated that this iPSC line could achieve pluripotency¹⁹. On the basis of the investigation using the 2A-3F-EGFPtg-4 clone, we examined various non-labelled lines of iPSCs and ES cells.

We first attempted to establish a transplantation assay system for epidermal tissue based on a previously reported transplantation system²⁰. We aggregated the GFP-positive iPSC clone 2A-3F-EGFPtg-4 with GFP-negative embryos to develop GFP-positive highly chimaeric

mice. Skin samples from the tails of the chimaeric mice were prepared, and then transplanted onto the backs of syngeneic GFP-negative C57BL/6 mice and allogeneic Balb/c mice (Fig. 2a). All of the six GFP-positive transplanted grafts generated could be sustained over a 10-month period. In contrast, in the control experiment, the transplanted grafts on the Balb/c mice remained physically attached to the backs of recipient mice for over a week but not as long as 2 weeks after transplantation (Fig. 2a). This system thus provides a rapid and highly efficient way of assaying the immunogenicity of epithelial tissues.

Using this same assay system, we subsequently examined four additional iPSC clones (2A-4F-1, -33, -60 and -100) and five ES-cell clones (B6ES2-2, B6ES2-9, B6ES5-1, B6ES7-13 and B6ES7-15). Three mouse strains—C57BL/6, C57BL/6-Tg(CAG-EGFP) and Balb/c—were used as recipients (Supplementary Fig. 4a). Because all of these cell lines are GFP negative, each clone was aggregated with GFP-positive embryos to ensure that the skin tissues of the chimaeric mice used for subsequent transplantation tests did not contain cells other than those derived from either an iPSC or an ES cell (Fig. 2b). Another motivation for using GFP-positive embryos for the aggregation step was to confer tolerance to the GFP molecules in the recipient mice used to analyse immune responses, such as T-cell infiltration (Fig. 2b, broken circle), as GFP molecules can elicit immune responses²¹. Between 4 and 12 replicate transplantations were conducted for each clone, and graft survival was measured 2 months after transplantation. Graft survival rates were $98.3 \pm 1.7\%$ and $92.5 \pm 5.0\%$ for iPSCs and ES cells, respectively (Fig. 2c and Supplementary Fig. 4). In contrast, no long-term survival was noted for grafts derived from Balb/c mice. These data suggest that iPSCs are not demonstrably more immunogenic than ES cells.

To analyse immunogenicity further, we used confocal microscopy to investigate the invasion of the grafts by GFP-positive cells produced by the recipient C57BL/6-Tg(CAG-EGFP) mice. In the control experiment, which involved transplantation of Balb/c tail skin, a large number of GFP-positive cells were observed within the grafts (Supplementary Fig. 5a). Moreover, as expected, subsequent histochemical staining with anti-CD3 antibody revealed the presence of CD3-positive cells within the GFP-positive population (Supplementary Fig. 6a). As a result, very few GFP-positive cells were detected around or within the transplanted tissues in any iPSC- or ES-cell-derived tissue sections 2 months after transplantation (Supplementary Figs 5b, c and 6b). However, we note the possibility that our assay system may have missed some lymphocytes with low GFP expression levels. Nevertheless, if such T cells existed, the number that invaded the graft must have been quite small, because flow cytometry analysis did not detect GFP-negative T cells in the whole blood of C57BL/6-Tg(CAG-EGFP) recipients (Supplementary Fig. 7c).

The first step in the assessment of the immunogenicity of bone marrow tissues involved mimicking the bone marrow transplantation treatment. We transplanted bone marrow from mice derived from the GFP-positive iPSC clone 2A-3F-EGFPtg-4 into C57BL/6 wild-type mice that had been irradiated with a lethal (9.5 Gy) dose of X-rays (Fig. 3a). Flow cytometry analysis demonstrated the presence of GFP-positive cells 5 months later (Fig. 3a, left, and Supplementary Fig. 7a). We also detected B lymphocytes, T lymphocytes and granulocytes in the GFP-positive cell population 4 months after transplantation (Fig. 3d, top) in each of the four mice that received transplants. This indicates that both short- and long-term haematopoietic stem cells were fixed and maintained. No major phenotypical or behavioural abnormalities were observed in any of these mice more than 5 months after transplantation, although some skin ulcers were observed in one recipient, IR-1 (Fig. 3a, left). As anticipated, bone marrow derived from the ES-cell line B6ES5-1 also reconstituted the bone marrow of each of four recipient mice after they received a lethal dose of irradiation (Fig. 3b, c).

It is noteworthy that although almost all B lymphocytes, T lymphocytes and granulocytes were replaced with iPSC-derived cells (Fig. 3d, top), recipient-derived cells still remained in all transplanted mice

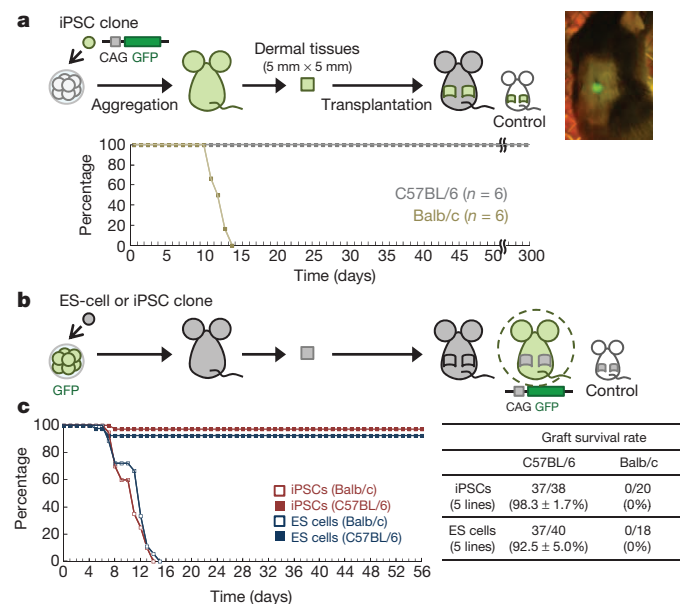


Figure 2 | Skin transplantation. **a**, Schematic diagram of the method for skin transplantation using a GFP-positive iPSC clone and time course of graft survival. Right, a mouse transplanted with GFP-positive skin at one month post transplantation. **b**, Schema of the skin transplantation assay for GFP-negative iPSCs and ES cells. **c**, Summary of the time course for graft survival.

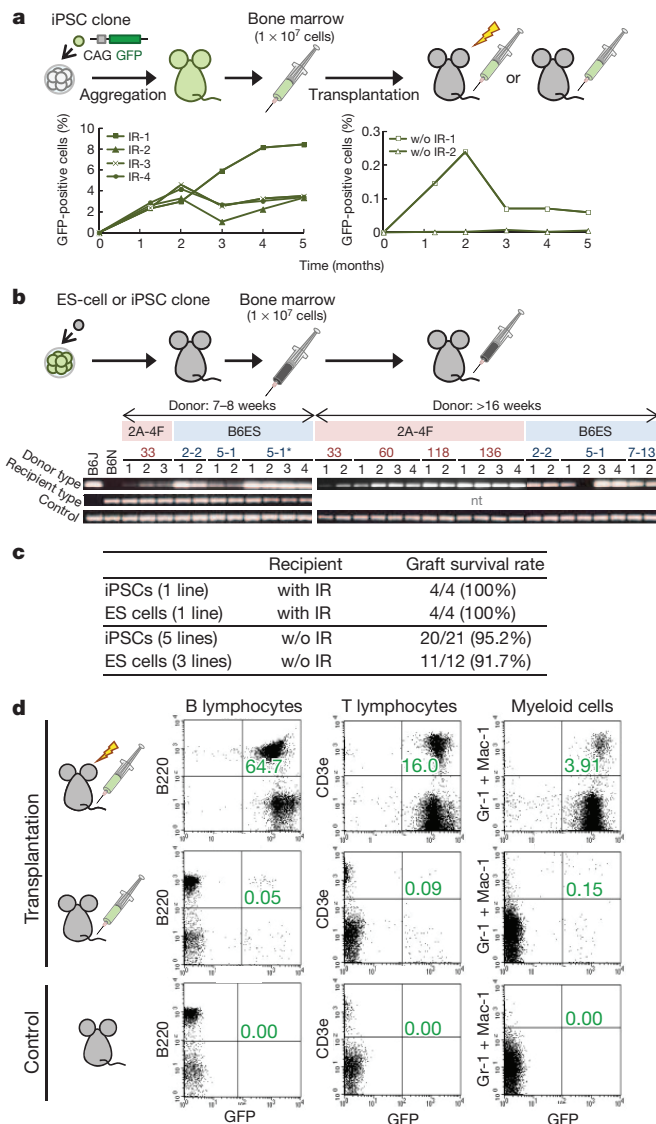


Figure 3 | Bone marrow transplantation. **a**, Schematic diagram of the bone marrow transplantation experiments using 2A-3F-EGFPtg-4 iPSCs and the survival of donor bone marrow cells. Time-course analysis of the survival of GFP-positive cells in the irradiated (left) and non-irradiated recipients (right) is shown. The percentage of GFP-positive cells to whole blood cells was measured by flow cytometry over 5 months (Supplementary Fig. 7a). IR-1, -2, and so on, indicate irradiated recipient 1, 2, and so on. w/o, without. **b**, Schematic diagram of the bone marrow transplantation experiments using non-labelled iPSCs and non-labelled ES cells, and of PCR assessment of the engraftment of donor-derived bone marrow cells. The existence of donor-derived bone marrow cells over 4 months was investigated by PCR using genomic DNA prepared from peripheral blood cells harvested at 4 months after transplantation. Asterisk indicates the use of irradiated recipients. **c**, Summary of the incidence of graft survival. **d**, Long-term reconstitution of bone marrow by 2A-3F-EGFPtg-4 iPSC-derived bone marrow cells. Peripheral blood cells at 4 months after transplantation were analysed using flow cytometry. The results of irradiation recipient IR-4 (top) and recipient without (w/o) irradiation IR-1 (middle), which are described in **a**, are shown as a representative case. The C57BL/6 mouse is shown as a control (bottom).

(Supplementary Fig. 7b). Importantly, the coexistence of donor- and recipient-derived bone marrow cells in the recipient mice more than 5 months from the time of transplantation is strongly suggestive of a limited immunogenicity of iPSC-derived bone marrow cells. This is because substantial immune responses must occur during the fixation and maintenance of iPSC-derived cells if the bone marrow cells derived from iPSCs are to show even a low level of immunogenicity.

Thus, these experiments indicate that iPSC-derived bone marrow cells have the same potential as ES-cell-derived bone marrow cells to reconstitute the bone marrow system, and indicate the low immunogenicity of the bone marrow cells derived from iPSCs and ES cells. These results with X-ray irradiation are consistent with those of a previous study that showed similar repopulation by iPSC- and ES-cell-derived haematopoietic progenitors⁷.

To assess whether low levels of immunogenicity had been overlooked, we next conducted transplantations under more severe conditions. This involved transplanting iPSC-derived bone marrow cells into wild-type C57BL/6 mice without any prior irradiation. Because the immune activity of the bone marrow in wild-type recipient mice must be normal, this enables better assessment of transplantation immunity. We injected 1×10^7 bone marrow cells from chimaeric mice developed using the iPSC line 2A-3F-EGFPtg-4 into the tail veins of recipient wild-type mice, and analysed peripheral blood samples at 1-month intervals for 5 months. Flow cytometry and semi-quantitative polymerase chain reaction (PCR) analysis indicated that donor cells derived from iPSCs were sustained over 5 months even after transplantation into non-irradiated mice (Fig. 3a, right, and Supplementary Fig. 7a). This indicates successful engraftment of both short- and long-term haematopoietic stem cells. In a comparison with the control, non-transplanted C57BL/6 bone marrow using flow cytometry, B lymphocytes, T lymphocytes and granulocytes derived from the donor cells were detected, although the number of GFP-positive cells was small (Fig. 3d). We also examined bone marrow cells prepared 6 months after transplantation to confirm the presence of GFP-positive lymphocytes and granulocytes (Supplementary Fig. 7d).

For the various non-labelled iPSCs and ES cells, similar bone marrow transplantations using non-irradiated recipient mice were performed (Fig. 3b, c and Supplementary Fig. 9a). Four iPSC and three ES-cell clones were also examined, and an assessment was done at 4 months after transplantation using genomic PCR, which enables discrimination between the genome of the donor and that of the recipient (Supplementary Fig. 8). In addition, we prepared bone marrow from mice of various ages (5–54 weeks). The results showed that 20 of 21 challenges involving bone marrow derived from any one of the five iPSC lines, and 11 of 12 challenges involving bone marrow derived from any one of the three ES-cell lines, were successful. Notably, the bone marrows of 1-year old chimaeric mice generated from either one of the two iPSC lines, 2A-4F-118 and 2A-4F-136, or from an ES-cell line, B6ES7-13, were successfully engrafted (Supplementary Fig. 9a). Moreover, semi-quantitative PCR showed donor-origin cells in B-lymphocyte, T-lymphocyte and granulocyte fractions prepared from mice developed using the non-labelled pluripotent stem cell lines 2A-4F-60 and B6ES5-1 (Supplementary Fig. 9b). These data indicate that iPSC-derived haematopoietic stem cells can be engrafted and sustained in recipients even under conditions of normal immunocompetence. Although seven-to-twelve months have now passed since the time of implantation, we have not observed abnormalities in any of the recipient mice.

The *Zg16* and *Hormad1* genes have been causally linked to the immunogenicity of iPSC-derived teratomas, and both genes are expressed at elevated levels in regressing teratomas¹¹. We also observed regression in both transplanted skin grafts and teratomas in these experiments, although no statistically significant difference was apparent between iPSC- and ES-cell-derived tissues (Supplementary Figs 10 and 11). Investigation of the expression of *Zg16* and *Hormad1* indicated no expression of *Zg16* in non-shrinking or shrinking grafts in dermal tissues, and a low level of expression of these genes in teratomas. A low level (less than 100-fold lower expression than that seen in the testis) of *Hormad1* expression was also observed in both transplanted grafts and teratomas. However, neither gene was expressed at an elevated level in the shrinking tissues. The expression profiles were quite similar between iPSC and ES-cell derivatives (Fig. 4a, b). Thus, the expression profiles of both genes were similar

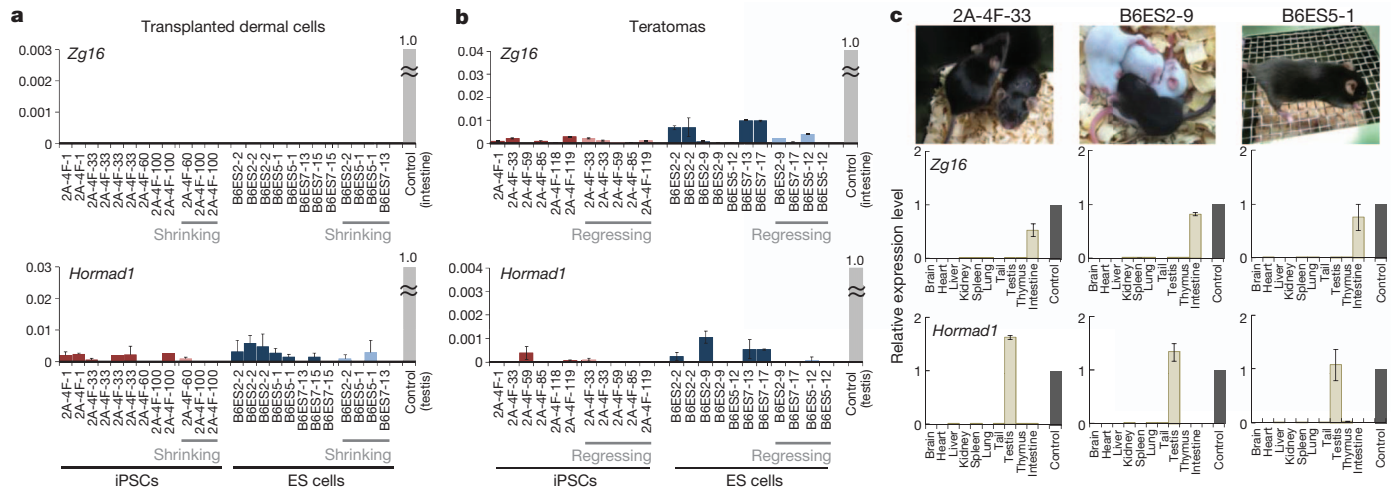


Figure 4 | Expression of *Zg16* and *Hormad1* genes in various tissues generated from iPSCs and ES cells. **a**, Expression of the *Zg16* and *Hormad1* genes in grafted skin 2 months after transplantation. **b**, Expression of the *Zg16* and *Hormad1* genes in the teratomas at 4 or 5 weeks after injection (Supplementary Fig. 11b). **c**, Expression of the *Zg16* and *Hormad1* genes in various tissues of iPSC tetraploid complementation chimaeric mice. Ten types

of tissues were prepared from adult, 2–8-month old, tetraploid-complementation chimaeric mice derived from iPSC clone 2A-4F-33 or from the ES-cell clones B6ES2-9 and B6ES5-1, and then subjected to semi-quantitative RNA analysis. The intestines and the testes of C57BL/6 wild-type mice were used as a control for *Zg16* and *Hormad1* gene expression, respectively. Error bars show standard deviation ($n = 2$).

in both non-regressing and regressing teratomas, and we could not confirm previous findings¹¹ that *Hormad1* is upregulated in regressing teratomas derived from the iPSC clone 2A-4F-33.

Finally, we examined whether *Zg16* and *Hormad1* are expressed at higher levels in the various differentiated tissues derived from iPSCs relative to differentiated cells derived from ES cells. Ten tissue types were prepared from the adult mice generated by tetraploid complementation^{22–24} with the iPSC line 2A-4F-33 and the ES-cell lines B6ES2-9 and B6ES5-1 for semi-quantitative expression analyses of the *Zg16* and *Hormad1* genes. The expression profiles of *Zg16* and *Hormad1* were indistinguishable between the three tissue panels derived from 2A-4F-33, B6ES2-9 and B6ES5-1 (Fig. 4c).

An important finding of this study is that the immunogenicity of iPSC-derived tissues is indistinguishable from that of ES-cell-derived tissues. Although all of the assays we performed demonstrated that the terminally differentiated cells developed from iPSCs elicit limited immune responses, it is not possible to exclude formally the possibility of immunogenicity, given the limitations of the experimental approaches at our disposal. Whether the immunogenicity of iPSCs is higher than that of ES cells therefore remains an important question. Addressing this issue effectively will require the analysis of substantial numbers of high-quality ES-cell lines, rather than relying on only a single ES-cell line as in a previous study¹¹. We have successfully established seven ES-cell lines derived from C57BL/6 mice and confirmed germline transmission for six of these (Supplementary Table 1). Our results using these ES cells contrast with previous data because the immunogenicities of iPSC- and ES-cell-derived tissues were indistinguishable when scored using all three immunogenicity assays tested—teratoma formation, skin transplantation and bone marrow transplantation. None of our data show meaningful differences between iPSCs and ES cells.

Our data may indicate that the differences between specific clones of iPSCs and ES cells are more crucial than the difference between iPSCs and ES cells *per se*. Indeed, we observed a variation among iPSC clones in another experiment involving three iPSC clones from which chimaeric mice exhibited low chimaerism and no germline transmission (Supplementary Fig. 12). We performed teratoma formation tests in each case followed by T-cell infiltration analysis. Intriguingly, several lines exhibited significant T-cell infiltration. Furthermore, considerable variations in T-cell infiltration were observed among teratomas generated even from identical cell lines, although the frequency was similar not only to that among the three

iPSC clones examined, but also to that of the lines of which fully developmental ability was confirmed. Our data may thus also indicate that the teratomas generated from the iPSCs for which developmental ability is not complete are prone to eliciting immune responses, and that this issue is crucial for the medical use of iPSCs. Because testing such as chimaera formation is not possible for human iPSCs, these findings underscore the need for careful discussion and longitudinal investigations of interclonal differences in iPSC and ES-cell lines^{25,26}, and the need to develop culture conditions that will achieve a pluripotent state^{27–29}. This is in addition to broader generalizations regarding the immunogenicities of the two cell types.

In this study, we used terminally differentiated cells of adult mice, which had been generated from either iPSCs or ES cells as donor cells, as our aim was to determine whether iPSC-derived differentiated cells are intrinsically immunogenic. In other words, we attempted to clarify whether iPSC-derived differentiated cells can be used as donor cells in the same way as ES cells when the complete *in vitro* differentiation of these stem cells became possible. In this regard it must be noted that our study does not directly contribute to resolving the possible immunogenicity of *in vitro* differentiated cells. Further investigations are needed to assess this issue and hence the actual clinical use of these pluripotent cells. Notably, we observed significant levels of T-cell infiltration when we used *in vitro* derived cells, cardiomyocytes, as donors (Supplementary Fig. 13).

We have demonstrated that the limited immunogenicity of iPSC-derived differentiated cells is indistinguishable from that of comparable ES-cell-derived cells. However, the possibility remains that even terminally differentiated cells derived from iPSCs might elicit some immune responses. For example, the genetic aberrations that have been demonstrated recently in iPSCs could account for their immunogenicity^{5,6}. However, considering the advantages of iPSCs compared with ES cells, such as the ease of direct establishment from patients without the same complex ethical considerations, the discussion surrounding the relative merits of using autologous iPSCs and autologous ES cells seems to be now less relevant. This might be further resolved by a direct comparison between autologous iPSCs and allogeneic and major histocompatibility complex (MHC)-matched ES cells¹².

METHODS SUMMARY

C57BL/6J Jms Slc and C57BL/6-Tg(CAG-EGFP)¹⁸ mice were used for iPSC and ES-cell generation. iPSCs were generated with pCX-OKS-2A and pCX-c-Myc

plasmids (Addgene) as described previously^{14,15}. We performed PCR analysis to confirm the absence of plasmid integration¹⁴ and established ES-cell lines as described previously³⁰. Established iPSC and ES-cell lines were evaluated on the basis of their morphologies, stem cell markers, neuploidy and pluripotency (Supplementary Fig. 1 and Supplementary Table 1). Skin and bone marrow were prepared from fully chimaeric adult male mice developed from either iPSCs or ES cells. The C57BL/6 and C57BL/6-Tg(CAG-EGFP) mouse strains were used as recipients.

Full Methods and any associated references are available in the online version of the paper.

Received 22 May; accepted 22 November 2012.

Published online 9 January 2013.

1. Takahashi, K. & Yamanaka, S. Induction of pluripotent stem cells from mouse embryonic and adult fibroblast cultures by defined factors. *Cell* **126**, 663–676 (2006).
2. Kiskinis, E. & Eggan, K. Progress toward the clinical application of patient-specific pluripotent stem cells. *J. Clin. Invest.* **120**, 51–59 (2010).
3. Polo, J. M. *et al.* Cell type of origin influences the molecular and functional properties of mouse induced pluripotent stem cells. *Nature Biotechnol.* **28**, 848–855 (2010).
4. Gore, A. *et al.* Somatic coding mutations in human induced pluripotent stem cells. *Nature* **471**, 63–67 (2011).
5. Puri, M. C. & Nagy, A. Concise review: embryonic stem cells versus induced pluripotent stem cells: the game is on. *Stem Cells* **30**, 10–14 (2012).
6. Martins-Taylor, K. & Xu, R. H. Concise review: genomic stability of human induced pluripotent stem cells. *Stem Cells* **30**, 22–27 (2012).
7. Hanna, J. *et al.* Treatment of sickle cell anemia mouse model with iPS cells generated from autologous skin. *Science* **318**, 1920–1923 (2007).
8. Wernig, M. *et al.* Neurons derived from reprogrammed fibroblasts functionally integrate into the fetal brain and improve symptoms of rats with Parkinson's disease. *Proc. Natl Acad. Sci. USA* **105**, 5856–5861 (2008).
9. Tsuji, O. *et al.* Therapeutic potential of appropriately evaluated safe-induced pluripotent stem cells for spinal cord injury. *Proc. Natl Acad. Sci. USA* **107**, 12704–12709 (2010).
10. Tucker, B. A. *et al.* Transplantation of adult mouse iPS cell-derived photoreceptor precursors restores retinal structure and function in degenerative mice. *PLoS ONE* **6**, e18992 (2011).
11. Zhao, T., Zhang, Z. N., Rong, Z. & Xu, Y. Immunogenicity of induced pluripotent stem cells. *Nature* **474**, 212–215 (2011).
12. Okita, K., Nagata, N. & Yamanaka, S. Immunogenicity of induced pluripotent stem cells. *Circ. Res.* **109**, 720–721 (2011).
13. Chen, Y. T. *et al.* Identification of CT46/HORMAD1, an immunogenic cancer/testis antigen encoding a putative meiosis-related protein. *Cancer Immun.* **5**, 9 (2005).
14. Okita, K., Nakagawa, M., Hyenjong, H., Ichisaka, T. & Yamanaka, S. Generation of mouse induced pluripotent stem cells without viral vectors. *Science* **322**, 949–953 (2008).
15. Jincho, Y. *et al.* Generation of genome integration-free induced pluripotent stem cells from fibroblasts of C57BL/6 mice without c-Myc transduction. *J. Biol. Chem.* **285**, 26384–26389 (2010).
16. Bosma, G. C., Custer, R. P. & Bosma, M. J. A severe combined immunodeficiency mutation in the mouse. *Nature* **301**, 527–530 (1983).
17. Dressel, R. *et al.* The tumorigenicity of mouse embryonic stem cells and *in vitro* differentiated neuronal cells is controlled by the recipients' immune response. *PLoS ONE* **3**, e2622 (2008).
18. Okabe, M., Ikawa, M., Kominami, K., Nakanishi, T. & Nishimune, Y. 'Green mice' as a source of ubiquitous green cells. *FEBS Lett.* **407**, 313–319 (1997).
19. Araki, R. *et al.* Crucial role of c-Myc in the generation of induced pluripotent stem cells. *Stem Cells* **29**, 1362–1370 (2011).
20. Billingham, R. E. & Medawar, P. B. The technique of free skin grafting in mammals. *J. Exp. Biol.* **28**, 385–391 (1951).
21. Bubnic, S. J., Nagy, A. & Keating, A. Donor hematopoietic cells from transgenic mice that express GFP are immunogenic in immunocompetent recipients. *Hematology* **10**, 289–295 (2005).
22. Boland, M. J. *et al.* Adult mice generated from induced pluripotent stem cells. *Nature* **461**, 91–94 (2009).
23. Kang, L., Wang, J., Zhang, Y., Kou, Z. & Gao, S. iPS cells can support full-term development of tetraploid blastocyst-complemented embryos. *Cell Stem Cell* **5**, 135–138 (2009).
24. Zhao, X. Y. *et al.* iPS cells produce viable mice through tetraploid complementation. *Nature* **461**, 86–90 (2009).
25. Miura, K. *et al.* Variation in the safety of induced pluripotent stem cell lines. *Nature Biotechnol.* **27**, 743–745 (2009).
26. Marks, H. *et al.* The transcriptional and epigenomic foundations of ground state pluripotency. *Cell* **149**, 590–604 (2012).
27. Ying, Q. L. *et al.* The ground state of embryonic stem cell self-renewal. *Nature* **453**, 519–523 (2008).
28. Carey, B. W. *et al.* Reprogramming factor stoichiometry influences the epigenetic state and biological properties of induced pluripotent stem cells. *Cell Stem Cell* **9**, 588–598 (2011).
29. Stadtfeld, M. *et al.* Ascorbic acid prevents loss of *Dlk1-Dio3* imprinting and facilitates generation of all-iPS cell mice from terminally differentiated B cells. *Nature Genet.* **44**, 398–405 (2012).
30. Nagy, A., Rossant, J., Nagy, R., Abramow-Newerly, W. & Roder, J. C. Derivation of completely cell culture-derived mice from early-passage embryonic stem cells. *Proc. Natl Acad. Sci. USA* **90**, 8424–8428 (1993).

Supplementary Information is available in the online version of the paper.

Acknowledgements We thank S. Yamanaka for providing the 2A plasmid vectors; K. Ito, N. Nakajima and K. Kawabata for technical advice on the transplantation experiments; H. Yoshida, K. Nishikawa, A. Ishibashi, R. Watanabe, M. Nakamura and T. Maeda for technical assistance. This work was partially funded by a research grant from Precursory Research for Embryonic Science and Technology (PRESTO), Japan Science and Technology Agency.

Author Contributions R.A. and M.A. designed the experiments, analysed the data and wrote the manuscript. R.A. and Y.H. established the iPSC and ES-cell lines. M.U., S.A., M.N. and Y.H. performed teratoma formation assays and transplantation assays. M. Sunayama and M. Sugiura performed molecular biological analyses. M.U., H.I., A.S. and A.N. performed immunohistochemical analyses.

Author Information Reprints and permissions information is available at www.nature.com/reprints. The authors declare no competing financial interests. Readers are welcome to comment on the online version of the paper. Correspondence and requests for materials should be addressed to M.A. (abemasum@nirs.go.jp).

METHODS

Mice. C57BL/6J Mm Slc mice were used for iPSC and ES cell generation, and C57BL/6J Mm Slc, C57BL/6-Tg(CAG-EGFP)¹⁸ and Balb/c mice were used for transplantation assays (Japan SLC). Only males were used for cell-line establishment and transplantation experiments. Animal experiments were performed in accordance with Institutional Animal Care and Use Committee guidelines.

iPSC and ES cell generation. iPSCs were generated with pCX-OKS-2A and pCX-c-Myc plasmids (Addgene) as described previously^{14,15}. Briefly, mouse embryonic fibroblasts (MEFs) were isolated from embryonic day (E)13.5 embryos of male C57BL/6 mice, and grown in DMEM supplemented with 10% FCS. The cells were transfected with the plasmids on days 1, 3, 5 and 7. Colonies were picked on day 15 after transfection. We carried out PCR analysis to confirm the absence of plasmid vector integration¹⁴. Established iPSC lines were evaluated on the basis of their morphologies, stem cell markers and pluripotency. Neuploidy was also investigated. We established ES cell lines as described previously³⁰. Briefly, E3.5 embryos were collected and plated individually onto mitomycin-C (Sigma-Aldrich) treated feeder MEFs. Established ES cell lines were evaluated on the basis of their morphologies, stem cell markers, neuploidy and pluripotency (Supplementary Fig. 1 and Supplementary Table 1).

Teratoma formation and T-cell immunostaining. Teratomas were produced by injecting cells (3×10^6 cells per injection) subcutaneously into the flanks of the mice. Four or five weeks after injection, the tumours were surgically dissected, fixed and embedded in paraffin. Tumour sections were immunostained with anti-CD3 antibody MCA-1477 (AbD serotec) as described previously³¹.

Statistics. Normally distributed data are expressed as the means \pm s.e.m., and the differences were tested using an unpaired *t*-test. *P* values < 0.05 were considered to be significant.

Immunocytochemistry of iPSC colonies. For immunocytochemical staining, anti-Nanog (1:50, ReproCELL), anti-Oct3/4 h-134 (1:100, Santa Cruz Biotechnology) and anti Sox-2 Y-17 (1:100, Santa Cruz Biotechnology) antibodies were used.

Generation of chimaeric mice from iPSCs and ES cells. Chimaeric mice were produced via the aggregation method, using 8-cell embryos or tetraploid embryo complementation³⁰.

Skin transplantation. Adult male chimaeric mice were used to prepare donor dermal tissues. Skin grafting was performed as described previously³². We used the tail as donor tissue. Because mouse tail tissue is resistant to ischaemia it can be transplanted efficiently without any technical troubles, and sensitive assays using tails have been developed for long-term (>1 month) investigations^{33,34}. Briefly, donor skin (5×5 mm) was grafted onto the back of recipient mice, and then covered with a bandage. The bandage was removed after 7 days, followed by analysis each day.

Bone marrow transplantation. Donor bone marrows were harvested from the femurs and tibias of fully chimaeric adult male mice (5–54 weeks old) derived from either iPSCs or ES cells. We used 7–8-week-old C57BL/6 or C57BL/6-Tg(CAG-EGFP) male mice as recipients with a single tail vein injection of the bone marrow cells. The animals were killed and the tibia and femurs were clipped into small pieces with scissors after removing the muscle and connective tissues. Bone chips were thoroughly rinsed with complete medium (DMEM supplemented with 5% FCS, 2 mM L-glutamine and antibiotics) in a 50-ml tube. The washed solution containing bone marrow cells was then transferred into a 50-ml tube after filtration through a 40- μ m nylon mesh filter, and centrifuged at 600g for 10 min. The supernatant was removed and 1 ml of 0.2% NaCl was added to the pellet and gently mixed for 1 min on ice. After addition of a further 1 ml of 1.6% NaCl, the mixture was centrifuged at 600g for 10 min and the pellet was resuspended in complete medium. Cells were counted and 10^7 cells in 0.4 ml of PBS were injected into the lateral tail veins using a 26-gauge needle for all animals, except for recipient without irradiation IR-2, for which 0.7×10^7 cells were injected.

Flow cytometric analysis. We used a capillary tube to collect 50 μ l of whole blood from the venous plexus of eye socket of the recipient mice. A 5- μ l aliquot of the

blood was diluted with PBS without haemolysis and used for the measurement of GFP-positive cells using flow cytometry, performed with an Epics XL instrument (Beckman Coulter). To detect B lymphocytes, T lymphocytes and granulocytes derived from donor bone marrow, the remaining collected whole blood was haemolysed using Versalys (Beckman-Coulter) to stain the cell-surface markers B220 (CD45R)-APC (clone; RA3-6B2, code no. 17-0452; eBioscience), CD3e-PE (clone; 145-2C11, code no. 12-0031; eBioscience), Gr-1 (Ly-6G)-PE (clone; RB6-8C5, code no. 12-5931; eBioscience) and Mac-1 (CD11b)-PE (clone; M1/70, code no. 101208; Biolegend). Four-colour flow cytometric analysis was performed using FACSCalibur, and the data were analysed using CellQuest software (BD Biosciences). In addition, using FACSaria (BD Bioscience), we sorted B220-positive, CD3e-PE-positive and Gr-1/Mac-1-positive fractions from the bone marrow preparations for semi-quantitative measurement of donor-origin cells.

Genotyping. Allele-specific PCR was performed to discriminate between donor and recipient tissues in the bone marrow transplantation experiments. Sequences of the primers used to characterize *Nnt* loci are listed in Supplementary Fig. 8³⁵. Genomic DNAs were prepared using the DNeasy Blood & Tissue Kit (Qiagen). PCR reactions were performed using Titanium Taq DNA polymerase (Clontech), and semi-quantitative PCR was performed using SYBR Premix EX Taq (Takara Bio) with the StepOnePlus Real-Time PCR System (Applied Biosystems).

Semi-quantitative expression analysis. Teratomas and tissues were homogenized using a Mixer mill MM300 (Qiagen), and total RNA fractions were prepared using the RNeasy Mini kit (Qiagen) in accordance with the manufacturer's protocol. All RT-PCR analyses were performed using the QuantiTect SYBR Green RT-PCR Kit (Qiagen). The data were normalized by comparison with *Gapdh* gene expression. The primers used were 5'-CATCACCGCCTTCGAT-3' and 5'-CGTTGAAACTTGTGCCTG A-3' for *Zg16*, and 5'-GCTGACACCAAG AAAGCAAG-3' and 5'-TTGGGACTTCTCCACATTT-3' for *Hormad1*.

Immunogenicity test for cardiomyocytes. Embryoid bodies were prepared with Iscove's modified Dulbecco's medium (Invitrogen) supplemented with 15% FBS, 1 mM sodium pyruvate (Invitrogen), 0.1 mM non-essential amino acids, 0.1 mM 2-mercaptoethanol, 50 U ml⁻¹ penicillin, 50 μ g ml⁻¹ streptomycin (1,000 cells per 200 μ l per well) using 96-well low cell-adhesion plates (Lipidure Coat; NOF Corp.)³⁶, then transferred to 0.3% gelatin-coated 12-well dishes (BD Falcon) in α MEM supplemented with 10% FBS, 0.1 mM non-essential amino acids, 0.1 mM 2-mercaptoethanol, 0.1% ascorbic acid, 50 U ml⁻¹ penicillin and 50 μ g ml⁻¹ streptomycin^{37,38}. Beating cardiomyocytes were implanted subcutaneously into C57BL/6-Tg(CAG-EGFP) recipient mice. Tissue sections were immunostained with anti-CD3 antibody (MCA-1477, AbD serotec).

31. Patten, P. E. *et al.* CD38 expression in chronic lymphocytic leukemia is regulated by the tumor microenvironment. *Blood* **111**, 5173–5181 (2008).
32. Le Moine, A. *et al.* Critical roles for IL-4, IL-5, and eosinophils in chronic skin allograft rejection. *J. Clin. Invest.* **103**, 1659–1667 (1999).
33. Surquin, M. *et al.* Skin graft rejection elicited by β_2 -microglobulin as a minor transplantation antigen involves multiple effector pathways: role of Fas-Fas ligand interactions and Th2-dependent graft eosinophil infiltrates. *J. Immunol.* **169**, 500–506 (2002).
34. Baruah, P. *et al.* Mice lacking C1q or C3 show accelerated rejection of minor H disparate skin grafts and resistance to induction of tolerance. *Eur. J. Immunol.* **40**, 1758–1767 (2010).
35. Huang, T. T. *et al.* Genetic modifiers of the phenotype of mice deficient in mitochondrial superoxide dismutase. *Hum. Mol. Genet.* **15**, 1187–1194 (2006).
36. Morizane, A., Doi, D., Kikuchi, T., Nishimura, K. & Takahashi, J. Small-molecule inhibitors of bone morphogenetic protein and activin/nodal signals promote highly efficient neural induction from human pluripotent stem cells. *J. Neurosci. Res.* **89**, 117–126 (2011).
37. Takahashi, T. *et al.* Ascorbic acid enhances differentiation of embryonic stem cells into cardiac myocytes. *Circulation* **107**, 1912–1916 (2003).
38. Guo, X. M. *et al.* Creation of engineered cardiac tissue *in vitro* from mouse embryonic stem cells. *Circulation* **113**, 2229–2237 (2006).

Studying arrhythmogenic right ventricular dysplasia with patient-specific iPSCs

Changsung Kim¹, Johnson Wong¹, Jianyan Wen^{1,2}, Shirong Wang¹, Cheng Wang¹, Sean Spiering³, Natalia G. Kan³, Sonia Forcales³, Pier Lorenzo Puri^{3,4}, Teresa C. Leone⁵, Joseph E. Marine⁶, Hugh Calkins⁶, Daniel P. Kelly⁵, Daniel P. Judge⁶ & Huei-Sheng Vincent Chen^{1,7}

Cellular reprogramming of somatic cells to patient-specific induced pluripotent stem cells (iPSCs) enables *in vitro* modelling of human genetic disorders for pathogenic investigations and therapeutic screens^{1–7}. However, using iPSC-derived cardiomyocytes (iPSC-CMs) to model an adult-onset heart disease remains challenging owing to the uncertainty regarding the ability of relatively immature iPSC-CMs to fully recapitulate adult disease phenotypes. Arrhythmogenic right ventricular dysplasia/cardiomyopathy (ARVD/C) is an inherited heart disease characterized by pathological fatty infiltration and cardiomyocyte loss predominantly in the right ventricle⁸, which is associated with life-threatening ventricular arrhythmias. Over 50% of affected individuals have desmosome gene mutations, most commonly in *PKP2*, encoding plakophilin-2 (ref. 9). The median age at presentation of ARVD/C is 26 years⁸. We used previously published methods^{1,10} to generate iPSC lines from fibroblasts of two patients with ARVD/C and *PKP2* mutations^{11,12}. Mutant *PKP2* iPSC-CMs demonstrate abnormal plakoglobin nuclear translocation and decreased β -catenin activity¹³ in cardiogenic conditions; yet, these abnormal features are insufficient to reproduce the pathological phenotypes of ARVD/C in standard cardiogenic conditions. Here we show that induction of adult-like metabolic energetics from an embryonic/glycolytic state and abnormal peroxisome proliferator-activated receptor gamma (PPAR- γ) activation underlie the pathogenesis of ARVD/C. By co-activating normal PPAR- α -dependent metabolism and abnormal PPAR- γ pathway in beating embryoid bodies (EBs) with defined media, we established an efficient ARVD/C *in vitro* model within 2 months. This model manifests exaggerated lipogenesis and apoptosis in mutant *PKP2* iPSC-CMs. iPSC-CMs with a homozygous *PKP2* mutation also had calcium-handling deficits. Our study is the first to demonstrate that induction of adult-like metabolism has a critical role in establishing an adult-onset disease model using patient-specific iPSCs. Using this model, we revealed crucial pathogenic insights that metabolic derangement in adult-like metabolic milieu underlies ARVD/C pathologies, enabling us to propose novel disease-modifying therapeutic strategies.

Mutations resulting in ARVD/C are frequently found in five components of the cardiac desmosome, which include junction plakoglobin, plakophilin-2 (*PKP2*), desmoplakin (*DSP*), desmoglein-2 and desmocollin-2⁹. Pathological hallmarks of ARVD/C are progressive fibro-fatty replacement of cardiomyocytes with increased cardiomyocyte apoptosis primarily in the right ventricle. Pathogenic processes of ARVD/C are difficult to study because obtaining cardiac samples from early stages of human ARVD/C hearts is not possible owing to ARVD/C being commonly diagnosed at advanced diseased stages or post-mortem⁸, and because primary cardiac tissues are difficult to biopsy safely from symptomatic ARVD/C patients owing to the risk of cardiac perforation. Moreover, mouse models of ARVD/C remain unproven for finding

clinically feasible therapy. These limiting factors impose significant constraints in developing therapies for human ARVD/C.

Using four retroviral vectors containing *Oct4*, *Sox2*, *Klf4* and *cMyc*, we first generated several iPSC lines from fibroblasts of a patient with clinical ARVD/C and a homozygous c.2484C>T mutation in *PKP2* that causes cryptic splicing with a 7-nucleotide deletion in exon 12, leading to frame-shift of the carboxy-terminal amino acids¹¹. Three iPSC lines were extensively characterized: JK#2, JK#7 and JK#11 (Fig. 1 and Supplementary Figs 1 and 2). All iPSC clones expressed pluripotent markers, including *Oct4*, *Tra1-81*, *Nanog* and *SSEA4*, had normal karyotypes, and formed teratoma when injected into severe combined immunodeficient (SCID) mice. Pluripotent status of mutant *PKP2*-iPSCs was also demonstrated by the methylation patterns of *Nanog* promoter regions (Fig. 1c) in comparison to parental mutant *PKP2* fibroblasts and H9 human embryonic stem cells (hESCs). Global transcriptome expression profiles showed that all mutant *PKP2*-iPSC lines showed a higher degree of similarity with H9 hESCs and normal iPSCs (CF-iPSCs, female, characterized in Supplementary Fig. 3) than their parental fibroblasts (Fig. 1f). Importantly, all three JK mutant iPSC lines showed silenced exogenous retroviral transgenes and activation of endogenous pluripotent genes (Supplementary Fig. 2). Genomic DNA sequencing and messenger RNA analysis confirmed the homozygous c.2484C>T mutation in *PKP2* that caused predominantly cryptic splicing in exon 12 of three JK lines (Supplementary Figs 1d and 2b). These results demonstrated the successful reprogramming of parental mutant *PKP2* fibroblasts to iPSC lines.

We differentiated human H9 hESCs, CF-iPSCs and mutant *PKP2*-iPSCs to beating EBs (Supplementary Videos 1 and 2) using a standard cardiogenic protocol¹⁴. Consistent with previous findings in ARVD/C cell line and mouse models with desmoplakin downregulation/deletion¹³, we observed abnormal nuclear translocation of junction plakoglobin proteins (PKG) (Fig. 2a, b), and very low β -catenin activity and expression in mutant iPSC-CMs (Supplementary Fig. 4) but not in normal hESC-CMs under baseline cardiogenic conditions. These results indicate that mutant *PKP2* proteins with frame-shifted C-terminals fail to anchor PKG to the sarcolemmal membrane, resulting in PKG nuclear translocation and downregulation of β -catenin activities¹³. However, no exaggerated lipogenesis (by Nile Red staining) or apoptosis (by TdT-mediated dUTP nick end labelling (TUNEL) assay) in H9 hESC- or mutant iPSC-CMs was found after culturing for 2–3 months in this baseline cardiogenic condition (Fig. 2c), an observation that is consistent with the delayed, adult-onset clinical course of ARVD/C.

We then focused our studies on the cardiomyocyte portions (positive for cardiac α -actinin or troponin I (CTNI)) of beating EBs. We counted (1) the percentage of cardiomyocytes that possessed positive TUNEL nuclear staining as the cardiomyocyte (CM) apoptotic index, and (2) the percentage of cardiomyocytes that contained any Nile-Red-positive

¹Del E. Webb Neuroscience, Aging & Stem Cell Research Center, Sanford-Burnham Medical Research Institute, La Jolla, California 92037, USA. ²Department of Cardiovascular Surgery, China-Japan Friendship Hospital, Beijing 100029, China. ³Muscle Regeneration and Development Program, Sanford-Burnham Medical Research Institute, La Jolla, California 92037, USA. ⁴Dulbecco Telethon Institute, IRCCS Fondazione Santa Lucia, 00179 Rome, Italy. ⁵Diabetes and Obesity Research Center, Sanford-Burnham Medical Research Institute, Orlando, Florida 32827, USA. ⁶Department of Medicine/Cardiology, Johns Hopkins University School of Medicine, Baltimore, Maryland 21287, USA. ⁷Department of Medicine/Cardiology, University of California-San Diego, San Diego, California, 92103, USA.

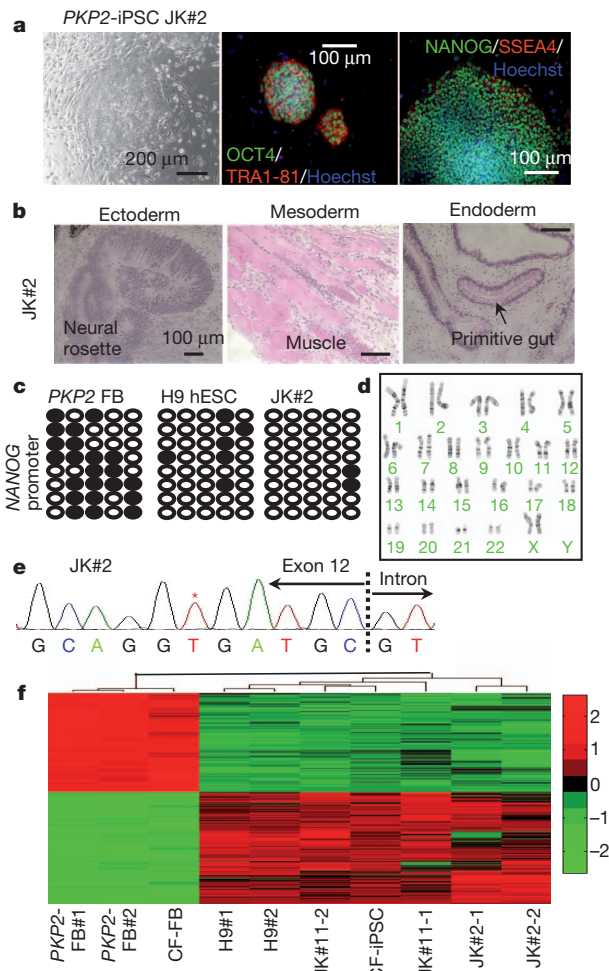


Figure 1 | Generation of c.2484C>T *PKP2* mutant iPSCs. **a**, The JK#2 clone of mutant iPSCs expressed significant levels of pluripotent proteins. **b**, Representative images of cells of three germ layers from teratoma sections. **c**, Bisulphite sequencing analysis of the CpG methylation patterns of NANOG promoter regions in mutant *PKP2* fibroblasts (FB), ESCs, and JK#2 clone of iPSCs. **d**, Normal karyotype of JK#2 iPSCs. **e**, Genomic DNA sequencing showed the homozygous c.2484C>T (asterisk) *PKP2* mutations in JK#2 iPSCs. **f**, Analysis of genome-wide mRNA expression profiles (heat map) of all iPSC lines, normal human FB (CF-FB)-derived CF-iPSC, and H9 hESC lines (see Methods and Supplementary Figs 1 and 2 for detailed description).

lipid droplets as the indicator of lipogenesis in cardiomyocytes. The baseline apoptotic index and percentages of lipid-laden cardiomyocytes are 1.8 ± 0.3 and $0.8 \pm 0.5\%$ for 60-day-old hESC-CMs, and 2.1 ± 0.6 and $0.9 \pm 0.1\%$ for 60-day-old mutant *PKP2* iPSC-CMs (no statistical difference between these two groups), respectively. Because the major metabolic differences between embryonic and adult cardiomyocytes are (1) embryonic cardiomyocytes use mostly glycolysis for energy production, and (2) adult cardiomyocytes produce most energy via fatty acid oxidation (FAO) but retain capacity to readily switch to glucose or other substrate utilization when fatty acid is not available or FAO is compromised^{15,16}, we first created a lipogenic milieu in beating EBs with an adipogenic cocktail (insulin, dexamethasone and 3-isobutyl-1-methylxanthine (IBMX), termed the 3-factor (3F) protocol)^{17–19} in an attempt to induce adult-like energy metabolism and accelerate pathogenesis in mutant iPSC-CMs. With this 3F protocol, we observed mildly increased lipogenesis with minimal apoptosis after 4–5 weeks of treatment (13.2 ± 4.3 and $4.8 \pm 1.0\%$ lipid-laden cardiomyocytes and 6.3 ± 1.4 and $3.9 \pm 1.8\%$ apoptotic cardiomyocytes in hESC-CMs and mutant *PKP2* iPSC-CMs, respectively, $P =$ non-significant between groups, Fig. 2d–k). Notably, this 3F protocol induced more expression of PPAR- α (PPAR- α), the major transcriptional regulator of fatty

acid metabolism in adult cardiomyocytes¹⁶, in beating mutant iPSC-EBs than in hESC-EBs (Fig. 2g). PPAR- γ , which should be minimally activated in normal cardiomyocytes, was slightly activated by this 3F protocol in both beating EBs. Because PPAR- γ pathway has been reported to be abnormally hyperactivated in right ventricle tissue samples of ARVD/C hearts²⁰ and transgene-induced overexpression of PPAR- γ in mouse cardiomyocytes leads to dilated cardiomyopathy²¹, we added 5 μ M rosiglitazone²² and 200 μ M indomethacin²³ to the 3F protocol to further induce abnormal PPAR- γ over-activation in beating EBs (termed the 5-factor (5F) protocol). After 4–5 weeks of treatment with 5F, mutant iPSC-CMs demonstrated exaggerated lipogenesis ($31.6 \pm 3.3\%$ versus $13.5 \pm 3.5\%$ in hESC-CMs, $P < 0.05$) and pronounced apoptosis ($39.6 \pm 8.5\%$ versus $5.4 \pm 0.9\%$ in hESC-CMs, $P < 0.05$, Fig. 2h–k). Quantitative real-time PCR with reverse transcription (qRT-PCR) analysis also confirmed the higher expression of adipogenic PPAR- γ /aP2 (fatty acid-binding protein, also known as FABP4) genes and downregulation of the pro-survival *Bcl2* gene in beating mutant *PKP2*-EBs when compared to normal hESC-EBs or CF-iPSC-EBs (Fig. 2g and Supplementary Fig. 5a, b). Results of cardiomyocytes apoptosis and lipogenesis in beating EBs after control, 3F or 5F treatment are summarized in Fig. 2j, k. We also observed abnormal PPAR- γ nuclear staining in mutant *PKP2* iPSC-CMs after 2 weeks of 5F treatment (Supplementary Fig. 5c), indicating that abnormal PPAR- γ activation may have a significant role in mediating mutant iPSC-CM pathology. We previously showed that we could use cardiac alpha-myosin heavy chain promoter-driven puromycin resistance (α -MHC-Puro^r) to efficiently isolate cardiomyocytes (>95% purity) from beating EBs¹⁴. We therefore generated mutant iPSC lines (JK#2 and JK#11) with α -MHC-Puro^r to enable purification of cardiomyocytes for further testing. In comparison to puromycin-isolated hESC-CMs, purified mutant iPSC-CMs showed higher PPAR- γ activation, lower *BCL2* mRNA levels, and higher apoptotic caspase 3 expressions after 5F treatment (Supplementary Fig. 5d). More importantly, rosiglitazone and indomethacin alone without the other three factors induced PPAR- γ activation only but did not induce exaggerated lipogenesis or apoptosis (Supplementary Fig. 5e–g), indicating that activation of both normal PPAR- α and abnormal PPAR- γ pathways in mutant *PKP2* iPSC-CMs is required for eliciting pathologies of ARVD/C.

We further verified that the pathogenic specificity of these ARVD/C phenotypes is due to the *PKP2* mutation in mutant iPSC-EBs by introducing the wild-type (WT) *PKP2* gene back into mutant iPSC-CMs, containing α -MHC-Puro^r, with a lentiviral transduction method (Fig. 3a). After transducing beating mutant iPSC-EBs with WT *PKP2* (verified by the expression of tagged green fluorescent protein, GFP), abnormal PKG nuclear localization (Fig. 3b), apoptosis (Fig. 3c) and lipogenesis (Fig. 3d) in puromycin-purified mutant iPSC-CMs were corrected by the expression of WT *PKP2* (GFP⁺), but not in isolated CMs without WT-*PKP2*-GFP after the 5F protocol. We measured the number of lipid droplets in each cardiomyocyte as the degree of lipogenesis in Fig. 3d because cardiomyocytes containing WT-*PKP2*-GFP still had few tiny lipid droplets remaining after 5F treatment (Fig. 3d, left image). Also, control GFP vector alone without WT-*PKP2* did not correct the PKG nuclear translocation (Fig. 3b) or the large number of big lipid droplets found in mutant *PKP2* iPSC-CMs (Fig. 3d, right image) after pathogenic induction. These findings support that observed pathological phenotypes are the result of mutated *PKP2* genes in iPSCs.

Among the components of pathogenic 5F protocol, insulin, dexamethasone and IBMX simulate natural hormonal regulation of cardiomyocyte metabolism, but rosiglitazone and indomethacin are not natural human ligands. Therefore, we searched for a natural ligand that could replace rosiglitazone and indomethacin for inducing abnormal PPAR- γ activation. We found that the endogenous PPAR- γ activator 13-hydroxyocta-decadienoic acid (13-HODE, a major component of the oxidized low-density lipoprotein (oxLDL))²² could replace rosiglitazone and indomethacin in the 5F protocol for abnormal PPAR- γ

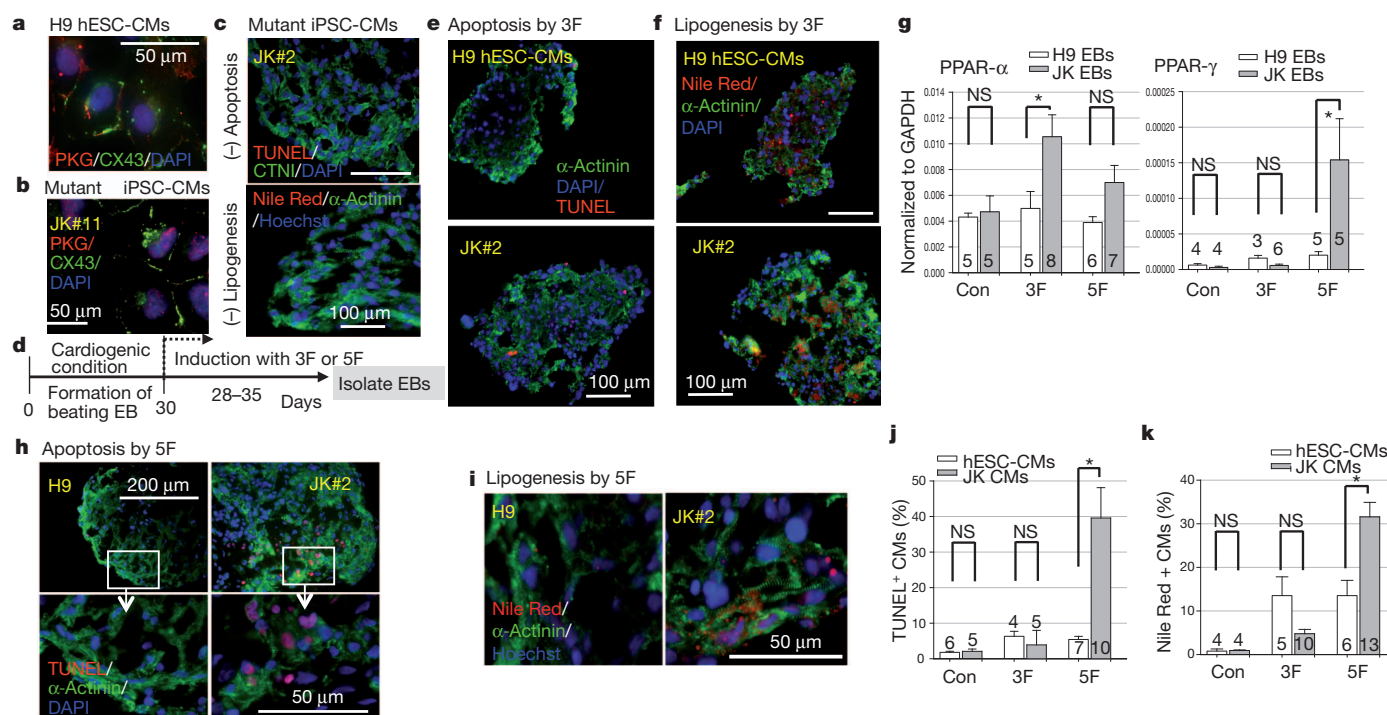


Figure 2 | Induction of pathognomonic features of ARVD/C using mutant *PKP2*-iPSCs. **a, b,** H9 hESC-CMs showed sarcolemmal connexin 43 (CX43) and PKG distribution (red) at both cell membrane and nucleus (DAPI) (**a**); yet PKG staining in mutant iPSC-CMs is restricted to the nuclei (**b**). **c,** At baseline, minimal TUNEL nuclear staining (apoptosis) or Nile Red labelling (lipogenesis) was found in mutant iPSC-CMs. Pictures with low magnification are used to show the lack of pathologies. **d,** Protocols for lipogenic (3F) and pathogenic (5F) induction. **e, f,** Minimal apoptosis (**e**) and mild increase of lipid-laden (red) CMs (**f**) were found after 3F treatment. **g,** Summary of mRNA expression levels of PPAR- α and PPAR- γ (relative to GAPDH) in beating EBs. PPAR- α : $4.3 \pm 0.3 \times 10^{-3}$ and

$4.7 \pm 1.2 \times 10^{-3}$ at control condition (Con), $5.0 \pm 1.3 \times 10^{-3}$ and $1.1 \pm 0.2 \times 10^{-2}$ after 3F and $3.9 \pm 0.5 \times 10^{-3}$ and $7.0 \pm 1.3 \times 10^{-3}$ after 5F for H9 hESC- and mutant iPSC-CMs, respectively. PPAR- γ : $6.1 \pm 2.1 \times 10^{-6}$ and $2.9 \pm 1.7 \times 10^{-6}$ at Con, $1.6 \pm 0.4 \times 10^{-5}$ and $5.6 \pm 1.8 \times 10^{-6}$ after 3F and $2.0 \pm 0.5 \times 10^{-5}$ and $1.5 \pm 0.6 \times 10^{-4}$ after 5F. **h, i,** Pictures with higher magnification are used to show significant increase of TUNEL-positive (**h**) and lipid-containing CMs after 5F (**i**). **j, k,** Summary of degrees of apoptosis (**j**) and lipid-laden CMs (**k**) in beating EBs. The number in each column represents the number of biological replicates tested. Asterisks indicate $P < 0.05$ and NS, no significant difference by ANOVA. All data are shown as mean \pm s.e.m.

activation, leading to extensive lipogenesis ($37.5 \pm 6.0\%$) and apoptosis ($22.4 \pm 4.0\%$) in mutant iPSC-CMs (Fig. 3e). Moreover, to support the crucial pathogenic role of coactivation of abnormal PPAR- γ and normal PPAR- α pathways in ARVD/C, we showed that blockade of PPAR- γ overactivation with PPAR- γ antagonists, GW9662 (GW)²² or T0070907 (T007)²³, during pathogenic induction with media containing 13-HODE and 3-factors, prevents apoptosis and lipogenesis in mutant iPSC-CMs (Fig. 3f–h). Also, blockade of PPAR- α activation with an antagonist, 2 μ M GW6471, after 5F treatment (Supplementary Fig. 6) or activation of PPAR- γ alone (Supplementary Fig. 5e–g) did not induce significant ARVD/C pathologies, supporting the crucial role of PPAR- α /PPAR- γ coactivation in ARVD/C pathogenesis. Significant FAO and β -oxidation activated by PPAR- α seem to be required for cardiomyocyte apoptosis as well (Supplementary Fig. 6b–e). Furthermore, because mitochondrial function is tightly linked to energy metabolism and apoptosis²⁴, we decreased reactive oxygen species (ROS) production from mitochondria with ROS scavengers, 1 mM N-acetyl-cysteine or ascorbic acid individually, in the 5F pathogenic protocol, which markedly decreased cardiomyocyte death in mutant *PKP2*-beating EBs (Fig. 3i, j).

Using a Seahorse XF96 Extracellular Flux Analyzer²⁵, functional assays of FAO and glycolysis in live cells showed that mutant *PKP2* iPSC-CMs and normal iPSC-CMs derived from a second normal iPSC line (hS-iPSC, male, characterized in Supplementary Fig. 7) had dominant glycolytic energetics (an embryonic pattern¹⁵) at the baseline (Fig. 4 and Supplementary Fig. 8). After activation of PPAR- α by 3F, mutant and normal iPSC-CMs had similar levels of glycolysis but significant activation of FAO (an adult-like pattern) when compared to the non-induced, baseline conditions (zero factor). Compared to 3F induction, mutant *PKP2* iPSC-CMs after pathogenic coactivation of

PPAR- α and PPAR- γ by 5F demonstrated overall depressed energy metabolism with 86% reduction in FAO and 74% reduction in glycolysis, resulting in a fuel shift from using both fatty acids and glucose to dominant glucose utilization (including glycolysis and pyruvate oxidation), much like the so-called metabolic burnt-out state observed in failing hearts²⁶ (Fig. 4). This fuel-shift after pathogenic induction is accompanied by significant downregulation of mRNA transcripts of carnitine palmitoyltransferase-1B (*CPT1B*) and pyruvate dehydrogenase kinase-4 (*PDK4*), leading to inhibition of FAO and activation of pyruvate dehydrogenase (PDH) for increased pyruvate oxidation^{16,26}, respectively (Fig. 4i–k). Thus, results from immunocytochemical, genetic and metabolic assays support strongly that coactivation of PPAR- α and PPAR- γ by hormones and small molecules accelerates the pathogenesis and establishes an efficient *in vitro* model of ARVD/C, recapitulating the metabolic and pathological signatures of failing ARVD/C hearts within 2 months.

We also used an episomal method¹⁰ to generate three lines of genome-integration free iPSC (SW#5, SW#6 and SW#7) from a second patient with clinical ARVD/C (Supplementary Fig. 9) and a heterozygous c.2013delC in exon 10 of *PKP2* (termed delC *PKP2* mutation) that causes frame-shift and premature termination in exon 10. Confirmation of pluripotent status and the heterozygous c.2013delC in *PKP2* of these three SW iPSC clones are shown in Supplementary Figs 10 and 11. Prematurely-terminated delC mutant *PKP2* transcripts are probably unstable and degraded to undetectable levels (see Supplementary Figs 10b, c and 11h). SW iPSC-CMs also showed increased nuclear PKG translocation (Supplementary Fig. 12a–c) and very low β -catenin nuclear localization (Supplementary Fig. 4) as described for the homozygous c.2484C>T mutant *PKP2* iPSC-CMs. We induced ARVD phenotypes from SW#5 and SW#7 mutant iPSC-CMs but not in normal female

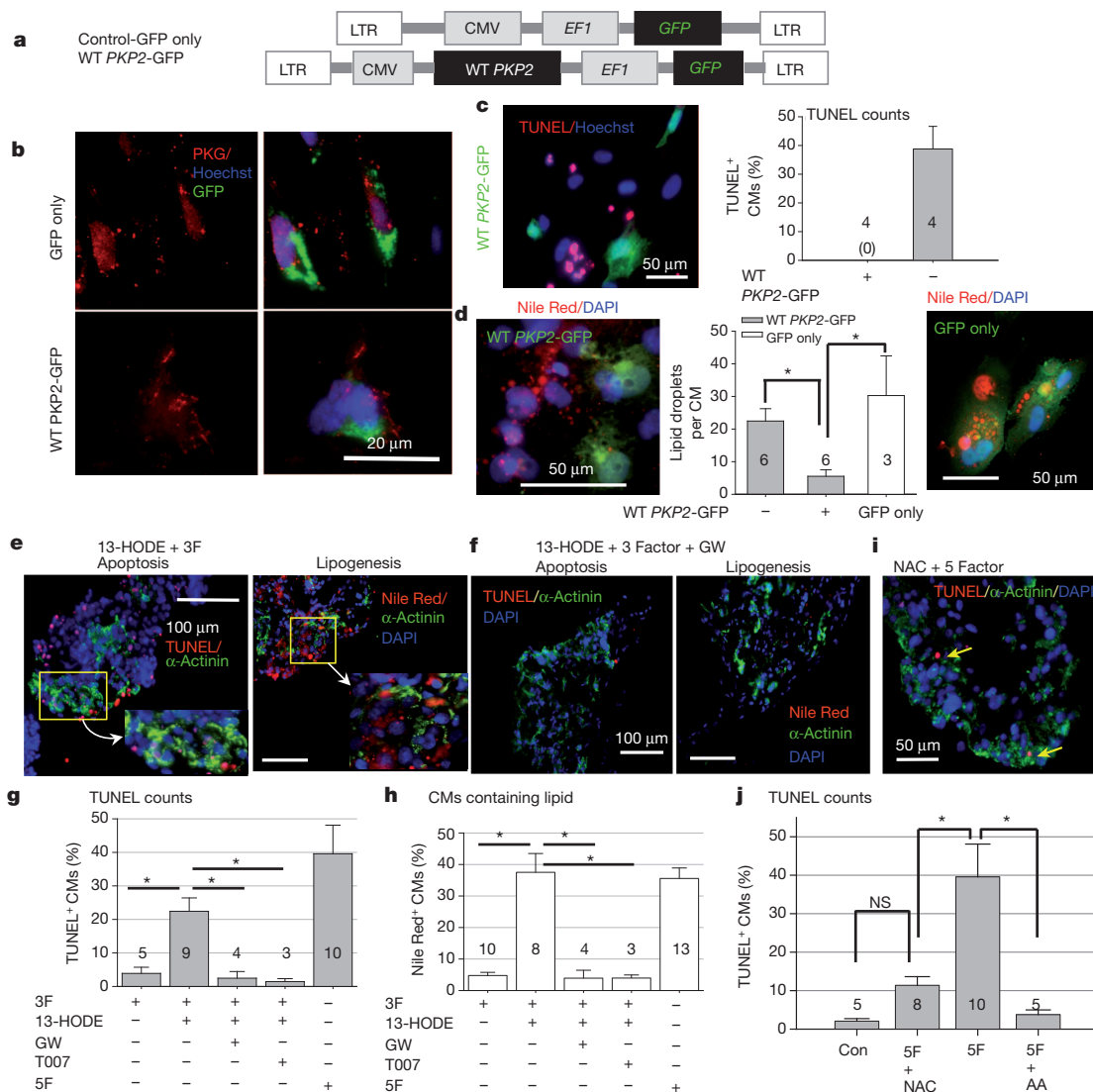


Figure 3 | Rescue of pathological features of mutant *PKP2*-iPSC-CMs.

a, Diagram of lentiviral vectors used to stably integrate control-GFP or WT-*PKP2*-GFP into mutant iPSC-CMs. **b**, Top panels, PKG (red) remained restricted to nuclei with control-GFP vectors; bottom panels, PKG distributed at both cell membrane and nucleus (Hoechst) with WT-*PKP2*-GFP of purified mutant iPSC-CMs. **c**, After 5F and WT *PKP2*-GFP lentiviral infection, TUNEL nuclear staining could only be found in GFP-negative CMs. **d**, Large number of lipid droplets (red) could only be found in WT *PKP2*-GFP-negative (left, 22.5 ± 3.8) or control-GFP-positive CMs (right, 30.3 ± 12.2 lipid droplets per CM), but not in WT *PKP2*-GFP-positive CMs (5.5 ± 2.0 small lipid droplets per CM). **e**, 13-HODE ($20 \mu\text{g ml}^{-1}$) with 3F could replace 5F for pathogenic induction. **f**, 3 μM GW and 0.5 μM T007 (not shown) prevent pathogenic

induction by 13-HODE+3F. **g**, **h**, Summary of CM apoptotic index (**g**) and degrees of lipogenesis (**h**) in mutant *PKP2*-CMs. The percentage of CMs that have TUNEL staining and lipid droplets in mutant iPSC-CMs after treatment with 3F, 13-HODE+3F, 13-HODE+3F+GW, 13-HODE+3F+T007 and 5F (re-plot from Fig. 2j, k) are: 3.9 ± 1.8 and $4.8 \pm 1.0\%$, 22.4 ± 4.0 and $37.5 \pm 6.0\%$, 2.5 ± 2.0 and $3.9 \pm 2.5\%$, 1.5 ± 0.9 and $4.0 \pm 1.0\%$ and 39.6 ± 8.5 and $31.6 \pm 3.3\%$, respectively. **i**, N-acetyl-cysteine (NAC) prevented CM apoptosis induced by 5F. **j**, The apoptotic index for mutant iPSC-CMs after 5F with 1 mM NAC or ascorbic acid (AA) is $11.4 \pm 2.3\%$ and $3.8 \pm 1.2\%$, respectively (versus $2.1 \pm 0.6\%$ in control and 39.6 ± 8.5 after 5F). The number in each column represents the number of biological replicates tested. Asterisks indicate $P < 0.05$ and NS, no significant difference by ANOVA.

CF-iPSC-CMs with the 5F protocol. Only the 5F protocol induced coactivation of normal PPAR- α and abnormal PPAR- γ pathways that led to exaggerated lipogenesis and cardiomyocyte apoptosis in delC *PKP2* iPSC-CMs (Supplementary Fig. 12), consistent with the results shown in Fig. 2. The second hS-iPSC line was also used to show that the 5F protocol did not induce exaggerated lipogenesis or cardiomyocyte apoptosis in normal male iPSC-CMs (Supplementary Fig. 7f).

We further used JK mutant iPSC-CMs to investigate other cardiomyocyte properties that may contribute to pathogenesis. Compared to H9 hESC-CMs in baseline conditions, mutant iPSC-CMs demonstrated slower intracellular calcium ($[\text{Ca}^{2+}]_i$) relaxation after pacing only in high extracellular Ca^{2+} media (5.8 mM) with a prolonged relaxation time constant, but not in normal Ca^{2+} media (1.8 mM). However, after 5F pathogenic induction, mutant iPSC-CMs demonstrated a

prolonged $[\text{Ca}^{2+}]_i$ relaxation phase even in normal Ca^{2+} media after pacing (Supplementary Fig. 13a–d), indicating abnormal $[\text{Ca}^{2+}]_i$ handling capability. Furthermore, using puromycin-purified cardiomyocytes and compared to hESC-CMs, qRT-PCR analysis of mutant iPSC-CMs in baseline conditions showed mildly decreased mRNA expression levels of sarcoplasmic reticulum Ca^{2+} -ATPase (*SERCA*, for Ca^{2+} re-uptake) with preserved $\text{Na}^+/\text{Ca}^{2+}$ exchanger 1 (*NCX1*, for $[\text{Ca}^{2+}]_i$ extrusion) expression, which may explain the impaired $[\text{Ca}^{2+}]_i$ relaxation of mutant iPSC-CMs only in high extracellular Ca^{2+} media at baseline. In contrast, after 5F treatment, both *NCX1* and *SERCA* expression levels were significantly downregulated (Supplementary Fig. 13e, f) relative to hESC-CMs, which would account for the further impaired $[\text{Ca}^{2+}]_i$ relaxation phase of mutant iPSC-CMs even in normal Ca^{2+} media. Also, electrophysiological

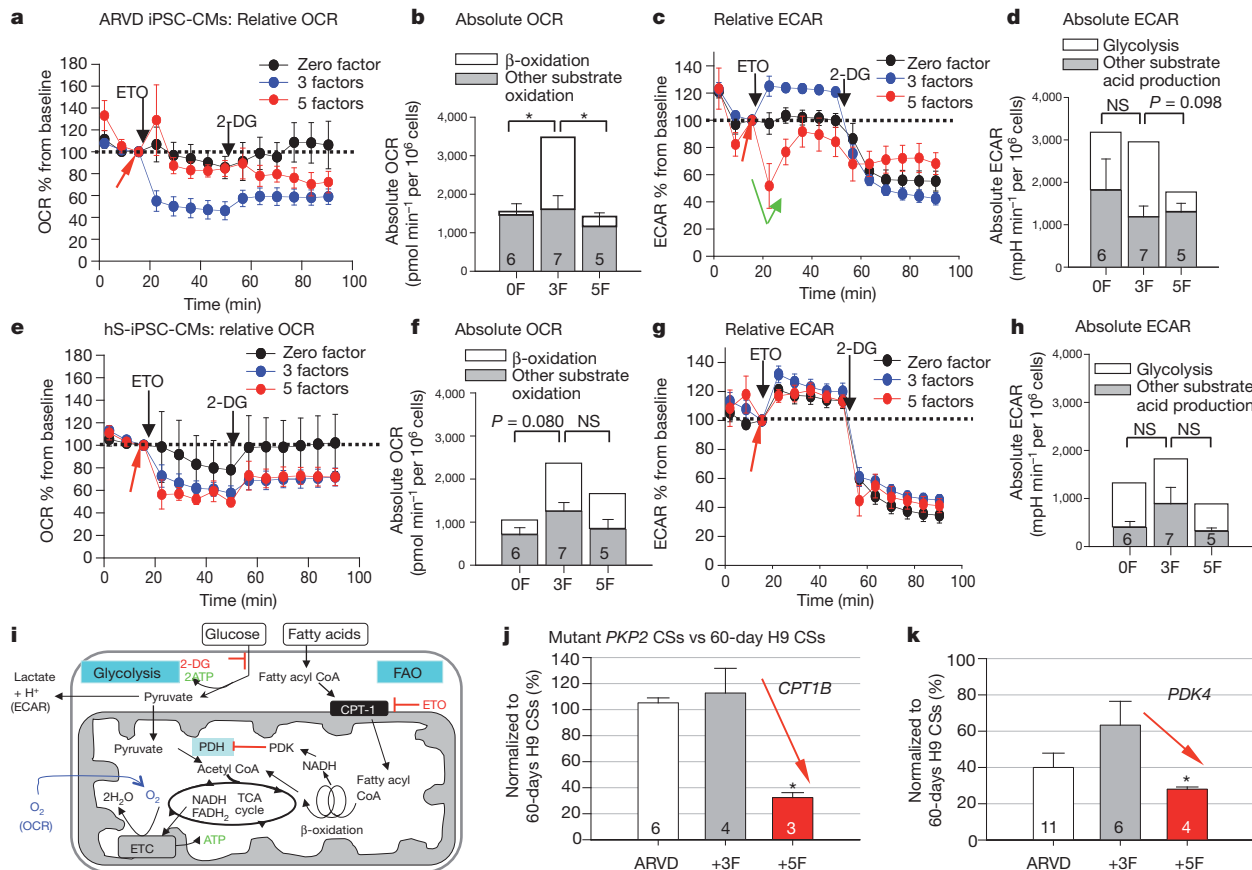


Figure 4 | Metabolic and qRT-PCR assays of glucose and fatty acid utilization of mutant (JK#11 and JK#2) and normal hS-iPSC-CMs. The Etomoxir (ETO, 100 μ M)-blocked component of oxygen consumption rate (OCR) and 2-deoxyglucose (2-DG, 50 mM)-blocked component of extracellular acidification rate (ECAR) represent FAO and glycolysis, respectively. Absolute values of OCR and ECAR are expressed as pmol min^{-1} per 10^6 cells and mpH min^{-1} per 10^6 cells, respectively. **a**, Real-time measurement of OCR showed that ETO blocked 14.4 ± 10.2 (0F), 53.9 ± 8.2 (3F) and 15.3 ± 8.5 (5F) of baseline OCR (red arrow) for mutant iPSC-CMs. **b**, ETO-blocked absolute OCR (white boxes) for mutant iPSC-CMs are 85.2 ± 196.6 (0F), 1865.3 ± 383.5 (3F) and 254.5 ± 115.4 (5F). **c**, ECAR measurement after ETO inhibition of β -oxidation showed a rapid $\sim 21\%$ compensatory increase of glycolysis only in the 3F condition (a switch in energy substrates); yet, after 5F, ETO transiently decreased ECAR by $\sim 45\%$ (green arrow) followed by $\sim 28\%$ compensatory increase in ECAR (glycolysis). **d**, 2DG-blocked absolute ECAR (glycolysis) for mutant iPSC-CMs after 0F, 3F or 5F are 1353.0 ± 313.6 , 1766.0 ± 579.7 and 457.2 ± 211.0 , respectively. **e–h**, Comparable patterns in absolute and relative OCR or ECAR in normal hS-iPSC-CMs (WS#4). **e, f**, For normal iPSC-CMs,

ETO-blocked FAO after 0F, 3F or 5F are (relative) $21.8 \pm 24.8\%$, $42.6 \pm 6.6\%$ and $50.5 \pm 4.06\%$ (**e**); or (absolute) 329.4 ± 235.8 , 1114.5 ± 316.6 and 807.8 ± 196.4 (**f**), respectively. **g, h**, 2DG-blocked glycolysis after 0F, 3F or 5F are (relative) $65.5 \pm 5.3\%$, $54.9 \pm 3.8\%$ and $58.8 \pm 4.8\%$ (**g**); or (absolute) 915.3 ± 270.6 , 929.4 ± 314.3 and 556.8 ± 217.9 (**h**), respectively. Combining data shown in **a–h**, these results support that both normal and mutant iPSC-CMs have embryonic metabolism at the baseline, and show significantly increased FAO after 3F with ability to switch between FAO and glucose utilization (an adult-like metabolic pattern). Mutant iPSC-CMs after 5F behave like failing cardiomyocytes (also see Supplementary Fig. 8) with pathological glucose-dominant metabolism. **i**, A simple diagram to illustrate substrate utilization pathways in cardiomyocytes. **j, k**, qRT-PCR analysis of puromycin-purified mutant iPSC-CMs showed that mutant iPSC-CMs displayed significantly decreased expression of *CPT1B* (**j**) and *PDK4* (**k**) mRNA transcripts when compared to control H9 hESC-CMs after 5F induction, leading to enhanced pyruvate oxidation and decreased FAO, respectively. Please see Supplementary Information for detailed legend of Fig. 4. Single asterisk indicates $P < 0.05$ and NS, no significant difference by ANOVA. P values are shown when unpaired t -test was performed.

properties of JK *PKP2* mutant iPSC-CMs are different from H9 hESC-CMs (Supplementary Fig. 14) at baseline and show further impairment after PPAR- α and PPAR- γ coactivation. Future mechanistic studies are needed to determine the roles of impaired $[\text{Ca}^{2+}]_i$ handling and altered electrical properties in mediating pathologies or arrhythmia of mutant iPSC-CMs^{8,27}.

Finally, to explain the predominant pathology in the right ventricle of ARVD/C hearts, we increased the number of Islet 1-positive (*Isl1*⁺) cardiac progenitor cells by approximately fourfold in JK#2 and JK#11 mutant *PKP2* iPSCs with 1 μ M 6-bromindirubin-3'-oxime (BIO)²⁸ to simulate natural right ventricle formation from *Isl1*⁺ progenitor cells of the secondary heart field²⁹ (Supplementary Fig. 15a–c). We also used 100 ng ml⁻¹ Dickkopf-1 (*Dkk1*)²⁸ to decrease the number of *Isl1*⁺ progenitor cells and, subsequently, right-ventricle-like cardiomyocytes. After 5F pathogenic induction, EBs with enriched *Isl1*⁺ cells had significantly more lipogenesis and apoptosis in cardiomyocytes than EBs with minimal numbers of *Isl1*⁺ progenitor cells

(Supplementary Fig. 15d–g). This result supports the notion that *Isl1*⁺ cells confer the dominant pathologies in the right ventricle³⁰.

In conclusion, using patient-specific mutant *PKP2*-iPSCs and various pathogenic conditions, we accelerate the pathogenesis of an adult-onset disease. We demonstrate the importance of PPAR- α /PPAR- γ coactivation, ROS production, fatty acid oxidation and *Isl1*⁺ cells in the pathogenesis of ARVD/C. These efficient *in vitro* iPSC models recapitulate the pathognomonic features of ARVD/C and enable pathogenic investigation and therapeutic screens.

METHODS SUMMARY

The retroviral and episomal methods of generating iPSCs from normal and patients' fibroblasts were performed as published previously¹⁰. Human ESC and iPSC culture methods, lentiviral transduction and derivation of cardiomyocytes using standard cardiogenic protocols were described previously¹⁴. ARVD/C fibroblasts were obtained from Johns Hopkins University and normal fibroblasts from UCSD with approved protocols at each institution. Genetic sequencing and

Illumina microarray data were performed at the Sanford-Burnham Medical Research Institute (SBMRI) core facility and Scripps Research Institute. Karyotyping was performed by Cell Line Genetics. Standard techniques were used for immunostaining, cryosections, qRT-PCR, TUNEL assay, teratoma formation/section, and Ca^{2+} imaging with Fura-2 AM dyes. Immunostaining sections were analysed with SlideBook software for lipid and TUNEL counts. Data were analysed with the StatView/JMP program (SAS Institute) and presented as mean \pm s.e.m. $[\text{Ca}^{2+}]$; relaxation curve fitting was performed with SigmaPlot 8.0 software using the Marquardt-Levenberg algorithm to achieve the best fit. Statistical difference was analysed by an ANOVA procedure for multiple comparisons and by the unpaired *t*-test for pair-wise comparisons with a *P*-value < 0.05 considered statistically significant.

Full Methods and any associated references are available in the online version of the paper.

Received 29 September 2011; accepted 15 November 2012.

Published online 27 January 2013.

1. Takahashi, K. *et al.* Induction of pluripotent stem cells from adult human fibroblasts by defined factors. *Cell* **131**, 861–872 (2007).
2. Yu, J. *et al.* Induced pluripotent stem cell lines derived from human somatic cells. *Science* **318**, 1917–1920 (2007).
3. Park, I. H. *et al.* Disease-specific induced pluripotent stem cells. *Cell* **134**, 877–886 (2008).
4. Carvajal-Vergara, X. *et al.* Patient-specific induced pluripotent stem-cell-derived models of LEOPARD syndrome. *Nature* **465**, 808–812 (2010).
5. Moretti, A. *et al.* Patient-specific induced pluripotent stem-cell models for long-QT syndrome. *N. Engl. J. Med.* **363**, 1397–1409 (2010).
6. Itzhaki, I. *et al.* Modelling the long QT syndrome with induced pluripotent stem cells. *Nature* **471**, 225–229 (2011).
7. Yazawa, M. *et al.* Using induced pluripotent stem cells to investigate cardiac phenotypes in Timothy syndrome. *Nature* **471**, 230–234 (2011).
8. Calkins, H. & Marcus, F. Arrhythmogenic right ventricular cardiomyopathy/dysplasia: an update. *Curr. Cardiol. Rep.* **10**, 367–375 (2008).
9. Awad, M. M., Calkins, H. & Judge, D. P. Mechanisms of disease: molecular genetics of arrhythmogenic right ventricular dysplasia/cardiomyopathy. *Nature Clin. Pract. Cardiovasc. Med.* **5**, 258–267 (2008).
10. Okita, K. *et al.* A more efficient method to generate integration-free human iPS cells. *Nature Methods* **8**, 409–412 (2011).
11. Awad, M. M. *et al.* Recessive arrhythmogenic right ventricular dysplasia due to novel cryptic splice mutation in *PKP2*. *Hum. Mutat.* **27**, 1157 (2006).
12. Dalal, D. *et al.* Clinical features of arrhythmogenic right ventricular dysplasia/cardiomyopathy associated with mutations in plakophilin-2. *Circulation* **113**, 1641–1649 (2006).
13. Garcia-Gras, E. *et al.* Suppression of canonical Wnt/ β -catenin signaling by nuclear plakoglobin recapitulates phenotype of arrhythmogenic right ventricular cardiomyopathy. *J. Clin. Invest.* **116**, 2012–2021 (2006).
14. Kim, C. *et al.* Non-cardiomyocytes influence the electrophysiological maturation of human embryonic stem cell-derived cardiomyocytes during differentiation. *Stem Cells Dev.* **19**, 783–795 (2010).
15. Onay-Besikci, A. Regulation of cardiac energy metabolism in newborn. *Mol. Cell. Biochem.* **287**, 1–11 (2006).
16. Lopaschuk, G. D., Ussher, J. R., Folmes, C. D., Jaswal, J. S. & Stanley, W. C. Myocardial fatty acid metabolism in health and disease. *Physiol. Rev.* **90**, 207–258 (2010).
17. Ali, A. T. *et al.* The relationship between alkaline phosphatase activity and intracellular lipid accumulation in murine 3T3-L1 cells and human preadipocytes. *Anal. Biochem.* **354**, 247–254 (2006).
18. Taura, D. *et al.* Adipogenic differentiation of human induced pluripotent stem cells: comparison with that of human embryonic stem cells. *FEBS Lett.* **583**, 1029–1033 (2009).
19. Gregoire, F. M., Smas, C. M. & Sul, H. S. Understanding adipocyte differentiation. *Physiol. Rev.* **78**, 783–809 (1998).
20. Djouadi, F. *et al.* A potential link between peroxisome proliferator-activated receptor signalling and the pathogenesis of arrhythmogenic right ventricular cardiomyopathy. *Cardiovasc. Res.* **84**, 83–90 (2009).
21. Son, N.-H. *et al.* Cardiomyocyte expression of PPAR γ leads to cardiac dysfunction in mice. *J. Clin. Invest.* **117**, 2791–2801 (2007).
22. Willson, T. M., Lambert, M. H. & Kliewer, S. A. Peroxisome proliferator-activated receptor gamma and metabolic disease. *Annu. Rev. Biochem.* **70**, 341–367 (2001).
23. Waku, N. *et al.* The nuclear receptor PPAR γ individually responds to serotonin- and fatty acid-metabolites. *EMBO J.* **29**, 3395–3407 (2010).
24. Scolletta, S. & Biagioli, B. Energetic myocardial metabolism and oxidative stress: let's make them our friends in the fight against heart failure. *Biomed. Pharmacother.* **64**, 203–207 (2010).
25. Ferrick, D. A., Neilson, A. & Beeson, C. Advances in measuring cellular bioenergetics using extracellular flux. *Drug Discov. Today* **13**, 268–274 (2008).
26. Neubauer, S. The failing heart — an engine out of fuel. *N. Engl. J. Med.* **356**, 1140–1151 (2007).
27. Kléber, A. G. & Rudy, Y. Basic mechanisms of cardiac impulse propagation and associated arrhythmias. *Physiol. Rev.* **84**, 431–488 (2004).
28. Qyang, Y. *et al.* The renewal and differentiation of *Isl1*⁺ cardiovascular progenitors are controlled by a Wnt/ β -catenin pathway. *Cell Stem Cell* **1**, 165–179 (2007).
29. Cai, C. L. *et al.* *Isl1* identifies a cardiac progenitor population that proliferates prior to differentiation and contributes a majority of cells to the heart. *Dev. Cell* **5**, 877–889 (2003).
30. Lombardi, R. *et al.* Genetic fate mapping identifies second heart field progenitor cells as a source of adipocytes in arrhythmogenic right ventricular cardiomyopathy. *Circ. Res.* **104**, 1076–1084 (2009).

Supplementary Information is available in the online version of the paper.

Acknowledgements We thank the patients for their participation, microarray core facilities at SBMRI and Scripps Research Institute for their support, T. Yi for technical assistance, and G. W. Rogers for assistance in metabolic assays. This work was supported by NIH grants (R01 HL058493 and R01 HL101189) (to D.P.K.); NIH grants (R01 AR056712 and R01 AR052779) (to P.L.P.); California Institute of Regenerative Medicine (CIRM) grants (RS1-00171-1, RB2-01512 and RB4-06276) and NIH grant (R01 HL105194) (to H.-S.V.C.).

Author Contributions C.K. and H.-S.V.C. designed experiments and wrote the manuscript; J.E.M., H.C. and D.P.J. provided clinical assessment and patient's fibroblasts as well as analysis of data and assistance with preparation of the manuscript; C.K., J.W., S.W., C.W., S.S., N.G.K. and H.-S.V.C. performed the experiments; S.F. and P.L.P. helped C.K. in performing bisulphide sequencing; J.W. analysed microarray, Seahorse and immunocytochemical data; D.P.K. and T.C.L. provided scientific advice and primers for metabolic assays; C.K., J.W. and H.-S.V.C. performed and interpreted the calcium imaging data; all authors read and approved the manuscript, and H.-S.V.C. supervised the entire research project.

Author Information Reprints and permissions information is available at www.nature.com/reprints. The authors declare no competing financial interests. Readers are welcome to comment on the online version of the paper. Correspondence and requests for materials should be addressed to H.-S.V.C. (hsv_chen@burnham.org).

METHODS

Culture conditions and generation of PKP2 iPSCs. We obtained normal and mutant *PKP2* human fibroblasts from University of California-San Diego and Johns Hopkins University after informed consent was obtained from all subjects under approved study protocols by respective Institutional Review Boards at both universities and SBMRI. The clinical presentation, diagnostic data and genetic analysis of the first patient and her family members were published previously¹¹. Normal fibroblasts were obtained from discarded heart and skin of aborted fetuses of pregnant females without ARVD/C and any family history of ARVD/C. HEK 293T cells and human fibroblasts were cultured in Dulbecco's modified Eagle media (DMEM, HyClone) containing 10% heat-inactivated fetal bovine serum (FBS), 1 mM non-essential amino acids (NEAAs), 1× GlutaMAX, and 100 unit ml⁻¹ penicillin with 100 µg ml⁻¹ streptomycin (penicillin/streptomycin). Human iPSCs and H9 hESCs were cultured on irradiated mouse embryonic fibroblast (MEF) feeders in stem cell media containing Knockout (KO)-DMEM, 20% KO Serum Replacement (SR), 1 mM NEAAs, 1× GlutaMAX, 0.1 mM β-mercaptoethanol, penicillin/streptomycin, and 8 ng ml⁻¹ bFGF (Sigma). Retroviral plasmids, pMXs-hc-MYC, pMXs-hSOX2, pMXs-hKLF4, and pMXs-hOCT3/4, were purchased from Addgene. The protocol to generate iPSC lines with retroviral plasmids is essentially the same as previously published¹. Briefly, each pMXs retroviral vector along with pMs-gag/pol and PCMV-VSV-G plasmids at the ratio of 2:2:1 (total 20 µg) were cotransfected to HEK-293T cells for viral particle production. At 36 h after transfection, DMEM containing viruses from each plate were collected, mixed with 8 µg ml⁻¹ polybrene (Sigma), and immediately used to infect human fibroblasts (100,000 cells) by spinning transduction. Six days after the first infection, a half-million infected fibroblasts were trypsinized and plated on 100-mm dishes containing irradiated MEF feeder layers in 10% FBS-containing DMEM. One day later, the media was changed to stem cell media as described above. Induced pluripotent colonies were selected based on stem cell-like morphologies at 12–14 days after the initial infection. All culture media and reagents were purchased from Invitrogen unless indicated otherwise.

The episomal method of generating integration-free iPSC colonies is the same as published previously using pCXLE-EGFP, pCXLE-hOCT3/4-shp53-F, pCXLE-hSK and pCXLE-hUL (Addgene) episomal vectors¹⁰.

Cardiomyocyte differentiation. Our standard cardiogenic protocol to produce beating EBs was published previously¹⁴ and the cardiogenic media was EB media: KO-DMEM with 20% FBS, 1 mM NEAAs, 1× GlutaMAX, 1 mM β-mercaptoethanol and penicillin/streptomycin. A modified method published previously³¹ to enrich cardiac progenitor cells was also used and optimized for our hESCs and iPSCs. After beating EBs were observed, they were maintained in the EB media containing only 2% FBS. The method to purify cardiomyocyte spheroids (CSs) from EBs containing α-MHC-Puro^r was published previously^{14,32}.

Adipogenic conditions and pharmacological investigation. In the presence of very low serum concentrations (2% FBS), we used low micromolar concentrations of insulin (50 µg ml⁻¹) and dexamethasone (0.5 µM) as well as 0.25 mM IBMX (3F protocol) to induce adipogenic environment in beating EBs. 5 µM rosiglitazone (Cayman Chemical) and 200 µM indomethacin were added to the 3F protocol to form the 5F protocol. Beating EBs at 30 days of differentiation were treated with 3F- or 5F-media for 4–5 weeks before further investigation. 20 µg ml⁻¹ 13-HODE (Cayman) was used to activate PPAR-γ based on published dose–response data³³. 3 µM GW9662 (Cayman)²² or 0.5 µM T0070907 (Cayman)²³ was chosen to block 13-HODE action based on their half maximal inhibitory concentrations of specific inhibition of PPAR-γ activation and assumed competitive antagonism from 13-HODE. N-acetyl-cysteine³⁴, ascorbate (1 mM)³⁴, BIO (Tocris, 1–2.5 µM)²⁸ and Dickkopf-1 (Invitrogen)²⁸ were used according to previous publications. All pharmacological agents were purchased from Sigma unless otherwise indicated.

Karyotype analysis and teratoma formation. Karyotype analysis was performed by Cell Line Genetics. For teratoma formation, we injected ~10⁶ undifferentiated human iPSCs under the kidney capsule of SCID beige mice (Harlan Laboratories). Tumours were collected 8 weeks after injection for histological sections as well as haematoxylin and eosin staining by the SBMRI Histology Core facility. All animal protocols were approved by the SBMRI Animal Care and Use Committee.

RNA isolation and quantitative RT-PCR. Total RNA from JK#11 and SW#5, SW#6 and SW#7 clones was prepared using mirVana miRNA Isolation Kit (Ambion) from 5–10 EBs or puromycin-selected CSs after respective treatments. Complementary DNA (cDNA) was synthesized by the QuantiTect RT kit (Qiagen). Quantitative real-time polymerase chain reaction (qRT-PCR) was performed on a Roche LightCycler 480 using the LightCycler 480 SYBR Green I Master kit (Roche) according to protocols recommended by the manufacturer. Real time PCR cycle was 40 cycles (95 °C for 20 s, 60 °C for 30 s, and 72 °C for 30 s). Quantification was carried out by correcting for amplification efficiency of the primer using a standard curve, followed by normalizing transcript levels to the amount of total ubiquitously expressed *GAPDH* transcripts. Two physical replicates from each of ≥ 3 respective

sets of experiments were used to construct the histograms in all figures. All qRT-PCR and regular reverse transcription PCR (RT-PCR) primers are listed in Supplementary Tables 1 and 2.

Genomic and cDNA sequence analysis. Genomic DNA from three to five colonies of undifferentiated H9 and *PKP2*-iPSCs was collected using QIAamp DSP DNA Mini Kit (Qiagen). Genomic DNA of the *PKP2* gene region was amplified with 5'-TGATGAATAATAGTCTTTGCAGGTGTG (sense) and 5'-CTGAGGGCTGACCAGATGATCTGG (antisense)¹¹ by PCR (95 °C for 2–3 min; 40 cycles of 95 °C for 1 min, 55 °C for 1 min, and 72 °C for 1 min; followed by 5 min at 72 °C). PCR products were directly used for sequencing with two primers as published previously¹¹.

For the expressed *PKP2*, cDNA was synthesized with Oligo-dT primer and Superscript III reverse transcriptase (Invitrogen) from puromycin-purified hESC- or *PKP2* iPSC-CSs. The exon 12–14 regions of *PKP2* cDNA were amplified with two primers: exon 12-F: CTCTCCCTGATTGTTTCC and exon 14-R: GTGGCCGGTATCTACTGGTG. PCR products were directly cloned into bacteria using the TOPO TA Cloning kit (Invitrogen) and sequenced using T7 primers at SBMRI DNA analysis facility.

Bisulphite sequencing. Genomic DNA purification from ~2 × 10⁴ cells and bisulphite conversion of purified DNA was performed using the EZ DNA Methylation Direct Kit (Zymo Research) according to the manufacturer's instructions. The NANOG promoter region of converted DNA was amplified by PCR using primers: NANOG-1F: AGAGATAGGAGGTAAGTTTTTTT and NANOG-1R: ACTCC CACACAACTAACTTTTATTC. PCR products were directly cloned into bacteria and sequenced as mentioned above.

Gene microarray analysis. Total RNA was extracted from ~10⁵ cultured fibroblasts, or 5–10 undifferentiated hESCs or iPSCs. Sample amplification, labelling, and hybridization on Illumina Human HT-12v4 arrays were performed for all arrays using Illumina BeadStations in the SBMRI and Scripps Research Institute Microarray Core facilities according to the manufacturer's instructions (<http://www.illumina.com>). Quality control of raw data was performed with the GenomeStudio software (Illumina) and analysed with various software detailed in the Supplementary Information. For the heat map, values across each probe were standardized to have mean 0 and standard deviation (s.d.) 1, and then plotted on a colour scale where green denotes negative s.d.; black, 0; and red, positive s.d. The heat map showed close hierarchical clustering between hESCs and iPSCs based on 5,559 genes with at least twofold changes in mRNA expression levels when compared to the average levels of three fibroblast lines.

Lentiviral construction and viral transduction. Wild-type (WT) *PKP2* cDNA was first cloned into pcDNA3.1 plasmid and the Xba1–EcoRI fragment containing WT *PKP2* cDNA was then sub-cloned into pCDH-CMV-MCS-EF1-GFP lentivector (System Biosciences). System Biosciences lenti packaging and concentration kit was used for lentiviral production following manufacturer's instructions. We used the same protocol to generate lentiviruses containing control GFP and pRex1:Blasticidin//α-MHC:puromycin (Addgene).

Undifferentiated mutant *PKP2* iPSCs with α-MHC-puromycin resistance were generated according to the detailed protocol published previously^{14,32}. To generate mutant *PKP2* iPSC-CMs with overexpression of control GFP or WT *PKP2*-GFP, we transduced mutant *PKP2* iPSC-CMs (~10,000 cells per well) with 8 µg ml⁻¹ polybrene and control GFP or WT *PKP2*-GFP lentiviruses. At 72 h after transduction, mutant *PKP2* iPSC-CMs were dissociated and plated into Geltrex (Invitrogen)-coated 96-well plates (~1,000 cells per well) for pathogenic induction experiments.

Beta-catenin luciferase assay. Production of lentiviruses containing 7xTcf-Fluc//SV40-Puro^r (Addgene) is the same as described above. At 72 h after transduction, cells were replated at 2,000 cells per well for 6 h, then treated with media containing no BIO or 2.5 µM BIO for 16 h, and subsequently Luciferase assay was performed with Promega Luciferase assay system (catalogue no. PRE4030) according to manufacturer's instructions. BIO treatment was used to assess the efficacy of the Luciferase assay and we used GloMax-96 Microplate Luminometer (Promega) to measure luminescent values.

Immunocytochemistry, TUNEL count and lipid-laden cardiomyocyte count. We prepared 8-µm cryosections of EBs or CSs, and performed immunostaining according to standard protocols published previously¹⁴. Primary antibodies used were listed in Supplementary Table 3. Alexa Fluor 488 and Alexa Fluor 594 anti-mouse or anti-rabbit IgG (Invitrogen) were the secondary antibodies used for the fluorescence imaging. Samples were imaged on a deconvolution microscope (Observer.Z1, Zeiss) using the SlideBook software (Intelligent Imaging Innovations).

TUNEL staining with *in situ* Cell Death Detection Kit, TMR Red (Roche) and Nile Red staining (10 µg ml⁻¹, Sigma) were conducted during the secondary antibody incubation period according to the manufacturer's instructions. TUNEL and Nile Red staining were co-stained with one cardiac marker (anti-CTNI or -α-actinin antibodies) so that cardiomyocyte-specific apoptosis and lipid-production could be counted. Cryosections with Nile Red staining were magnified using

SlideBook so as to count the number of cardiomyocytes that contained any cytoplasmic, round lipid droplets as the lipid-laden cardiomyocytes. Supplementary Table 4 summarized all clones of each type of iPSCs used for various experiments. **Ca²⁺ imaging and curve fitting.** Puromycin-purified CSs were manually dissected to small clusters and clusters with slow beating rates (see Supplementary Fig. 16 for details) with or without pathogenic induction at approximately 60-day-old were loaded with Fura-2 AM (Molecular Probe). Ca²⁺ imaging was conducted with an inverted microscope (IX71, Olympus) and a cooled CCD camera (Hamamatsu) controlled by SlideBook. The [Ca²⁺]_i was calculated from fluorescence ratio at 500 nm after excitation at 340 and 380 nm with a LAMBDA DG-4 system (Sutter Instrument) according to the standard method³⁵. CSs were externally paced at 1 Hz with 8 V/8 ms stimulus strength, and the relaxation phase of Ca²⁺ signals of the last paced beat was analysed with the SigmaPlot software (SPSS) using the Marquardt–Levenberg algorithm to obtain the relaxation time constant (τ) of the best single-exponential curve fit. These CSs were then perfused with extra-cellular DMEM containing 5.8 mM Ca²⁺ (high Ca²⁺ media) for 10 min to reach steady-state¹⁴. The τ after a similar pacing protocol was then obtained for comparison. All experiments were conducted at 37 °C with all extracellular solutions pre-oxygenated with 95% O₂/5% CO₂. More than three sets of experiments were performed to construct Supplementary Fig. 13.

Seahorse metabolic assay. We used a Seahorse XF96 Extracellular Flux Analyzer²⁵ to measure oxygen consumption rate (OCR, pmol min⁻¹) and extracellular acidification rate (ECAR, the H⁺ production rate, mpH min⁻¹) of JK mutant PKP2 iPSC-CMs and normal hS-iPSC-CMs in XF96 well plates according to Installation and Operation Manual from Seahorse Bioscience. XF assay media contain unbuffered

DMEM, 5.5 mM glucose, and 0.5 mM carnitine. We used Etomoxir (ETO, 100 μ M), a specific CPT-1 inhibitor, to assess the degree of fatty acid oxidation, and 2-deoxyglucose (2-DG, 50 mM), a blocker of glycolysis and pyruvate oxidation, to assess glucose utilization³⁶.

Intracellular recording. Standard intracellular recording of action potentials was performed as described previously¹⁴.

Statistical analysis. Data were presented as the mean \pm s.e.m. Using the StatView/JMP program (SAS institute), statistical difference was analysed by an ANOVA procedure with post-hoc Tukey–Kramer test for multiple comparisons and by the unpaired *t*-test for pair-wise comparisons. A difference with a *P*-value < 0.05 was considered statistically significant and was labelled with an asterisk (*) in all figures.

31. Kattman, S. J. *et al.* Stage-specific optimization of activin/nodal and BMP signaling promotes cardiac differentiation of mouse and human pluripotent stem cell lines. *Cell Stem Cell* **8**, 228–240 (2011).
32. Kita-Matsuo, H. *et al.* Lentiviral vectors and protocols for creation of stable hESC lines for fluorescent tracking and drug resistance selection of cardiomyocytes. *PLoS ONE* **4**, e5046 (2009).
33. Nagy, L. *et al.* Oxidized LDL regulates macrophage gene expression through ligand activation of PPAR γ . *Cell* **93**, 229–240 (1998).
34. Dhalla, N. S., Elmoselhi, A. B., Hata, T. & Makino, N. Status of myocardial antioxidants in ischemia-reperfusion injury. *Cardiovasc. Res.* **47**, 446–456 (2000).
35. Grynkiewicz, G., Poenie, M. & Tsien, R. Y. A new generation of Ca²⁺ indicators with greatly improved fluorescence properties. *J. Biol. Chem.* **260**, 3440–3450 (1985).
36. Seahorse BioScience. <http://www.seahorsebio.com/learning/tech-writing.php>.

Obesity-induced overexpression of miR-802 impairs glucose metabolism through silencing of *Hnf1b*

Jan-Wilhelm Kornfeld^{1,2,3}, Catherina Baitzel^{1,2,3}, A. Christine Könnner^{1,2,3}, Hayley T. Nicholls^{1,2,3}, Merly C. Vogt^{1,2,3}, Karolin Herrmanns⁴, Ludger Scheja⁵, Cécile Haumaitre^{6,7}, Anna M. Wolf⁸, Uwe Knippschild⁸, Jost Seibler⁹, Silvia Cereghini^{6,7}, Joerg Heeren⁵, Markus Stoffel⁴ & Jens C. Brüning^{1,2,3}

Insulin resistance represents a hallmark during the development of type 2 diabetes mellitus and in the pathogenesis of obesity-associated disturbances of glucose and lipid metabolism^{1–3}. MicroRNA (miRNA)-dependent post-transcriptional gene silencing has been recognized recently to control gene expression in disease development and progression, including that of insulin-resistant type 2 diabetes. The deregulation of miRNAs miR-143 (ref. 4), miR-181 (ref. 5), and miR-103 and miR-107 (ref. 6) alters hepatic insulin sensitivity. Here we report that the expression of miR-802 is increased in the liver of two obese mouse models and obese human subjects. Inducible transgenic overexpression of miR-802 in mice causes impaired glucose tolerance and attenuates insulin sensitivity, whereas reduction of miR-802 expression improves glucose tolerance and insulin action. We identify *Hnf1b* (also known as *Tcf2*) as a target of miR-802-dependent silencing, and show that short hairpin RNA (shRNA)-mediated reduction of *Hnf1b* in liver causes glucose intolerance, impairs insulin signalling and promotes hepatic gluconeogenesis. In turn, hepatic overexpression of *Hnf1b* improves insulin sensitivity in *Lepr^{db/db}* mice. Thus, this study defines a critical role for deregulated expression of miR-802 in the development of obesity-associated impairment of glucose metabolism through targeting of *Hnf1b*, and assigns *Hnf1b* an unexpected role in the control of hepatic insulin sensitivity.

To identify novel miRNAs that are deregulated during obesity development and that may contribute to the development of obesity-associated insulin resistance and type 2 diabetes, we carried out 'miRNome' expression profiling using miRNA microarrays on RNA isolated from liver of two mouse models of obesity and insulin resistance: (1) high fat diet (HFD)-fed mice compared to normal chow diet fed mice, and (2) mice homozygous for the diabetes *db* mutation of the leptin receptor (*Lepr^{db/db}*) compared to wild-type controls. Out of 769 miRNA-specific probe sets, 334 (43.4%) and 311 (40.4%) miRNAs were detectable in liver of normal chow diet/HFD and control/*Lepr^{db/db}* livers, respectively (Supplementary Fig. 1a, b). In the liver of HFD-fed mice, expression of 66 miRNAs was significantly changed compared to miRNAs in normal chow diet controls, of which 90.1% were increased and 9.9% decreased (Supplementary Table 1). In *Lepr^{db/db}* livers, 156 miRNAs were significantly changed, the vast majority (99%) were upregulated in *Lepr^{db/db}* mice compared to controls (Supplementary Table 2). This screen confirmed an increased expression of miRNAs previously associated with obesity-induced insulin resistance, such as miR-103 and miR-107 (ref. 6), miR-143 (ref. 4) and miR-335 (ref. 7). In addition to these reported changes in obesity-associated miRNA expression, our screen revealed an even more pronounced overexpression of miR-802 in the liver of HFD and *Lepr^{db/db}* mice compared to controls (Supplementary Tables 1 and 2).

Increased miR-802 expression in obese mouse models was further confirmed by quantitative real-time PCR with reverse transcription (qRT-PCR) analyses, which revealed a 5.5-fold upregulation of miR-802 expression in the liver of HFD-fed mice and a 30-fold increase of miR-802 expression in the liver of *Lepr^{db/db}* mice (Fig. 1a). Northern blot analyses confirmed miR-802 expression in the liver of control mice, and hepatic overexpression in HFD and *Lepr^{db/db}* mice (Fig. 1a and Supplementary Fig. 1c). In addition, our analysis revealed that murine miR-802 expression is highly enriched in the liver of lean mice (Supplementary Fig. 1d). Moreover, we compared miR-802 expression in primary hepatocytes versus non-hepatocytes isolated from control mice, revealing that miR-802 expression was tenfold higher in hepatocytes versus non-hepatocytes, indicating that liver parenchymal cells represent the main source of miR-802 expression in this tissue (Supplementary Fig. 1e). miR-802 expression was also increased in other tissues of obese mice, such as in kidney, pancreatic islets, skeletal muscle, white adipose tissue (WAT) and the brain, particularly in *Lepr^{db/db}* mice (Fig. 1a), although to a lesser extent than the overexpression observed in the liver. Next, we quantified miR-802 expression in liver of a cohort of human individuals. miR-802 levels were significantly increased in overweight (body mass index (BMI) > 25) compared with lean individuals (Fig. 1b) and hepatic miR-802 expression significantly correlated with the BMI of these subjects (Fig. 1c). Taken together, hepatic expression of miR-802 is increased in dietary and genetic mouse models of obesity as well as in overweight human subjects.

To address whether increased miR-802 expression may contribute to the development of insulin resistance, we overexpressed miR-802 in the murine hepatoma cell line Hepa1-6 (Supplementary Fig. 2a). This resulted in a diminished ability of insulin to phosphorylate Akt, a central signalling node of insulin action (Fig. 2a). To further address potential mechanisms leading to insulin resistance upon miR-802 overexpression, we investigated the messenger RNA expression of insulin signalling mediators and known inducers of insulin resistance in the presence of miR-802 overexpression. This analysis revealed unaltered expression of mRNAs for *Akt1*, *Igf1r*, *Insr* and *Irs1* (Supplementary Fig. 2c), but showed significantly increased mRNA expression of suppressor of cytokine signalling *Socs1* and *Socs3* upon miR-802 overexpression (Fig. 2b). Because deregulation of hepatic glucose production represents a key step in the development of type 2 diabetes, we assessed the effect of miR-802 expression on the transcriptional regulation of glucose 6 phosphatase (*G6pc*) and phosphoenolpyruvate carboxykinase 1 (*Pck1*). This analysis revealed that in addition to inducing insulin resistance, overexpression of miR-802 enhanced both basal and forskolin-induced expression of *G6pc* (Fig. 2c), but not *Pck1* (Supplementary Fig. 2b).

¹Max-Planck-Institute for Neurological Research, Gleueler Strasse 50a, 50931 Cologne, Germany. ²Cologne Excellence Cluster on Cellular Stress Responses in Aging Associated Diseases (CECAD), Zùlpicher Strasse 47a, 50674 Cologne, Germany. ³Department of Mouse Genetics and Metabolism, Institute for Genetics, University of Cologne, Center for Endocrinology, Diabetes and Preventive Medicine (CEDP), University Hospital Cologne and Center for Molecular Medicine Cologne, Zùlpicher Strasse 47a, 50674 Cologne, Germany. ⁴Swiss Federal Institute of Technology (ETH Zurich), Institute of Molecular Health Science, Schafmattstrasse 22, 8093 Zurich, Switzerland. ⁵Department of Biochemistry and Molecular Cell Biology, University Hospital Hamburg-Eppendorf, Martinistrasse 52, 20246 Hamburg, Germany. ⁶INSERM U 969, 9 Quai Saint Bernard, 75005 Paris, France. ⁷CNRS Université Pierre et Marie Curie UMR7622, 9 Quai Saint Bernard, 75005 Paris, France. ⁸Department of General and Visceral Surgery, University Hospital of Ulm, Albert-Einstein-Allee 23, 89081 Ulm, Germany. ⁹TaconicArtemis GmbH, Neurather Ring 1, 51063 Cologne, Germany.

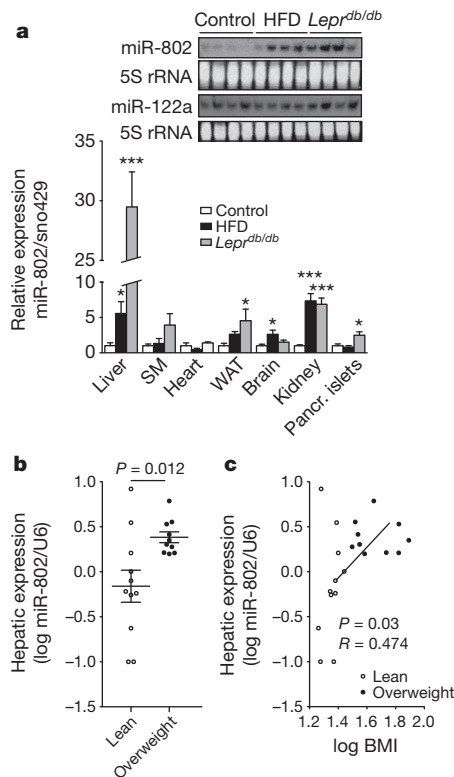


Figure 1 | miR-802 expression is increased in obese mice and humans.

a, Comparative qRT-PCR analysis (bottom) of miR-802 expression in high fat diet (HFD)-fed mice (liver, *n* = 6; skeletal muscle (SM), *n* = 8; heart, *n* = 6; white adipose tissue (WAT), *n* = 8; brain, *n* = 8; kidney, *n* = 7; pancreatic islets, *n* = 7), *Lepr^{db/db}* (liver, *n* = 6; SM, *n* = 8; heart, *n* = 6; WAT, *n* = 7; brain, *n* = 8; kidney, *n* = 6; pancreatic islets, *n* = 5) and chow-fed control mice (liver, *n* = 6; SM, *n* = 8; heart, *n* = 7; WAT, *n* = 7; brain, *n* = 8; kidney, *n* = 14; pancreatic islets, *n* = 12). Northern blot analysis (top) of miR-802 expression in liver of control, HFD-fed and *Lepr^{db/db}* mice (*n* = 4 in each group). **b**, qRT-PCR quantification of human miR-802 expression in liver of lean (*n* = 11) and obese (*n* = 10) individuals. **c**, Correlation between hepatic miR-802 levels and BMI (*n* = 21) in lean (*n* = 11) and obese (*n* = 10) individuals. Expression was normalized to *sno429* in mice and to *U6* in humans; all error bars indicate mean \pm s.e.m.; and **P* < 0.05, ****P* < 0.001.

To verify whether overexpression of miR-802 also causes insulin resistance and impairs glucose metabolism *in vivo*, we aimed to mimic the obesity-associated increase of miR-802 expression via transgenic overexpression of miR-802 in lean mice. To do this we generated mice with the capacity for doxycycline (Dox)-induced overexpression of miR-802 (hereafter referred to as miR-802 mice, Supplementary Fig. 2d–f). Insertion of the transgenic miR-802 expression cassette in the absence of Dox stimulation did not alter body weight, glucose tolerance or insulin tolerance (Supplementary Fig. 2g–i). Upon Dox administration, we observed an increase of miR-802 expression in the liver, skeletal muscle, white adipose tissue, pancreatic islets and kidney of transgenic compared to control animals (Supplementary Fig. 2j). Profiling of global miRNA-expression of Dox-treated control and transgenic mice revealed no major differences in global miRNA-expression between both groups, indicating that transgenic overexpression of miR-802 does not interfere with transcription and processing of small RNAs in a non-specific manner (Supplementary Fig. 2k). Thus, transgenic overexpression of miR-802 mimicked the miR-802 expression observed in obese mice, with the exception of a higher degree of miR-802 expression in skeletal muscle and white adipose tissue compared to the obese state. Although we detected no differences in blood glucose concentrations (Supplementary Fig. 2l), transgenic mice developed glucose intolerance and insulin resistance upon miR-802 overexpression (Fig. 2d, e). Furthermore, homeostatic model assessment

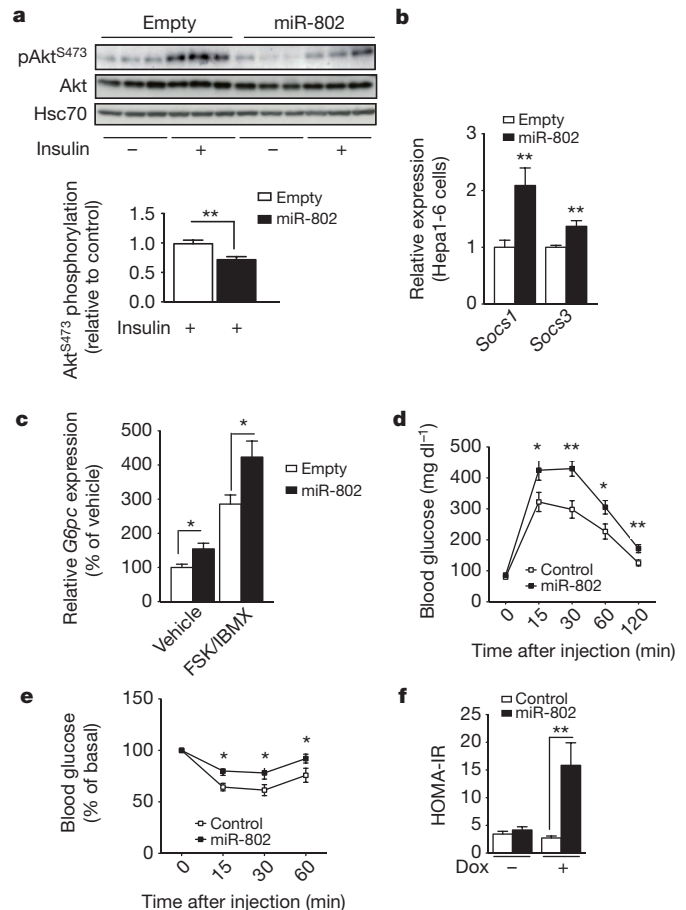


Figure 2 | Overexpression of miR-802 impairs insulin action and glucose metabolism. **a**, Immunoblot analysis (top) and quantification (bottom) of insulin-stimulated Akt Serine 473 phosphorylation versus total Akt protein levels in Hepa1-6 cells in the absence (empty vector) or presence of miR-802 overexpression. For quantification, the mean value for insulin-stimulated intensity of cells transfected with empty vector was set to 1. The results were obtained from three independent experiments, each performed in triplicate and a representative immunoblot is shown. Hsc70 is also known as Hspa8. **b**, qRT-PCR analysis of *Socs1* and *Socs3* expression in Hepa1-6 cells upon transfection with control or miR-802 expression vector. **c**, qRT-PCR analysis of *G6pc* expression in Hepa1-6 cells upon transfection with empty vector or miR-802 expression vector following stimulation with vehicle or forskolin (FSK) and 3-isobutyl-1-methylxanthine (IBMX). **d**, Glucose tolerance tests of miR-802 (*n* = 11) and control mice (*n* = 11) treated with doxycycline. **e**, Insulin tolerance tests of miR-802 (*n* = 11) and control mice (*n* = 9) after doxycycline administration. **f**, HOMA-IR of miR-802 (*n* = 11) and control littermates (*n* = 11). Dox, doxycycline. In all panels error bars indicate mean \pm s.e.m.; **P* < 0.05, ***P* < 0.01.

of insulin resistance (HOMA-IR) indices of mice overexpressing miR-802 were significantly increased (Fig. 2f). Collectively, overexpression of miR-802 in mice impairs glucose homeostasis *in vivo*.

Next, we assessed the functional contribution of increased miR-802 expression to the development of insulin resistance by reducing miR-802 expression in obese mice. We synthesized locked nucleic acids (LNA) specifically targeting the seed sequence of miR-802, as well as appropriate control LNA in which four nucleotides of the seed sequence were mutated. C57BL/6 mice, which had been receiving a HFD for 12 weeks, were injected with either anti-miR-802 or control LNA. We observed an 80% reduction of hepatic miR-802 expression in mice that had received the anti-miR-802 LNA compared to those receiving control LNA (Fig. 3a). Although anti-miR-802 treatment also efficiently reduced miR-802 expression in the kidney of obese mice, it only slightly reduced miR-802 expression in skeletal

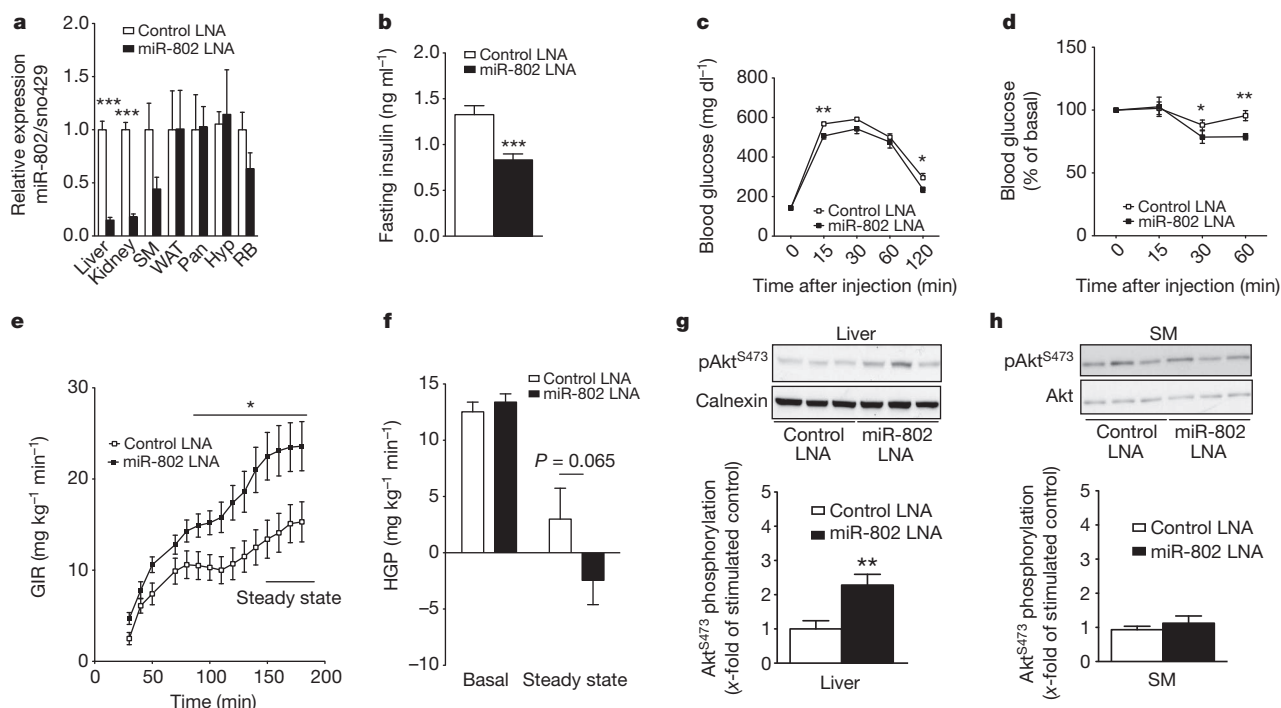


Figure 3 | Suppression of miR-802 expression improves obesity-associated insulin resistance and glucose intolerance. **a**, miR-802 expression after intravenous injection of HFD-fed mice with miR-802 locked nucleic acids (LNA) (liver, $n = 9$; kidney, $n = 10$; SM, $n = 6$; WAT, $n = 6$; pancreatic islets, $n = 3$; hypothalamus (Hyp), $n = 10$; rest of brain (minus the hypothalamus) (RB), $n = 9$) or control LNA (liver, $n = 7$; kidney, $n = 8$; skeletal muscle, $n = 6$; WAT, $n = 6$; Pan, $n = 4$; Hyp, $n = 7$; RB, $n = 6$). **b**, Serum insulin levels of HFD-fed mice treated with miR-802 LNA ($n = 8$) or control LNA ($n = 8$). **c**, Glucose tolerance tests of HFD-fed mice administered with miR-802 LNA ($n = 19$) or control LNA ($n = 17$). **d**, Insulin tolerance tests of HFD-fed mice treated with miR-802 LNA ($n = 14$) or control LNA ($n = 16$). **e**, Glucose infusion rates (GIR) during euglycaemic-hyperinsulinaemic clamps

in HFD-fed mice treated with control LNA ($n = 9$) or miR-802 LNA ($n = 12$). **f**, Hepatic glucose production (HGP) of HFD-fed mice treated with control LNA ($n = 9$) or miR-802 LNA ($n = 12$) before (basal) and during (steady state) euglycaemic-hyperinsulinaemic clamp analysis. $P = 0.065$ in unpaired one-tailed (based on the improved insulin sensitivity of miR-802 LNA treated mice) Student's *t*-test. **g**, **h**, Immunoblot analysis of insulin-stimulated Akt^{S473} phosphorylation in liver (**g**) and skeletal muscle (**h**) of HFD-fed mice treated with control and miR-802 LNA (top). Densitometric quantification of Akt phosphorylation in liver (**g**) and skeletal muscle (**h**) of control ($n = 9$) or miR-802-LNA-treated mice ($n = 12$) (bottom). In all panels error bars indicate mean \pm s.e.m.; * $P < 0.05$, ** $P < 0.01$, *** $P < 0.001$.

muscle and did not affect miR-802 expression in the pancreas, WAT, hypothalamus or other brain areas (Fig. 3a). Anti-miR-802 treatment had no effect on body weight, body fat content or circulating serum leptin concentrations (Supplementary Fig. 3a–c) as well as no effect on adipocyte size or gene expression of pro-inflammatory mediators in WAT (Supplementary Fig. 3d–f). On the other hand, the obesity-associated rise in serum insulin concentrations was diminished in HFD animals treated with miR-802 LNA (Fig. 3b). In accordance with this, glucose tolerance tests revealed an improvement of glucose tolerance upon miR-802 inhibition (Fig. 3c). Moreover, insulin sensitivity was also improved upon inhibition of miR-802 (Fig. 3d). To further examine the exact mechanisms and cell type through which reducing miR-802 expression improves glucose metabolism, we performed euglycaemic-hyperinsulinaemic clamps in HFD-fed mice, which had received either control or anti-miR-802 LNA. Reduction of miR-802 expression significantly increased glucose infusion rate by 1.5-fold during the clamp (Fig. 3e and Supplementary Fig. 4a), whereas analysis of insulin-stimulated glucose uptake in skeletal muscle and WAT did not reveal any differences between mice receiving control or anti-miR-802 LNA (Supplementary Fig. 4b). By contrast, the ability of insulin to suppress glucose production was enhanced in mice receiving anti-miR-802 compared to those receiving control LNA, although this effect did not reach statistical significance (Fig. 3f). Moreover, the ability of insulin to inhibit *G6pc* expression in the liver as well as *G6pc* and *Pck1* expression in the kidney was enhanced upon inhibition of miR-802 expression (Supplementary Fig. 4c). Consistent with improved hepatic insulin sensitivity, insulin-stimulated Akt phosphorylation was enhanced in the liver (Fig. 3g),

but not in the skeletal muscle of anti-miR-802 treated animals during the clamp (Fig. 3h). Taken together, the findings show that reduction of miR-802 expression in diet-induced obese mice results in improvement of insulin sensitivity predominantly by increasing insulin action in the liver.

We aimed to identify those mRNA(s) that are targeted by miR-802 and serve as its molecular effector(s) in disease progression. Using a stringent bioinformatics approach, we identified 26 putative murine miR-802 target genes (Supplementary Fig. 5a), among which the gene encoding hepatocyte nuclear factor 1 beta (*Hnf1b*; also known as transcription factor 2, *Tcf2*) harboured a miR-802 binding site, which is also conserved in the human *HNF1B* gene (Supplementary Fig. 5b). *HNF1B* has been causally linked to the development of maturity onset diabetes of the young (MODY) type 5 (ref. 8) and variants in *HNF1B* have also been linked to predisposition for type 2 diabetes⁹. Inclusion of the *Hnf1b* 3' untranslated region (UTR) into a luciferase reporter construct reduced luciferase activity compared to a reporter lacking the *Hnf1b* 3' UTR upon transfection into Hepa1-6 cells (Fig. 4a and Supplementary Fig. 5c). Overexpression of miR-802 led to a further reduction of luciferase activity when the reporter construct contained the *Hnf1b* 3' UTR (Fig. 4a). In contrast, mutation of the conserved miR-802 binding motif abrogated reduced luciferase expression (Fig. 4a). Moreover, overexpression of miR-802 in Hepa1-6 cells led to reduced *Hnf1b* protein expression (Supplementary Fig. 5d). *In vivo*, hepatic *Hnf1b* protein expression was reduced by 50% in *Lepr^{db/db}* mice, which exhibit increased miR-802 expression compared to controls (Fig. 4b), whereas hepatic *Hnf1b* protein expression was significantly increased in mice that had been treated with anti-miR-802 LNA

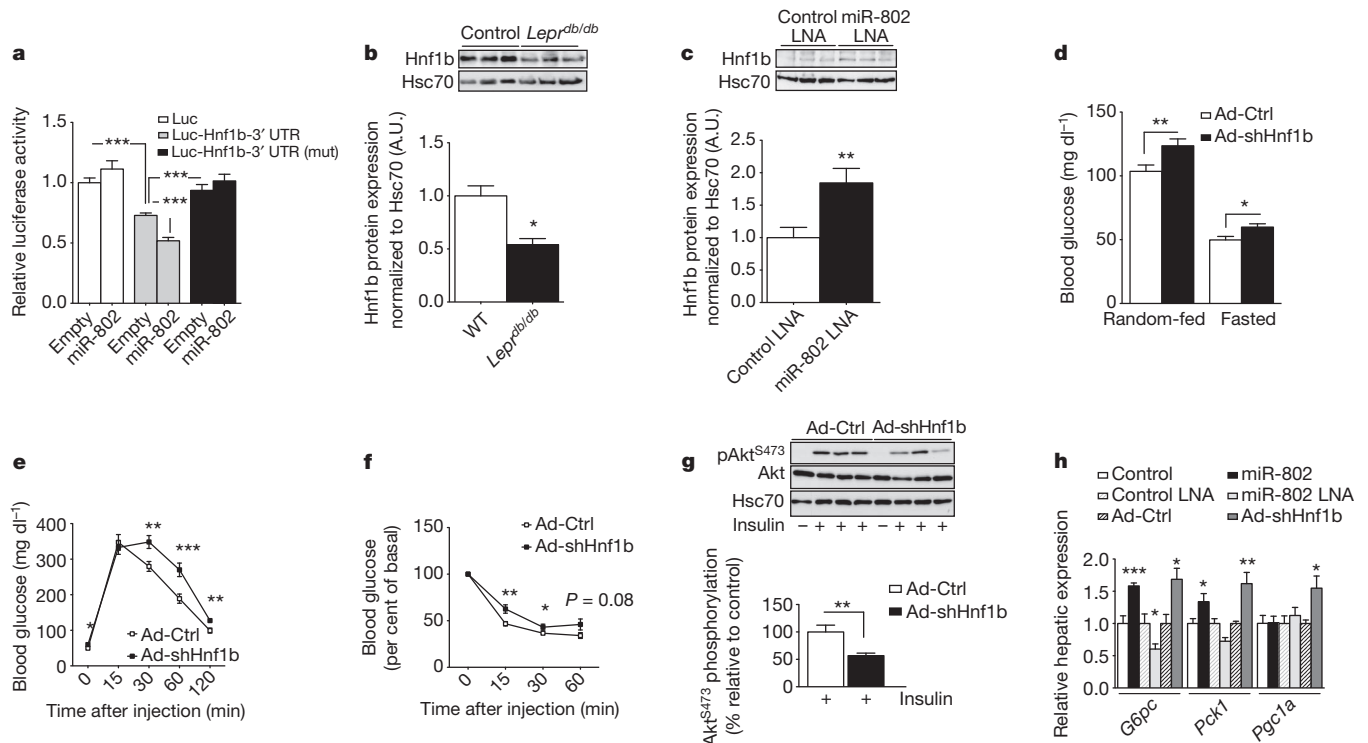


Figure 4 | Silencing of the miR-802 target *Hnf1b* impairs insulin action and glucose metabolism. **a**, Relative luciferase activity of the firefly reporter constructs containing either the wild-type or mutated 3' UTR of the murine *Hnf1b* gene. Firefly luciferase activity was normalized to the activity of *Renilla* luciferase. Luciferase activity of the luciferase-only containing construct was set to 1. One-way ANOVA was carried out followed by Bonferroni post-hoc analysis, * $P < 0.05$, ** $P < 0.01$, *** $P < 0.001$. **b**, Immunoblot analysis (top) and densitometry quantification (bottom) of hepatic *Hnf1b* expression in the liver of *Lep^{db/db}* ($n = 3$) and control mice ($n = 3$). **c**, Representative immunoblot analysis (top) and densitometric quantification (bottom) of hepatic *Hnf1b* expression in HFD-fed control LNA treated mice ($n = 10$) and miR-802 LNA treated mice ($n = 9$). **d**, Blood glucose concentrations of random-fed and overnight-fasted mice treated with Ad-shHnf1b ($n = 20$) or

Ad-Ctrl ($n = 20$). **e**, Glucose-tolerance tests of mice treated with Ad-shHnf1b ($n = 20$) or Ad-Ctrl ($n = 20$). **f**, Insulin tolerance tests of mice administered Ad-shHnf1b ($n = 20$) or Ad-Ctrl ($n = 20$). **g**, Representative immunoblot analysis (top) and quantification (bottom) of insulin-stimulated Akt Serine 473 phosphorylation versus total Akt protein levels in liver of mice delivered Ad-shHnf1b ($n = 7$) or Ad-Ctrl ($n = 7$). For quantification, the mean value for insulin-stimulated intensity of control animals was set to 100%. **h**, qRT-PCR analysis of *G6pc*, *Pck1* and *Pgc1a* mRNA expression in liver of Dox-treated miR-802 transgenic ($n = 6$) versus control animals ($n = 6$); HFD-fed mice treated with miR-802 LNA ($n = 9$) and control LNA ($n = 7$); and wild-type mice treated with Ad-shHnf1b ($n = 9$) and Ad-Ctrl ($n = 9$). In all panels error bars indicate mean \pm s.e.m.; * $P < 0.05$, ** $P < 0.01$, *** $P < 0.001$.

(Fig. 4c). Functionally, shRNA-mediated silencing of *Hnf1b* in Hepa1-6 cells led to enhancement of basal and forskolin-induced *G6pc* and *Pck1* expression (Supplementary Fig. 6a) and to increased expression of *Socs1* and *Socs3* (Supplementary Fig. 6b), similar to what was observed upon miR-802 overexpression. Taken together, these experiments define *Hnf1b* as a target of miR-802-dependent post-transcriptional silencing in liver *in vitro* and *in vivo*.

To gain further insights into how partial reduction of *Hnf1b* expression affects glucose metabolism, we performed glucose and insulin tolerance tests in heterozygous *Hnf1b*^{+/-} mice (*Hnf1b*^{+/-}) and control littermates¹⁰. However, these analyses revealed no differences in glucose or insulin tolerance between these groups of mice (Supplementary Fig. 7a, b). Surprisingly, analysis of *Hnf1b* mRNA and protein expression revealed only a negligible reduction of *Hnf1b* mRNA and unaltered protein expression in liver (Supplementary Fig. 7c, d) and kidney of *Hnf1b*^{+/-} mice (Supplementary Fig. 7e, f). Interestingly, *Hnf1b*^{+/-} mice exhibited reduced hepatic miR-802 expression (Supplementary Fig. 7g), potentially contributing to unaltered *Hnf1b* protein expression in these animals. Thus, we next aimed to acutely and efficiently reduce hepatic *Hnf1b* expression through generation of adenoviruses expressing shRNA targeting *Hnf1b* (Ad-shHnf1b) and control viruses (Ad-Ctrl). When administered intravenously to the control mice, injection of Ad-shHnf1b led to a significant, 40% reduction of hepatic *Hnf1b* mRNA expression (Supplementary Fig. 8a). Importantly, analysis of global miRNA expression in these animals revealed that pol-III-dependent expression

of the *Hnf1b*-shRNA did not generally interfere with expression and processing of small RNA molecules (Supplementary Fig. 9). Ad-shHnf1b-mediated reduction of hepatic *Hnf1b* protein expression had no effect on body weight, fat mass, adipocyte size or WAT inflammation (Supplementary Fig. 8b–e), whereas it resulted in significantly increased blood glucose concentrations (Fig. 4d). Moreover, glucose and insulin tolerance tests (GTT and ITT, respectively) revealed a profound reduction in glucose tolerance and insulin sensitivity in Ad-shHnf1b-treated animals (Fig. 4e, f), and insulin-evoked phosphorylation of Akt was significantly impaired in these mice (Fig. 4g). In addition, microarray gene expression profiling of mRNAs isolated from liver of Ad-shHnf1b- and Ad-Ctrl-treated mice revealed the coordinate induction of key catabolic, fasting-associated gene ontology (GO) pathways such as gluconeogenesis, beta-oxidation of fatty acids, oxidative phosphorylation and the tricarboxylic acid cycle upon reduction of *Hnf1b* expression (Supplementary Fig. 10 a–d). qRT-PCR analyses confirmed the significant induction of *Pgc1a* and its gluconeogenic target genes *Pck1* and *G6pc* upon reduction of *Hnf1b* protein expression (Fig. 4h). Conversely, expression of *G6pc* and *Pck1* mRNA was reduced in anti-miR-802 LNA treated HFD mice and increased in the liver of mice with conditional overexpression of miR-802 (Fig. 4h).

We next investigated whether adenoviral overexpression of *Hnf1b* can affect the increased *G6pc* expression observed upon miR-802 overexpression in Hepa1-6 cells. Indeed, a 1.5-fold increase in *Hnf1b* expression reversed the increased *G6pc* mRNA expression upon concomitant miR-802 overexpression (Supplementary Fig. 11 a, b). Next,

we aimed to restore hepatic Hnf1b expression via adenovirus-mediated overexpression of Hnf1b in liver of *Lepr^{db/db}* mice. Injection of a Hnf1b-expressing adenovirus resulted in a ninefold increase in hepatic Hnf1b expression compared to *Lepr^{db/db}* mice, which had been injected with a GFP-expressing control vector (Supplementary Fig. 11c). Increasing hepatic Hnf1b expression led to an improvement of insulin sensitivity in *Lepr^{db/db}* mice and to a reduction of HOMA-IR indices (Supplementary Fig. 11d, e), supporting the model that miR-802-mediated reduction of hepatic Hnf1b expression contributes to the metabolic impairment observed upon development of obesity.

Our study reveals an important role for obesity-induced overexpression of miR-802 in the development of obesity-associated insulin resistance. Interestingly, the degree of increased hepatic expression of miR-802 in *Lepr^{db/db}* mice exceeded that of miRNAs, whose upregulation has been described so far in the context of obesity-associated insulin resistance. The observation that overexpression of miR-802 causes insulin resistance and impairs glucose tolerance, whereas reducing miR-802 expression in obese mice improves these metabolic parameters, clearly indicates a functional role for increased miR-802 expression in the development of obesity-associated insulin resistance. Importantly, increased miR-802 expression is not restricted to murine obesity models, but is also detected in obese humans, thus characterizing miR-802 and its target gene(s) as potential new targets for the treatment of obesity-associated insulin resistance and type 2 diabetes. Among these potential target genes, we have functionally validated Hnf1b as a bona fide miR-802 target both *in vitro* and *in vivo*. Hnf1b constitutes a member of the homeodomain-containing superfamily of liver-enriched transcription factors, and truncated or loss-of-function HNF1B alleles cause MODY type 5 in humans^{8,11}. In addition, some genome-wide association studies revealed an association between HNF1B variants with the susceptibility to develop type 2 diabetes, whereas others failed to observe this effect in different populations¹². Although the functional consequences of dysfunctional HNF1B alleles are well understood for the development of MODY type 5 in humans, as they affect not only pancreatic β -cell function but also cause insulin resistance^{13,14}, surprisingly few studies have addressed the role of Hnf1b in liver. Our experiments clearly reveal an important role for Hnf1b in control of hepatic insulin sensitivity and glucose metabolism *in vivo*. We demonstrate that both overexpression of miR-802 or knockdown of Hnf1b leads to upregulation of hepatic *Socs1* and *Socs3* expression. These findings are consistent with earlier reports that Hnf1b represses *Socs3* expression and in turn enhances hepatocyte growth factor signalling in kidney¹⁵. Because both *Socs1* and *Socs3* are characterized mediators of insulin resistance *in vitro* and *in vivo*^{16,17}, miR-802-evoked, Hnf1b-dependent derepression of *Socs* transcription represents a candidate pathway to cause insulin resistance. Although the mechanism(s) of how Hnf1b controls hepatic glucose metabolism clearly requires further investigation, our study reveals an important role for miR-802- and Hnf1b-dependent regulation of insulin sensitivity and glucose metabolism *in vivo*.

METHODS SUMMARY

LNA synthesis and administration. Custom-made miRCURY locked nucleic acids (LNA) for *in vivo* application were designed and synthesized as unconjugated and fully phosphorothiolated oligonucleotides by Exiqon. The sequence of the LNA targeting miR-802 was fully complementary to the mature miRNA

sequence: 5'-AATCTTTGTTACTG-3' (miR-802 LNA); the appropriate mismatch LNA control was mutated in four nucleotide positions: 5'-TATGTACTTACTG-3' (control LNA). LNA were intravenously delivered to HFD-fed mice at a concentration of 25 mg kg⁻¹ body weight in 1×PBS. Mice were injected on two consecutive days and killed two weeks after LNA administration.

Received 16 May; accepted 15 November 2012.

1. Saltiel, A. R. & Kahn, C. R. Insulin signalling and the regulation of glucose and lipid metabolism. *Nature* **414**, 799–806 (2001).
2. Gregor, M. F. & Hotamisligil, G. S. Inflammatory mechanisms in obesity. *Annu. Rev. Immunol.* **29**, 415–445 (2011).
3. Glass, C. K. & Olefsky, J. M. Inflammation and lipid signaling in the etiology of insulin resistance. *Cell Metab.* **15**, 635–645 (2012).
4. Jordan, S. D. *et al.* Obesity-induced overexpression of miRNA-143 inhibits insulin-stimulated AKT activation and impairs glucose metabolism. *Nature Cell Biol.* **13**, 434–446 (2011).
5. Zhou, B. *et al.* Downregulation of miR-181a upregulates sirtuin-1 (SIRT1) and improves hepatic insulin sensitivity. *Diabetologia* **55**, 2032–2043.
6. Trajkovski, M. *et al.* MicroRNAs 103 and 107 regulate insulin sensitivity. *Nature* **474**, 649–653 (2011).
7. Nakanishi, N. *et al.* The up-regulation of microRNA-335 is associated with lipid metabolism in liver and white adipose tissue of genetically obese mice. *Biochem. Biophys. Res. Commun.* **385**, 492–496 (2009).
8. Horikawa, Y. *et al.* Mutation in hepatocyte nuclear factor-1 β gene (*TCF2*) associated with MODY. *Nature Genet.* **17**, 384–385 (1997).
9. Han, X. *et al.* Implication of genetic variants near *SLC30A8*, *HHEX*, *CDKAL1*, *CDKN2A/B*, *IGF2BP2*, *FTO*, *TCF2*, *KCNQ1*, and *WFS1* in type 2 diabetes in a Chinese population. *BMC Med. Genet.* **11**, 81 (2010).
10. Barbacci, E. *et al.* Variant hepatocyte nuclear factor 1 is required for visceral endoderm specification. *Development* **126**, 4795–4805 (1999).
11. Lindner, T. H. *et al.* A novel syndrome of diabetes mellitus, renal dysfunction and genital malformation associated with a partial deletion of the pseudo-POU domain of hepatocyte nuclear factor-1 β . *Hum. Mol. Genet.* **8**, 2001–2008 (1999).
12. Wen, J. *et al.* Investigation of type 2 diabetes risk alleles support *CDKN2A/B*, *CDKAL1*, and *TCF7L2* as susceptibility genes in a Han Chinese cohort. *PLoS ONE* **5**, e9153 (2010).
13. Haumaitre, C. *et al.* Severe pancreas hypoplasia and multicystic renal dysplasia in two human fetuses carrying novel *HNF1 β /MODY5* mutations. *Hum. Mol. Genet.* **15**, 2363–2375 (2006).
14. Bellanné-Chantelot, C. *et al.* Clinical spectrum associated with hepatocyte nuclear factor-1 β mutations. *Ann. Intern. Med.* **140**, 510–517 (2004).
15. Ma, Z. *et al.* Mutations of HNF-1 β inhibit epithelial morphogenesis through dysregulation of SOCS-3. *Proc. Natl Acad. Sci. USA* **104**, 20386–20391 (2007).
16. Howard, J. K. & Flier, J. S. Attenuation of leptin and insulin signaling by SOCS proteins. *Trends Endocrinol. Metab.* **17**, 365–371 (2006).
17. Ueki, K., Kondo, T., Tseng, Y. H. & Kahn, C. R. Central role of suppressors of cytokine signaling proteins in hepatic steatosis, insulin resistance, and the metabolic syndrome in the mouse. *Proc. Natl Acad. Sci. USA* **101**, 10422–10427 (2004).

Supplementary Information is available in the online version of the paper.

Acknowledgements J.-W.K. was supported by stipends from EMBO and CECAD. S.C. received funds from INSERM, CNRS and EU FP7 (Marie Curie Initial Training Network BOLD). This work was in part supported by ERC grant 'Metabolomirs' (to M.S.), by a grant to J.H. by the DFG (SFB 841) and DFG funding to J.C.B. (Br1492-7). We thank D. Wagner-Stippich, J. Alber, P. Scholl and B. Hampel for technical assistance.

Author Contributions J.C.B. and J.-W.K. conceived the study and wrote the manuscript. J.-W.K. and C.B. performed most experiments. A.C.K. performed the euglycaemic-hyperinsulinaemic clamp experiments. H.T.N. performed adenoviral treatments of mice. M.C.V. contributed to bioinformatical analyses. K.H. and M.S. analysed miR-802 expression in murine tissues. J.S. aided in the generation of miR-802 transgenic mice. C.H. and S.C. provided tissues and analysed glucose metabolism in *Hnf1b^{+/-}* mice. A.M.W., U.K., L.S. and J.H. provided and analysed human liver explants for miR-802 expression. All authors approved the manuscript.

Author Information Gene expression data was deposited with Gene Expression Omnibus (GEO) under accession number GSE42188. Reprints and permissions information is available at www.nature.com/reprints. The authors declare no competing financial interests. Readers are welcome to comment on the online version of the paper. Correspondence and requests for materials should be addressed to J.C.B. (bruening@nf.mpg.de).

Microbiota restricts trafficking of bacteria to mesenteric lymph nodes by CX₃CR1^{hi} cells

Gretchen E. Diehl¹, Randy S. Longman^{1,2*}, Jing-Xin Zhang^{1†*}, Beatrice Breart^{1†}, Carolina Galan¹, Adolfo Cuesta^{1,3}, Susan R. Schwab¹ & Dan R. Littman^{1,3}

The intestinal microbiota has a critical role in immune system and metabolic homeostasis, but it must be tolerated by the host to avoid inflammatory responses that can damage the epithelial barrier separating the host from the luminal contents^{1–6}. Breakdown of this regulation and the resulting inappropriate immune response to commensals are thought to lead to the development of inflammatory bowel diseases such as Crohn's disease and ulcerative colitis⁷. We proposed that the intestinal immune system is instructed by the microbiota to limit responses to luminal antigens. Here we demonstrate in mice that, at steady state, the microbiota inhibits the transport of both commensal and pathogenic bacteria from the lumen to a key immune inductive site, the mesenteric lymph nodes (MLNs). However, in the absence of *Myd88* or under conditions of antibiotic-induced dysbiosis, non-invasive bacteria were trafficked to the MLNs in a CCR7-dependent manner, and induced both T-cell responses and IgA production. Trafficking was carried out by CX₃CR1^{hi} mononuclear phagocytes, an intestinal-cell population previously reported to be non-migratory⁸. These findings define a central role for commensals in regulating the migration to the MLNs of CX₃CR1^{hi} mononuclear phagocytes endowed with the ability to capture luminal bacteria, thereby compartmentalizing the intestinal immune response to avoid inflammation.

How the intestinal immune system discriminates between commensal and pathogenic microorganisms remains an enigma. Commensals have the same immunostimulatory molecules as pathogenic bacteria and have been shown to trigger inflammation and disease if they penetrate the intestinal epithelial barrier. Host sensing of commensals has been shown to be important for the proper development and functionality of the immune system, as germ-free mice have an altered immune system organization and reduced cellularity, especially in the small-intestinal lamina propria, compared to mice harbouring a complex microbiota (reviewed in ref. 9). This feature of host immune system dependence on the microbiota led us to examine whether commensal bacteria have a role in modulating mucosal immune responses to specific microbes. To this end, we investigated the consequences of antibiotic-mediated depletion of the intestinal microbiota⁵ (Supplementary Fig. 1a) on the host response to a non-invasive strain of *Salmonella enterica* serovar Typhimurium. We used this strain because, although it has limited CD18-dependent access to the blood and spleen, it cannot cross the epithelium overlying intestinal lymphoid tissues, and hence does not reach the Peyer's patches^{10,11}. We were thus able to investigate a potential role for commensals in regulating access of this non-invasive strain of *Salmonella* to the lamina-propria-draining lymphatics that traffic luminal contents to the MLNs, sites of immune system induction.

Oral infection with non-invasive *Salmonella* normally induces an IgG but not an IgA response¹⁰ (Fig. 1a). Unexpectedly, after treatment with antibiotics, infected mice mounted a strong *Salmonella*-specific

faecal IgA response in addition to an IgG response (Fig. 1a). In untreated mice, *Salmonella*-specific T cells were limited to the spleen and small-intestinal lamina propria, but antibiotic-treated mice additionally had antigen-specific T cells in the MLNs (Fig. 1b and Supplementary Fig. 1b). This was a *Salmonella*-specific response, as there was no difference in interferon- γ (IFN- γ)-producing T cells after anti-CD3 stimulation and there was little IFN- γ production from MLN T cells isolated from mice that did not receive antigenic stimulation or that were *Salmonella*-naïve (Supplementary Fig. 1b and data not shown). This indicates that immune responses specific for non-invasive *Salmonella* are only observed in the lamina-propria-draining MLNs if commensal bacteria are depleted before infection.

We proposed that commensals could influence the amount of antigen (in this case, *Salmonella*) that reaches the MLNs. In untreated mice, infection with both pathogenic and non-pathogenic strains of

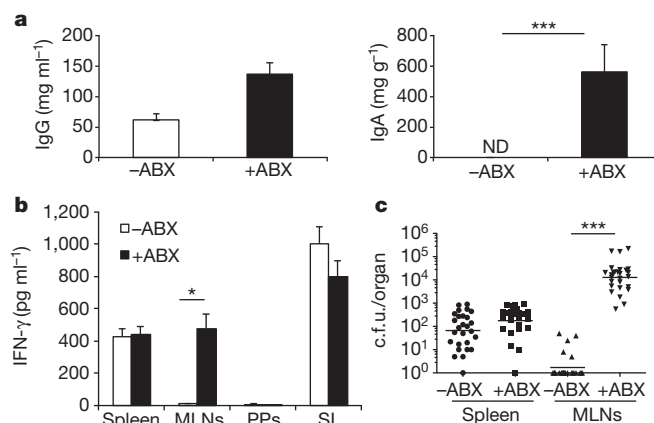


Figure 1 | Induction of immune response against non-invasive *Salmonella* after antibiotic treatment. **a–c**, Mice were left untreated (–ABX) or treated with antibiotic (+ABX) for 4 weeks. **a**, Mice were orally infected with non-invasive, non-pathogenic *Salmonella* (*invA/aroA*), and *Salmonella*-specific IgG in the blood and IgA in the faeces were measured by ELISA. Bars represent the average from five mice from one of three independent experiments. ND, not detected. *** $P < 0.001$, unpaired t -test. Error bars represent standard error of the mean (s.e.m.). **b**, T cells from spleen, mesenteric lymph nodes (MLNs), Peyer's patches (PPs) and small-intestinal lamina propria (SI) of mice infected with non-invasive *Salmonella* were cultured with irradiated splenocytes and boiled *Salmonella* antigen, and IFN- γ was measured by ELISA. Bars represent three mice per treatment group and are representative of two independent experiments. * $P < 0.05$, unpaired t -test. Error bars represent s.e.m. **c**, Bacterial titres in the spleen and MLNs were determined for mice infected with non-invasive *Salmonella* (*invA*). c.f.u., colony-forming units. Data points represent organs from a single mouse; data were pooled from six experiments. *** $P < 0.0001$, Mann–Whitney Test. Error bars represent the geometric mean.

¹Molecular Pathogenesis Program, The Kimmel Center for Biology and Medicine of the Skirball Institute, New York University School of Medicine, New York, New York 10016, USA. ²Division of Digestive and Liver Diseases, Department of Medicine, Columbia University, New York, New York 10032, USA. ³Howard Hughes Medical Institute, New York University School of Medicine, New York, New York 10016, USA. [†]Present addresses: Sanofi Oncology, Cambridge, Massachusetts 02139, USA (J.-X.Z.); Dynamics of Immune Responses, Institut Pasteur, 75015 Paris, France, and Institut National de la Santé et de la Recherche Médicale U668, Equipe Avenir, 75015 Paris, France (B.B.).

*These authors contributed equally to this work.

non-invasive *Salmonella* resulted in bacteria reaching the spleen, but very few bacteria were observed in the MLNs (Fig. 1c and Supplementary Fig. 1c). Importantly, after antibiotic treatment, there were high titres of the bacteria in the MLNs, as previously reported¹², in addition to the spleen (Fig. 1c and Supplementary Fig. 1c). As expected, no bacteria were found in the Peyer's patches in either condition (data not shown). The increase in bacteria reaching the MLNs was unlikely to be the result of increased epithelial permeability after treatment with antibiotics, as we did not observe an increase in bacteria reaching the spleen. This was confirmed by using a direct test for intestinal permeability with fluorescein isothiocyanate (FITC)-conjugated dextran (FITC-dextran) gavage (Supplementary Fig. 1d). In addition, the increased *Salmonella* in the MLNs was not a consequence of impaired colonization resistance on depletion of the microbiota, as there was equivalent expansion of *Salmonella* in the presence of any individual antibiotic, yet only vancomycin or ampicillin treatment allowed for its trafficking to the MLNs and induction of the bacterium-specific IgA (Supplementary Fig. 2).

Our results raised the question of whether commensal bacteria could gain access to the MLNs in the same way as non-invasive *Salmonella*, allowing for the induction of mucosal-specific immune responses. Antibiotic-treated and untreated mice were infected by oral gavage with a non-invasive, non-pathogenic bacterium, *Escherichia coli* K-12. In the control mice, the bacteria could not be found in the MLNs, nor was there induction of *E. coli*-specific IgA (Supplementary Fig. 3a, b). By contrast, in antibiotic-treated mice *E. coli* was detected in the MLNs and there was induction of a specific IgA response (Supplementary Fig. 3a, b). These results indicate that the microbiota functions to limit the colonization of the MLNs by both commensal and pathogenic bacteria, thereby constraining the induction of intestinal immune responses against both.

To investigate whether a specific microbial recognition system is involved in microbiota-dependent restraint of *Salmonella* trafficking to the MLNs, we examined mice bearing mutations in diverse signalling pathways. As observed in antibiotic-treated mice, *Myd88*^{-/-} mice infected with non-invasive *Salmonella* had increased bacterial counts in the MLNs compared to *Myd88*^{+/-} littermate controls (Fig. 2a). Consistent with our observations in commensal-depleted animals, there was also induction of *Salmonella*-specific IgA and antigen-induced IFN- γ -producing T cells in the MLNs in *Myd88*^{-/-} animals but not in littermate controls (Fig. 2b, c). In contrast, there was no increase in bacteria reaching the MLNs or induction of IgA in NOD2- or NALP3-deficient (NALP3 also known as NLRP3) animals, suggesting that MyD88 specifically relays a microbial signal via a Toll-like receptor (TLR) (Supplementary Fig. 4a). This indicates that detection of commensals in a MyD88-dependent manner functions to reduce bacterial colonization of the MLNs and thereby reduce intestinal immune responses.

We next sought to identify microbial products that could prevent trafficking of non-invasive *Salmonella* to the MLNs in antibiotic-treated mice. Re-colonizing antibiotic-treated mice with the caecal contents of unmanipulated mice reduced the amount of *Salmonella* that reached the MLNs (Supplementary Fig. 4b), as did short pre-treatment with caecal contents (2 days before infection with non-invasive *Salmonella*) or with heat-killed *E. coli* or *Salmonella* (Fig. 2d). These results indicate that complete re-colonization was not required to abrogate trafficking of the bacteria. Pre-feeding mice with heat-killed bacteria before infection did not reduce the load of *Salmonella* in the intestine, even though the amount of bacteria reaching the MLNs was reduced (Fig. 2d and Supplementary Fig. 4c). This indicates that recognition of bacterial products can function to reduce colonization of internal organs with a non-invasive bacterium without affecting the intestinal load of that bacterium. As expected, pre-treating MyD88-deficient animals with heat-killed *Salmonella* had no effect (Supplementary Fig. 4d). Pre-treating mice with lipopolysaccharide (LPS), bacterial DNA or zymosan (Fig. 2d and data not shown) also

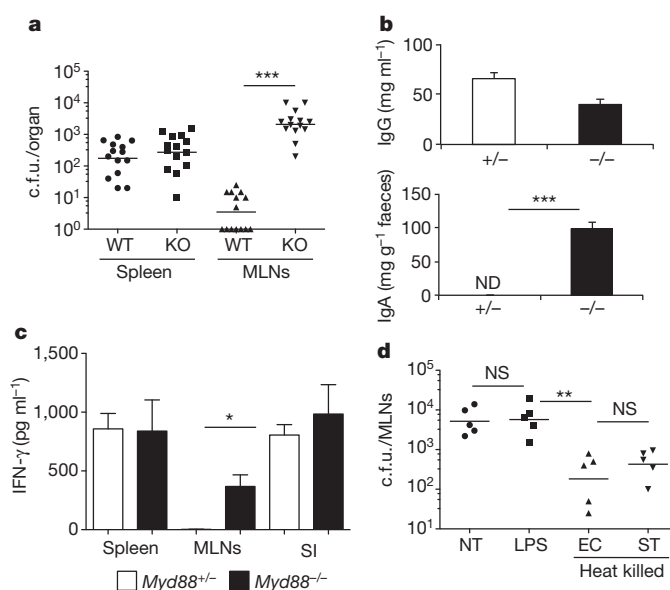


Figure 2 | MyD88-dependent signals limit non-invasive *Salmonella* entry in the MLN. **a**, *Myd88*^{-/-} (knockout; KO) or heterozygous (wild-type; WT) littermates were infected with non-invasive *Salmonella* (*invA*) and bacterial titres were determined in the spleen and MLNs. Data points represent organs from a single mouse. Data were pooled from three independent experiments. ****P* < 0.0001, Mann–Whitney Test. Error bars represent the geometric mean. **b**, *Myd88*^{-/-} or heterozygous littermates were infected with non-invasive, non-pathogenic *Salmonella*, and blood and faeces were analysed for *Salmonella*-specific IgG and IgA. ND, not detected. Bars represent data from three mice per genotype. Data are representative of three independent experiments. ****P* < 0.001, unpaired *t*-test. Error bars represent s.e.m. **c**, IFN- γ production by spleen, MLNs and small-intestinal lamina propria (SI) T cells from *Salmonella*-infected mice of the indicated genotype. Analysis was as in Fig. 1b. Bars represent three animals per genotype. Data are representative of two independent experiments. **P* < 0.05, unpaired *t*-test. Error bars represent s.e.m. **d**, Antibiotic-treated B6 mice were left untreated (NT) or gavaged twice with LPS or heat-killed *E. coli* (EC) or *Salmonella* (ST). Twenty-four hours later the mice were infected orally with non-invasive *Salmonella*. Bacterial titres in the MLNs were determined 2 days later. Each point represents individual mice from one of two independent experiments. ***P* < 0.002, one-way analysis of variance (ANOVA). Error bars represent the geometric mean. NS, not significant.

failed to limit MLN titres of *Salmonella*, despite the ability of LPS to induce upregulation of the antimicrobial protein Reg-3 γ (Supplementary Fig. 4e). Thus, commensal-dependent intestinal epithelial responses may not be sufficient to prevent trafficking of non-invasive *Salmonella* to the MLNs.

Antigens and pathogens that can penetrate the mucus layer and cross the intestinal epithelium to enter the lamina propria are thought to be trafficked by dendritic cells to the MLNs, where they can prime immune responses^{13,14}. This conclusion was based on experiments with invasive bacteria that colonized Peyer's patches^{14,15}. Although lamina propria CD11c⁺ cells were also shown to be required for non-invasive *Salmonella* colonization of the lamina propria and the MLNs, it was concluded that the dendritic cells were required only for bacterial translocation across the epithelium^{12,16}. We wanted to determine whether non-invasive bacteria, which cannot colonize Peyer's patches, would also be transported to the MLNs by lamina propria dendritic cells. Our observation that *Salmonella* trafficked to the MLNs only after dysbiosis induced by antibiotics, in the absence of barrier disruption, suggested a specific mechanism that restricts access of bacteria to intestinal immune-priming sites. We therefore examined whether dendritic cells or other lamina propria myeloid cells were responsible for transporting *Salmonella* to the MLNs and initiating immune responses to it. We first used CD11c–diphtheria toxin receptor (DTR) mice, in which injection of diphtheria toxin results in

selective depletion of CD11c⁺ cells^{17,18}. CD11c-DTR bone marrow chimaeric mice were treated with antibiotics and then injected with diphtheria toxin to deplete dendritic cells (Supplementary Fig. 5) before oral infection with non-invasive *Salmonella*. There was no decrease in splenic titres of non-invasive *Salmonella* in diphtheria-toxin-treated versus untreated mice (Fig. 3a), arguing against a role for dendritic cells in bacterial entry to the tissue. However, bacterial titres in the MLNs were significantly reduced after ablation of CD11c⁺ cells (Fig. 3a). Thus, in microbiota-depleted mice, CD11c⁺ cells are at least partially responsible for transporting non-invasive *Salmonella* to the MLNs. As dendritic cell migration to the MLNs requires their expression of CCR7 (refs 19, 20), we treated *Ccr7*^{+/+} or *Ccr7*^{-/-} mice with antibiotics to deplete commensal bacteria before infecting mice orally with non-invasive *Salmonella*. There was a substantial reduction in *Salmonella* in the MLNs of commensal-depleted *Ccr7*^{-/-} mice compared to wild-type mice (Fig. 3b), indicating that this chemokine receptor is required for transport of the bacteria to the MLN.

The CD11c⁺ mononuclear phagocytes within the lamina propria have been subdivided into two major populations: CX₃CR1⁺ and CD103⁺ cells (Supplementary Fig. 6a and reviewed in ref. 21). CX₃CR1⁺ cells can be further divided into cells expressing high and intermediate levels of the chemokine receptor. CX₃CR1^{hi} cells, which also express CD14 and low levels of CD103 (Supplementary Fig. 6a)^{16,21}, have been described to have both dendritic cell- and macrophage-like characteristics. They differentiate from monocyte precursors^{15,16,22}, are thought to be non-migratory in response to *in vivo* TLR activation⁸, and are poorly immunostimulatory *in vitro*. CX₃CR1^{int} cells, which also differentiate from monocyte precursors, have been described to have dendritic cell-like characteristics²². CD103⁺ cells, which do not express CX₃CR1, are thought to be conventional myeloid dendritic cells, as they develop from a classical dendritic cell precursor^{15,16}, express CCR7, can activate naive T cells *in vitro*, and migrate to the MLNs on TLR stimulation^{8,15,23}. In contrast with previous reports that found CCR7 only expressed on CD103⁺ cells^{8,15}, we observed upregulation of CCR7 on both CX₃CR1⁺ and

CD103⁺ cells after *in vitro* stimulation with LPS (Supplementary Fig. 6b), suggesting that both have migratory potential.

To assess whether intestinal CD103⁺ or CX₃CR1⁺ cells were involved in transporting *Salmonella* to the MLNs in the absence of commensals, we next examined mice in which a *loxP*-flanked stop cassette upstream of the DTR-coding region was knocked into the *Cx3cr1* locus (Supplementary Fig. 7a). Expression of CD11c-Cre excises the stop cassette, allowing for DTR expression and selective depletion of CD11c⁺ CX₃CR1^{hi} cells on administration of diphtheria toxin, with no effect on CD11c⁺ CX₃CR1^{int} or CD11c⁺ CD103⁺ cells (Supplementary Fig. 7b, c). Because monocytes have been reported to take up wild-type *Salmonella*²⁴, we determined that they were not depleted in the diphtheria-toxin-treated animals, but were actually increased in number (Supplementary Fig. 8). When mice were orally infected with non-invasive *Salmonella* after diphtheria-toxin-mediated depletion of the CX₃CR1^{hi} mononuclear cells, there was a marked reduction in the number of bacteria reaching the MLNs (Fig. 3c). This result, which was unexpected in the light of recent studies showing that only the CD103⁺ cells migrate from the lamina propria to the MLNs after TLR activation, suggested that CX₃CR1^{hi} cells are responsible for trafficking of the non-invasive bacteria to the MLNs on disturbance of the microbiota.

To evaluate further the hypothesis that CX₃CR1^{hi} cells are responsible for trafficking of non-invasive *Salmonella* to the MLNs, we orally infected antibiotic-treated CX₃CR1-green fluorescent protein (GFP) mice²⁵ with the bacterium and analysed the cell populations in the MLNs. There was an increase in dendritic cells of all subsets after antibiotic treatment (Supplementary Fig. 9a), but after infection with non-invasive *Salmonella* there was a further increase only in CX₃CR1^{hi} cells (Fig. 3d and Supplementary Fig. 9a), and this was not observed if mice were pre-treated with heat-killed *Salmonella* before infection (Supplementary Fig. 9b), consistent with the limited number of bacteria reaching the MLNs in these animals (Fig. 2d). Furthermore, the co-stimulatory molecule CD80 was upregulated on CX₃CR1^{hi} cells, but not on CD103⁺ dendritic cells, after infection of antibiotic-treated mice with non-invasive *Salmonella* (Fig. 3e), implicating the CX₃CR1^{hi}

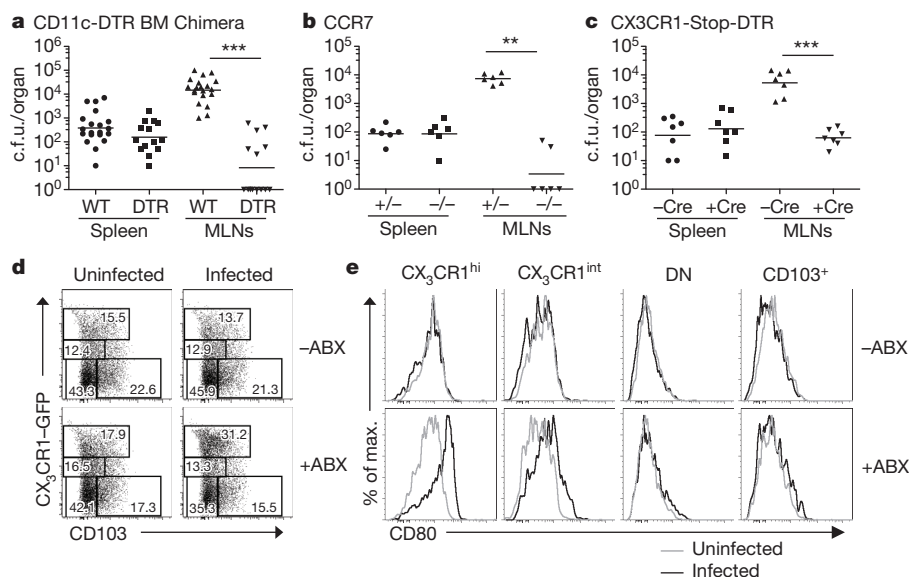


Figure 3 | Colonization of MLNs by non-invasive *Salmonella* requires CCR7-dependent trafficking of CX₃CR1^{hi} cells. **a–c**, Antibiotic-treated mice of the indicated genotype and littermate controls were orally infected with non-invasive *Salmonella*, and bacterial titres in the spleen and MLNs were determined. **a**, **c**, Mice were treated with diphtheria toxin for two consecutive days before infection. **a**, ****P* < 0.0001; **b**, ***P* < 0.005; **c**, ****P* = 0.0006; all Mann–Whitney test. Error bars represent the geometric mean. **d**, Analysis of dendritic cell subsets in MLNs of untreated or antibiotic-treated *Cx3cr1*^{gfp/+}

mice that were mock infected or infected with non-invasive *Salmonella*. MLN cells were isolated at 48 h, gated on the MHCII⁺ CD11c⁺ population, and analysed for expression of CX₃CR1 and CD103. Percentages are shown in each gate. Absolute numbers are shown in Supplementary Fig. 9a. **e**, Expression of CD80 on intestinal myeloid cell subsets. Cells were gated on the indicated cell populations as shown in **d**. For data in **a–c**, points represent individual mice pooled from independent experiments. Panels **d** represent individual mice from one of five independent experiments.

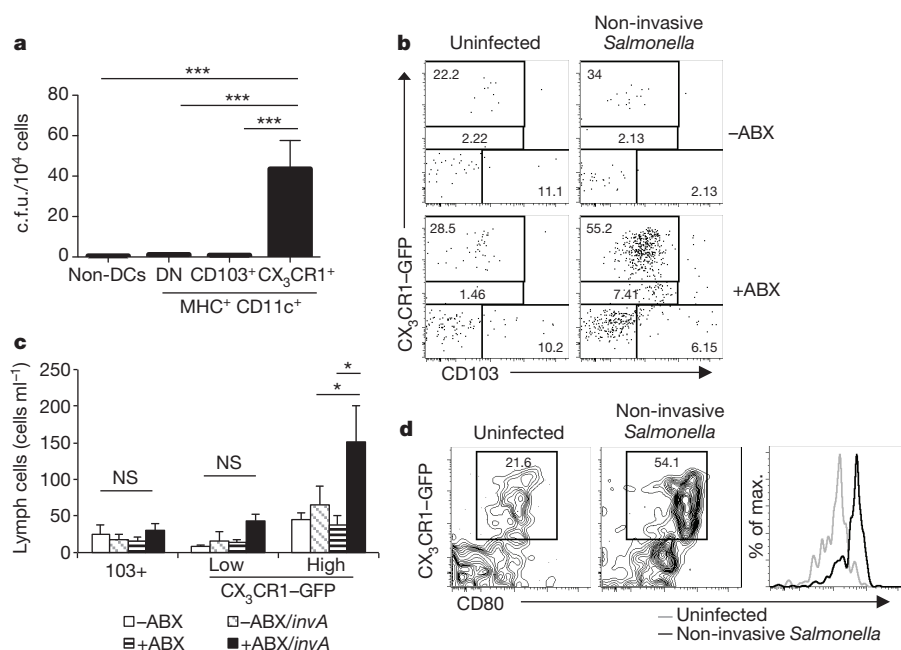


Figure 4 | CD103⁻ CX3CR1⁺ cells migrate into afferent lymphatics of antibiotic-treated animals. **a**, CX3CR1⁺ CD103⁺ or CX3CR1⁻ CD103⁻ (double-negative; DN) cells (gated on the MHCII⁺ CD11c⁺ population, as in Fig. 3d) from the MLNs were isolated from antibiotic-treated, non-invasive *Salmonella*-infected mice. The numbers of bacteria per 10⁴ cells were determined by plating. No bacteria were observed from cells isolated from uninfected or infected but antibiotic-untreated mice. DCs, dendritic cells. Bars represent pooled data from 15 individual mice from 4 independent experiments. ****P* < 0.0001, one-way ANOVA with Bonferroni correction. Error bars represent s.e.m. **b–d**, Untreated or antibiotic-treated *Cx3cr1*^{sfp/+}

mice were left uninfected or were infected with non-invasive *Salmonella*. At 48 h, cells in the intestinal lymph were isolated and analysed by flow cytometry. **b**, Cells were gated on the MHCII⁺ CD11c⁺ population and analysed for expression of CX3CR1-GFP and CD103. Data are representative of three independent experiments. **c**, Quantification of MHCII⁺ CD11c⁺ CX3CR1-GFP⁺ cells in the afferent lymph of the indicated mice. ***P* < 0.01, one-way ANOVA with Bonferroni correction. Error bars represent s.e.m. **d**, CD80 expression on CX3CR1-GFP⁺ cells from lymph of antibiotic-treated mice with and without *Salmonella* infection.

cells in priming the anti-*Salmonella* T-cell response. To confirm that CX3CR1⁺ cells had taken up non-invasive *Salmonella*, we sorted CX3CR1⁺ and CD103⁺ cells from the MLNs of infected antibiotic-treated mice (Supplementary Fig. 9c) and assayed for cells containing colony-forming units. Most of the bacteria were recovered from the CX3CR1⁺ cells rather than the CD103⁺ cells, and no bacteria could be detected from cells derived from untreated infected mice (Fig. 4a). These results suggest that commensal-derived signals prevent CX3CR1⁺ cells from ferrying bacteria to the MLNs, although we cannot rule out additional mechanisms, for example, reduced killing of internalized bacteria under these conditions.

To examine more directly whether CX3CR1⁺ cells migrate from the small intestine to the MLNs, we assayed the afferent intestinal lymph in antibiotic-treated or untreated CX3CR1-GFP mice after oral infection with non-invasive *Salmonella*. In uninfected or non-antibiotic-treated animals, very few cells were detected and, as expected, TLR activation with R848 resulted in the preferential release of CD103⁺ dendritic cells into the lymph (Supplementary Fig. 9d). Unlike previous reports⁸, we observed CX3CR1⁺ cells in the afferent lymph of unmanipulated animals, with a higher proportion of CX3CR1^{hi} than CX3CR1^{int} cells (Fig. 4b, c and Supplementary Fig. 9d). The number and proportion of these cells in the afferent lymph was markedly higher after infection of antibiotic-treated mice with non-invasive *Salmonella* (Fig. 4b, c). Additionally, in antibiotic-treated mice infected with non-invasive *Salmonella* there was upregulation of CD80 in lymph-derived CX3CR1⁺ cells (Fig. 4d).

Our results indicate the existence of a novel CX3CR1^{hi}-cell-mediated pathway for antigen access from the intestinal lumen and for immune priming. Inhibition of this pathway through a MyD88-dependent mechanism may contribute to maintenance of immunological tolerance towards commensal microbes. There is thus another role for microbiota-initiated signalling in the host: limiting immune

priming against intestinal antigens by inhibiting trafficking of a lamina propria cell population and phagocytosed bacteria to the MLNs. We speculate that disruption of this pathway for inhibition of antigen trafficking may be an important defence strategy on infection with invasive microbes, but could also contribute to inflammatory bowel disease in humans. Inflammatory bowel disease is thought to result from an inappropriate immune response against commensal microorganisms, and it has been reported that patients with inflammatory bowel disease have changes in their microbiota²⁶. Our results suggest that this could lead to increased intestinal priming and intestinal inflammation, which can itself cause dysbiosis^{27,28}, thus amplifying the pathogenic process. Furthermore, in a susceptible individual, reductions in certain classes of bacteria might be sufficient to trigger this increased trafficking. In conditions of infection, the dysbiosis that results from intestinal inflammation^{28,29} may be beneficial, as it may allow for the induction of immune responses against pathogens and not commensals. Further work will be needed to determine if a particular microbe or microbial signal is required for regulation of CX3CR1⁺-cell migration. Therapeutic modulation of these cells may attenuate intestinal inflammation or enhance priming for mucosal vaccines.

METHODS SUMMARY

Mice. C57BL/6 mice were purchased from Taconic Farms or Jackson Laboratories. For inducible CX3CR1-DTR mice, we introduced a *loxP*-floxed stop cassette followed by DTR into the *Cx3cr1* locus. Mice were subsequently crossed to CD11c-Cre mice (Jackson Laboratories).

Depletion of gut commensal microbiota. Animals were treated with antibiotics as described⁷. Mice were switched to water without antibiotics for 2 days before infecting them as described later.

Infection with *Salmonella Typhimurium* and *E. coli*. Mice were infected orally with 1 × 10⁸ *Salmonella AinvA* c.f.u. (stationary phase) or 2 × 10⁸ *AaroA/AinvA* c.f.u. Organ titres were determined 2 days after infection. For T-cell analysis, mice

were analysed 10 days after infection. For antibody titres, mice were infected on day 0 and day 15.

Measurement of T-cell and antibody responses. Analyses of serum and faecal proteins for *Salmonella*-specific IgG and IgA by ELISA were performed as described¹⁰. For T-cell responses, T cells from the indicated organ were stimulated *in vitro* for 72 h. IFN- γ in the supernatant was measured by ELISA (BD Biosciences).

Cell isolation. Small-intestinal lamina propria cells were isolated as previously described³⁰.

Lymph collection. Afferent lymph was isolated as described⁸.

Antibodies, cell staining and flow cytometry. Flow cytometric analysis was performed on a LSR II (BD Biosciences) instrument and analysed using FlowJo software (Tree Star). All antibodies were from BD Pharmingen or eBiosciences.

Heat-killed *Salmonella* and *E. coli*. *Salmonella* or *E. coli* were heated to 85 °C for 60 min. Mice were administered 1×10^{10} heat-killed bacteria orally daily for 2 days before infecting with non-invasive *Salmonella*.

Statistical analysis. One-way ANOVA with Bonferroni's post-test or unpaired *t*-test was performed using a 95% confidence interval. All analyses were performed using GraphPad Prism version 4.0. Differences were considered significant at *P* values of <0.05.

Full Methods and any associated references are available in the online version of the paper.

Received 5 May; accepted 21 November 2012.

Published online 13 January 2013.

- Macpherson, A. J. & Uhr, T. Compartmentalization of the mucosal immune responses to commensal intestinal bacteria. *Ann. NY Acad. Sci.* **1029**, 36–43 (2004).
- Hooper, L. V. & Gordon, J. I. Commensal host-bacterial relationships in the gut. *Science* **292**, 1115–1118 (2001).
- Hooper, L. V., Midtvedt, T. & Gordon, J. I. How host-microbial interactions shape the nutrient environment of the mammalian intestine. *Annu. Rev. Nutr.* **22**, 283–307 (2002).
- Hooper, L. V. *et al.* Molecular analysis of commensal host-microbial relationships in the intestine. *Science* **291**, 881–884 (2001).
- Rakoff-Nahoum, S., Paglino, J., Eslami-Varzaneh, F., Edberg, S. & Medzhitov, R. Recognition of commensal microflora by toll-like receptors is required for intestinal homeostasis. *Cell* **118**, 229–241 (2004).
- Mazmanian, S. K., Liu, C. H., Tzianabos, A. O. & Kasper, D. L. An immunomodulatory molecule of symbiotic bacteria directs maturation of the host immune system. *Cell* **122**, 107–118 (2005).
- Balfour Sartor, R. Bacteria in Crohn's disease: mechanisms of inflammation and therapeutic implications. *J. Clin. Gastroenterol.* **41** (suppl. 1), S37–S43 (2007).
- Schulz, O. *et al.* Intestinal CD103⁺, but not CX3CR1⁺, antigen sampling cells migrate in lymph and serve classical dendritic cell functions. *J. Exp. Med.* **206**, 3101–3114 (2009).
- Macpherson, A. J. & Harris, N. L. Interactions between commensal intestinal bacteria and the immune system. *Nature Rev. Immunol.* **4**, 478–485 (2004).
- Vazquez-Torres, A. *et al.* Extraintestinal dissemination of *Salmonella* by CD18-expressing phagocytes. *Nature* **401**, 804–808 (1999).
- Griffin, A. J. & McSorley, S. J. Development of protective immunity to *Salmonella*, a mucosal pathogen with a systemic agenda. *Mucosal Immunol.* **4**, 371–382 (2011).
- Hapfelmeier, S. *et al.* Microbe sampling by mucosal dendritic cells is a discrete, MyD88-independent step in *ΔinvG* *S. Typhimurium* colitis. *J. Exp. Med.* **205**, 437–450 (2008).
- Mowat, A. M. Anatomical basis of tolerance and immunity to intestinal antigens. *Nature Rev. Immunol.* **3**, 331–341 (2003).
- Macpherson, A. J. & Uhr, T. Induction of protective IgA by intestinal dendritic cells carrying commensal bacteria. *Science* **303**, 1662–1665 (2004).
- Bogunovic, M. *et al.* Origin of the lamina propria dendritic cell network. *Immunity* **31**, 513–525 (2009).
- Varol, C. *et al.* Intestinal lamina propria dendritic cell subsets have different origin and functions. *Immunity* **31**, 502–512 (2009).
- Jung, S. *et al.* *In vivo* depletion of CD11c⁺ dendritic cells abrogates priming of CD8⁺ T cells by exogenous cell-associated antigens. *Immunity* **17**, 211–220 (2002).
- Vallon-Eberhard, A., Landsman, L., Yagci, N., Verrier, B. & Jung, S. Trans epithelial pathogen uptake into the small intestinal lamina propria. *J. Immunol.* **176**, 2465–2469 (2006).
- Jang, M. H. *et al.* CCR7 is critically important for migration of dendritic cells in intestinal lamina propria to mesenteric lymph nodes. *J. Immunol.* **176**, 803–810 (2006).
- Worbs, T. *et al.* Oral tolerance originates in the intestinal immune system and relies on antigen carriage by dendritic cells. *J. Exp. Med.* **203**, 519–527 (2006).
- Varol, C., Zigmund, E. & Jung, S. Securing the immune tightrope: mononuclear phagocytes in the intestinal lamina propria. *Nature Rev. Immunol.* **10**, 415–426 (2010).
- Rivollier, A., He, J., Kole, A., Valatas, V. & Kelsall, B. L. Inflammation switches the differentiation program of Ly6C^{hi} monocytes from anti-inflammatory macrophages to inflammatory dendritic cells in the colon. *J. Exp. Med.* **209**, 139–155 (2012).
- Johansson-Lindbom, B. *et al.* Functional specialization of gut CD103⁺ dendritic cells in the regulation of tissue-selective T cell homing. *J. Exp. Med.* **202**, 1063–1073 (2005).
- Rydstrom, A. & Wick, M. J. Monocyte recruitment, activation, and function in the gut-associated lymphoid tissue during oral *Salmonella* infection. *J. Immunol.* **178**, 5789–5801 (2007).
- Jung, S. *et al.* Analysis of fractalkine receptor CX3CR1 function by targeted deletion and green fluorescent protein reporter gene insertion. *Mol. Cell. Biol.* **20**, 4106–4114 (2000).
- Frank, D. N. *et al.* Molecular-phylogenetic characterization of microbial community imbalances in human inflammatory bowel diseases. *Proc. Natl Acad. Sci. USA* **104**, 13780–13785 (2007).
- Kaser, A., Zeissig, S. & Blumberg, R. S. Inflammatory bowel disease. *Annu. Rev. Immunol.* **28**, 573–621 (2010).
- Thienmuth, P., Winter, S. E. & Bauml, A. J. *Salmonella*, the host and its microbiota. *Curr. Opin. Microbiol.* **15**, 108–114 (2012).
- Lupp, C. *et al.* Host-mediated inflammation disrupts the intestinal microbiota and promotes the overgrowth of Enterobacteriaceae. *Cell Host Microbe* **2**, 119–129 (2007).
- Valdez, Y. *et al.* Nramp1 expression by dendritic cells modulates inflammatory responses during *Salmonella* Typhimurium infection. *Cell. Microbiol.* **10**, 1646–1661 (2008).

Supplementary Information is available in the online version of the paper.

Acknowledgements We thank H. Yue and J. Hall for comments on the manuscript and members of the Littman laboratory for their suggestions. We thank the NYU Histology Core, which is supported in part by grant 5P30CA016087-32 from the National Cancer Institute. Supported by the American Cancer Society and National Institutes of Health (NIH) T32 CA009161 (G.E.D.), NIH T32 DK083256-02 (R.S.L.), Human Frontier Science Program Long-Term Fellowship (B.B.), NIH R01AI085166 (S.R.S.) and the Howard Hughes Medical Institute (D.R.L.).

Author Contributions G.E.D. designed and performed the experiments. G.E.D. and D.R.L. planned experiments and wrote the manuscript with input from all co-authors. R.S.L., J.-X.Z., S.R.S., B.B., C.G. and A.C. helped plan and perform experiments.

Author Information Reprints and permissions information is available at www.nature.com/reprints. The authors declare no competing financial interests. Readers are welcome to comment on the online version of the paper. Correspondence and requests for materials should be addressed to G.E.D. (Gretchen.Dieh@med.nyu.edu).

METHODS

Mice. C57BL/6 mice were purchased from Taconic Farms or Jackson Laboratories. *Ccr7*- and *Nod2*-mutant mice were purchased from Jackson Laboratories. CX₃CR1-GFP and CD11c-DTR mice were as previously described^{17,25}. *Myd88*- and *Nalp3*-mutant mice were from R. Medzhitov and J. Tschoopp, respectively. For inducible CX₃CR1-DTR mice, we introduced a *loxP*-floxed stop cassette followed by DTR into the *Cx3cr1* locus. Mice were subsequently crossed to CD11c-Cre mice (Jackson Laboratories), allowing deletion of the stop cassette in CD11c⁺ cells and induction of DTR in CX₃CR1⁺ cells. All animal experiments were performed in accordance with approved protocols for the NYU Institutional Animal Care and Usage Committee.

Depletion of gut commensal microbiota. Animals were given ampicillin (A; 1 g l⁻¹; Sigma), vancomycin (V; 500 mg l⁻¹; Amresco), neomycin sulphate (N; 1 g l⁻¹; Sigma), and metronidazole (M; 1 g l⁻¹; Sigma) in drinking water for 4 weeks as described⁵. Mice were switched to water without antibiotics for 3 days before infecting them as described later.

Infection with *Salmonella* Typhimurium and *E. coli*. Mice were infected orally with 1 × 10⁸ *Salmonella* *Ainva* c.f.u. or 2 × 10⁸ *AroA/Ainva* c.f.u. in 100 µl of PBS. For titres, organs were homogenized 2 days after infection, diluted in phosphate-buffered saline (PBS) and plated on LB agar with streptomycin (strep) (50 µg ml⁻¹). Colony counts were expressed as c.f.u. per organ. For T-cell analysis, mice were analysed 10 days after infection. For antibody titres, mice were infected on day 0 and day 15. Blood and faeces were collected 2 weeks after the second infection. Mice were infected with 1 × 10⁹ *E. coli* K12 (American Type Culture Collection no. 29425) and analysed for bacterial titres or for induction of antibodies as described earlier. A description of *Salmonella* strains can be found in Supplementary Table 1.

Measurement of T-cell and antibody responses. Analyses of serum and faecal proteins for *Salmonella*-specific IgG and IgA by ELISA were performed as described¹⁰. Concentrations were determined by interpolating from a standard curve generated by plating IgG or IgA. For T-cell responses, single-cell suspensions from the indicated organ were first negatively depleted with anti-B220 and anti-CD8 magnetic microbeads (Miltenyi Biotec). The depleted fraction was stained and cell sorting was performed on an Aria flow cytometer (BD Biosciences) to obtain memory/effector TCR⁺CD4⁺CD44⁺CD62L⁻ T cells (>99% purity). These cells were plated at 1 × 10⁵ cells per well with 5 × 10⁵ irradiated splenocytes and 1 µg of heat-killed *Salmonella*. At 72 h, IFN-γ in the supernatant was measured by ELISA (BD Biosciences).

Generation of CD11c-DTR bone marrow chimaeras. Six-week old Ly5.1 congenic mice (Jackson Labs) were lethally irradiated and reconstituted with bone marrow from wild-type or CD11c-DTR transgenic mice (Ly5.2). After 8–10 weeks, recipients were examined for immune reconstitution by analysing blood for Ly5.2⁺ haematopoietic cells before treating with antibiotics.

Cell isolation. Small-intestinal lamina propria cells were isolated as previously described³⁰. Spleen and MLN cells were isolated by injecting the organ with complete Roswell Park Memorial Institute medium (RPMI) containing 100 U ml⁻¹ type VIII collagenase (Sigma) and 150 µg ml⁻¹ DNaseI (Sigma). The organ was dissociated using frosted glass slides and the tissue was incubated at 37 °C for 45 min.

Lymph collection. Afferent lymph was isolated as described⁸. Mice were gavaged with 200 µl corn oil 1 h before isolating lymph to visualize the lymphatics. Afferent lymphatics were identified by anatomical location and confirmed by cellular

composition, as afferent lymph contains a majority of MHCII⁺ cells whereas efferent lymph contains a majority of T cells.

Antibodies, cell staining and flow cytometry. Flow cytometric analysis was performed on an LSR II (BD Biosciences) and analysed using FlowJo software (Tree Star). Antibodies were from BD Pharmingen or eBiosciences. 4',6-Diamidino-2-phenylindole (DAPI) was used to exclude dead cells.

In vivo cytokine analysis. Mice were infected with 2 × 10⁸ *AroA/Ainva* c.f.u., and 9 days later mice were injected with Brefeldin A (Sigma) as described³¹. Four hours later, mice were injected with 50 µg of boiled *Salmonella*. Spleen and MLN T cells were isolated 2 h later. During cell isolation and extracellular staining, all solutions contained Brefeldin (GolgiPlug, BD Biosciences). Cells were stained for cytokines as per the manufacturer's instructions (BD Bioscience).

RNA extraction and real-time RT-PCR. The terminal ileum was disrupted in Trizol (Ambion) using a TissueLyserII (Qiagen). Real-time PCR for Reg-3γ was performed as described³².

Intestinal permeability. Intestinal permeability was assessed by oral administration of FITC-dextran (Sigma-Aldrich) at 400 mg kg⁻¹ as described³³. Serum FITC-dextran concentrations were determined using an Envision 2104 Multiplate Reader (Perkin Elmer).

Quantification of faecal bacterial DNA. Faecal pellets were weighed and resuspended in 200 mM Tris pH 8, 20 mM NaCl, 20 mM EDTA with 3% SDS. Bacteria were lysed by mechanical disruption with silica beads using a Retsch TissueLyser. DNA was extracted using phenol-chloroform. qPCR was performed on a Lightcycler 480 (Roche Applied Science) using SYBR green (Qiagen). 16S rRNA was amplified using forward primer 5'-ACTCCTACGGGAGGCAGCAGT-3' and reverse primer 5'-ATTACCGCGGCTGCTGGC-3'. A standard curve was generated using limiting dilutions of bacterial DNA to allow conversion of 16S rRNA amplification to nanograms of bacterial DNA. The data were normalized to faecal pellet weight and expressed as ng bacterial DNA/mg of faecal pellet.

Sorting *Salmonella*-infected cells. *Cx3cr1^{sf/p}+* mice were treated with antibiotics and infected with non-invasive *Salmonella*. Two days later MLN cells were isolated and stained. Cell sorting was performed on an Aria cytometer (BD Biosciences). TCR-β⁺CD19⁻MHCII⁺CD11c⁺ cells were sorted into CX₃CR1⁺, CD103⁺ or CX₃CR1⁻CD103⁻ cell populations. CD19⁺ or TCR-β⁺ cells were plated as non-dendritic cells. Sorted cells were plated on LB-strep plates.

Heat-killed *Salmonella* and *E. coli*. *Salmonella* or *E. coli* were heated to 85 °C for 60 min. Bacteria were plated and allowed to grow overnight to confirm death. Mice were administered 1 × 10¹⁰ heat-killed bacteria orally daily for 2 days before infecting with non-invasive *Salmonella*.

Statistical analysis. One-way ANOVA with Bonferroni's post-test or unpaired *t*-test was performed using a 95% confidence interval. All analyses were performed using GraphPad Prism version 4.0. Differences were considered to be significant at *P* values of <0.05.

1. Liu, F. & Whitton, J. L. Cutting edge: re-evaluating the *in vivo* cytokine responses of CD8⁺ T cells during primary and secondary viral infections. *J. Immunol.* **174**, 5936–5940 (2005).
2. Vaishnava, S., Behrendt, C. L., Ismail, A. S., Eckmann, L. & Hooper, L. V. Paneth cells directly sense gut commensals and maintain homeostasis at the intestinal host-microbial interface. *Proc. Natl Acad. Sci. USA* **105**, 20858–20863 (2008).
3. Napolitano, L. M., Koruda, M. J., Meyer, A. A. & Baker, C. C. The impact of femur fracture with associated soft tissue injury on immune function and intestinal permeability. *Shock* **5**, 202–207 (1996).

ATP-directed capture of bioactive herbal-based medicine on human tRNA synthetase

Huihao Zhou¹, Litao Sun¹, Xiang-Lei Yang¹ & Paul Schimmel¹

Febrifugine is the active component of the Chinese herb Chang Shan (*Dichroa febrifuga* Lour.)^{1,2}, which has been used for treating malaria-induced fever for about 2,000 years. Halofuginone (HF), the halogenated derivative of febrifugine, has been tested in clinical trials for potential therapeutic applications in cancer and fibrotic disease^{3–6}. Recently, HF was reported to inhibit T_H17 cell differentiation by activating the amino acid response pathway⁷, through inhibiting human prolyl-transfer RNA synthetase (ProRS) to cause intracellular accumulation of uncharged tRNA^{8,9}. Curiously, inhibition requires the presence of unhydrolysed ATP. Here we report an unusual 2.0 Å structure showing that ATP directly locks onto and orients two parts of HF onto human ProRS, so that one part of HF mimics bound proline and the other mimics the 3' end of bound tRNA. Thus, HF is a new type of ATP-dependent inhibitor that simultaneously occupies two different substrate binding sites on ProRS. Moreover, our structure indicates a possible similar mechanism of action for febrifugine in malaria treatment. Finally, the elucidation here of a two-site modular targeting activity of HF raises the possibility that substrate-directed capture of similar inhibitors might be a general mechanism that could be applied to other synthetases.

ProRS is a member of the aminoacyl-tRNA synthetase family of enzymes that activate amino acids for protein synthesis through formation of aminoacyl adenylates (AA-AMP) and subsequent transfer of

the activated amino acids to the 3' ends of the cognate tRNAs. Because of their crucial role in protein synthesis, inhibition halts the growth and suppresses the viability of all cell types. Consequently, aminoacyl-tRNA synthetases are attractive targets for discovering types of drugs such as antibiotics and suppressors of cell hyperproliferation^{10,11}. Many tRNA synthetase inhibitors mimic AA-AMPs; the AA-AMP mimics directly occupy and block the active site for ATP and amino acid and compete out the substrate ATP. By contrast, ATP was reported to be essential for HF binding to ProRS⁸. This ATP dependence suggests that HF binds to ProRS through a different mechanism and not as a mimetic of Pro-AMP. Thus, understanding how HF inhibits human ProRS is of great interest.

In its simplest description, HF is composed of a hydroxypiperidine ring joined by bridging atoms to a double-ring halogenated 4-quinazolinone (Fig. 1a). To clarify the mechanism of inhibition of HF, we cloned and expressed human ProRS and were able to obtain co-crystals with a non-hydrolysable ATP analogue ((adenosine 5'-(β, γ-imido)triphosphate) (ATP^a)) and HF, which diffracted to 2.0 Å resolution (Supplementary Table 1). The structure was solved by molecular replacement using *Thermus thermophilus* ProRS as template. The asymmetric unit contained two ProRS molecules that formed a homodimer (Fig. 1b), as also seen in gel filtration experiments (data not shown). Each subunit encoded an amino-terminal catalytic domain characteristic of a class II tRNA synthetase, an

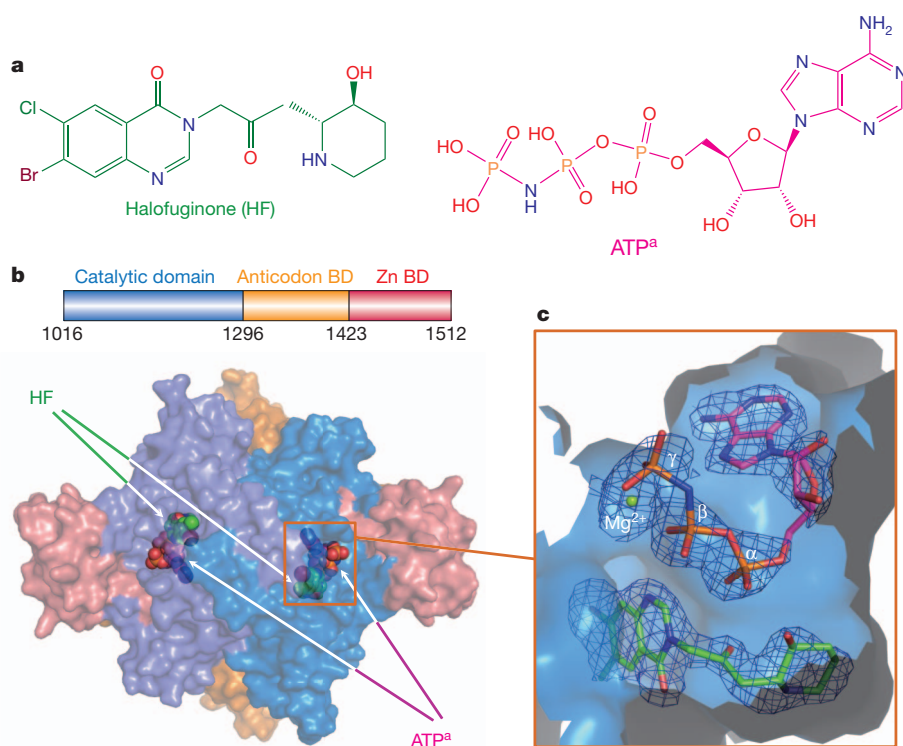


Figure 1 | Structure of human ProRS with bound ligands.

a, Chemical structures of halofuginone (HF) and the ATP analogue (ATP^a). The colour scheme for HF (green) and ATP^a (red) is the same throughout the manuscript. **b**, Two ProRS monomers form an asymmetric unit that is a homodimer. The domains of ProRS are shown in the colour-coded diagram; BD, binding domain. HF and ATP^a are shown as spherical models at the active site of both subunits. **c**, HF is buried at the bottom of the pocket and covered by co-bound ATP^a. A simulated annealing omit map was calculated with Fourier coefficients $2F_o - F_c$ and contoured at 1.5σ .

¹The Skaggs Institute for Chemical Biology, Department of Molecular Biology, The Scripps Research Institute, 10550 North Torrey Pines Road, La Jolla, California 92037, USA.

anticodon-binding domain and a carboxy-terminal zinc-binding domain (Fig. 1b). In the two catalytic domains of the ProRS homodimer, HF and ATP^a were bound to the active site for Pro-AMP formation (Fig. 1b, c).

ATP^a was located at the canonical ATP-binding pocket of class II aminoacyl-tRNA synthetases¹². Three hydrogen bonds contributed by Thr 1164 and Thr 1276 and hydrophobic stacking of Phe 1167 stabilized the adenosine group (Supplementary Fig. 2). The ribose moiety was bound by three hydrogen bonds with Gln 1237, Thr 1240 and Arg 1278. The hydrogen bonds from Arg 1152 and Arg 1163 contributed to stabilizing the α -, β - and γ -phosphate groups of ATP^a (Supplementary Fig. 2), which form a cap over the HF-binding pocket (Fig. 1c). These extensive hydrophilic and hydrophobic interactions positioned the ATP in a 'U'-like bent conformation with the α -phosphate group exposed at the bottom of the U shape. Superposition of the catalytic domains of human ProRS with that of the previously determined structure of *T. thermophilus* ProRS showed that the conformation and location of ATP was the same (Supplementary Fig. 3), with the α -phosphate

group poised for proline activation. In the human ProRS–HF–ATP^a ternary complex, the α -phosphate group is proximal to the hydroxypiperidine ring of HF and forms two hydrogen bonds with its hydroxyl group (Fig. 2a, b). It also forms an additional hydrogen bond with the keto group in the bridge between the piperidine ring and the quinazolinone moiety of HF (Fig. 2a, b). These direct hydrogen-bond interactions may enable ATP to lock onto and orient HF.

In addition to the interactions with ATP, ProRS itself forms seven hydrogen bonds and several hydrophobic contacts with each moiety of HF (Fig. 2a, b). Thus, the pocket for the HF piperidine ring, built by Thr 1121, Glu 1123, Trp 1169, Glu 1171, His 1173, Thr 1240, His 1242 and Ser 1272 (Fig. 2c), has both hydrophobic and hydrophilic character. These residues are highly conserved among eukaryotic ProRS (Supplementary Fig. 4), and were found to be also important for proline recognition in the structure of *T. thermophilus* eukaryotic-like ProRS with proline (Fig. 2d)¹³. Overlay of the catalytic domains of human and *T. thermophilus* ProRS structures showed the piperidine ring of HF bound to the same site as proline (Fig. 2e). In particular, the

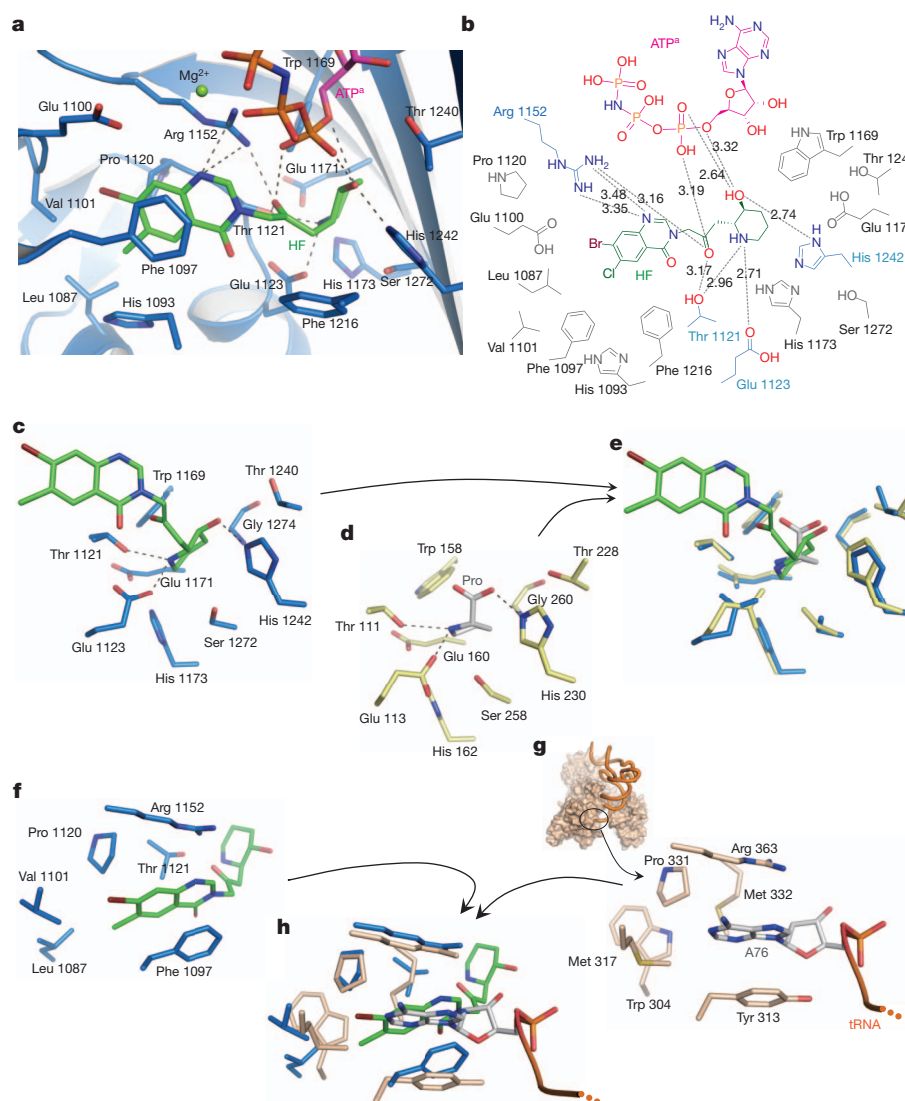


Figure 2 | Mechanistic basis for ATP-dependent inhibition of ProRS by halofuginone. **a**, HF forms extensive hydrophobic contacts and hydrogen-bonding interactions with ProRS and with ATP^a. **b**, Two-dimensional presentation of HF binding. The HF, ATP^a and hydrogen-bonded residues are coloured as previously, and other residues within 4 Å of HF are coloured in grey. **c**, A stick model showing the binding of the piperidine ring of HF to human ProRS. **d**, The proline binding pocket of *T. thermophilus* ProRS in complex with proline (Protein Data Bank 1H4T, protein is coloured as yellow

and proline as grey-white). **e**, Structure superposition of the catalytic domain of human ProRS with *T. thermophilus* ProRS reveals the piperidine ring of HF directly occupies the proline-binding pocket. **f**, Stick model showing the binding of the halogenated 4-quinazolinone group of HF to human ProRS. **g**, Structure of *E. coli* ThrRS–tRNA complex, with the pocket for the adenosine group for A76 (PDB 1QF6). **h**, Overlay of the catalytic domain of human ProRS onto *E. coli* ThrRS (brown) reveals that HF uses the binding pocket for A76 of the CCA⁷⁶ 3' end for binding the quinazolinone moiety.

orientations of the proline pyrrolidine ring and of the HF piperidine ring, and the locations of nitrogen and oxygen atoms, are similar. Thus, the HF piperidine ring structurally mimics a proline-like group, and would directly compete with proline and block proline activation. The proline mimic mechanism is consistent with the observation that HF or febrifugine derivatives with piperidine ring modifications are unable to bind to the proline-binding pocket and therefore are rendered unable to inhibit or bind to ProRS or affect cell function (for example, MAZ1310 ref. 8). In contrast, derivatives that replaced the piperidine ring by the pyrrolidine ring of proline retained similar or superior biological activity¹⁴.

The halogenated 4-quinazolinone group is buried in a pocket mainly composed of Leu 1087, Phe 1097, Val 1101, Pro 1120, Thr 1121 and Arg 1152 (Fig. 2a, f). In addition to the hydrogen bonds between Arg 1152 and the quinazolinone nitrogen atom, the quinazolinone group was mainly stabilized by hydrophobic contacts, particularly by the hydrophobic stack effect from Phe 1097 (Fig. 2a, f). Threonyl-tRNA synthetase (ThrRS) also belongs to class II aminoacyl-tRNA synthetases, and it is most similar to ProRS. Arg 1152 and Phe 1097 of ProRS are conserved in class II synthetases. The corresponding residues Arg 363 and Tyr 313 in the structure of *Escherichia coli* ThrRS were found to flank the two sides of the adenosine A76 of tRNA^{Thr} and thus play crucial roles in CCA 3'-end binding (Fig. 2g)¹⁵. In addition to these two residues, other parts of the A76 adenosine pocket are also quite similar to the quinazolinone group binding pocket in the ProRS structure (Fig. 2g). Overlay of the ProRS and ThrRS structures by aligning the conserved 7-strand β -sheet core of their catalytic domains showed that the quinazolinone group of HF bound to the same position as bound A76, and with a similar orientation and side-chain contacts (Fig. 2h). This structural similarity indicates that the quinazolinone group of HF binds to ProRS by using a strategy of mimicking the terminal adenosine of the tRNA substrate. Thus, in contrast to the single-site and conventional AA-AMP mimics, HF is a dual-site inhibitor by virtue of simultaneously occupying two active site pockets, the proline binding pocket and the binding pocket for the 3' end of the tRNA (Supplementary Fig. 1).

We used our crystal structure of the ProRS-ATP-HF complex to further dissect the mechanism of action of HF. Earlier work by other groups showed that HF specifically inhibits overall aminoacylation of tRNA^{Pro} and that binding of HF to ProRS is greatly enhanced by ATP⁸ (the level of HF binding, in the absence of ATP, was unknown and presumably weak). According to our structure, HF is 'two-headed' and, with bound ATP, uses the piperidine ring to block the proline binding site and the quinazolinone group to block the site for docking

the 3' end of tRNA^{Pro}. We designed experiments to probe the function of each site, the site for adenylate formation/binding and the site for docking the 3' end of tRNA. In addition to HF, we used another inhibitor, Pro-SA (5'-O-(N-(L-prolyl)-sulphamoyl-adenosine), as a comparator. Pro-SA is a tight-binding non-reactive adenylate analogue of Pro-AMP¹⁶.

We first determined that the thermal melting of ProRS was barely affected by either proline or ATP^a. In contrast, in the presence of HF the melting curve was shifted to a higher temperature by about 10 °C by HF alone, and by about 18 °C with HF plus ATP^a (Fig. 3a). These data show that HF binds even in the absence of ATP, and also confirm that HF binds much tighter in the presence of ATP. Not surprisingly, the largest thermal shift was obtained with Pro-SA.

To probe the adenylate-formation site, we studied the first step of aminoacylation, which is the activation of proline by ProRS to form a tightly bound Pro-AMP adenylate complex and release of pyrophosphate (PPi). This reaction step is $\text{ProRS} + \text{Pro} + \text{ATP} \rightarrow \text{ProRS-Pro-AMP} + \text{PPi}$.

The conventional proline-dependent ATP-PPi exchange reaction was used to investigate this reaction. As expected, both Pro-SA and HF were potent inhibitors of this reaction in a dose-dependent fashion, with Pro-SA being more effective (Fig. 3b). This result is consistent with the thermal melting data of Fig. 3a showing the tighter binding of Pro-SA, and with our X-ray crystal structure showing the docking of one 'head' of HF at the site for the prolyl moiety of Pro-AMP.

Next, we investigated the ability of HF to mimic the docking of A76 of tRNA^{Pro} to ProRS. For this purpose we studied the effect of HF on the relatively stable preformed ProRS-Pro-AMP complex, isolated using a column. Because binding of tRNA to tRNA synthetases is generally associated with conformational changes that mobilize the active site for transfer of the activated amino acid to A76, we reasoned that binding of the A76-mimicking quinazolinone group of HF would result in an abortive transfer and thereby release Pro-AMP from ProRS. Accordingly, the ProRS-Pro-AMP complex was incubated separately with Pro-SA (which should not have access to the A76 site) and with HF (without ATP). As expected, Pro-SA caused some reduction in the bound Pro-AMP, which is attributed to an exchange on the enzyme between bound Pro-AMP and Pro-SA. In contrast, free HF, while having a much lower affinity than Pro-SA for ProRS, completely released Pro-AMP from the complex (Fig. 3c). This result supports the conclusion (from our X-ray structure) that HF also mimics A76 of tRNA.

HF is a halogenated derivative of febrifugine, which is the bioactive constituent in the Chang Shan herb that has long been used to treat malaria. The ProRS binding sites of both human and the malaria

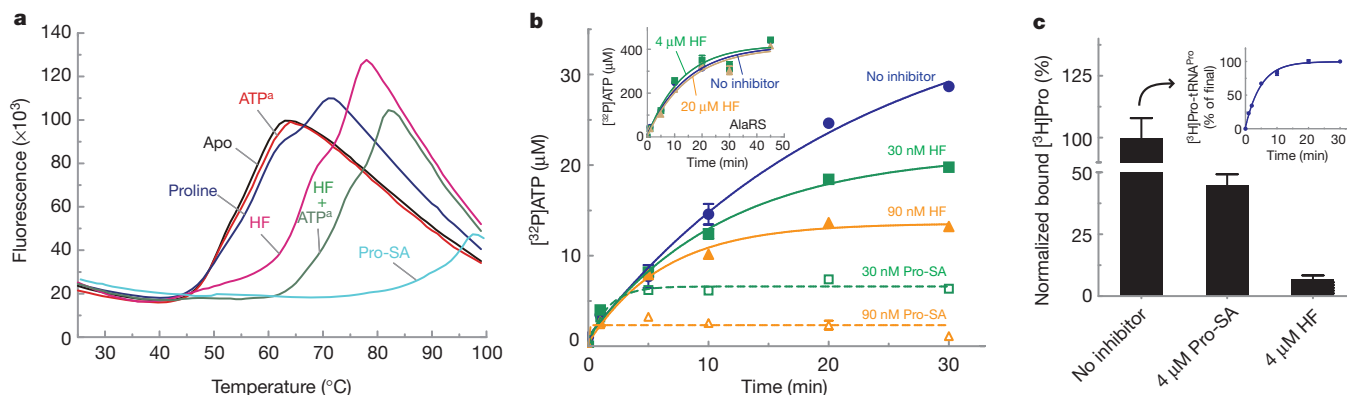


Figure 3 | HF interacts with both the site for amino acid activation and the site for docking the 3'-end of tRNA. **a**, Thermal melting¹⁹ of ProRS in the presence of different ligands. HF binds in the absence of ATP^a, and binds more strongly in the presence of ATP^a. Apo, apoenzyme. Fluorescence units are arbitrary. **b**, HF and the comparator Pro-SA block formation of Pro-AMP, in the proline-dependent ATP-PPi exchange reaction. The inset shows that HF had no effect on the alanine-dependent ATP-PPi exchange reaction with

AlaRS. **c**, HF mobilizes the release of Pro-AMP from ProRS. The ProRS-[³H]Pro-AMP complex was prepared on ice and then isolated on a column and for 10 min was left untreated, or exposed to HF, or exposed to Pro-SA, respectively. The complex was then re-run on the column and the amount of bound [³H]Pro-AMP was determined. The inset shows that the isolated [³H]Pro was activated (as [³H]Pro-AMP) and could be transferred to tRNA. Error bars are s.e.m. ($n = 2$).

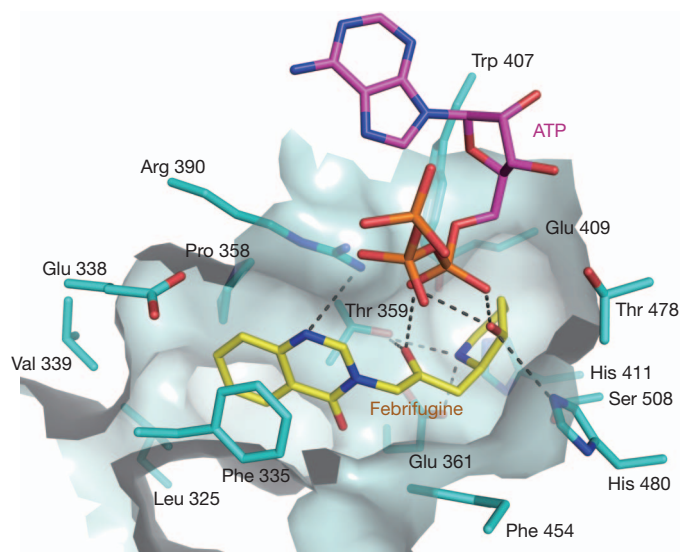


Figure 4 | Febrifugine blocks ProRS. Febrifugine docked to the active site of *P. falciparum* ProRS (UniProtKB code Q8I5R7). ProRS and Febrifugine are coloured cyan and yellow, respectively. The hydrogen bonds are indicated with dashes. The *P. falciparum* ProRS structure was generated by the protein structure homology-modelling server SWISS-MODEL²⁰. Febrifugine was docked into the *P. falciparum* ProRS active site based on the structure of ProRS–halofuginone–ATP^a complex, whereas ATP was docked based on the structure of the *T. thermophilus* ProRS–tRNA–ATP complex (PDB code 1H4Q).

parasite *Plasmodium falciparum* are highly similar (Supplementary Fig. 4). With that in mind, using our ATP-dependent docking of HF to human ProRS as a template, we were able to show the potential for febrifugine docking to *P. falciparum* ProRS (Fig. 4). Thus, our analysis suggests malarial ProRS may also be the target of febrifugine. This possibility could also explain why the lethal effect of febrifugine on *P. falciparum* in culture is reversed by proline⁸.

Interestingly, in addition to the inhibition of amino acid activation by mimics of AA-AMP (including the ‘operational’ mimic pseudomonic acid (mupirocin)¹⁷), the ATP-dependent two-site HF inhibition mechanism reported here, and the single-site tRNA-dependent editing-site-trapping mechanism reported earlier¹⁸, illustrate two entirely different and unusual mechanisms for substrate participation in capture of an inhibitor (Supplementary Fig. 5). In addition, by substitution of the piperidine ring with other amino acid mimics, dual-site inhibitors could in principle be designed for other aminoacyl-tRNA synthetases.

METHODS SUMMARY

Human ProRS was overexpressed in *E. coli* and purified by fast protein liquid chromatography. The protein–ligand complex was generated by mixing the protein with 3 mM halofuginone, 5 mM ATP analogue adenosine 5′-(β,γ -imido)triphosphate, 5 mM MgCl₂ and 5 mM β -mercaptoethanol. Crystals were obtained by the sitting-drop vapour-diffusion method, and diffraction data were collected using a single flash-frozen crystal. The ProRS–ligand complex structure was determined by the molecular replacement method, using the structure of *T. thermophilus* ProRS (PDB code 1HC7) as the searching model. Standard refinement procedures were performed to get the final model. The ATP–pyrophosphate exchange was as described²¹ and the ProRS–Pro-AMP complex was isolated with a desalting column. Results were analysed with GraphPad Prism software.

Full Methods and any associated references are available in the online version of the paper.

Received 15 June; accepted 9 November 2012.

Published online 23 December 2012.

- Koepfli, J. B., Mead, J. F. & Brockman, J. A. Jr. An alkaloid with high antimalarial activity from *Dichroa febrifuga*. *J. Am. Chem. Soc.* **69**, 1837 (1947).
- Coatney, G. R., Cooper, W. C., Culwell, W. B., White, W. C. & Imboden, C. A. Jr. Studies in human malaria. XXV. Trial of febrifugine, an alkaloid obtained from *Dichroa febrifuga* Lour., against the Chesson strain of *Plasmodium vivax*. *J. Natl. Malar. Soc.* **9**, 183–186 (1950).
- Pines, M., Snyder, D., Yarkoni, S. & Nagler, A. Halofuginone to treat fibrosis in chronic graft-versus-host disease and scleroderma. *Biol. Blood Marrow Transplant.* **9**, 417–425 (2003).
- Pines, M. & Nagler, A. Halofuginone: a novel antifibrotic therapy. *Gen. Pharmacol.* **30**, 445–450 (1998).
- de Jonge, M. J. et al. Phase I and pharmacokinetic study of halofuginone, an oral quinazolinone derivative in patients with advanced solid tumours. *Eur. J. Cancer* **42**, 1768–1774 (2006).
- Koon, H. B. et al. Phase II AIDS Malignancy Consortium trial of topical halofuginone in AIDS-related Kaposi sarcoma. *J. Acquir. Immune Defic. Syndr.* **56**, 64–68 (2011).
- Sundrud, M. S. et al. Halofuginone inhibits T_H17 cell differentiation by activating the amino acid starvation response. *Science* **324**, 1334–1338 (2009).
- Keller, T. L. et al. Halofuginone and other febrifugine derivatives inhibit prolyl-tRNA synthetase. *Nature Chem. Biol.* **8**, 311–317 (2012).
- Kilberg, M. S., Pan, Y. X., Chen, H. & Leung-Pineda, V. Nutritional control of gene expression: how mammalian cells respond to amino acid limitation. *Annu. Rev. Nutr.* **25**, 59–85 (2005).
- Schimmel, P., Tao, J. & Hill, J. Aminoacyl tRNA synthetases as targets for new anti-infectives. *FASEB J.* **12**, 1599–1609 (1998).
- Hill, J. Aminoacyl sulfamides for the treatment of hyperproliferative disorders. US Patent 5,824 657 (1998).
- Carter, C. W. Jr. Cognition, mechanism, and evolutionary relationships in aminoacyl-tRNA synthetases. *Annu. Rev. Biochem.* **62**, 715–748 (1993).
- Yaremchuk, A., Tukalo, M., Grotli, M. & Cusack, S. A succession of substrate induced conformational changes ensures the amino acid specificity of *Thermus thermophilus* prolyl-tRNA synthetase: comparison with histidyl-tRNA synthetase. *J. Mol. Biol.* **309**, 989–1002 (2001).
- Zhu, S. et al. Synthesis and biological evaluation of febrifugine analogues as potential antimalarial agents. *Bioorg. Med. Chem.* **17**, 4496–4502 (2009).
- Sankaranarayanan, R. et al. The structure of threonyl-tRNA synthetase-tRNA^{Thr} complex enlightens its repressor activity and reveals an essential zinc ion in the active site. *Cell* **97**, 371–381 (1999).
- Heacock, D., Forsyth, C. J., Shiba, K. & Musier-Forsyth, K. Synthesis and aminoacyl-tRNA synthetase inhibitory activity of prolyl adenylate analogs. *Bioorg. Chem.* **24**, 273–289 (1996).
- Nakama, T., Nureki, O. & Yokoyama, S. Structural basis for the recognition of isoleucyl-adenylate and an antibiotic, mupirocin, by isoleucyl-tRNA synthetase. *J. Biol. Chem.* **276**, 47387–47393 (2001).
- Rock, F. L. et al. An antifungal agent inhibits an aminoacyl-tRNA synthetase by trapping tRNA in the editing site. *Science* **316**, 1759–1761 (2007).
- Pantoliano, M. W. et al. High-density miniaturized thermal shift assays as general strategy for drug discovery. *J. Biomol. Screen.* **6**, 429–440 (2001).
- Arnold, K., Bordoli, L., Kopp, J. & Schwede, T. The SWISS-MODEL workspace: a web-based environment for protein structure homology modeling. *Bioinformatics* **22**, 195–201 (2006).
- Beebe, K. et al. A universal plate format for increased throughput of assays that monitor multiple aminoacyl transfer RNA synthetase activities. *Anal. Biochem.* **368**, 111–121 (2007).

Supplementary Information is available in the online version of the paper.

Acknowledgements We thank K. Musier-Forsyth for providing the ProRS gene plasmid and Pro-SA, staff at beamline 7-1 of Stanford Synchrotron Radiation Lightsources for assistance in X-ray diffraction data collection, and M. Guo for comments. This work was supported by National Institutes of Health grants GM15539, GM23562 and GM88278 and by a fellowship from the National Foundation for Cancer Research.

Author Contributions H.Z., L.S., X.-L.Y. and P.S. designed the experiments. H.Z. and L.S. performed the experiments and all authors analysed the data. All authors discussed the results and H.Z. and P.S. wrote the manuscript.

Author Information Atomic coordinates and structure factors for the reported crystal structure have been deposited in the Protein Data Bank under accession code 4HVC. Reprints and permissions information is available at www.nature.com/reprints. The authors declare no competing financial interests. Readers are welcome to comment on the online version of the paper. Correspondence and requests for materials should be addressed to P.S. (schimmel@scripps.edu).

METHODS

Protein expression and purification. The cDNA fragment encoding human prolyl-tRNA synthetase (ProRS) was cloned into *E. coli* plasmid pET21a (Novagen), with an additional N-terminal His₆ tag. The plasmid encoding ProRS was transformed into *E. coli* strain BL21(DE3) pLysS (Life Technologies) and was induced overnight for overexpression with 0.5 mM isopropyl- β -D-thiogalactoside (IPTG) at room temperature. The *E. coli* cell lysate was first loaded onto a nickel-nitrilotriacetic (Ni-NTA) column (Qiagen), and the elution fraction was further purified with mono Q ion-exchange chromatography (GE Healthcare) to a single band as indicated on SDS-polyacrylamide gel electrophoresis with Coomassie brilliant blue staining. The purified protein was found as a single peak with the elution volume consistent with a homogeneous ProRS homodimer on the Superdex 200 analytical gel filtration column (GE Healthcare). The purified ProRS was concentrated to 50 mg ml⁻¹ and stored at -80 °C in a buffer of 50 mM NaCl, 2 mM Tris buffer, pH 8.0.

Crystallization and data collection. ProRS was crystallized with the sitting-drop vapour-diffusion method using a Mosquito robot (TTP Labtech). Prior to crystallization, ProRS was diluted to 40 mg ml⁻¹ with 3 mM halofuginone (HF) (Sigma-Aldrich), 5 mM ATP analogue adenosine 5'-(β , γ -imido)triphosphate (Sigma-Aldrich), 5 mM MgCl₂ and 5 mM β -mercaptoethanol, and then incubated on ice for 30 min. Next, sitting drops were set up by mixing 100 nl of protein (40 mg ml⁻¹) and 100 nl of reservoir solution containing 20% (w/v) polyethylene glycol 3350, 0.6 M CaCl₂ and 50 mM HEPES, pH 7.5, and equilibrated against a 70 μ l of reservoir solution at 30 °C for 2 to 3 days before data collection. The X-ray diffraction data were collected using a single crystal at 1.000 Å (0.1000 nm) and temperature of 100 K at beamline 7-1 of Stanford Synchrotron Radiation Lightsource. The complete data set contains 500 images with the oscillation angle of 0.5° for each image. The ProRS-HF-ATP^a crystal belonged to space group *P*2₁. Data were integrated and scaled with the program HKL2000 (ref. 22).

Structure determination and refinement. The initial model was determined by molecular replacement using the program MOLREP²³. The crystal structure of *T. thermophilus* ProRS (PDB code 1HC7), which has 43% amino acid sequence identity to human ProRS, was used as the searching model. The structure was further refined by iterative cycles of positional refinement and translation-libration-screw refinement with Refmac5²⁴ and Phenix²⁵ and model building with COOT²⁶, and the final model was refined to 2.0 Å resolution with $R_{\text{work}}/R_{\text{free}}$ of 20.4%/22.7%. The model has good geometry quality, and 98.9%/99.8% residues are in favoured or allowed regions of the MolProbity²⁷ Ramachandran plot. Statistics of data collection and structure refinement are given in Supplementary Table 1. The atomic coordinates and structural factors have been deposited into Protein Data Bank under the accession code 4HVC.

Sequence analysis and structure presentation. Protein sequences were aligned using the program Multalin²⁸. The alignment result was submitted to ESPript²⁹ for figure generation. All protein structure illustrations were prepared with the program PyMOL (<http://www.pymol.org>).

Thermal shift assay. ProRS (3 μ g) was diluted in 30 μ l buffer containing 500 mM NaCl, 20 mM Tris, pH 8.0, 1 to 2,500 dilution SYPRO orange dye (Life Technologies) and different ligands (5 mM ATP^a, 5 mM proline, 1 mM HF, 1 mM HF plus 5 mM ATP^a or 1 mM Pro-SA, respectively), and incubated at room

temperature for 10 min. Then ProRS samples were heated from 25 °C to 98 °C at a rate of 1 °C min⁻¹, and the fluorescence signals were monitored by the StepOnePlus quantitative real-time PCR system (Life Technologies). Each curve was an average of three measurements.

ATP-pyrophosphate exchange assays. The ATP-pyrophosphate exchange was as described²¹. The reaction buffer contained 100 mM HEPES, pH 7.5, 20 mM KCl, 10 mM MgCl₂, 1 mM dithiothreitol, 2 mM ATP, 1 mM Na pyrophosphate (NaPPi), 20 μ Ci ml⁻¹ [³²P]PP_i and 0.5 mM proline. Inhibitor HF and Pro-SA (5'-O-(N-(L-prolyl)-sulphamoyl)adenosine (gift of K. Musier-Forsyth) were added at different concentrations (0, 30 or 90 nM). The reactions were started by adding ProRS into buffer at the final ProRS concentration of 10 nM, and then incubated at 20 °C. 20 μ l of each of the reactions was quenched at different time points in 200 μ l of quench buffer (1 M HCl, 200 mM NaPPi and 4% charcoal). The free [³²P]PP_i was removed by flowing through the 96-well polyvinylidene fluoride (PVDF) filter plates, and the residual [³²P]PP_i was washed five times using 200 μ l of washing buffer (1 M HCl and 200 mM NaPPi). Then the produced [³²P]ATP remaining in filter plates was transferred to scintillation vials and counted. The data were analysed with GraphPad Prism (GraphPad Software). The experiments here and following subsequently were independently repeated three times with duplicated measurements each time.

HF-Pro-AMP competition assay. The isolation of ProRS-Pro-AMP was slightly modified from that of a previous report³⁰. In brief, 2 μ M ProRS was added to the buffer containing 50 mM HEPES, pH 7.5, 20 mM KCl, 5 mM MgCl₂, 2 mM ATP, 2 mM dithiothreitol, 20 μ M proline and 1 μ M [³H]proline, and then incubated at 4 °C for 10 min to create ProRS-[³H]Pro-AMP. The reaction containing ProRS-[³H]Pro-AMP flowed through a desalting column (SpinTrap G-25, GE Healthcare) to isolate the complex and remove the extra ATP and proline. HF and Pro-SA were added at the concentration of 4 μ M to the complex to compete for 10 min at 20 °C. The reaction was passed through a desalting column again to remove dissociated [³H]Pro-AMP. The eluted [³H]Pro-AMP still bound to ProRS was then measured.

22. Otwinowski, Z. & Minor, W. Processing of X-ray diffraction data collected in oscillation mode. *Methods Enzymol.* **276**, 307–326 (1997).
23. Vagin, A. & Teplyakov, A. MOLREP: an automated program for molecular replacement. *J. Appl. Crystallogr.* **30**, 1022–1025 (1997).
24. Murshudov, G. N., Vagin, A. A. & Dodson, E. J. Refinement of macromolecular structures by the maximum-likelihood method. *Acta Crystallogr. D* **53**, 240–255 (1997).
25. Adams, P. D. *et al.* PHENIX: a comprehensive Python-based system for macromolecular structure solution. *Acta Crystallogr. D* **66**, 213–221 (2010).
26. Emsley, P. & Cowtan, K. Coot: model-building tools for molecular graphics. *Acta Crystallogr. D* **60**, 2126–2132 (2004).
27. Chen, V. B. *et al.* MolProbity: all-atom structure validation for macromolecular crystallography. *Acta Crystallogr. D* **66**, 12–21 (2010).
28. Corpet, F. Multiple sequence alignment with hierarchical clustering. *Nucleic Acids Res.* **16**, 10881–10890 (1988).
29. Gouet, P., Courcelle, E., Stuart, D. I. & Metz, F. ESPript: analysis of multiple sequence alignments in PostScript. *Bioinformatics* **15**, 305–308 (1999).
30. Shi, J. P. & Schimmel, P. Aminoacylation of alanine minihelices. 'Discriminator' base modulates transition state of single turnover reaction. *J. Biol. Chem.* **266**, 2705–2708 (1991).

Mitotic cell rounding accelerates epithelial invagination

Takefumi Kondo¹ & Shigeo Hayashi^{1,2}

Mitotic cells assume a spherical shape by increasing their surface tension and osmotic pressure by extensively reorganizing their interphase actin cytoskeleton into a cortical meshwork and their microtubules into the mitotic spindle^{1,2}. Mitotic entry is known to interfere with tissue morphogenetic events that require cell-shape changes controlled by the interphase cytoskeleton, such as apical constriction^{3–5}. However, here we show that mitosis plays an active role in the epithelial invagination of the *Drosophila melanogaster* tracheal placode. Invagination begins with a slow phase under the control of epidermal growth factor receptor (EGFR) signalling; in this process, the central apically constricted cells, which are surrounded by intercalating cells^{6,7}, form a shallow pit. This slow phase is followed by a fast phase, in which the pit is rapidly depressed, accompanied by mitotic entry, which leads to the internalization of all the cells in the placode. We found that mitotic cell rounding, but not cell division, of the central cells in the placode is required to accelerate invagination, in conjunction with EGFR-induced myosin II contractility in the surrounding cells. We propose that mitotic cell rounding causes the epithelium to buckle under pressure and acts as a switch for morphogenetic transition at the appropriate time.

The invagination of epithelial placodes converts flat sheets into the three-dimensional structures that form complex organs, and it is a key morphogenetic process in animal development⁸. A major mechanism of invagination is apical constriction, which is driven by actomyosin contraction⁹. However, not all constricted cells invaginate^{10,11}, and some cell internalization occurs without apical constriction^{6,7,12,13}, suggesting that additional mechanisms of inward cell movement contribute to invagination.

To obtain three-dimensional information about cell behaviour during invagination, we performed live imaging of the *Drosophila* tracheal placode. Ten pairs of tracheal placodes, each of which is composed of about 40 cells, are formed in the ectoderm at mid-embryogenesis, and each placode initiates invagination simultaneously¹⁴. Using an adherens junction marker, DE-cadherin–green fluorescent protein (E-cad–GFP)¹⁵, we found that the adherens junctions of the central placode cells slowly created a depression by apical constriction, which became the tracheal pit⁷ (Fig. 1a). After 30 to 60 min of slow movement (slow phase), the tracheal pit was suddenly enlarged, and the tracheal cells were rapidly internalized (fast phase) and eventually formed L-shaped tube structures (Fig. 1a, b, e, Supplementary Fig. 1 and Supplementary Video 1).

After the fast transition, all the tracheal cells and surrounding epidermal cells entered mitosis 16, the final round of embryonic mitosis¹⁶. We noticed that the fast invagination was always associated with the mitotic entry of central cells that were frequently the first to enter mitosis 16 (10 out of 14 cases) (Fig. 1b, c and Supplementary Fig. 1a). Intriguingly, mitotic rounding of the central constricted cells occurred simultaneously with the rapid depression of their apices, followed by chromosome condensation 10 min later (Fig. 1d and Supplementary Video 2). In this study, we call this atypical mitotic rounding associated

with apical depression ‘internalized cell rounding’, to distinguish it from canonical surface mitosis (surface cell rounding).

To determine whether cell rounding is required for invagination, we analysed zygotic mutants of the cell-cycle gene *Cyclin A* (*CycA*), which fail to enter mitosis 16 (ref. 17), and *double parked*^{a3} (*dup*^{a3}), which show a prolonged S phase 16 and delayed entry into mitosis 16 (ref. 18). Tracheal invagination was initiated normally in the *CycA* and *dup*^{a3} mutants, but proceeded more slowly than in controls (Fig. 2a, d, Supplementary Fig. 2 and Supplementary Video 3), indicating that entry into mitosis 16 is required for proper timing of the fast phase.

Although delayed, the accelerated invagination in the *CycA* or *dup*^{a3} mutants eventually occurred, allowing the formation of tube structures (Fig. 2d and Supplementary Fig. 2b) and suggesting that additional mechanisms are involved. After invagination, fibroblast growth factor (FGF) signalling is activated in the tracheal cells to induce branching morphogenesis through chemotaxis^{19,20}. To examine the contribution of FGF signalling to invagination, we analysed mutants of the FGF ligand *branchless* (*bnl*) or the FGF receptor *breathless* (*btl*) (Fig. 2b, e and Supplementary Fig. 3a, c). These mutants invaginated normally, indicating that chemoattraction to FGF is dispensable for invagination.

Next, to assess FGF’s role in the mitosis-defective condition, we analysed double mutants for *CycA* and *bnl* or *CycA* and *btl*, and found that they showed slower invagination than *CycA* single mutants (Fig. 2c, f and Supplementary Fig. 3b, d). Furthermore, the invagination in these double mutants was incomplete, in that the cells failed to form L-shaped tubular structures (Fig. 2c, Supplementary Fig. 3b and Supplementary Video 4, see 120-min time point). Therefore, FGF signalling is critical for invagination when mitosis is blocked, serving a back-up role. Tracheal-specific *CycA* expression rescued the defects in invagination speed and tube structure in the *CycA btl* mutants (Supplementary Fig. 4). In addition, we occasionally observed mitosis of cells outside the pit that occurred before the mitosis of the central apically constricted cells and was not correlated with the fast invagination phase (Supplementary Fig. 1c). Thus, mitosis of the surrounding epidermal cells is dispensable for tracheal invagination. Taken together, we conclude that mitotic entry of central cells is a major mechanism for accelerating tracheal invagination.

To distinguish the role of cell rounding from that of cell division in the fast phase, we used the microtubule inhibitor colchicine to arrest the cell cycle after cell rounding. Colchicine treatment after mitosis 15 induced M-phase arrest at mitosis 16, but the fast invagination movement accompanied by cell rounding was not affected (Fig. 3 and Supplementary Video 5). This result indicates that cell rounding, but not cell division, is responsible for the acceleration phase of the tracheal invagination.

Mitosis of cells in the columnar epithelium normally occurs at the apical surface after surface rounding^{21,22}. We next asked how the apical surface of the central cells becomes depressed during internalized cell rounding. One possible model explains internalized cell rounding as

¹Laboratory for Morphogenetic Signaling, RIKEN Center for Developmental Biology, 2-2-3, Minatojima-Minamimachi, Chuo-ku, Kobe, Hyogo 650-0047, Japan. ²Department of Biology, Kobe University Graduate School of Science, Kobe, Hyogo 657-8501, Japan.

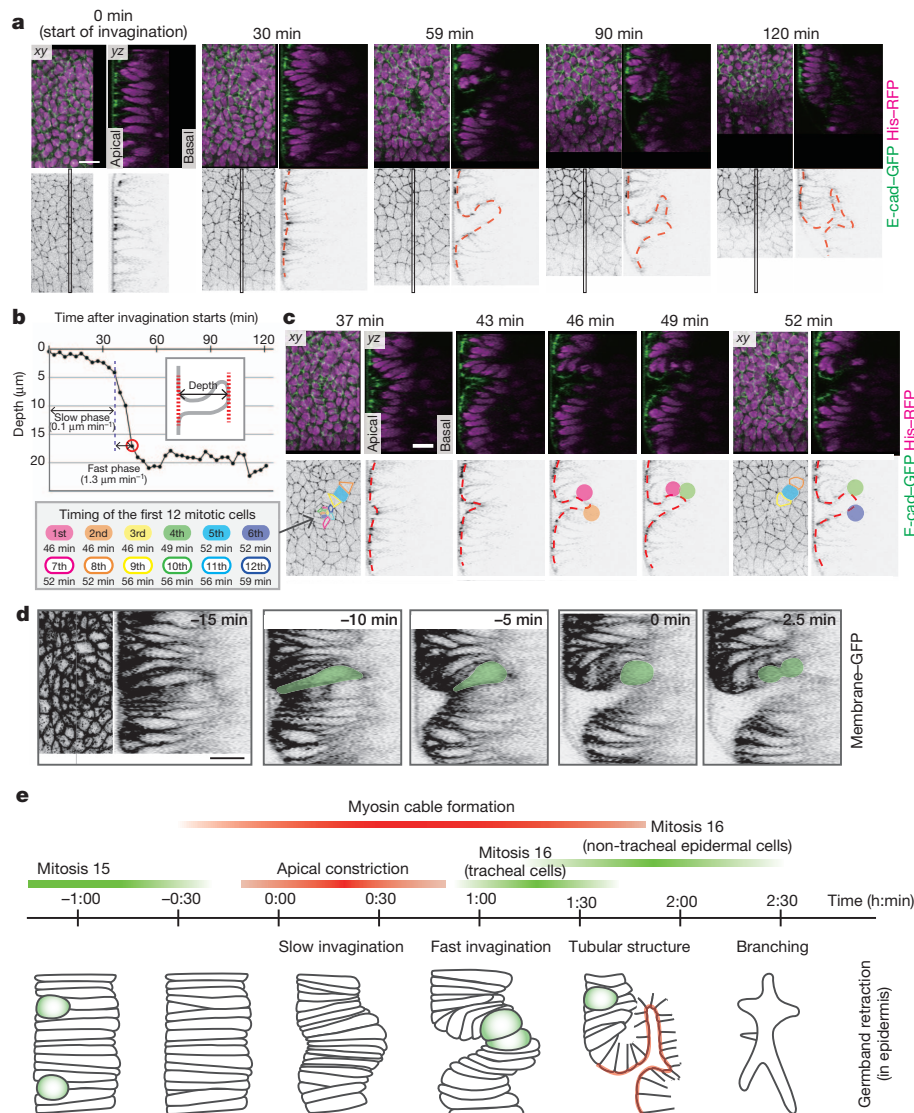


Figure 1 | Two-step process of tracheal invagination. **a**, Time-lapse images of E-cad-GFP (green) and histone H2Av-red fluorescent protein (His-RFP) (magenta) during tracheal invagination. Red dashed lines outline the adherens junctions. Time zero was the initiation of adherens junction depression. **b**, Time course of pit-depth change measured for the images in **a**. Red circle indicates the timing of the first appearance of condensed chromosomes (46 min

cell-autonomously controlled by the association of the cells with the basement membrane or underlying mesodermal cells. However, genetic removal of basement-membrane adhesion by the maternal and zygotic mutation of *βPS-integrin* (also known as *mys*)²³ did not compromise the speed of invagination, and *snail/twist* double-mutant embryos, which lack mesodermal cells²⁴, still showed tracheal invagination with internalized cell rounding (Supplementary Fig. 5). These results suggest that anchoring to the basal side is probably not required.

A second model proposes that the apical depression of the rounding cells is driven by local planar interactions among the tracheal cells. Before and during tracheal invagination, myosin II is enriched at the cell boundaries tangential to the centre of the placode and regulates cell intercalation⁷ (Supplementary Fig. 6a). We noted that the myosin II level in the central cells was lower than in the surrounding, intercalating cells (Supplementary Fig. 6a, compare to myosin II distribution in the ventral furrow in Supplementary Fig. 6c). Nevertheless, the apices of the central cells were constricted during the slow phase (Supplementary Fig. 6b), strongly suggesting that the surrounding cells exerted centripetal pressure on the central cells through myosin II cables⁷.

in **c**. **c**, Time-lapse images of the fast transition. The first 12 mitotic cells are coloured as shown. **d**, Time-lapse images of GFP-CAAX (membrane-GFP). Cells that became spherical are coloured green. Time zero was defined by the complete mitotic rounding of the green cell. **e**, Schematic of tracheal invagination. Scale bars, 10 μm.

Myosin II cables fail to form in EGFR signalling mutants (such as *rho*, the rhomboid endopeptidase required for EGF ligand maturation, and *Egfr*), and apical constriction is impaired in these mutants^{6,7}. The first few cells undergoing mitosis 16 in the tracheal placode of *rho* or *Egfr* mutants showed surface cell rounding with expanded apices (Supplementary Figs 7 and 8b), indicating that EGFR signalling is required to couple the mitotic cell rounding with fast apical depression. We speculate that the columnar shape of the central cells resists centripetal movements, resulting in the accumulation of inward pressure during the slow phase. The existence of such resistance was supported by the results of a physical perturbation experiment using a pulsed ultraviolet laser (Supplementary Fig. 9, Supplementary Videos 7–9, and Supplementary Notes). The cell rounding associated with mitotic entry would release the stored inward pressure by means of cytoskeletal remodelling that causes rapid depression of apical surface together with the active shortening of cell height, leading to rapid buckling of the apical surface and the fast phase of invagination (Fig. 4m and Supplementary Fig. 10a).

Even with the loss of both EGFR and FGF signalling, the tracheal placodes form moderately invaginated structures⁶ (Fig. 4e–h,

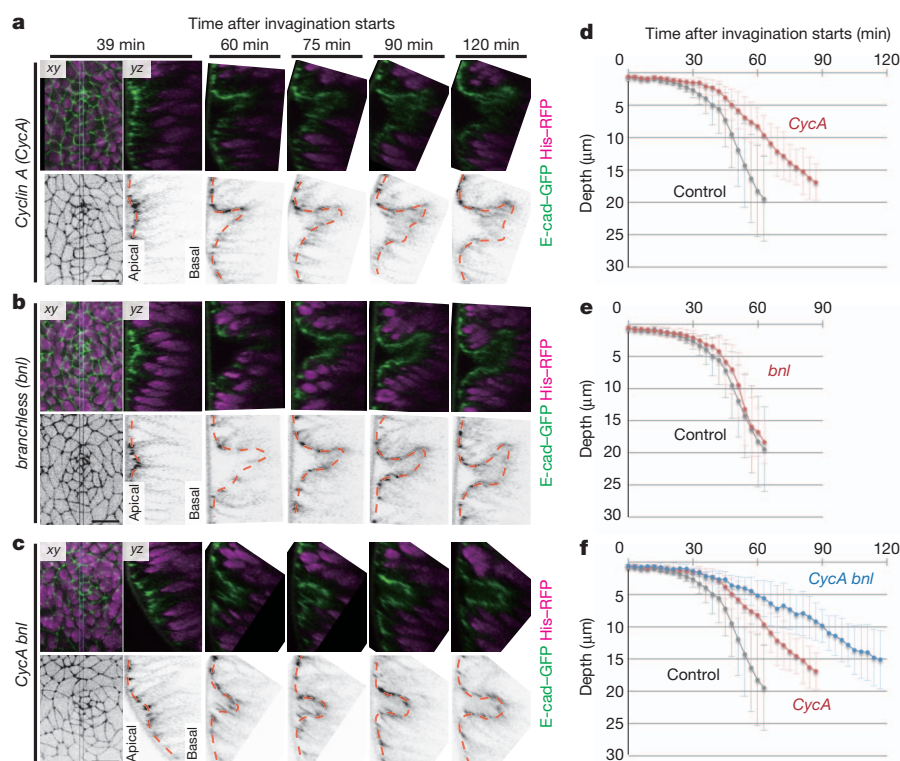


Figure 2 | Mitosis is required for the acceleration of invagination.
a–c, Time-lapse images of tracheal invagination in *CycA* (a), *bnl* (b) and *CycA bnl* (c) mutants carrying E-cad-GFP (green) and His-RFP (magenta).

d–f, Depth of tracheal pits in the mutants and control. Error bars indicate s.d. (control: $n = 14$; *CycA*: $n = 9$; *bnl*: $n = 8$; and *CycA bnl*: $n = 7$). Scale bars, 10 μm.

Supplementary Fig. 8d and Supplementary Video 6), compared to the flat tracheal placode observed in the *rho bnl CycA* triple mutant at the same stage (Fig. 4i–l and Supplementary Video 10), indicating that cells needed to undergo mitosis 16 to induce invagination, independent of EGFR and FGF signalling. In *rho bnl* double mutants, although the cells undergoing the earliest mitoses showed surface cell rounding (Fig. 4f), some of the subsequent mitotic events were coupled to apical depression and internalized cell rounding (Fig. 4g), and invaginated structures eventually appeared (Fig. 4h and Supplementary Video 6). Unlike the earlier mitotic events on the surface, the internalized rounding cells in the *rho bnl* embryos showed constricted apices and were surrounded by apically rounded cells before mitosis (Supplementary Fig. 8b). Internalized rounding with a constricted apical surface were shared properties of cells in mitoses leading to invagination, in both

control and *rho bnl* embryos (Supplementary Fig. 8c). We suggest that the first few cells undergoing surface cell rounding compress the adjacent interphase cells and restrict their apical area, so that they are forced to move internally after rounding, causing the epithelial layer to buckle and invaginate.

Although invagination was largely blocked in the *rho bnl CycA* triple mutants, any double mutant combination permitted invagination to some degree (Figs 2 and 4 and Supplementary Figs 3, 8 and 11), indicating that three qualitatively distinct mechanisms, mitotic cell rounding, myosin II contractility (EGFR) and active cell motility (FGFR), can independently trigger invagination (Supplementary Fig. 11m and Supplementary Notes). In the normal context of wild-type development the combination of cell rounding and EGFR signalling may optimize the timing and speed of invagination, and then

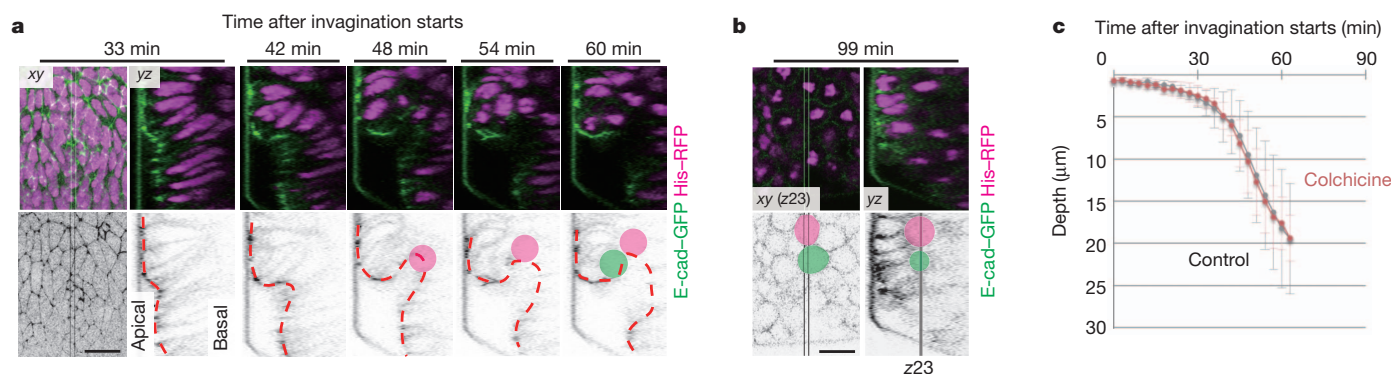


Figure 3 | Mitotic cell rounding is sufficient for the fast transition.
a–b, Time-lapse images of tracheal invagination in a colchicine-treated embryo with E-cad-GFP (green) and His-RFP (magenta). The first rounding cell is coloured magenta, and an additional rounding cell is coloured green. In b, z23 indicates single plane at the z section 23 from the top. c, Mean pit depth of the

colchicine-treated tracheal invagination. Error bars indicate s.d. (control: $n = 14$ and colchicine: $n = 8$). Although almost all the cells arrested at the M phase and the epithelial structure were eventually disrupted (b), the tracheal placodes invaginated normally (c) with cell rounding identical to those of controls (a). Scale bar, 10 μm.

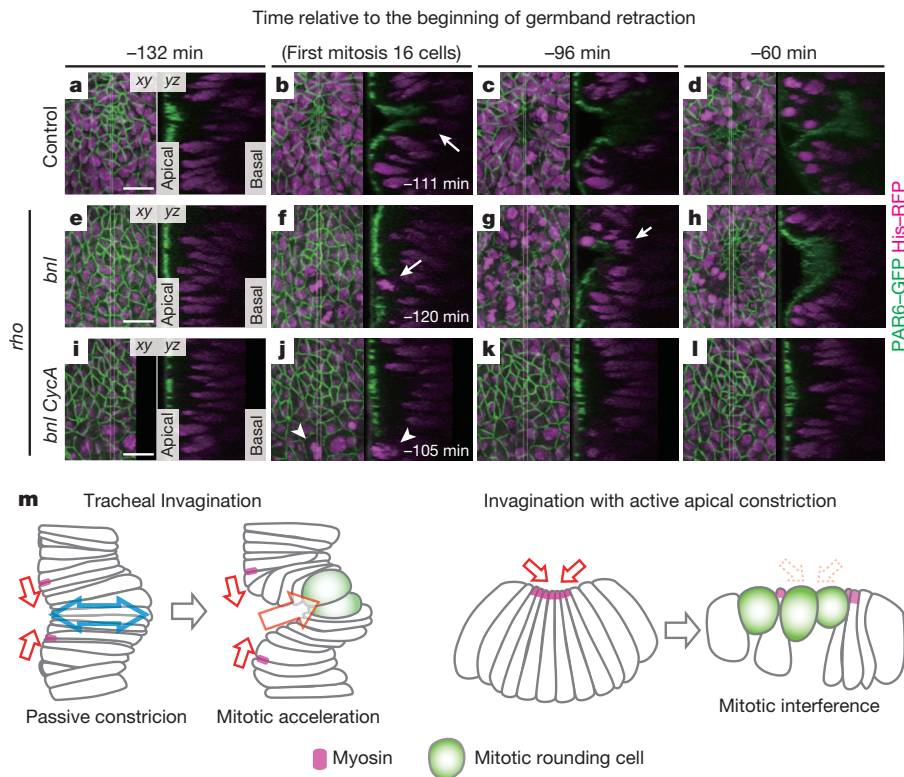


Figure 4 | Mitosis triggers invagination independent of EGF and FGF signalling. a–l, Time-lapse images of tracheal placode in control (a–d), *rho bnl* (e–h) and *rho bnl CycA* (i–l) embryos with PAR-6–GFP, which labels the subapical region, and His–RFP (magenta). Time zero is the initiation of germband retraction. Arrows indicate mitotic cells. Arrowheads in j indicate delayed mitosis 15. m, Model for tracheal invagination with mitotic rounding

invaginated tracheal sacs subsequently respond to FGF emanating from several target tissues guiding branching morphogenesis.

Our observations demonstrates a new role for mitosis in tissue morphogenesis to generate mechanical force through cell rounding, independent of cell division. This is distinct from previously described invagination mechanisms involving cell-autonomous constriction by the apical activation of actomyosin contractility^{25,26}, which is incompatible with mitosis^{3–5} (Fig. 4m and Supplementary Fig. 10). Mitosis 16 outside the tracheal placode occurs in clusters on the ectoderm surface, but does not lead to invagination, suggesting that the tracheal placode is sensitized to invaginate upon mitosis, independent of EGFR and FGFR signalling. Future research to uncover the properties of the tracheal placode that enables it to respond to clustered mitosis will explain not only this new mode of morphogenesis, but also the homeostasis mechanisms of epithelial architecture.

METHODS SUMMARY

Drosophila eggs were collected at 25 °C. Dechorionated embryos were mounted on a glass-bottomed dish (IWAKI) with glue and covered with water. Fluorescent images were captured by a confocal laser-scanning microscope (Olympus FV1000 with 15 mW laser diode 473 nm and 15 mW laser diode 559 nm lasers) with a $\times 60$ oil immersion objective (PLAPON 60XO, numerical aperture 1.42, Olympus) at 25 °C, until the initiation of germband retraction (end of stage 11). All the acquired images were smoothed with a 1-pixel-radius median filter and a 1-pixel full-width at half-maximum Gaussian filter, and movements along the x–y position between time points were corrected by iSEMS²⁷. The y–z or x–z projected views were generated by software developed by K. Kato (unpublished software). The apical area and depth of the apical surface were measured using Image J and calculated with Microsoft Excel.

Detailed information about the reagents and methods used in this paper, including the *Drosophila* stocks, live imaging, laser ablation, image processing, plasmid construction, drug treatment and immunohistochemistry is included in the Methods.

(left). Mitotic cell rounding releases the resistance of central cells (blue arrow) to centripetal forces (red arrows) as the cells shorten, leading to rapid epithelial buckling (large red arrow). In the model (right) of invagination with active apical constriction (red arrows above constricted cells labelled with magenta), mitotic entry interferes with invagination owing to the disappearance of inward forces (red dashed arrows). See Supplementary Fig. 10 for details. Scale bars, 10 μ m.

Full Methods and any associated references are available in the online version of the paper.

Received 11 May; accepted 13 November 2012.

Published online 13 January 2013.

- Théry, M. & Bornens, M. Get round and stiff for mitosis. *HFSP J.* **2**, 65–71 (2008).
- Stewart, M. P. *et al.* Hydrostatic pressure and the actomyosin cortex drive mitotic cell rounding. *Nature* **469**, 226–230 (2011).
- Großhans, J. & Wieschaus, E. A genetic link between morphogenesis and cell division during formation of the ventral furrow in *Drosophila*. *Cell* **101**, 523–531 (2000).
- Mata, J., Curado, S., Ephrussi, A. & Rørth, P. Tribbles coordinates mitosis and morphogenesis in *Drosophila* by regulating String/CDC25 proteolysis. *Cell* **101**, 511–522 (2000).
- Seher, T. C. & Leptin, M. Tribbles, a cell-cycle brake that coordinates proliferation and morphogenesis during *Drosophila* gastrulation. *Curr. Biol.* **10**, 623–629 (2000).
- Brodu, V. & Casanova, J. The RhoGAP *crossveinless-c* links *trachealess* and EGFR signaling to cell shape remodeling in *Drosophila* tracheal invagination. *Genes Dev.* **20**, 1817–1828 (2006).
- Nishimura, M., Inoue, Y. & Hayashi, S. A wave of EGFR signaling determines cell alignment and intercalation in the *Drosophila* tracheal placode. *Development* **134**, 4273–4282 (2007).
- Lecuit, T. & Lenne, P.-F. Cell surface mechanics and the control of cell shape, tissue patterns and morphogenesis. *Nature Rev. Mol. Cell Biol.* **8**, 633–644 (2007).
- Sawyer, J. M. *et al.* Apical constriction: a cell shape change that can drive morphogenesis. *Dev. Biol.* **341**, 5–19 (2010).
- Escudero, L. M., Bischoff, M. & Freeman, M. Myosin II regulates complex cellular arrangement and epithelial architecture in *Drosophila*. *Dev. Cell* **13**, 717–729 (2007).
- Corrigall, D., Walther, R. F., Rodriguez, L., Fichelson, P. & Pichaud, F. Hedgehog signaling is a principal inducer of Myosin-II-driven cell ingression in *Drosophila* epithelia. *Dev. Cell* **13**, 730–742 (2007).
- Vincent, A., Blankenship, J. T. & Wieschaus, E. Integration of the head and trunk segmentation systems controls cephalic furrow formation in *Drosophila*. *Development* **124**, 3747–3754 (1997).
- Wang, Y.-C., Khan, Z., Kaschube, M. & Wieschaus, E. F. Differential positioning of adherens junctions is associated with initiation of epithelial folding. *Nature* **484**, 390–393 (2012).

14. Ghabrial, A., Luschnig, S., Metzstein, M. M. & Krasnow, M. A. Branching morphogenesis of the *Drosophila* tracheal system. *Annu. Rev. Cell Dev. Biol.* **19**, 623–647 (2003).
15. Oda, H. & Tsukita, S. Real-time imaging of cell-cell adherens junctions reveals that *Drosophila* mesoderm invagination begins with two phases of apical constriction of cells. *J. Cell Sci.* **114**, 493–501 (2001).
16. Campos-Ortega, J. A. & Hartenstein, V. *The Embryonic Development of Drosophila melanogaster* (Springer, 1997).
17. Lehner, C. F. & O'Farrell, P. H. Expression and function of *Drosophila* cyclin A during embryonic cell cycle progression. *Cell* **56**, 957–968 (1989).
18. Garner, M., van Kreeveld, S. & Su, T. T. *mei-41* and *bub1* block mitosis at two distinct steps in response to incomplete DNA replication in *Drosophila* embryos. *Curr. Biol.* **11**, 1595–1599 (2001).
19. Klämbt, C., Glazer, L. & Shilo, B. Z. *breathless*, a *Drosophila* FGF receptor homolog, is essential for migration of tracheal and specific midline glial cells. *Genes Dev.* **6**, 1668–1678 (1992).
20. Sutherland, D., Samakovlis, C. & Krasnow, M. A. *branchless* encodes a *Drosophila* FGF homolog that controls tracheal cell migration and the pattern of branching. *Cell* **87**, 1091–1101 (1996).
21. Baker, J. & Garrod, D. Epithelial cells retain junctions during mitosis. *J. Cell Sci.* **104**, 415–425 (1993).
22. Meyer, E. J., Ikmi, A. & Gibson, M. C. Interkinetic nuclear migration is a broadly conserved feature of cell division in pseudostratified epithelia. *Curr. Biol.* **21**, 485–491 (2011).
23. Bunch, T. A. *et al.* Characterization of mutant alleles of *myospheroid*, the gene encoding the β subunit of the *Drosophila* PS integrins. *Genetics* **132**, 519–528 (1992).
24. Leptin, M. & Grunewald, B. Cell shape changes during gastrulation in *Drosophila*. *Development* **110**, 73–84 (1990).
25. Martin, A. C., Kaschube, M. & Wieschaus, E. F. Pulsed contractions of an actin-myosin network drive apical constriction. *Nature* **457**, 495–499 (2009).
26. Martin, A. C., Gelbart, M., Fernandez-Gonzalez, R., Kaschube, M. & Wieschaus, E. F. Integration of contractile forces during tissue invagination. *J. Cell Biol.* **188**, 735–749 (2010).
27. Kato, K. & Hayashi, S. Practical guide of live imaging for developmental biologists. *Dev. Growth Differ.* **50**, 381–390 (2008).

Supplementary Information is available in the online version of the paper.

Acknowledgements We thank the Kyoto and Bloomington *Drosophila* Stock Centers, the Developmental Studies Hybridoma Bank, E. Wieschaus, H. Oda and T. Nishimura for fly stocks and antibodies; K. Kato and H. Wada for assistance with data analysis and experiments; G. Sheng, E. Kuranaga, K. Kato, T. Otani and B. Dong for comments on the manuscript; and members of the Hayashi, Nishimura and Kuranaga laboratories for discussions. This work was supported by Grant-in-Aid for Scientific Research on Innovative Areas (22111007 to S.H.); Grant-in-Aid for Young Scientists (B) (23770624 to T.K.) from The Ministry of Education, Culture, Sports, Science and Technology, Japan; and the RIKEN Special Postdoctoral Researcher Program (T.K.).

Author Contributions T.K. and S.H. conceived the project and wrote the manuscript, and T.K. performed the experiments.

Author Information Reprints and permissions information is available at www.nature.com/reprints. The authors declare no competing financial interests. Readers are welcome to comment on the online version of the paper. Correspondence and requests for materials should be addressed to S.H. (shayashi@cdb.riken.jp).

METHODS

Imaging. Eggs were collected at 25 °C. Dechorionated embryos were mounted on a glass-bottomed dish (IWAKI) with glue and covered with water. Fluorescent images were captured by a confocal laser-scanning microscope (Olympus FV1000 with 15 mW laser diode 473 nm and 15 mW laser diode 559 nm lasers) with a $\times 60$ oil immersion objective (PLAPON 60XO, numerical aperture 1.42, Olympus) at 25 °C. The confocal aperture was opened to 200 μm . Forty to sixty z stacks with a 0.7- μm interval were taken every 1–4 min for up to 300 min until the beginning of germband retraction. All the acquired images were smoothed with a 1-pixel-radius median filter and 1-pixel full-width at half-maximum Gaussian filter, and movements along the x – y position between time points were corrected by iSEMS²⁷. The y – z or x – z -projected views were generated by software developed by K. Kato (unpublished software). ‘ xy ’ shows the Z -projection view (except for Fig. 3b) and ‘ yz ’ and ‘ xz ’ show X -projection and Y -projection views of the boxed area in the ‘ xy ’ view, respectively. In Supplementary Figs 1 and 8, ‘ yz ’ and ‘ xz ’ views are generated along the position of the mitotic cell. The apical area and depth of the apical surface were measured using Image J and calculated with Microsoft Excel. The depth of the tracheal pits was measured as the minimum length between the line of adherens junctions of the surrounding epidermal cells and the most internalized adherens junctions of tracheal pit as shown in Fig. 1b, inset. In Supplementary Fig. 8, the depth of the apical surface was measured as the minimum length between the line of PAR-6–GFP labelling of surrounding epidermal cells and that of each rounded cell (coloured). The developmental timing was determined in a variety of ways depending on the mutant conditions, as described in the figure legends. When obvious tracheal pits were observed (control, *CycA* and FGF-signalling mutants), the initiation of adherens junction depression at the centre was taken as time zero. Under conditions in which no clear tracheal pit formation was observed (EGFR-signalling mutants), the onset of germband retraction (initiation of the distance shortening between two adjacent tracheal pits) was set as time zero. In some cases, onset of the first mitosis 16 was set as time zero.

Fly strains. The following fly strains were used: *ubi-DE-cadherin-GFP* (*E-cad-GFP*)^{15,28}, *histone H2Av-mRFP* (*His-RFP*)²⁹, *sqh-mCherry* (*myosin-mCherry*)²⁵, *par-6-GFP*³⁰, *UAS-mCherry-CAAX*³¹ and *UAS-CycA*³². Information on the following stocks can be found in FlyBase (<http://flybase.net/>): *rho^{del1}*, *Egfr^{J24}*, *btl^{P1}*, *btl^{AOH10}*, *CycA^{C8LR1}*, *dup^{a3}*, *snail^{IIIG}*, *twist^{IIH}*, *mys^{XG43}* and *lele1* (*trh-lacZ*). *btl^{AOH24}* is an imprecise excision mutant³³ from *btl⁶⁻⁸¹*, in which a region including *btl*, *Fbp1* and *Sox21a* is deleted. In this study, *btl^{AOH10/AOH10}* and *btl^{AOH10/AOH24}* were used as *btl* mutants. We noticed that *btl^{AOH24/AOH24}* mutant embryos showed the proper invagination movement, but could not initiate branching morphogenesis, the same as *btl^{AOH10/AOH10}*. Zygotic mutant embryos were distinguished using green balancers (*CyO*, *twi-GAL4 UAS-2xEGFP* or *TM3*, *twi-GAL4 UAS-2xEGFP*)³⁴. Germline clones of *mys^{XG43}* were generated in females of the genotype *mys^{XG43} FRT19A/Ovo^{D1} hsFLP FRT19A*; *ubi-DE-cad-GFP* and mated to *FM7a Dfd-GMR-YFP/Y*; *ubi-DE-cad-GFP* using the *Ovo^{D1}* system³⁵. Embryos that were negative for *Dfd-GMR-YFP*³⁶, were identified as maternal/zygotic *mys* mutant embryos. *ubi-GFP-CAAX* (membrane-GFP) and *trh66-GAL4* strains were generated by Φ C31-mediated transgene integration into attP target sites of the 22A or 86Fa strain³⁷ with the pUbi-GFP-CAAX and pGAL4-*trh66* plasmid, respectively.

Plasmid construction. All plasmids were constructed using PCR with PrimeSTAR (Takara Bio) and the In-Fusion PCR cloning kit (Clontech). For pUbi-attB, the promoter sequence of the ubiquitin gene³⁸ was amplified by PCR and used to replace the UAS enhancer and *hsp70* promoter region of pUAST-attB. In addition, the 3′ untranslated region (UTR) region of the ubiquitin gene was amplified by PCR from the genomic DNA of the Oregon R strain, and cloned into the KpnI site of the previously mentioned plasmid. The resulting plasmid was named pUbi-attB. For Ubi-GFP-CAAX, GFP fused with a 20-amino-acid carboxy terminal CAAX motif of human HRAS was amplified by PCR and cloned into NotI/KpnI-digested pUbi-attB. For pGAL4-attB, GAL4 was amplified by PCR and cloned into NotI/KpnI-digested pUAST-attB. Then the *hs43* promoter with the multi-cloning site of pCaSpeR-*hs43-lacZ* was amplified by PCR and cloned into the above plasmid digested with HindIII/NotI. The resulting plasmid was named pGAL4-attB. For pGAL4-*trh66*, the early tracheless enhancer (*trh66*)³⁹ was amplified from genomic DNA by PCR and cloned into KpnI/NotI-digested pGAL4-attB.

Drug treatment. Dechorionated embryos were treated with heptane for 5–10 s, and immediately washed with PBS containing 0.9 mM CaCl₂ and 0.5 mM MgCl₂

(PBS+). Embryos were mounted on a glass-bottomed dish (IWAKI) with glue and covered with PBS+, and fluorescent images were captured by a confocal laser-scanning microscope as already described. After mitosis 15, the covering PBS+ was replaced with PBS+ containing 50 mM or 500 mM colchicine, and time-lapse imaging was restarted. Only samples in which cells entered and were arrested at mitosis 16 were used for this analysis. (In the rest of the samples, the cells did not enter mitosis 16 and embryogenesis was arrested.)

Laser ablation. Laser ablation was performed using a confocal laser-scanning microscope (Olympus FV1000 with 15 mW laser diode 473 nm and 15 mW laser diode 559 nm lasers) equipped with an ultraviolet laser system (Olympus UV-ASU-P2) and a $\times 60$ oil immersion objective (UPLSAPO 60XO, numerical aperture 1.35, Olympus). For fluorescent image acquisition, six z stacks with a 1- μm interval were taken every 3.53 s. Simultaneously with the image acquisition, a single pulse of a 349-nm laser (pulse duration <5 ns) was applied to cells at a specific time and defined depth. The area and depth of the cells were measured as described previously. A box plot was drawn using R software, showing the median as a line, the upper and lower quartiles as boxes, and the 1.5-interquartile range as whiskers. The P values were calculated using a Student's t -test (for two samples with similar variances, two-tailed) or Welch's t -test (for two samples with passively unequal variances, two-tailed).

Immunohistochemistry. Dechorionated embryos were fixed in 4% paraformaldehyde for 30 min at room temperature, and blocked with 0.1% bovine serum albumin, 0.2% Triton X-100 and 0.2% Tween-20 in PBS. The first antibody was diluted in the blocking solution and incubated overnight with gentle rotation at 4 °C. After washing, the second antibody, diluted in the blocking solution, was added, and the tissue was further incubated for 2 h at room temperature. After washing, the embryos were mounted in Vectashield mounting medium with 4′, 6-diamidino-2-phenylindole (DAPI, Vector Laboratories) and photographed using an Olympus FV1000 confocal microscope with a $\times 20$ objective lens (UPLSAPO 20X numerical aperture 0.75, Olympus) and a $\times 60$ water immersion objective lens (UPLSAPO 60XW numerical aperture 1.2, Olympus). The following antibodies were used: mouse anti- β -galactosidase (1:100, 40a-1, DSHB), rabbit anti- β -galactosidase (1:1,000, Cappel), rabbit anti-DsRed (1:5,000, BD Biosciences), rat anti-DEcad (1:20, DSHB), anti-mouse IgG Alexa 488 (1:500, Molecular Probes), anti-rabbit IgG Alexa 555 (1:500, Molecular Probes) and anti-rat IgG Dylight649 (1:500, Jackson Laboratory).

28. Haruta, T., Warrior, R., Yonemura, S. & Oda, H. The proximal half of the *Drosophila* E-cadherin extracellular region is dispensable for many adherin-dependent events but required for ventral furrow formation. *Genes Cells* **15**, 193–208 (2010).
29. Pandey, R., Heidmann, S. & Lehner, C. F. Epithelial re-organization and dynamics of progression through mitosis in *Drosophila* separase complex mutants. *J. Cell Sci.* **118**, 733–742 (2005).
30. Wirtz-Peitz, F., Nishimura, T. & Knoblich, J. A. Linking cell cycle to asymmetric division: Aurora-A phosphorylates the par complex to regulate numb localization. *Cell* **135**, 161–173 (2008).
31. Kakiyama, K., Shinmyozu, K., Kato, K., Wada, H. & Hayashi, S. Conversion of plasma membrane topology during epithelial tube connection requires Arf-like 3 small GTPase in *Drosophila*. *Mech. Dev.* **125**, 325–336 (2008).
32. Hayashi, S. & Yamaguchi, M. Kinase-independent activity of Cdc2/Cyclin A prevents the S phase in the *Drosophila* cell cycle. *Genes Cells* **4**, 111–122 (1999).
33. Ohshiro, T. & Saigo, K. Transcriptional regulation of *breathless* FGF receptor gene by binding of TRACHELESS/dARNT heterodimers to three central midline elements in *Drosophila* developing trachea. *Development* **124**, 3975–3986 (1997).
34. Halfon, M. S. *et al.* New fluorescent protein reporters for use with the *Drosophila* Gal4 expression system and for vital detection of balancer chromosomes. *Genesis* **34**, 135–138 (2002).
35. Chou, T. B. & Perrimon, N. Use of a yeast site-specific recombinase to produce female germline chimeras in *Drosophila*. *Genetics* **131**, 643–653 (1992).
36. Le, T. *et al.* A new family of *Drosophila* balancer chromosomes with a w⁺ *dfd-GMR* yellow fluorescent protein marker. *Genetics* **174**, 2255–2257 (2006).
37. Bischof, J., Maeda, R. K., Hediger, M., Karch, F. & Basler, K. An optimized transgenesis system for *Drosophila* using germ-line-specific ϕ C31 integrases. *Proc. Natl Acad. Sci. USA* **104**, 3312–3317 (2007).
38. Lee, H. S., Simon, J. A. & Lis, J. T. Structure and expression of ubiquitin genes of *Drosophila melanogaster*. *Mol. Cell. Biol.* **8**, 4727–4735 (1988).
39. Sotillos, S., Espinosa-Vázquez, J. M., Foglia, F., Hu, N. & Hombria, J. C.-G. An efficient approach to isolate STAT regulated enhancers uncovers STAT92E fundamental role in *Drosophila* tracheal development. *Dev. Biol.* **340**, 571–582 (2010).

CORRIGENDUM

doi:10.1038/nature11788

Corrigendum: The zebrafish dorsal axis is apparent at the four-cell stage

Aniket V. Gore, Shingo Maegawa, Albert Cheong, Patrick C. Gilligan, Eric S. Weinberg & Karuna Sampath

Nature **438**, 1030–1035 (2005); doi:10.1038/nature04184

In Fig. 3p and q and Supplementary Table 3 of this Letter, the data for sqt MO2 and sqt MO3 were inadvertently mislabelled and should be swapped. The text on page 1033 that describes Fig. 3p and q should therefore read ‘sqt MO2’ not ‘sqt MO3’ on lines 4 and 13 of the second full paragraph of the left column. All our other figures and conclusions stand. In addition, Fig 1a–c and the labelling of sqt MO2 and sqt MO3 is correct in our Reply to the Brief Communication Arising (*Nature* **450**, E2–E4 (2007); doi:10.1038/nature06315). We regret the error.

CORRIGENDUM

doi:10.1038/nature11827

Corrigendum: How cancer metabolism is tuned for proliferation and vulnerable to disruption

Almut Schulze & Adrian L. Harris

Nature **491**, 364–373 (2012); doi:10.1038/nature11706

We inadvertently omitted to cite reference 101, which should have been cited on page 267 at the end of the following sentence: “Recent evidence suggests that renal cyst formation after Fh1 deletion is independent of HIF, but involves activation of the NRF2 pathway by fumarate, and that activation of NRF2 may contribute to the development of fumarate-hydratase-deficient cancers^{51,101}.”

101. Ooi, A. et al. An antioxidant response phenotype shared between hereditary and sporadic type 2 papillary renal cell carcinoma. *Cancer Cell* **20**, 511–523 (2011).

ERRATUM

doi:10.1038/nature11828

Erratum: Making sense of palaeoclimate sensitivity

PALAEOSSENS Project Members

Nature **491**, 683–691 (2012); doi:10.1038/nature11574

The surname of author V. Masson-Delmotte was misspelled as Masson-Demotte. In Table 1 of this Perspective, the ‘Source’ for ‘Label in Fig. 3’ entry 13 should be ref. 61 (not ref. 65). In addition, the x-axis labels of Fig. 3c were misplaced. Figure 1 shows the corrected panel and the original Perspective has been corrected online.

C

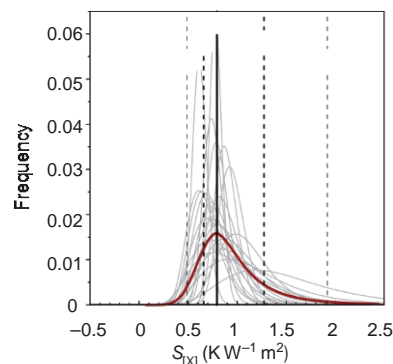


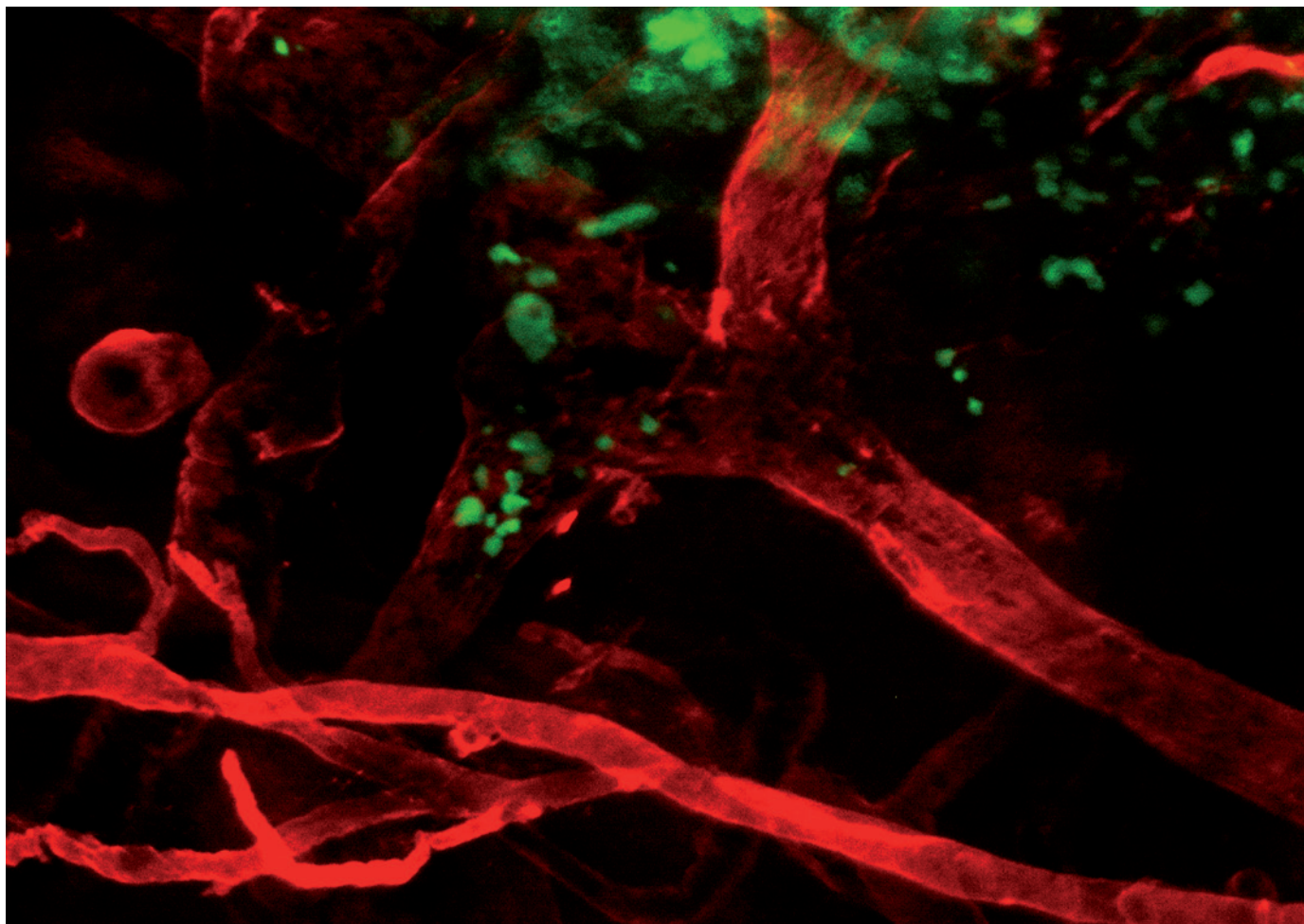
Figure 1 | This is the corrected Fig. 3c.

TECHNOLOGY FEATURE

TRACKING METASTASIS AND TRICKING CANCER

Physics – and engineering – based approaches are helping researchers stop the spread of cancer by anticipating tumour cells' moves and habits.

W. KILARSKI, A. LUND/EPFL



Live fluorescence microscopy imaging of metastasis — the spread of cancer — showing melanoma cells (green) invading lymphatic vessels (thick red vessels).

BY VIVIEN MARX

In the 1880s, British surgeon Stephen Paget examined autopsy reports from more than 900 patients with advanced breast cancer. He was trying to understand metastasis — the process by which tumours spread through the body. Paget reasoned that if all the organs were equally susceptible, with the location of tumour fragments governed by chance alone, then all the organs should be equally affected.

Instead, he found that the breast cancers had spread mainly to the uterus and the bones. He suggested that when tumours shed cells that move through the bloodstream, the cells are like seeds that grow only where they find congenial soil. To understand metastasis, it might be useful, he wrote, to study not only the seeds, but the soil too¹.

Paget's 'seed and soil' hypothesis "still holds forth today", writes Isaiah Fidler of the University of Texas MD Anderson Cancer Center

in Houston². It informs present-day efforts to understand every detail of metastasis — including the genetic pathways that direct a cancer's growth, the factors that set some tumour cells free to travel through the bloodstream, and their interactions with the environments at the organs in which they settle³.

Only a few of those cells manage to seed new tumours. Metastasis is a "low-probability event", says Robert Gillies of the H. Lee Moffitt Cancer Center in Tampa, Florida. Even ►

► so, more than 90% of cancer deaths are the result of metastasis. Understanding the processes involved is therefore something of a priority.

Studying metastasis in patients would require unethical experimentation, so scientists are creating artificial conditions similar to those in the body. They are developing approaches based on physics, chemistry and engineering, and are increasingly using three-dimensional assays for experiments that are usually two-dimensional. For example, they have created mimics of the extracellular matrix (ECM) — the body's tissue scaffolding — in devices that are hooked up to imaging systems. This set-up allows them to track tumour cells over extended periods of time to see how they detach from one spot and attach at another, and how they creep through tissue that should be too dense to let them pass. Other approaches involve scooping migrating tumour cells out of the blood and locking them in highly engineered cages to discover how they seed secondary tumours.

Scientists are making rapid progress thanks to an array of approaches that consider networks of interacting genes and proteins, and breakthroughs in imaging and animal

modelling are yielding increasingly comprehensive data (see 'Technology timeline in metastasis research'). Such technological innovations are galvanizing efforts to overcome gaps in the scientific understanding of metastasis, as Yibin Kang, a cancer biologist at Princeton University in New Jersey, and Nilay Sethi, a former member of Kang's lab now at the University of California, San Francisco, have pointed out⁴.

READY TO SPREAD

Metastasis is thought to begin with the epithelial–mesenchymal transition (EMT), a cascade of events in which tumour cells lose many of their 'epithelial' characteristics and become more like mesenchymal cells with the ability to spread and invade tissue⁵. This process occurs naturally in healthy cells but is poorly understood in tumours. Researchers are not even sure whether it happens early in tumour development or only in advanced tumours. But they know that the transformation involves a chatter of signalling, both within a tumour cell and between cells. For example, both normal cells and tumour cells shed small vesicles, known as exosomes, into the bloodstream. Previously considered a cell's way of putting out the rubbish, exosomes are now known to contain proteins and signalling molecules — like messages in a bottle — that prepare the target tissues to accept metastatic cells.

Even before cells migrate, tumours create

their own microhabitat that promotes metastasis. "We believe there are components of the microenvironment that matter in the adaptive changes in tumour cells," Gillies says. Clinicians can identify genetic signatures in patients' cancers and prescribe drugs to attack the specific tumour type, but this treatment often fails because tumours activate alternative genetic pathways instead, he says. If clinicians can understand the adaptive landscape of the tumour and its environment, they will have more lines of attack and may even be able to create a habitat that inhibits metastasis.

Researchers have found that as tumours grow they create a unique microclimate with highly acidic areas that are low in oxygen — conditions that seem to favour metastasis. Combining imaging with technology that characterizes cancer metabolism in this microhabitat helps to reveal how tumour cells shift to a metastatic state, Gillies says. Rapid cancer growth is fuelled by a metabolic process called glycolysis. Gillies and his team are able to detect this — and thereby identify cancer cells — using an instrument from Seahorse Bioscience in Billerica, Massachusetts, that allows them to analyse both tumour metabolism and the microenvironment in an automated fashion. "Since we got the device, it has been running non-stop," he says.

The instrument, an XF Analyzer, measures the acid produced by glycolysis in cells, thereby identifying tumour cells, which have a high

TECHNOLOGY TIMELINE IN METASTASIS RESEARCH

Adapted from ref. 4.

1994 ► Advances in mass spectrometry allow identification of individual cancer proteins.	1995 ► DNA-microarray technology shows many patterns of gene expression.	1996–1998 ► Advances in microscope technology and biomarker tagging allow live imaging of tumour metastasis.	1998 ► Therapies emerge that use an antibody to target a specific tumour protein.	Tissue microarrays are developed to detect specific proteins in a large number of tumour samples.
1999–2000 ► Assays pinpoint the target sites of DNA-binding proteins that shape gene expression.	2000–2002 ► Gene-expression profiling helps to find metastasis genes and reveals cancer subtypes in patients.	Protein microarrays can screen for markers of cancer progression.	2002 ► Gene-expression profiles show cancer progression signatures. Metastatic behaviour of single breast cancer cell is imaged.	2003 ► Microarray profiling identifies factors that influence bone metastases.
2004 ► Drug based on monoclonal antibody is approved for inhibiting angiogenesis in metastatic colon cancer.	2005 ► Discovery of a niche that forms before the arrival of metastatic cancer cells in secondary organs to nurture their growth.	2006 ► High-throughput sequencing increasingly used to sequence cancer genomes.	Mass spectrometry and new types of protein labels pinpoint changes in proteins co-opted by tumours.	2007 ► First metastasis-related microRNA identified.
2008 ► RNA sequencing applied to cancer genomes to quantify expression of cancer genes.	2009 ► Experiments indicate that tumour self-seeding may even drive the growth of primary tumours.	2010 ► Drugs targeting tumour oncogenes or supporting host cells approved to address some types of metastasizing cancers.	2011 ► Sequencing reveals the natural history of metastatic progression in human cancer patients.	2012 ► Recognition of tumour exosomes as means of long-distance communication in cancer metastasis.

glycolysis rate, says Min Wu, director of biology at Seahorse Bioscience. A sensor cartridge positioned above the cells creates a temporary microchamber and measures oxygen and pH levels. This arrangement lets scientists detect cell metabolism in real time, typically within 1–2 hours, says Wu.

Buffers that neutralize the tumour's acidity have been shown to make chemotherapies more effective and inhibit metastasis. To determine the right buffer mix, Gillies uses the analyser to type cells according to their metabolic profile. Several research groups are also exploring how drugs can be tailored to release a warhead loaded with anticancer drugs into tissue areas with a profile characteristic of cancer.

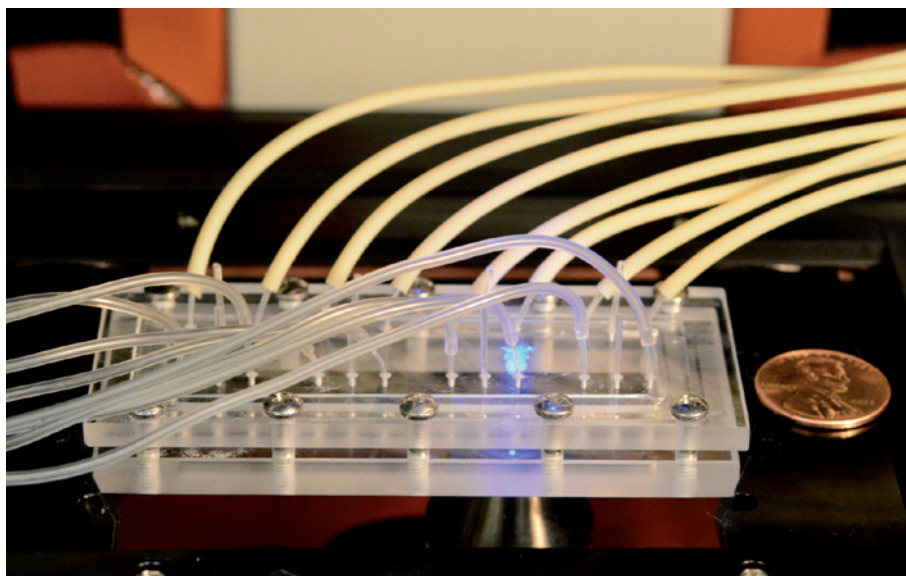
ON THE MOVE

The next step in metastasis is for cells to break away from the tumour so that they can enter the bloodstream. Several relatively low-tech but tried-and-tested assays can help scientists watch this migration. Companies such as EMD Millipore of Billerica, Massachusetts, and Cell Biolabs in San Diego, California, offer two-dimensional assays that help researchers track and quantify migration and chemotaxis (the movement of cells towards a chemical signal).

Scientists sometimes build these assays themselves, but the companies say that standardized products result in more comparable experimental results. One technique developed in the 1960s to study cell migration is the Boyden chamber, which is essentially a small cup containing cells placed inside a larger cup containing growth medium or chemoattractant to attract cancer cells. The two chambers are separated by a porous membrane through which cells can migrate. In this way, scientists can track chemotaxis and see which cells migrate through the membrane.

In a similar test known as a scratch assay, tumour cells are spread in a layer across growth medium in a plate. When the surface is scratched — by a researcher running a pipette tip across it, for example — cells move together to fill in the artificial gap, much as they would when closing a wound in the body. Richard Klemke, a cell biologist at the University of California, San Diego, and a consultant at EMD Millipore, developed a comb for the scratch assay, putting “a new spin on a very old technique”, says Jun Ma, a product manager at EMD Millipore. The comb makes uniform, high-density scratches that induce large numbers of cells to migrate synchronously for scientists to image, says Klemke.

A German company, Ibidi, based in Munich, offers what it believes is an improved migration assay. Most labs use the Boyden chamber to study chemotaxis, but Ibidi's president, Roman Zantl, is aware of its limitations. “I doubt that it gives valid results in case of adherent cancer and other cell types,” he says. The synthetic membrane between the two cups is unlike the material through which cells travel in the



Scientists have engineered an environment that lets them follow metastatic tumour cells while chemokines and growth factors flow in from the side to mimic the tumour microenvironment.

body and might alter the cells' behaviour. And although the assays work well enough for fast-migrating cells, such as leukocytes, they are less suited to the slower movement of tumour cells, which might not be counted if they take too long to complete their journey across the membrane from one cup to another.

To address these issues, Ibidi developed a migration assay based on the Zigmond chamber, an approach developed in the 1970s that uses two reservoirs, one containing cells and a second containing a chemoattractant. In Ibidi's version, cells move along a chemoattractant gradient across a small area that can be viewed under a microscope. Diffusion of the chemoattractant is slow, allowing researchers

“It’s a physics problem in some ways, it’s an integrated problem.”

Mingming Wu, a bioengineer at Cornell University in Ithaca, New York. Wu says she uses them because “cancer metastasis is a game of going somewhere”. But she hopes to be able to model migration in three dimensions.

SEEING 3D

“What you see in two dimensions has very little apparent correlation with what you see in three dimensions,” says Wu. In a two-dimensional assay, tumour cells use adhesion molecules to inch along. “If you disable the adhesion molecules, the cells cannot move,” she says. But in a three-dimensional assay, cancer cells switch to a different type of movement when their adhesion molecules are disabled. “A cancer cell is very smart in some ways,” Wu says.

Imaging experiments by several researchers, including John Condeelis at Albert Einstein

College of Medicine in New York, have provided a visual, three-dimensional view of metastasis in mice, says Wu. Now she wants to bring this observational power to an engineered environment that realistically mimics human physiology. “It’s a physics problem in some ways, it’s an integrated problem.”

Wu has developed a device in which tumour cells move through a synthetic version of an ECM. As they move, they generate force and migrate along the ECM fibrils to reach the bloodstream. “Some of them climb the ropes. They extend and cling onto fibres and pull themselves, which makes them more elongated, but some are more rounded,” she says. Where the matrix is too dense, tumour cells secrete chemicals to create a passageway.

The device has three tiny channels patterned into the surface of a growth medium, and Wu places tumour cells embedded in ECM in the middle channel. Chemoattractants known to affect cancer cells are added to another channel. Wu uses time-lapse microscopy to observe what happens. To explore why breast cancer cells first metastasize to lymph nodes, the researchers use chemoattractants that correspond to molecules present in lymph nodes. The device makes it possible to observe tumour cells interacting as naturally as possible with one another, with healthy tissue cells and with the body's immune cells.

Once again, commercial alternatives are available for scientists who do not want to build their own microfluidic platform. Last year, for example, EMD Millipore began selling one after acquiring CellASIC, which launched the platform in 2007.

The company's programmable perfusion system is hooked up to a microscope and lets scientists use software-based commands instead of manual ones to make cells or molecules flow in or out of a microenvironment.

They can investigate factors that might promote or thwart a metastasis-like state in cells and “get real-time movies of these cells as they’re behaving”, says bioengineer Alex Mok, who was in Luke Lee’s lab at the University of California, Berkeley, where the device was developed, and is now a product manager at EMD Millipore. Mok describes the device as “a semiconductor chip for biologists” that should allow more researchers to do this kind of experiment.

SCOOPING UP THE SEEDS

Once the malignant cells enter the bloodstream they are known as circulating tumour cells (CTCs). Clinicians can gauge how a breast, prostate or colon cancer patient is faring from the number of CTCs in the blood and from their molecular characteristics. However, CTCs are extremely difficult to isolate. Test instruments typically sample 5–10 millilitres of blood, a tiny fraction of the body’s total of 5 litres. And a cancer patient’s blood may contain only one metastatic cell for every 1 billion to 5 billion other cells, says Mehmet Toner, a bio-engineer at Massachusetts General Hospital in Boston. “It’s a statistical nightmare.”

One device that can help to improve the odds of finding CTCs is the CellSearch, made by Veridex, a subsidiary of Johnson & Johnson based in Raritan, New Jersey. Approved by the US Food and Drug Administration in 2004, it tags tumour cells with magnetic beads coated with antibodies that adhere to proteins found on the surface of tumour cells. The CTCs are then separated using a magnet and are then stained and imaged.

Toner and other scientists want devices that capture CTCs to be more sensitive and to keep the cells viable for further analysis, which CellSearch does not. The technical challenge and its commercial promise have led to a flurry of device-building. “There are lots of good ideas out there,” Toner says.

His own team has been developing different types of bank-card-sized devices coated with antibodies that trap CTCs by attaching to proteins on their cell surface. In his most recent device, the herringbone-chip (HB-chip), blood flows in a see-through channel that lets scientists image the captured cells. The herringbone pattern of grooves on the inside of the channel’s roof creates a gentle vortex in the blood, increasing the number of tumour cells that stick to the antibody-coated surface, he says.

A LIQUID BIOPSY

Toner thinks that CTC chips such as this will help cancer researchers understand the separate steps in the transformation from tumour cells to the metastatic seeds of a new tumour. The devices make it possible to use extremely high-definition imaging, which can enhance the work of pathologists, he says.

In a test using blood from patients with metastatic prostate cancer, Toner’s team was

able to distinguish between circulating tumour cells before and after medical treatment, an ability that could help to guide therapy. In a separate test, the researchers found higher levels of a signalling molecule called WNT2 in circulating pancreatic tumour cells than in primary tumour cells⁶. This difference is a potential biomarker that could help drug developers find ways to inhibit metastasis.

The test also revealed metastatic cells’ survival strategies. Cells need to be anchored if they are to survive — once they are in the bloodstream, even tumour cells should die, Toner says. But turning on the *Wnt2* gene helps them avoid cell death. “Cells that express *Wnt2* can survive in a suspended state,” he says.

In contrast to CellSearch, Toner’s chip does not need blood samples to be preprocessed. It also keeps cells viable for further profiling. In 2011, his team landed a five-year, US\$30-million collaboration agreement with Johnson & Johnson to refine CellSearch technology with a new approach to characterize tumour cells. Toner says he cannot comment on the progress yet, but he challenges views that metastatic cells are too scarce to capture in sufficient numbers or that microfluidics cannot be used for large-scale blood analysis. Using

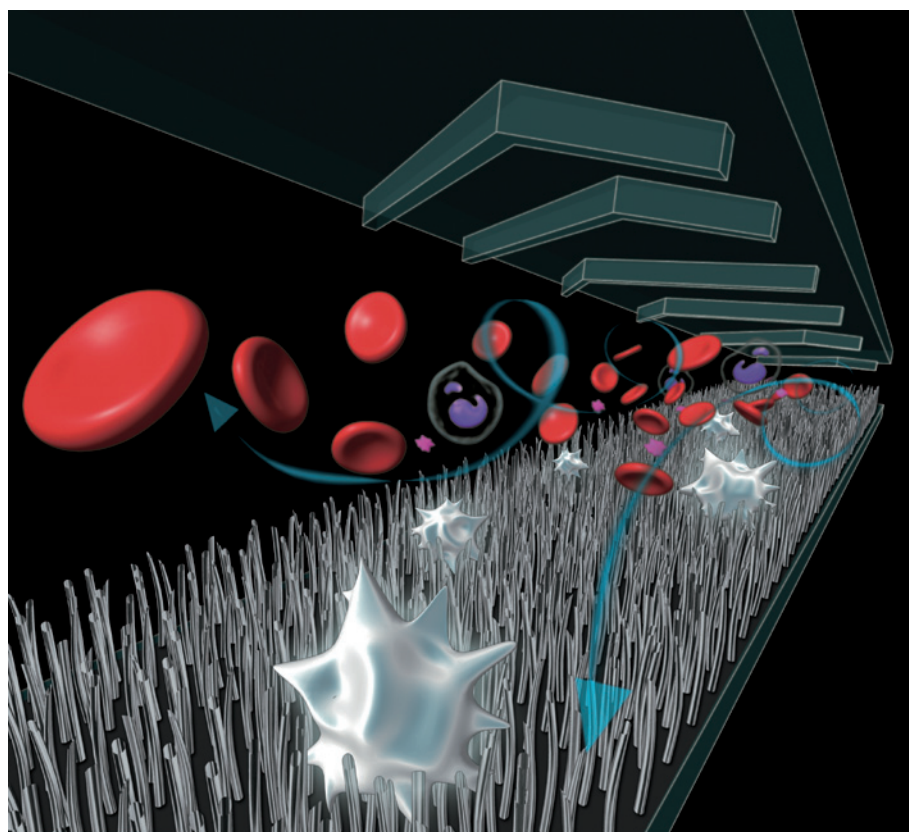
A cancer patient’s blood may harbour only one metastatic cell for every 1 billion to 5 billion other cells.

such a tiny device has engineering efficiencies. “Microfluidics gives us multiplexing, building redundancy into the system, and it gives us very uniform conditions,” he says.

Many other labs are also working on CTC chips, including the National University of Singapore, Stanford University in California, Louisiana State University and the University of California, Los Angeles (UCLA). Hsian-Rong Tseng, a chemist at UCLA, says CellSearch has raised awareness among scientists, physicians and patients that CTCs allow “a biopsy directly from the blood”. Tseng’s team has developed a microfluidic ‘Nano-Velcro’ assay, in collaboration with researchers at the RIKEN Advanced Science Institute in Saitama, Japan, and several institutions in China, including Wuhan University. Tseng’s group has now founded a company called CytoLumina Technologies to commercialize the instrument.

Tseng’s device can capture and release live CTCs from a blood sample. When the team used it to analyse CTCs from patients with metastatic melanoma, they sequenced the cells’ DNA and identified clinically relevant mutations. To ramp up the scale at which it can be used with genetic testing, Tseng teamed up with the Beijing Genomics Institute in China.

The device contains polymer-coated silicon nanowire brush hairs studded with antibodies that match proteins on the surface of metastatic cells. As the blood flows through the device, also aided by a herringbone pattern, the tumour cells stick to the surface — hence



A ‘Nano-Velcro’ device captures circulating tumour cells and keeps them viable for further analysis.

the Nano-Velcro name. “We can release them simply by changing the temperature,” he says. Lowering the temperature changes the polymer’s configuration, pulling the antibodies inwards, allowing the tumour cells to detach and flow out of the channel — viable, intact and ready for further study.

LESSONS FROM THE HEART

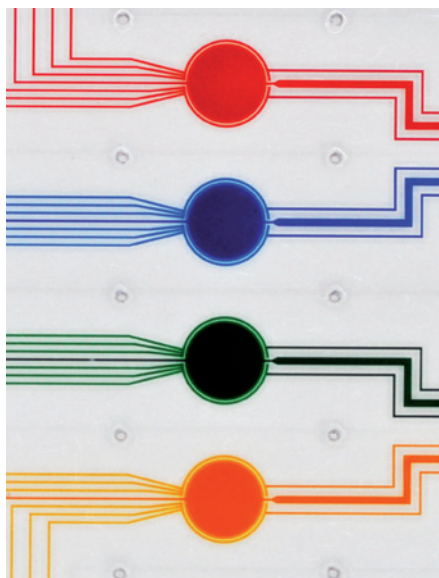
The final stage of metastasis is when the CTCs find fertile ‘soil’ in the body, to use Paget’s term, and begin to grow. It’s not clear what makes particular environments hospitable to certain tumour cells, but one place to look for answers is the heart — “the one organ in the body that has actually beaten cancer,” according to cardiology researcher Jay Schneider at the University of Texas Southwestern Medical Center in Dallas. Some cancers such as melanoma can metastasize to the heart, but it is “very, very rare”, he says. Attempts to achieve metastasis to the heart experimentally have worked only with one cancer cell line, he adds.

The heart’s defence mechanism remains unknown, but it seems to be shielded by either mechanical or physical barriers that make the microenvironment hostile to CTCs. It’s likely that some component of the heart’s microenvironment — maybe its tissue, cells or the scaffolding around the cells — is protecting it. One way to understand the mechanism is to identify what aspect of the ‘soil’ makes healthy tissue vulnerable to metastatic seeds.

Biomedical engineer Sangeeta Bhatia and her graduate student Nathan Reticker-Flynn at the Massachusetts Institute of Technology (MIT) in Cambridge have built a platform to help them study the interactions between tumour cells and various synthetic models of the ECM (the dense weave of fibrils that make up the scaffolding connecting cells in tissues). The pair want to learn which components of the ECM are most hospitable to metastatic seeds and favour cell migration and adhesion.

Far from being mere stabilizing mortar, the ECM has “its own universe of biology; it is a signalling hub”, she says. “And the cells are constantly modifying it, so it’s a dynamic and biologically active glue.” In a primary tumour, cancer cells stick to one another. To spread, metastatic cells must first detach from their mooring, then move within the ECM to the bloodstream, travel in the blood until they reach a suitable destination, and then attach to the ECM and grow into a tumour there. “The attachment at that metastatic site is what this experiment was about,” she says.

Bhatia’s team used robots to print arrays of ECM dots, each with a different composition. The researchers scoured catalogues to find all the synthetic ECM molecules on the market and developed 800 unique combinations. They coated glass slides with polyacrylamide, which swells to trap the ECM molecules in one spot, and then seeded metastatic lung cancer cells on the spots. “We developed a platform



This system uses software-based commands to flow cells in a controlled microenvironment.

to query these all at once,” Bhatia says, and it has attracted so much interest that she plans to distribute it commercially.

The researchers imaged the different ways the cells adhered to the ECM spots and compared the adhesion profiles. “We found they have gained the ability to stick to different things than in the primary tumour,” she says. As the cells grew over a period of time, the scientists used a clustering algorithm to find patterns in the data. They hope that understanding how tumour cells adhere to the ECM could open the way for a potential therapeutic to interfere with this ability.

THE GAZE OF PHYSICISTS

Metastasis research is benefiting from a multi-disciplinary approach that includes biologists, physicists, chemists and engineers. In 2009, for example, the US National Cancer Institute (NCI) started funding a network of 12 Physical Science–Oncology Centers (PSOCs). In 2010 it launched a Provocative Questions initiative requesting research proposals that address “perplexing” problems in cancer, such as devising engineering approaches to improve the study of metastasis.

Another NCI scheme, the Innovative Molecular Analysis Technologies (IMAT) programme, launched in 1998, also fosters these partnerships and aims to develop tools that could accelerate cancer research, says IMAT director Tony Dickherber. “Our understanding of how metastasis works, and the importance and complexity of the microenvironment, is significantly influenced by what tools we have to tell us about either of those things,” he says. Several IMAT-funded projects have become widespread research tools as well as commercial products. “I really appreciate the community they have brought together,” says Tseng, who received a grant from IMAT.

“We don’t prescribe what kinds of innovations we’re interested in, we want investigators to come to us and surprise us with their innovative ideas,” Dickherber says. The programme puts together interdisciplinary review panels to score prospective research tools according to their potential impact.

Tyler Jacks, who directs the MIT’s David H. Koch Institute for Integrative Cancer Research, says his institute is “expressly about bringing biologists and engineers together under one roof”. Collaborations are encouraged by ensuring that everyone circulates in the same sections. “We’re neighbours now and we interact much more extensively,” he says.

Physicist Jean-François Joanny at the Curie Institute in Paris is also using his expertise to benefit cancer biology. Building on work by the late Malcolm Steinberg, a Princeton University biologist, Joanny’s team has looked at how pressure affects the growth of clusters of cancer cells known as spheroids. Perhaps a physical property is what distinguishes cancer cells. “Could you characterize the degree of invasiveness by looking at properties like this?” he says. “That’s the idea at the back of our minds.”

One cancer biologist proposed a scientific challenge for Joanny’s group. He asked the physicists to make pressure measurements in a mouse with multiple tumours and determine, from those measurements alone, which cancer is most likely to metastasize. As the biologist knows the correct answer, his team will use biology to validate the physics-based results.

The Curie Institute has a tradition of cross-disciplinary collaboration, with cancer biologists approaching suggestions from physicists with open minds, Joanny says. “We are used to the idea that they might consider us crazy.” But if wild ideas from physicists can boost the fight against cancer — and their work to help biologists understand the various processes of metastasis suggests that they can — then maybe they’re not quite so crazy after all. ■

Vivien Marx is technology editor at *Nature* and *Nature Methods*.

1. Paget, S. *Lancet* **133**, 571–573 (1889).
2. Fidler, I. J. *Nature Rev. Cancer* **3**, 453–458 (2003).
3. Hanahan, D. & Weinberg, R. A. *Cell* **144**, 646–674 (2011).
4. Sethi, N. & Kang, Y. *Nature Rev. Cancer* **11**, 735–748 (2011).
5. Polyak, K. & Weinberg, R. A. *Nature Rev. Cancer* **9**, 265–273 (2009).
6. Yu, M. *et al.* *Nature* **487**, 510–513 (2012).

CORRECTION

The Technology Feature ‘Two microscopes are better than one’ (*Nature* **492**, 293–297; 2012) wrongly stated that the enzyme APEX is a singlet oxygen generator, it is a peroxidase. Also, Alice Ting was a postdoc in the lab of Roger Tsien, not Mark Ellisman.

CAREERS

TURNING POINT Mentoring young students boosts theoretical physicist's profile **p.139**

EQUALITY Data suggest that white men dominate UK professoriate **p.139**

NATUREJOBS For the latest career listings and advice www.naturejobs.com

F. MAKSYM/SHUTTERSTOCK



COMMUNICATION

Two minutes to impress

With ruthless revision, researchers can compose a punchy 'elevator speech' to sell their science to a neighbour, potential employer or politician.

BY ROBERTA KWOK

In a buzzing exhibition hall at the Moscone Center in San Francisco, California, cell biologist Cecilia Seixas steps in front of a video camera and prepares to sell her science in two minutes or less.

"Hi, my name is Cecilia," says Seixas, a post-doc at the New University of Lisbon's Chronic Diseases Research Center in Portugal. "I am studying how cells assemble an organelle, the cilium, that is like an antenna sticking out of the surface..."

She explains that the cilium acts as a receptor for signals, often needs its parts replaced and can cause diseases when not functioning properly. "Really nice!" says John Fleischman, a science writer at the American Society for Cell Biology (ASCB) in Bethesda, Maryland, who is operating the camera. "And you were 10 seconds short."

Seixas was competing in the ASCB's inaugural Elevator Speech Contest. Brevity is not many scientists' strong suit, but 20 attendees at the society's 2012 annual meeting gamely tried to pitch their research to a hypothetical

layperson in the time it takes to travel several floors in a lift. Although Seixas didn't win, she found the competition a useful exercise. "I usually go a little bit longer in my explanation," she says. "I think the system is complex, so I always give more details."

Giving an effective elevator speech is a crucial skill. Aside from fielding questions about their jobs at cocktail parties, researchers may need to summarize their work briefly while interviewing for a position, asking for money, taking a visiting politician on a lab tour or wooing a potential collaborator at a conference. ►

► Even casual conversations with friends and neighbours can educate about the importance of taxpayer-funded research. “Everybody goes to Thanksgiving dinner and gets seated next to Aunt Kelly, and she goes, ‘And what do you do, dear?’” says Fleischman. “You have to be able to explain it without her tearing up in boredom.”

But that is a struggle for many scientists. Researchers are notorious for using jargon, spouting streams of facts or becoming so bogged down in the details of their experiments that they forget to mention why they are doing them at all. They sometimes explain their research to lay audiences in the same way as they would to a lab colleague — resulting in a lot of glazed eyes and wrinkled brows.

With thoughtful preparation, however, researchers can compress their work into a few key points. Emphasizing everyday relevance, tailoring the speech to the audience and using simple terms and analogies can turn a garbled, dissertation-length discussion into a punchy two-minute pitch.

HONING THE MESSAGE

One of the most common pitfalls is cramming an overwhelming number of details into the speech. “The biggest challenge for scientists is they suffer the curse of too much knowledge,” says Nancy Baron of Santa Barbara, California, who is director of science outreach at COMPASS, an organization that helps scientists to communicate their research. “They’ve got a bunch of things they want to talk about. But really, at the core of it, if someone has just one moment, what do you want to say?”

Baron suggests thinking about four key topics: the problem, why it matters, potential solutions and the benefits of fixing it. To address these questions concisely, scientists should list all the points that they might want to make, and then winnow them down to the most important ones. At one of Baron’s workshops, a scientist who studies jellyfish population trends started by writing a description of his research problem that mentioned how the life stage called a polyp tolerates harsh conditions; the lack of long-term data on population trends; and the complex interactions between factors such as overfishing, eutrophication and aquaculture. But in the end, he kept only his first point: “Humans have degraded marine ecosystems, making them more favourable for jellyfish.”

To articulate the purpose of the work, researchers should step back and consider the bigger picture. For example, particle physicists often say that the goal of their research is to measure some property to high precision. “I have to remind them, ‘No, no, no, that’s not the goal,’” says Kurt Riessmann, head of the office of public information at the Fermi National Accelerator Laboratory (Fermilab) in Batavia, Illinois. “That’s the measurement you want to do. But the goal is that you want to better understand a particle or you want to verify a theory.”

Scientists sometimes forget to explain the

broader benefits of the work, too. “They talk about the details of the mechanism, but they don’t talk about why it matters to other people or how it could improve our lives,” says Nancy Blount, assistant director for society communications at the American Chemical Society in Washington DC. For example, most people won’t care about research on one step in the synthesis of a molecule. But they do care if a scientist tells them that he or she is working on a drug for Alzheimer’s disease, says Blount. Even if practical applications are a long way off, think about how the research might eventually improve health, food, safety, everyday technology or some other aspect of people’s lives.

It is important to tailor the speech to the listener. A good sound bite for a visiting politician might be something like, “This research is going to make this community a focal point in nanotechnology,” says Richard Fox, a partner at research-commercialization organization Astralis Group in Orlando, Florida, and a judge of a 2011 elevator-pitch contest for the US National Science Foundation’s Engineering Research Centers. The head of a conservation organization will want to know how the research helps to preserve biodiversity, whereas a potential employer is looking for information about a scientist’s skill set.

The same goes for conversations about the commercialization potential of the research. An elevator speech to the vice-president “sounds nothing like what you’re going to say to the junior engineer,” says Fox. Engineers are curious about how the technology works, but executives are seeking a high-level conceptual picture that tells them how they will save money or get an edge on the competition.

It is often best to omit caveats and exceptions, or to mention them only at the end. Scientists can be afraid that other researchers will criticize them for being inaccurate, says Riessmann. But most of the time, the exception to the rule is not important unless the study focuses on it, he says. Some scientists even make the mistake of leading with caveats, which undermines their credibility and diminishes the listener’s interest, says Baron.

NO MUMBO-JUMBO

Deciding what to say is only the first step; sorting out how to say it is just as important. Avoiding technical jargon such as gene names is key. Navneeta Pathak, a cell biologist at the University of California, San Diego, and one of the

winners of the ASCB elevator-speech contest, studies cancer metastasis but chose not to use that word in her speech. Instead, she described how tumour cells break away and travel through the blood to other parts of the body.

Some words or phrases that may not seem too technical, such as ‘synthesis’ or ‘mechanism of the reaction’, should be avoided because they sound too vague, says Blount. A better phrase would be something like, “I’m looking for a greener way to make this chemical.”

Elevator speeches to other scientists can be more technical, but should avoid specialist vocabulary. Non-chemists may know what anions and cations are, but they are unlikely to remember the finer points of the Fischer-Tropsch process. And even biologists may not be familiar with a specific protein or pathway.

Analogies and strong images are effective ways of capturing attention. In her winning elevator speech, Pathak compared a cell structure to a drill bit that pokes holes through blood vessels. Analogies can be helpful in explaining phenomena such as the hard-to-conceptualize invisible subatomic world. For example, Riessmann recalls an article in the March 2005 issue of *symmetry*, a magazine co-produced by Fermilab, in which a particle physicist wrote that the theory of supersymmetry “describes a grand dance of particles through the universe, but we can currently see only one partner from each pair”. Every analogy will have shortcomings, but speakers have to compromise to give the audience a memorable image, says Riessmann.

Crafting an elevator speech doesn’t mean composing it word for word. It is best to jot down bullet points and remain flexible enough to think on one’s feet, says Fox. Researchers who do write out a complete oration should not try to memorize and repeat it verbatim, because that can come across as unnatural. It is helpful to practise with family and friends, or to convene a small group of people from different backgrounds to give feedback. Using Twitter is good training in being concise, says Baron.

Energy and body language are important: make eye contact and use natural gestures to convey enthusiasm and draw the listener in, says Blount. Watch for cues, too; if the listener is glazing over, stop and let them ask a question, or bring in details that might pique their interest. Someone talking about work on an Alzheimer’s drug, for example, might mention their grandmother’s experience with the condition to convey how devastating the symptoms are.

Finally, resist the nervous urge to ramble. The purpose of an elevator speech is to get someone interested, not to tell them everything there is to know. As ASCB contest judge Lynne Cassimeris, a cell biologist at Lehigh University in Bethlehem, Pennsylvania, notes: “They’ll ask if they want to know more.” ■

Robert Kwok is a freelance science writer in Burlingame, California.



“The biggest challenge for scientists is they suffer the curse of too much knowledge.”

Nancy Baron

TURNING POINT

Yogesh Joglekar

Yogesh Joglekar, a theoretical physicist at Indiana University–Purdue University Indianapolis (IUPUI), this year became a visiting scholar at the Kavli Institute for Theoretical Physics at the University of California, Santa Barbara.

How did you move from India to Indiana?

After my master's degree in abstract mathematical physics at the Indian Institute of Technology Kanpur, I wanted to do something more concrete. I applied to numerous places for a PhD, but ended up at Indiana University in Bloomington, in part because I had the chance to combine theoretical and applied research by doing condensed-matter physics. I studied quantum Hall conductance, which is found in two-dimensional electron systems in strong magnetic fields.

You did one short and one long postdoc. Why?

I went to the University of Kentucky in Lexington for nine months with a short-term goal — to learn a method for studying the quantum Hall effect, with Ganpathy Murthy. But to expand my skills, I also applied for multi-year postdocs. I moved to Los Alamos National Laboratory in New Mexico to learn about high-temperature superconductivity. It was not academia, but not industry, and I wanted to experience that. But it became obvious that high-impact research could be difficult in a 15-year-old field where advances were incremental — especially at that stage of my career.

How did you carve out your faculty niche?

I came to the IUPUI in December 2005, when graphene research was taking off. I saw an opportunity because electrons in graphene are two-dimensional systems, like those I worked with on the quantum Hall effect.

You have done a short stint as a visitor at Kavli before. How did that help your career?

At Kavli, theorists and experimentalists are given space to work together and exchange ideas. In 2009, I attended a workshop there for three weeks. It was helpful to interact with a variety of experts who could help me to figure out how to run my experiments. The IUPUI has a 13-person physics faculty, whereas other, larger universities can have 20 faculty members in condensed-matter physics alone. Kavli visits are ideal for active researchers at smaller institutions.

How has branching out altered your teaching?

I have been able to find research areas that



are amenable to involving undergraduate and school students. I strongly believe that research should be accessible at every level, to help future scientists to learn problem-solving. In the past few years, I have had 19 peer-reviewed publications — of which six are with undergraduate students, and two with high-school students. My youngest co-author, Jacob Barnett, was 13 years old when we published on theoretical physics in 2011. He was the youngest-ever author in *Physical Review A*, and was featured on the US television news programme *60 Minutes*.

What has been the impact of involving students in your work?

It was a key to my career success — one that I did not appreciate at first. I had not been including my mentoring efforts in grant applications for graphene research because the students were working on different topics. But I kept being told that the broader-impact elements of my proposals were not strong enough. A programme officer pointed out that any research involving younger students counts on grants. I included it in my next application and received a CAREER grant for faculty early-career development from the US National Science Foundation.

Do you encourage colleagues to involve young students, too?

Yes. Research and teaching are two sides of the same coin. If you focus on research accessible to the postdoc or PhD student, you are tapping only a small part of the work that can be done. With MATLAB and other sophisticated software, what a student can do has changed dramatically. For theoretical physicists, it is definitely worth exploring. ■

INTERVIEW BY VIRGINIA GEWIN

GOVERNANCE

A voice for adjunct staff

US universities should let adjunct and contingent faculty members participate in setting policy, argues the American Association of University Professors (AAUP) in a report published on 21 January. *The Inclusion in Governance of Faculty Members Holding Contingent Appointments* says that excluding full- and part-time non-tenure-track teachers, as well as graduate students, postdocs and librarians who teach or do research, leaves them unrepresented and undermines equity among colleagues. It recommends paying contingent staff for time devoted to governance. Gwendolyn Bradley, senior programme officer for the AAUP in Washington DC, says that faculty senates and AAUP union representatives will work with universities to adopt the recommendations.

EQUALITY

Bias in UK recruitment

Just one in five professors at UK higher education institutions (HEIs) is female, although women comprise nearly half of other academic staff, according to a report. Black and minority ethnic (BME) researchers account for only 7% of professors, but 13% of other academics. Four times more men than women applied for professorial posts between 2008 and 2011, says *The Position of Women and BME Staff in Professorial Roles in UK HEIs*, released on 29 January by the University and College Union (UCU) in London and based on data from the UK Higher Education Statistics Agency. In its report, the UCU calls for universities to track recruitment and retention, create and monitor equality targets and investigate why so few women apply to be professors.

UNIVERSITIES

Minority enrolment falls

Minority enrolment in natural-sciences doctoral and master's programmes has fallen by 19% in California, Florida, Texas and Washington following bans on affirmative action in admissions, says a study (L. M. Garces *Am. Educ. Res. J.* <http://doi.org/kb9>; 2013). Liliana Garces, who studies higher education at the George Washington University in Washington DC, examined enrolment data from 118 graduate institutions, including 33 in the target states. "Students may be receiving a message that they're not welcome," she says.

LOCAL 623

Protect yourself.

BY DONALD S. CRANKSHAW

The following was found on the bulletin board of Local 623 of The Fraternal Order of Mad Science Assistants, Test Subjects and Abominations:

KNOW YOUR RIGHTS!

The Executive Leadership Council of your Local 623 has negotiated the following rights and privileges for all members:

You are entitled to a fair wage. Gone are the days when three square meals a week and a cell in the dungeon were considered adequate compensation for the discomfort and social stigma of mutations and experimental surgery. You are entitled to at least minimum wage — minus tips (such as from a grotesquery) — room and board. Remember, any room you are locked into is not considered in this calculation, nor is raw meat if it is not fresh.

You are not required to take part in any experiment with a lower than 43% survival rate without adequate hazard pay. Although risking life and limb is part and parcel for a career in the Mad Sciences, you should expect to be rewarded for any higher-than-average risk. Do not allow your employer to convince you that the cut-off is 40%. That number was negotiated upwards last year, thanks to your hard-working Local 623.

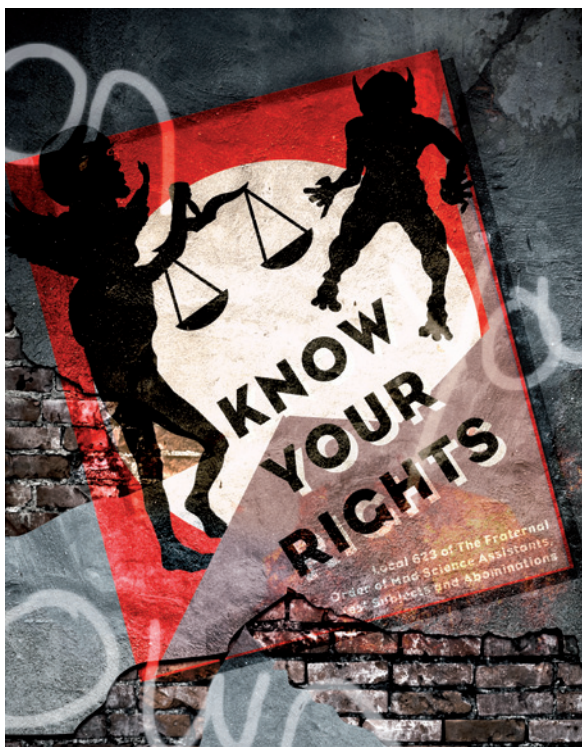
If you are horribly disfigured by an experiment, you are entitled to compensation. Accidents, and absurdly unethical experiments, happen. When they do, you could pursue expensive, and unacceptably public, litigation, which we cannot in good conscience support, or you can choose one of the generous compensation packages your Local 623 has negotiated for you. You are entitled to either enhanced physical or cognitive abilities, experimental corrective surgery (up to and including a brain transplant) or a life mate as horribly disfigured as you are.

You are not required to participate in any time-travel experiment with a greater than 30% chance of a catastrophic paradox. This includes the standard grandfather, grandmother and great aunt paradoxes, as well

as the less common chicken-egg and green wallaby paradoxes. You may still be required to kill

Hitler or Stalin, although to the best of our knowledge, doing so has never resulted in a stable timeline.

You have a right to a workplace free from discrimination on the basis of race, species, current or former sex or orientation thereof, religion, politics, disfigurement, natural, unnatural, supernatural or subnatural origin, current or former deceased status, old age, regressed age, immortality, disability or



super-ability. Life is difficult enough when you are a fiendish conglomeration of half-a-dozen human and animal corpses brought back to an unholy mockery of life. You should not also have to worry about being passed over for advancement or hazardous (but well-compensated) experimentation in favour of a more attractive colleague, or one with a better origin story, if you have an equal chance of success and/or survival. If you feel that you have been discriminated against on any basis, you are entitled to a hearing before the Mad Science Advisory Board Discrimination Subpanel.

You have the right to a workplace free from harassment. Although it is expected that your employer will want to play God with your body and sanity, that does not give him (or her) the right to demand sexual, sadistic

or otherwise indecent favours, even if she (or he) offers remuneration, advancement, surgery or repairs, transformation, mutation or transplantation in return. He (or she) is likewise prohibited from performing any transformation, mutation, transplantation, programming or conditioning designed to induce said favours. If you feel that you have been harassed, you are entitled to a hearing before the Mad Science Advisory Board Sexual, Sadistic and Indecent Subpanel. Leather outfits are *not* provided for the hearing. Please bring your own.

If you are required to work more than 57 hours a week, you are entitled to overtime equal to twice your basic pay. Given the complexities of a live-in job, requiring long sessions on the operating table and tedious hours of testing, not to mention the effects of time dilation and compression, it can sometimes be difficult to determine how many hours you work each week, or even what constitutes work, or a week. For this reason, we offer a convenient online calculator into which you can enter your hours of work, surgery, captivity, testing and sleep, as well as the rate of time dilation and duration of any time travel, to determine if you are owed overtime.

You are not required to participate in any world domination and/or destruction plan unless it has been approved by the Mad Science Advisory Board World Domination and Destruction Subpanel. We at Local 623 realize that many of you will have qualms about letting your employer run the world, much less destroy it, or even make it uninhabitable for your non-mutant friends and relatives. Therefore, you have a right to conscientious objection and refusal to participate in such plans unless they have been approved by the subpanel as having no more than a 13% chance of success. In the unlikely event that such a plan does succeed ...

The rest of the poster was burned away. Carved into the corkboard below it was the following:

YOU ARE ON YOUR OWN ■

Donald S. Crankshaw has a PhD in electrical engineering from the Massachusetts Institute of Technology, and has published stories in *Black Gate* and *Daily Science Fiction*. Read more at www.donaldsrankshaw.com.

JACEY

Looking from both sides

ARISING FROM J. A. Scholl, A. L. Koh, & J. A. Dionne *Nature* **483**, 421–427 (2012)

The size-dependent properties of a nanoscale object can be studied in two ways. In the top-down approach the nanoscale object is made smaller and smaller. In the bottom-up approach one starts from the smallest possible size—sometimes an atom. Scholl *et al.*¹ studied the electronic properties of silver particles using the top-down approach¹. However, experimental^{2–4} and theoretical^{5–8} results are available from several bottom-up approaches and these results do not support the results of ref. 1.

Scholl *et al.*¹ deposited silver particles on carbon substrates suitable for electron microscopy, and measured the size dependence of the surface plasmon. This collective electronic resonance is a powerful optical antenna, which has been used for the non-fading colouring of church windows⁹ for centuries. Figure 1 shows the data of ref. 1, but also included are results from four earlier publications^{2–5}, which have not been cited by ref. 1; in fact, Scholl *et al.*¹ have overlooked nearly 30 years of cluster science^{2–14}. The theoretical papers^{5–8} support the experimental results^{2–4}. Plasmon energies are plotted in Fig. 1 as a function of $1/D$. Here D is a nominal particle diameter, which is defined² as $D = 2r_s N^{1/3}$, where N is the number of atoms in a particle, and $r_s = 1.6$ nm is the electronic density parameter of bulk silver. The parameter $1/D$ allows a size evolution to be plotted from the bulk ($1/D = 0$) to the molecule ($N \leq 8$).

All data show a blue shift, which is caused^{1–9} by the size-dependent interplay of the delocalized 5s conduction electrons of silver with its more localized 4d electrons. The data from well defined measurements in vacuum² or in weakly interacting rare-gas matrices^{3,4} are in agreement with theory^{5–8} and give a consistent picture if one takes the experimental differences into account (see Methods). The data of ref. 1 overlap with those of refs 4 and 5 for large particles ($N > 4,000$), but show a stronger blue shift and large oscillations for smaller sizes.

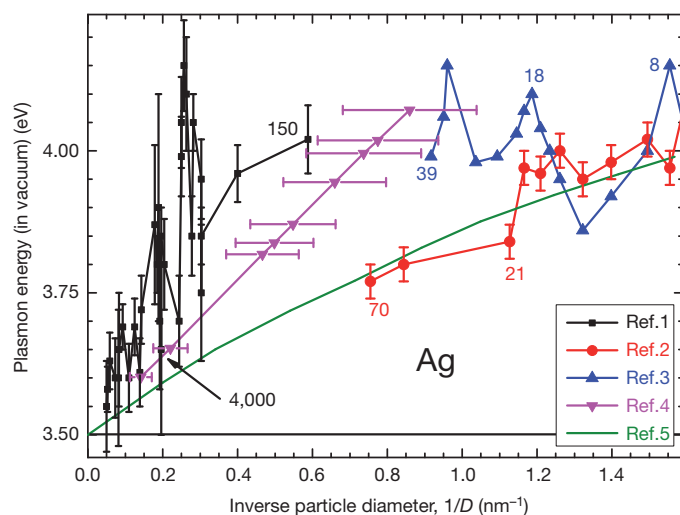


Figure 1 | Surface plasmon resonance of silver particles in vacuum. The plasmon energy is plotted against the inverse particle diameter $1/D$. The dipolar bulk limit (Mie plasmon⁹) is at 3.5 eV. The data of refs 1, 3 and 4 have been scaled to obtain the resonance energies in vacuum (see Methods). The horizontal error bars on the data of ref. 4 give the widths of the size distributions of their Ag particles. For ref. 1, this width is smaller than their data points. The average number N of atoms in a particle is indicated; for $N \leq 39$ this number is exactly known. The data of ref. 1 show a larger blue shift as well as oscillations not reported by refs 4 and 5.

One explanation for these deviations could be that the particles studied by ref. 1 are influenced by interactions with the underlying surface and residual ligand molecules. Scholl *et al.*¹ admit some interaction that is due to the influence of the carbon substrate. Their inhomogeneous situation (the particles are in a vacuum, but sit on a carbon substrate and probably have ligand molecules attached) might also be responsible for the overlarge width^{4–6,9} of their plasmon peaks.

Both the small and large size limit should be considered for a convincing study of a size dependence, that is, one should look at the problem from both sides. What is the small-particle limit of the surface plasmon? It has been shown experimentally¹⁰ and theoretically^{11,12} that at low temperatures small sodium clusters show molecule-like electronic spectra. For example, a cluster containing nine atoms can be viewed at low temperatures as a nine-atom molecular entity, characterized by distinct geometrical isomers^{10–12}. At high temperatures the cluster essentially ‘melts’, and fast interconversion between a large number of structural forms leads to a coalesced broadened plasmon-like absorption feature^{10,12}. These observations suggest that to understand the evolution of quantum plasmon effects better, it will be of interest to explore in detail the temperature dependence of the optical spectra of small Ag clusters^{7,13}.

Methods

The dipolar plasmon resonance of bulk silver^{2,5,6,9} occurs at 3.5 eV. For silver particles embedded in a solid argon matrix this shifts^{3,4} to 3.21 eV. Given that the Ag dielectric function is nearly linear between 3 eV and 4 eV, the data obtained in argon can simply be shifted by 0.29 eV to obtain the corresponding resonance energies in vacuum^{2,3,6} (see Fig. 1). The data transformation from the experimental to the vacuum values is much more involved for ref. 1. Some problems that might influence this transformation include that their larger particles might not be completely spherical, compensating for the image potential of the plasmon, the possible presence of impurities, and so on. None of these problems is easy to solve, so I also simply shifted their data so that their experimental bulk limit aligns with the vacuum value of the Mie plasmon. The clusters of ref. 2 are positively charged and their distribution of inner energies corresponds to an ‘evaporative ensemble’¹⁰ (for an appreciation of the ‘evaporative ensemble’ concept regarding silver clusters, see ref. 14), that is, they are ‘boiling hot’, whereas the clusters of refs 3 and 4 are neutral and have been measured near 10 K. It is not known how to compensate for these differences, and the original data of ref. 2 are plotted in Fig. 1. These differences might explain some of the discrepancies between the data of refs 2 and 3.

Hellmut Haberland¹

¹Department of Physics and Freiburg Materials Research Center, University of Freiburg, 79104 Freiburg, Germany.
e-mail: haberland@physik.uni-freiburg.de

Received 12 May 2012; accepted 7 December 2012.

- Scholl, J. A., Koh, A. L. & Dionne, J. A. Quantum plasmon resonances of individual metallic nanoparticles. *Nature* **483**, 421–427 (2012).
- Tiggesbäumker, J., Köller, L., Meiwes-Broer, K. H. & Liebsch, A. Blue shift of the Mie plasma frequency in Ag clusters and particles. *Phys. Rev. A* **48**, R1749–R1752 (1993).
- Harbich, W., Federigo, S. & Buttet, J. The optical absorption spectra of small silver clusters ($n=8-39$) embedded in rare gas matrices. *Z. Phys. D* **26**, 138–140 (1993).
- Charlé, K.-P., König, L. & Nepijko, S. Rabin, I. & Schulze, W. The surface plasmon resonance of free and embedded Ag-clusters in the size range $1.5 \text{ nm} < D < 30 \text{ nm}$. *Cryst. Res. Technol.* **33**, 1085–1096 (1998).
- Kasperovich, V. & Kresin, V. V. Ultraviolet absorption spectra of silver and gold nanoclusters. *Phil. Mag.* **78**, 385–396 (1998).
- Lermé, J. Size evolution of the surface plasmon resonance damping in nanoparticles: confinement and dielectric effects. *J. Phys. Chem. C* **115**, 14098–14110 (2011).

BRIEF COMMUNICATIONS ARISING

7. Bonačić-Koutecký, V., Veyret, V. & Mitrić, R. *Ab initio* study of the absorption spectrum of Ag_n ($n=5-8$) clusters. *J. Chem. Phys.* **114**, 10450–10460 (2001).
8. Yabana, K. & Bertsch, G. F. Optical response of small silver clusters. *Phys. Rev. A* **60**, 3809–3814 (1999).
9. Kreibig, U. & Vollmer, M. *Optical Properties of Metal Clusters* (Springer, 1995).
10. Schmidt, M., Ellert, E., Kronmüller, W. & Haberland, H. Temperature dependence of the optical response of sodium cluster ions Na_n^+ with $4 \leq n \leq 16$. *Phys. Rev. B* **59**, 10970–10979 (1999).
11. Bonačić-Koutecký, V. *et al.* *Ab initio* predictions of structural and optical response properties of Na_n^+ clusters: interpretation of depletion spectra at low temperature. *J. Chem. Phys.* **104**, 1427–1440 (1996).
12. Moseler, M., Hakkinen, H. & Landman, U. Photoabsorption spectra of Na_n^+ clusters: thermal line-broadening mechanisms. *Phys. Rev. Lett.* **87**, 053401 (2001).
13. Federmann, F., Hoffmann, K., Quaas, N. & Toennies, J.-P. Spectroscopy of extremely cold silver clusters in helium droplets. *Eur. Phys. J. D* **9**, 11–14 (1999).
14. Schmidt, M., Cahuzac, Ph, Bréchnac, C. & Cheng, H.-P. The stability of free and oxidized silver clusters. *J. Chem. Phys.* **118**, 10956–10962 (2003).

Competing Financial Interests Declared none.

doi:10.1038/nature11886